

Form and flow of the Devon Island Ice Cap, Canadian Arctic

J. A. Dowdeswell, T. J. Benham, and M. R. Gorman

Scott Polar Research Institute, University of Cambridge, Cambridge, UK

D. Burgess and M. J. Sharp

Department of Earth and Atmospheric Sciences, University of Alberta, Edmonton, Alberta, Canada

Received 15 September 2003; revised 15 January 2004; accepted 29 January 2004; published 10 April 2004.

[1] In this study, 3370 km of 100 MHz ice-penetrating radar data were acquired from Devon Ice Cap, Arctic Canada. Bed returns were obtained from >90% of flight tracks. Mean crossing point errors in ice surface elevation and ice thickness were 7–8 m. Digital elevation models of ice cap surface and bed elevation, and ice thickness, were produced and can be used as boundary conditions in numerical modeling. Devon Ice Cap, including 1960 km² of contiguous stagnant ice to its west, is 14,010 km². The ice cap proper is 12,050 km². Its largest drainage basin is 2630 km². The ice cap crest has a maximum measured elevation of 1921 m. Maximum recorded ice thickness is 880 m. Ice cap volume is 3980 km³ (about 10 mm sea level equivalent). The bed, 8% of which lies below sea level, is an upland plateau dissected by steep-sided valleys that control the locations of the major outlet glaciers which dominate ice cap drainage. About 73 km, 4%, of the ice cap margin ends in tidewater. The margin is not floating. Icebergs of <100 m were observed offshore. Only a single outlet glacier showed signs of past surge activity. All major outlet glaciers along the eastern ice cap margin have retreated 1–3 km since 1960. Synthetic aperture radar-interferometric velocity structure shows slow, undifferentiated flow predominating in the west and center, with fast-flowing outlet glaciers and intervening slow-flowing ridges typical elsewhere. Outlet glacier velocities are 7–10 times higher than in areas of undifferentiated flow. This velocity structure, of fast-flowing units within slower-flowing ice, appears typical of many large (10³ km²)

Arctic ice caps. *INDEX TERMS*: 1827 Hydrology: Glaciology (1863); 1824 Hydrology: Geomorphology (1625); 6969 Radio Science: Remote sensing; 9315 Information Related to Geographic Region: Arctic region; *KEYWORDS*: glaciology, radio-echo sounding, Arctic

Citation: Dowdeswell, J. A., T. J. Benham, M. R. Gorman, D. Burgess, and M. J. Sharp (2004), Form and flow of the Devon Island Ice Cap, Canadian Arctic, *J. Geophys. Res.*, 109, F02002, doi:10.1029/2003JF000095.

1. Introduction

[2] The ice caps and glaciers of the Arctic islands make up about 45% of the 540,000 km² or so of ice outside Antarctica and Greenland, forming a significant area and volume fraction of the world's ice [Dyurgerov and Meier, 1997a, 1997b; Dowdeswell *et al.*, 1997; Dowdeswell and Hagen, 2004; Dowdeswell, 1995]. Over 151,000 km² of this ice is located in the Canadian Arctic islands [Andrews, 2002; Koerner, 2002]. The distribution of these ice masses within the Canadian Arctic archipelago is a function of the regional climate and climate gradients, together with the large-scale topography of the area. Major ice caps are present on the mountainous eastern sides of Ellesmere, Devon, and Baffin Islands (Figure 1), associated with a predominant moisture source from the southeast [Koerner, 1979]. The largest ice caps in the Canadian Arctic, and indeed in the Arctic as a whole, include the Devon Ice Cap

(~14,000 km²) on Devon Island and the Agassiz Ice Cap (~17,300 km²) on Ellesmere Island (Figure 1).

[3] Deep ice cores, collected from ice caps on Devon, Ellesmere, and Baffin Islands, have been used to reconstruct the climate history of the eastern Canadian Arctic [e.g., Koerner, 1977a, 1997; Koerner and Fisher, 1990; Fisher *et al.*, 1998], and the mass balance of a number of glaciers and ice caps has been investigated systematically over the past 40 years or so [e.g., Koerner, 2002]. However, numerical modeling of Canadian Arctic ice caps, and thus predictions of their likely responses to future and past climate changes, has been largely precluded because very little information is available on their three-dimensional morphology; this applies particularly to model boundary conditions of ice thickness and the topography of the underlying bedrock [cf. Koerner, 1977b].

[4] In this paper we present detailed observations of the form and flow of the Devon Ice Cap (Figure 1), derived mainly from airborne 100 MHz ice-penetrating radar survey and ancillary satellite data. This ice cap was selected for investigation because of the existence of evidence on its

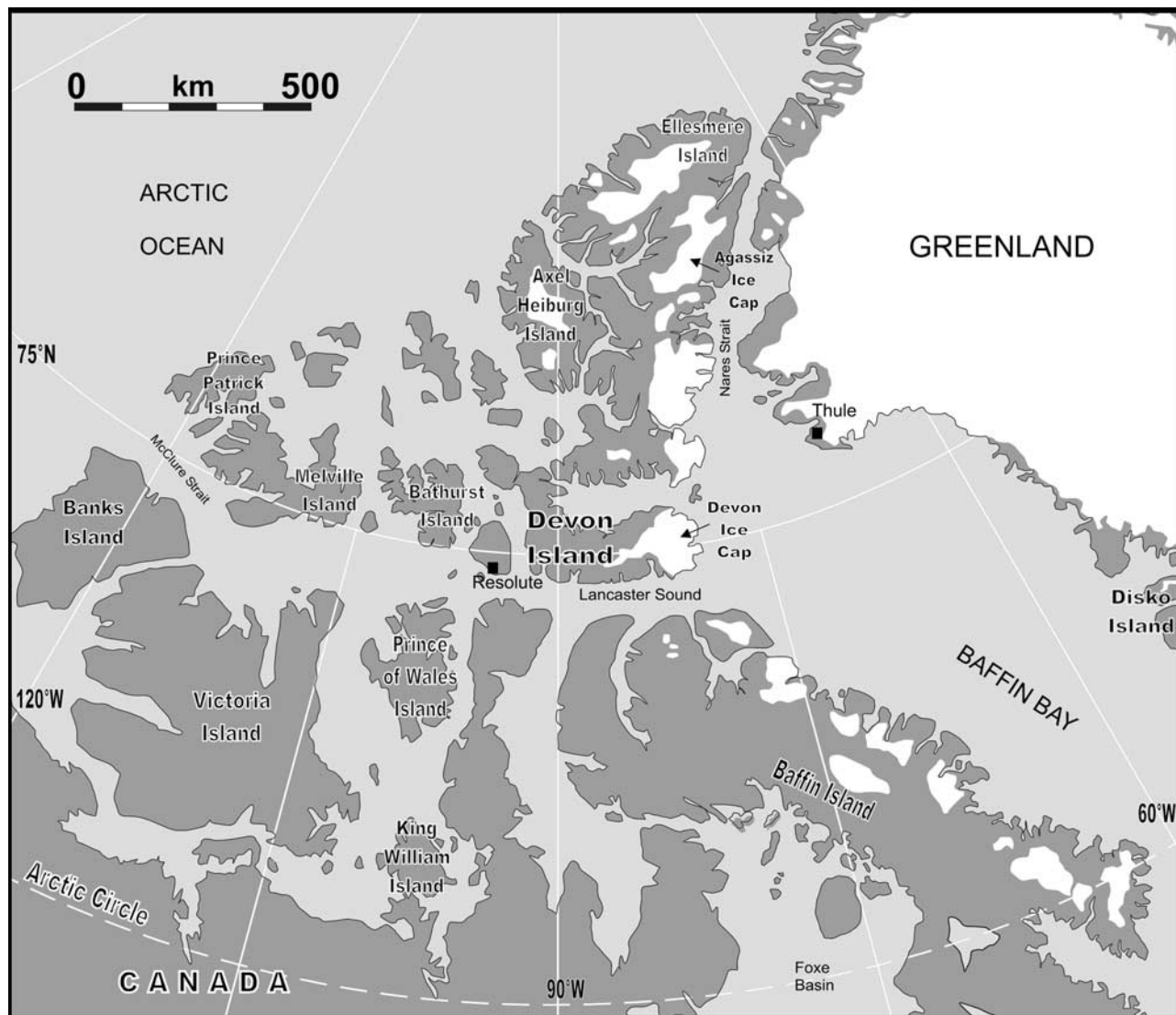


Figure 1. Map of the Canadian Arctic islands, with the Devon Ice Cap and other ice masses in northern Canada and Greenland shown in white.

climate and mass balance history [e.g., Koerner, 1977a, 2002] and because of its relatively large size but simple surface form. In a broader environmental context, general circulation models (GCMs) predict that the Arctic will warm preferentially over the next hundred years or so relative to lower latitudes, thus making the changing form and flow of Arctic glaciers and ice caps important to future projections of global sea level in a warming world [e.g., Cattle and Crossley, 1995].

2. Methods

2.1. Airborne Radar Investigations

[5] Our airborne radar studies of the ice thickness of the Devon Ice Cap used a 100 MHz system. The radar instrument was the same as that fabricated by M. R. Gorman and used previously in our radar investigations of the ice caps on Russian Severnaya Zemlya [Dowdeswell *et al.*, 2002]. The specifications of the radar system are given in Table 1. The antennae were two half-wave dipoles mounted beneath

the aircraft wings, with one for transmitting and the second for receiving. Antenna gain was 8 dB (one way). A digital data acquisition system recorded data, employing a fast digitizer to record complete waveforms, allowing the recovery of absolute power levels and power reflection coefficients. An example of a digital radar record across the Devon Ice Cap is given in Figure 2.

[6] The program of airborne radio echo sounding on the Devon Ice Cap took place between 4 April and 14 April 2000. Data acquisition well before the beginning of the melt season insured that there was no increase in signal absorption associated with summer meltwater in the snowpack [Smith and Evans, 1972]. Scientific flying was undertaken from a de Havilland Twin Otter fixed-wing aircraft, operated from Resolute Bay on Cornwallis Island with refueling at Grise Fjord on Ellesmere Island during some missions (Figure 1). The flights were at a nominal air speed of ~ 230 km hr⁻¹ and were flown at a constant pressure altitude, which ranged from 700 to 1100 m, depending on weather conditions. A series of seven scientific flights of up

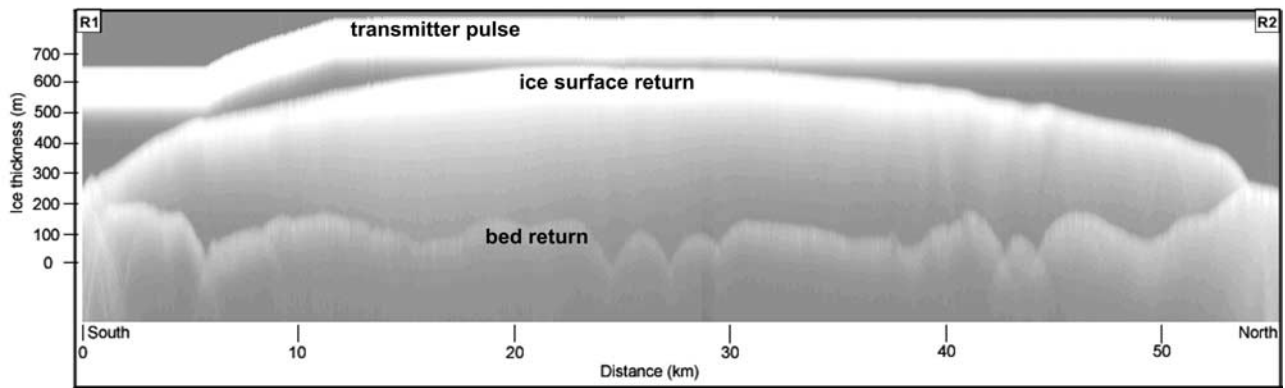


Figure 2. Example of 100 MHz ice-penetrating radar data obtained from the Devon Ice Cap. The y axis has been converted from time delay into ice thickness using a radio wave velocity in ice of $168 \text{ m } \mu\text{s}^{-1}$. The flight line (R1–R2) is located in Figure 3.

to 3 hours duration was undertaken. On each flight a significant amount of time was required for positioning legs over land or water. Dedicated flights were also made for equipment testing after installation and for over-water calibration of the radio echo sounding system. To locate the aircraft position and altitude, GPS positions and pressure altimeter data were recorded.

[7] GPS records of aircraft position were collected and differentially postcorrected using data from base stations at Resolute ($74^{\circ}43'N$, $94^{\circ}59'W$), Thule ($76^{\circ}32'N$, $68^{\circ}47'W$), and on the Devon Ice Cap itself ($75^{\circ}21'N$, $82^{\circ}08'W$) (Figure 1). Differential correction accuracy degrades as the distance between the aircraft and base stations increases. Distances from the Resolute and Thule base stations to the nearest and furthest margins of the Devon Ice Cap are 290–455 km and 315–465 km, respectively. Average errors in navigation are ~ 5 m for horizontal positions and ~ 9 m in the vertical at a 95% level of confidence.

[8] A map of the flight lines over the Devon Ice Cap is given in Figure 3. The ice cap was covered by a nominal 10 km spaced grid of flight lines. Several additional lines were also acquired from flow lines down specific outlet glaciers that were unsuitable for coverage by the gridding scheme. A total of 3370 km of radar data were obtained over the Devon Ice Cap.

[9] The digital radar data were analyzed by plotting waveforms in Z-scope mode, in raw data number, differentiated, or start-of-rise-point form. Reference was made to individual A-scope waveforms where necessary. Tracking algorithms for delineating horizons for first surface and bed returns need to locate the start of sustained rises in returned power levels and to identify continuity of the tracked horizon in subsequent waveforms [Cooper, 1987]. While automated tracking of interfaces had some success on relatively smooth horizons, loss of lock meant that the algorithm needed restarting frequently. We found that the optimal means of tracking interfaces was in a semimanual fashion, with the operator tracing along the approximate location of an interface on a Z-scope display and the delineated points being “snapped” to the nearest start of power rise. For suppression of noise in individual waveforms we typically averaged five waveforms (~ 7 m in along-track distance), although in areas of noisier data, it was possible to average greater numbers of waveforms to

better identify reflectors. The interfaces thus tracked could be overlain on the raw mode Z-scope display for assessment. In areas where there was potential for misidentification of interfaces due to off-nadir echoes from subaerial valley walls, Landsat Enhanced Thematic Mapper Plus (ETM+) imagery was overlain by flight position and interface-tracking information to assist identification of echo sources [Benham and Dowdeswell, 2003].

[10] Differentially corrected GPS records provided absolute aircraft altitudes. Aircraft pressure-altimeter measurements were also calibrated over the sea surface adjacent to the ice cap. Where three-dimensional GPS positions were either absent or unreliable, pressure-derived altitude data were used. Ice surface elevations were then derived by subtracting aircraft terrain clearance measured by the radar from the absolute altitude of the aircraft.

[11] Analysis of the differences in measured ice surface elevation and ice thickness at points where flight tracks crossed was used to assess random errors in our measurements. The distribution of these errors was not constant over the ice cap. Larger errors in ice surface elevation were generally distributed around areas of steeper slope or more complicated topography, such as at the steeper margins of the ice cap. The mean difference in ice surface elevation measurements at crossing points was 7.7 m, with 155 of the 165 crossing points located within 20 m of one another.

[12] The largest crossing point errors in the measurements of ice thickness were generally in areas of more complicated bedrock and/or surface topography. Some of these were concentrated in areas of thicker ice southeast of the center of

Table 1. System Parameters of the 100 MHz Radar Used in the Canadian Arctic

Parameter	Value
Center frequency, MHz	100
Transmitter pulse length, μs	0.35 or 1.1
Transmitter peak pulse power, W	250 or 1000
Transmitter pulse rate, kHz	10
Receiver bandwidth, MHz	30 or 3
Receiver type	successive detection log amplifier
Receiver noise, dB	6
System performance (excluding antenna gain), dB	
Short pulse	150
Long pulse	160

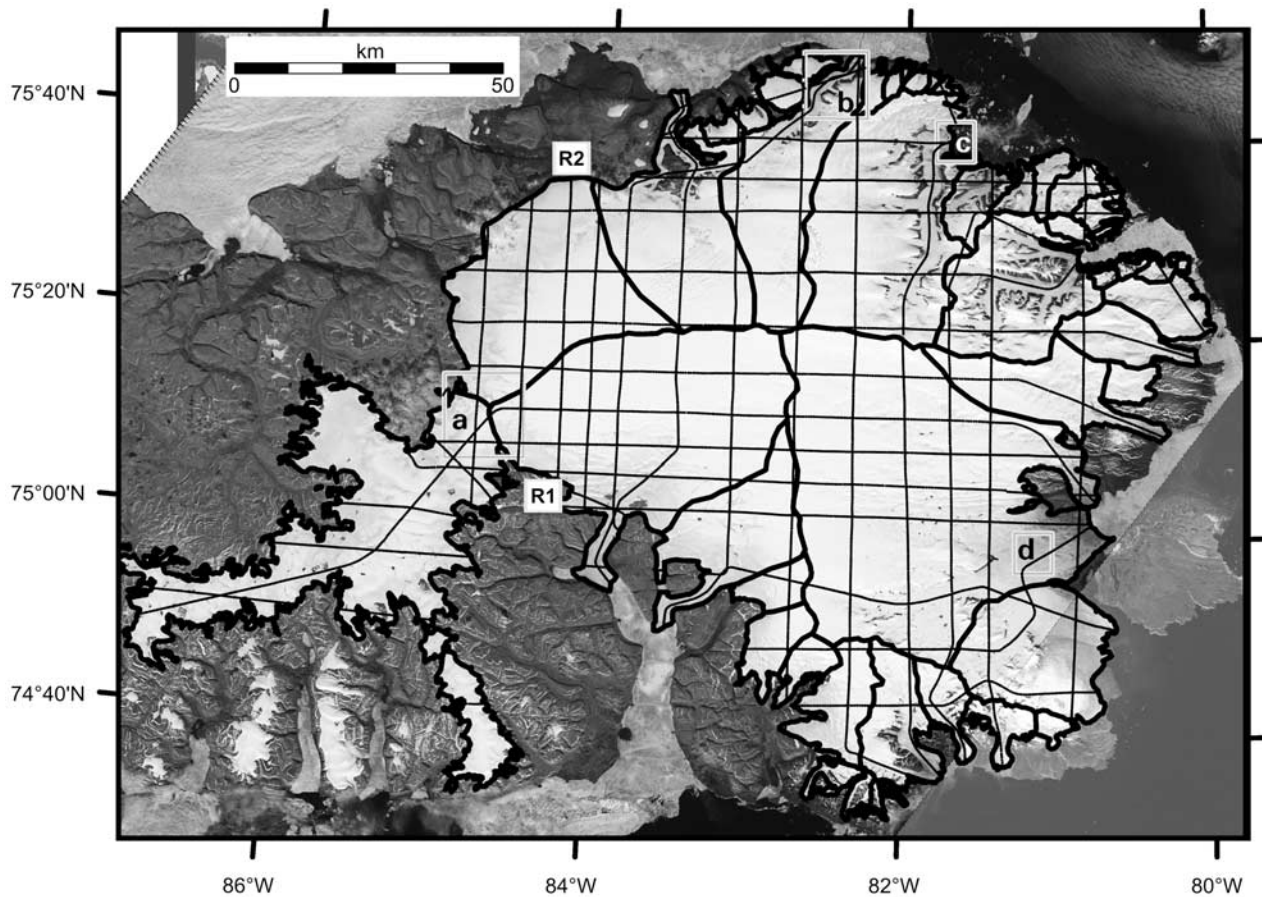


Figure 3. Landsat Enhanced Thematic Mapper Plus (ETM+) image mozaic of the Devon Ice Cap, showing the boundaries of major ice cap drainage basins (thick black lines) and the grid of flight lines from which airborne radio echo sounding data was obtained (thin black lines). The radar transect shown in Figure 2 (R1–R2) is located. The boxes labeled a–d locate the four subscenes making up Figure 4.

the ice cap, where radio echo returns from the ice cap bed were weakest due to greater absorption of electromagnetic energy along a longer two-way path length and to scattering by ice inclusions within firn of the accumulation zone. The mean crossing point error in ice thickness measurements was 7.5 m, with 111 of 116 crossing points located within 20 m.

[13] Our reduced radar measurements of ice surface elevation and ice thickness along flight lines were then interpolated over the whole ice cap to produce digital elevation models (DEMs) for use in, for example, numerical modeling of the Devon Ice Cap. For modeling purposes the DEM grid cell size used should be greater than the ice thickness. Given a maximum observed ice thickness of ~900 m, a cell size of 1 km was selected. In line with the practice of the Antarctic BEDMAP project [Lythe *et al.*, 2001], we extracted data at regular intervals along track from each flight line. While the ice surface elevation, as a property that tends to vary smoothly, could be characterized adequately by sampling at regular intervals, the ice thickness and bedrock data exhibited more high-frequency variability. We therefore added a number of additional “points of interest” from visual inspection of Z-scope profiles and included these as data points.

[14] For interpolation of our reduced radar measurements of ice surface elevation and ice thickness over the whole ice

cap we had envisaged using ordinary kriging with prior semivariogram analysis [Isaaks and Srivastava, 1989]. Kriging is an optimal interpolator of irregularly spaced point data. However, we were not able to apply this technique to our satisfaction for the Devon Ice Cap. No single semivariogram model fitted the data adequately, and trial interpolations carried out using kriging and other methods such as splining did not yield results that were consistent with the input point data. Given that the intention was to generate DEMs which characterize the average elevation or thickness in 1 km cells, an inverse distance weighting (IDW) method was chosen.

[15] To address artifacts from the directional effects of the radar survey pattern (Figure 3), we implemented, in line with the BEDMAP approach [Lythe *et al.*, 2001], our own IDW interpolation algorithm using an eight-point directional search for input data points. This method was generally successful in removing the bias toward data points from the nearest flight line, and the use of a block-smoothing approach further reduced such effects. However, for the surface elevation DEM we encountered artifacts in maximum slope calculations which we believed to result from the additional smoothing used. We therefore generated surface elevation DEM values using the ArcInfo TOPOGRIDTOOL facility [Hutchinson, 1993]. This uses a

locally adaptive splining model which enforces hydrological rules. Bed elevation DEM values used in final products were derived from ice surface elevation minus ice thickness values for the same grid cell. This is in keeping with the fact that ice thickness is the primary parameter extracted from radio echo sounding data and that bed elevation is a derived quantity. For the purposes of numerical modeling, grid cells were also defined for 5 km beyond the present ice cap margin from our radar data, allowing ice advance as well as retreat to be reconstructed effectively during modeling work.

[16] It is clear from Landsat ETM+ imagery of the Devon Ice Cap that outlet glaciers constrained within rock walls are an important component of ice cap form and flow (Figure 3). Ignoring such boundaries to flow resulted in ice thickness and bedrock elevation interpolation artifacts. Using Landsat imagery as a backdrop within a geographic information system (GIS), a polygon coverage of rock wall boundaries to ice flow was produced. This was then used to restrict the choice of input points for our interpolation to those relevant to the channelized ice flow and prevented such important topographic features from being removed or subdued in the interpolation.

2.2. Satellite Remote Sensing

2.2.1. Landsat Imagery

[17] Landsat ETM+ digital imagery (Figure 3), with a spatial resolution of 15 m in panchromatic mode [Bindschadler *et al.*, 2001], was used for several purposes during our investigations of the Devon Ice Cap. First, Landsat imagery was used to map the margins of the ice cap after georeferencing to ground control points. Secondly, the qualitative topography of the ice cap surface, including the location of ice divides defining ice cap drainage basins, was derived from digitally enhanced Landsat pixel brightness values [e.g., Martin and Sanderson, 1980; Dowdeswell *et al.*, 1995]. This surface topographic information was used in the planning of aircraft flight lines for radio echo sounding.

[18] Landsat imagery and aerial photography from 1959/1960 were examined for the presence of indicators of surge behavior on both Devon Ice Cap and also, more generally, over the ice masses of Ellesmere and Axel Heiberg Islands [Copland *et al.*, 2003]. A number of ice surface features have been used as indicators of whether or not glaciers and larger ice masses have undergone periodic surge behavior during the residence time of the ice within a given drainage basin. These features include [Meier and Post, 1969] (1) looped medial moraines, formed as fast-flowing, active-phase surge-type glaciers flow past less active or stagnant neighbors and deform the medial moraines between them and preserved over the residence time of ice within the system; (2) potholes on the glacier surface during the quiescent phase; and (3) a heavily crevassed surface indicative of a glacier in the active phase of the surge cycle and often, although not always, associated with rapid terminus advance. These features can be recognized readily on Landsat imagery and aerial photography [e.g., Dowdeswell and Williams, 1997].

2.2.2. Synthetic Aperture Radar (SAR) Interferometry

[19] Few velocity measurements of the Devon Ice Cap have been made; Doake *et al.* [1976] measured a velocity of

2.4 m yr^{-1} near the ice cap crest using radar fading patterns, and Cress and Wyness [1961] recorded winter and summer velocities of 36 and 65 m yr^{-1} , respectively, $\sim 5 \text{ km}$ from the terminus of Sverdrup Glacier, an outlet draining the northwest side of the ice cap. Satellite radar interferometry provides a tool for measuring velocity structure synoptically across whole ice masses. The interferograms produced for the Devon Ice Cap are derived from pairs of ERS-1/2 synthetic aperture radar (SAR) images acquired during the 1996 tandem-mode mission over the southeast and western regions and from 1992 3 day repeat pass data over the northeast quadrant. The phase difference in an interferogram is a result of range change between two satellite passes, where range is affected by both horizontal and vertical ice displacement as well as by the interferometric baseline between passes. The effects of ice surface topography are removed by subtracting a synthetic interferogram generated from an external DEM [Massonet *et al.*, 1993] or by double differencing between two tandem-mode interferometric pairs [Gabriel *et al.*, 1989]. Errors in interferometric baseline estimates can also introduce a quasi-linear phase ramp of several fringes across an image [Joughin *et al.*, 1996]. This ramp has been removed through subpixel coregistration between the slave and master images together with tie points selected over areas of bare land [Zebker *et al.*, 1994], where displacement should be zero.

[20] Interferograms of the Devon Ice Cap were generated using the above methods and corrections. They can be viewed as contour maps of surface displacement in the satellite look direction, with each fringe (i.e., cycle of the color wheel) representing a change of 20 m yr^{-1} . The errors in the velocity estimates, which are dependent on the interferometric baseline and the accuracy of the external DEM, were 0.92, 1.26, and 2.7 m yr^{-1} for the southeast, west, and northeast sectors of the ice cap, respectively. Coherent interferometric fringes were produced over almost the whole ice cap. These data were phase unwrapped and then used to produce ice surface velocities in the look direction of the SAR. Look direction velocities, rather than those in the direction of ice flow, are presented in this study because they are well suited for identifying coherent flow units as well as subtle changes in ice motion over large areas.

3. Results: Ice Cap Morphology, Thickness, and Velocity Structure

3.1. Ice Surface Morphology

[21] The total area of the Devon Ice Cap is $14,010 \text{ km}^2$, measured digitally from Landsat ETM+ imagery. However, the ice-covered area extending westward from the main ice cap is a subsidiary ice body (Figure 3). This ice appears from Landsat imagery to be both dynamically separate from the main ice cap and also likely to be of very low surface gradient (Figure 4a). The entire margin of this subsidiary, 1960 km^2 ice body ends on land; it is referred to informally as the “western Devon Ice Cap” here. Subtracting this from the total ice-covered area yields an area of $12,050 \text{ km}^2$ for the Devon Ice Cap proper.

[22] The surface of the Devon Ice Cap is relatively simple and dome-like in shape. A DEM of the ice surface, derived from our airborne radar data, is shown in Figure 5. This ice

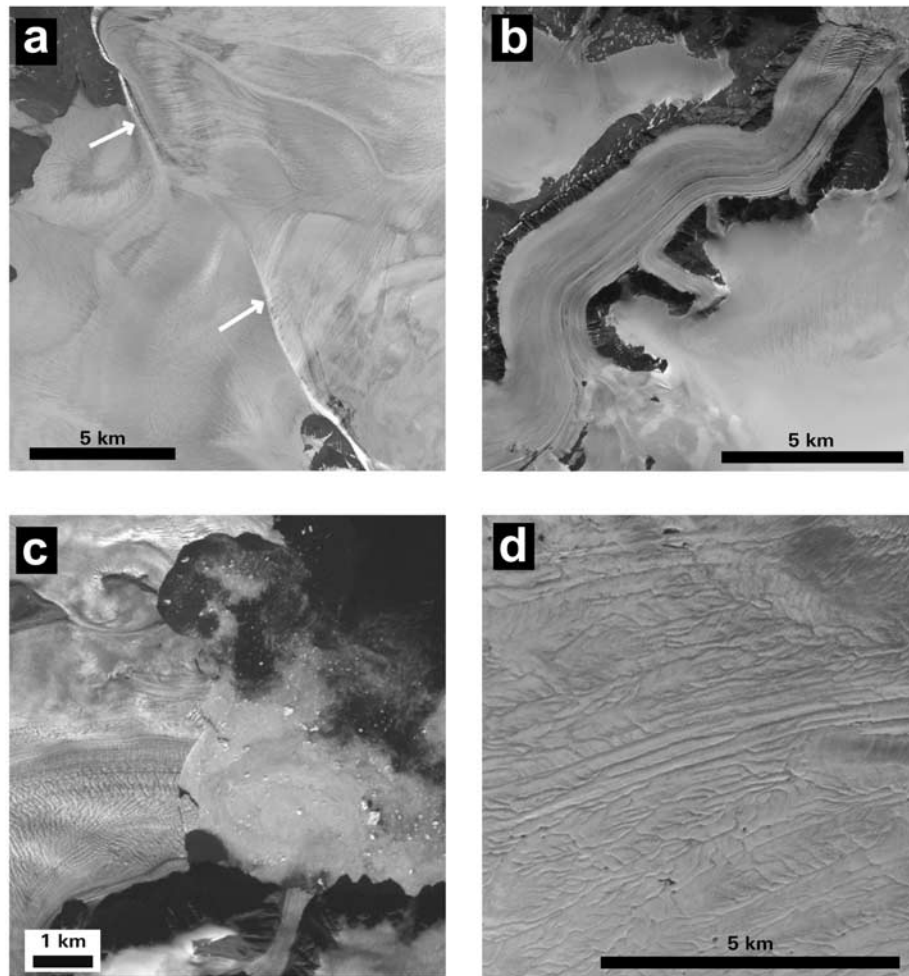


Figure 4. Landsat ETM+ images of parts of the ice cap on Devon Island. Each subscene is located in Figure 3. Glacier names are shown in Figure 8. (a) The well-defined boundary (marked with arrows) between the main Devon Ice Cap to the right and the thin and inactive “western Devon Ice Cap” to the left. (b) Eastern Glacier, an outlet glacier constrained by valley walls and ending in a crevassed tidewater margin. (c) The heavily crevassed tidewater terminus of Belcher Glacier, with several icebergs located within brash ice offshore. (d) A closely spaced network of supraglacial stream channels incised into the surface of the low-gradient lobe on the southeast of the Devon Ice Cap. Note that some streams terminate at moulins, implying that supraglacial meltwater probably reaches the glacier bed.

surface DEM, together with those for ice thickness and bed elevation, are obtainable as auxiliary material to this paper¹. The crest of the ice cap reaches a maximum measured elevation of 1921 m. Ice surface ridges run east, north, and south from the summit, with the eastward being the most pronounced. To the west, the ice cap surface has a very simple form, sloping down gently to terminate on land. Mountain ridges rise above the ice surface to the north and south of the crest in particular (Figure 3). The rock ridges form the walls of outlet glaciers that drain the central area of the ice cap. In addition, the area-altitude distribution, or hypsometry, of the ice cap is an important control on snow accumulation and surface melting and is a vital parameter in

mass balance studies [Hagen and Reeh, 2004]. The distribution of ice cap surface elevation with altitude is illustrated in Figure 6a. The area-elevation curve is relatively smooth, with a minor peak at ~ 1000 – 1100 m above sea level.

[23] The Devon Ice Cap is drained by a number of outlet glaciers. Examples include Eastern and Belcher Glaciers (Figures 4b and 4c). These outlet glaciers are constrained by valley walls, with the ice-filled valleys probably being similar in configuration to the series of steep-walled canyons cut into bedrock that are typical of the terrain beyond the ice cap margin. Among the largest of these outlet glaciers, Belcher and Sverdrup Glaciers draining northward into Jones Sound and Cunningham Glacier flowing south into Lancaster Sound are 35, 25, and 20 km long, respectively. The southeastern region of the ice cap is rather different in surface form from the rest of the ice cap margins, being less well constrained by mountain topogra-

¹Auxiliary material is available at <ftp://ftp.agu.org/apend/jf/2003JF000095>.

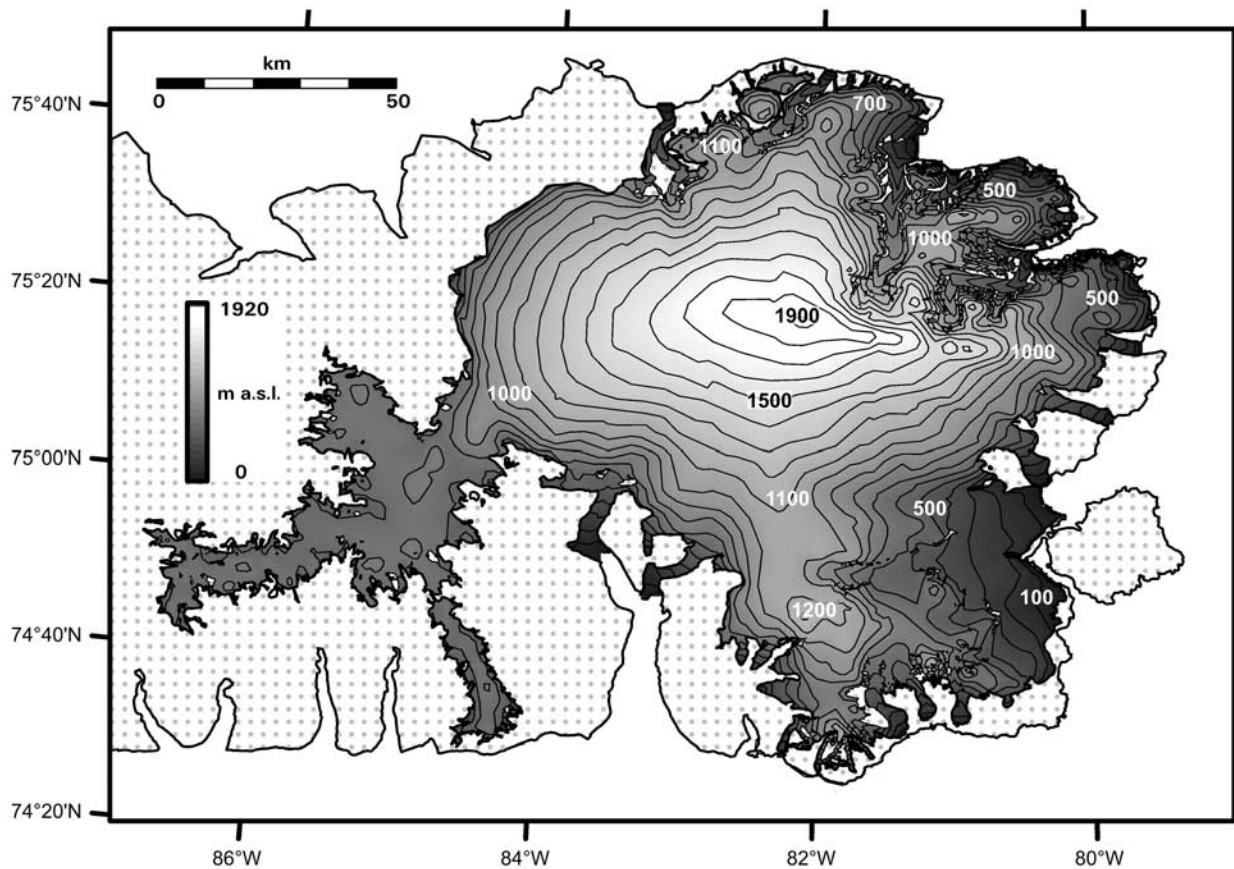


Figure 5. Ice surface elevation map of the Devon Ice Cap (contour interval 100 m).

phy; the marginal 15 km or so of the ice cap flows into marine waters at a gentle gradient here.

[24] The total length of tidewater ice cliffs at the margins of the Devon Ice Cap is 73 km. This makes up $\sim 4\%$ of the ice cap edge, with the remainder ending on land. Over 75% of these ice cliffs are the termini of outlet glaciers that are, individually, less than ~ 2.5 km in width. The longest section of ice cliffs, in the southeast of the ice cap, totals about 18 km in length. Icebergs are produced from the crevassed tidewater margins of the ice cap. The largest icebergs observed on Landsat imagery and during airborne radar work were <100 m in maximum diameter (Figure 4c). There is little evidence that these tidewater ice margins are floating in the form of either significant areas of very low ice surface slope or the production of large tabular icebergs. These criteria have been used previously to infer the presence of floating ice margins in Greenland and the Russian Arctic islands [Higgins, 1991; Dowdeswell *et al.*, 1994; Williams and Dowdeswell, 2001].

3.2. Ice Thickness and Bed Elevations

[25] The thickness of Devon Ice Cap, measured using our 100 MHz radar system, is illustrated as a DEM in Figure 7. The maximum recorded ice thickness is 880 m, slightly southeast of the center of the ice cap at $75^{\circ}10'N$, $81^{\circ}18'W$. From this DEM a volume of 3980 km^3 is calculated for the main Devon Ice Cap. The additional volume of the western Devon Ice Cap is a further 130 km^3 . If the Devon Ice Cap were to melt completely, it would contribute ~ 10 mm to the global sea level.

[26] In general, ice thickness increases most rapidly close to the ice cap margin and then continues to increase more slowly and monotonically toward the central dome. The thickest ice, between ~ 700 and 880 m deep, is located to the northeast and southeast of the geographical center of the ice cap (Figure 7). An extensive area of thin ice, <350 m thick and covering $\sim 400 \text{ km}^2$, occurs in the southeast of the ice cap. This piedmont area is fed by several outlet glaciers, which flow through the mountains to the west. The western Devon Ice Cap, by contrast, forms only a thin carapace of ice over bedrock (Figure 4a), with a maximum recorded thickness of 240 m.

[27] The absolute altitude of the bed of the Devon Ice Cap is presented as a DEM in Figure 8. The ice cap bed hypsometry is also shown in Figure 6b. The vast bulk of the bed of the main ice cap, and all of the smaller ice body to the west, lies above sea level. The bed appears to be an upland plateau, dissected by a series of steep-sided valleys (Figure 8). Mountain summits and ridges break the ice cap surface in the north and south; the Treuter and Cunningham Mountains are most prominent. The subglacial valleys and subaerial valley walls appear to control the locations of the major outlet glaciers draining the Devon Ice Cap. Subglacial valleys also influence the direction of ice flow into the southeastern piedmont lobe.

[28] Only 8% of the ice cap bed lies below present sea level (Figure 6b). This is confined to two types of areas: First, the marginal few kilometers of most outlet glaciers, including their tidewater termini, have beds below sea level;

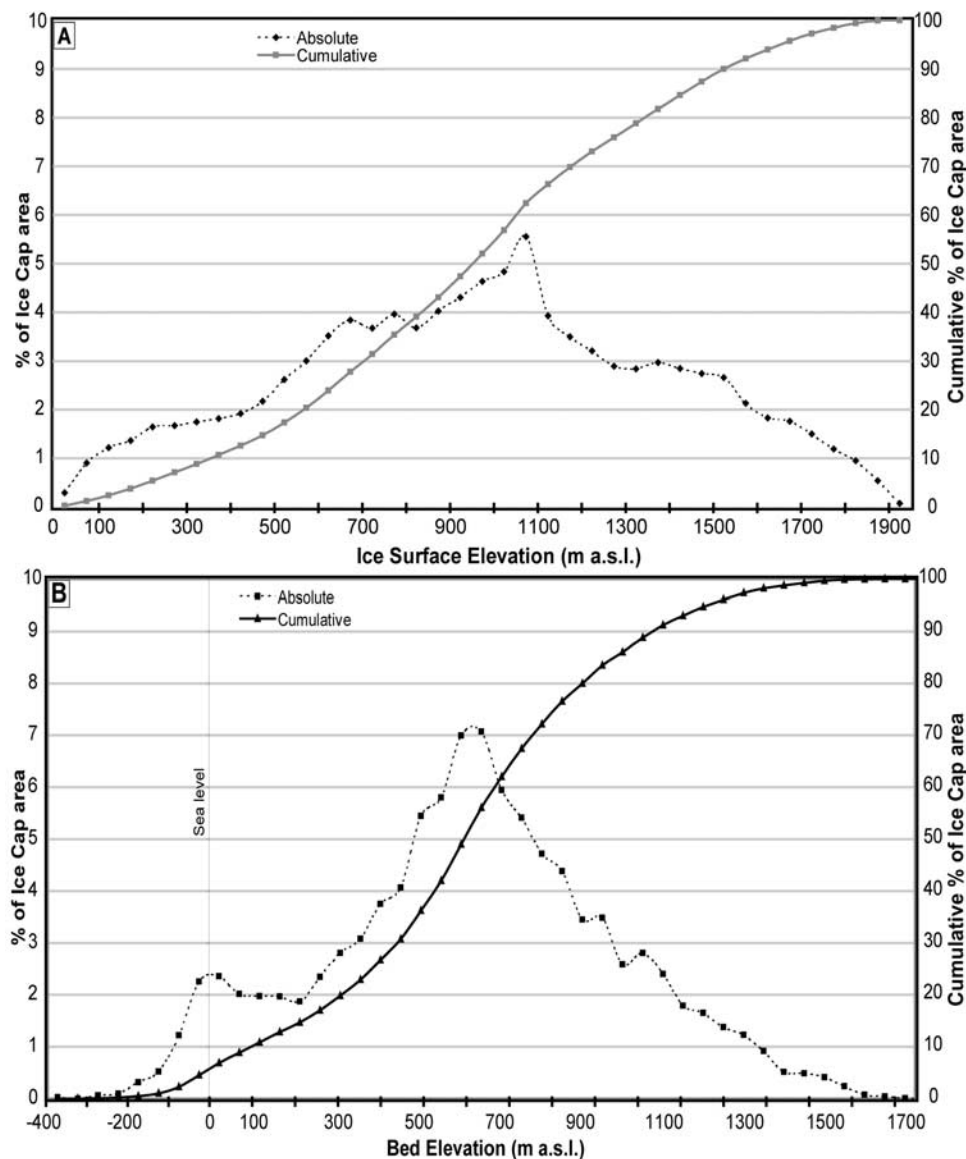


Figure 6. Hypsometry of the 12,050 km² Devon Ice Cap. (a) Ice surface elevation (m). (b) Subglacial bed elevation (m). Hypsometric curves are given for each elevation band and for the cumulative percentage. The 1960 km² western Devon Ice Cap is excluded.

secondly, the piedmont ice cover in the southeast of the ice cap is largely grounded below sea level (Figure 8). Several of the larger outlet glaciers, including Sverdrup and Belcher Glaciers draining northward and the two tidewater glaciers flowing south into Croker Bay, have beds lying several hundred meters below present sea level that extend between 15 and 20 km from the ice margin. It is likely that the bed in these areas is made up of glacier-influenced marine sediments, which would have accumulated at times over the late Quaternary when the Devon Ice Cap was smaller or disappeared, as environmental records from the deep ice core taken close to the ice cap summit and investigations of Holocene sedimentation in Bear Lake adjacent to the northwestern ice cap margin indicate [Koerner, 1977a; Lamoureux *et al.*, 2002].

[29] Radar returns from the bed of the Devon Ice Cap were acquired from $\sim 91\%$ of the flight tracks. The main

areas where bed echoes were absent were in zones of intense surface crevassing, associated particularly with steep icefalls on outlet glaciers, or where bed returns were masked by significant valley sidewall echoes. Some loss of bed reflection may be a result of nonoptimal terrain clearance or aircraft attitude while repositioning with respect to terrain elevation change.

3.3. Velocity Structure From SAR Interferometry

[30] SAR interferometry was used to map the velocity structure of the Devon Ice Cap and, in particular, the extent and distribution of fast-flowing ice (Figure 9). The most notable pattern in the interferogram is the slow and undifferentiated velocities in the west and central region of the ice cap as compared with outlet glaciers and intervening slow-flowing ridges elsewhere (Figures 9 and 10). A number of fast-flowing units identified in SAR interferometry usually

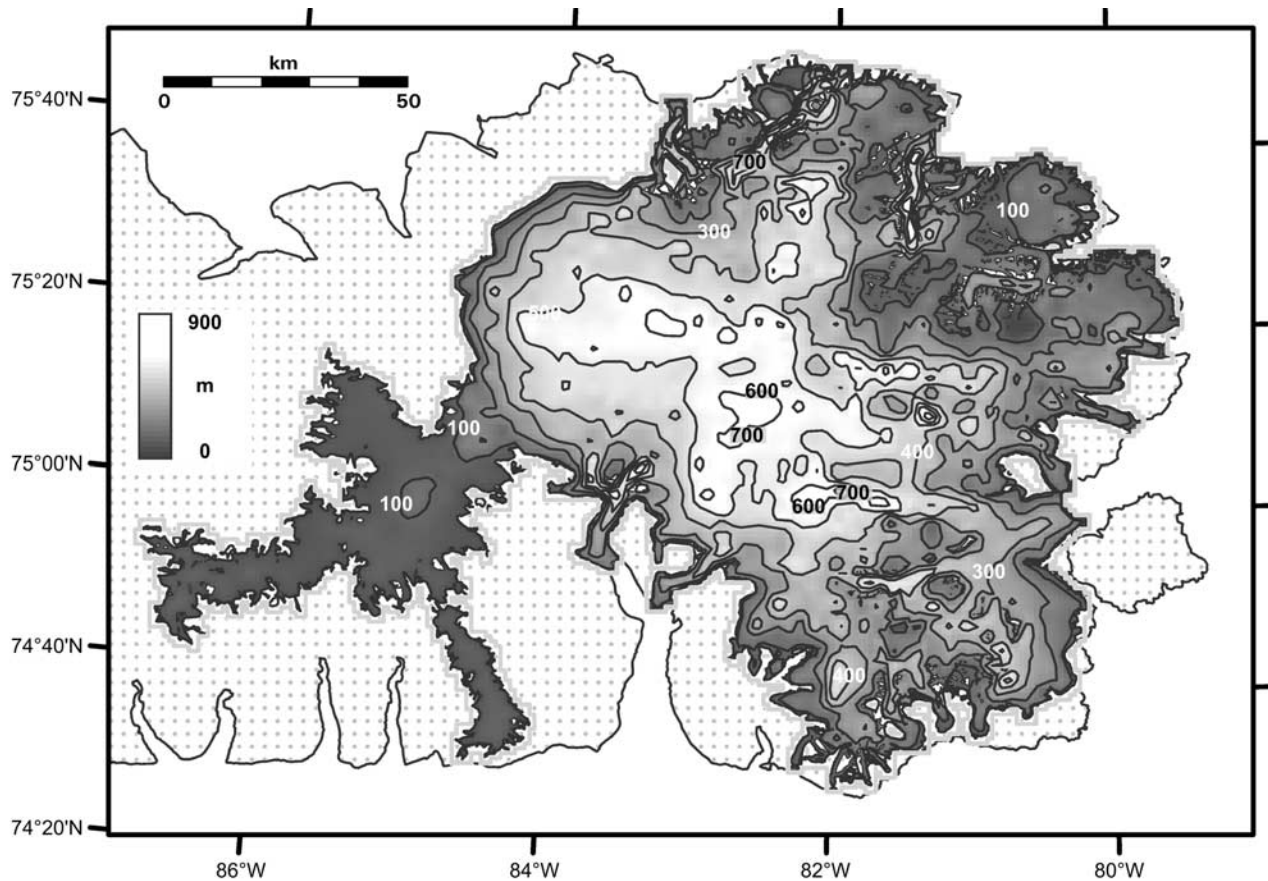


Figure 7. Ice thickness distribution on the Devon Ice Cap (contour interval 100 m).

occupy troughs in the bedrock topography over all or part of their length (Figures 10a and 10b). Surface velocities in these outlet glaciers of the ice cap are typically 7–10 times higher than in adjacent areas of undifferentiated flow.

4. Flow of the Devon Ice Cap

4.1. Inferences From Landsat Imagery

[31] Landsat ETM+ imagery of the Devon Ice Cap shows clearly that ice flow outward from the crest of the ice cap is mainly through outlet glaciers channeled within a series of bedrock-sided valleys (Figure 3). Most of these outlet glaciers end in tidewater (Figures 4b and 4c). Their margins are usually crevassed, with the crevasses generally oriented perpendicularly to ice flow, indicating longitudinal tension. This is typical of the stress regime found close to the unconstrained ice walls of tidewater glaciers [e.g., *Hodgkins and Dowdeswell, 1994*].

[32] Where mountainous terrain is absent (Figure 8), the ice cap surface appears largely smooth on Landsat imagery; the northwest sector of the ice cap is the best example of this form of simple radial flow (Figure 3). By contrast, the piedmont lobes on the southeast side of the ice cap have a very distinctive ice surface morphology developed on a surface of very low gradient. Dense networks of supraglacial stream channels appear almost ubiquitous on Landsat imagery in this area (Figure 4d). Many of these channel systems end abruptly, with meltwater presumably descending to the glacier bed via moulins.

[33] Landsat imagery was also used to examine the drainage basins and outlet glaciers of the Devon Ice Cap for indicators of present or past surge activity. *Copland et al.* [2003] reported that a single outlet glacier of the ice cap, the western branch of Cunningham Glacier (74°34'N, 81°25'W), exhibited extensive surface folding combined with a 2 km retreat between 1959 photographs and 1999 imagery, implying past surge activity. Other outlet glaciers of the ice cap showed no indicators of past surges [*Copland et al., 2003*], according to the criteria of *Meier and Post* [1969]. However, all the major outlet glaciers along the eastern margin of the ice cap have experienced retreat ranging from 1 to 3 km since 1960 (D. Burgess and M. J. Sharp, personal communication, 2003). Given the lack of evidence of ice surface features indicative of past nonsteady flow, such retreat is more likely to be a response to climate change than to past surge activity.

[34] Finally, the major ice divides and drainage basins on the ice cap have been mapped using a combination of the Canadian Digital Elevation Dataset (CDED) DEM, Landsat imagery, SAR interferometry, and bedrock topography (Figure 3). Basins were originally delineated based on the surface topography represented by the CDED DEM using the hydrological modeling tools in ArcView GIS. Placement of the modeled basin boundaries was guided by interpretation of the surface topography evident in the 1999 Landsat 7 ETM+ orthomosaic. Drainage divides were refined further by comparing the drainage basin boundaries with the source regions of major outlet glaciers

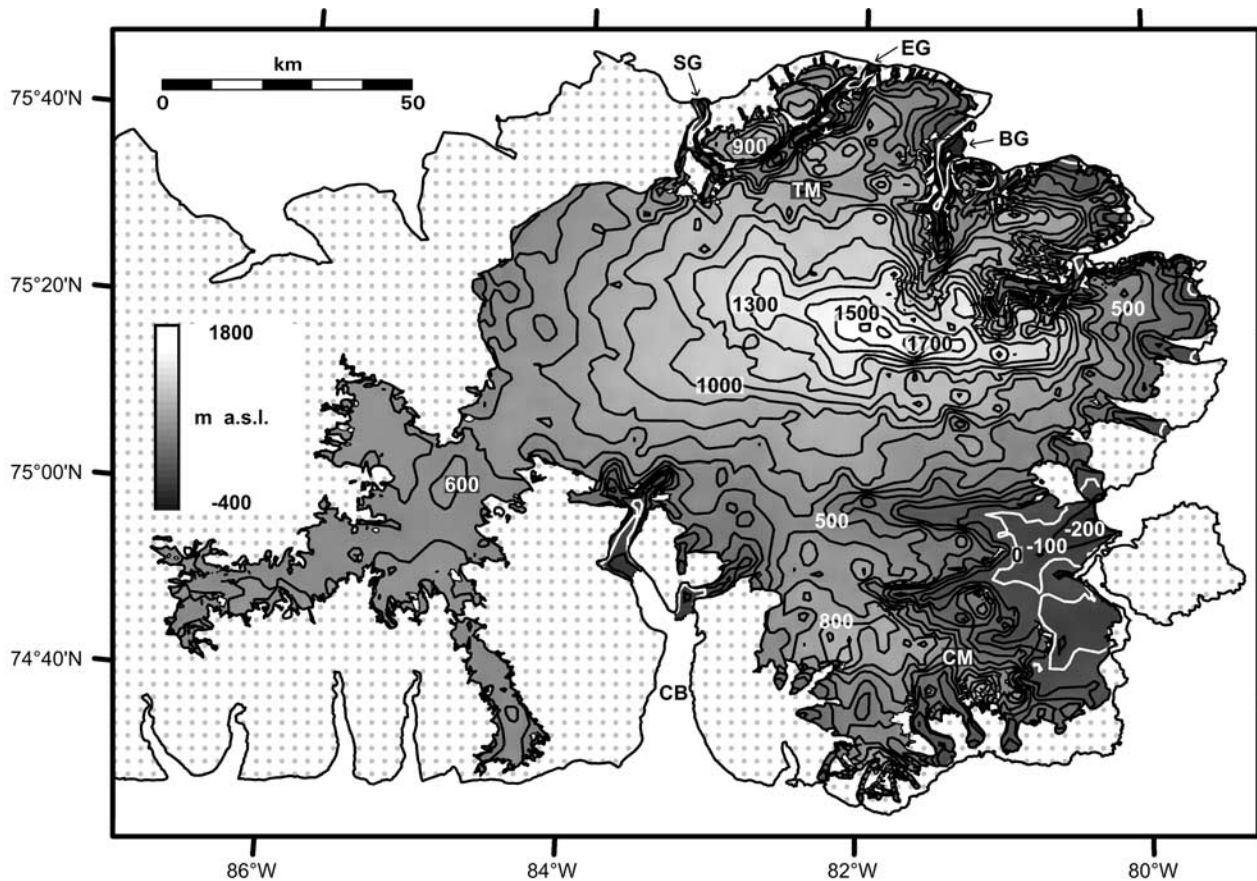


Figure 8. Bed elevation map of the Devon Ice Cap (contour interval 100 m). Note that the zero, or sea level, contour is white. SG, Sverdrup Glacier; EG, Eastern Glacier; BG, Belcher Glacier; CB, Croker Bay; CM, Cunningham Mountains; TM, Treuter Mountains.

and ice streams. Source regions were effectively highlighted by the pattern of accelerated ice flow in the SAR interferometry throughout the interior regions, where surface topography is subtle (Figure 9). Finally, the bedrock topography derived in this study was used to identify divides based on subglacial ridges (not evident at the surface) to mark the point of flow divergence throughout regions of uniform sheet flow. The largest drainage basin is 2630 km² in area and is drained primarily by the two large outlet glaciers in the southeast sector of the ice cap (Figure 3).

4.2. Pattern of Ice Flow

[35] The velocity pattern derived from SAR interferometric analysis of the Devon Ice Cap, of slow and undifferentiated flow in the west and center and relatively fast-flowing outlet glaciers separated by slower-flowing ice, is linked to several factors: (1) the relatively smooth bed topography of the west side of the ice cap as compared to the more mountainous and much more dissected bedrock topography elsewhere (Figure 8) and (2) the relative lack of precipitation and hence mass turnover on the northwestern side of the ice cap [Koerner, 1979]. This flow pattern appears typical of many large (10³ km²) Arctic ice caps, which are also differentiated into fast- and slow-flowing elements, for example, Academy of Sciences Ice Cap, Severnaya Zemlya, and Austfonna, Svalbard [Dowdeswell *et al.*,

1999, 2002]. In addition, SAR interferometry of the Academy of Sciences Ice Cap also shows a region of undifferentiated flow in the precipitation shadow of the ice cap crest [Dowdeswell *et al.*, 2002].

[36] Fast-flowing features in the velocity structure of the Devon Ice Cap are usually associated with troughs in the bedrock beneath the ice (Figures 10a and 10b). This is consistent with the likely thermal structure of the ice cap, where basal melting will take place first beneath thick ice located in bedrock troughs [e.g., MacAyeal, 1993]. Analysis of the subglacial topography in regions near the onset of fast flow at the heads of outlet glaciers indicates that the transition from slow to fast glacier flow tends to occur in two different bedrock-topographic settings. The first type of transition zone is characterized by the presence of a bedrock step at the location where marked acceleration occurs. An example is provided by the two glaciers that drain from the southwest region of the ice cap into Croker Bay (Figure 10a). Ice flow from ~15 km up-glacier of the area where rapid flow begins is strongly convergent, and the ice surface slope increases from ~1° to ~7° over a bedrock step. These characteristics are similar to those of a number of outlet glaciers that drain the East Antarctic Ice Sheet [McIntyre, 1985], where a step in the subglacial topography is associated with the initiation of fast flow and also provides a “pinning point” that appears to restrict the propagation of fast flow farther inland.

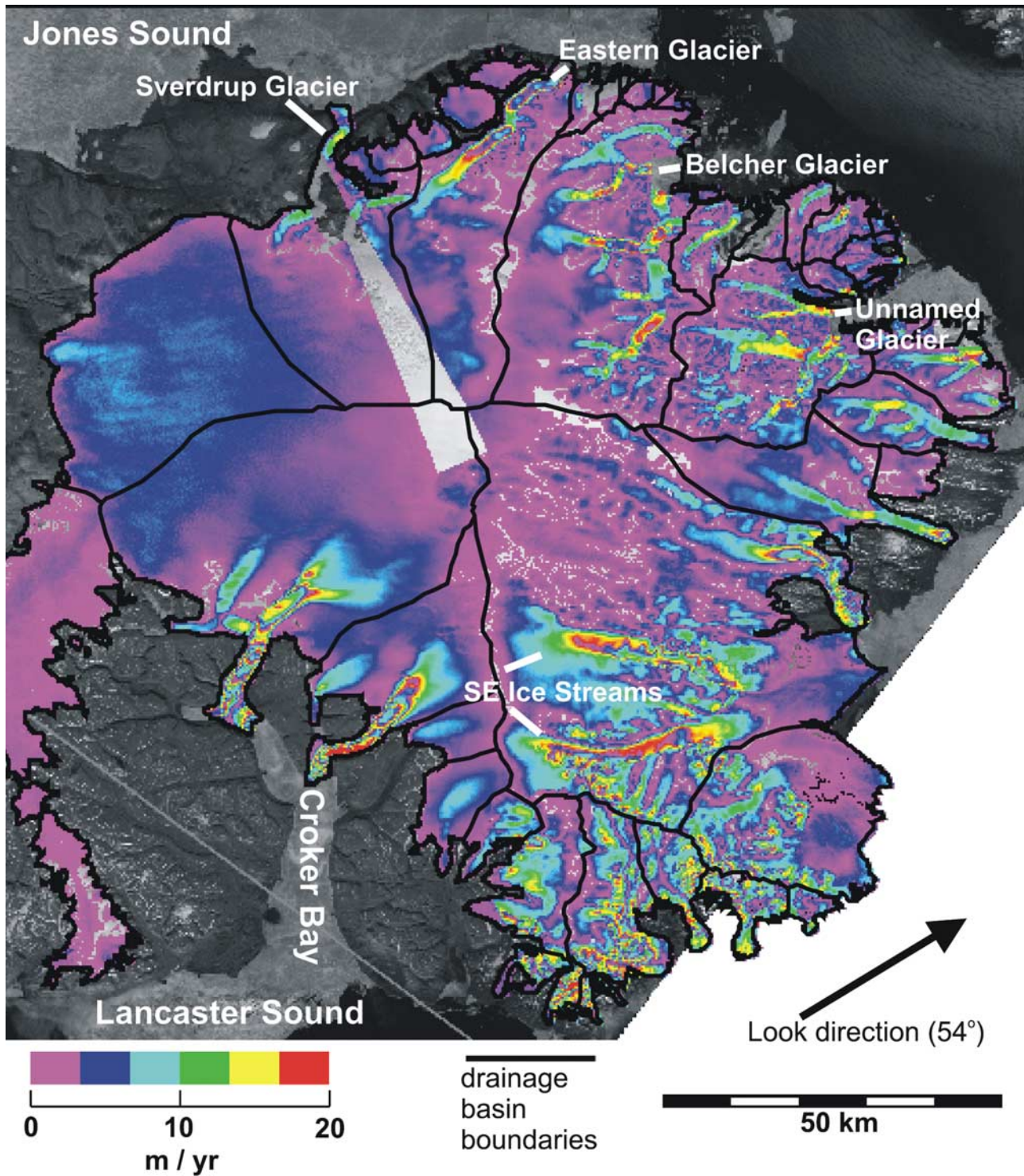


Figure 9. Synthetic aperture radar interferogram of the Devon Ice Cap. Ice surface velocities are given in the look direction of the satellite, which is indicated by an arrow. The interferometric fringes are overlaid on a 1999 Landsat 7 ETM+ image.

[37] A second type of transition between slow and fast glacier flow occurs at the head of most of the outlet glaciers that drain the eastern half of the Devon Ice Cap. Here ice flow is generally nonconvergent, surface slopes are consistently low ($\sim 1^\circ$), and surface velocities increase gradually down-glacier (Figure 9). The lack of distinct pinning points along

these outlet glaciers suggests that there is no constraint on the up-glacier propagation of enhanced glacier flow. This may explain why the two well-developed fast-flow units in the southeast region of the ice cap currently extend inland almost to the main north-south ice divide (Figure 9). The velocities of these two fast-flowing glaciers also decrease significantly

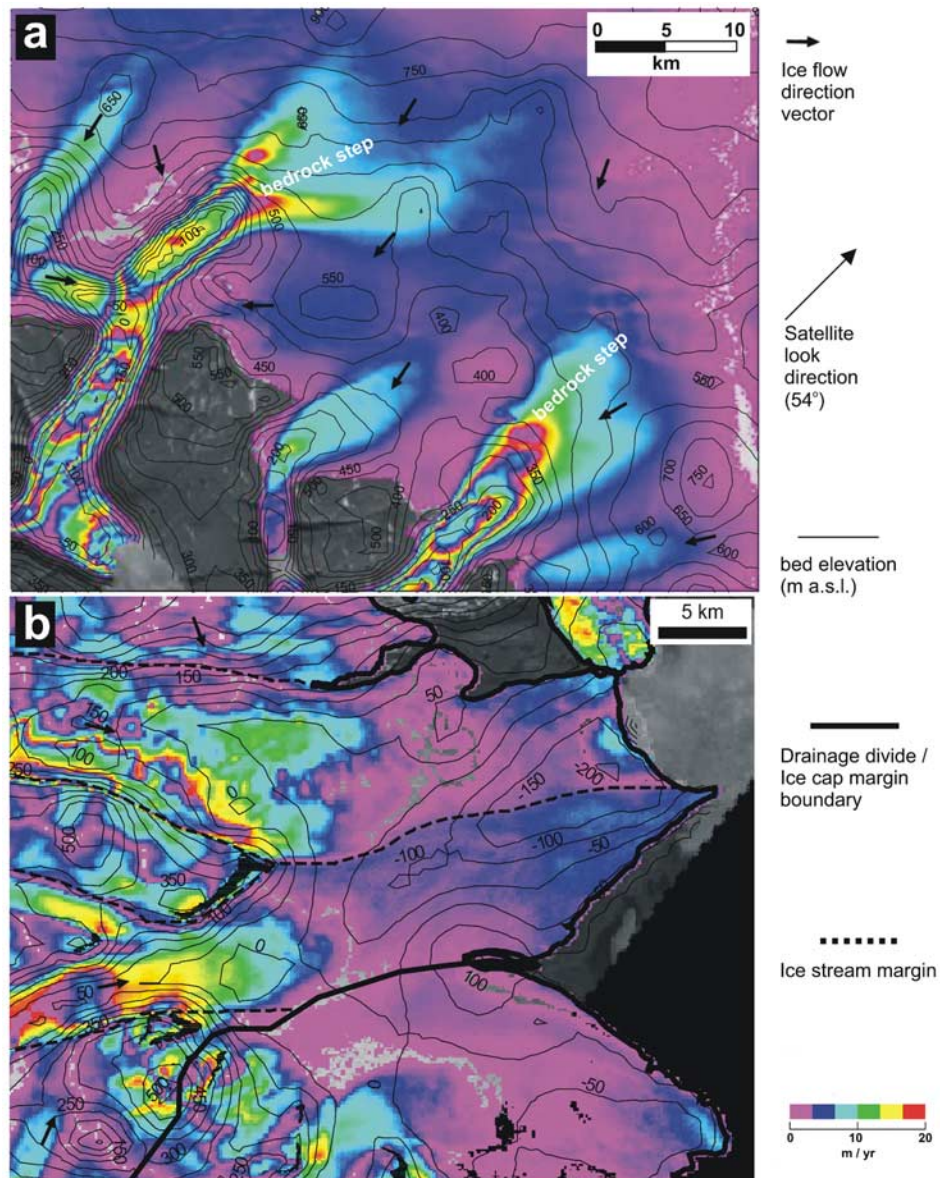


Figure 10. Ice surface velocity (in the satellite look direction) and subglacial bedrock topography (from radio echo data) for two parts of the Devon Ice Cap. (a) Two outlet glaciers draining southwest into Croker Bay. (b) Low-gradient piedmont lobe draining east from the Devon Ice Cap and fed by several outlet glaciers. The ice flow direction (inferred from the direction of maximum ice surface slope) is shown by arrows.

down-glacier of the point beyond which ice flow is no longer constrained laterally by bedrock structures and the ice streams are no longer fed by tributary ice flows (Figure 10b).

4.3. Driving Stresses From Radar-Derived Topographic Data

[38] The pattern of driving stresses (τ) on the Devon Ice Cap is calculated from the data on ice surface slope (α) and ice thickness (h) in our radar-derived digital elevation models (Figures 5 and 7). The driving stresses mapped in Figure 11 are calculated using the equation $\tau = \rho_i g h \sin \alpha$, where ρ_i is ice density and g is the acceleration due to gravity. The absolute values of calculated driving stress will vary with the amount of smoothing of the ice surface slopes [Paterson, 1994], but the spatial pattern of the stresses will remain unaltered.

[39] Driving stresses are generally lowest close to the ice divides on the Devon Ice Cap (Figures 3 and 11) and also on the piedmont lobes draining the southeast of the ice cap, where they reach <50 kPa. Although low in relative terms, the driving stresses in the piedmont lobe are significantly higher than those recorded in the ice streams of West Antarctica [e.g., Cooper *et al.*, 1983; Bentley, 1987].

5. Conclusions

[40] 1. Our airborne 100 MHz radar investigations of the morphology of the Devon Ice Cap acquired a total of 3370 km of radar data. The ice cap was covered by a nominal 10 km spaced grid of flight lines, with additional lines obtained from a number of outlet glaciers (Figure 3).

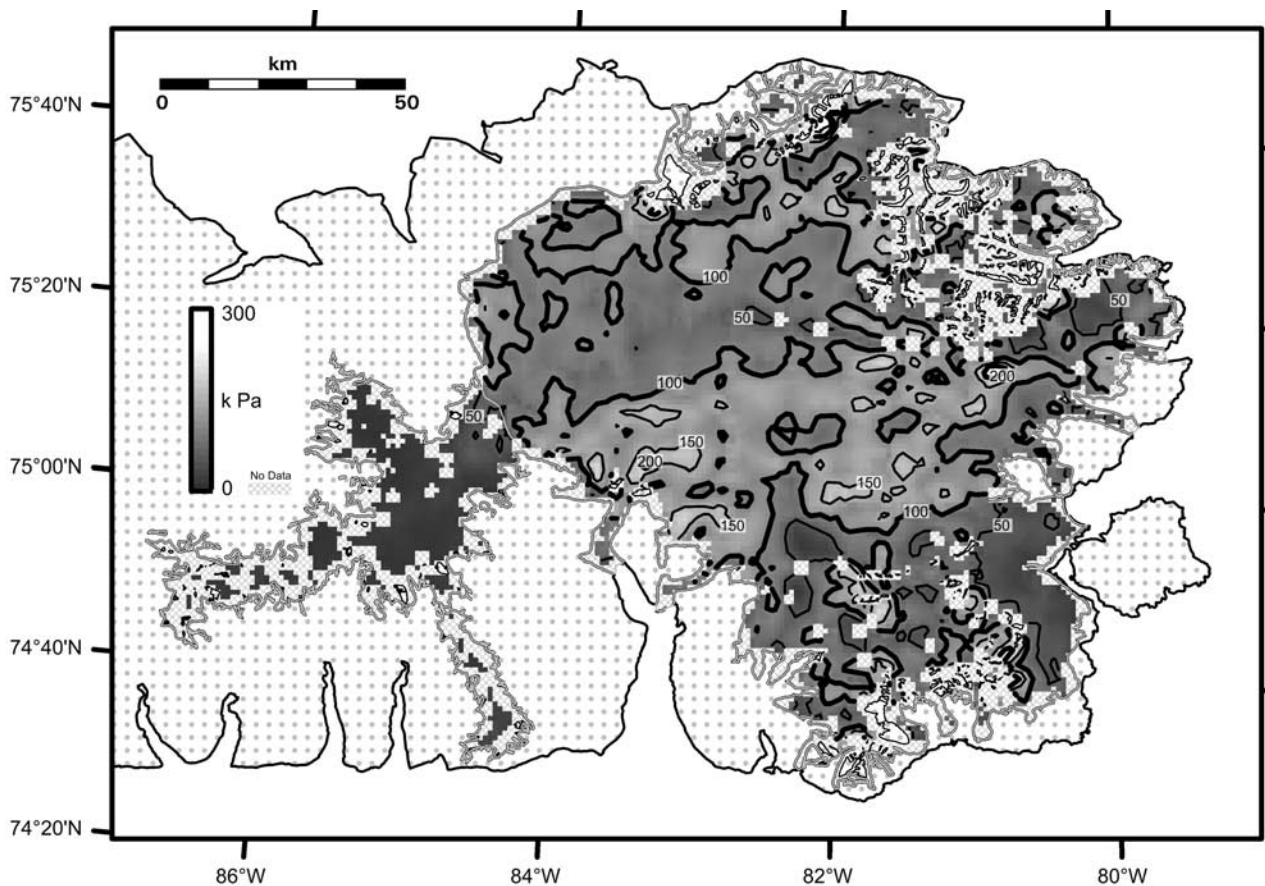


Figure 11. Distribution of driving stresses on the Devon Ice Cap (contour interval 50 kPa).

Radar returns from the ice cap bed were obtained from over 90% of flight tracks. Mean crossing point errors in ice surface elevation and ice thickness were 7–8 m.

[41] 2. Reduced radar measurements were interpolated over the whole ice cap to produce DEMs of ice cap surface and bed elevation, together with ice thickness. These DEMs can be used in numerical modeling studies of the ice cap. Until now, numerical modeling of Canadian Arctic ice caps, and thus predictions of their likely responses to future and past climate changes, has been largely precluded because very little information has been available on their three-dimensional morphology.

[42] 3. The total area of the Devon Ice Cap is 14,010 km², measured digitally from Landsat imagery (Figure 3). However, a 1960 km² ice-covered area extending westward from the main ice cap is stagnant and dynamically separate (Figure 4a). Subtracting this gives an area of 12,050 km² for the Devon Ice Cap proper. The largest drainage basin is 2630 km² in area (Figure 3).

[43] 4. The central area of the Devon Ice Cap is relatively simple and dome-like in shape (Figures 3 and 5). The ice cap crest has a maximum measured elevation of 1921 m. The area-elevation curve, important in mass balance studies, is relatively smooth, with a minor peak at ~1000–1100 m above sea level (Figure 6). The ice cap is drained by a number of outlet glaciers, usually constrained by valley walls and up to ~35 km long.

[44] 5. The total length of tidewater ice cliffs at the margins of the Devon Ice Cap is 73 km (~4% of the ice

cap edge). Icebergs are produced from the crevassed tidewater margins of the ice cap. The largest icebergs observed on Landsat imagery and during airborne radar work were <100 m in maximum diameter (Figure 4c). There is little evidence that these tidewater ice margins are floating.

[45] 6. The maximum thickness of ice recorded on Devon Island is 880 m, just southeast of the center of the ice cap. An ice volume of 3980 km³ is calculated, which is equivalent to ~10 mm of global sea level.

[46] 7. Only 8% of the ice cap bed lies below present sea level (Figure 6b). The bed is an upland plateau, dissected by a series of steep-sided valleys (Figure 8). The subglacial valleys and subaerial valley walls appear to control the locations of the major outlet glaciers draining the Devon Ice Cap.

[47] 8. Landsat imagery was used to examine the drainage basins and outlet glaciers of the Devon Ice Cap for indications of present or past surge activity. Only a single outlet glacier of the ice cap showed signs of past instability [Copland *et al.*, 2003]. However, all the major outlet glaciers along the eastern margin of the ice cap have experienced retreat, ranging from 1 to 3 km since 1960.

[48] 9. SAR interferometry was used to map the velocity structure of the Devon Ice Cap and, in particular, the extent and distribution of fast-flowing ice (Figure 9). Slow and undifferentiated flow predominates in the west and central region of the ice cap, with fast-flowing outlet glaciers and intervening slow-flowing ridges typical elsewhere (Figures 9 and 10). Outlet glacier velocities are

typically 7–10 times higher than in adjacent areas of undifferentiated flow.

[49] 10. Fast-flowing outlets usually occupy troughs in the bedrock topography (Figures 8 and 10), consistent with an ice cap thermal structure where basal melting is likely to take place first beneath thick ice located in bedrock troughs [e.g., *MacAyeal*, 1993]. This velocity structure, of fast-flowing units set within slower-flowing ice, appears typical of many large Arctic ice caps as well as of the great ice sheets of Antarctica and Greenland.

[50] **Acknowledgments.** This study was funded by the NERC Centre for Polar Observation and Modelling, UK, by NERC grant GR3/12469, and by the EU SPICE Project to J.A.D. as well as by grants from the Meteorological Service of Canada (CRYSYS program) to M.J.S. D.B. acknowledges receipt of an NSERC IPS scholarship. We thank Kenn Borek Aviation for air support and the Polar Continental Shelf Project (PCSP), Canada, for ground support at Resolute Bay. The paper is PCSP contribution 02003. We are grateful to R. M. Koerner, who provided advice and support throughout the project and who read the manuscript. Robin Bassford assisted with the field program. Liz Morris kindly assisted with data and support for GPS differential postprocessing. Waleed Abdalati, Douglas Mair, and Liz Morris provided surface elevation points.

References

- Andrews, J. T. (2002), *Glaciers of Canada: Glaciers of Baffin Island*, *U.S. Geol. Surv. Prof. Pap.*, 1386-J, 165–198.
- Benham, T. J., and J. A. Dowdeswell (2003), A simple visualisation method for distinguishing between subglacial-bed and side-wall returns in radio-echo records from outlet and valley glaciers, *J. Glaciol.*, 49, 463–468.
- Bentley, C. R. (1987), Antarctic ice streams: A review, *J. Geophys. Res.*, 92, 8843–8858.
- Bindschadler, R., J. A. Dowdeswell, D. Hall, and J.-G. Winther (2001), Glaciological applications with Landsat-7: Early assessments, *Remote Sens. Environ.*, 78, 163–179.
- Cattle, H., and J. Crossley (1995), Modelling Arctic climate change, *Philos. Trans. R. Soc. London, Ser. A*, 352, 201–213.
- Cooper, A. P. R. (1987), Interface tracking in digitally recorded glaciological data, *Ann. Glaciol.*, 9, 50–54.
- Cooper, A. P. R., N. F. McIntyre, and G. de Q. Robin (1983), Driving stresses in the Antarctic ice sheet, *Ann. Glaciol.*, 3, 59–64.
- Copland, L., M. Sharp, and J. A. Dowdeswell (2003), The distribution and flow characteristics of surge-type glaciers in the Canadian High Arctic, *Ann. Glaciol.*, 36, 73–81.
- Cress, P., and R. Wyness (1961), The Devon Island expedition: Observations of glacial movement, *Arctic*, 14, 257–259.
- Doake, C. S. M., M. Gorman, and W. S. B. Paterson (1976), A further comparison of glacier velocities measured by radio-echo and survey methods, *J. Glaciol.*, 17, 35–38.
- Dowdeswell, J. A. (1995), Glaciers in the High Arctic and recent environmental change, *Philos. Trans. R. Soc. London, Ser. A*, 352, 321–334.
- Dowdeswell, J. A., and J. O. Hagen (2004), Arctic glaciers and ice caps, in *Mass Balance of the Cryosphere*, edited by J. L. Bamber and A. J. Payne, pp. 527–557, Cambridge Univ. Press, New York.
- Dowdeswell, J. A., and M. Williams (1997), Surge-type glaciers in the Russian High Arctic identified from digital satellite imagery, *J. Glaciol.*, 43, 489–494.
- Dowdeswell, J. A., M. R. Gorman, A. F. Glazovsky, and Y. Y. Macheret (1994), Evidence for floating ice shelves in Franz Josef Land, Russian High Arctic, *Arct. Alp. Res.*, 26, 86–92.
- Dowdeswell, J. A., A. F. Glazovsky, and Y. Y. Macheret (1995), Ice divides and drainage basins on the ice caps of Franz Josef Land, Russian High Arctic, defined from Landsat, Russian KFA-1000 and ERS-1 SAR satellite imagery, *Arct. Alp. Res.*, 27, 264–270.
- Dowdeswell, J. A., et al. (1997), The mass balance of circum-Arctic glaciers and recent climate change, *Quat. Res.*, 48, 1–14.
- Dowdeswell, J. A., B. Unwin, A.-M. Nuttall, and D. J. Wingham (1999), Velocity structure, flow instability and mass flux on a large Arctic ice cap from satellite radar interferometry, *Earth Planet. Sci. Lett.*, 167, 131–140.
- Dowdeswell, J. A., et al. (2002), Form and flow of the Academy of Sciences Ice Cap, Severnaya Zemlya, Russian High Arctic, *J. Geophys. Res.*, 107(B4), 2076, doi:10.1029/2000JB000129.
- Dyurgerov, M. B., and M. F. Meier (1997a), Year-to-year fluctuations of global mass balance of small glaciers and their contribution to sea-level change, *Arct. Alp. Res.*, 29, 392–402.
- Dyurgerov, M. B., and M. F. Meier (1997b), Mass balance of mountain and subpolar glaciers: A new global assessment for 1961–1990, *Arct. Alp. Res.*, 29, 379–391.
- Fisher, D. A., et al. (1998), Penny Ice Cap cores, Baffin Island, Canada, and the Wisconsin Foxe Dome connection: Two states of Hudson Bay ice cover, *Science*, 279, 692–695.
- Gabriel, A. K., R. M. Goldstein, and H. A. Zebker (1989), Mapping small elevation changes over large areas: Differential radar interferometry, *J. Geophys. Res.*, 94, 9183–9191.
- Hagen, J. O., and N. Reeh (2004), Mass balance measurements, in *Mass Balance of the Cryosphere*, edited by J. L. Bamber and A. J. Payne, pp. 11–42, Cambridge Univ. Press, New York.
- Higgins, A. K. (1991), North Greenland glacier velocities and calf ice production, *Polarforschung*, 60, 1–23.
- Hodgkins, R., and J. A. Dowdeswell (1994), Tectonic processes in Svalbard tidewater glacier surges: Evidence from structural glaciology, *J. Glaciol.*, 40, 553–560.
- Hutchinson, M. F. (1993), Development of a continent-wide DEM with applications for terrain and climate analysis, in *Environmental Modelling With GIS*, edited by M. F. Goodchild et al., pp. 392–399, Oxford Univ. Press, New York.
- Isaaks, E. H., and R. M. Srivastava (1989), *Applied Geostatistics*, Oxford Univ. Press, New York.
- Joughin, I., S. Tulaczyk, M. Fahnestock, and R. Kwok (1996), A mini-surge on the Ryder Glacier, Greenland, observed by satellite radar interferometry, *Science*, 274, 228–230.
- Koerner, R. M. (1977a), Devon Island Ice Cap—Core stratigraphy and paleoclimate, *Science*, 196, 15–18.
- Koerner, R. M. (1977b), Ice thickness measurements and their implications with respect to past and present ice volumes in the Canadian High Arctic ice caps, *Can. J. Earth Sci.*, 14, 2697–2705.
- Koerner, R. M. (1979), Accumulation, ablation and oxygen isotope variations in the Queen Elizabeth Island ice caps, Canada, *J. Glaciol.*, 22, 25–41.
- Koerner, R. M. (1997), Some comments on climatic reconstructions from ice cores drilled in areas of high melt, *J. Glaciol.*, 43, 90–97.
- Koerner, R. M. (2002), Glaciers of Canada: Glaciers of the High Arctic islands, *U.S. Geol. Surv. Prof. Pap.*, 1386-J, 111–146.
- Koerner, R. M., and D. A. Fisher (1990), A record of Holocene summer climate from a Canadian High-Arctic ice core, *Nature*, 343, 630–631.
- Lamoureux, S. F., R. Gilbert, and T. Lewis (2002), Lacustrine sedimentary environments in High Arctic proglacial Bear Lake, Devon Island, Nunavut, Canada, *Arct. Antarct. Alp. Res.*, 34, 130–141.
- Lytke, M. B., D. G. Vaughan, and BEDMAP Consortium (2001), BEDMAP: A new ice thickness and subglacial topographic model of Antarctica, *J. Geophys. Res.*, 106, 11,335–11,352.
- MacAyeal, D. R. (1993), Binge/purge oscillations of the Laurentide Ice Sheet as a cause of the North Atlantic's Heinrich events, *Paleoceanography*, 8, 775–784.
- Martin, P. J., and T. J. O. Sanderson (1980), Morphology and dynamics of ice rises, *J. Glaciol.*, 25, 33–45.
- Massonnet, D., M. Rossi, C. Carmona, F. Adragna, G. Peltzer, K. Feigl, and T. Rabaute (1993), The displacement field of the Landers earthquake mapped by radar interferometry, *Nature*, 364, 138–142.
- McIntyre, N. F. (1985), The dynamics of ice-sheet outlets, *J. Glaciol.*, 31, 99–107.
- Meier, M. F., and A. S. Post (1969), What are glacier surges?, *Can. J. Earth Sci.*, 6, 807–817.
- Paterson, W. S. B. (1994), *The Physics of Glaciers*, 3rd ed., Pergamon, New York.
- Smith, B. M. E., and S. Evans (1972), Radio echo sounding: Absorption and scattering by water inclusions and ice lenses, *J. Glaciol.*, 11, 133–146.
- Williams, M., and J. A. Dowdeswell (2001), Historical fluctuations of the Matushevich Ice Shelf, Severnaya Zemlya, Russian High Arctic, *Arct. Antarct. Alp. Res.*, 33, 211–222.
- Zebker, H. A., C. L. Werner, P. A. Rosen, and S. Hensley (1994), Accuracy of topographic maps derived from ERS-1 interferometric radar, *IEEE Trans. Geosci. Remote Sens.*, 32, 823–836.

T. J. Benham, J. A. Dowdeswell, and M. R. Gorman, Scott Polar Research Institute, University of Cambridge, Lensfield Road, Cambridge CB2 1ER, UK. (tjb52@cam.ac.uk; jd16@cam.ac.uk)

D. Burgess and M. J. Sharp, Department of Earth and Atmospheric Sciences, University of Alberta, Edmonton, Alberta, Canada T6G 2E3. (dob@ualberta.ca; martin.sharp@ualberta.ca)



Last Glacial Maximum and deglaciation of Devon Island, Arctic Canada: support for an Inuitian ice sheet

Arthur S. Dyke*

Terrain Sciences Division, Geological Survey of Canada, 601 Booth Street, Ottawa, Ont., Canada K1A 0E8

Abstract

The extent and origin of Quaternary glaciers in the Queen Elizabeth Islands of Arctic Canada, especially during the Last Glacial Maximum (LGM), has been debated for well over a century. No consensus has yet emerged and the spectrum of interpretations within the last decade is the broadest ever. The glacial geology of Devon Island strongly supports the Late Wisconsinan Inuitian Ice Sheet hypothesis. During LGM, the southeastern part of the Queen Elizabeth Islands was covered by an ice sheet flowing from a centre, or a divide centrally located, in the archipelago. Another ice divide extended from the centre across Devon Island. Flow from the Inuitian centre and convergent flow from Devon Island, and probably also from Cornwallis and Bathurst Islands, sustained an ice stream in Wellington Channel. Ice was locally advancing to its LGM limit about 23 ka BP. Recession in the vicinity of the present coastline was underway by 10 ka BP and final ice remnants west of the present Devon Ice Cap vanished about 8 ka BP. The island bears the same two-part landscape zonation as do other islands and peninsulas in the region. These reflect a cold-based core and warm-based periphery at LGM. © 1999 Elsevier Science Ltd. All rights reserved.

1. Introduction

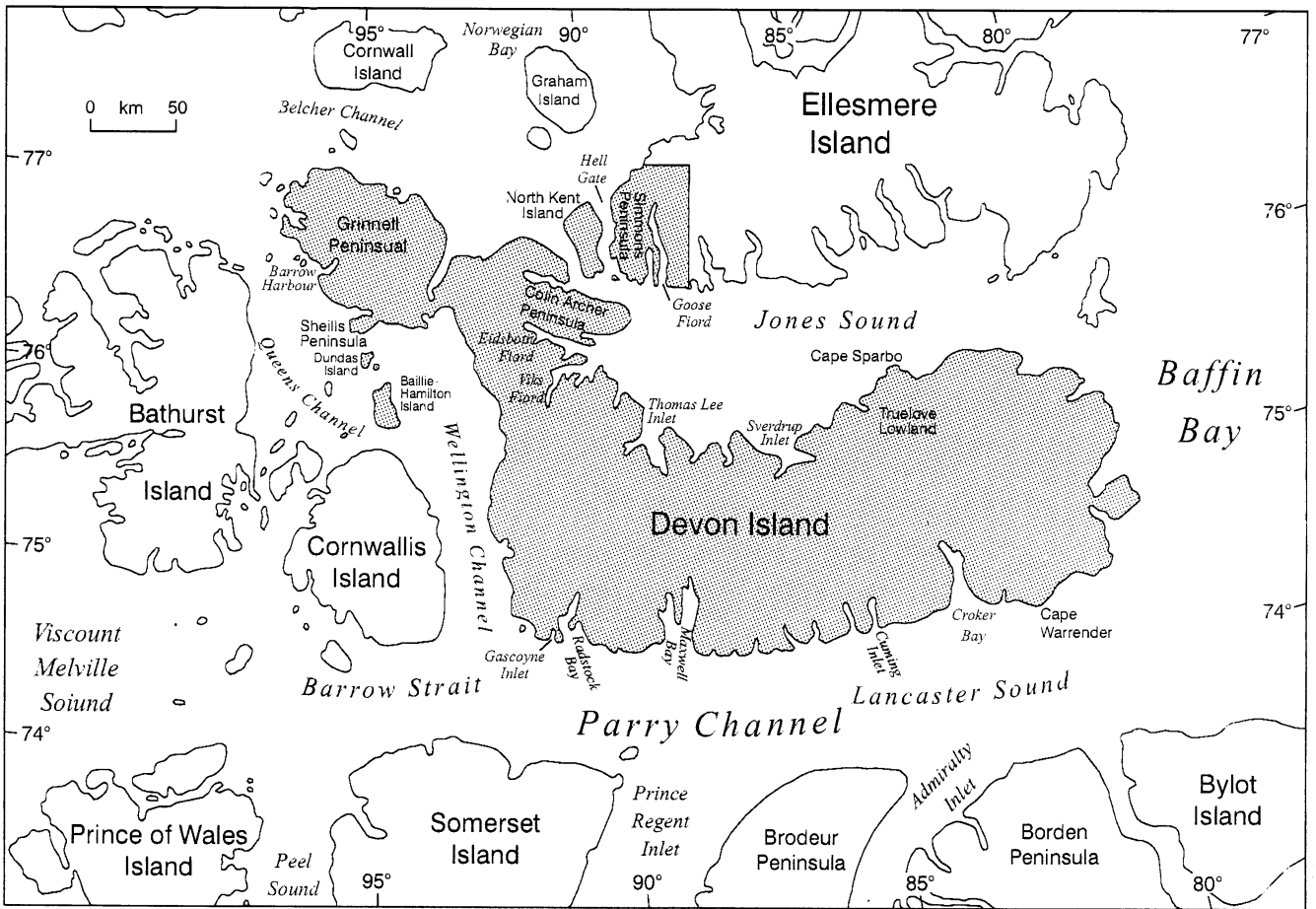
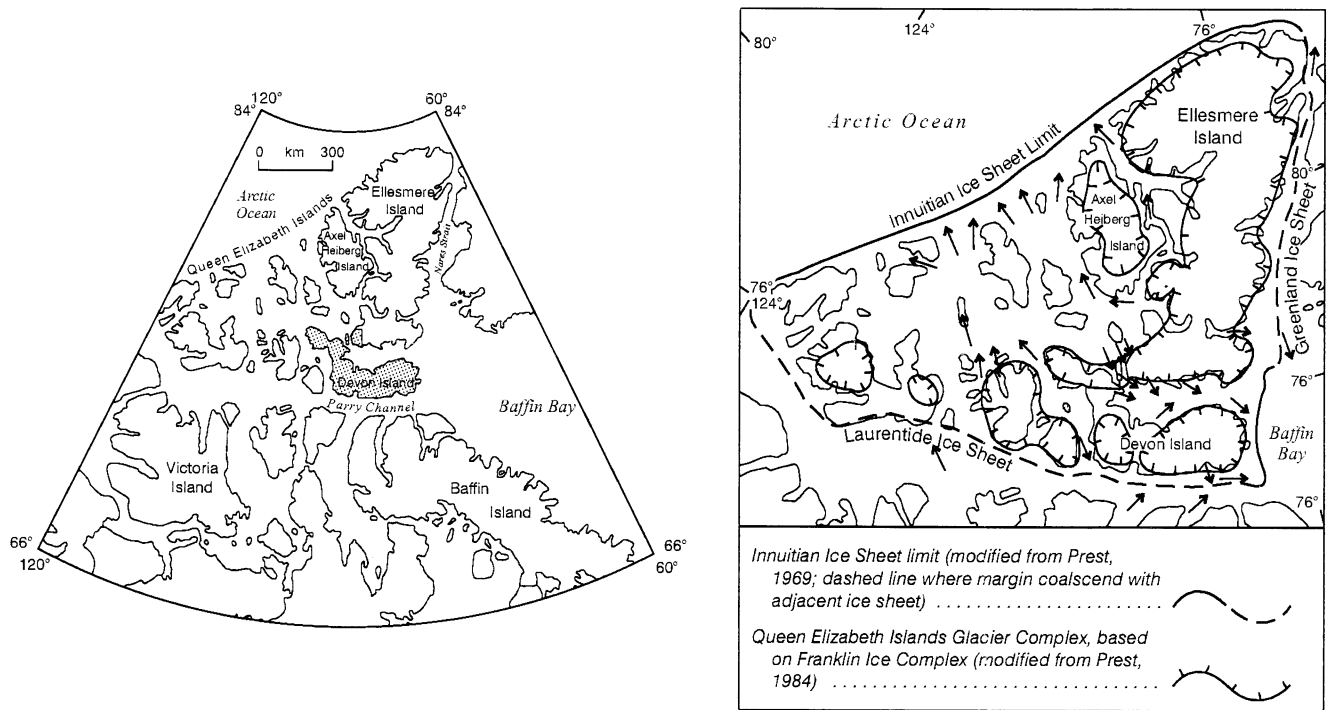
This paper offers a substantial resolution of the debate about Late Wisconsinan glaciation of the Canadian High Arctic, based on new data from Devon Island and its vicinity (Fig. 1). The focus is on ice configuration during the Last Glacial Maximum (LGM) and during early Holocene deglaciation. Holocene relative sea-level history will be treated in a later paper. In this paper, LGM is defined as the *time interval* of generally maximal ice extent during marine isotope stage 2. According to the Devon Island ice core $\delta^{18}\text{O}$ record (e.g. Fisher, 1979), the last major regional temperature depression began about 20,000 calendar years ago and persisted until about 12,000 calendar years ago [ca. 10,300 radiocarbon years BP (10.3 ka BP)], when temperatures began to rise sharply. This chronology agrees with the geological evidence presented below. Although the ice core chronology is in calendar years, its >5% uncertainty before 5 ka BP (Koerner and Fisher, 1985) means that it cannot be safely converted to the radiocarbon time scale. Events discussed herein are referred to the latter scale because all previous publications on regional glacial history use it.

Data presented here support the general Inuitian Ice Sheet model of Blake (1970). However, a full definition of the ice sheet, in terms of its maximal limits and flow configuration, is not yet possible. The glacial history of this region is as well known for its long debate as for its geology (Hodgson, 1989). Because the debate has been prominent, a review of interpretations is presented to illustrate the nature of the arguments. Scanty previous work on Devon Island is outlined before turning to regional interpretations.

2. Geographic setting

Devon Island spans half the Queen Elizabeth Islands (QEI), that part of the Canadian Arctic Archipelago (CAA) north of Parry Channel (Fig. 1). Its western tip lies near the centre of the proposed Inuitian Ice Sheet. The eastern part faces Baffin Bay, which deepens near shore to 500–1000 m and must have limited advances of grounded ice during the Quaternary. Hence, no part of the QEI is better situated for addressing the debate about regional glaciation. The eastern part of the island lies adjacent to a significant regional moisture source, the North Water polynya and, in part because of this, is covered by the Devon Ice Cap (15,570 km²; Koerner, 1970).

* E-mail address: ad@gsc.nrcan.gc.ca



GSC

Fig. 1. Location of the study area (stippled) and main place names mentioned. Eureka Sound separates southeastern Axel Heiberg and Ellesmere islands. The upper-right map shows the Innuitian Ice Sheet limit as portrayed by Prest (1969, 1970), along with the Innuitian ice flow pattern of Blake (1970). It also shows the Franklin Ice Complex, the inner ticked lines, as portrayed by Prest (1984).

Much of the island is a simple plateau. Bounded by cliffs on the north and the south, it rises in most places gradually from the west coast to elevations in the east of about 600 m. Nunataks in the fretted, but still mostly subglacial, Cunningham Mountains rise to 900 m. Well-developed fiords indent the north and particularly the south coast. With the exception of Viks Fiord, they are not tectonically controlled (cf. Thorsteinsson and Mayr, 1987); thus, they provide evidence of glaciation, probably repeatedly, by ice flowing off the island. In its central and western parts, the plateau truncates sedimentary rocks, which dip westward at angles slightly greater than the surface slope. These rocks are mostly Paleozoic carbonates with sandstone, shale and gypsum (Thorsteinsson and Mayr, 1987). Gneisses of the Precambrian Canadian Shield underlie the eastern part (Frisch, 1988).

Grinnell Peninsula is joined to the main island by a low isthmus and was a separate island in the early Holocene. It has a maturely dissected plateau and a more rugged relief than most of Devon Island; its higher ground is mainly in the 300–500 m range. The sedimentary rocks there were involved in the orogeny that produced the Cornwallis Fold Belt and the Parry Islands—Jones Sound Fold Belt (Trettin, 1991) and the structural complexity accounts for the more varied topography.

Devon Island is bounded by large channels. Belcher Channel and Norwegian Bay to the northwest are at the marginal parts of a shallow epicontinental sea, mostly less than 200 m deep, and are floored by the clastic rocks of the Sverdrup Basin (Fig. 1; Okulitch, 1991). Queens and Wellington Channels on the west are about 50 km wide and attain depths in excess of 300 m (MacLean *et al.*, 1989). They are floored mainly by carbonate rocks, as are Barrow Strait and Prince Regent Inlet. Jones and Lancaster Sounds are about 100 km wide and their depths exceed 500 m. Most of Lancaster Sound and the eastern half of Jones Sound are floored by Cretaceous—Tertiary clastic sediments occupying grabens in Precambrian gneisses. The origin of the inter-island channels remains a problem (e.g. Fortier and Morley, 1956; Pelletier, 1966; Blake, 1970; England, 1987; Trettin, 1991; Dyke *et al.*, 1992). However, Jones and Lancaster sounds are clearly localized along major rift structures related to the formation of Baffin Bay (e.g. Okulitch and Trettin, 1991), whereas the channels to the west and northwest of Devon Island show little sign of structural control and were, therefore, formed by some combination of fluvial and glacial erosion. The rock formations that floor the latter channels are simply offshore extensions of those on land.

3. Previous work

3.1. Bordering channels

Lancaster Sound has been taken as the dividing line between Wisconsinan Laurentide ice to the south and

other ice to the north (e.g. Prest *et al.*, 1968; see, however, Andrews, 1973; Fulton, 1989). Grounded ice extended past the mouth of Lancaster Sound during the Early Wisconsinan and terminated in northern Baffin Bay (Klassen, 1993). Ice-rafted detrital carbonate (DC) layers were deposited in Baffin Bay whenever many icebergs were released into or from channels around the head of the bay (Aksu, 1985; Hiscott *et al.*, 1989; Andrews *et al.*, in press). In general, the Baffin Bay DC record indicates repeated glaciation of the CAA during the Quaternary but this record does not constrain ice configurations within the archipelago. In a major revision of the original chronology of these DC layers (Aksu, 1985), the base of the uppermost DC layer now has been dated at 12.5 ka BP, much younger than its original assignment (Andrews and Meese, 1997; Andrews *et al.*, in press). A thick layer at about 4 m depth was dated > 48 ka and was correlated with an interstadial layer in the Greenland Ice Sheet dated about 51.5 ka BP, rather than to marine isotopic stage 6, as originally. The thicker DC layer may thus correlate with recession from the Early Wisconsinan limit. Three thin, intermediate DC layers were correlated with Greenland interstadial ice layers dated about 45, 38 and 28 ka BP. In general, the chronology of DC layers in Baffin Bay, although still preliminary, suggests the presence of glacier ice extending into the channels north and west of Baffin Bay during marine isotope stages 3 and 2.

Acoustically chaotic deposits, interpreted as till, are widespread in Lancaster Sound and Wellington Channel and the thickest of these, the most extensive of which is at the south end of Wellington Channel, may comprise end or lift-off moraines (MacLean *et al.*, 1989). Although there is little control on the age of these glacial deposits, the till is overlain only by a glaciomarine-marine sequence, compatible with deposition during the last deglaciation. Cores of the marine sequence have been described from Wellington Channel and Barrow Strait but only one (HU86-027-144; Fig. 2) has radiocarbon age control. A shell from the postglacial mud dated 7970 ± 70 BP (TO-752). If the deposition rate of this unit was constant, its base is about 10 ka old (MacLean *et al.*, 1989) (p. 24).

A core (HU83-023-053; Fig. 2) of surficial marine sediment from outer Jones Sound has a near-basal date on acid-insoluble, disseminated organic matter of $25\,830 \pm ?$ yr BP [Williams, 1990 (p. 1489); no laboratory number reported]. This date was adjusted to 17.5 ka BP using a calculation intended to correct for the possible presence of redeposited organic matter (Andrews *et al.*, 1985). If this date is approximately correct, the last glaciation of outer Jones Sound was in earliest Late Wisconsinan time or possibly earlier. Another core of marine sediment (HU83-023-052; Fig. 2) from the mouth of Jones Sound has a basal date on a marine shell of $30,290 \pm 2490$ (Williams, 1990 (p. 1489); no laboratory number reported). If we assume that ice from Jones Sound extended

into Baffin Bay about as far as the ice did from Lancaster Sound (Klassen, 1993), that site probably was covered by ice during the Early Wisconsinan.

3.2. *Devon Island*

The Quaternary geology of Devon Island has almost escaped attention and no glacial geological map of the island has been published. Previous comments on glaciation resulted mainly from observations during bed-rock mapping (Prest, 1952; Fortier *et al.*, 1963; Thorsteinsson and Mayr, 1987).

The most complete statement regarding glaciation is by Roots (1963), who was mainly concerned with physiography. He proposed (p. 176) that the island, possibly excluding Grinnell Peninsula, had been covered by an ice cap, with possibly a separate ice cap on Colin Archer Peninsula. He identified the areas of prominent glacial erosion and an area of hummocky moraine on northern Colin Archer Peninsula. He also referred to striated spurs that indicate ice flow down Croker and Maxwell bays but did not map their locations. Greiner (1963) (p. 201) recorded the only mapped glacial striae from the island before the present work. Thorsteinsson and Mayr (1987) (p. 8) reported that 'sparsely distributed metamorphic and igneous rocks of pebble to boulder size occur at all elevations in those parts of Devon Island that are underlain by Phanerozoic rocks' and inferred that they were derived from the eastern part of the island.

Later studies focused on Truelove Lowland because of the Arctic Institute of North America base camp there. Müller and Barr (1966) concluded that Holocene rebound resulted from deglaciation but did not speculate on the style of glaciation. Barr *et al.* (1968) provided the only elevation of the Holocene marine limit yet available from the northern east coast of Devon Island. Barr (1971) amended the original rebound curve and discarded spurious pre-Holocene marine shell age determinations. He thus revised the age of marine limit from 15.5 to 9.45 ka BP. He also reported age determinations in the Middle Wisconsinan range (about 30 ka BP) on shells from the surface of raised beaches and considered several possible histories that might account for them. Young and King (1989) and King (1991) described lake sediments and reported two radiocarbon dates on marine mud below the lacustrine sediments. They further revised the age of marine limit to 9.7 ka BP.

Other parts of Devon Island have been little studied. Grosswald (1973) examined southwestern Grinnell Peninsula and concluded that the area had been glaciated. He incorrectly concluded that the postglacial marine limit extended to at least 150 m altitude based on the occurrence of 'somewhat subdued terraces' and marine shells. His samples provided a radiocarbon date on a marine-limit delta at the head of Barrow Harbour (Blake, 1987) and other dates that are discussed below

(Glushankova *et al.*, 1980). W. Blake, Jr provided several radiocarbon dates on deglaciation of the Jones Sound region (Lowdon *et al.*, 1971; Lowdon and Blake, 1975; Blake, 1987). S.B. McCann contributed radiocarbon dates from Radstock Bay and Eidsbotn (Blake, 1988; McNeely, 1989), and R.B. Taylor added dates around Gascoyne Inlet (R.B. Taylor, *pers. comm.*, 1996).

Important inferences regarding Quaternary glaciation have been drawn from the Devon Island ice core, which extends back to last interglacial times (120 ka BP; Paterson *et al.*, 1977). Koerner and Fisher (1985) (p. 312) summarized these as follows: 'The Devon Ice Cap, at least throughout the Holocene and the last ice age, is believed to have remained independent from both the Laurentide Ice Sheet and other Queen Elizabeth Islands ice masses (Paterson, 1977; Fisher, 1979). As an independent ice cap it is unlikely that the ice at the drill site location was more than 100–200 m thicker than it is at present because the dimensions of the ice cap are constrained by deep channels at its margins.' The drill site is within 2 km of the present main ice dome and the term 'last ice age' refers to the entire Wisconsinan Stage.

Some general and preliminary conclusions from the present Devon Island project have been presented by England *et al.* (1995), Dyke *et al.* (1996a,b), and Hättestrand and Stroeve (1996).

4. Regional glaciation of QEI

4.1. *Trends of Argument*

The recent debate about glaciation of the QEI sets the Franklin Ice Complex model (England, 1976a) against the Innuitian Ice Sheet model (Blake, 1970). Although the dichotomy is firmly identified with the two major proponents, it captures the essence of a much longer debate about the extent of late Quaternary ice, as summarized chronologically in Table 1. Specifically, it involves the question as to whether the archipelago was covered at LGM by multiple, noncontiguous ice caps or by an extensive and continuous ice sheet. Neither Blake nor England illustrated his model with a map of ice cover, but the Innuitian model was illustrated by Prest (1969, 1970) and the Franklin model by Prest (1984). Both are sketched in Fig. 1 using Prest's rendering of the margins but Blake's ice flow pattern. This section and the next highlight the more important trends emerging from Table 1.

Prior to radiocarbon dating, discussion centred on the extent of glaciation, but most assessments seem to pertain to the last glaciation. Interpretations of plant geography as indicating ice-age refugia (Simmons, 1913; Fernald, 1925; Hultén, 1937; Brassard, 1970) influenced portrayals of limited ice cover, and *vice versa*. Washburn (1947) tabulated records of striations, erratics, and

Table 1
Interpretations of the extent of glaciation of the Queen Elizabeth Islands

Reference	Interpretation
Shaler and Davis (1881)	All then-known islands of CAA glaciated; channels ice-free
Chamberlin (1894)	No glaciation of the CAA except southeastern Baffin Island; see Fig. 3 in Prest (1990)
Upham (1895)	Complete glaciation of then-known extent of CAA including inter-island channels; see Fig. 4 in Prest (1990)
Schei (1903)	Glaciation of Ellesmere and Axel Heiberg islands never much more than at present
Low (1906)	Glaciation of Baffin and Devon islands never much more than at present
Chamberlin and Salisbury (1906, 1907)	No glaciation of the CAA including southeastern Baffin Island; see Fig 7 in Prest (1990)
Young (1909)	Glaciation of CAA apparently never more than at present
McMillan (1910)	Recorded first striae from QEI; westward flow at head of Liddon Gulf, probably by local ice cap on Melville Island
Chamberlin (1913)	Complete glaciation of then-known extent of CAA including channels; ice divides on Ellesmere and Devon islands; see Fig. 8 in Prest (1990)
Simmons (1913)	CAA free of ice during maximum glaciation because of lack of precipitation; phytogeography indicative of CAA refugium
Schuchert (1914, 1915)	Nearly complete lack of glaciation of CAA
Tarr and Martin (1914)	Complete glaciation of then-known extent of CAA; local ice caps on all islands but no ice in channels; see Fig. 10 in Prest (1990)
Coleman and Parks (1922)	No glaciation of the CAA except for two ice caps on Baffin Island; see Fig. 11 in Prest (1990)
Alden (1924)	Keewatin Ice Sheet extends across Foxe Basin and onto parts of Baffin Island; no ice in QEI; see Fig. 12 in Prest (1990)
Fernald (1925)	Large parts of the CAA remained unglaciated; phytogeography indicative of refugium
Nordenskjöld (1928)	CAA contained large ice-free areas during the Pleistocene, based on limited extent of present glaciation and supposed climate during glaciations
Antevs (1929)	Pleistocene glaciation reached south coast of Victoria Island; local ice cap on Prince Patrick Island in QEI based on misinformed presence of modern ice cap there
Billings and Williams (1932)	No glaciation of western CAA except for independent ice cap on Victoria Island
Snider (1932)	Nearly complete glaciation of CAA
Martin (1932, 1935)	Keewatin Ice Sheet reached south coast of Victoria Island; local ice caps covered Baffin and Ellesmere islands; see Fig. 13 in Prest (1990)
Shepard (1936)	Ice cap filled entire Arctic basin
Hultén (1937)	CAA shows no traces of glaciation; phytogeography indicates refugium
Maull (1938)	Complete glaciation of CAA
Longwell <i>et al.</i> (1939)	Complete glaciation of CAA
Shepard (1941)	Inter-island channels are evidence of glacial erosion by thick, pervasive ice sheet
Coleman (1941)	Large portions of the CAA not glaciated
Hobbs (1945)	Wisconsinan Laurentide glacial limit south of Parry Channel; QEI ice-free
Flint <i>et al.</i> (1946)	Glacial Map of North America; left open the question of glaciation in least known parts of the Arctic, based in part on Washburn (1947)
Washburn (1947)	Widespread recent emergence of the QEI indicates widespread regional glaciation
Wickenden (1947)	Complete glaciation of the CAA including channels based on widespread evidence of postglacial emergence
Flint (1947)	Complete glaciation of CAA including channels
Jenness (1952)	Western QEI glaciated by local ice caps, if at all; second striae measurements from QEI (Resolute Bay, measured by R.L. Nichols)
Tozer (1956)	Local ice cap on Prince Patrick Island based on striae at Mould Bay, erratics and rock-basin lakes
Heywood (1957)	Ellef Ringnes Island never glaciated as indicated by complete absence of till and glacial landforms
Prest (1957)	Eastern QEI ice sheet with centre of flow on each island and western limit on eastern Bathurst Island; local ice caps on Melville and Prince Patrick islands; derived from compilation of Wilson <i>et al.</i> (1958)
Thorsteinsson (1958)	Local ice cap on Cornwallis Island based on striae at Resolute Bay and Reid Bay; shield erratics above marine limit probably indicative of older Laurentide glaciation
Wilson <i>et al.</i> (1958)	Glacial Map of Canada; same as Prest, 1957; central and western QEI explicitly mapped as unglaciated along with Beringia; striae from Tozer (1956) and Thorsteinsson (1958)
Craig and Fyles (1960)	<i>Ellesmere-Baffin Glacier Complex</i> over eastern QEI during Late Wisconsinan with western limit as in Prest (1957); possible local Late Wisconsinan ice caps and possible pre-Late Wisconsinan regional ice sheet in central and western QEI
Fyles (in Jenness, 1962)	Last glaciation covered only part of western Ellesmere where freshly glaciated areas are restricted to flanks of some fiords
Boesch (1963)	Weathering zones on Axel Heiberg Island indicate limited LGM ice extent near present ice margins

Table 1 (Continued)

Reference	Interpretation
Fortier <i>et al.</i> (1963)	Local ice caps on Devon, Ellesmere, Axel Heiberg islands; glaciation of eastern Bathurst Island; no clear evidence of glaciation of central and western QEI except for Lougheed Island; two striae sites and distribution of erratics based on extensive field work in 1955; concepts influenced 1958 Glacial Map of Canada
Blake (1964)	Local ice cap covered Bathurst Island during Late Wisconsinan deglaciation based on mapped ice-flow features and retreat pattern; possibly part of a larger ice sheet that earlier covered inter-island areas to north, based on delevelling pattern
St-Onge (1965)	Glaciation of Ellef Ringnes Island by ice flowing from islands to the east and south indicated by erratics, probable esker, lake basins, and postglacial emergence
Fyles (1965)	Pre-Late Wisconsinan Laurentide glaciation of western QEI based on erratics
Prest <i>et al.</i> (1968)	Glacial Map of Canada; complete glaciation of CAA except western Banks Island and part of Melville Island; glaciation of QEI based on Innuitian Ice Sheet concept (Prest, 1984) (p. 26)
Hattersley-Smith (1969)	Younger of two tills at head of Tanguary Fiord, northern Ellesmere Island indicates very limited last glaciation and an extensive ice-free area from here to the Axel Heiberg Island
Bryson <i>et al.</i> (1969)	Northern limit of Laurentide Ice Sheet 'proper' close to Arctic mainland coast; glaciation of all but western fringe of QEI by ice mass independent of Laurentide; however, no evidence of break between QEI and Laurentide postglacial uplift
Andrews (1969)	Distinct uplift cell over QEI separated by saddle from Laurentide uplift
Prest (1969)	Complete glaciation of QEI based on Innuitian Ice Sheet concept; however, ice retreat pattern also compatible with Flint (1971)
Brassard (1970)	Evidence of Wisconsinan botanical refugium on northern Ellesmere Island
Blake (1970)	Complete glaciation of QEI by <i>Innuitian Ice Sheet</i> during Late Wisconsinan based primarily on Holocene uplift pattern; ice flow pattern based on inter-island channels; ice sheet fully coalescent with both Laurentide and Greenland ice
Prest (1970)	Complete glaciation of QEI based on Blake (1970) but ice mass referred to <i>Queen Elizabeth Islands Glacier Complex</i>
Tedrow (1970)	Threefold soil chronosequence on tills of Inglefield Land, northwest Greenland indicates limited advance at LGM and non-coalescence of Ellesmere and Greenland ice
Mercer (1970)	Pre-Late Wisconsinan glaciation of QEI by southward flowing ice emanating from a marine ice sheet over the Canada Basin of the Arctic Ocean based on analogous West Antarctic Ice Sheet and glacially redeposited marine shells in CAA
Flint (1971)	Complete glaciation of CAA except western Banks Island; eastern islands covered by Ellesmere-Baffin Glacier Complex; western islands, including QEI, covered by Laurentide Ice Sheet
Davies (1972)	LGM advance on northwest Greenland restricted to fiords; Greenland and Ellesmere ice not coalescent
Andrews (1973)	At 12 ka BP QEI mostly covered by Laurentide Ice Sheet with ice spreading from a north-plunging ice divide extending from Somerset Island to Ellesmere Island
England (1976a, 1978, 1983, 1990, 1992, 1996)	Noncontiguous glaciation of the eastern QEI by <i>Franklin Ice Complex</i> ; similar to Prest (1957) but less ice offshore
Hughes <i>et al.</i> (1977)	Late Wisconsinan Arctic Ice Sheet
England and Bradley (1978); England <i>et al.</i>	Beyond LGM ice limit on NE Ellesmere Island are ice shelf moraines of Ellesmere ice advance dated >30 ka BP and still older features related to advance of Greenland ice onto Ellesmere
Boulton (1979)	Available evidence does not favour the existence of a large Innuitian Ice Sheet; postglacial uplift can be explained in an infinite variety of ways
Völk (1980); King (1981)	LGM ice limit in the Kreiger Mountains, NW Ellesmere Island only a few kilometres beyond present ice margins
Mayweski <i>et al.</i> (1981)	Complete glaciation of QEI by Innuitian Ice Sheet
England (1983, 1987b)	Sea level stable at marine limit in full glacial sea beyond LGM ice margin, followed by slow initial emergence as theoretically expected for sea in ice marginal depression
Grosswald (1984)	Late Wisconsinan <i>Panarctic Ice Sheet</i> ; Innuitian Ice Sheet part of one contiguous Northern Hemisphere ice sheet-ice shelf complex
Prest (1984)	Noncontiguous glaciation of the eastern QEI by <i>Queen Elizabeth Islands Glacier Complex</i> ; largely ice free western islands; essentially equivalent to Franklin Ice Complex of England (1976); not equivalent to QEIGC of Prest (1970)
Hodgson (1985)	Major early Holocene drift belt along west-central Ellesmere Island; ice extended beyond it during LGM; data compatible with either Innuitian or Franklin models
England (1985)	Northern Nares Strait occupied by full glacial (LGM) sea from 33 to 8 ka BP
Retelle (1986)	Northern Nares Strait ice free at LGM; Early Quaternary advance of Greenland ice onto Ellesmere Island
England (1987a)	Only regional ice sheet in QEI, if ever, predated faulting that formed inter-island channels, possibly during late Tertiary; thereafter channels precluded ice sheets
Dyke and Prest (1987); Hodgson (1989)	Noncontiguous glaciation of eastern and southern QEI, Melville Island; essentially Franklin Ice Complex of England (1976) and Queen Elizabeth Islands Glacier Complex of Prest (1984) though more ice cover than latter

Table 1 (Continued)

Reference	Interpretation
Fulton (1989)	Complete Wisconsinan glaciation of QEI: Laurentide ice covered southern and western islands; 'Innuitian Ice Sheet' covered only Ellesmere and Axel Heiberg islands; more limited ice cover during Late Wisconsinan
Andrews (1989)	Same map as in Fulton (1989) except Laurentide ice cover of QEI assigned to Late Wisconsinan and eastern ice referred to Franklin Ice Complex
Funder (1989)	Nares Strait filled by coalescent Ellesmere and Greenland ice during Late Wisconsinan
Funder (1990)	Late Wisconsinan maximum advance of Greenland Ice Sheet in Wolstenholme Fiord, NW Greenland only 10 km beyond present
England (1990; 1992)	Innuitian Ice Sheet supplanted by <i>Innuitian Sea</i> in its central areas at LGM; Innuitian Sea and Franklin Ice Complex near their limits during the interval 38–8 ka BP
Lemmen and England (1992)	Late Wisconsinan Franklin Ice Complex more extensive than any other Wisconsinan ice
Blake (1992a)	Smith Sound Ice Stream drained southward from Kane Basin fed by coalescent Innuitian and Greenland ice during LGM
Kelly and Bennike (1992)	Northern Nares Strait occupied by ice lobe derived from coalescent Ellesmere and Greenland ice during LGM; extensive ice-free land on both sides of strait
Bednarski (1995)	Peninsulas adjacent central Nansen Sound covered by coalesced local ice caps during last glaciation
Bell (1996)	Eureka Sound region, part of the axis of proposed Innuitian Ice Sheet, ice-free at LGM and occupied by Innuitian Sea
England (1996)	Northern Nares Strait and Kane basin ice free at LGM
Funder and Hansen (1996)	Nares Strait filled by coalescent Ellesmere and Greenland ice during Late Wisconsinan
England (1997)	Nares Strait filled by coalescent Ellesmere and Greenland ice during Late Wisconsinan

marine submergence for the CAA and summarized interpretations of the extent of glaciation. For the entire QEI, he listed striae at only one site. Erratics were more widely recorded but were regarded as problematic because many are below the limits of marine submergence and hence probably were ice rafted. Distinguishing between ice rafting and glacial transport remains a problem (Thorsteinsson, 1958; Hodgson, 1990). Evidence of emergence was widely noted but not well measured; nor was the extent of the rebounding region well defined. This virtual absence of data allowed a plethora of early opinions regarding glaciation (Table 1).

Table 1 shows that the debate about extent of glaciation has dominated since the beginning of publication on the region more than a century ago. It started well ahead of substantive observation and no consensus has even briefly emerged. The list of early interpretations overwhelms the list of observations (four striae recorded to 1958 but 34 published interpretations). Washburn (1947) (p. 47) reflected this imbalance when he ended his summary of previous work with the statement: 'These widely divergent views reflect our lack of facts regarding the area.' Four decades later, Hodgson (1989) concluded: 'Notwithstanding local studies... there is still insufficient evidence for models of late Quaternary ice cover to be anything but speculative.' Thus, this problem has remained intractable to the present day.

Narrowing of the spectrum of interpretations also has been limited. The option that the present glacier cover is the largest of the Quaternary (e.g. Schei, 1903; Low, 1906) seems to have been abandoned. Apart from that, the range of interpretations has continued to ex-

pand. For example, England (1987) reasoned that if there ever was a regional ice sheet over the islands, it likely preceded formation of the inter-island channels during the late Tertiary because the large channels would have precluded formation of regional ice sheets by the efficacy of calving in deep water. Lemmen and England (1992) further concluded that the LGM Franklin Ice Complex, which extended only modestly beyond present glacier margins, was the most extensive of the entire Wisconsinan Stage. In contrast, Fulton (1989) suggested that the Wisconsinan *Laurentide* Ice Sheet covered all islands except Ellesmere and Axel Heiberg. The other extreme in terms of extent of Late Wisconsinan ice cover is the Panarctic Ice Sheet concept of Hughes *et al.* (1977) and Grosswald (1984), wherein an Innuitian dome is part of one continuous Northern Hemisphere ice sheet and ice shelf complex.

Some terminological confusion has arisen and hampers attempts to understand interpretations. For example, the Queen Elizabeth Islands Glacier Complex of Prest (1970) was based on the Innuitian Ice Sheet model, but Prest (1984) used the same name for a very different ice configuration based on the Franklin Ice Complex model. Prest's Glacier Complex, therefore, has become an ambiguous alternative for both and its continuance would not be helpful. Fulton (1989) restricted the Wisconsinan 'Innuitian Ice Sheet' to Ellesmere and Axel Heiberg Islands, while showing Laurentide ice over the rest of the QEI. Thus, his Innuitian Ice Sheet inappropriately becomes smaller and takes on an even more alpine character than the Franklin Ice Complex. On another map showing the same ice distribution

(Andrews, 1989), Fulton's Innuitian Ice Sheet is more appropriately labelled 'Franklin Ice Complex', but both, itself and the neighbouring Laurentide ice over the QEI are assigned to the Late Wisconsinan. We must bear in mind that both contending models are hypothetical but strictly pertain only to Late Wisconsinan time.

The foregoing should not be taken to mean that little progress has been made in studying the Quaternary history of the QEI. Despite lack of clear evidence for extensive *Late Wisconsinan* glaciation in many areas, with the exception of the Smith Sound region (Blake, 1992), a rich database has grown for Holocene emergence, mainly from the efforts of Blake (1970, 1975, 1992, 1993), England (1976b, 1978, 1982, 1985, 1990, 1996), McLaren and Barnett (1978), Hodgson (1982, 1985), Bednarski (1986, 1995), Retelle (1986), Lemmen (1989), and Evans (1990). Nevertheless, the nature of QEI glaciation during the Late Wisconsinan remains a prominent issue in North American Quaternary geology.

4.2. Interpretations of postglacial uplift

Two proposals of regional glaciation based on postglacial uplift were published in 1947 (Table 1). Because much of the subsequent discussion has centred on uplift, it is worth acknowledging these original statements. In considering the extent of glaciation, Washburn (1947) (p. 58) stated: 'Another line of evidence is suggested by the widespread recent emergence of the Arctic Archipelago.... To the extent that emergence in the definitely glaciated regions of the Canadian Arctic is a result of isostatic adjustment from removal of ice load, it suggests that considerable recent emergence of the less definitely glaciated areas may be of the same character. This would indicate widespread glaciation of the whole Arctic Archipelago.' Wickenden (1947) (p. 334) similarly reasoned: 'Doubt has been expressed that all the eastern islands were covered by glaciers. Much of them, however, show emerged beaches and marine sediments similar to those of areas... where these features are supposedly due to uplift following the melting of the ice load that had depressed the land... It seems probable, therefore, that the islands that show raised beaches may have been depressed by a load of ice in the same way as the mainland to the south.' Uplift, therefore, has historically provided the most conspicuous indication of glaciation in this region. But it has not been accepted as direct evidence of any one particular ice configuration.

Radiocarbon dating allowed measurement of uplift rates and a general advance of interpretation (Table 1). Andrews (1969) (p. 53) illustrated an uplift centre over the QEI but offered no explicit interpretation of ice configuration. He later (in Bryson *et al.*, 1969) stressed the lack of a 'break' between QEI and Laurentide uplift. Blake (1970) defined the pattern of emergence more precisely. Mainly on the basis of an axis of uplift since 5 ka BP that

trends through the centre of the archipelago, he proposed the *Innuitian Ice Sheet*. He inferred that it connected the Laurentide Ice Sheet to the Greenland Ice Sheet but that it spread from an independent ice divide (Fig. 1). Walcott (1972) drew a similar emergence pattern and inferred a similar ice configuration. In contrast, Andrews (1973) interpreted the QEI uplift centre as resulting from a northward extension of the central Laurentide ice divide. This model has never been discussed by regional workers, but it dictates different ice flow patterns in places and a somewhat different uplift pattern. England (1976b) figured QEI uplift as a westward protrusion of the Greenland uplift cell, with a saddle separating this from Laurentide uplift. Andrews (1989b) presented an isobase map on the 7 ka BP shoreline that showed a ridge of uplift over the QEI *rising* toward Greenland but a series of emergence-rate maps that showed maxima over the QEI *decreasing* toward Greenland. Thus, the pattern of uplift, as figured by different authors, has remained rather fluid.

The Innuitian Ice Sheet model offered perhaps the simplest explanation of the uplift. However, it was vulnerable because there was next-to-no direct glacial geological evidence of such an ice sheet *of that age*. The inter-island channels, for example, the basis of the Innuitian ice flow pattern as drawn by Blake (1970) (p. 658), must be older than Late Wisconsinan because the volume of Late Wisconsinan sediment in the adjacent marine basins is far too small to backfill them (e.g. Aksu, 1985). With the same implicit assumptions, the channels could be used to explain the flow pattern of any Quaternary ice sheet, just as they have been used to infer Tertiary river systems (Fortier and Morley, 1956) and tectonic rifting patterns (Kerr, 1980). Furthermore, Quaternary geological mapping in the central and western parts of the proposed Innuitian Ice Sheet yielded no direct evidence of a Late Wisconsinan regional ice sheet (Barnett *et al.*, 1976; 1977, Hodgson, 1977, 1982, 1990, 1992; Hodgson *et al.*, 1984; Hodgson, 1985; Edlund, 1991; Lemmen *et al.*, 1994; Bednarski, 1995; Bell, 1996), except possibly on Lougheed Island (Hodgson, 1981), where the ice flow features might also reflect an earlier Laurentide event (Glenister and Thorsteinsson, 1963; Fyles, 1965). Throughout large areas of sedimentary rocks, periglacial weathering and mass movement have removed most of the striae that may have existed and generated a colluvial cover similar to till (Dyke, 1983; Hélie and Elson, 1984; Hodgson, 1989).

More importantly, the recognition of broad zones of crustal depression (ca. 200 km) beyond the margins of ice caps and of other crustal loads (Brotchie and Silvester, 1969; Walcott, 1970; Farrell and Clark, 1976) opened the way for an alternative explanation of the uplift. In this alternative, the Laurentide and Greenland ice sheets depressed swaths of the QEI in their forefields and a series of intervening, noncontiguous ice caps accounted for the

rest (England, 1976a, 1983), or else tectonics did (Dyke, 1993a). While ice sheet reconstructions based on rebound continued to bolster the Innuitian Ice Sheet model (e.g. Walcott, 1972; Clark, 1980; Tushingham and Peltier, 1991; Tushingham, 1991), reasonable counter arguments were at hand (England *et al.*, 1991). Furthermore, nonunique glacial histories, reasonably compatible with the two contending models, were used to account for the same rebound data (cf. Tushingham, 1991; Peltier, 1994), thus illustrating the contention of Boulton (1979) and Andrews (1982) that only primary glacial geological evidence would constitute sufficient proof of former ice sheets, such as the Innuitian and Barents Sea (Schytt *et al.*, 1968) ice sheets, that had been inferred mainly from uplift patterns. One reviewer of the problem went so far as to state that Blake's (1970) proposition of an Innuitian Ice Sheet '... represents a misuse of uplift data. For a given isostatic history there is no unique history of glacial loading and unloading; the same pattern of uplift can be produced in an infinite variety of ways' (Boulton, 1979) (p. 377).

4.3. The current problem

Broader recent syntheses of glacial history have favoured both the Innuitian model (Hughes *et al.*, 1977; Mayewski *et al.*, 1981) and the Franklin model (Boulton, 1979; Dyke *et al.*, 1982; Prest, 1984; Dyke and Prest, 1987). Paterson (1977) considered the glaciological and geological evidence for both models and declared a draw. Similarly, glaciological modelling demonstrated little more, in this regard, than that realistic flow patterns will result when flowlines are computed from assumed margins (Mayewski *et al.*, 1981; Reeh, 1984). These would (will) be useful if there were independently mapped flow patterns and (or) margins against which to check the models. But there were none for the Innuitian Ice Sheet, and this approach will not resolve the issue of whether or not an ice sheet existed.

The nature of the debate, therefore, indicates that it will be resolved only by mustering one of the following: (1) direct evidence, other than uplift, of an LGM ice configuration that supports the Innuitian Ice Sheet model; or (2) firm evidence that ice cover was much less extensive, along with a means of explaining the thereby incongruent uplift pattern. The Quaternary geology of Devon Island appears to provide the first of these.

5. Methods

This study of Devon Island resembles previous efforts in the region south of Parry Channel (Dyke, 1983, 1984; Dyke *et al.*, 1992). These studies defined the landscape zonation resulting from glaciation by cold-centred ice

caps and the chronological implication of that zonation (Dyke, 1993b).

The approach was as follows: (1) map the glacial deposits and landforms from airphotos; (2) conduct field studies to gather samples to radiocarbon date deglaciation and emergence, to confirm apparent ice flow directions, and to determine till composition; and (3) finalise airphoto mapping as field work progressed.

Field work involved traversing by small all-terrain vehicles out of 15 camps, each for about a week, in 1993 and 1994. Airphotos served as traverse maps and were constantly checked and interpreted in several iterations to yield the final Quaternary geology maps. These are the basis of generalized maps presented below, but the full maps will be published elsewhere.

Only those radiocarbon dates pertaining to the advance to LGM limits and to deglaciation are considered here. Most of these are on marine mollusc shells and the ages are reported with a 400 yr marine reservoir correction, as has been the convention in this region (e.g. Blake, 1975). Elevations of radiocarbon samples and raised shore features were measured by Wallace and Tiernan surveying altimeter as detailed by Dyke *et al.* (1991).

6. Results

6.1. Events before LGM

Events prior to LGM have a limited geological record. Fossiliferous sediments are known from three locations and redeposited marine shells provide additional information.

Pre-Late Wisconsinan sediments. Pre-Late Wisconsinan glaciomarine sediment outcrops in a 40 m section on northwestern Grinnell Peninsula (Fig. 2). Poorly lithified pre-Quaternary mudstone is overlain by dropstone-rich mud containing abundant *Mya truncata* and *Hiatella arctica* in growth positions. These sediments extend to about 50 m altitude and the shells are > 34 ka old (GSC-5956; Table 2). They are overlain in places by oxidized gravel, which is capped by Holocene beach gravel. Because of the ice-proximal appearance of the sediment, its altitude, and indications of emergence and weathering, it is interpreted as recording recession of the penultimate or an earlier local glaciation despite lack of an overlying till.

A 0.5 m thick, shell-rich marine bed at 6.5 m altitude at Cape Ricketts has been dated > 34 ka old (GSC-5556). It directly overlies an oxidized zone and is overlain by 25 m of material that consists of Holocene beach sediment at the top (R.B. Taylor, pers. comm., 1996). The shell bed may record a marine transgression following a nonglacial interval, presumably in the early part of the last glacial cycle.

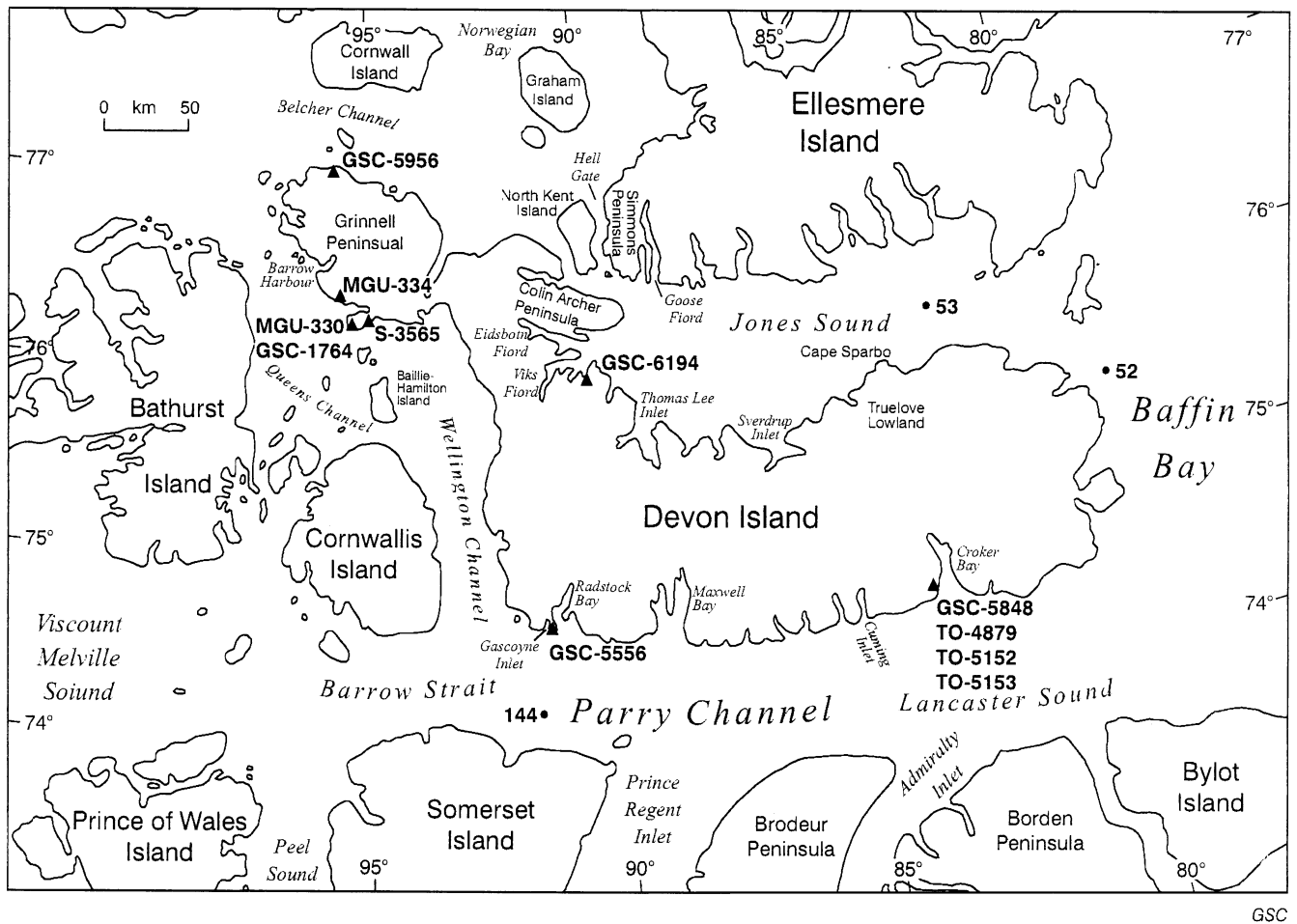


Fig. 2. Locations of radiocarbon samples related to pre-LGM events (Table 2) and marine sediment cores, HU83-023-053 (53), HU83-023-052 (52), and HU86-027-144 (144).

A bowhead whale (*Balaena mysticetus*) skull, collected half-way up the face of a 20 m stream-cut section on Sheills Peninsula, has been dated to > 33 ka BP (S-3565). The entire section is covered in colluvium, but most of the deposit appears to be well-rounded gravel. The section is capped by Holocene beach gravel. The underlying gravel and fossil apparently predate the last glaciation.

These three occurrences of pre-Late Wisconsinan sediment are within the limits of Late Wisconsinan ice. They thus represent the apparently rare occurrences of older sediment that escaped complete erosion during the last glaciation.

6.2. Redeposited marine shells

Glacially transported shells have been dated from five sites (Table 2). Those from Goose Fiord and Sheills Peninsula have nonfinite ages. However, a sample from Grinnell Peninsula yielded an age of $14,540 \pm 300$ yr (MGU-334). Although the collector (M.G. Grosswald) stated that these shells were from an 'ancient shore line',

the site is about 50 m above the Holocene marine limit as here recognized from the upper limit of shore features and the lower limit of meltwater channels. At face value, this result indicates ice-free conditions in Queens Channel at that time and advance to LGM limits thereafter. This result is anomalous and it is, therefore, unfortunate that no description of the dated shells is available. However, most surface shells in this area are encrusted with secondary (younger) carbonate, and this may explain the anomalous age determination.

Shells from two sites below the Holocene marine limit have given pre-Holocene conventional ages: (i) Barr (1971) reported four samples of this sort from Truelove Lowland. The oldest ages are finite and in the Middle Wisconsinan range (Table 2). However, because they were below marine limit, these samples may well have included postglacial shells. Hence, the dates should be taken as the minimum ages of an older group of shells. The two dates that fall in the Late Wisconsinan range are probably on mixtures with higher proportions of Holocene material. (ii) A sample from Sheills Peninsula

TABLE 2
Radiocarbon dates pertaining to pre-Late Wisconsinan events

Lab no. Field no.	Age	Species dated	Latitude, longitude	Location and Comments
GSC-5956 94DCA78	> 34,000	<i>Mya truncata</i>	77°02'58" N 95°42'07" W	13 km WNW of Lyall River, north coast of Grinnell Peninsula; paired valves in glaciomarine silt below oxidized gravel
GSC-5556 9208010	> 34,000	<i>M. truncata</i>	74°37.68' N 91°16.50' W	Cape Ricketts, inner Lancaster Sound coast; distinct shell bed in silty fine sand overlying an orange oxidized layer 5.5 cm thick (R.B. Taylor, <i>pers. comm.</i> , 1996)
S-3565 94DCA44	> 33,000	<i>Balaena mysticetus</i>	76°15'06" N 94°59'28" W	Sheills Peninsula, southern Grinnell Peninsula; skull protruding from gravel in midsection below Holocene beaches
GSC-865	> 34,000	Shells including <i>Hiatella arctica</i>	76°54' N 88°38' W	Inland of Goose Fiord, Ellesmere Island, at 98–101 m altitude; believed transported from Norwegian Bay (Blake, 1970)
GSC-1764 72MGG14	> 25,000	<i>M. truncata?</i>	76°17' N 95°01' W	Sheills Peninsula at 150 m altitude, well above marine limit; younger limiting age due to small sample (single shell, 3.0 g; Lowdon and Blake, 1973 (p. 39))
MGU-334	14,540 ± 300	Marine shells	76°23' N 95°37' W	near Stewart Point, Grinnell Peninsula at 150 m altitude; reported to be from a raised shore feature (Glushankova <i>et al.</i> , 1980) (p. 90) but well above marine limit
Y-1734	31,200 ± 1800	Marine shells		Lowland south of Cape Skogn, outer Jones Sound coast at 27 m altitude; below marine limit (Barr, 1971) (p. 253)
Y-1733	30,100 ± 1500	Marine shells		Truelove Lowland, outer Jones Sound coast at 36 m altitude; below marine limit (Barr, 1971) (p. 253)
Y-1297	16,000 ± 240	Marine shells		Truelove lowland at 23 m altitude; from surface of raised beach (Barr, 1971) (p. 253)
S-412	12,800 ± 160	<i>H. arctica</i> , mainly		Truelove Lowland at 15.5 m altitude; from surface of raised beach (Barr, 1971) (p. 253)
MGU-330	11,280 ± 160	Marine shells	76°15' N 95°16' W	Cape Becher, Sheills Peninsula at 84 m altitude, below marine limit (Glushankova <i>et al.</i> , 1980) (p. 90)
GSC-6194	39,900 ± 1800	<i>H. arctica</i>	75°53.36' N 90°14.41' W	Mouth of Viks Fiord at 70–80 m; numerous whole valves presumably redeposited in foreset sand of early Holocene delta (85.5 m terrace)
GSC-5848 94DCA226	23,200 ± 290	<i>H. arctica</i>	74°36'18" N 83°37'43" W	West side of outer Croker Bay, outer Lancaster Sound coast at 35 m altitude; marine limit at 37.5 m dated about 10,000 yr BP (See S-3595, Table 3)
TO-4879 94DCA226	27,240 ± 270	<i>H. arctica</i> , 1 shell	74°36'18" N 83°37'43" W	See GSC-5848
TO-5152 94DCA226	23,830 ± 250	<i>H. arctica</i> , 1 shell	74°36'18" N 83°37'43" W	See GSC-5848
TO-5153 94DCA226	25,410 ± 510	<i>H. arctica</i> , 1 shell	74°36'18" N 83°37'43" W	See GSC-5848

Laboratories: GSC, Geological Survey of Canada; MGU, Moscow MV Lomonosov State University; S, Saskatchewan Research Council; TO, IsoTrace, University of Toronto; Y, Yale University.

yielded an age of 11,280 ± 160 yr (MGU-330). Because this is much older than any reliable postglacial shell date from the region, it too is here regarded as a blended age.

Glacial transport and redeposition of shells is not always self-evident to the collector. A raised delta close to marine limit and deposited by glacial meltwater near the mouth of Viks Fiord (Fig. 2) yielded abundant whole

valves of *Hiatella arctica* from foreset sand. These shells were expected to date close to time of deglaciation in the early Holocene and they bore no signs of abrasion. However, they yielded an age of 39,900 ± 1800 yr (GSC-6194). Nevertheless, the delta is evidently part of the early Holocene sequence and the shells must have been recycled from an older deposit by ice or meltwater. Shells

that are contemporaneous with delta deposition and that were redeposited in the foreset beds from the delta top are indistinguishable from such older recycled shells from their sedimentary context.

Four ages were determined for a sample of shells collected from the till surface in front of a glaciomarine fan near Croker Bay (Fig. 2). As with the last sample discussed, these shells were expected to date about 10 ka BP and this age for marine limit was confirmed by dates on whale bones (see below). However, the shells gave a conventional age of $23,200 \pm 290$ yr BP (GSC-5848), which suggested redeposition. Three AMS determinations on individual shells from this sample, run to ascertain the range of ages, also returned finite ages between 23.8 and 27.2 ka BP. The spread of ages is compatible with the inferred redeposition.

Of the samples considered above, only the one from Croker Bay reasonably indicates an advance to LGM position within the range of radiocarbon dating. Elsewhere, the last advance of the ice margin appears to have occurred at an undetermined time before 33 ka BP. The clean, robust, unaltered shell material used for dating the Croker Bay sample, its radioactivity well above background, and the clustering of ages all argue against the finite age determinations being due to contamination. Therefore, the ages are accepted as accurate. This implies that, in the interval 27–23 ka BP, at least outer parts of Croker Bay and Lancaster Sound were occupied by the sea. The Devon ice core $\delta^{18}\text{O}$ record shows values intermediate between those of LGM and the Holocene at that time, as does the core from Agassiz Ice Cap on northern Ellesmere Island (Koerner *et al.*, 1987) and the Camp Century core from northwest Greenland (Dansgaard *et al.*, 1971).

Although there is no evidence of a general Middle Wisconsinan deglaciation of the central QEI, extensive ice recession may have occurred around the periphery. Blake (1980) assigned marine deposits dating 35–40 ka BP at Cape Storm to an interstade, the Cape Storm Nonglacial Interval, thus suggesting that much or all of Jones Sound was then free of glacier ice. Smith Sound and some eastern Ellesmere Island fiords also appear to have been ice-free around 30 ka BP (Blake, 1992b). Possibly, all of Nares Strait (England, 1996) and parts of western Ellesmere Island (England, 1990) and north west Greenland (Kelly, 1985) were ice-free around that time as well.

6.3. The Last Glacial Maximum

6.3.1. Ice extent

If any part of Devon Island escaped glaciation at LGM, it was the seaward-facing slopes of the mountains along Lancaster Sound near Cape Warrender (Fig. 1). These slopes show no apparent signs of glacial erosion. Inactive alluvial fans, unlike any others on the island, are

perched on the lower slopes as though graded to a base level that was stable for a while above the present.

6.3.2. Basal thermal zonation and ice flow pattern

The island displays a twofold landscape zonation similar to that described for Somerset Island, Borden Peninsula, Brodeur Peninsula, Cornwallis Island and Bathurst Island. These zones reflect the basal thermal zonation of the ice cover: an inner, cold-based zone and an outer, warm-based zone (Dyke, 1993b; cf. Sugden, 1978).

The outer zone (Fig. 3) bears evidence of weak to moderate glacial scouring. Scouring has created a roughened bedrock relief with numerous rock-basin lakes and ice molded eminences. Where freshly exposed from beneath till, the rock is striated. Till is widespread and is flow streaked or fluted in places. In general, the ice flow features describe a coastward flow from an ice divide over the axis of the island. End moraines are common (Fig. 4). The moraines, along with numerous lateral meltwater channels (Fig. 5), reveal the pattern of ice marginal recession in detail, thought to be of annual resolution where the channels are optimally developed (Dyke, 1993b).

The inner zone bears little evidence of subglacial erosion. The surface here may have changed little since the Tertiary and preglacial river valleys show little sign of modification. The bedrock surface is thinly mantled by coarse residuum on broad interfluves and on long, graded slopes with scarcely an outcrop. The clast composition of the residuum precisely reflects that of the underlying rock. Most valley floors and lower slopes have a mantle of material that is difficult to interpret but is tentatively mapped as till. On Somerset Island, a similar valley-floor mantle was mapped as colluvium (Dyke, 1983), because it seemed derived from residuum upslope. On Devon Island, however, there are many instances where this material does not seem to be a simple colluvial slope facies and in places it extends to upper slopes. Perhaps it is till derived from colluvium. If so, it represents some slight movement of debris at the base of the ice.

Only one glacial landform occurs in the inner zone. Lateral meltwater channels extend right back to the final remnants of the ice cap.

The contact between the rough outer zone and smooth inner zone (Fig. 3) can be readily mapped from airphotos along much of its length. A similar, though less accurate, zonation could be derived by simply drawing a line between terrain with and without lakes (cf. Sugden, 1978). The lake basins are best developed on flat lying sedimentary rocks and on Precambrian gneisses. On dipping sedimentary rocks, glacial erosion seems mainly to have enhanced the structural grain. The contact does not commonly coincide with any abrupt change in slope but its configuration reflects both general and rather fine topographic control of ice flow. For example, it reaches the coast over broad interfluves that might be expected to

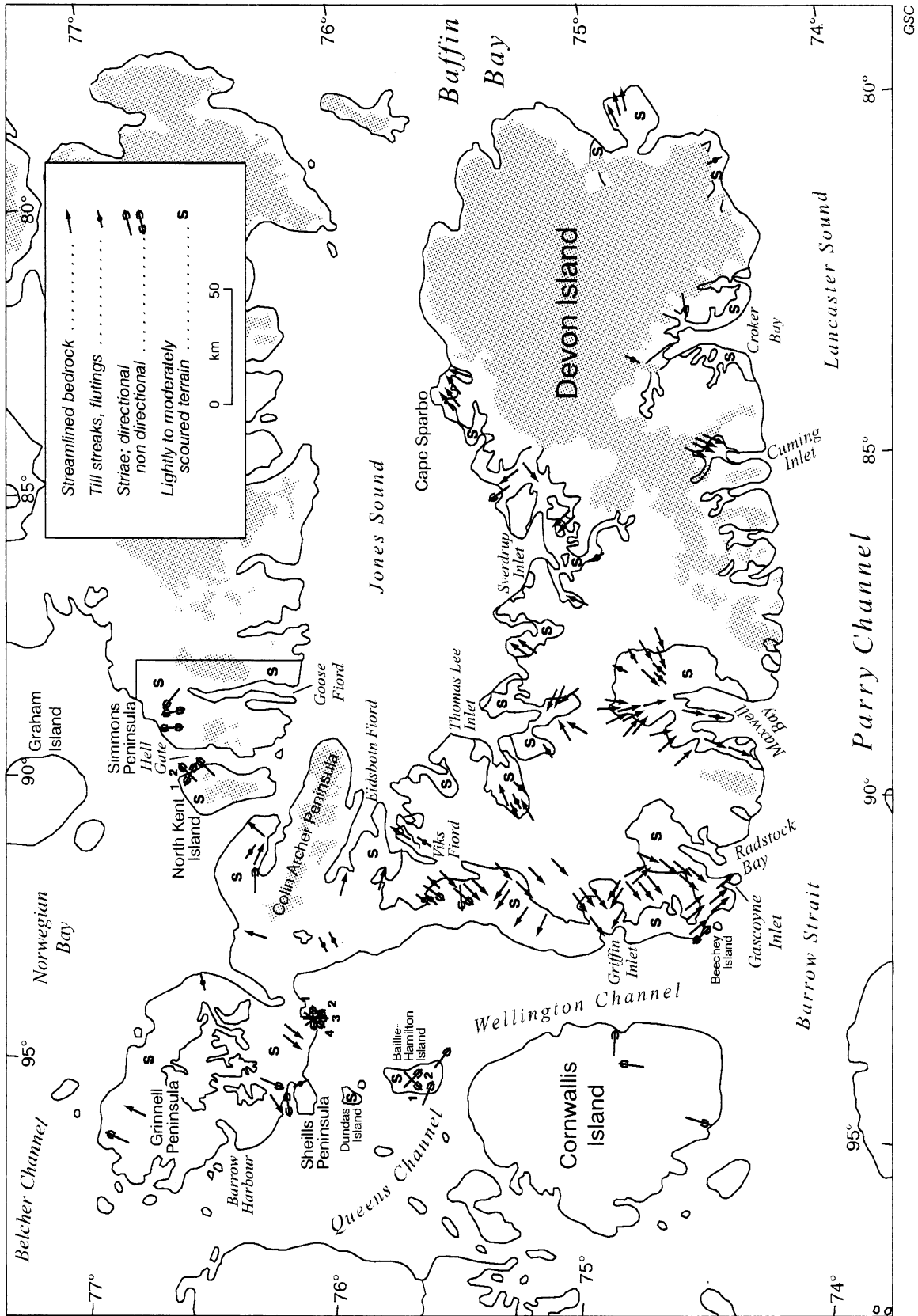


FIG. 3. Ice flow features and zones of glacial scouring of Devon Island and vicinity. The areas of scour are outlined and labeled "s". The present ice cover is stippled.

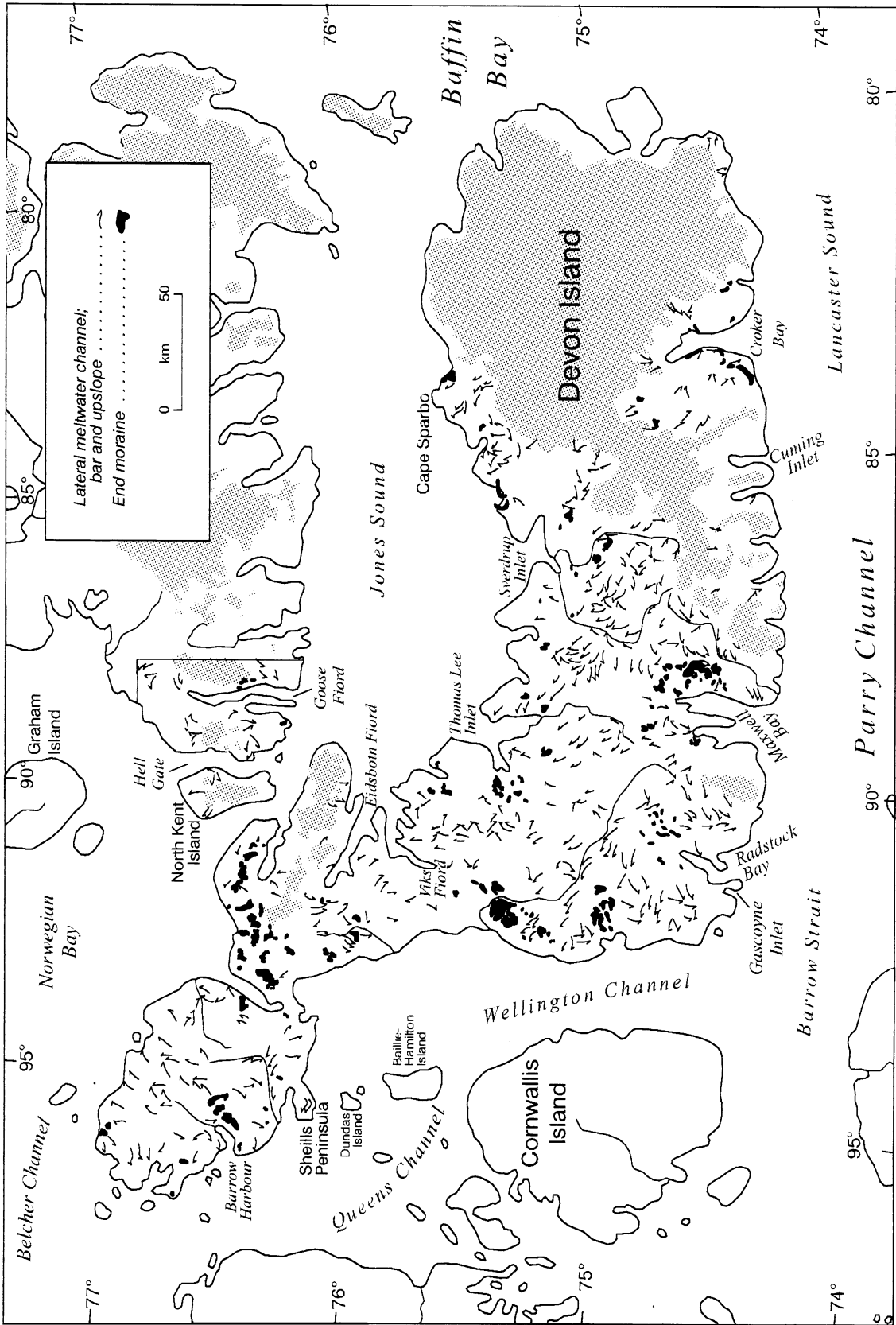


FIG. 4. Ice marginal features of Devon Island and vicinity. The black areas are end moraine accumulations; the arrows are lateral meltwater channels with the barb on the side away from the ice.

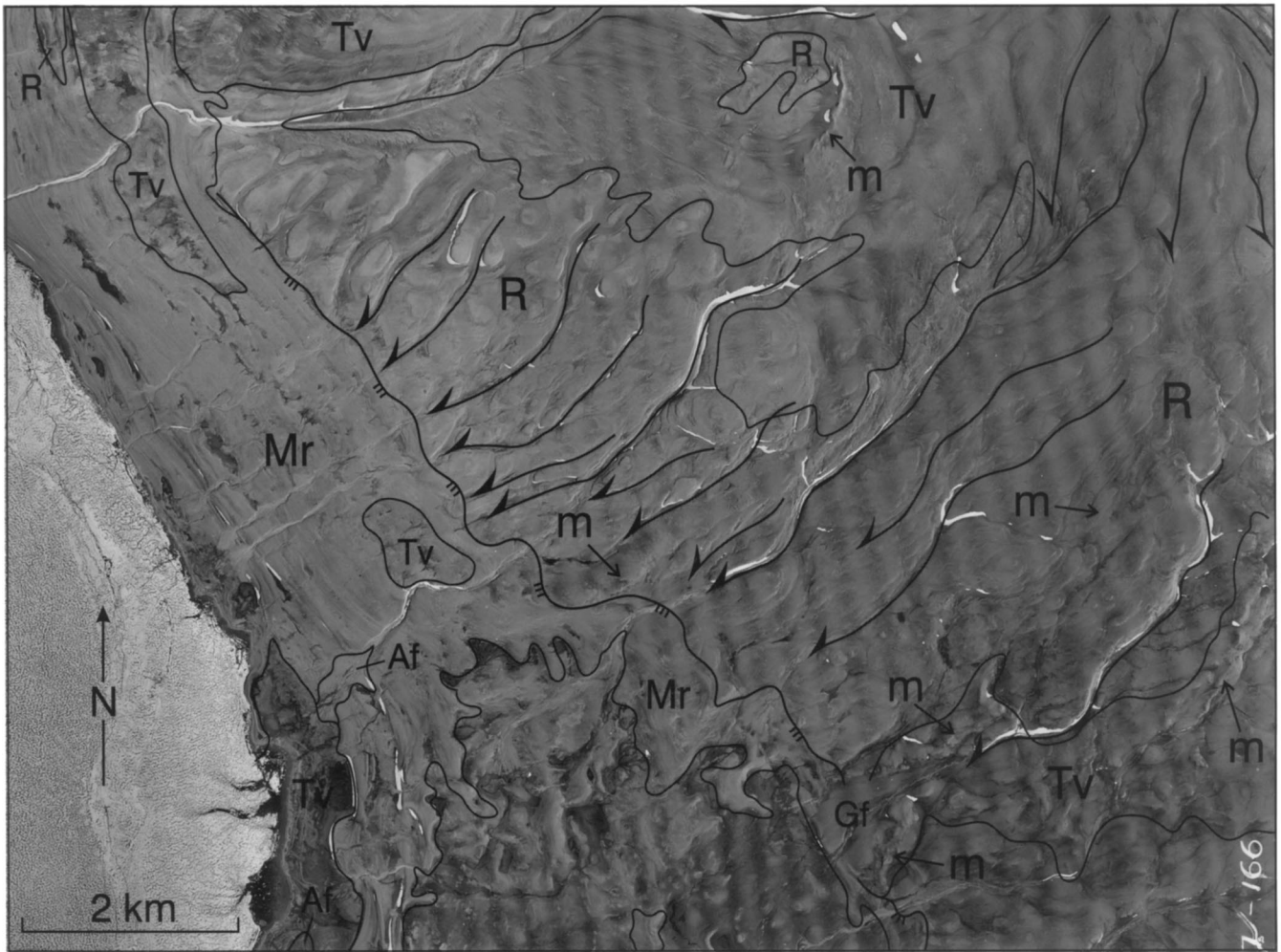


Fig. 5. Lateral meltwater channels (arrows with barbs on the upslope side) descending to marine limit (line with triple ticks) along Wellington Channel. End moraines are labeled 'm'; map units are alluvial fan (Af), glaciofluvial fan (Gf), raised marine beach ridges (Mr), bedrock (R), and till veneer (Tv). National Airphoto Library A16747-166; scale 1 : 60,000.

have set up ice flow divergence and is recessed inland along topographic lows that might be expected to have set up flow convergence. The largest recesses are inland of the largest inlets: Maxwell Bay, Radstock Bay, and Thomas Lee Inlet. Smaller recesses occur inland of Griffin Inlet and the valleys leading to Sverdrup Inlet, each in proportion to valley size. The pattern of mapped ice flow features confirms these relationships. Note, for example, the strong convergence into Maxwell Bay. Along several of these scour-zone reentrants there is an apparent increase in intensity of scouring toward the flow axes.

It takes more than 10 ka, probably more than 20 ka, for subglacial permafrost comparable to present thicknesses to dissipate after establishment of an ice cap the size of Devon Island [see Dyke, 1993b (p. 230) for calculations]. More time was then required to erode the glacier bed in the outer zone and to adjust the configuration of the thermal zones to the flow pattern. Considering

these requirements, it is unrealistic to ascribe either the zones or the related flow pattern to any transient deglacial phase. For these reasons, I ascribe these features as illustrated in Fig. 3 broadly to the LGM, that is to an interval well before the earliest phases of deglaciation. This time, rather than an earlier glacial maximum, is most reasonable because, as shown below, deglaciation patently occurred during the early Holocene.

6.3.3. Ice flow along Wellington Channel

To this point, the interpretation of the glacial features requires only flow from an ice divide over the island at LGM. Left there, the interpretation would better fit the Franklin Ice Complex model than the Innuitian Ice Sheet model. However, two areas also bear direct evidence of ice flow along Wellington Channel.

On the summit of Beechey Island and on two other adjacent plateaux at about 300 m elevation, ice flow

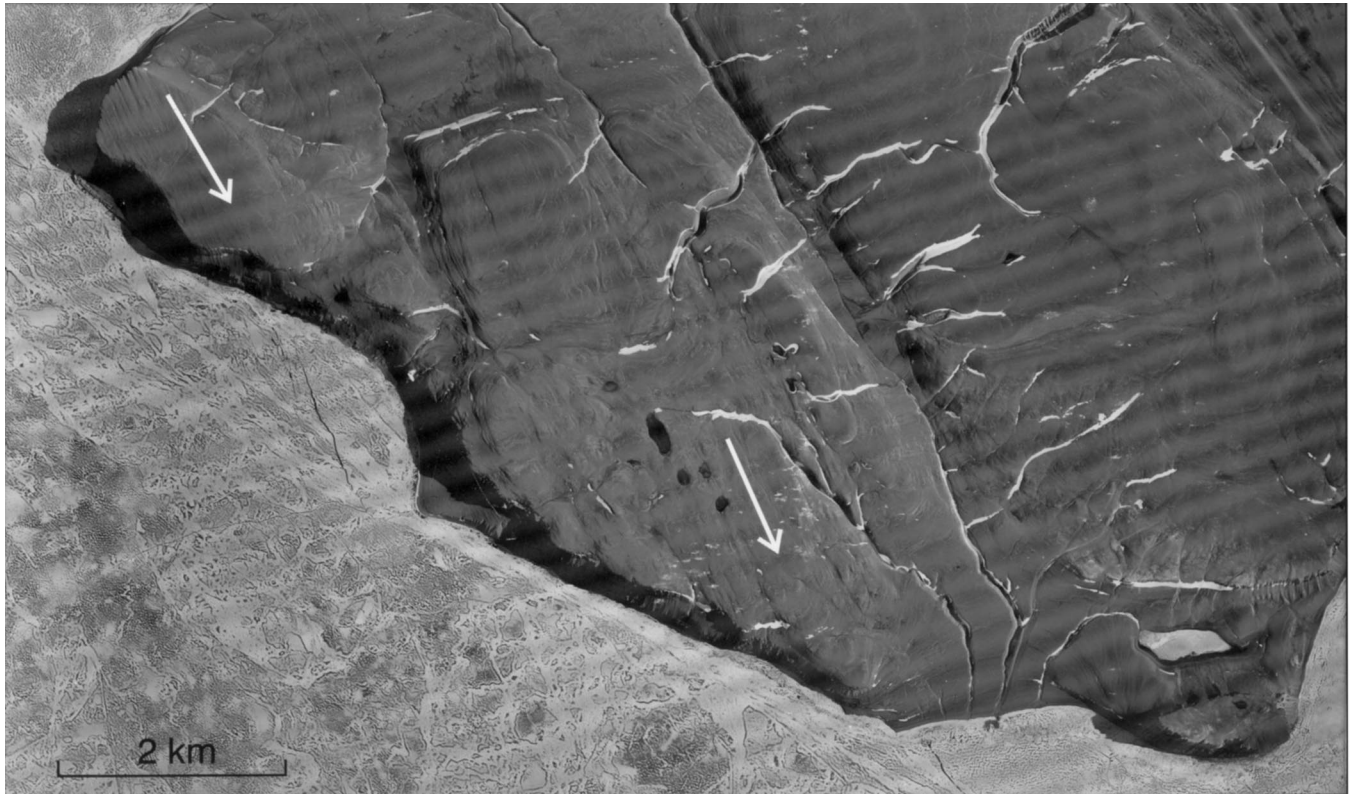


Fig. 6. Ice flow to the southeast (arrow) inscribed in horizontally bedded carbonate rock on the plateau west of Gascoyne Inlet. North is at the top. National Airphoto Library A16747-108; scale 1 : 60,000.

trending northwest-southeast is strongly inscribed in bedrock (Fig. 6). The slight bedform asymmetries (long tails) indicate that this flow debouched from Wellington Channel. Greiner (1963) recorded 'glacial striae with a westerly trend' on the top of Beechey Island. On his sketch map (p. 202), he plotted these striae as nondirectional, but with a trend nearly northwest-southeast. I take these striae as confirmation of the interpretation of the airphoto lineaments. On the main geological map in Fortier *et al.* (1963) and on the Glacial Map of Canada (Prest *et al.*, 1968) these striae incorrectly appear as indicating flow from the southeast; i.e. onshore from Lancaster Sound. This is a highly improbable flow direction given that all other indications are that ice in Lancaster Sound flowed eastward to Baffin Bay.

On Baillie-Hamilton Island, broad tonal streaks of till, as viewed on airphotos, indicate smearing of debris toward the southeast. Rat-tail striae, bedrock faceting and plucking confirm that these streaks are ice flow features (Fig. 3; Hättestrand and Stroeven, 1996). The till streaks, or weak flutings, are rather typical of the appearance of ice flow features on airphotos in the extra-Laurentide part of the CAA. Although weak, they form coherent, parallel sets independent of rock structure and are usually confirmed to be of glacial origin whenever striae can be found.

6.3.4. Age of ice flow along Wellington channel

The Innuitian Ice Sheet, as proposed, is a Late Wisconsinan feature because it was inferred from Holocene uplift. Thus, evidence of ice flow along Wellington Channel bears on the existence of this ice sheet only if that flow can be shown to have occurred during LGM or later. We must, therefore, consider whether it might have occurred earlier.

Lancaster Sound once carried an outlet glacier well into Baffin Bay (Klassen and Fisher, 1988). It deposited the Eclipse Moraines at its limit on the north slope of Bylot Island (Hodgson and Haselton, 1974; Klassen, 1985, 1993). Admiralty Inlet and Prince Regent Inlet carried tributaries, as shown by drift composition (Klassen, 1993). At the same time, Wellington Channel must have carried either a northward flowing tongue of Laurentide ice or a southward flowing tributary of QEI ice.

Klassen (1993) assigned the Eclipse Moraines to the Early Wisconsinan (his Early Foxe) because apparent post-eclipse marine sediments contain molluscs dated >40 ka old. That age assignment recently has been supported by ^{10}Be dating of Eclipse drift boulders to about 60 ka BP (McCuaig, 1994). In the absence of a cogent argument to the contrary, ice flowing along Wellington Channel might be assumed to be of the same age.

At present, we have no means of directly dating the ice flow along Wellington Channel because it left no ice marginal features that can be traced to dateable marine deposits. The preservation of striae on Baillie-Hamilton Island is not, in itself, proof of a Late Wisconsinan age because the striating phase could have been followed by a phase of till deposition, or of cold-based ice, under which the striae were preserved. Other lines of evidence are needed for convincing assignment of the Wellington Channel ice flow to the Late Wisconsinan. Three lines will be considered.

First, over a distance of about 200 km along the west coast of Devon Island, there is a parallel ice flow pattern toward the southwest (Fig. 3). That pattern is interrupted in places by younger flow oriented more directly toward the coast or into local basins. The older flow predates deglaciation and was strongly deflected from the path that it would have taken if there were no ice flowing along, or at the least nearly filling, Wellington Channel. If the earlier argument that the main ice flow pattern and landscape zonation on Devon Island date from LGM or a little later is correct, so does the Wellington Channel flow. The extensive convergent flow into the channel suggests that the style of flow there was that of an ice stream.

Second, an outcrop of sandstone on southeast Grinnell Peninsula (Fig. 3) illustrates the following flows: non-directional striae on an old facet trend along Wellington Channel and probably were formed by the ice stream; the younger facet bears cross-cutting striae that indicate a clockwise rotation of flow, culminating in southwestward flow. There is no reason to suspect that the earliest flow belongs to a different glacial stage than the youngest because the facets are not differently weathered. The youngest striae on Baillie-Hamilton Island also indicate southwestward flow (Fig. 3; Hättestrand and Stroeven, 1996). That flow was too brief to obliterate striae left by the earlier flow. Because the youngest striae there occur on the same rock facets as the older (Fig. 7), there probably was very little time separating their inscription. That is, the flow along Wellington Channel evidently dates from the same glacial stage as the younger flow.

There is further evidence that Devon ice flowed onto Baillie-Hamilton Island during the earliest phase of local deglaciation. Lateral meltwater channels on southern Sheills Peninsula (Fig. 4) record the thinning of an ice lobe centred off the present shore and emanating from the east. Extrapolation of these ice margins suggests that this lobe would have covered Dundas Island and probably Baillie-Hamilton Island. A parallel set of ice-marginal channels on northeast Baillie-Hamilton Island indicates ice recession towards Devon Island.

The Wellington Channel Ice Stream, therefore, is thought to have immediately preceded deglaciation. Its head must have been upstream of Baillie-Hamilton Is-

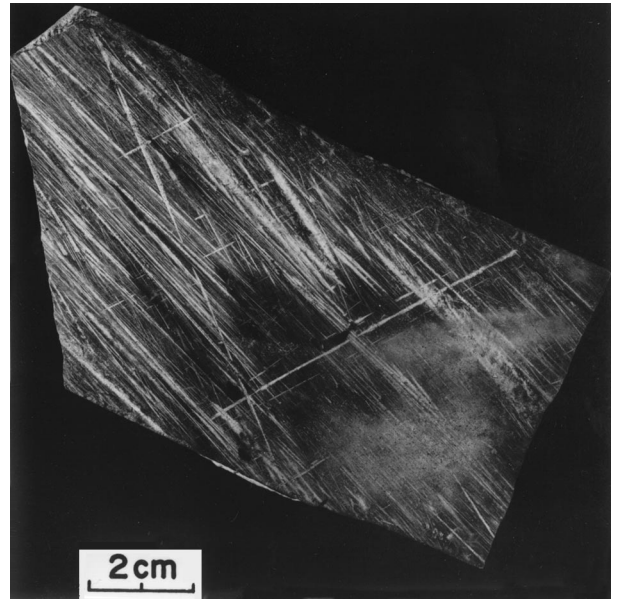


FIG. 7. Three sets of striae on a single rock facet on Baillie-Hamilton Island. The main, denser set is from the northwest. The final set is from Devon Island to the northeast.

land, which it crossed without deflection. The rebound data for Devon Island (Dyke, unpublished) indicate that the divide probably lay farther away than the western tip of Grinnell Peninsula.

If we accept Klassen's (1985, 1993) Early Wisconsinan age assignment of the Eclipse Moraines, the end of Wellington Channel Ice Stream must have been somewhere between these moraines and Gascoyne Inlet (Fig. 3). Dyke and Prest (1987) speculated that the Button Drift limit, which is just above sea level, and essentially horizontal, along the north coast of Bylot Island, represents the Late Wisconsinan limit of an ice shelf in Lancaster Sound. This is the first younger drift limit behind the Eclipse Moraines and it remains the most reasonable Late Wisconsinan limit, without more definitive studies. The lift-off line separating the Wellington Channel Ice Stream from the putative ice shelf has not been identified. The moraine at the south end of Wellington Channel mapped by MacLean *et al.* (1989) probably dates from an early phase of retreat.

6.3.5. Jones sound ice stream

Evidence of ice flowing along Jones Sound has been found on only one part of Devon Island. On the lowland and the adjacent plateau near Cape Sparbo, ice molded bedrock trending northeastward could only have been formed by ice flowing along the sound (Fig. 3). However, there is no evidence that coastward flow from the island was deflected by ice flowing along the sound. Hence, no strong argument can yet be made that the Jones Sound Ice Stream was a Late Wisconsinan feature. The relatively early date on marine sediment in the outer part of the

sound (discussed above) might also indicate a pre-Late Wisconsinan age for last glaciation of that site. Furthermore, ice filling Jones Sound is indicative of a regional ice extent and volume comparable to Eclipse Glaciation. On the other hand, a Late Wisconsinan age cannot be disproved and shoreline delevelling (Dyke, unpublished) indicates a greater Late Wisconsinan ice load in Jones Sound than in Lancaster Sound.

6.3.6. *Ice flow from Norwegian Bay*

Ice flow out of Norwegian Bay at LGM has been invoked to explain the otherwise anomalous position of Goose Fiord and the parallel, fiord-sized channels bounding North Kent Island (Fig. 3; Blake, 1970). However, erosion of the fiords could have occurred during any glaciation(s). The glacially transported marine shells collected north of Goose Fiord (Fig. 2; Table 2) may be supporting evidence of flow out of Norwegian Bay, but their nonfinite age does not constrain its timing.

Hättestrand and Stroeven (1996), as part of the current study, measured striae on four outcrops on North Kent Island. With one exception, these are best explained by flow during recession of a local ice cap. The other striae are oriented west-northwest to east-southeast and are non-directional (Fig. 3; unpublished GSC field notes). They could indicate flow into Hell Gate from Norwegian Bay or flow splaying onto the island from a glacier flowing northward through Hell Gate. The pattern of lateral meltwater channels in the region indicates a north-flowing glacier occupying Hell Gate during deglaciation.

Another indication of ice flow southward from Norwegian Bay was found on northwestern Grinnell Peninsula. A small patch of shelly red till occurs on the plateau, otherwise mantled by non-fossiliferous, light yellowish brown till, overlooking the bay. All other indicators of ice flow in this area are coastward.

6.3.7. *Distribution of erratics*

Despite the reference to a ubiquitous scatter of metamorphic and igneous erratics at all elevations on the Phanerozoic rocks Thorsteinsson and Mayr, 1987, p. 8, no Precambrian Shield erratics were noted above marine limit in eight camps involving several thousand kilometres of ground traversing on western Devon Island. One was noted on Baillie-Hamilton Island (Hättestrand and Stroeven, 1996), but they are common in places on Cornwallis Island (Edlund, 1991). Such erratics occur sparsely below marine limit on western Devon Island and are, hence, probably ice rafted. Shield erratics were noted above marine limit just east of Thomas Lee Inlet. LGM flow into the east side of Thomas Lee Inlet probably tapped the Precambrian rocks under the present ice cap (Fig. 3). The only common distinctive erratics on western Devon Island are sandstones on the carbonate rocks and carbonate stones on the sandstones. Black

shale supplied a till dispersal train on southern Grinnell Peninsula.

6.4. *Deglaciation*

6.4.1. *Method*

Because of the abundant ice-marginal features, the deglaciation of Devon Island can be mapped in detail. The generalized ice margins shown in Fig. 8 were derived as follows: (i) ice marginal features were drawn on 1:60,000 scale airphotos and correlated in stereoscopic view to ensure that reasonable ice surface gradients were employed in connecting features along and across valleys and across interfluves; (ii) these lines were plotted on 1:250,000 scale topographic maps and probable correlations were added based on trend and topography; (iii) the maps were reduced to 1:1,000,000 scale and selected ice marginal positions (generally, one out of about five to ten shown on the 1:250,000 scale maps) were drawn; (iv) radiocarbon dates pertaining to deglaciation (Table 3) were plotted and the ice marginal positions were assigned to age classes; and (v) the map was generalized and reduced to publication scale. Note that the pattern of ice recession was drawn completely, independently of the radiocarbon age determinations. Indeed, it was drawn on the airphotos and the 1:250,000 scale maps before the field work was started. The radiocarbon dates, thus, constitute a test of the interpreted ice retreat pattern.

6.4.2. *Pattern*

The deglaciation pattern is simple. The ice retreated inland and split into many small ice caps that finally melted at sites strung roughly along the LGM ice divide (cf. Figs. 3 and 8). Thus it appears that the pattern was largely dictated by the ice thickness and ice surface elevation at LGM. At least 17 retreat centres are recognized west of the present ice cap. Additionally, one each occurs on North Kent Island and Simmons Peninsula in the vicinity of extant ice caps. Additional retreat centres probably lie beneath the ice caps on Colin Archer Peninsula. The ice caps that occupy early Holocene retreat centres possibly survived throughout.

In contrast, the multidomed complex of ice that extends southwest from the main ice cap lies discordantly across the early Holocene retreat pattern (Fig. 8). Thus, these areas have been newly glaciated, presumably in the Neoglacial. However, the core, at least, of the main ice cap did not disappear during the Holocene as illustrated by the continuity of the summit ice core record. Survival of the central part of the Devon Ice Cap, while ice beneath other parts of the LGM ice divide completely ablated, could be due simply to the higher elevations of the eastern part of the island. The elevation difference from west to east across the island, typically about 300 m, was 130 m more at 8.8 ka BP because of isostatic tilting.

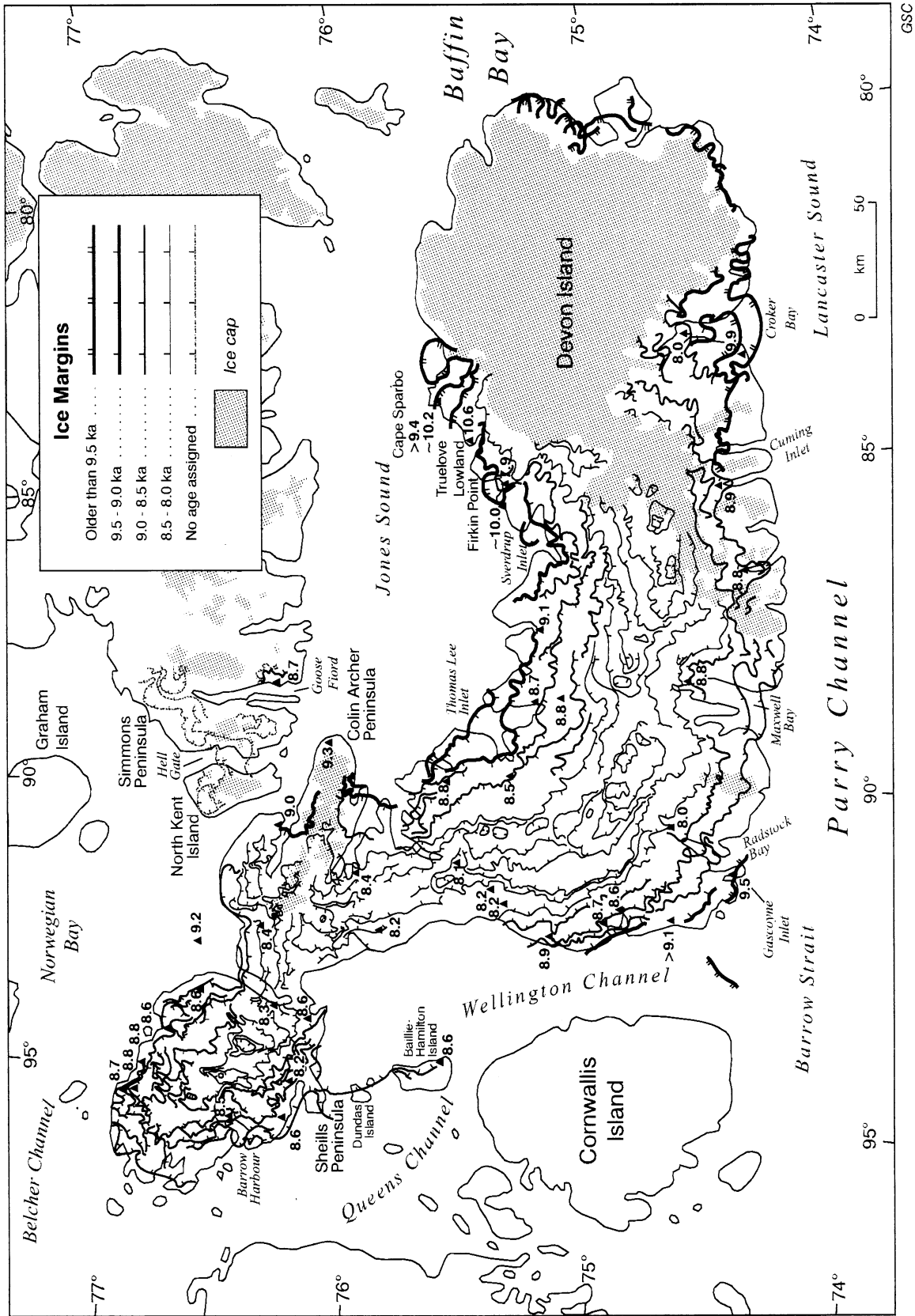


FIG. 8. Deglaciation of Devon Island and vicinity. Numbers are radiocarbon ages on deglaciation in millennia (cf. Table 3).

Table 3
Radiocarbon dates pertaining to deglaciation of Devon Island and adjacent areas

Lab no. Field no.	Age in ¹⁴ C yr	Species or material dated	Latitude, Longitude	Elev. (m) Sample (ML)*	Location and comments
Beta-14819	8920 ± 140	<i>Balaena mysticetus</i>	75°40' N 84°30' W	69 (86)	Truelove Lowland, outer Jones Sound coast; highest dated postglacial marine fossil from lowland (King, 1991)
MGU-331	8570 ± 120	Marine shells	76°23' N 95°31' W	98	Stewart Point, south coast of Grinnell Peninsula (Glushankova <i>et al.</i> , 1980) (p. 90)
GSC-858 67BS163	8720 ± 110	<i>Hiatella arctica</i>	76°28' N 88°18' W	120 (~120)	Goose Fiord, Ellesmere Island; surface of highest beaches (Lowdon and Blake, 1975) (p. 24)
GSC-866 67BS171	9260 ± 100	<i>H. arctica</i> , <i>Mya truncata</i>	76°17' N 89°22' W	114 (~120)	Cape Hawes, inner Jones Sound; highest beaches; close minimum date for marine limit (Lowdon and Blake, 1975) (p. 24)
GSC-874 67BS190	8950 ± 80	<i>Mya</i> sp., <i>H. arctica</i>	76°28.5' N 90°45' W	114 (≤125)	Berkeley Bay, inner Jones Sound; surface and active layer of muddy gravel (Lowdon and Blake, 1975) (p. 24)
GSC-907 67BS145	9780 ± 200	<i>H. arctica</i> , <i>M. truncata</i>	76°49' N 90°13' W	29-33	Norwegian Bay coast of North Kent Island; possibly mix of postglacial and older shells (Lowdon <i>et al.</i> , 1971) (p. 312)
GSC-1128 67BS204	8430 ± 140	<i>M. truncata</i>	76°57.5' N 95°22' W	94 ± 5	Lyall River, north coast of Grinnell Peninsula; shells from surface within 30 m of marine limit (Lowdon <i>et al.</i> , 1971) (p. 311)
GSC-1502 69MC104	9260 ± 150	<i>Balanus balanus</i>	74°40' N 91°25' W	105	Near west side of mouth of Radstock Bay, Lancaster Sound; elevation estimated (Blake, 1988) (p. 60)
GSC-1661 70BS252	8490 ± 160	<i>M. truncata</i>	75°32.5' N 89°59.5' W	73–76 (81)	Inland of west arm, Thomas Lee Inlet, Jones Sound; shells from gully incised in delta terrace (Blake, 1987) (p. 23)
GSC-1765 72MGG14	8500 ± 150	<i>M. truncata</i>	76°35' N 95°31.5' W	110 (116)	Head of Barrow Harbour, Grinnell Peninsula; from section in delta (Blake, 1987) (p. 23)
GSC-1810 72MGG16c	10,200 ± 140	Marine algae (seaweed)	76°35.2' N 95°33' W	51 (116)	Head of Barrow Harbour; from frozen sand and clay; very anomalous date (Blake, 1987) (p. 24)
GSC-3006 79MC1a	8400 ± 80	<i>M. truncata</i>	76°09.5' N 91°31' W	48	Eidsbotn, inner Jones Sound; from silt with dropstones and sand and gravel lenses (McNeely, 1989) (p. 73)
GSC-5653 93DCA100	8550 ± 70	<i>M. truncata</i>	76°19'59" N 93°53'49" W	86 (95)	Prince Alfred Bay, Wellington Channel; from slightly stony clay in small basin near marine limit
GSC-5659 93DCA12	8230 ± 90	<i>H. arctica</i>	75°37'04" N 91°33'29" W	66 (78)	Inland of Providence Mountain, Wellington Channel; whole and paired valves from glaciomarine silty clay with 10% dropstones
GSC-5662 93DCA158	8630 ± 90	<i>M. truncata</i>	76°51'28" N 94°13'56" W	84–90 (99)	Bere Bay, north coast of Grinnell Peninsula; whole and paired valves from section in marine-limit delta
GSC-5667 93DCA215	8830 ± 100	<i>M. truncata</i>	75°20'34" N 88°38'02" W	65–70 (79)	Inland of east arm, Thomas Lee Inlet, Jones Sound coast; whole valves from stony mud bottomset beds in marine-limit delta
GSC-5682 93DCA222	8720 ± 100	<i>H. arctica</i> , <i>M. truncata</i>	75°27'15" N 88°44'06" W	76 (102)	Head of east arm, Thomas Lee Inlet; fragments from till surface in front of glaciomarine fan marking marine limit
GSC-5698 93DCA155	8310 ± 110	<i>Astarte borealis</i>	76°27'18" N 93°41'49" W	75 (80)	Head of Arthur Fiord, Grinnell isthmus; from foreset sand in marine-limit delta
GSC-5732 93DCA204	8840 ± 80	<i>M. truncata</i>	76°57'35" N 94°52'28" W	86 (114)	Whitmore Point, north coast of Grinnell Peninsula; whole valves eroding from section in marine-limit delta
GSC-5733 93DCA45	8240 ± 110	<i>H. arctica</i> , <i>M. truncata</i>	76°04'21" N 92°21'56" W	71 (84)	Inland of Owen Point, Wellington Channel; surface of stony silt close to marine limit shoreline
GSC-5737 93DCA264	7930 ± 90	<i>H. arctica</i>	75°33'25" N 85°21'16" W	26 (43)	East of Firkin Point, Jones Sound; whole valves from surface of stony mud on foreslope of marine-limit delta behind end moraine
GSC-5739 93DCA195	8610 ± 80	<i>H. arctica</i>	76°45'55" N 93°32'42" W	90–96 (101)	Wilmer Bay, northeastern Grinnell Peninsula; whole valves from gullies in glaciomarine stony silt; gravel pad at 101 m probably remnant of original delta terrace

TABLE 3. (Continued)

Lab no. Field no.	Age in ¹⁴ C yr	Species or material dated	Latitude, Longitude	Elev. (m) Sample (ML)*	Location and comments
GSC-5850 94DCA24	8200 ± 90	<i>M. truncata</i>	76°22'33" N 94°55'22" W	84 (91)	Inland of Inglis Sound, south coast of Grinnell Peninsula; paired valves from section in delta at mouth of meltwater channel
GSC-5853 94DCA67	8680 ± 110	<i>H. arctica</i>	77°00'45" N 95°23'00" W	126 (131)	Lyall River, north coast of Grinnell Peninsula; fragments and whole valves from surface of beach gravel 5 m below highest beach; site stratigraphically older than GSC-5859 despite slightly younger age determination
GSC-5856 94DCA113	8440 ± 90	<i>H. arctica</i>	76°32'29" N 92°24'33" W	100 (110)	Triton Bay, Norwegian Bay coast; fragments and whole valves from surface of glaciomarine stony silt
GSC-5859 94DCA64	8760 ± 100	<i>H. arctica</i>	76°57'37" N 95°15'16" W	107 (117)	Lyall River; whole valves eroding from stony mud in section in marine-limit delta
GSC-5874 94DCA426	8620 ± 80	<i>M. truncata</i>	75°46'30" N 94°21'00" W	103 (≥ 110)	Central east coast of Baillie-Hamilton Island, Wellington Channel; from surface of raised beaches; highest beaches at 110 m
GSC-5940 9208015	9470 ± 90	<i>H. arctica</i>	74°39.3' N 91°17.9' W	115 (115)	Gascoyne Inlet, inner Lancaster Sound coast; from surface of silty pebble gravel on highest marine terrace (R.B. Taylor, <i>unpublished</i>)
GSC-6184 97DCA8	9090 ± 110	<i>H. arctica</i>	75°25.89' N 87°36.01' W	60 (69.5)	Fiord south of Nookap Island, Jones Sound coast; whole valves from freshly cut section in foreset beds of marine-limit delta
GSC-6185 97DCA13	8820 ± 100	<i>H. arctica</i>	74°37.04' N 86°47.08' W	39 (55)	Head of Stratton Inlet, Lancaster Sound coast; whole valves from foreset sandy gravel in section through marine-limit delta
GSC-6187 97DCA14	8760 ± 100	<i>H. arctica</i>	74°50.64' N 88°25.27' W	30–36 (56)	Ryder Inlet, Maxwell Bay, Lancaster Sound coast; whole valves from stony mud at toe of marine-limit delta
GSC-6189 97DCA16	8040 ± 80	<i>H. arctica</i>	74°54.18' N 90°34.74' W	40 (64.75)	Head of Radstock Bay, Lancaster Sound coast; whole valves from stony mud on lower foreslope of marine-limit delta; delta attached to end moraine
GSC-6191 97DCA11	8860 ± 80	<i>H. arctica</i>	74°41.42' N 85°34.10' W	19 (41.5)	Head of Powell Inlet, Lancaster Sound coast; whole valves eroding from stony mud just in front of marine-limit delta
GSC-6192 97DCA7	8750 ± 100	<i>M. truncata</i>	75°47.45' N 90°04.33' W	55 (94.5)	Sandhook Bay, inner Jones Sound coast; whole valves from foreset sand of delta with terrace at 86 m; this delta is glaciofluvial but an adjacent delta occupies marine limit at 94.5 m altitude
GSC-6197 97DCA5	8130 ± 90	<i>H. arctica</i>	75°45.33' N 91°12.40' W	55 (55–60)	Head of Viks Fiord; inner Jones Sound coast; whole valves from surface of eroding slightly stony silt at edge of a large delta terrace
GSC-6198 97DCA3	8900 ± 100	<i>H. arctica</i>	75°23.04' N 92°14.19' W	75–90 (102)	Macormick Bay, Wellington Channel coast; whole valves from surface of eroding stony mud just in front of marine-limit delta
GSC-6200 97DCA4	8170 ± 90	<i>H. arctica</i>	75°36.06' N 91°47.17' W	34–40 (83)	Dragleybeck Inlet, Wellington Channel coast; whole valves eroding from thick glaciomarine silt in front of marine-limit delta
GSC-6201 97DCA1	8610 ± 90	<i>H. arctica</i>	75°07.98' N 91° 46.35' W	35–40 (66.5)	Sophia Cove, Wellington Channel coast; whole valves eroding from stony prodelta mud in front of marine-limit delta terrace
GSC-6203 97DCA2	8730 ± 80	<i>H. arctica</i> & <i>M. truncata</i>	75° 11.29' N 92° 00.83' W	75 (90.5)	Griffith Inlet, Wellington Channel coast; fragments and whole valves from surface of till and thin marine mud in front of marine-limit delta
S-413	9570 ± 130	<i>H. arctica</i> , mainly	75°40' N 84°33' W	23 (86)	Truelove Lowland, outer Jones Sound coast; oldest dated postglacial shells from lowland (Barr, 1971; King, 1991)
S-3572 94DCA173	9420 ± 200	<i>B. mysticetus</i>	75°46'24" N 83°51'17" W	64.5 (114)	Cape Sparbo-Hardy Lowland, outer Jones Sound coast; highest and oldest dated marine material; beach well below marine limit
S-3580 94DCA203	9540 ± 200	<i>B. mysticetus</i>	74°34'27" N 83°39'27" W	32.5 (37.5)	Cape Home, Croker Bay, outer Lancaster Sound coast; highest dated postglacial marine fossil; see S-3595

TABLE 3. (continued)

Lab no. Field no.	Age in ¹⁴ C yr	Species or material dated	Latitude, Longitude	Elev. (m) Sample (ML)*	Location and comments
S-3595 94DCA245	9920 ± 180	<i>B. mysticetus</i>	74°35'39" N 83°31'45" W	13 (37.5)	Cape Home; oldest dated postglacial marine fossil; close minimum age for marine limit
S-3597 94DCA261	9120 ± 200	<i>B. mysticetus</i>	74°57'38" N 91°59'55" W	76.5 (91)	Lovell Point, outer Wellington Channel coast; oldest dated postglacial marine fossil
TO-564	10,600 ± 160	Organic fraction of marine mud	75°39' N 84°33' W	4.53	Phalarope Lake, Truelove Lowland; total organic carbon from core (Young and King, 1989) (p. 211)
TO-566	10,570 ± 200	Organic fraction of marine mud	75°39' N 84°33' W	21	Fish Lake, Truelove Lowland; total organic carbon from core; agrees with TO-564 (Young and King, 1989) (p. 211)
TO-2012	9230 ± 90	<i>Astarte montagui</i>	76°47.1' N 92°42.0' W	– 184	Core 87-027-08 (GSC Atlantic) off mouth of Arthur Fiord, Norwegian Bay coast (P.J. Mudie, <i>pers. comm.</i> 1997)
TO-6317	8020 ± 110	<i>Macoma calcaria</i>	74°45.7' N 83°13.1' W	– 394	Core HU74-026-095, Croker Bay, about 5 km off present calving glacier front (W. Blake, Jr, <i>pers. comm.</i> 1997)

Laboratories: Beta, Beta Analytic; GSC, Geological Survey of Canada, MGU, Moscow State MV Lomonosov University; S, Saskatchewan Research Council; TO, IsoTrace, University of Toronto.

Note: GSC reports ages with a 2σ error term; the other ages are reported with a 1σ error term. All marine shell ages from GSC are reported with a reservoir correction of 400 yr. A 410 yr reservoir correction was applied to 'TO' shell ages, as is the practice at that laboratory. Whale bone ages from SRC are reported uncorrected for either carbon isotope fractionation or for marine reservoir effect. The reporting protocol for the Beta Analytic whale bone age was not published.

*ML: marine limit.

The extent of Holocene retreat of the Devon Ice Cap is unknown. However, supraglacial debris in places on the southeastern part of the ice cap appear to be remnants of terminal moraines which suggests that this part of the margin has readvanced at least 20 km.

6.4.3. Chronology

Deglaciation of the eastern coasts was underway by 10 ka BP (Fig. 8). The two dates of 10.6 ka BP on disseminated organic matter in marine sediment on Truelove Lowland (King, 1991; Table 3) may be slightly too old because this kind of sediment commonly contains some redeposited organic matter. The marine limit shoreline at Cape Sparbo, which was deglaciated somewhat earlier, dates about 10.2 ka BP by extrapolation of the local relative sea-level curve. The marine limit shoreline at Firkin Point, which was deglaciated about the same time as Truelove Lowland, has an age of about 10 ka by the same procedure. Thus, by 10 ka BP the margin lay close to the northern, eastern and southern margins of the present ice cap. Given the configuration of this ice margin, any contemporaneous ice in Jones Sound probably did not extend beyond Sverdrup Inlet and any ice in Lancaster Sound probably did not extend beyond Cuming Inlet.

The sea reached the mouth of Wellington Channel by 9.5 ka BP and the head of Jones Sound by 9.3 ka BP

(Fig. 8). Ice retreat appears to have been minimal between 9.5 and 9.0 ka BP. However, the sea reached the north coast of Grinnell Peninsula by 8.8 ka BP, probably from the northwest, and ice did not extend far off that shore at 9.2 ka BP (TO-2012; Table 3). Ice flowing into Wellington Channel was able to prevent full penetration of the sea until 8.2 ka BP. Retreat after 8.1 ka BP is not dated. However, if the rate of ablation remained similar, the final ice remnants west of the ice cap probably were gone about 8 ka BP. The Devon Ice Cap, therefore, probably reached its Holocene minimum after 8 ka BP. The Devon δ¹⁸O record shows least negative values, which are usually interpreted as maximum local temperatures, about 5 ka BP, so presumably recession continued until then (Fisher, 1979; Koerner, 1989). Either the retreat rate slackened after 8 ka BP or most of the ice cap had melted by 5 ka BP. Alternatively, the Devon δ¹⁸O record may reflect influences aside from temperature such as location of moisture sources and season of precipitation (cf. Dyke *et al.*, 1996).

6.4.4. The Cockburn interval on Devon island

The Cockburn Substage was defined as the interval 9–8 ka BP (Andrews and Ives, 1978). The distinctive Cockburn event was the construction of large end moraines around the northern and northeastern Laurentide Ice Sheet (Falconer *et al.*, 1965), which suggests

that this was a period of positive mass balance. Dyke and Morris (1990) proposed that the positive mass balance that allowed construction of the northern moraines was made possible by the newly established summer-open sea in the CAA, which supplied moisture and fog to the still glaciated areas.

The deglaciation record of Devon Island is equivocal with respect to this glaciological interpretation of the Cockburn Substage. On the one hand, ice retreat on land apparently was slower before 9 ka BP than between 9 and 8 ka BP (Fig. 8). On southwestern Devon Island, where chronological control is best, recession before 9 ka BP proceeded at about 30 m a^{-1} . Recession between 9 and 8.1 ka BP ranged from about 30 to 75 m a^{-1} where it can be best measured. On the other hand, many end moraines were deposited throughout the entire interval of recession prior to 8.1 ka BP (cf. Figs 4 and 8). These moraines may indicate that the whole interval 10–8.1 ka BP was one of only slightly negative mass balance, punctuated by positive mass balance excursions. The apparently slower terrestrial retreat during the interval 10–9 ka BP could be due to ice-profile equilibration after calving in the channels. Nevertheless, the formal lower boundary of the Cockburn Substage at 9 ka BP has no apparent paleoclimatic significance here in either the deglaciation or the ice-core records.

6.4.5. *An anomalous deglaciation date*

One of the age determinations listed in Table 3 is anomalous and needs to be explained and discarded. M.G. Grosswald collected marine macroalgae (Phaeophyta, identified by M. Kuc, GSC unpublished Bryological Report 205) from deltaic sediment near the head of Barrow Harbour and Blake (1987) (p. 24) reported an age determination of $10,200 \pm 180 \text{ yr}$ (GSC-1810). This result is far older than any other date on deglaciation from Grinnell Peninsula, and molluscs from just below marine limit near this site returned an acceptable age of 8.5 ka (Fig. 8). The laboratory notes on the sample indicate that algae comprised no more than 5% of the weight of material utilized based on its CO_2 yield on burning; the remaining material was mainly dolomitic sand. Although the mixture was subjected to dissolution in HCl, the anomalous age suggests that some of the gas that was used may have evolved from fluxing of carbonate.

7. Discussion and conclusion

It has been persistently difficult to establish the primary glacial geological record of the QEI, even that of the last glaciation. For over a century, therefore, scientists have argued widely divergent interpretations. Those who have viewed the problem from afar have generated

as diverse a spectrum of opinions as have the relatively few regional field scientists. The more general, and at times persuasive, arguments have been in play from early days and have remained forceful (Table 1): for example, hyperaridity as the cause of limited glaciation; low temperatures as the cause of complete glaciation; plant distributions indicative of refugia; inter-island channel patterns as the basis of ice sheet configuration; and regional emergence as evidence of regional glaciation. The latter has provided the most substantive evidence because at least it has a firm chronology, but the pattern of uplift has not been consistently drawn, nor have glacioisostatic interpretations converged on a single ice sheet history. Boulton (1979) even pronounced inference from uplift to be a *misuse* of data.

Field geologists typically have reported the lack of any definitive evidence of glaciation, sometimes even where it is relatively conspicuous, or only evidence of an apparently early Laurentide glaciation in the form of sparse erratics. Certainly, the glacial landform record of the CAA beyond the Late Wisconsinan Laurentide margin and outside the eastern mountain rim is subtle in comparison to that farther south. Interpretation has been further plagued by the difficulty of distinguishing between till and closely similar diamictos produced by periglacial weathering of sedimentary bedrock (e.g. Dyke, 1983). Rapid weathering has also largely eradicated the striation record. Thus, the primary glacial record has gone under-recognized (e.g. Fulton, 1995).

Proponents of a large ice sheet have at times admitted a complete lack of definitive geological evidence, excepting the rebound pattern. They have explained this through the contention that the ice sheet was cold based and left *no* geological record. This argument was never convincing, because even a cold-based ice sheet must melt and leave a landform and sediment record. In fact, cold-based ice leaves a more detailed record of recession, in the form of lateral meltwater channels, than does warm-based ice (Dyke, 1993b), as the record on Devon Island further exemplifies.

However, the regional ice cover was not entirely cold-based. It did leave a record of basal flow, at least in the vicinity of Devon Island. Although that record is subtle in comparison to the obvious landforms of the Laurentide Ice Sheet, the main evidence is caught on airphotos. Indeed, the main conclusions presented here were in place as firm hypotheses arising from initial airphoto interpretation in 1992.

During LGM a regional ice sheet, compatible with Blake's (1970) proposition of an Innuitian Ice Sheet, inundated the southeastern QEI. It must have also extended much farther to the west and northwest. The central dome, or part of the central divide, of the ice sheet lay either over Grinnell Peninsula or more probably, on the basis of the rebound pattern (Dyke, unpublished),

farther northwest. Flow from the centre, combined with flow from an ice divide over Devon Island and probably also from domes over Bathurst and Cornwallis Islands, sustained an ice stream in the Wellington Channel. This flow is not compatible with Andrews' (1973) hypothesis of a northward-plunging Laurentide ice divide over the QEI. At least one part of the Devon ice margin was advancing to its LGM limit about 23 ka BP. Recession was underway by 10 ka BP and was probably complete west of the ice cap about 8 ka BP. Throughout that interval, recession was slow and, until 8.1 ka BP, was punctuated by moraine building. The retreat pattern appears to have been controlled by the ice thickness and ice surface elevations at LGM.

As presently resolved, the record of Wisconsinan terrestrial glacial events is simple in comparison to that inferred from ice-rafted detrital carbonate layers in Baffin Bay cores (Andrews and Meese, 1997). These layers are thought to record regional iceberg release during ice-marginal recessions brought on by sudden warming events. Perhaps the details of ice marginal fluctuations of the near-maximal ice sheets in the High Arctic will be found most clearly in Baffin Bay sediments. However, most of the carbonate terrain around the head of Baffin Bay was deglaciated, presumably largely by iceberg calving, after 10 ka BP. Yet there does not appear to be a correlative DC layer in the deep Baffin Bay cores. Such a layer may be present on the northeastern Baffin Shelf, though carbonate levels there are low and the chronology not yet well established (Andrews *et al.*, 1989).

If the existence of the Late Wisconsinan Innuitian Ice Sheet can now be accepted, we can move forward to addressing the next tier of questions. The major unresolved problems of the Late Wisconsinan glacial history within the QEI include (1) defining the extent of northward or northwestward Innuitian ice flow, (2) defining the extent of Innuitian ice penetration into Eureka Sound between Ellesmere and Axel Heiberg islands (Fig. 1) and its interaction with alpine ice on these islands, and (3) defining the limit of grounded ice in Lancaster and Jones sounds. Evolution of the Innuitian Ice Sheet from pre-Late Wisconsinan ice covers is entirely unresolved, as is the manner in which ice filled the large marine channels. The age of Laurentide glaciation of the QEI is also unresolved so it remains tenable that the Innuitian Ice Sheet evolved from an earlier Wisconsinan Laurentide ice cover (Fulton, 1989), although growth from island ice caps seems more in line with the modern climate and state of glacierization. Delimiting Middle Wisconsinan deglaciation is critical to addressing these problems, but this will remain difficult because of the uncertainty about the meaning of finite radiocarbon age determinations, at least those in the middle and older part of that age range.

Acknowledgements

Field work in 1993, 1994 and 1997 was supported with its usual excellence by Polar Continental Shelf Project, Natural Resources Canada. No less valued is the support of GSC's Radiocarbon Laboratory through its Director R.N. McNeely and the services of the Saskatchewan Research Council and IsoTrace laboratories, University of Toronto. My appreciation goes to W. Blake, Jr. (GSC Ottawa), R.B. Taylor, and P.J. Mudie (GSC Atlantic) for advising me of their unpublished radiocarbon dates. Field assistance was provided by Cheryl Miller in 1993 and Matthew Dance in 1994, working out of my field camps, and by volunteer graduate students, Clas Hättestrand and Arjen Stroeven (Stockholm University) in 1994, working separately. J. England and C. ÓCofaigh (University of Alberta) accompanied the author in the field in 1997. Graphics were rendered by Jill Coulthart and Ed Bélec (GSC Ottawa). My thanks to W. Blake, Jr and D.A. Hodgson (GSC Ottawa), J. Bednarski (GSC Calgary), and I.A. Brookes (York University) for informal reviews and to P.U. Clark (Oregon State University) and J.T. Andrews (University of Colorado) for helpful formal reviews.

References

- Aksu, A. E. (1985). Climatic and oceanographic changes over the past 400,000 years: evidence from deep-sea cores on Baffin Bay and Davis Strait. In Andrews, J. T. (Ed.), *Quaternary Environments: Eastern Canadian Arctic, Baffin Bay and Western Greenland*, pp. 181–209. Allen and Unwin, Boston.
- Alden, W. C. (1924). Physical features of central Massachusetts. *United States Geological Survey Bulletin*, 760-B, 145–160.
- Andrews, J. T. (1969). The pattern and interpretation of restrained, post-glacial and residual rebound in the area of Hudson Bay. *Geological Survey of Canada Paper* 68-53, 49–62.
- Andrews, J. T. (1973). The Wisconsin Laurentide Ice Sheet: Dispersal centers, problems of rates of retreat, and climatic implications. *Arctic and Alpine Research*, 5, 185–199.
- Andrews, J. T. (1982). On the reconstruction of Pleistocene ice sheets: A review. *Quaternary Science Reviews*, 1, 1–30.
- Andrews, J. T. (1989a). Nature of the last glaciation in Canada. In R.J. Fulton, (Ed.), *Quaternary Geology of Canada and Greenland* (pp. 544–546). Geological Survey of Canada, Geology of Canada, No. 1.
- Andrews, J. T. (1989b). Postglacial emergence and submergence. In R.J. Fulton, (Ed.), *Quaternary Geology of Canada and Greenland*, (pp. 546–562). Geological Survey of Canada, Geology of Canada, No. 1.
- Andrews, J. T., Geirsdóttir, A., & Jennings, A. E. (1989). Late Quaternary spatial and temporal changes in clay- and silt-size mineral assemblages of fiord and shelf cores, western Baffin Bay, northwest Atlantic. *Continental Shelf Research*, 9, 445–463.
- Andrews, J. T., & Ives, J. D. (1978). 'Cockburn' nomenclature and the late Quaternary history of the eastern Canadian Arctic. *Arctic and Alpine Research*, 10, 617–633.
- Andrews, J. T., Jull, A. J. T., Donahue, D. J., & Short, S. K. (1985). Sedimentation rates in Baffin Island fjord and shelf cores from comparative radiocarbon dates. *Canadian Journal of Earth Sciences*, 22, 1827–1837.

- Andrews, J. T., Kirby, M., Aksu, A., Barber, D. C., & Meese, D. (1999). Late Quaternary detrital carbonate (DC) layers in Baffin Bay marine sediments (67–74 N): Correlation with Heinrich events in the North Atlantic? *Quaternary Science Reviews*, in press.
- Andrews, J. T., & Meese, D. (1997). Inferred glacial events in NW Greenland and the Canadian High Arctic (~Baffin Bay): Deglaciation linked to major isotope stage 2 and 3 interstadials? Program and Abstracts, 27th Arctic Workshop, (pp. 11–13). Department of Geography, University of Ottawa.
- Antevs, E. (1929). Maps of Pleistocene glaciations. *Geological Society of America Bulletin*, 40, 631–720.
- Barnett, D. M., Dredge, L. A., & Edlund, S. A. (1976). Terrain Inventory: Bathurst, Cornwallis, and adjacent islands. *Report of Activities. Geological Survey of Canada Paper 76-1A*, 201–204.
- Barnett, D. M., Edlund, S. A., & Dredge, L. A. (1977). Terrain characterization and evaluation: an example from eastern Melville Island. *Geological Survey of Canada Paper 76–23*.
- Barr, W. (1971). Postglacial isostatic movements in northeastern Devon Island: A reappraisal. *Arctic*, 24, 249–268.
- Barr, W., Barrett, P. E., Hussell, D. J. T., King, R. H., & Koerner, R. M. (1968). Devon Island Programs, 1967. *Arctic*, 21, 44–50.
- Bednarski, J. (1986). Late Quaternary glacial and sea level events, Clements Markham Inlet, northern Ellesmere Island, Arctic Canada. *Canadian Journal of Earth Sciences*, 23, 1343–1355.
- Bednarski, J. (1995). Glacial advances and stratigraphy in Otto Fiord and adjacent areas, Ellesmere Island, Northwest Territories. *Canadian Journal of Earth Sciences*, 32, 52–64.
- Bell, T. (1996). The last glaciation and sea level history of Fosheim Peninsula, Ellesmere Island, Canadian High Arctic. *Canadian Journal of Earth Sciences*, 33, 1075–1086.
- Billings, M. P., & Williams, C. R. (1932). Origin of the Appalachian highlands. *Appalachia*, 19, 1–33.
- Blake, W. Jr (1964). Preliminary account of the glacial history of Bathurst Island, Arctic Archipelago. *Geological Survey of Canada Paper 64-30*.
- Blake, W. Jr (1970). Studies of glacial history in Arctic Canada I: pumice, radiocarbon dates, and differential postglacial uplift in the eastern Queen Elizabeth Islands. *Canadian Journal of Earth Sciences*, 7, 634–664.
- Blake, W. Jr (1975). Radiocarbon age determinations and postglacial emergence at Cape Storm, southern Ellesmere Island. *Geografiska Annaler*, 57A, 1–11.
- Blake, W. Jr (1980). Mid-Wisconsinan interstadial deposits beneath Holocene beaches, Cape Storm, Ellesmere Island, Arctic Canada. In *Abstracts, AMQUA 6th Biennial Meeting*, pp. 26–27. Orono, Maine.
- Blake, W. Jr (1987). Geological Survey of Canada radiocarbon dates XXVI. *Geological Survey of Canada Paper 86-7*.
- Blake, W. Jr (1988). Geological Survey of Canada radiocarbon dates XXVII. *Geological Survey of Canada Paper 87-7*.
- Blake, W. Jr (1992a). Holocene emergence at Cape Herschel, east-central Ellesmere Island, Arctic Canada: Implications for ice sheet configuration. *Canadian Journal of Earth Sciences*, 29, 1958–1980.
- Blake, W. Jr (1992b). Shell-bearing till along Smith Sound, Ellesmere Island-Greenland: age and significance. *Sverges Geologiska Undersökning, Series Ca, 81*, 51–58.
- Blake, W. Jr (1993). Holocene emergence along the Ellesmere Island coasts of northernmost Baffin Bay. *Norsk Geologisk Tidsskrift*, 73, 147–160.
- Boesch, H. (1963). Notes on the geomorphological history. In F. Müller (Ed.), *Axel Heiberg Research Reports, Preliminary Report 1961–62*, (pp. 163–167). Montreal: McGill University.
- Boulton, G. S. (1979). A model of Weichselian glacier variation in the North Atlantic regions. *Boreas*, 8, 373–395.
- Brassard, G. R. (1970). The mosses of northern Ellesmere Island, arctic Canada: Ecology and phytogeography, with an analysis for the Queen Elizabeth Islands. *The Bryologist*, 74, 234–281.
- Brotchie, J. F., & Silvester, R. (1969). On crustal flexure. *Journal of Geophysical Research*, 74, 5240–5252.
- Bryson, R. A., Wendland, W. M., Ives, J. D., & Andrews, J. T. (1969). Radiocarbon isochrones on the disintegration of the Laurentide Ice Sheet. *Arctic and Alpine Research*, 1, 1–13.
- Chamberlin, T. C. (1894). Glacial phenomena of North America. In J. Geike (Ed.), *The great ice age* (3rd ed., pp. 724–775). London: Edward Stanford.
- Chamberlin, T. C. (1913) *Map of North America during the Great Ice Age*, scale 1 inch to 104 miles. Chicago: Rand McNally.
- Chamberlin, T. C., & Salisbury, R. D. (1906) *Geology* (Vol. 1). New York: Henry Holt and Company.
- Chamberlin, T. C., & Salisbury, R. D. (1907) *Earth history* (2nd ed.). American Science Series, Advanced Course. New York: Henry Holt and Company.
- Clark, J. A. (1980). The reconstruction of the Laurentide Ice Sheet of North America from sea level data: Method and preliminary results. *Journal of Geophysical Research*, 85, 4307–4323.
- Coleman, A. P. (1941) *The last million years*. Toronto: University of Toronto Press.
- Coleman, A. P., & Parks, W. A. (1922) *Elementary geology with special reference to Canada*. Toronto: I.M. Dent and Sons.
- Craig, B. G., & Fyles, J. G. (1960). Pleistocene geology of Arctic Canada. *Geological Survey of Canada Paper 60-10*.
- Dansgaard, W., Johnsen, S. J., Clausen, H. B., & Langway, C. C. (1971). Climate record revealed by Camp Century ice core. In K.K. Turekian (Ed.), *The late Cenozoic glacial ages* (pp. 37–56). New Haven: Yale University Press.
- Davies, W. E. (1972). Landscape of northern Greenland. *Cold Regions Research and Engineering Laboratory Special Report 164*.
- Dyke, A. S. (1983). Quaternary geology of Somerset Island, District of Franklin. *Geological Survey of Canada Memoir 404*.
- Dyke, A. S. (1984). Quaternary geology of Boothia Peninsula and northern District of Keewatin, central Canadian Arctic. *Geological Survey of Canada Memoir 407*.
- Dyke, A. S. (1993a). Glacial and sea level history of Lowther and Griffith Islands, Northwest Territories: A hint of tectonics. *Géographie physique et Quaternaire* 47, 133–146.
- Dyke, A. S. (1993b). Landscapes of cold-centred Late Wisconsinan ice caps, Arctic Canada. *Progress in Physical Geography*, 17, 223–247.
- Dyke, A. S., Dale, J. E., & McNeely, R. N. (1996a). Marine molluscs as indicators of environmental change in glaciated North America and Greenland during the last 18,000 years. *Géographie physique et Quaternaire*, 50, 125–184.
- Dyke, A. S., Dredge, L. A., & Vincent, J.-S. (1982). Configuration and dynamics of the Laurentide Ice Sheet during the Late Wisconsinan maximum. *Géographie physique et Quaternaire*, 36, 5–14.
- Dyke, A. S., Hooper, J., & Savelle, J. M. (1996b). A history of sea ice in the Canadian Arctic Archipelago based on the postglacial remains of the bowhead whale (*Balaena mysticetus*). *Arctic*, 49, 235–255.
- Dyke, A. S., & Morris, T. F. (1990). Postglacial history of the bowhead whale and of driftwood penetration: Implications for paleoclimate, central Canadian Arctic. *Geological Survey of Canada Paper 8–24*.
- Dyke, A. S., Morris, T. F., & Green, D. E. C. (1991). Postglacial tectonic and sea level history of the central Canadian Arctic. *Geological Survey of Canada Bulletin 397*.
- Dyke, A. S., Morris, T. F., Green, D. E. C., & England, J. (1992). Quaternary geology of Prince of Wales Island, Arctic Canada. *Geological Survey of Canada Memoir 433*.
- Dyke, A. S., & Prest, V. K. (1987). Late Wisconsinan and Holocene history of the Laurentide Ice Sheet. *Géographie physique et Quaternaire*, 41, 237–263.
- Edlund, S. A. (1991). Preliminary surficial geology of Cornwallis and adjacent islands, Northwest Territories. *Geological Survey of Canada Paper 89-12*.

- England, J. (1976a). Late Quaternary glaciation of the eastern Queen Elizabeth Islands, northwest Territories, Canada: Alternative models. *Quaternary Research*, 6, 185–202.
- England, J. (1976b). Postglacial isobases and uplift curves from the Canadian and Greenland High Arctic. *Arctic and Alpine Research*, 8, 61–78.
- England, J. (1978). The glacial geology of northeastern Ellesmere Island, Northwest Territories, Canada. *Canadian Journal of Earth Sciences*, 15, 603–617.
- England, J. (1982). Postglacial emergence along northern Nares Strait. *Meddelelser om Grønland, Geoscience*, 8, 65–75.
- England, J. (1983). Isostatic adjustments in a full glacial sea. *Canadian Journal of Earth Sciences*, 20, 895–917.
- England, J. (1985). The late Quaternary history of Hall Land, Northwest Greenland. *Canadian Journal of Earth Sciences*, 22, 1394–1408.
- England, J. (1987a). Glaciation and the evolution of the Canadian high arctic landscape. *Geology*, 15, 419–424.
- England, J. (1987b). Application of AMS dating to the Paleogeography of the Canadian High Arctic. *Nuclear Instruments and Methods in Physics Research*, B29, 216–222.
- England, J. (1990). The late Quaternary history of Greely Fiord and its tributaries, west-central Ellesmere Island. *Canadian Journal of Earth Sciences*, 27, 255–270.
- England, J. (1992). Postglacial emergence in the Canadian High Arctic: Integrating glacioisostasy, eustasy, and late deglaciation. *Canadian Journal of Earth Sciences*, 29, 984–999.
- England, J. (1996). Glacier dynamics and paleoclimate change during the last glaciation of eastern Ellesmere Island, Canada. *Canadian Journal of Earth Science*, 33, 779–799.
- England, J. (1997). The last glaciation of Nares Strait: Ice configuration, deglacial chronology, and regional implications. *Program and Abstracts, 27th Arctic Workshop*, pp. 70–72. Department of Geography, University of Ottawa.
- England, J., & Bradley, R. S. (1978). Past glacial activity in the Canadian High Arctic. *Science*, 200, 265–270.
- England, J., Bradley, R. S., & Miller, G. H. (1978). Former ice shelves in the Canadian High Arctic. *Journal of Glaciology*, 83, 393–404.
- England, J., Bradley, R. S., & Stuckenrath, R. (1981). Multiple glaciations and marine transgressions, western Kennedy Channel, Northwest Territories, Canada. *Boreas*, 10, 71–89.
- England, J., Dyke, A. S., & Hodgson, D. A. (1995). A review of the glacial and sea level history of the Canadian High Arctic. In: *Program with Abstracts, Joint Meeting of CANQUA/CGRG*, St. John's.
- England, J., Sharp, M., Lemmen, D. S., & Bednarski, J. (1991). On the extent and thickness of the Innuitian Ice Sheet: a postglacial-adjustment approach: discussion. *Canadian Journal of Earth Sciences*, 28, 1689–1695.
- Evans, D. J. A. (1990). The last glaciation and relative sea level history of northwest Ellesmere Island, Canadian High Arctic. *Journal of Quaternary Science*, 5, 67–82.
- Falconer, G., Ives, J. D., Løken, O. H., & Andrews, J. T. (1965). Major end moraines in eastern and central Arctic Canada. *Geographical Bulletin*, 7, 137–153.
- Farrell, W. E., & Clark, J. A. (1976). On postglacial sea level. *Geophysical Journal of the Royal Astronomical Society*, 46, 647–667.
- Fernald, M. L. (1925). Persistence of plants in unglaciated areas of the boreal North America. *American Academy of Arts and Sciences Memoirs*, XV(III), 241–342.
- Fisher, D. A. (1979). Comparison of 10^5 years of oxygen isotope and insoluble impurity profiles from the Devon Island and Camp Century ice cores. *Quaternary Research*, 11, 299–305.
- Flint, R. F. (1946) *Glacial Map of North America*, two sheets, scale 1:4,555,000. Geological Society of America, 2 sheets. Washington.
- Flint, R. F. (1947) *Glacial geology and the pleistocene epoch*. New York: Wiley.
- Flint, R. F. (1971) *Glacial and quaternary geology*. New York: Wiley.
- Fortier, Y. O., Blackadar, R. G., Glenister, B. F., Greiner, H. R., McLaren, D. J., McMillan, N. J., Norris, A. W., Roots, E. F., Souther, J. G., Thorsteinsson, R., & Tozer, E. T. (1963). Geology of the north central part of the Arctic Archipelago, Northwest Territories (Operation Franklin). *Geological Survey of Canada Memoir* 320.
- Fortier, Y. O., & Morley, L. W. (1956). Geological unity of the Arctic Islands. *Transactions of the Royal Society of Canada Series 3*, 50, 3–12.
- Frisch, T. (1988). Reconnaissance geology of the Precambrian Shield of Ellesmere, Devon and Coburg Islands. *Geological Survey of Canada Memoir* 409.
- Fulton, R. J. (1989). Foreword. In R.J. Fulton (Ed.), *Quaternary geology of Canada and Greenland*, (pp. 1–11). Geological Survey of Canada, Geology of Canada, No. 1.
- Fulton, R. J. (1995). *Surficial Materials Map of Canada*. Geological Survey of Canada, Map 1880A, scale 1:5,000,000.
- Funder, S. (1989). Quaternary geology of the ice-free areas and adjacent shelves of Greenland. In R. J. Fulton (Ed.), *Quaternary Geology of Canada and Greenland* (pp. 743–792). Geological Survey of Canada, Geology of Canada, No. 1.
- Funder, S. (1990). Late Quaternary stratigraphy and glaciology in the Thule area, northwest Greenland. *Meddelelser om Grønland, Geoscience* 22.
- Funder, S., & Hansen, L. (1996). The Greenland ice sheet - a model for its culmination and decay during and after the last glacial maximum. *Bulletin of the Geological Society of Denmark*, 42, 137–152.
- Fyles, J. G. (1965). Surficial geology, western Queen Elizabeth Islands. *Report of Activities; Field, 1964. Geological Survey of Canada Paper* 65-1, 3–5.
- Glenister, B. F., & Thorsteinsson, R. (1963). Southern Lougheed Island. *Geology of the north-central part of the Arctic Archipelago, Northwest Territories (Operation Franklin)*, (pp. 571–575). *Geological Survey of Canada Memoir* 320.
- Glushankova, N. I., Parunin, O. B., Timashkova, T. A., Khait, V. Z., & Shlukov, A. I. (1980). Moscow MV Lomonosov State University radiocarbon dates I. *Radiocarbon*, 22, 82–90.
- Greiner, H. R. (1963). Vicinity of Beechey Island to Radstock Bay. In *Geology of the north-central part of the Arctic Archipelago, Northwest Territories (Operation Franklin)*, (pp. 201–207). *Geological Survey of Canada Memoir* 320.
- Grosswald, M. G. (1973). Reconnaissance glacial geology of south-western Grinnell Peninsula, Devon Island. *Report of Activities. Geological Survey of Canada Paper* 73-1A, 199–200.
- Grosswald, M. G. (1984). Glaciation of the continental shelves (Part II). *Polar Geography and Geology*, 8, 287–351.
- Hattersley-Smith, G. (1969). Glacial features of Tanguary Fiord and adjoining areas of northern Ellesmere Island, N.W.T. *Journal of Glaciology*, 8, 23–50.
- Hättestrand, C., & Stroeven, A. P. (1996). Field evidence for wet-based ice sheet erosion from the south-central Queen Elizabeth Islands, Northwest Territories, Canada. *Arctic and Alpine Research*, 28, 466–474.
- Hélie, R. G., & Elson, J. A. (1984). Discrimination between glacial and weathering residue diamictos, Somerset Island, Northwest Territories. *Current Research, Part A. Geological Survey of Canada Paper* 84-1A, 339–344.
- Heywood, W. W. (1957). Isachsen area, Ellef Ringnes Island, District of Franklin, Northwest Territories. *Geological Survey of Canada Paper* 56-8.
- Hiscott, R. N., Aksu, A. E., & Nielsen, O. B. (1989). Provenance and dispersal patterns, Pliocene-Pleistocene section at site 645, Baffin Bay. In: S.P. Srivastava, M.A., Arthur, & B. Clement, et al. (Eds.), *Proceedings of the Ocean Drilling Program, Scientific Results*, (Vol. 105, pp. 31–52).

- Hobbs, W. H. (1945). The boundary of the last glaciation in Arctic Canada. *Science*, 101, 549–551.
- Hodgson, D. A. (1977). A preliminary account of surficial materials, geomorphological processes, terrain sensitivity, and Quaternary history of King Christian and southern Ellef Ringnes Islands, District of Franklin. *Report of Activities. Geological Survey of Canada Paper 77-1A*, 485–493.
- Hodgson, D. A. (1981). Surficial geology, Lougheed Island, northwest Arctic Archipelago. Current Research, Part C. *Geological Survey of Canada Paper 81-1C*, 27–34.
- Hodgson, D. A. (1982). Surficial materials and geomorphological processes, western Sverdrup and adjacent islands, District of Franklin. *Geological Survey of Canada Paper 81-9*.
- Hodgson, D. A. (1985). The last glaciation of west-central Ellesmere Island, Arctic Archipelago, Canada. *Canadian Journal of Earth Sciences*, 22, 347–368.
- Hodgson, D. A. (1989). Quaternary geology of the Queen Elizabeth Islands. In R.J. Fulton (Ed.), *Quaternary Geology of Canada and Greenland*, pp. 441–478. Geological Survey of Canada, Geology of Canada, No. 1.
- Hodgson, D. A. (1990). Were erratics moved by glaciers or icebergs to Prince Patrick Island, western Arctic Archipelago, Northwest Territories? *Current Research, Part D. Geological Survey of Canada Paper 90-1D*, 67–70.
- Hodgson, D. A., & Haselton, G. M. (1974). Reconnaissance glacial geology, northeast Baffin Island. *Geological Survey of Canada Paper 74-20*.
- Hodgson, D. A., Taylor, R. B., & Fyles, J. G. (1994). Late Quaternary sea level changes on Brock and Prince Patrick Islands, western Canadian Arctic Archipelago. *Géographie physique et Quaternaire*, 48, 69–84.
- Hodgson, D. A., Vincent, J.-S., & Fyles, J. G. (1984). Quaternary geology of central Melville Island, Northwest Territories. *Geological Survey of Canada Paper 83-16*.
- Hughes, T. J., Denton, G. H., & Grosswald, M. G. (1977). Was there a late Wurm Arctic ice sheet? *Nature*, 266, 596–602.
- Hultén, E. (1937) *Outline of the history of Arctic and boreal biota during the Quaternary Period*. Stockholm: Aktiebolaget Thule.
- Jenness, J. L. (1952). Problem of glaciation in the western islands of arctic Canada. *Geological Society of America Bulletin*, 63, 939–952.
- Jenness, S. E. (1962). Fieldwork, 1961. *Geological Survey of Canada Information Circular No. 5*.
- Kelly, M. (1985). A review of the Quaternary geology of western Greenland. In J.T. Andrews (Ed.), *Quaternary Environments: Eastern Canadian Arctic, Baffin Bay and Western Greenland*, (pp. 428–460). Boston: Allen and Unwin.
- Kelly, M., & Bennike, O. (1992). Quaternary geology of western and central North Greenland. *Grønlands Geologiske Undersøgelse Rapport* 153.
- Kerr, J. W. (1980). Structural framework of the Lancaster aulacogen, Arctic Canada. *Geological Survey of Canada Bulletin* 319.
- King, L. (1981). Studies in glacial history of the area between Oobloyah Bay and Esayoo Bay, northern Ellesmere Island, N.W.T., Canada. In *Results of the Heidleberg Ellesmere Island Expedition. Heidelberger Geographische Arbeiten*, 69, 233–267.
- King, R. H. (1991). Paleolimnology of a polar oasis, Truelove Lowland, Devon Island, N.W.T., Canada. *Hydrobiologia*, 214, 317–325.
- Klassen, R. A. (1985). An outline of the glacial history of Bylot Island, District of Franklin, N.W.T. In J. T. Andrews (Ed.), *Quaternary Environments: Eastern Canadian Arctic, Baffin Bay and Western Greenland*, (pp. 428–460). Boston: Allen and Unwin.
- Klassen, R. A. (1993). Quaternary geology and glacial history of Bylot Island, Northwest Territories. *Geological Survey of Canada Memoir* 429.
- Klassen, R. A., & Fisher, D. A. (1988). Basal flow conditions at the northeastern margin of the Laurentide Ice Sheet, Lancaster Sound. *Canadian Journal of Earth Sciences* 25, 1740–1750.
- Koerner, R. M. (1970). The mass balance of the Devon Island Ice Cap. *Journal of Glaciology*, 9, 325–336.
- Koerner, R. M., & Fisher, D. A. (1985). The Devon Island ice core and the glacial record. In J.T. Andrews (Ed.), *Quaternary Environments: Eastern Canadian Arctic, Baffin Bay, and Western Greenland* (pp. 309–327). Boston: Allen and Unwin.
- Koerner, R. M. Fisher, D. A., & Paterson, W. S. B. (1987). Wisconsinan and pre-Wisconsinan ice thicknesses on Ellesmere Island, Canada: Inferences from ice cores. *Canadian Journal of Earth Sciences* 24, 296–301.
- Lemmen, D. S. (1989). The last glaciation of Marvin Peninsula, northern Ellesmere Island, High Arctic, Canada. *Canadian Journal of Earth Sciences*, 26, 2578–2590.
- Lemmen, D. S., Aitken, A. E., & Gilbert, R. (1994). Early Holocene deglaciation of Expedition and Strand fiords, Canadian High Arctic. *Canadian Journal of Earth Sciences*, 31, 943–958.
- Lemmen, D. S., & England, J. (1992). Multiple glaciations and sea level changes, northern Ellesmere Island, high arctic Canada. *Boreas*, 21, 137–152.
- Longwell, C. R., Knopf, A., & Flint, R. F. (1939). *A textbook of geology, Part I: Physical geology* (2nd ed.). New York: Wiley.
- Low, A. P. (1906) *Report of the Dominion Government Expedition to Hudson Bay and the Arctic Islands on board the D.G.S. Neptune, 1903–1904*, (pp. 183–247) Ottawa: King's Printer.
- Lowdon, J. A., & Blake, W. Jr (1975). Geological Survey of Canada radiocarbon dates XV. *Geological Survey of Canada Paper 75-7*.
- Lowdon, J. A., Robertson, I. M., & Blake, W. Jr (1971). Geological Survey of Canada radiocarbon dates XI. *Geological Survey of Canada Paper 71-7*.
- Martin, L. (1932). The physical geography of Wisconsin, (2nd ed.). *Wisconsin Geological and Natural History Survey Bulletin* 36.
- Martin, L. (1935). Patrician Ice Sheet on North American glacial maps. *Pan-American Geologist*, 65, 8–11.
- MacLean, B., Sonnichsen, G., Vilks, G., Powell, C., Moran, K., Jennings, A., Hodgson, D., & Deonarine, B. (1989). Marine geological and geotechnical investigations in Wellington, Byam Martin, Austin, and adjacent channels, Canadian Arctic Archipelago. *Geological Survey of Canada Paper 89-11*.
- Maull, O. (1938) *Geomorphologie*. Leipzig und Wien: Franz Deuticke.
- Mayewski, P. A., Denton, G. H., & Hughes, T. J. (1981). Late Wisconsin ice sheets of North America. In G.H. Denton & T.J. Hughes, (Eds.), *The Last Great Ice Sheets*, (pp. 67–162). New York: Wiley.
- McCuaig, S. J. (1994). Glacial chronology of the south Bylot and Salmon River lowlands, N.W.T., using erratic dispersal patterns, cosmogenic dating, radiocarbon dating and lichenometry. M.Sc. thesis, Carleton University, Ottawa, Unpublished.
- McLaren, P., & Barnett, D. M. (1978). Holocene emergence of the south and east coasts of Melville Island, Queen Elizabeth Islands, Northwest Territories, Canada. *Arctic* 31, 415–427.
- McMillan, J. G. (1910). Report of J.G. McMillan, geologist of the Arctic expedition, 1908–1909. In J.E. Bernier (Ed.), *Report of the Dominion of Canada Government Expedition to the Arctic Islands and Hudson Strait on board the D.G.S. Arctic*, (pp. 382–479). Ottawa: King's Printer.
- McNeely, R. (1989). Geological Survey of Canada radiocarbon dates XXVIII. *Geological Survey of Canada Paper 88-7*.
- Mercer, J. H. (1970). A former ice sheet in the Arctic Ocean? *Palaeogeography, Palaeoclimatology, Palaeoecology*, 8, 19–27.
- Müller, F., & Barr, W. (1966). Postglacial isostatic movement in north-eastern Devon Island, Canadian Arctic Archipelago. *Arctic*, 19, 263–269.
- Nordenskjöld, O. (1928). Polar nature: A general characterization. In O. Nordenskjöld & L. Mecking, (Eds), *The geography of the polar regions* (pp. 3–90). American Geographical Society, Special Publication No. 8.

- Okulitch, A. V. (1991). Geology of the Canadian Arctic Archipelago and North Greenland. In H.P. Trettin (Ed.), *Geology of the Innuitian Orogen and the Arctic Platform of Canada and Greenland*, Figure 2, scale 1:2,000,000. Geological Survey of Canada, Geology of Canada, No. 3.
- Okulitch, A. V., & Trettin, H. P. (1991). Late Cretaceous—Early Tertiary deformation, Arctic Islands. In H.P. Trettin (Ed.), *Geology of the Innuitian Orogen and the Arctic Platform of Canada and Greenland*, pp. (469–489). Geological Survey of Canada, Geology of Canada, No. 3.
- Paterson, W. S. B. (1977). Extent of late-Wisconsin glaciation in north-west Greenland and northern Ellesmere Island: A review of the glaciological and geological evidence. *Quaternary Research*, 8, 180–190.
- Paterson, W. S. B., Koerner, R. M., Fisher, D. A., Johnsen, S. J., Clausen, H. R., Dansgaard, W., Bucher, P., & Oeschger, H. (1997). An oxygen isotope climate record from the Devon Ice Cap, Arctic Canada. *Nature*, 266, 508–511.
- Pelletier, B. R. (1966). Development of submarine physiography in the Canadian Arctic and its relation to crustal movements. In G.D. Garland (Ed.), *Continental drift* (pp. 77–101). Toronto: University of Toronto Press.
- Peltier, W. R. (1994). Ice age paleotopography. *Science*, 265, 195–201.
- Prest, V. K. (1952). Notes on the geology of parts of Ellesmere and Devon Islands, Northwest Territories. *Geological Survey of Canada Paper* 52-32.
- Prest, V. K. (1957). Pleistocene geology and surficial deposits. In C.H. Stockwell (Ed.), *Geology and economic minerals of Canada* (4th ed., pp. 443–494). Economic Geology Series No. 1, Geological Survey of Canada.
- Prest, V. K. (1969). *Retreat of Wisconsin and Recent Ice in North America*. Geological Survey of Canada, Map 1257A, scale 1:5,000,000.
- Prest, V. K. (1970). Quaternary Geology of Canada. In R.J.W. Douglas, (Ed.), *Geology and economic minerals of Canada* (5th ed., pp. 675–764). Economic Geology Series No. 1, Geological Survey of Canada.
- Prest, V. K. (1984). The Late Wisconsinan glacier complex. In R.J. Fulton (Ed.), *Quaternary Stratigraphy of Canada—A Canadian Contribution to IGCP Project 24*, (pp. 21–36). Geological Survey of Canada, Paper 84-10.
- Prest, V. K. (1990). Laurentide ice-flow patterns: a historical review, and implications of the dispersal of Belcher Islands erratics. *Géographie Physique et Quaternaire*, 44, 113–136.
- Prest, V. K., Grant, D. R., & Rampton, V. N. (1968) *Glacial Map of Canada*. Geological Survey of Canada, Map 1253A, scale 1:5,000,000.
- Reeh, N. (1984). Reconstruction of the glacial ice cover of Greenland and the Canadian Arctic Islands by three-dimensional perfectly plastic ice sheet modeling. *Annals of Glaciology*, 5, 115–128.
- Retelle, M. (1986). Glacial geology and Quaternary marine stratigraphy of the Robeson Channel area, northeastern Ellesmere Island, Northwest Territories. *Canadian Journal of Earth Sciences*, 23, 1001–1012.
- Roots, E. F. (1963). Physiography, Devon Island. In: *Geology of the north-central part of the Arctic Archipelago, Northwest Territories (Operation Franklin)*, (pp. 164–179). *Geological Survey of Canada Memoir* 320.
- Schei, P. (1903). Summary of geological results. *Geographical Journal*, 22, 56–69.
- Schuchert, C. (1914). *Climates of Geologic Time*. Carnegie Institution Publication No. 192, 263–298.
- Schuchert, C. (1915). Geological history. In L.V. Pirsson, & C. Schuchert, (Eds), *Textbook of Geology*, Part II, (pp. 405–992). New York: Wiley.
- Schytt, V. G., Hoppe, G., Blake, W., Jr & Grosswald, M. G. (1968). The extent of Würm glaciation in the European Arctic. *International Association of Hydrological Sciences*, 79, 207–216.
- Shaler, N. S., & Davis, W. M. (1881). *Illustrations of the earth's surface: Glaciers*. Boston: Osgood and Company
- Shepard, F. P. (1936). The underlying causes of submarine canyons. *National Academy of Sciences Proceedings*, 22, 496–502.
- Shepard, F. P. (1941). Origin and history of submarine canyons. In F. P. Shepard, & K. O. Emery, (Eds.), *Submarine topography of the California coast: Canyons and interpretation* (pp. 109–166). Geological Society of America Special Paper No. 31.
- Simmons, H. G. (1913). A survey of the phytogeography of the Arctic American Archipelago. Lunds University Aarskrift, N.F. Afd. 2, Bd. 9, No. 19.
- Snider, L. C. (1932). *Earth history*. New York: Century Company.
- St-Onge, D. (1965). La géomorphologie de l'Île Ellef Ringnes, Territoires du Nord-Ouest, Canada. *Étude Géographique* 38, Direction de la Géographie, Ministère des Mines et des Relevés techniques, Ottawa.
- Sugden, D. E. (1978). Glacial erosion by the Laurentide Ice Sheet. *Journal of Glaciology*, 20, 367–391.
- Tarr, R. S., & Martin, L. (1914) *College physiography*. New York: Macmillan.
- Tedrow, J. C. F. (1970). Soil investigations in Inglefield Land, Greenland. *Meddelelser om Grønland* 188.
- Thorsteinsson, R. (1958). Cornwallis and Little Cornwallis Islands, District of Franklin, Northwest Territories. *Geological Survey of Canada Memoir* 294.
- Thorsteinsson, R., & Mayr, U. (1987). The sedimentary rocks of Devon Island, Canadian Arctic Archipelago. *Geological Survey of Canada Memoir* 411.
- Tozer, E. T. (1956). Geological reconnaissance, Prince Patrick, Eglinton, and western Melville Islands, arctic Archipelago, Northwest Territories. *Geological Survey of Canada Paper* 55-5.
- Trettin, H. P. (1991). *Geology of the Innuitian Orogen and the Arctic Platform of Canada and Greenland*. Geological Survey of Canada, Geology of Canada, No. 3.
- Tushingham, M. (1991). On the extent and thickness of the Innuitian Ice Sheet: a postglacial-adjustment approach. *Canadian Journal of Earth Sciences*, 28, 231–239.
- Upham, W. (1895). The Glacial Lake Agassiz. *United States Geological Survey Monograph* XXV.
- Völk, H. R. (1980). Records of emergence around Oobloyah Bay and Neil Peninsula in connection with the Wisconsin deglaciation pattern, Ellesmere Island, Northwest Territories, Canada: a preliminary report. *Polarforschung*, 50, 29–44.
- Walcott, R. I. (1970). Isostatic response to loading of the crust in Canada. *Canadian Journal of Earth Sciences*, 7, 716–726.
- Walcott, R. I. (1972). Late Quaternary vertical movements in eastern North America: quantitative evidence of glacio-iso-static rebound. *Reviews of Geophysics and Space Physics*, 10, 849–884.
- Washburn, A. L. (1947). Reconnaissance geology of portions of Victoria Island and adjacent regions. *Geological Society of America Memoir* 22, 142 pp.
- Wickenden, R. T. D. (1947). Pleistocene glacial deposits. *Geology and economic minerals of Canada* (3rd ed., pp. 325–346). Geological Survey of Canada.
- Williams, K. M. (1990). Late Quaternary paleoceanography of the western Baffin Bay region: Evidence from fossil diatoms. *Canadian Journal of Earth Sciences* 27, 1487–1494.
- Wilson, J. T., Falconer, G., Mathews, W. H., & Prest, V. K. (1958) *Glacial Map of Canada*, scale 1:3,801,600. Geological Association of Canada.
- Young, G. A. (1909) *Geology and Economic Minerals of Canada*. Geological Survey of Canada.
- Young, R. B., & King, R. H. (1989). Sediment chemistry and diatom stratigraphy of two High Arctic isolation lakes, Truelove Lowland, Devon Island, N.W.T., Canada. *Journal of Paleolimnology* 2, 207–225.

Changes in late-Neoglacial perennial snow/ice extent and equilibrium-line altitudes in the Queen Elizabeth Islands, Arctic Canada

Gabriel J. Wolken,^{1*} John H. England¹ and Arthur S. Dyke²

¹Department of Earth and Atmospheric Sciences, University of Alberta, Alberta T6G 2E3, Canada;

²Terrain Sciences Division, Geological Survey of Canada, 601 Booth Street, Ottawa, Ontario K1A 0E8, Canada)

Received 8 February 2007; revised manuscript accepted 3 December 2007



Abstract: Changes in late Neoglacial climate resulted in extensive modification of Arctic terrestrial ice cover. A substantial reduction in terrestrial ice cover in the Queen Elizabeth Islands (QEI) following the ‘Little Ice Age’ (LIA) (~AD 1250–1900), is indicated by widespread, light-toned patches of poorly vegetated terrain, extending back to the modern ice mass. These patches display abrupt outer margins (trimlines), which record the former position and maximum extent of perennial snow/ice and, in many cases, mark the former equilibrium-line altitude (ELA). Trimlines surrounding terrain formerly covered by LIA perennial snow/ice were mapped using multispectral classification approaches applied to high-resolution satellite imagery. ELAs were reconstructed from trimlines associated with former perennial snow/ice produced by long-term snowline lowering. Between the end of the LIA and 1960, the area of terrestrial ice in the QEI decreased by 37% (62 387 km²). Most of this reduction (94%) occurred in the eastern QEI where the majority of the ice exists today; however, a 100% reduction in ice cover occurred on many of the western islands by 1960, an effect largely controlled by the subtle topography of these islands. The reconstructed LIA ELA trend surface was used with the 1960 mapped ELAs to calculate spatial variations in the change in height (Δh) of the ELA trend surface throughout the QEI during the first half of the twentieth century. ELA Δh between the LIA and 1960 reveal a high degree of local variability in the mountainous regions, ranging from 0 to >600 m; however a strong regional-scale pattern of change is shown over the QEI as a whole.

Key words: Trimlines, ‘Little Ice Age’, snow extent, ice cover change, glaciers, equilibrium-line altitude, climate variability, Arctic Canada, Queen Elizabeth Islands.

Introduction

Among the many indicators of climatic variability in the Arctic is the large-scale fluctuation of glaciers, ice caps and ice sheets. Recent studies have documented glacier responses to recent climate change in the Arctic (Dyurgerov and Meier, 1997; Church *et al.*, 2001; Arendt *et al.*, 2002; Arctic Climate Impacts Assessment (ACIA), 2004), and in the Canadian High Arctic, our knowledge of the behaviour of terrestrial ice masses in response to late twentieth-century warming is being advanced by a growing body of research (Dowdeswell *et al.*, 1997; Burgess and Sharp, 2004; Braun *et al.*, 2004; Burgess *et al.*, 2005; Mair *et al.*, 2005; Shepherd *et al.*, 2007). Little is known, however, about the changes in terrestrial ice extent during the early twentieth century,

following the ‘Little Ice Age’ (LIA; ~AD 1250–1900, Grove, 2001), and even less is known about the climatic forcing responsible for these changes.

The terrestrial ice configuration in the Canadian Arctic during the LIA is widely recognized to mark the maximum Neoglacial ice extent (post 4500 BP, England, 1977; Blake, 1981; Bradley, 1990; Evans and England, 1992; Miller *et al.*, 2005; Wolken *et al.*, 2005). In addition to the widespread evidence of glaciers attaining their maximum late-Holocene extents within the last few centuries (LIA), this time period in the QEI is regarded as the coldest of the entire Holocene (Bradley, 1990; Koerner and Fisher, 1990). Onset of ice retreat since the LIA coincides with the beginning of the twentieth century, when significant warming occurred in the Arctic, resulting in rapid melting of terrestrial ice, ice shelves and sea ice (Koerner and Fisher, 1990; Overpeck *et al.*, 1997; Bengtsson *et al.*, 2004; Johanessen *et al.*, 2004). This large-scale

*Author for correspondence (e-mail: gwolken@ualberta.ca)

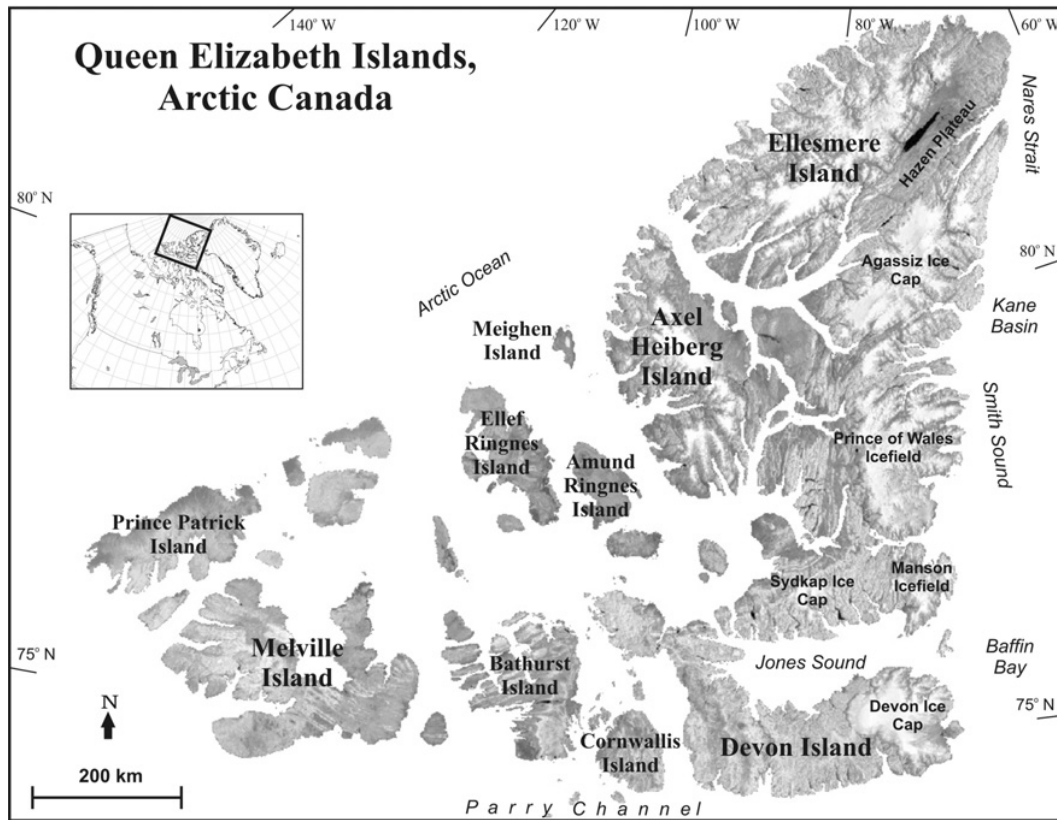


Figure 1 Map of the Queen Elizabeth Islands, Arctic Canada (Radarsat Orthomosaic, courtesy of the Canadian Centre for Remote Sensing)

reduction of terrestrial ice is delimited by prominent trimlines, within which the terrain is characterized by an absence of vegetation and/or a reduction in oxidized and weathered substrates. These lighter-toned surfaces are often evident on both aerial photographs and satellite imagery (Ives, 1962; Wolken *et al.*, 2005). Wolken *et al.* (2005) provide an important baseline from which palaeoenvironmental information can be extracted and evaluated (Wolken *et al.*, 2005; Wolken, 2006).

This study documents the magnitude and nature of terrestrial ice reduction in the QEI following the termination of the LIA, by comparing reconstructed LIA ice cover with that of 1960, when full aerial photograph coverage of the region was first acquired. The distribution of mapped trimlines, associated with former perennial snow/ice fields, taken to mark the position of ice margins at the end of the LIA, is then used to compute trend surfaces of equilibrium-line altitude (ELA) during the LIA. These results are compared with mid-twentieth century ELAs (1960) previously reconstructed from topographic maps (1:250 000; Miller *et al.*, 1975). The trend surface of difference in ELA (Δh) between the end of the LIA and 1960 is then used to indicate the primary spatial changes in perennial snow/ice extent caused by post-LIA warming.

Study area

The QEI comprise the part of the Canadian Arctic Archipelago (74–83°N, Figure 1) lying north of Parry Channel. The QEI are bounded by the Arctic Ocean to the north and northwest and by Nares Strait, Smith Sound and Baffin Bay to the east. The total land area of the QEI is ~416 000 km², with the four largest islands (Ellesmere, Axel Heiberg, Devon and Melville) accounting for ~80% of the area. More than 25% of the QEI is covered by ice

(~110 000 km²), the largest concentration of terrestrial ice after Antarctica and Greenland (Williams and Ferrigno, 2002). The eastern QEI (Devon, Axel Heiberg and Ellesmere Islands) have high relief reaching 2500 m and support widespread ice caps and glaciers. ELAs (1960) in the eastern QEI range from less than 200 m along the north coast of Ellesmere Island to nearly 1200 m in island interiors, where the climate is more continental (Miller *et al.*, 1975). Numerous plateaus occur close to the regional glaciation level in the eastern QEI and provide important surfaces where small changes in climate have the potential to either form new ice caps, or expand/remove existing ones. In contrast, the physiography of the western QEI is characterized by low (<400 m) dissected plateaus separated by wide marine channels. Consequently, the western QEI support few ice caps, which are currently restricted to higher terrain on western Melville Island (above 600 m) and to Meighen Island where a solitary, low elevation (<250 m) ice cap faces the Arctic Ocean (Koerner and Paterson, 1974).

Data sources

The reconstruction of LIA perennial snow/ice in the QEI, and its subsequent reduction up to ~1960, is based on Visual and Near Infrared (VNIR) data from two high-resolution multispectral sensors: Enhanced Thematic Mapper Plus (ETM+) on the Landsat 7 satellite (1999–2004), and Advanced Spaceborne Thermal Emission and Reflection Radiometer (ASTER) aboard the Terra satellite (2000–2004). ETM+ has a swath width of 185 km and a spatial resolution of 30 m, and ASTER has a swath width of 60 km and a 15 m spatial resolution. Other sensor details can be found in the methodological companion to this paper (Wolken, 2006).

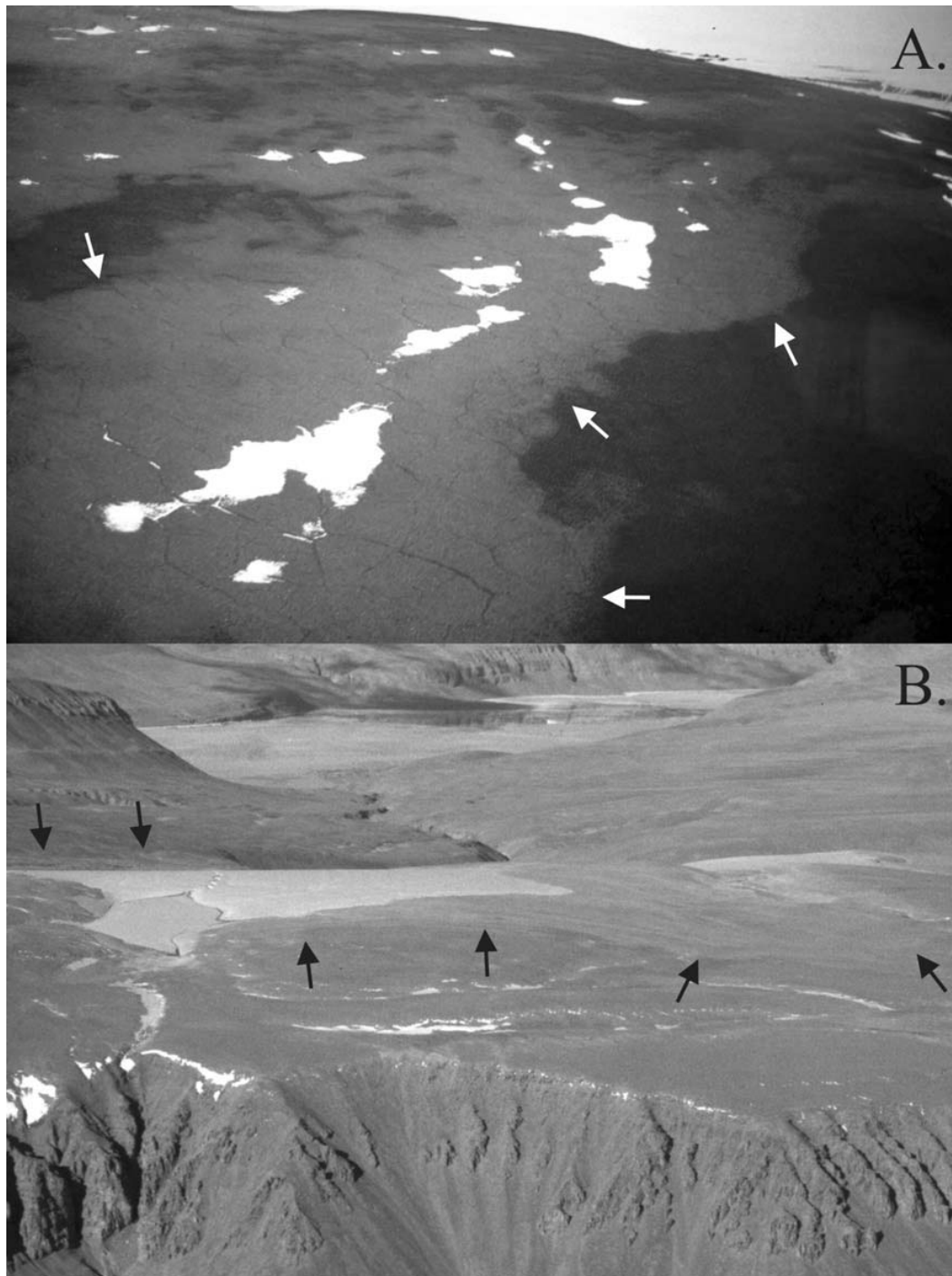


Figure 2 Trimlines (arrows) surrounding recently exposed terrain associated with (A) former perennial snowfields on siliceous terrain, central Axel Heiberg Island, and (B) a small plateau ice cap on calcareous terrain, Knud Peninsula, Ellesmere Island

In lieu of ETM+ and ASTER imagery, aerial photographs from the 1959/1960 (hereafter referred to as 1960) survey of the Canadian Arctic Archipelago (acquired by the Government of Canada) were used for N Ellesmere Island above 82.7°N. In addition to the aerial photographs, 1960 ice margins were obtained from the National Topographic Database (NTDB, provided by Geomatics Canada), which are thematic digital reproductions of the National Topographic System (NTS) maps derived from the 1960 aerial photographs. Digital Elevation Models (DEMs) used in this study were created from the Canadian Digital Elevation Data set, derived from

the 1:250 000 NTS map series. This study utilized 149 DEMs, which were reprojected to a resolution of 100 m on a NAD83 UTM grid, and later used to create a DEM mosaic of the QEI.

Methods

Trimlines in Arctic Canada

Trimlines are distinct transitions on a glaciated landscape resulting from differential weathering and erosion of a surface formerly covered

by a perennial snow/ice mass (Wolken *et al.*, 2005). In the QEI, trimlines are most visible when expressed as vegetation trimlines, typically occurring on siliceous substrates that are otherwise well vegetated (lichens and plants), but they are also detectable on calcareous substrates, where they are much subtler in appearance owing to the sparsity of vegetation on such terrains (Figure 2). Trimlines record the former extent of glaciers, ice caps and perennial snowfields and have been used for palaeoenvironmental reconstruction in Arctic Canada (Ives, 1962; Andrews *et al.*, 1975, 1976; Locke and Locke, 1977; Dyke, 1978; Edlund, 1985; Braun *et al.*, 2004). When using trimlines to reconstruct former ELAs, however, it is important to consider the type of ice mass that was responsible for the formation of the trimlines (Wolken *et al.*, 2005). For instance, trimlines found at distinctly lower elevations than other nearby trimlines are either associated with ice flow from glaciers below the ELA or with topography-influenced perennial snowbanks, which are the products of wind drifting and aspect. While both flow-produced and topography-influenced trimlines represent a record of the former extent of these perennial ice masses, they do not record the former ELA and should not be used for its regional reconstruction. Alternatively, trimlines outlining the former position of perennial snowfields, which are widespread on fiord uplands and plateaus in the Canadian Arctic, are commonly found at the same elevation as neighbouring trimlines surrounding thin cold-based ice caps that have limited or no flow (Wolken *et al.*, 2005). Because of the comparable elevation at which these trimlines are located and the overwhelming number of instances in which this occurs, their formation has been attributed to long-term snowline lowering during the late Neoglacial rather than ice cap expansion resulting from internal flow, and they are used in this study to represent the lowest Neoglacial multiyear ELA. Although the precise age of the perennial snow/ice expansion event that produced these trimlines is unknown, the existing age determinations associated with trimlines in Arctic Canada place the event in the late Neoglacial (Falconer, 1966; Andrews *et al.*, 1975), which is consistent with widespread cooling in the QEI during the LIA (Bradley, 1990; Koerner and Fisher, 1990). Therefore, we make the assumption that the late Neoglacial snow/ice expansion that produced the trimlines occurred during the LIA.

Trimline mapping

Reconstructing the extent of former perennial snow/ice cover in the QEI using remotely sensed data poses numerous challenges because of the size, topographic and lithologic diversity, and sparsity of vegetation in this region. Image processing and classification procedures for mapping trimlines in the QEI follow Wolken (2006).

Automated and semi-automated classifications were applied according to the estimated ratio of siliceous (automated) versus calcareous (semi-automated) terrain in each image. This effort was guided by the use of surficial and bedrock geology maps, ground observations (where available) and intensive examination of the images. For example, if an image was comprised mostly ($\geq 75\%$) of igneous (siliceous) Precambrian bedrock, then an automated classification was employed. However, if an image was comprised of nearly equal parts of siliceous and calcareous terrains, then both automated and semi-automated classifications were applied separately to the image, followed by masking and elimination of classified pixels on the unsought terrain (either siliceous or calcareous) of each new classified image. To reduce overclassification of the imagery caused by the inclusion of features that mimic trimlines (eg, lithological contacts, talus slopes and escarpments), data reduction procedures were applied to each classified image, thus identifying and removing these areas from the final classified maps (Wolken, 2006).

On northernmost Ellesmere Island, where multispectral coverage is either missing or unusable owing to extensive cloud cover,

the former coverage of perennial snow/ice was mapped manually from aerial photographs scanned at high-resolution (spatial resolution ~ 5 m). On-screen, three-dimensional mapping from aerial photograph stereo-pairs, minimized errors associated with the inadvertent mapping of features similar in appearance to trimlines. The raster data from the classified images were then converted into vector coverages and merged with the manually digitized sections of N Ellesmere Island. This produced a single vector coverage for the entire QEI comprised of polygons demarcating recently deglaciated terrain (inside designated trimlines).

ELA reconstruction

The DEM mosaic of the QEI was used to extract low point elevation and coordinate data from each polygon of recently deglaciated terrain. Where trimlines outlining the former margins of thin plateau ice caps and trimlines marking former perennial snowfields exist at corresponding elevations (± 40 m), they are interpreted to record the LIA ELA for that locality (see above section 'Trimlines in Arctic Canada'). Point data meeting this criterion were selected manually from the trimline data set to create a new data set consisting of 4334 elevation points representing the altitude of the LIA equilibrium-line throughout the QEI (Figure 3). A three-dimensional LIA ELA trend surface, with 250 m resolution, was then created from the array of elevation points using Topogrid in ArcInfo 8.0, and was later resampled to a 1-km resolution grid for trend surface analysis (discussed below). Topogrid uses ANU-DEM, a DEM interpolation program that calculates elevations using finite difference interpolation on a discretized smooth surface regular grid (Hutchinson, 1989). Topogrid is effective in modelling surface topography where steep gradients occur locally in the data and, for this reason, was chosen to model the variable ELA trend surface over the QEI. Although some uncertainty in the reconstructed LIA ELA trend surface can be attributed to sensor spatial resolution, low image classification accuracy and errors associated with image processing procedures (see Wolken, 2006 for a detailed discussion of these errors), most of the error can be ascribed to the vertical accuracy of the DEMs, which is estimated to be ± 20 m over bedrock to ± 90 m over complex terrain and ice-covered regions (Centre for Topographic Information, 2000; Burgess and Sharp, 2004). Another source of uncertainty in the LIA ELA trend surface stems from uneven LIA ELA point distribution which is largely a function of lithology (Figure 3); some areas in the QEI have better LIA ELA representation than others. Figure 3 shows the spatial distribution of LIA ELA points and qualitative uncertainties associated with the LIA ELA trend surface over the QEI.

'Little Ice Age' and 1960 ice covers

The polygon coverage of recently deglaciated terrain provides a minimum measure of former LIA perennial ice extent, because some formerly ice-covered sites have been obscured by periglacial processes or are otherwise undetectable with available sensors (Wolken, 2006). In order to provide a more realistic estimate of LIA perennial ice extent, the LIA ELA trend surface, which delineates the former LIA accumulation area, was used to interpolate ice cover between mapped (detectable) areas of former ice extent. The land area above the LIA ELA trend surface was determined by subtracting the ELA trend surface from the DEM mosaic of the study area. Positive pixel values in the new raster data set represent areas above the ELA, and hence ice-covered land during the LIA. However, this data set only includes perennial snow/ice cover above the LIA ELA and does not account for outlet glaciers that would have extended below the ELA. In his investigation into Neoglacial fluctuations of glaciers in SE Ellesmere Island, Blake (1981) reported widespread evidence indicating that many outlet glaciers were (in the late 1970s) at their maximum Neoglacial

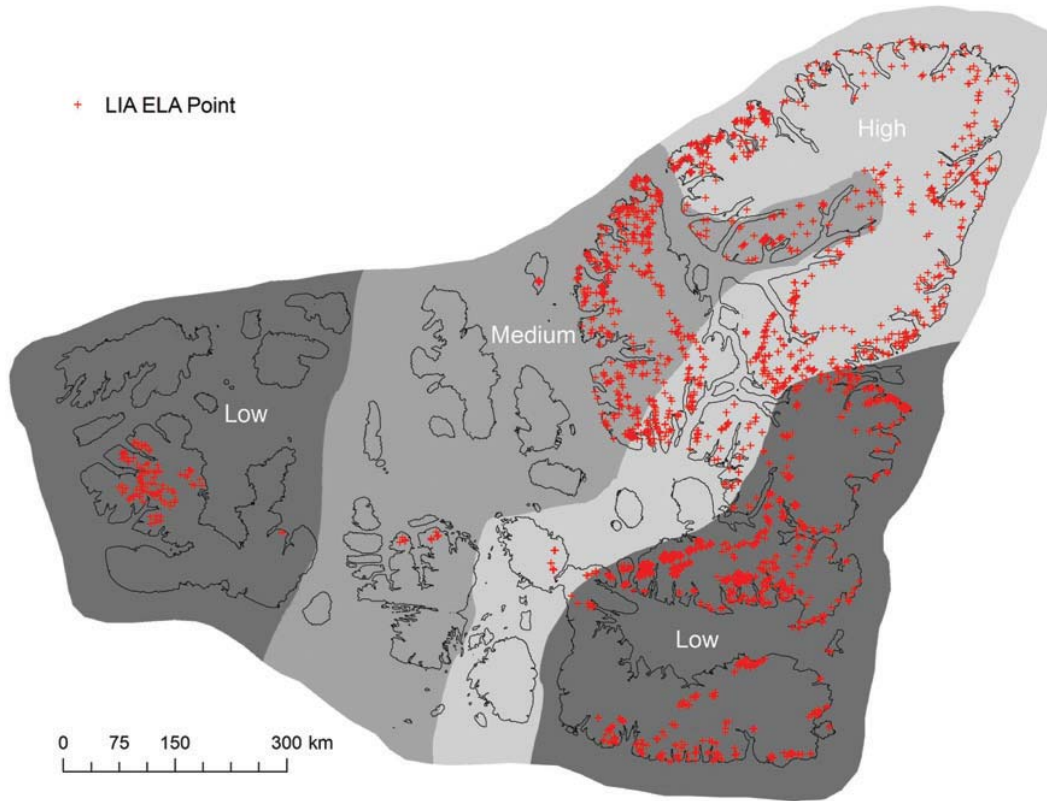


Figure 3 Spatial distribution of 4334 points representing local LIA ELA estimates and uncertainties (qualitative: low; medium; and high) associated with the LIA ELA trend surface over the QEI. Uncertainties are largely a function of surface lithology, and hence the distribution of LIA ELA points

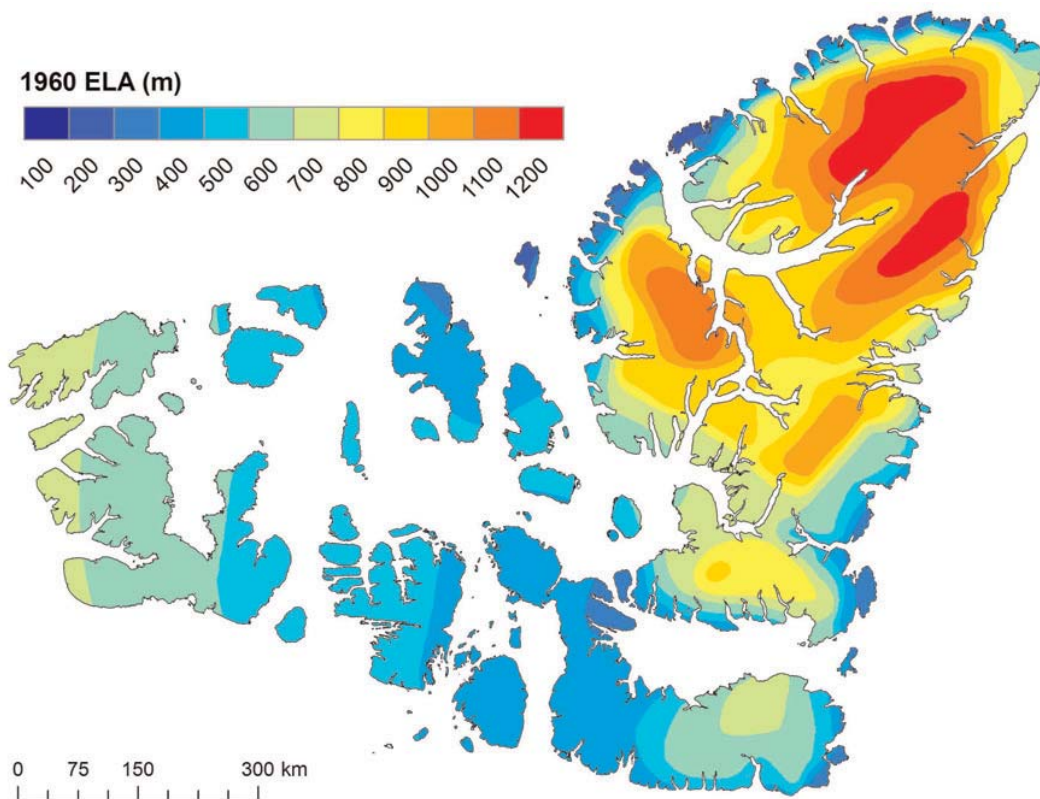


Figure 4 1960 ELA trend surface recreated from Miller *et al.* (1975)

extent, or slightly retreated from this position, which they likely reached within the last 100 years. For outlet glaciers elsewhere in the QEI, it is likely that only minimal marginal retreat would have occurred by the time of Blake's observations, in fact, it is possible that some glaciers at this time were still advancing in response to LIA cooling (Miller *et al.*, 1975; England, 1977). While it is beyond the scope of this investigation to determine changes in the geometry of outlet glaciers in the QEI, our observations confirm minimal marginal retreat for most outlet glaciers at the time of the 1960 airphoto survey. Thus, in order to obtain a more realistic estimate of LIA perennial snow/ice cover, 1960 glacier outlines extending below the LIA ELA trend surface were amalgamated with the LIA ice cover above the ELA. Area calculations of LIA and 1960 ice covers were performed by converting each ice cover into raster grids (30 m resolution), then multiplying the total pixel count for each grid by 900 m² (the area of one pixel).

1960 ELAs

ELAs for the QEI (1960; Figure 4) were derived from a map by Miller *et al.* (1975). The map was georeferenced and the ELA contours were digitized manually in point form. The ELA points were then used to create a DEM (or ELA trend surface) by interpolating the points onto a 1-km resolution grid.

Miller *et al.* (1975) determined 'steady-state' ELAs throughout the QEI (based on at least one point per 2500 km²) using one of three different traditional methods: (i) Accumulation Area Ratio (AAR; 0.65) on the lowest small cirque glacier; (ii) AAR (0.65) on the lowest small ice cap; and (iii) elevation of the change of contour inflection from convex to concave down-glacier on larger outlet glaciers. Although the AAR method performed on cirque glaciers was preferred, in the absence of cirque glaciers the second method was used where only ice caps existed, and the third option was used in extensively glacierized areas. Overall, 1960 ELA estimates produced from the first method are believed to be valid, given the methods used, and generally consistent with multiyear ELA estimates derived from mass balance records from a limited number of glaciers in the region (Dyurgerov, 2002; Dyurgerov and Meier, 2005). However, the second method systematically underestimates the ELA by using ice masses that were not in equilibrium with the contemporary climate. During the 1960 aerial photography surveys, many small plateau ice caps were entirely below the ELA, as evidenced by their missing accumulation area (Figure 5) and local ELA estimates determined from mass balance records (Dyurgerov, 2002; Dyurgerov and Meier, 2005). Therefore, under these conditions, the use of the AAR method on the lowest small ice cap in a given area would produce an erroneously low ELA. Based on an extensive photogrammetric evaluation of the study area using the 1960 aerial photographs and the QEI DEM mosaic, the 1960 ELA is thought to have been seriously underestimated in two areas: (i) central and western Devon Island; and (ii) S Ellesmere Island. For this area of the QEI, long-term mass balance monitoring exists only on the Devon Ice Cap, with records from 1961 to present (Dyurgerov, 2002; Dyurgerov and Meier, 2005). In order to estimate the multiyear ELA for the early 1960s, a fourth-order polynomial was used to statistically fit the observed ELA data. Based on this 'best-fit' model, the multiyear ELA for the Devon Ice Cap during the early-1960s was determined to be ~1200 m, which is >400 m above the corresponding estimates produced by Miller *et al.* (1975). To account for the underestimated ELAs over the southern QEI, the multiyear ELA for the Devon Ice Cap was used to create a grid of correction values, which was then applied to the original 1960 ELA trend surface (Miller

et al., 1975). The correction area was delineated according to two assumptions: (i) the 1960 ELA trend surface is correct in areas where cirque glaciers existed in 1960; and (ii) the 1960 ELA trend surface on Melville Island is correct (Figure 1). In the SE QEI, a correction value of 400 m was assigned to both the Devon and S Ellesmere Island ice caps (Figure 1), and a value of 0 m was assigned to areas containing small cirque glaciers (ie, central and E Ellesmere Island and E Devon Island), as well as to all points distal to these glaciers and those to the west beyond the underestimated region. These correction values were used as fixed limits in a tensional spline interpolation on a 1-km resolution grid to create an elevation model of correction values over the QEI (Figure 6). As an independent evaluation of the validity of the 1960 ELA corrections, NCEP/NCAR reanalysis was used to spatially model the height of the mean July 0°C isotherm over the QEI on a 2.5° resolution regular grid for the period 1958–1962 (Figure 7; Kalnay *et al.*, 1996; Kistler *et al.*, 2001). Bradley (1975) showed that in the Canadian High Arctic a strong positive correlation exists between the height of the July 0°C isotherm (freezing level) and the ELA; high July 0°C isotherm heights in the SE QEI suggest a correspondingly high ELA trend surface, which includes the area of underestimated ELAs (1960). Furthermore, the decreasing trend in isotherm heights to the northwest across the QEI corresponds to the tendency of correction values determined for the area of underestimated ELAs. The correction grid was added to the original 1960 ELA grid to produce a corrected 1960 ELA trend surface across the QEI (ELA.2, Figure 8). The map of corrected 1960 ELAs (ELA.2) replaces the original 1960 ELA trend surface map (from Miller *et al.*, 1975) for all analyses in forthcoming sections. The contrast between the 1960 and LIA ELA trend surfaces is used as a basis for interpreting differences in climatic conditions between the LIA and the mid-twentieth century, which led to post-LIA changes in perennial snow/ice extent across the QEI (Wolken *et al.*, 2008, this issue).

Changes in ELAs and perennial snow/ice cover

The ELA trend surface during the LIA shows a significant departure from the corrected 1960 ELA trend surface (Figure 9). The LIA ELA trend surface indicates lower elevations along coasts and increasing heights inland. For example, exceptionally low ELAs (0–200 m) are found along the coasts of SE Ellesmere and E Devon Islands that face Baffin Bay. In the northwest QEI a very low ELA (0–200 m) also characterizes the coastlines extending from Ellef Ringnes Island to N Ellesmere Island. ELAs gradually increase towards the southwest QEI where higher ELAs (400–600 m) are found on western Melville Island. Highest LIA ELAs (>1000 m) are over the interiors of Axel Heiberg and Ellesmere Islands.

In their mapping of ELAs and glaciation levels (GL) in the QEI, Miller *et al.* (1975) identified the existence of sharp gradients in the GL in coastal areas, in particular along the north coast of Ellesmere Island (Figure 4). Although the trend surfaces for both 1960 and the LIA exhibit similar spatial patterns, comparatively, LIA ELA gradients tend to be much shallower, which is especially apparent along the coasts of Devon and SE Ellesmere Islands bordering Baffin Bay and along the north coasts of Axel Heiberg and Ellesmere Islands. For instance, LIA ELA gradients along the north coast of Ellesmere Island to inland locations were ~6 m/km compared with ELA gradients of ~14 m/km for the same area in 1960. Changes in ELA gradients between the LIA and 1960 were the result of disproportionate changes in ELAs over the elevation

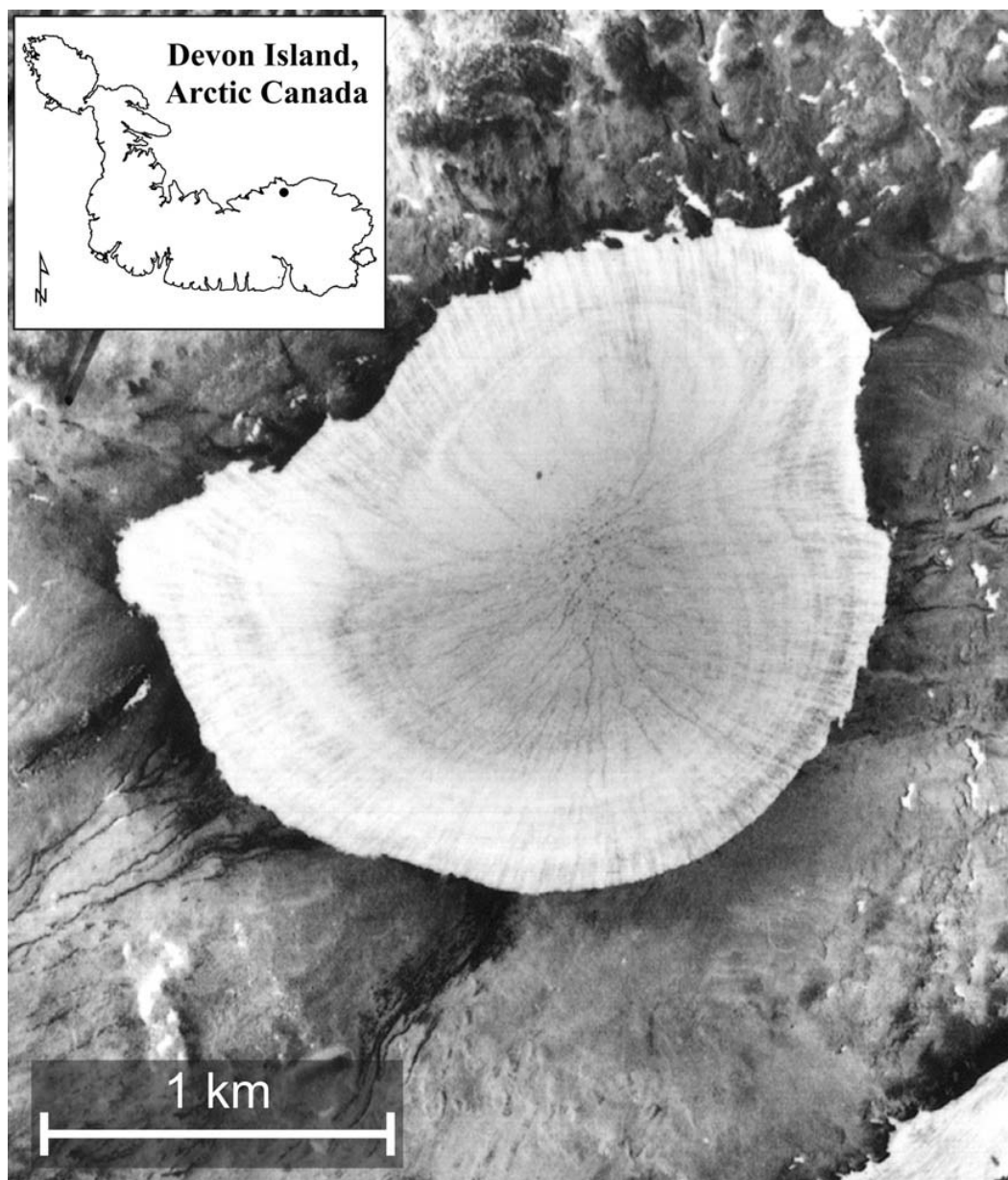


Figure 5 1959 aerial photograph of a small plateau ice cap on N Devon Island near Brae Bay (dark dot on inset map shows the location of the ice cap; Government of Canada, NAPL-A16684-5). The ice cap in this photo is entirely below the regional ELA, as evidenced by its missing accumulation area, and is indicative of many small plateau ice caps on Devon Island during the 1959/1960 aerial photography survey. Several supraglacial ponds are visible at the summit and numerous supraglacial meltwater channels can be seen clearly at all levels of the ice cap

range of the QEI; greater changes in ELAs occurred at higher elevation. Lower ELAs and accompanying shallow ELA gradients during the LIA may have been due to high precipitation rates during the LIA, influenced by cooler temperatures (ie, a lower lifting condensation level (LCL)) and/or more frequent storms. Indeed, in some parts of the QEI, palaeoclimate proxies indicate higher precipitation rates during the LIA (Lamoureux, 2000), while drier conditions seem to be prevalent during the early twentieth century, following the end of the LIA.

Throughout the QEI, a rise in the ELA following the LIA resulted in a substantial decrease in ice cover and a considerable exposure of predominantly unoxidized and unvegetated bedrock and/or unconsolidated substrates (Figure 2). ELA Δh from the LIA to 1960 show a strong regional-scale pattern of change

across the QEI, with considerable variability at the local-scale in the mountains of the eastern QEI (Figure 10). The region of greatest change (~300–600 m) extends from Devon Island, into S Ellesmere and S Axel Heiberg Islands and north into the lowlands separating Axel Heiberg and Ellesmere Islands, including the high plateaus and mountains of N Ellesmere Island. The smallest change (<100 m) occurs generally in the central to western QEI and in coastal localities, especially along N Axel Heiberg and NW Ellesmere Islands, the southeast sector of the QEI bordering Baffin Bay and W Melville Island. Collectively, these changes in the ELA resulted in a 62 387 km² or 37% decrease in perennial snow/ice cover across the QEI (Figure 11 and Table 1). Most of this ice cover loss (58 677 km², 94%) occurred on the three largest islands (Ellesmere, Axel Heiberg

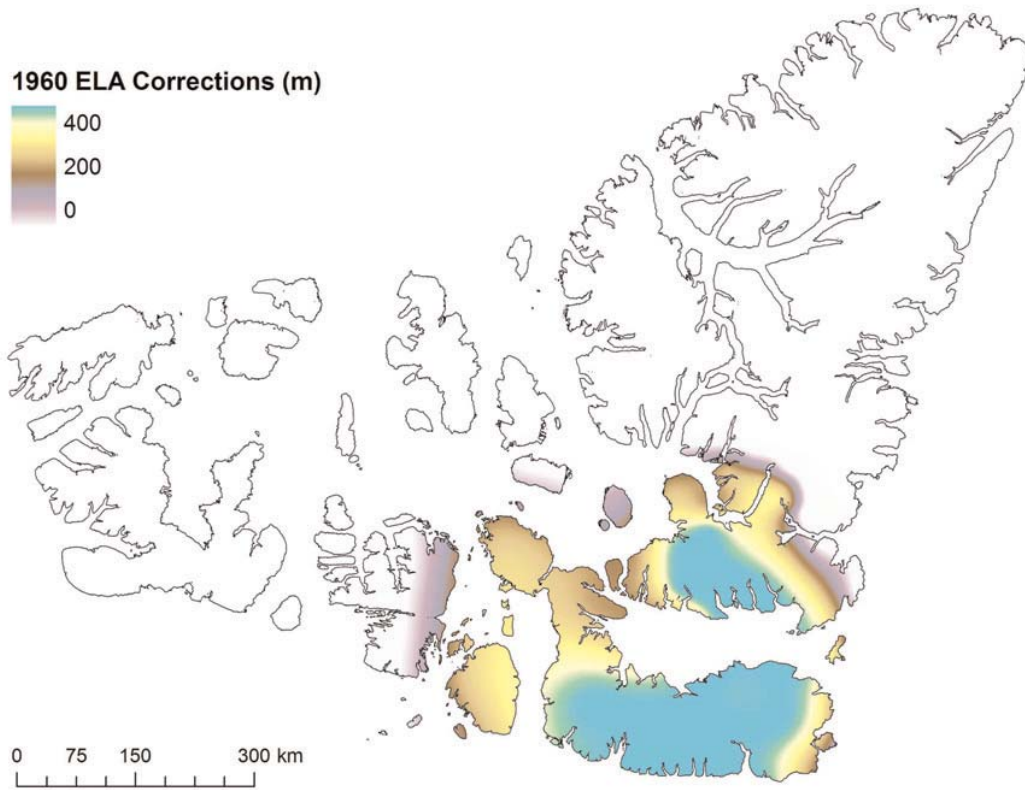


Figure 6 Correction values for 1960 ELAs. Values were interpolated over underestimated areas of the SE QEI based on the early 1960s multi-year ELA on the Devon Ice Cap

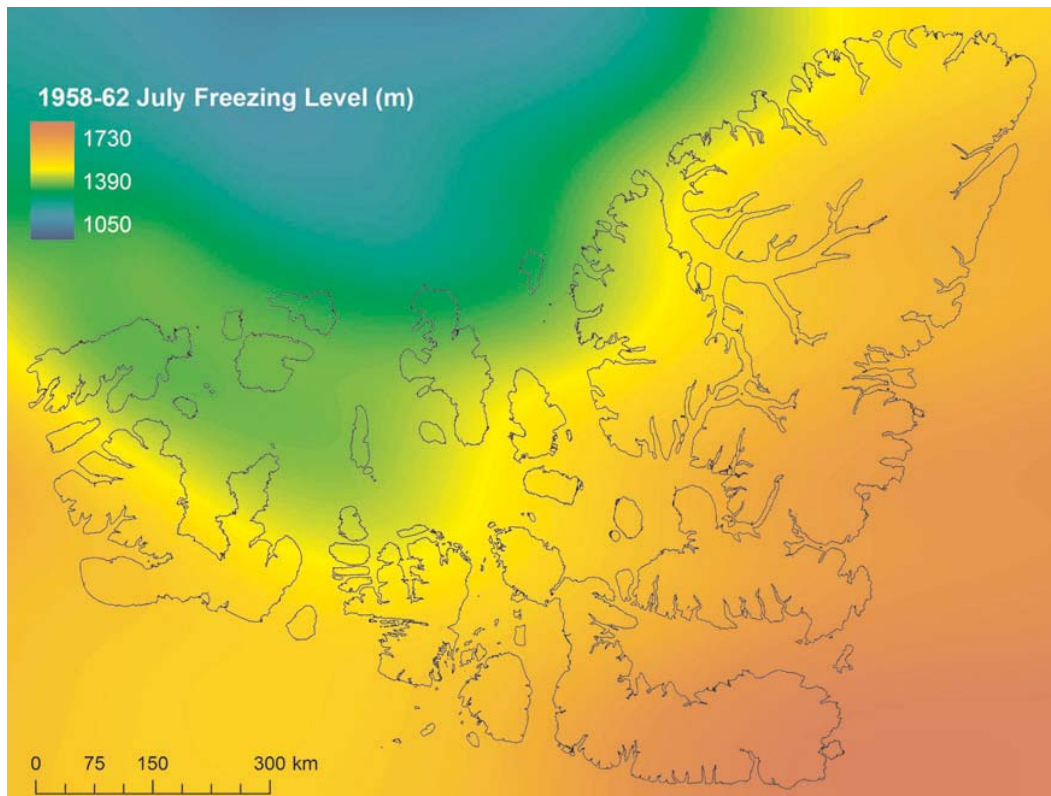


Figure 7 Mean July 0°C isotherm heights (freezing level) over the QEI for the period 1958–1962

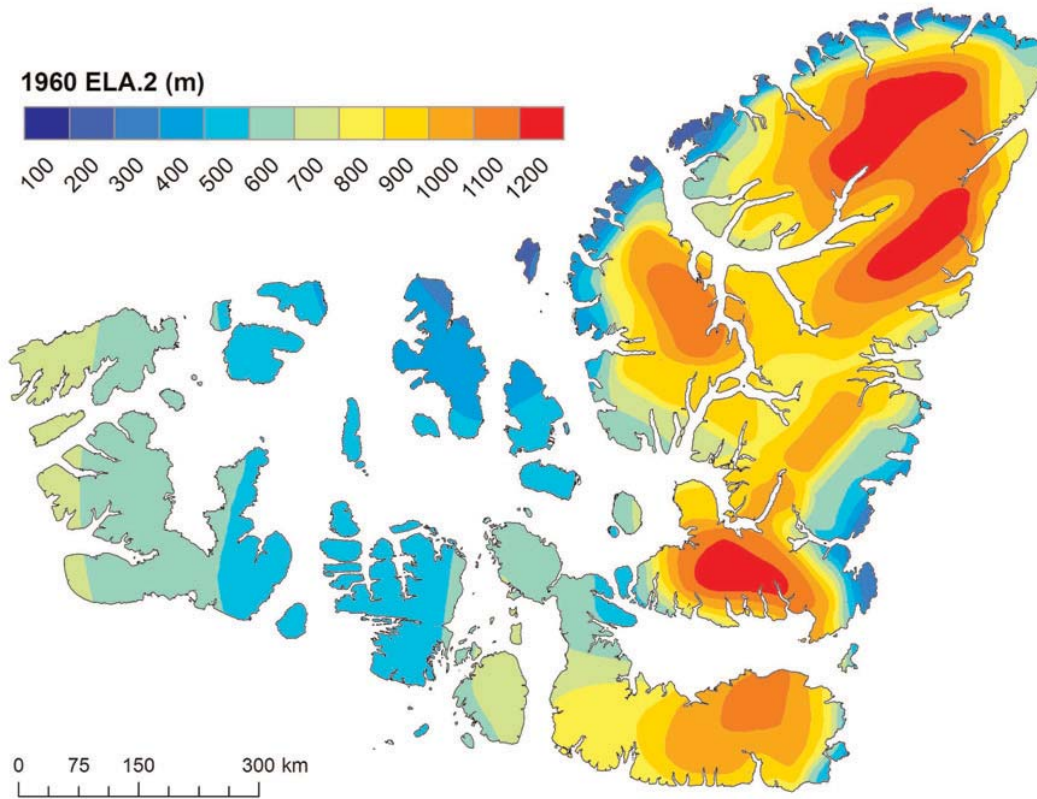


Figure 8 Corrected 1960 ELA trend surface (ELA.2); interpolated correction values (Figure 6) added to original 1960 ELAs (Figure 4; Miller *et al.*, 1975)

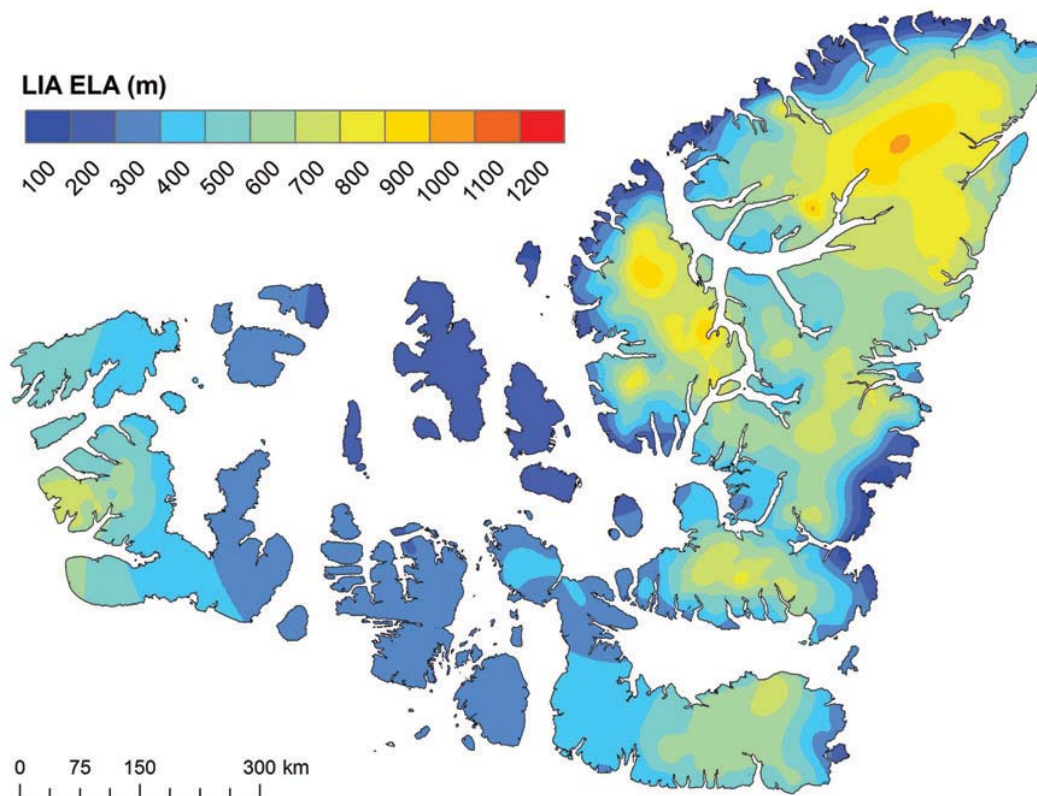


Figure 9 Reconstructed LIA ELAs for the QEI

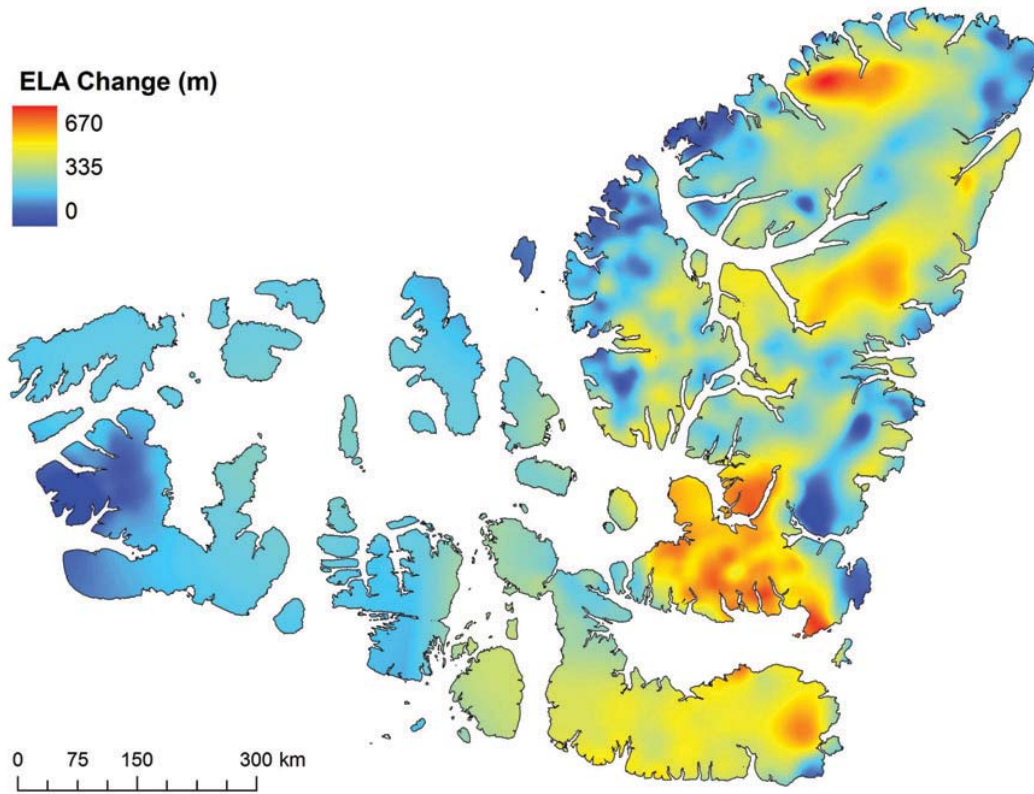


Figure 10 ELA change (Δh) between the LIA and 1960

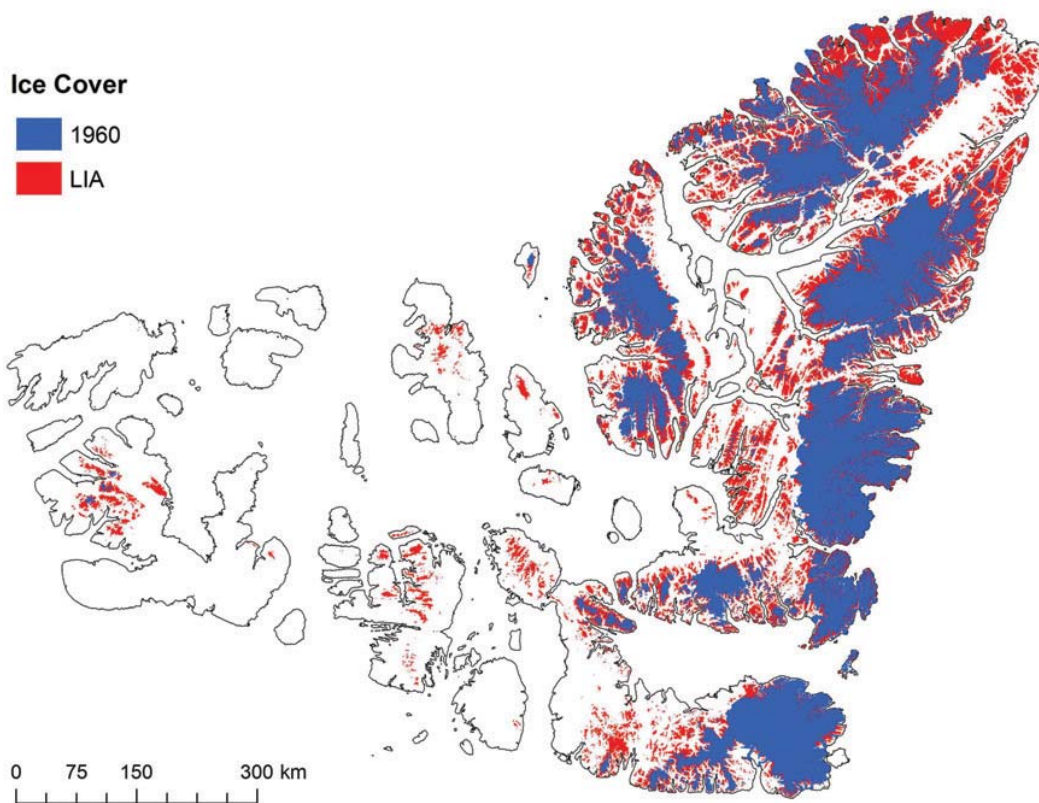


Figure 11 Reconstructed LIA and 1960 perennial snow/ice cover for the QEI

Table 1 LIA and 1960 ice area and area change totals (1960-LIA) for the QEI.

Island	LIA (km ²)	1959/60 (km ²)	Area change (km ²)	% Area change
Ellesmere	122 993.0	79 317.5	-43 675.6	-35.5
Axel Heiberg	20 039.4	11 987.2	-8052.2	-40.2
Devon	22 942.8	15 993.1	-6949.7	-30.3
Melville	1860.8	153.2	-1707.6	-91.8
Bathurst	1065.4	0.0	-1065.4	-100.0
Ellef Ringnes	497.1	0.0	-497.1	-100.0
Amund Ringnes	246.7	0.0	-246.7	-100.0
Cornwall	69.4	0.0	-69.4	-100.0
Meighen	155.6	93.1	-62.5	-40.1
Coburg	226.9	188.0	-39.0	-17.2
Cornwallis	22.8	0.0	-22.8	-100.0

and Devon Islands) where most of the ice in the QEI is concentrated today. Area changes for individual islands ranged from 17 to 40% for the eastern QEI (Ellesmere, Axel, Devon and Coburg Islands). With the exception of Meighen Island (40%), reductions in the low-lying central and western QEI (Bathurst, Cornwallis, Cornwall, Amund Ringnes, Ellef Ringnes and Melville Islands) ranged from 90 to 100%.

A change in the distribution of ice cover in the QEI with respect to the position of the ELA is dependent not only on the prevailing climatic conditions, but also on the aspect (Williams, 1975) and the hypsometry (area–elevation distribution) of the land. Figure 12 shows area–elevation relationships for the LIA and 1960 ice covers. During the LIA, lower ELAs resulted in more land incorporated in the accumulation zone; hence, a higher percentage of ice-covered land. The maximum areal coverage of perennial snow/ice in the QEI during this time was centred on an elevation of ~700 m. By 1960, however, this had increased to ~1100 m. Consequently, the greatest reduction of ice cover following the LIA was on intermediate elevation plateaus (700–1000 m) rather than in surrounding mountains where higher accumulation zones have helped to maintain many outlet glaciers close to their LIA margins.

Climatically induced lowering (rising) of the ELA will result in an increase (decrease) in ice-covered area as more land is added to the accumulation area (ablation area). This effect is enhanced if ELA lowering (or rising) occurs in areas where topographic complexity is low (ie, few large undulations) and orographic amplitude is high (ie, high land elevation), such as in intermediate and high plateaus. Such areas may provide the most suitable setting for glacial inception (Oerlemans, 2002), but they are also the most vulnerable to large-scale reductions in perennial snow/ice cover as a result of a small increase in the ELA. For instance, on western Melville Island, extensive high plateaus rise abruptly from sea level to >700 m in the west and descend gently eastward to >400 m over ~100 km. Between the LIA and 1960, an average increase in the ELA of only ~50 m over the plateaus of W Melville led to a 92% reduction in ice cover (Figures 10 and 11). Substantial reductions in ice cover since the LIA are characteristic of many of the plateaus in the central and western QEI, where orographic range is limited to only a few hundred metres over hundreds of square kilometres, and the change in ELA was generally <100 m. By 1960, most of these islands were devoid (or nearly so) of perennial snow/ice (Figure 11 and Table 1). In contrast, the least amount of areal change in perennial snow/ice cover, coincident with the largest change in Δh , occurred in the highest mountains of Axel Heiberg and Ellesmere Islands, where large ice caps and many glaciers persist today. In these highly glacierized areas, large changes in the ELA have little short-term (10^1 – 10^2 yr) impact because the ice coverage above the ELA remains substantial.

Conclusions

The areal extent of perennial snow/ice in the QEI underwent a considerable reduction between the end of the LIA and 1960 as a consequence of early twentieth-century warming. Trimlines were used to map former LIA perennial snow/ice extent throughout the QEI, revealing a 37% (62 387 km²) reduction in snow and ice cover between the end of the LIA and 1960. The largest areal reduction in snow and ice extent occurred in the eastern QEI where most ice persists today; however, the most substantial reductions occurred on intermediate and high plateaus where small increases in the ELA caused vast areas to enter the ablation zone. On several of the central and western islands, a complete removal of snow/ice cover occurred by 1960, which was largely controlled by the low relief of these islands, which in turn makes them especially vulnerable to a rise in the ELA. ELA changes (Δh) between the LIA and 1960 range from 0 to >600 m; the spatial distribution of Δh reveals a high degree of local variability in the mountains of the eastern QEI, but it exhibits a strong regional-scale pattern of change over the QEI as a whole.

This research demonstrates the usefulness of trimlines for reconstructing ELAs and former perennial snow/ice extent in the Canadian High Arctic. Reconstructed LIA ELAs represent important indicators of LIA climate and the change in the ELA trend surface between the LIA and 1960 can serve as a valuable proxy for early twentieth-century climatic change in a region with exceptionally limited observational data during this time. Furthermore, data presented in this study significantly advance our knowledge about the configuration and extent of perennial ice across the QEI during the late Neoglacial and improve our understanding of the nature and magnitude of its reduction from the LIA to the mid-twentieth century.

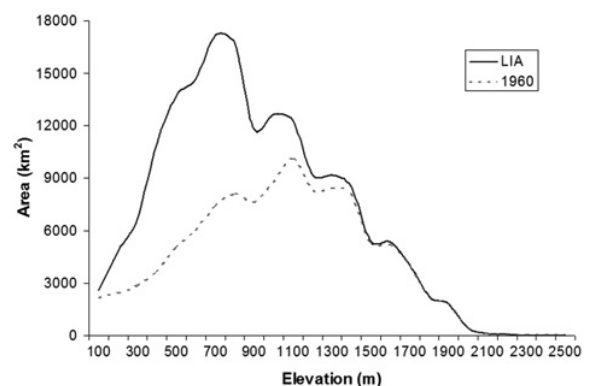


Figure 12 Area–elevation (hypsometric) relationships for LIA and 1960 ice covers in the QEI

Acknowledgements

Financial support for this research was provided by the Natural Sciences and Engineering Research Council of Canada (NSERC Discovery Grant A6680) and the NSERC Northern Chair Award, both to J. England. Additional support to the G. Wolken was provided by the Canadian Circumpolar Institute (University of Alberta, Edmonton, Alberta). The Polar Continental Shelf Project, Natural Resources Canada, provided logistical support during the summers of 2001 and 2003 (PCSP/ÉPCP contribution # 003-07). Special thanks to M. Sharp for providing Landsat 7 ETM+ imagery, purchased through support from CRYSYS (Cryospheric System to Monitor Global Change in Canada). ASTER (Advanced Spaceborne Thermal Emission and Reflection Radiometer) imagery was provided by the GLIMS (Global Land Ice Measurements from Space) project. We are grateful to R. Bradley (University of Massachusetts), A. Bush (University of Alberta) and D. Hik (University of Alberta) for their comments on an earlier draft of the manuscript. Finally, we thank Atle Nesje and an anonymous referee for their comments and suggestions of how to improve this manuscript.

References

- Andrews, J.T., Barry, R.G., Davis, P.T., Dyke, A.S., Mahaffy, M., Williams, L.D. and Wright, C. 1975: The Laurentide Ice Sheet: problems of the mode and speed of inception. *World Meteorological Publication* 421, 87–94.
- Andrews, J.T., Davis, P.T. and Wright, C. 1976: Little Ice Age permanent snowcover in the Eastern Canadian Arctic: extent mapped from Landsat-1 satellite imagery. *Geografiska Annaler* 58A, 71–81.
- Arctic Climate Impact Assessment (ACIA) 2004: *Arctic climate impacts assessment*. Cambridge University Press, 1046 pp.
- Arendt, A.A., Echelmeyer, K.A., Harrison, W.D., Lingle, C.S. and Valentine, V.B. 2002: Rapid wastage of Alaska glaciers and their contribution to rising sea level. *Science* 297, 382–86.
- Bengtsson, L., Semenov, V.A. and Johannessen, O.M. 2004: The early twentieth-century warming in the Arctic – a possible mechanism. *Journal of Climate* 17, 4045–57.
- Blake, W.J. 1981: Neoglacial fluctuations of glaciers, Southeastern Ellesmere Island, Canadian Arctic Archipelago. *Geografiska Annaler* 63, 201–18.
- Bradley, R.S. 1975: Equilibrium-line altitudes, mass balance, and July freezing-level heights in the Canadian High Arctic. *Journal of Glaciology* 14, 267–74.
- 1990: Holocene paleoclimatology of the Queen Elizabeth Islands, Canadian High Arctic. *Quaternary Science Reviews* 9, 365–84.
- Braun, C., Hardy, D.R. and Bradley, R.S. 2004: Mass balance and area changes of four High Arctic plateau ice caps, 1959–2002. *Geografiska Annaler Series A-Physical Geography* 86A, 43–52.
- Burgess, D.O. and Sharp, M.J. 2004: Recent changes in areal extent of the Devon Ice Cap, Nunavut, Canada. *Arctic, Antarctic, and Alpine Research* 36, 261–71.
- Burgess, D.O., Sharp, M.J., Mair, D.W.F., Dowdeswell, J.A. and Benham, T.J. 2005: Flow dynamics and iceberg calving rates of the Devon Ice Cap, Nunavut, Canada. *Journal of Glaciology* 51, 219–30.
- Centre for Topographic Information (C.S.G.) 2000: *Canadian digital elevation data standards and specifications*. Natural Resources Canada, 15 pp.
- Church, J.A., Gregory, J.M., Huybrechts, P., Kuhn, M., Lambeck, K., Niu, M.T., Qin, D. and Woodworth, P.L. 2001: Changes in sea level. In Intergovernmental Panel on Climate Change, *Climate change 2001: the scientific basis*. Cambridge University Press, 641–93.
- Dowdeswell, J.A., Hagen, J.O., Bjornsson, H., Glazovsky, A.F., Harrison, W.D., Holmlund, P., Jania, J., Koerner, R.M., Lefauconnier, B., Ommanney, C.S.L. and Thomas, R.H. 1997: The mass balance of circum-Arctic glaciers and recent climate change. *Quaternary Research* 48, 1–14.
- Dyke, A.S. 1978: *Indications of neoglaciation on Somerset Island, District of Franklin*. Scientific and Technical Notes, Current Research, Part B; Geological Survey of Canada, 215–17.
- Dyrgerov, M.B. 2002: *Glacier mass balance and regime: data of measurements and analysis*. Institute of Arctic and Alpine Research, University of Colorado, 268 pp.
- Dyrgerov, M.B. and Meier, M.F. 1997: Mass balance of mountain and subpolar glaciers: a new global assessment for 1961–1990. *Arctic and Alpine Research* 29, 379–91.
- 2005: *Glaciers and the changing Earth system: a 2004 snapshot*. Institute of Arctic and Alpine Research, University of Colorado, 118 pp.
- Edlund, S.A. 1985: *Lichen-free zones as neoglaciation indicators on western Melville Island, District of Franklin*. Current Research, Part A, Geological Survey of Canada Paper 85-1A, 709–712.
- England, J. 1977: The glacial geology of northeastern Ellesmere Island, N. W. T., Canada. *Canadian Journal of Earth Science* 15, 603–17.
- Evans, D.J.A. and England, J. 1992: Geomorphological evidence of Holocene climatic change from northwest Ellesmere Island, Canadian High Arctic. *The Holocene* 2, 148–58.
- Falconer, G. 1966: Preservation of vegetation and patterned ground under a thin ice body in north Baffin Island, N.W.T., Canada. *Geographical Bulletin* 8, 194–200.
- Grove, J.M. 2001: The initiation of the ‘Little Ice Age’ in regions round the North Atlantic. *Climatic Change* 48, 53–82.
- Hutchinson, M.F. 1989: A new procedure for gridding elevation and stream line data with automatic removal of spurious pits. *Journal of Hydrology* 106, 211–32.
- Ives, J.D. 1962: Indication of recent extensive glaciation in north central Baffin Island, N.W.T. *Journal of Glaciology* 4, 197–205.
- Johannessen, O.M., Bengtsson, L., Miles, M.W., Kuzmina, S.I., Semenov, V.A., Alekseev, G.V., Nagurnyi, A.P., Zakharov, V.F., Bobylev, L.P., Pettersson, L.H., Hasselmann, K. and Cattle, A.P. 2004: Arctic climate change: observed and modelled temperature and sea-ice variability. *Tellus Series a-Dynamic Meteorology and Oceanography* 56, 328–41.
- Kalnay, E., Kanamitsu, M., Kistler, R., Collins, W., Deaven, D., Gandin, L., Iredell, M., Saha, S., White, G., Woollen, J., Zhu, Y., Chelliah, M., Ebisuzaki, W., Higgins, W., Janowiak, J., Mo, K.C., Ropelewski, C., Wang, J., Leetmaa, A., Reynolds, R., Jenne, R. and Joseph, D. 1996: The NCEP/NCAR 40-year reanalysis project. *Bulletin of the American Meteorological Society* 77, 437–71.
- Kistler, R., Kalnay, E., Collins, W., Saha, S., White, G., Woollen, J., Chelliah, M., Ebisuzaki, W., Kanamitsu, M., Kousky, V., van den Dool, H., Jenne, R. and Fiorino, M. 2001: The NCEP-NCAR 50-year reanalysis: monthly means CD-ROM and documentation. *Bulletin of the American Meteorological Society* 82, 247–67.
- Koerner, R.M. and Fisher, D.A. 1990: A record of Holocene summer climate from a Canadian high-Arctic ice core. *Nature* 343, 630–31.
- Koerner, R.M. and Paterson, W.S. 1974: Analysis of a core through Meighen Ice Cap, Arctic Canada, and its paleoclimatic implications. *Quaternary Research* 4, 253–63.
- Lamoureux, S. 2000: Five centuries of interannual sediment yield and rainfall-induced erosion in the Canadian High Arctic recorded in lacustrine varves. *Water Resources Research* 36, 309–18.
- Locke, C.W. and Locke, W.W. 1977: Little Ice Age snow-cover extent and paleoglaciation thresholds: North-central Baffin Island, N.W.T., Canada. *Arctic and Alpine Research* 9, 291–300.
- Mair, D., Burgess, D. and Sharp, M. 2005: Thirty-seven year mass balance of Devon Ice Cap, Nunavut, Canada, determined by shallow ice coring and melt modeling. *Journal of Geophysical Research-Earth Surface* 110, F01011, doi:10.1029/2003JF000099.
- Miller, G.H., Bradley, R.S. and Andrews, J.T. 1975: The glaciation level and lowest equilibrium line altitude in the High Canadian Arctic: maps and climatic interpretation. *Arctic and Alpine Research* 7, 155–68.
- Miller, G.H., Wolfe, A.P., Briner, J.P., Sauer, P.E. and Nesje, A. 2005: Holocene glaciation and climate evolution of Baffin Island Arctic Canada. *Quaternary Science Reviews* 24, 1703–21.

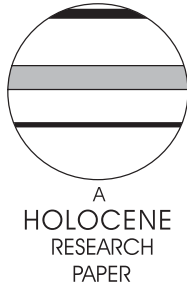
- Oerlemans, J.** 2002: On glacial inception and orography. *Quaternary International* 95, 5–10.
- Overpeck, J.K., Hughen, K., Hardy, D., Bradley, R., Case, R., Douglas, M., Finney, B., Gajewski, K., Jacoby, G., Jennings, A., Lamoureux, S., Lasca, A., MacDonald, G., Moore, J., Retelle, M., Smith, S., Wolfe, A. and Zielinski, G.** 1997: Arctic environmental change of the last four centuries. *Science* 278, 1251–56.
- Shepherd, A., Du, Z., Benham, T.J., Dowdeswell, J.A. and Morris, E.M.** 2007: Mass balance of Devon Ice Cap, Canadian Arctic. *Annals of Glaciology* 46, 249–54.
- Williams, L.D.** 1975: The variation of corrie elevation and equilibrium line altitude with aspect in Eastern Baffin Island, N.W.T., Canada. *Arctic and Alpine Research* 7, 169–81.
- Williams, R.S.J. and Ferrigno, J.G.** 2002: Introduction. In Williams, R.S.J. and Ferrigno, J.G., editors, *Satellite image atlas of glaciers of the world. Glaciers of North America – glaciers of Canada*. U.S. Geological Survey, 405 pp.
- Wolken, G.J.** 2006: High-resolution multispectral techniques for mapping former Little Ice Age terrestrial ice cover in the Canadian High Arctic. *Remote Sensing of Environment* 101, 104–14.
- Wolken, G.J., England, J.H. and Dyke, A.S.** 2005: Re-evaluating the relevance of vegetation trimlines in the Canadian Arctic as an indicator of Little Ice Age paleoenvironments. *Arctic* 58, 341–53.
- Wolken, G.J., Sharp, M.J. and England, J.H.** 2008: Changes in late-Neoglacial climate inferred from former equilibrium-line altitudes in the Queen Elizabeth Islands, Arctic Canada. *The Holocene* 18, 00–000.

Changes in late-Neoglacial climate inferred from former equilibrium-line altitudes in the Queen Elizabeth Islands, Arctic Canada

Gabriel J. Wolken,* Martin J. Sharp and John H. England

(Department of Earth and Atmospheric Sciences, University of Alberta, Alberta T6G 2E3, Canada)

Received 8 February 2007; revised manuscript accepted 3 December 2007



Abstract: Regional-scale spatial variation in the change in equilibrium-line altitude (ELA) trend surface in the Queen Elizabeth Islands (QEI), Arctic Canada between the ‘Little Ice Age’ (LIA) and 1960 corresponds to Empirical Orthogonal Functions (EOFs) representing specific patterns of summer climate variability found in the modern record. Extreme warm (1953–1962) and cold (1965–1974) decades in the modern record were used as modern analogues of climatic conditions during the early twentieth century and the LIA, respectively. Because of the minimal influence of precipitation during both extreme decades, temperature is the variable upon which the fluctuation of the ELA is dependent. Hence, the ELA Δh pattern describes the spatial pattern of change in SAT across the QEI between the LIA and 1960. This pattern is consistent with the primary mode of variability of mean summer surface air temperature (SAT) in the modern record (ie, EOF-1, 1949–2002), the positive (negative) phase of which is strongly in place during the extreme warm (cold) decade. SAT anomalies in the QEI during the warm (cold) decade are positively correlated with a weak (strong) QEI-distal (QEI-proximal) polar vortex, higher (lower) than normal SSTs in the North Atlantic, and one of the lowest (highest) periods of sea-ice extent during the twentieth century. The climatic conditions during the cold decade are believed to describe conditions, which if sustained, would lead to a LIA-type cold episode capable of long-term snowline lowering and perennial snow/ice expansion. The climatic conditions during the warm decade represent possible modern analogues for those that might have occurred during the early twentieth century in the Canadian High Arctic, which led to a substantial reduction in perennial snow/ice.

Key words: Trimlines, ‘Little Ice Age’, snow extent, ice-cover change, glaciers, equilibrium-line altitude, climate variability, polar vortex, Arctic Canada, Queen Elizabeth Islands.

Introduction

Climate change and the role of anthropogenic forcing have become focal issues in the last few decades, and concerns have escalated with regard to observed and predicted modifications to Polar Regions (Arctic Climate Impacts Assessment (ACIA), 2004). The most recognized impacts pertain to Northern Hemisphere sea ice reduction and thinning (Johannessen *et al.*, 1999; Vinikov *et al.*, 1999) and the simultaneous reduction of glaciers and ice caps that are contributing to global sea-level rise (Dyurgerov and Meier, 1997; Intergovernmental Panel on Climate Change (IPCC), 2001). Part of the problem with accurately assessing modern climate change is the inability to differentiate between changes resulting from natural climatic variability from those occasioned by forcing from greenhouse gases and sulphate

aerosols. This uncertainty is accentuated in the Canadian High Arctic because of the brevity of the instrumental record (~56 yr), which precludes direct observations of climate change prior to the mid-twentieth century. Consequently, one must rely on palaeoclimate proxies in high latitudes in order to better evaluate the record of natural variability; such records can be used as a baseline to better profile modern changes.

This study uses the change in the extent of perennial snow/ice and the variation in the equilibrium-line altitude (ELA) trend surface between the ‘Little Ice Age’ (LIA; ~AD 1250–1900, Grove, 2001) and 1960 in the Queen Elizabeth Islands (QEI; Figure 1). This comparison of LIA and 1960 ELAs records the impact of early twentieth-century warming in the Canadian High Arctic (Wolken *et al.*, 2008, this issue) and provides the basis for exploring the complex feedbacks internal to the climate system that may have contributed to these reported changes. The assumption is made that all atmosphere/ocean boundary conditions occurring

*Author for correspondence (e-mail: gwolken@ualberta.ca)

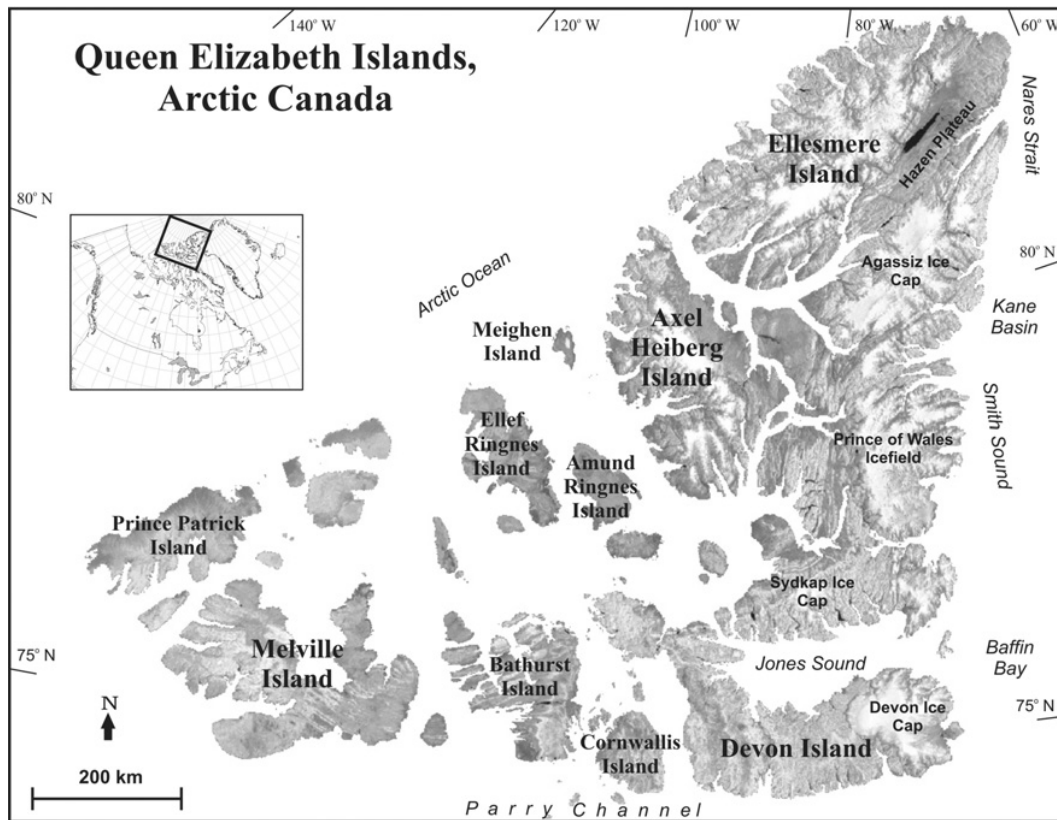


Figure 1 Map of the Queen Elizabeth Islands, Arctic Canada (Radarsat Orthomosaic, courtesy of the Canadian Centre for Remote Sensing)

during the LIA and early twentieth century can also occur in the modern record. Thus, patterns of ELA Δh (the trend surface of difference in ELA; Wolken *et al.*, 2008, this issue) are referenced against specific modes of variability associated with climatological variables in the modern record (1949–2002) that serve as analogues for those that might have occurred during the early twentieth century in the Canadian High Arctic. Changes in the ELA (Δh) from LIA to 1960 provide first-order estimates of climate change in the QEI and implicate possible patterns of atmospheric circulation that may explain the observed changes in early twentieth-century perennial snow/ice extent. The objective of the climatic analyses is to provide a better understanding of the synoptic scale conditions that influence the extent of terrestrial ice cover in Arctic Canada.

Study area climatology

The climate of the Canadian Arctic is strongly influenced by complex interactions between the atmosphere, ocean, sea ice and land (Serreze and Barry, 2005). Although topographically diverse, most of the land surface of the QEI has been classified as polar desert, which is indicative of the aridity of this region. However, Maxwell (1981) partitions the Canadian High Arctic into climatic subregions, indicating high precipitation and greater warmth around Baffin Bay compared with colder areas in the more continental central and northwest QEI (Edlund and Alt, 1989). Systematic meteorological observations in the QEI began in the late 1940s, with the establishment of five coastal weather stations (Alert, Eureka, Mould Bay, Isachsen and Resolute Bay). Observations have been at times intermittent, and Mould Bay and

Isachsen have been closed in recent years. Efforts have been made to characterize the synoptic climatology of the region (Bradley, 1973, 1975; Bradley and England, 1978b, 1979; Alt, 1987), which revealed substantial variability in synoptic types and their influence on regional glaciers and ice caps.

Data sources

NCEP/NCAR reanalysis

The NCEP/NCAR reanalysis (NNR, following Bromwich *et al.*, 2002) uses data from 1948 to the present for data assimilation conducted four times per day (every six hours starting at 0Z), with a T-62 coordinate system (horizontal resolution of ~208 km) at 28 levels vertically (Kalnay *et al.*, 1996; Kistler *et al.*, 2001). As per standard procedure, these four times daily values are averaged, and the daily means are compiled to monthly means, which are then output to a global grid with a spatial resolution of 2.5° latitude by 2.5° longitude. The monthly mean data (1949–2002) for this study were obtained from the NCEP/NCAR Reanalysis Project (<http://www.cdc.noaa.gov/cdc/reanalysis/reanalysis.shtml>) and include: 2 m temperature (hereafter referred to as surface air temperature, SAT); surface precipitation rate (SPR); sea-level pressure (SLP); and 850, 500 and 200 hPa geopotential heights. Gridded NNR variables are ranked according to the relative influence of observational data versus model output, where a rank of *A* indicates that the variable selected is most reliable, based strongly on observational data, whereas rank *B* indicates less reliability owing to diminished observational influence on the variable and a greater dependence on the model.

Rank *C* indicates a variable that is fully model dependent, ie, direct observational data associated with the variable are unavailable (Kalnay *et al.*, 1996). For the variables used in this study, NNR ranks geopotential height and SLP as *A*, SAT as *B* and SPR as *C*.

Gridded reanalysis allows a more comprehensive assessment of climate in remote regions than does individual station analysis and is generally preferred in climate studies of the Arctic (Bromwich *et al.*, 2002). Some high-latitude studies, however, have revealed inaccuracies in certain NNR variables. For example, topographic smoothing related to the low resolution of gridded NNR oversimplifies mountainous terrain, which leads to inaccuracies in the derived modelled temperatures (Bromwich *et al.*, 2002). In the QEI, the potential for this error is greatest in its eastern sector, where topographic complexity is greatest. Compounding this problem is the paucity and variable quality of observational climate data from this region, which cause inhomogeneities in the assimilation data, especially in the early part of the record (pre-1958) when only limited radiosonde coverage occurred (Serreze and Barry, 2005: 257). Furthermore, only two long-term weather stations exist in the mountainous eastern sector of the QEI (Alert and Eureka), both of which are located in coastal lowlands, thereby limiting their climatic representation of this area (Maxwell, 1981).

Additional inaccuracies are associated with NNR modelled precipitation in the Arctic. Over land areas, NNR tends to overestimate summer precipitation, an effect resulting from excessive (modelled) convective precipitation (Serreze and Hurst, 2000). For the period of interest in this study (1949–2002), however; summer precipitation rate over the QEI is very low and any overestimation inherent to this variable is believed to have little impact on subsequent analyses (discussed below). NNR generated spatial patterns of precipitation rate has also been shown to be too simplistic, especially in its inability to produce observed interannual variability in snow cover (Serreze and Maslanik, 1997; Cullather *et al.*, 2000). Serreze *et al.* (2003) report consistent NNR underestimation of precipitation variability in Arctic regions, and similar accounts of underestimated precipitation variability are also noted by Bromwich *et al.* (2002) in their work over Baffin Island. Nevertheless, they noted that the normalized, long-term record still captures the relative variability in SPR, which is also true over the QEI.

ERSST data

Climate variability is strongly linked to variations in oceanic boundary conditions (Hansen and Bezdek, 1996). Thus, the influence of Sea Surface Temperatures (SSTs) on variations in atmospheric cir-

culaton is considered for high latitude regions. The Extended Reconstructed Sea Surface Temperature (ERSST v.2) data set (Smith and Reynolds, 2004) was obtained from the National Oceanic and Atmospheric Administration's Cooperative Institute for Research in Environmental Sciences (NOAA-CIRES), Climate Diagnostic Center (CDC) (<http://www.cdc.noaa.gov/cdc/data.noaa.ersst.html>). The ERSST v.2 was developed using the SST data and enhanced statistical techniques provided by the International Comprehensive Ocean–Atmosphere Data Set (ICOADS). The ERSST v.2 has a 2° latitude by 2° longitude grid, and was designed to manage more effectively regions with weak-variance while improving high-latitude SST analyses by using sea-ice concentration data (Smith and Reynolds, 2004).

Analysis and discussion

This section presents a three-part analysis and discussion of the spatial changes in perennial snow and ice extent and ELA Δh between the LIA and 1960 in the QEI, as reported in Wolken *et al.* (2008, this issue). The first section analyses NCEP/NCAR reanalysis and identifies extreme cold and warm decades, and specific modes of variability associated with climatological variables in the modern record (1949–2002). These cold and warm decades serve as possible analogues for those that might have occurred between the LIA and the early twentieth century in the QEI. In the second section, important atmosphere–ocean interactions related to the assumed modern analogues of LIA and the early twentieth-century climates (cold and warm decades) are further identified and discussed. The third section identifies important connections between the pattern of ELA Δh and the primary modes of variability of climatological variables found in the modern record, and provides a spatial reconstruction of post-LIA to 1960 temperature change in the QEI.

Climate variability: 1949–2002

In the QEI, variability in net mass balance is dominated by climate conditions during the summer (ie, temperature and precipitation). This is largely because winter accumulation is low and relatively consistent, allowing interannual variability in ablation to predominantly control variations in the height of the equilibrium-line (Dowdeswell *et al.*, 1997). It is, therefore, assumed that the reduction of perennial snow/ice extent since the LIA has also been dominated by changes in summer climate; if so, this reduction provides a proxy record of summer climate change. Hence, the variability in

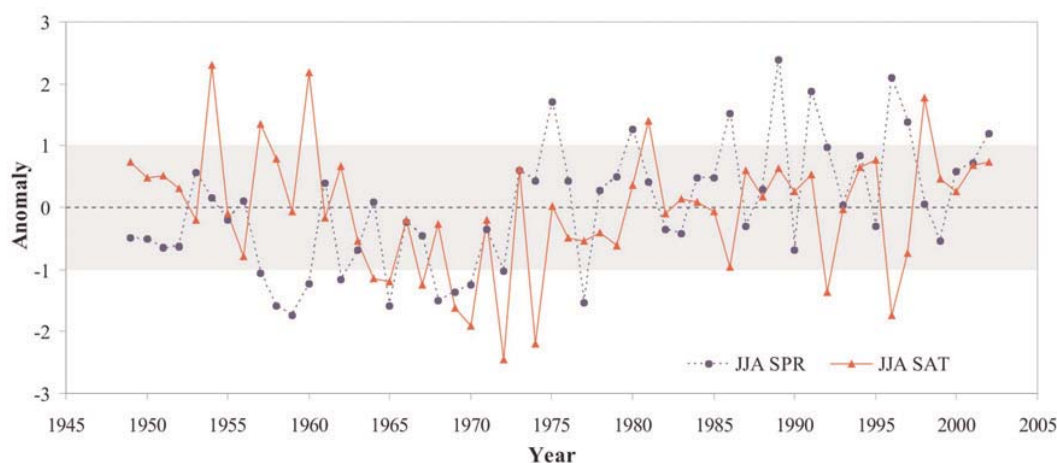


Figure 2 Standardized anomaly time series of summer 2 m temperature (SAT; red) and winter surface precipitation rate (SPR; blue) for the period 1949–2002. Extreme years are those with standardized anomaly values exceeding one standard deviation

summer temperature and precipitation in the QEI between the end of the LIA and 1960 is of primary interest for this study. However, because the instrumental record in the QEI (~56 yr) extends only a decade into the record of ELA change (LIA to 1960), the contemporary record was searched for potential modern analogues of climatic conditions that would have favoured, and hence help to explain, the high summer ablation and the large spatial differences in Δh in the QEI during the early twentieth century (noted above).

All NNR variables were spatially averaged across the QEI based on a 2.5° resolution grid. All climate variables used in this study (NNR and ERSST) span the interval 1949–2002 and

annual, summer (JJA) and winter (SONDJFMAM) averages were obtained for each year. Long-term seasonal means (1949–2002) and standard deviations were calculated, and used to compute standardized anomalies from the long-term mean by,

$$X_N = (X_i - X_m) / S_x \quad (1)$$

where X_i is the mean of a meteorological variable (annual or seasonal) for a particular year, X_m is the long-term mean (annual or seasonal), and S_x is the long-term standard deviation (annual or seasonal) for a meteorological variable.

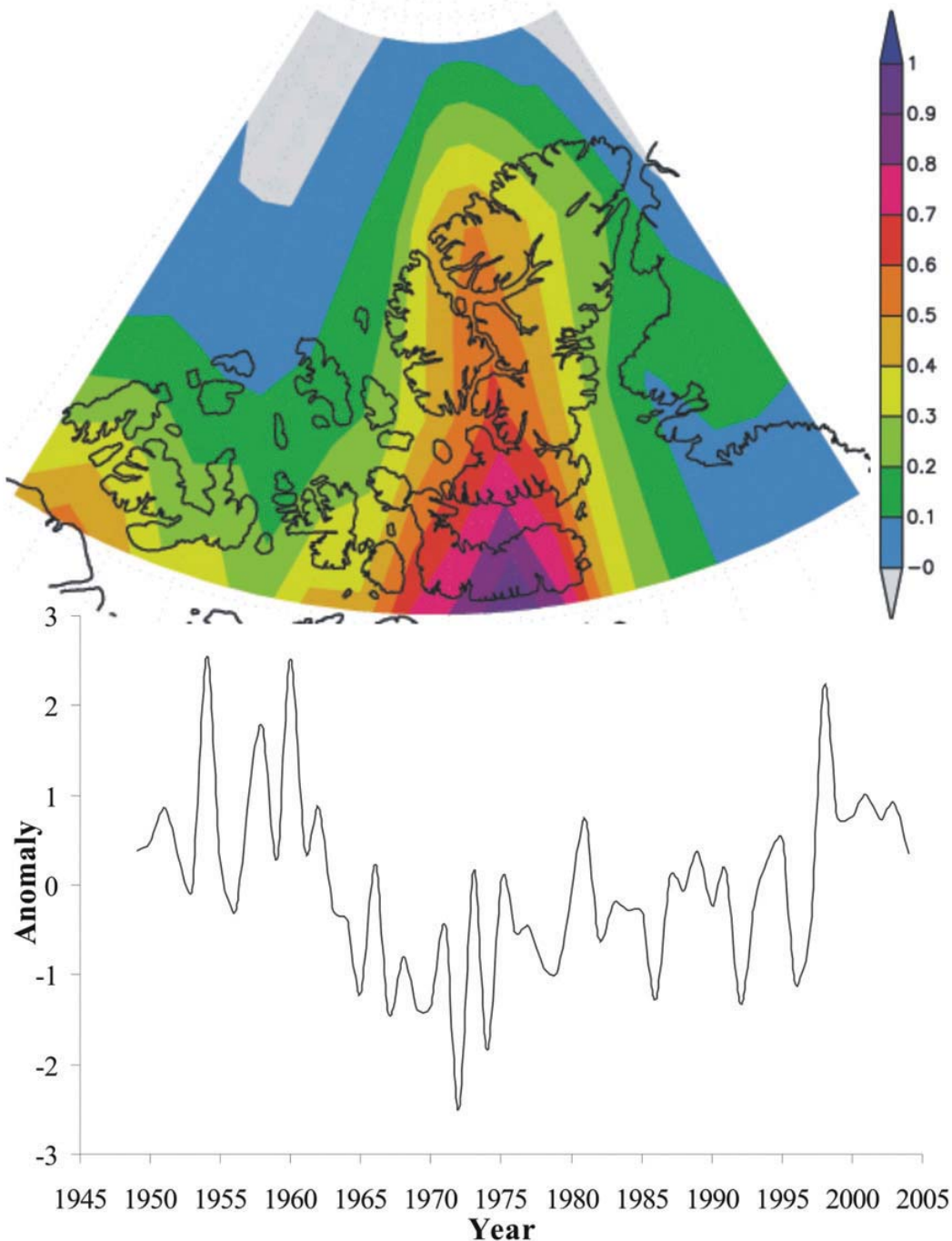


Figure 3 The first Empirical Orthogonal Function (EOF-1) of SAT (top), centred over the QEI, and corresponding principal component (PC-1) time series (bottom) for the period 1949–2002

The NNR time series (1949–2002) of QEI standardized mean summer SAT and SPR anomalies are shown in Figure 2. Both temperature and precipitation records show substantial interannual variability, and only a slight correlation ($r = 0.01$) is found between the two variables. Summer SAT anomalies in the time series range from -2.5 to 2.3 standard deviations, equivalent to -1.0 to 0.9°C . The highest (warmest) anomalies in the period occurred during the late 1950s to early 1960s, before a step-like change to the lowest (coldest) anomalies from the mid-1960s to mid-1970s. The period from the late 1970s to the present is characterized by less interannual variability with more positive temperature anomalies resulting in a gradual increase in mean summer

temperature. The time series contains nine extreme cold years (those exceeding one standard deviation: 1964, 1965, 1967, 1969, 1970, 1972, 1974, 1992 and 1996) and five extreme warm years (1954, 1957, 1960, 1981 and 1998). Seven of the cold years occurred during the mid-1960s to mid-1970s, with the coldest mean summer temperature (1972) falling 0.9°C below the 1949–2002 mean (-0.8°C). Three of the five warm years occurred during the warmer than normal part of the record, from the late 1950s to early 1960s; the warmest mean summer SAT for the entire record (0.1°C ; 1954) reached 0.9°C above the 1949–2002 mean. QEI averaged winter SPR anomalies in the time series (1949–2002) range from -1.7 to 2.4 standard deviations, and

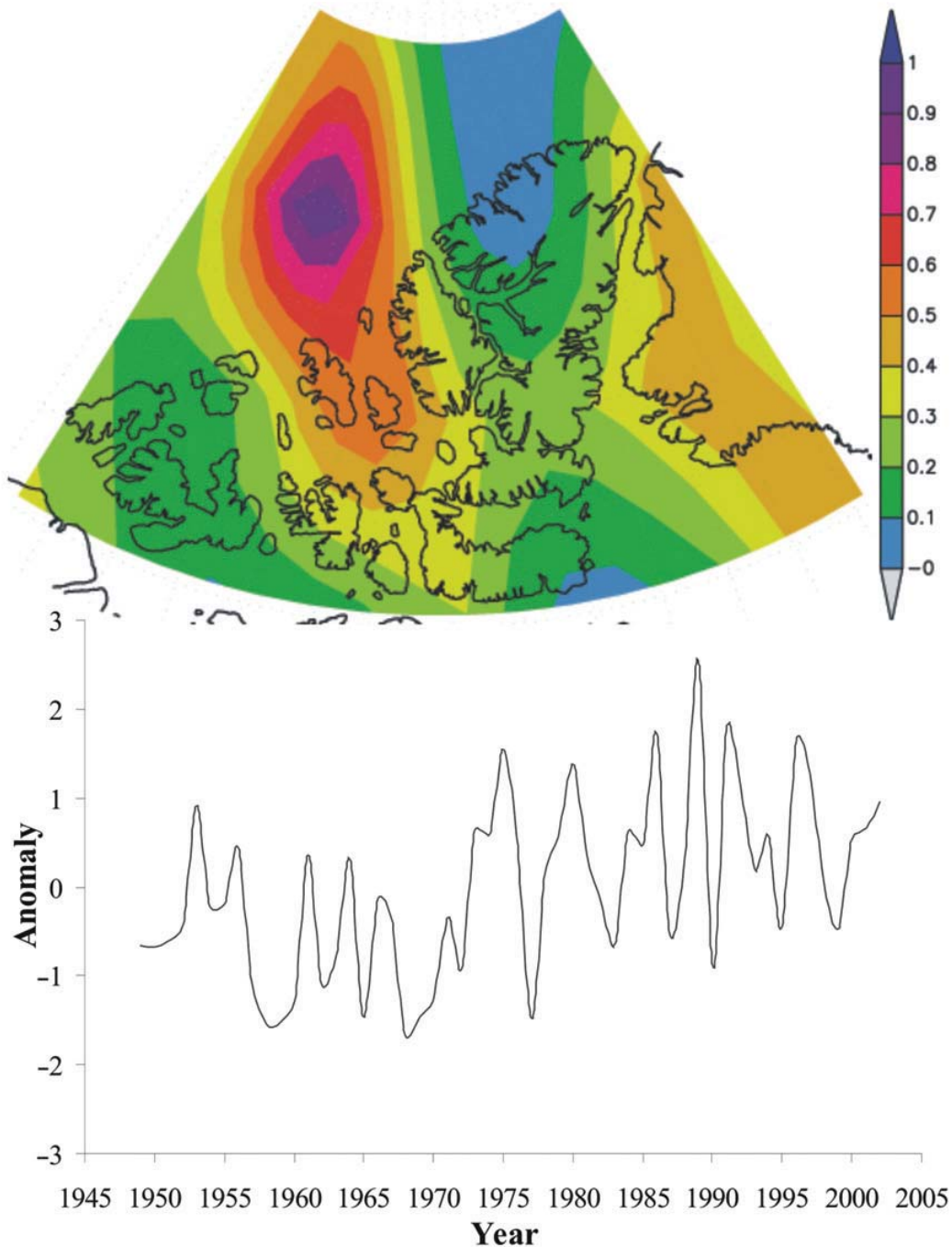


Figure 4 EOF-1 of SPR (top), centred over the QEI, and corresponding PC-1 time series (bottom) for the period 1949–2002

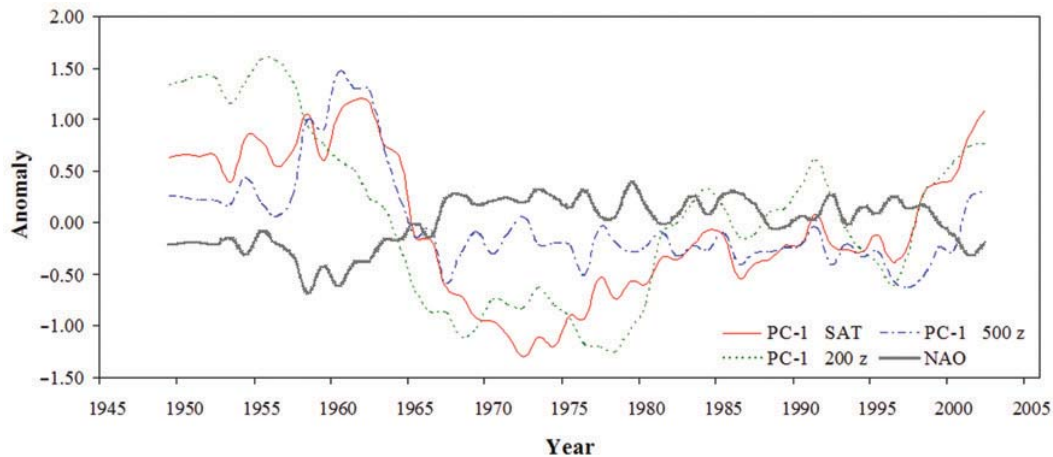


Figure 5 Five-year running mean time series of the first principal components of SAT and 500 and 200 hPa geopotential heights, and standardized anomalies of the NAO index (1949–2002). In the early part of the record, strong decadal extremes are evident as each of the time series covary. During the latter part of the record decadal trend are much weaker, and interannual variability dominates

trends in the time series show drier than normal conditions in the first half of the record (1949–1974), with several extreme dry (1957–1960, 1962, 1965, 1968–1970 and 1972) but no extreme wet summers. The latter half of the record (1975–2002), however, shows wetter than normal conditions, with several extreme wet (1975, 1980, 1986, 1989, 1991–1992, 1996–1997 and 2002) and only one extreme dry summer (1977).

Patterns of variability

Empirical Orthogonal Functions (EOFs) provide a compressed description of the variability of a spatially distributed time series, often referred to as a mode of variability. Principal Components (PCs) associated with these modes of variability demonstrate how the EOFs oscillate in time. In this study, EOFs were used to describe the main modes of variability of NNR meteorological variables over the QEI for the 1949–2002 (summer) period. EOFs were computed to a cumulative explained variance of 80% for the following meteorological variables: SAT, SPR, SST, SLP and geopotential heights at 850, 500 and 200 hPa levels.

Figure 3 shows the leading mode of variability (EOF-1) for summer SAT for the QEI and the corresponding PC time series for 1949–2002. EOF-1 explains 55% of the variance (EOFs 2 and 3 explain 12 and 8%, respectively) and illustrates a strong pattern of variability over the eastern QEI. Higher values of variance occur in the southeast part of the islands (principally Devon Island) and extend northward into the intermontane basin between Axel Heiberg and Ellesmere Islands. The pattern of variability illustrated by EOF-1 (Figure 3) coincides with the pattern of ELA Δh (Wolken *et al.*, 2008, this issue: figure 11). The principal component time series associated with EOF-1 shows how this preferred temperature pattern evolves over time (Figure 3). The positive phase of this pattern was strongly established during the early part of the record, concomitant with the highest summer temperatures during the period (1949–2002). Conversely, negative scores (PC-1) of this mode are dominant from the mid 1960s to the late 1970s, indicating cool summer temperatures in the same spatial pattern.

EOF-1 of SPR (1949–2002) explains 40% of the variability in the period (Figure 4). The spatial pattern of variability shows a band of positive loadings extending from the north-central to east-central QEI, with the high values over the Arctic Ocean and running through Meighen Island and Amund and Ellef Ringnes

Islands. The associated PC time series (Figure 4) shows high inter-annual variability, with the first half of the record showing mainly negative anomalies in the SPR (1949–1974), whereas positive anomalies are prevalent during the latter part of the record (1975–2002). EOFs 2 and 3 (not shown) explain another 16 and 11% of the variability within the period of record, respectively.

The distinct pattern of variability that is expressed in EOF-1 of SPR represents the dominant storm track through the QEI. The QEI is situated between relatively high SLP associated with the perennially ice-covered Arctic Ocean and low SLP in the commonly open waters of Baffin Bay (Alt, 1987). This configuration causes cyclones to take a S-SE track through the QEI towards Baffin Bay, where there is an increase in cyclone frequency and cyclogenesis (Serreze and Barry, 2005: 98). Higher than normal precipitation occurs in the QEI when there is an increase in the frequency of cyclones along this track (ie, the positive phase of the leading EOF of SPR); however, anomalously low SPR during approximately the first half of the record (1949–1974) suggests a decrease in the frequency of cyclones following this S-SE trajectory through the QEI.

Correlations and decadal trends

Variations in summer temperature and precipitation in the QEI (1949–2002) are due in part to fluctuations in the distribution of atmospheric mass in the Arctic. PC-1 of QEI averaged summer SAT is positively correlated with summer geopotential height at the 500z and 200z levels ($r = 0.57$ and 0.59 , respectively) and negatively correlated with the summer North Atlantic Oscillation (NAO) index ($r = -0.48$). Only slight correlations, however, are apparent with other climate indices (eg, Pacific North American pattern (PNA), $r = 0.19$; Southern Oscillation Index (SOI), $r = 0.17$; Arctic Oscillation (AO), $r = 0.03$). PC-1 of summer QEI SPR is negatively correlated with fluctuations in the height of the summer 500 hPa geopotential surface ($r = -0.64$) and positively correlated with the summer AO index ($r = 0.53$).

Figure 5 shows five-year running mean time series of the first principal components of QEI averaged summer SAT and summer geopotential height at the 500z and 200z levels, and the summer NAO index for the period 1949–2002. Decadal- and multidecadal-scale fluctuations in PC-1 of summer SAT are strongly coupled to changes in both the upper troposphere (500z) and lower stratosphere (200z). Moreover, decadal shifts in the phase of the NAO

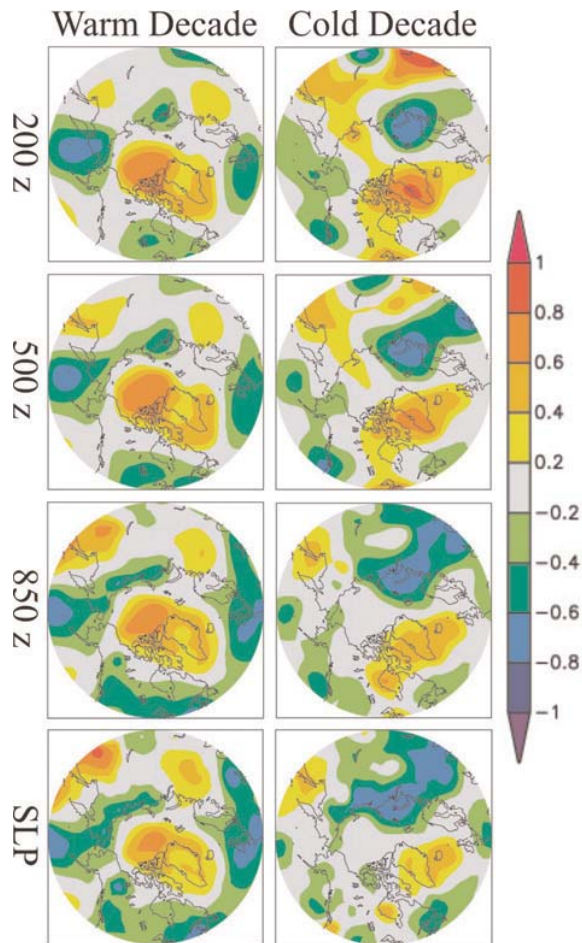


Figure 6 Correlation coefficients for linear regression of PC-1 of QEI averaged SAT with SLP and 850, 500 and 200 hPa geopotential height surfaces (1949–2002) at each grid point north of 45°N

are coincident with decadal-scale modifications in PC-1 of summer SAT, which suggests regional-scale influences on summer surface temperature fluctuations in the QEI. Distinct trends in the time series in approximately the first half of the record illustrate contrasting periods of warm and cold conditions, which will serve as the basis for the following analyses.

Warm and cold decades

Two decadal episodes representing extreme (exceeding one standard deviation of the decadal mean for the period 1949–2002) warm (1953–1962) and cold (1965–1974) periods are recoded in the NNR spatially averaged time series for the QEI. The warm decade is consistent with reports of net ablation on glaciers on the Hazen Plateau, E Ellesmere Island (Hattersley-Smith and Serson, 1973), and the cold decade is characterized by a lowering of the ELA and positive mass balance on some QEI glaciers and ice caps (Bradley and Miller, 1972; Bradley, 1973, 1975; Bradley and England, 1978a, b; Alt, 1987; Braun *et al.*, 2004). These contrasting temperature regimes are examined and analysed in order to identify potential modern analogues for LIA and early twentieth-century climates.

Relation to atmospheric circulation

In order to examine the influence of atmospheric circulation patterns on summer SAT in the QEI during both warm and cold decades, PC-1 of QEI averaged summer SAT was regressed upon mean summer sea-level pressure and 850, 500 and 200 hPa geopo-

tential height fields at each grid point north of 45°N (Figure 6). For the warm decade, anomalously high temperatures in the QEI are positively correlated with higher than normal SLP (Figure 7) and elevated geopotential heights up to 200z over the Canadian Arctic, most of the Arctic Basin and southeastwardly over Iceland, the western North Atlantic Ocean and the Labrador Sea (ie, a warm core high). In this region, a barotropic structure exists, that is, the positive geopotential anomaly occurs from the surface to the lower stratosphere, which coincides with a weak summer polar vortex, the centre of which lies northwest of the QEI over the Arctic Ocean (Figure 8). This barotropic structure is similar to that associated with the negative phase of the AO (Thompson and Wallace, 1998), and to a lesser extent with the NAO. Hence, a negative correlation exists between warm decade PC-1 of QEI averaged summer SAT and both the AO and NAO indices ($r = -0.38$ and -0.57 , respectively). During the cold decade, PC-1 of QEI averaged summer SAT is positively correlated with geopotential height at the 200 and 500 hPa levels over the QEI (Figure 6). In the lower troposphere, however, only a slight negative correlation exists between geopotential height (850 hPa to surface) and PC-1 (summer SAT) in the Arctic Basin and the western QEI, whereas, in the eastern Canadian Arctic, Greenland and Iceland a positive correlation occurs between these variables. In the Arctic basin and western QEI, a core of cold dense air resides in the lower troposphere, resulting in high SLP and anomalously high geopotential heights below ~850 hPa (ie, a cold core high; Figure 7). Above this surface high, a strong, QEI-proximal summer polar vortex occurs in the upper troposphere and lower stratosphere (Figure 8). From northern Ellesmere Island to southern Hudson Bay and eastwards across the North Atlantic, the negative geopotential anomaly occurs consistently from the lower troposphere to the lower stratosphere, while in the mid-Atlantic, areas of negative correlation represent positive geopotential anomaly (Figure 6). Anomalously low pressure in the North Atlantic relative to high pressure in the mid-Atlantic during the cold decade, is characteristic of a positive NAO (Figures 5 and 7); a negative correlation exists between PC-1 of QEI averaged summer SAT and the NAO index, but the correlation is weak ($r = -0.32$).

Atmosphere–ocean interactions

At high latitudes, complex energy exchanges between the atmosphere and ocean can occasion positive feedbacks affecting atmospheric circulation, SSTs, and SATs (Hansen and Bezdek, 1996; Mysak *et al.*, 1996; Rogers *et al.*, 1998). To investigate the influence of SST on temperature changes during the warm and cold decades across the QEI, PC-1 of mean summer SAT was regressed upon mean summer SST (using the ERSST reanalysis) at each grid point for the extended circumpolar region north of 45°N (Figure 9). During the warm decade, PC-1 of QEI averaged SAT is positively correlated with SST in the central and western North Atlantic, Labrador Sea and Hudson Bay and north into Baffin Bay and along the east coast of Greenland. In these areas, the correlation is robust ($r = 0.65$) and the variation in summer SST explains approximately 42% of the variability in the mean summer temperature for the QEI. Additional areas of positive correlation also occur in the Bering Sea, extending northward through Bering Strait, as well as in the Gulf of Alaska. During the cold decade, PC-1 of QEI averaged SAT is positively correlated with SST across the North Atlantic, with the most robust correlation located in the east-central North Atlantic ($r = 0.70$), where variation in summer SST accounts for about 50% of the variation in summer temperature in the QEI. Other areas of positive correlation are shown in Hudson Bay and the Labrador Sea, extending north into Davis Strait. Anomalously cool SAT in the QEI during this decade is negatively correlated with a broad area of warm SST in the North Pacific, as well as a much smaller area along the northeast coast of Greenland.

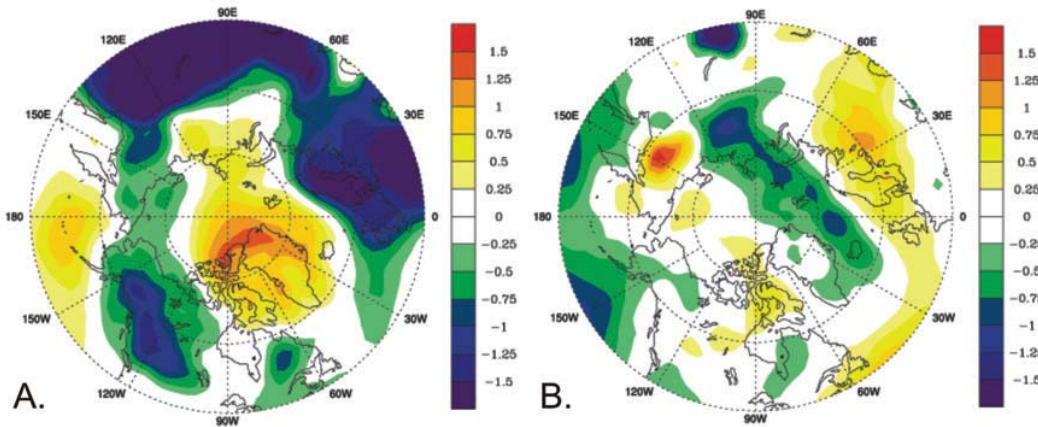


Figure 7 Summer mean SLP anomalies (45–90°N) during warm (1953–1962) and cold (1965–1974) decades in the QEI. Anomalies are in reference to the 1949–2002 climatology period

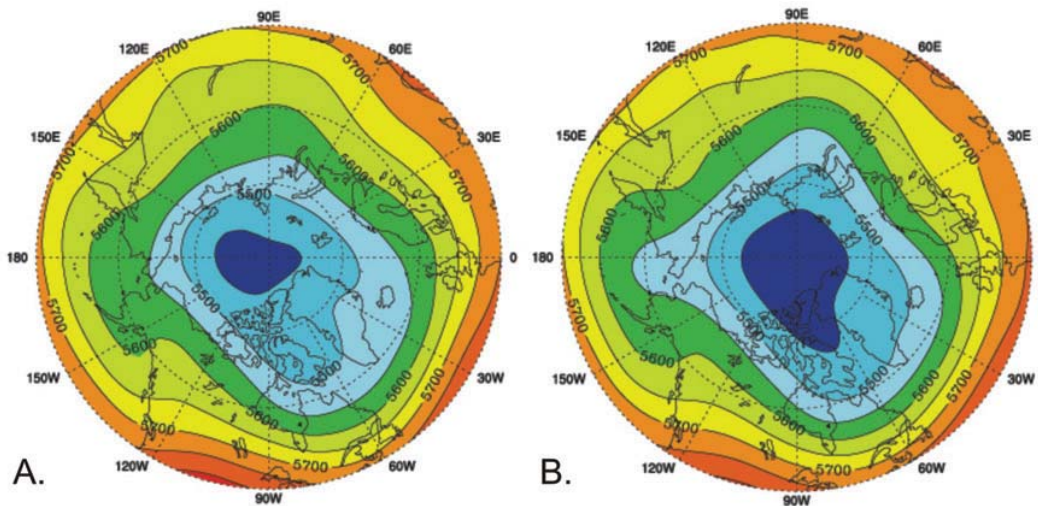


Figure 8 Mean 500 hPa geopotential height surface indicating a weak, QEI-distal (strong, QEI-proximal) polar vortex during the warm (cold) decade

EOFs of summer SST were computed for the area north of 45°N for the period 1949–2002. Figure 10 shows the leading two EOFs and their corresponding principal component time series. EOF-1 accounts for 29% of the variance and depicts a spatial pattern of variability whereby positive loadings are in the North Pacific and Bering Strait and lesser positive values are in the North Atlantic. For the full period of record, a positive correlation is revealed between PC-1 of SST and PC-1 of QEI summer SAT ($r = 0.32$), with a positive correlation during the warm decade ($r = 0.32$) and a weak negative correlation during the cold decade ($r = -0.10$). EOF-2 explains 18% of the variance in the data set and shows strongly positive values of variance in the North Atlantic, Davis Strait and Hudson Bay, and slightly negative values in the Bering Sea, Bering Strait and the Gulf of Alaska. A positive correlation was found between PC-2 of SST and PC-1 of QEI summer SAT for the period 1949–2002 ($r = 0.54$), with stronger positive correlations during both the warm and cold decades ($r = 0.65$ and 0.76 , respectively), explaining 42% (warm) and 58% (cold) of the variance in PC-1 of QEI SAT. Strong coupling in these time series reflects the influence of changes in SSTs in the North Atlantic on SAT in the QEI during both extreme decades (Figure 11).

The distribution of SST is largely influenced by surface winds resulting from strong gradients in the sea-level pressure fields. During the cold decade, anomalously low SSTs across the North Atlantic were influenced by enhanced westerly winds across the North Atlantic, resulting from lower than normal pressure near Iceland (extending northeast into the Greenland and Barents seas) in combination with anomalously high pressure in the central Atlantic. Although less intense, the cold decade atmospheric circulation pattern is similar to that of the 1972 extreme cold year described by Bromwich *et al.* (2002), where strong westerly winds across the North Atlantic increased the stress on the Ekman layer causing enhanced divergence and upwelling (lower SSTs) in the North Atlantic (Figure 9). In both patterns (cold decade and 1972), a deeper than normal Icelandic low was coupled with anomalously high pressure over the Arctic Ocean and the Canadian Arctic Archipelago, which created an intense zonal pressure gradient across the central and eastern QEI and Greenland and caused strong northerly airflow over this region. This persistent high pressure also serves as an effective obstruction to cyclones that typically track through this region (Alt, 1987), thereby reducing the precipitation during such cold intervals. Low SSTs in the North

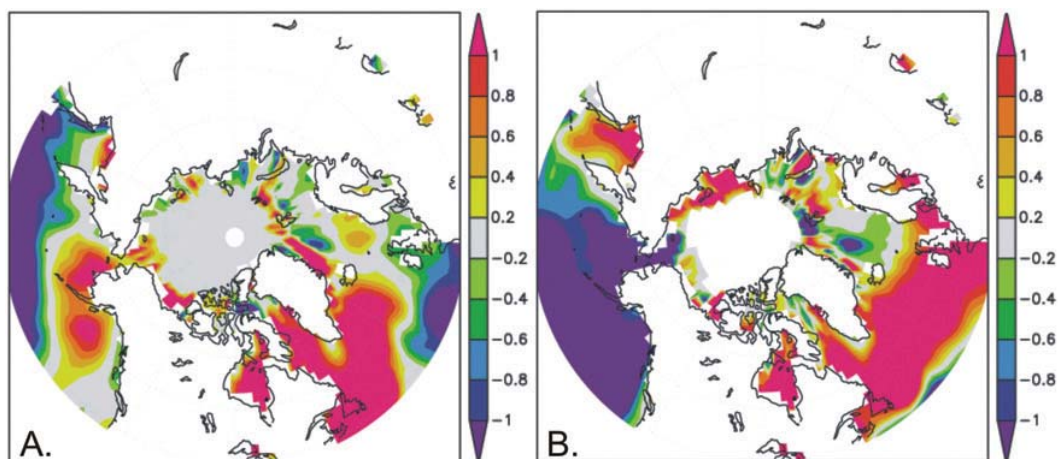


Figure 9 Correlation coefficients of linear regression of PC-1 of QEI averaged SAT with SST (1949–2002) at each grid point north of 45°N

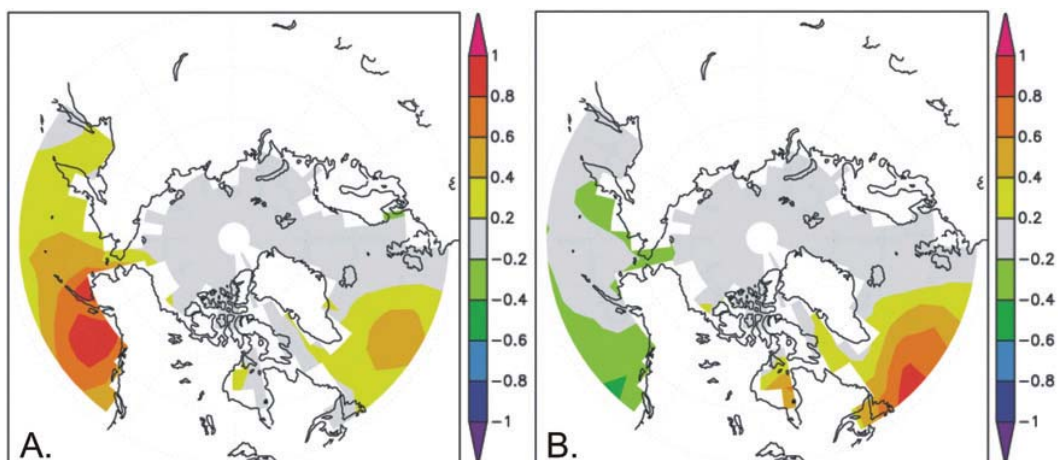


Figure 10 First and second EOFs of summer SST (1949–2002) north of 45°N for the period 1949–2002

Atlantic increase low-level mid-latitude baroclinicity, resulting in enhanced low pressure over Iceland and stronger than normal cold northerly flow over the eastern Canadian Arctic (Bromwich *et al.*, 2002). In 1972, this northerly flow resulted in exceptionally low snowlines and positive summer mass balances on QEI glaciers (Alt, 1987), as well as one of the lowest percentages of summer open water on record throughout the QEI (Koerner, 1977). It has been hypothesized that the anomalous SSTs during the summer of 1972 were related to transient pools of cold water associated with the Great Salinity Anomaly (1968–1982; Dickson *et al.*, 1988; Rogers *et al.*, 1998; Bromwich *et al.*, 2002); it is possible that the migration of the salinity anomaly through the North Atlantic may have had an influence on the anomalous SSTs that were recorded during the cold decade, and ultimately, the low SATs throughout the QEI during this time. However, anomalously low SSTs in the North Pacific may also have influenced QEI SATs during the cold decade by modifying the Northern Hemisphere atmospheric circulation, which has also been credited for the abrupt lowering of summer freezing level heights over the QEI in 1963 (Bradley, 1973). Changes in the freezing level height in the atmosphere have been shown to be directly related to fluctuations in the ELA in the High Arctic (Bradley, 1975). Another influence on the low SAT across the QEI during the cold decade may have been the injection of volcanic aerosols into the stratosphere in response to increased volcanic activity during the 1960s and 1970s, starting with the

massive eruption of Mt Agung (Indonesia, 1963) (Bradley and England, 1978a, b; Hansen *et al.*, 1978).

During the warm decade, high SSTs in the W North Atlantic Ocean and the Labrador Sea coincided with lower than normal pressure over northern Quebec, and anomalously high pressure over Greenland and most of the Canadian Arctic Archipelago. The anomalous circulation pattern resulted in the cessation of typically strong westerly winds in the W North Atlantic, which, to first order, would have decreased the evaporative heat loss from the ocean surface layer. In addition, a pressure gradient reversal led to anomalous easterly wind stresses on the Ekman layer in this region, which would have caused a convergence of flow, leading to downwelling and a thickening of the warm surface layer in the western North Atlantic and Labrador Sea. Advection of warm water into Davis Strait and Baffin Bay would have significantly reduced sea-ice extent and increased the thermodynamic efficiency of warm southeasterly winds directed into the QEI, effectively increasing the ELA and enhancing ablation on perennial snow/ice masses in this region.

Temperature variability in the Arctic has also been linked to fluctuations in sea-ice extent (Chapman and Walsh, 1993; Parkinson *et al.*, 1999; Bengtsson *et al.*, 2004; Johannessen *et al.*, 2004). In order to examine the role of sea-ice extent in variations in QEI SAT during the extreme warm and cold decades, the 100 yr ‘Zakharov’ data set is used. This includes observations of Arctic

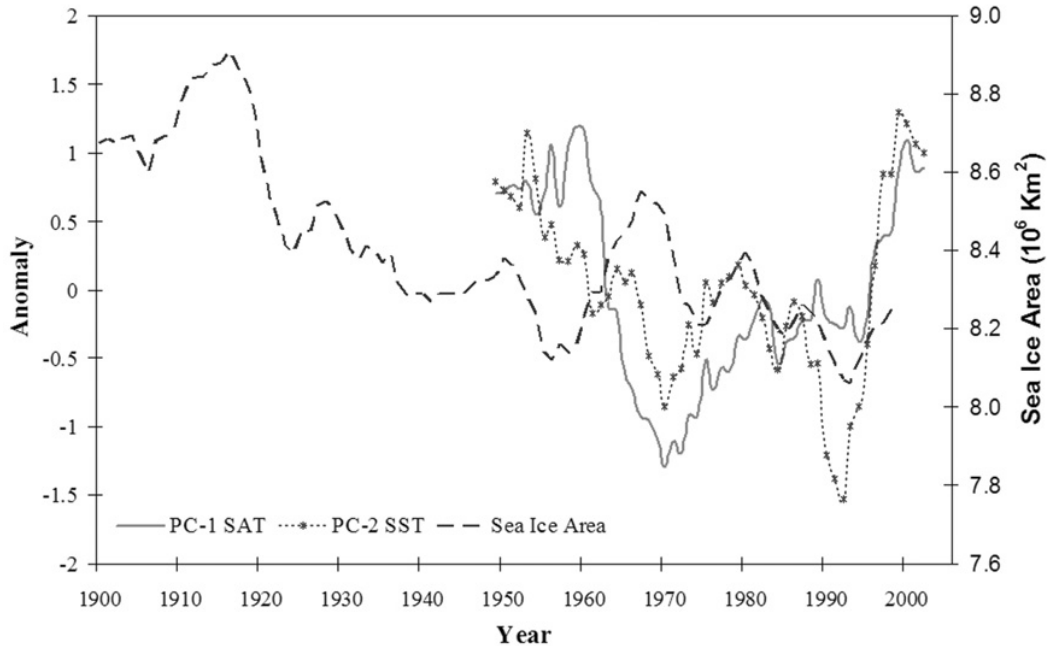


Figure 11 Five-year running mean time series of sea-ice area (1900–1999) (Zakharov, 1997; Johannessen *et al.*, 2004), PC-1 of QEI averaged SAT (1949–1999), and PC-2 of summer SST (1949–2002) north of 45°N showing strongly coupled decadal and multidecadal variation during warm (1953–1962) and cold (1965–1974) decades in the QEI

sea-ice extent within the ice-ocean margin (Zakharov, 1997; Johannessen *et al.*, 2004). Figure 11 shows 5-yr running mean time series of PC-1 of summer SAT for the QEI compared with PC-2 of summer SST north of 45°N and mean annual sea-ice extent (1900 to 1999). SAT and sea-ice extent time series are negatively correlated ($r = -0.31$) for the overlapping period of record (1949–1999), with stronger negative correlations occurring during both warm and cold decades ($r = -0.52$). Thus, on decadal and multidecadal timescales, it is evident that QEI SAT co-varies with North Atlantic SST and Northern Hemisphere sea-ice extent. During the cold decade (1965–1974), the QEI experienced anomalously low mean summer temperatures ($\sim -0.42^\circ\text{C}$ cooler), corresponding to the largest increase in sea-ice extent in the Arctic since the end of the LIA. In contrast, however, a pronounced decrease in sea-ice extent corresponds to the warm decade, when the mean summer SAT throughout the QEI was $\sim 0.24^\circ\text{C}$ warmer than the 1949–2002 mean. These trends are also apparent in the early twentieth century, when anomalously low Arctic mean annual SATs (~ 1900 –1919) correspond to the largest sea-ice area during the century-long record, and anomalously high SATs (~ 1920 –1939) match a significant decrease in sea-ice extent (Figure 5, Johannesson *et al.*, 2004). This sizeable decrease in sea-ice extent is coincident with an increase (~ 0.5 – 1.0°C) in the observed spring/summer/autumn SAT across the QEI, likely marking the end of the LIA there (Figure 2, Johannessen *et al.*, 2004).

ELA changes and twentieth-century analogues

The above analyses of climatic conditions in the QEI during the extreme cold and warm decades of the modern record, lead to the hypothesis that these decades can be used as analogues for describing climatic conditions that could be linked to LIA cooling and early twentieth-century warming in the QEI. Regional spatial variations in twentieth-century climate across the QEI are reflected in the change in the distribution of perennial snow/ice cover and ELA Δh between the end of the LIA and 1960 (Wolken *et al.*, 2008, this issue). Although the spatial distribution of Δh

shows substantial meso- and microscale variability across the QEI, especially in the mountainous regions (where orographic effects are amplified), the data set also exhibits distinctive synoptic-scale patterns, indicative of regional climate forcing. For example, the area of greatest change in the ELA (Figure 11, Wolken *et al.*, 2008, this issue) is qualitatively similar to the pattern of the primary mode of summer temperature variability in the QEI (EOF-1, 1949–2002, Figure 3). This pattern shows the greatest amount of variability occurring in the eastern QEI, extending from central Devon Island northward across SW Ellesmere Island through the axis of Eureka Sound. The positive phase of EOF-1 (PC-1, summer SAT, Figure 3) characterizes the warm decade (1953–1962), when the mean temperature rose 1.5 standard deviations over the 1949–2002 mean (Figure 2). Strong qualitative similarities between EOF-1 (summer SAT) during the warm decade and the pattern of ELA Δh indicate that the warm decade may serve as a suitable analogue for climatic conditions during the early twentieth century that caused an increase in melt of perennial snow/ice masses across the QEI. Furthermore, dry conditions dominated throughout the QEI during the warm decade (Figures 2 and 4), and palaeoprecipitation proxy records from the central QEI suggest that similar dry conditions persisted there during the early twentieth century (Lamoureux, 2000). While the effect of low summer precipitation on net mass balance in the QEI is important (Dowdeswell *et al.*, 1997), such dry conditions indicate that the regional pattern of ELA Δh is largely a reflection of the variation in summer temperature.

Reconstructed temperature change across the QEI from the end of the LIA to 1960 is shown in Figure 12. This reconstruction is calculated from ELA Δh based on a summer near-surface temperature lapse rate of $-4.3^\circ\text{C}/\text{km}$, empirically derived from an observational network on Prince of Wales Icefield, Ellesmere Island (Figure 1; Marshall *et al.*, 2007). Resulting mean temperature change for the QEI was $+1.1^\circ\text{C}$ (SD = 0.4°C), ranging from $<0.5^\circ\text{C}$ along NW Axel Heiberg and Ellesmere Islands and W Melville Island, to $>2.9^\circ\text{C}$ in localized areas of Ellesmere and Devon

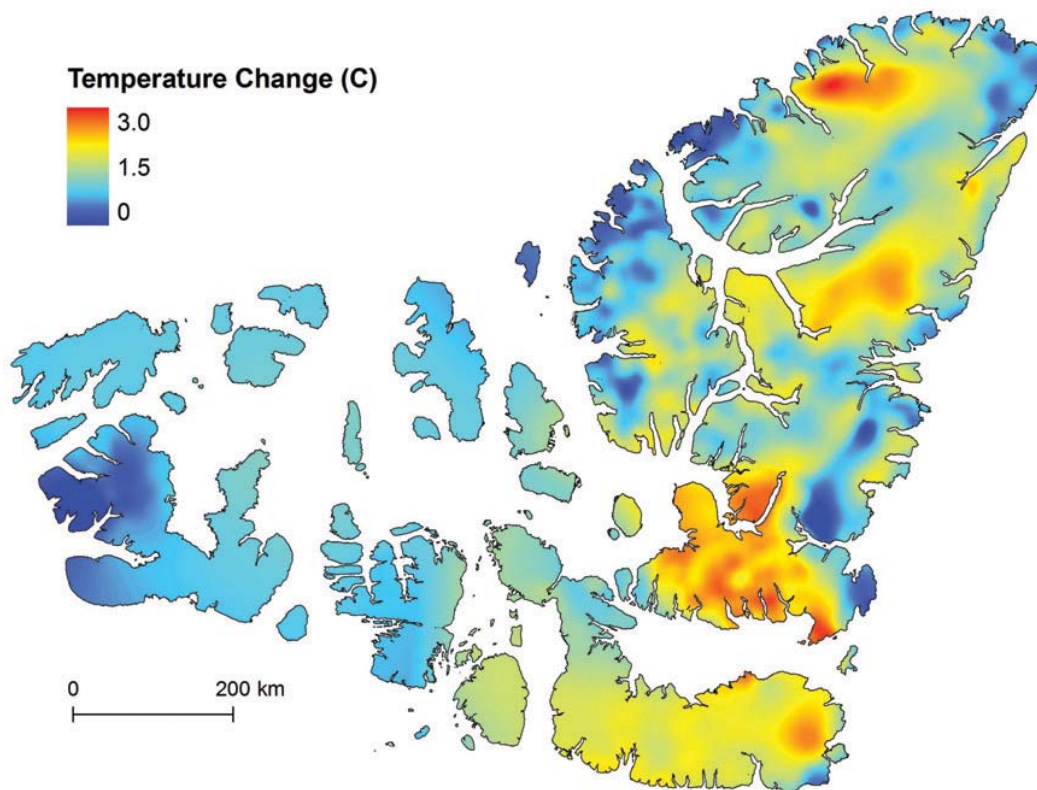


Figure 12 Temperature change between the LIA and 1960, estimated from ELA Δh (Wolken *et al.*, 2008, this issue) using a summer near-surface temperature lapse rate of $-4.3^{\circ}\text{C}/\text{km}$ (Marshall *et al.*, 2006)

Islands. The ELA-derived temperature changes are consistent with changes related to circum-Arctic gridded surface air temperatures (MJJASO) during the early twentieth century (Figure 2, Johannessen *et al.*, 2004), and they are also in broad agreement with other temperature reconstructions from the High Arctic. For instance, based on proxy data from lakes, ice cores, wetlands and marine sources Overpeck *et al.* (1997: figure 3) reported an average summer-weighted Arctic warming of $\sim 1.5^{\circ}\text{C}$ from the end of the LIA to ~ 1960 , with changes in the Canadian Arctic between 1 and 3°C . Also in the Canadian High Arctic, melt layer and $\delta^{18}\text{O}$ analyses from ice cores extracted from the Devon and Agassiz ice caps (Figure 1) reveal marked warming in summer temperatures (~ 0.5 to 1.5°C) between the end of the LIA and modern times (Koerner, 1977; Koerner and Fisher, 1990), which is broadly consistent with warming between the mid-nineteenth and the mid-twentieth centuries, as indicated by high sedimentation rates seen in lake core records from the QEI (Lamoureux and Bradley, 1996; Gajewski *et al.*, 1997; Lamoureux and Gilbert, 2004; Smith *et al.*, 2004) and by a rapid colonization of diatoms in QEI lakes in response to a reduction in lake-ice cover (Perren *et al.*, 2003).

Large-scale atmospheric circulation patterns during the cold and warm decades can also be used as analogues for those patterns that may have occurred during the LIA and the early twentieth century. Atmospheric circulation causing strong northerly flow into Arctic Canada during the cold decade is responsible for producing temperature anomalies in the QEI similar to those estimated from temperature reconstructions noted above. This atmospheric circulation pattern is similar to the synoptic types producing 'cool and dry' conditions (types 1, 4, 6 and 9) described by Bradley and England (1979), as well as the synoptic type *I* suggested by Alt (1987), which produces strong northerly flow through the QEI and is associated with melt suppression on QEI

ice caps. Although the seasonal atmospheric circulation patterns characterizing the cold decade produced temperatures comparable with those reported to have occurred during the LIA, other patterns observed in the contemporary record are capable of producing similar cool episodes, some of which are accompanied by increased precipitation (Bradley and England, 1979; Alt, 1987; Bromwich *et al.*, 2002). Indeed, some palaeoclimatic reconstructions for the central QEI suggest enhanced summer precipitation in these areas during the LIA (Lamoureux, 2000); some precipitation events during this time may have been related to increased volcanic activity (Lamoureux *et al.*, 2001).

One of the characteristic atmospheric circulation features during the warm decade in the Arctic is the strong S-SE flow across the QEI, which undoubtedly played a major role in the spatial distribution of positive SAT anomalies throughout this region. The similarity in the spatial pattern of temperatures reconstructed from ELA Δh , indicates that this circulation feature may also have been important during the post-LIA to 1960 period. However, other elements of high latitude atmospheric circulation have also been suggested to contribute to circum-Arctic warming during the early twentieth century. For instance, Bengtsson *et al.* (2004) propose that enhanced winter oceanic and atmospheric heat transport into the Arctic, initiated by an increase in the S-SW winds into the Barents Sea, was associated with regional warming that provided the main contribution to Arctic SAT anomalies from 1920 to 1940. While this feature does not appear during the winter months (NDJFMA) of the warm decade, there is indication of a possible pre-conditioning associated with the winter atmospheric circulation pattern (a weakened pressure gradient between the Icelandic low and central Atlantic high), which would have favoured warmer temperatures in the QEI during the warm decade summers.

Conclusions

Reconstructed ELA trend surfaces modelled throughout the QEI represent important proxies of climate in a region with limited or no observational data during the late nineteenth and early twentieth centuries (Wolken *et al.*, 2008, this issue), and have been used here to assess climate variability and provide a model of the spatial variability of temperature and precipitation change in the QEI between the end of the LIA and 1960.

Warm (1953–1962) and cold (1965–1974) decades of summer SAT in the QEI were identified in the 1949–2002 NNR as potential analogs of LIA (cold) and early twentieth-century (warm) climates. The spatial pattern of Δh between the LIA and 1960 (Wolken *et al.*, 2008, this issue) is qualitatively similar to the primary mode of variability for mean summer SAT in the modern record (ie, EOF-1, 1949–2002, Figure 3), the positive (negative) phase of which is strongly in place during the warm (cold) decade. During the cold decade, lower than normal SATs are associated with atmospheric circulation patterns producing strong northerly winds over the study region. Warmer than normal SATs during the warm decade are linked to warm southeasterly flow through the QEI resulting from a pressure gradient reversal in the W North Atlantic, caused by anomalously high pressure over Greenland and the Canadian Arctic Archipelago coupled with lower than normal pressure over N Quebec and NW mainland Canada. SAT anomalies in the QEI during the warm (cold) decade are positively correlated with a weak (strong) QEI-distal (QEI-proximal) polar vortex, higher (lower) than normal SSTs in the North Atlantic, and lower (higher) Northern Hemisphere sea-ice extent.

Owing to the low precipitation in the QEI during both warm and cold decades, and its minimal influence on the pattern of ELA Δh compared with temperature, Δh is considered to reflect regional changes in summer SAT between the end of the LIA and 1960. Estimates of temperature change between the LIA and 1960 are calculated from Δh based on a summer near-surface temperature lapse rate of $-4.3^\circ\text{C}/\text{km}$. The mean estimated temperature change in the QEI from the LIA to 1960 is 1.1°C , and ranges from $<0.5^\circ\text{C}$ near the northwest coasts of Axel Heiberg and Ellesmere Islands and the west coast of Melville Island, to $>2.9^\circ\text{C}$ in the mountains of Ellesmere Island. While the large-scale atmospheric circulation changes required to produce this warming are not clear, plausible circulation patterns based on modern analogues have been proposed.

Investigating and understanding ice mass responses to past changes in climate is imperative to our understanding of future modifications to the cryosphere. Data presented in this study (and Wolken *et al.*, 2008, this issue) demonstrate the extent to which ice reduction occurred in the QEI in response to an average estimated temperature increase of 1.1°C between the end of the LIA and 1960, and highlight the sizeable changes in sea ice extent during this same interval. These data are particularly important for providing a perspective on the continued warming and melt in the Arctic (Krabill *et al.*, 1999; Arendt *et al.*, 2002; Burgess and Sharp, 2004; Abdalati *et al.*, 2004) and the accelerated warming trend seen globally (Mann *et al.*, 1998). Furthermore, this study helps to clarify the considerable sensitivity of both terrestrial- and sea-ice systems to small changes in summer temperature, reinforcing the changes that will continue under ongoing global warming.

Acknowledgements

This work was financially supported by the Natural Sciences and Engineering Research Council of Canada (NSERC Discovery Grant A6680) and the NSERC Northern Chair Award, both to J. England. Additional support to G. Wolken was provided by the Canadian Circumpolar Institute (University of Alberta, Edmonton, Alberta).

The Polar Continental Shelf Project, Natural Resources Canada, provided logistical support during the summers of 2001 and 2003 (PCSP/ÉPCP contribution # 003-07). Grants awarded to M. Sharp from the Meteorological Service of Canada CRYSYS (Cryospheric System to Monitor Global Change in Canada) programme and from the GLIMS (Global Land Ice Measurements from Space) project provided access to satellite data used in the study. We express our gratitude to R. Bradley (University of Massachusetts), A. Bush (University of Alberta) and D. Hik (University of Alberta) for their comments on an earlier draft of the manuscript. We also thank Atle Nesje and an anonymous referee for their comments and suggestions of how to improve this manuscript.

References

- Abdalati, W., Krabill, W., Frederick, E., Manizade, S., Martin, C., Sonntag, J., Swift, R., Thomas, R., Yungel, J. and Koerner, R. 2004: Elevation changes of ice caps in the Canadian Arctic Archipelago. *Journal of Geophysical Research-Earth Surface* 109, doi:10.1029/2003JF000045.
- Ait, B.T. 1987: Developing synoptic analogs for extreme mass balance conditions on Queen Elizabeth Island ice caps. *Journal of Climate and Applied Meteorology* 26, 1605–23.
- Arctic Climate Impact Assessment 2004: *Arctic climate impacts assessment*. Cambridge University Press, 1046 pp.
- Arendt, A.A., Echelmeyer, K.A., Harrison, W.D., Lingle, C.S. and Valentine, V.B. 2002: Rapid wastage of Alaska glaciers and their contribution to rising sea level. *Science* 297, 382–86.
- Bengtsson, L., Semenov, V.A. and Johannessen, O.M. 2004: The early twentieth-century warming in the Arctic – a possible mechanism. *Journal of Climate* 17, 4045–57.
- Bradley, R.S. 1973: Recent freezing level changes and climatic deterioration in the Canadian Arctic archipelago. *Nature* 243, 398–400.
- 1975: Equilibrium-line altitudes, mass balance, and July freezing-level heights in the Canadian High Arctic. *Journal of Glaciology* 14, 267–74.
- Bradley, R.S. and England, J. 1978a: Volcanic dust influences on glacier mass balance at high latitudes. *Nature* 271, 736–38.
- 1978b: Recent climatic fluctuations of the Canadian High Arctic and their significance for glaciology. *Arctic and Alpine Research* 10, 715–31.
- 1979: Synoptic climatology of the Canadian High Arctic. *Geografiska Annaler* 61, 187–201.
- Bradley, R.S. and Miller, G.H. 1972: Recent climatic change and increased glacierization in Eastern Canadian Arctic. *Nature* 237, 385–87.
- Braun, C., Hardy, D.R. and Bradley, R.S. 2004: Mass balance and area changes of four High Arctic plateau ice caps, 1959–2002. *Geografiska Annaler Series A-Physical Geography* 86A, 43–52.
- Bromwich, D.H., Toracinta, E.R. and Wang, S.H. 2002: Meteorological perspective on the initiation of the Laurentide Ice Sheet. *Quaternary International* 95, 113–24.
- Burgess, D.O. and Sharp, M.J. 2004: Recent changes in areal extent of the Devon Ice Cap, Nunavut, Canada. *Arctic, Antarctic, and Alpine Research* 36, 261–71.
- Chapman, W.L. and Walsh, J.E. 1993: Recent variations of sea ice and air-temperature in high-latitudes. *Bulletin of the American Meteorological Society* 74, 33–47.
- Cullather, R.I., Bromwich, D.H. and Serreze, M.C. 2000: The atmospheric hydrologic cycle over the Arctic basin from reanalyses. Part I: comparison with observations and previous studies. *Journal of Climate* 13, 923–37.
- Dickson, R.R., Meincke, J., Malmberg, S.A. and Lee, A.J. 1988: The great salinity anomaly in the northern North-Atlantic 1968–1982. *Progress in Oceanography* 20, 103–51.
- Dowdeswell, J.A., Hagen, J.O., Björnsson, H., Glazovsky, A.F., Harrison, W.D., Holmlund, P., Jania, J., Koerner, R.M., Lefauconnier, B., Ommanney, C.S.L. and Thomas, R.H. 1997: The mass balance of circum-Arctic glaciers and recent climate change. *Quaternary Research* 48, 1–14.

- Dyrgerov, M.B.** and **Meier, M.F.** 1997: Mass balance of mountain and subpolar glaciers: a new global assessment for 1961–1990. *Arctic and Alpine Research* 29, 379–91.
- Edlund, S.A.** and **Alt, B.T.** 1989: Regional congruence of vegetation and summer climate patterns in the Queen Elizabeth Islands, Northwest Territories, Canada. *Arctic* 42, 3–23.
- Gajewski, K., Hamilton, P.B.** and **McNeely, R.** 1997: A high resolution proxy-climate record from an arctic lake with annually-laminated sediments on Devon Island, Nunavut, Canada. *Journal of Paleolimnology* 17, 215–25.
- Grove, J.M.** 2001: The initiation of the ‘Little Ice Age’ in regions round the North Atlantic. *Climatic Change* 48, 53–82.
- Hansen, D.V.** and **Bezdek, H.F.** 1996: On the nature of decadal anomalies in North Atlantic sea surface temperature. *Journal of Geophysical Research-Oceans* 101, 8749–58.
- Hansen, J.E., Wang, W.C.** and **Lacis, A.A.** 1978: Mount Agung eruption provides test of a global climatic perturbation. *Science* 199, 1065–68.
- Hattersley-Smith, G.** and **Serson, H.** 1973: Reconnaissance of a small ice cap near St. Patrick Bay, Robeson Channel, Northern Ellesmere Island, Canada. *Journal of Glaciology* 12, 417–21.
- Intergovernmental Panel on Climate Change (IPCC)** 2001: *Climate change 2001: the scientific basis*. Cambridge University Press, 408 pp.
- Johannessen, O.M., Shalina, E.V.** and **Miles, M.W.** 1999: Satellite evidence for an Arctic sea ice cover in transformation. *Science* 286, 1937–39.
- Johannessen, O.M., Bengtsson, L., Miles, M.W., Kuzmina, S.I., Semenov, V.A., Alekseev, G.V., Nagurnyi, A.P., Zakharov, V.F., Bobylev, L.P., Pettersson, L.H., Hasselmann, K.** and **Cattle, A.P.** 2004: Arctic climate change: observed and modelled temperature and sea-ice variability. *Tellus Series a-Dynamic Meteorology and Oceanography* 56, 328–41.
- Kalnay, E., Kanamitsu, M., Kistler, R., Collins, W., Deaven, D., Gandin, L., Iredell, M., Saha, S., White, G., Woollen, J., Zhu, Y., Chelliah, M., Ebisuzaki, W., Higgins, W., Janowiak, J., Mo, K.C., Ropelewski, C., Wang, J., Leetmaa, A., Reynolds, R., Jenne, R.** and **Joseph, D.** 1996: The NCEP/NCAR 40-year reanalysis project. *Bulletin of the American Meteorological Society* 77, 437–71.
- Kistler, R., Kalnay, E., Collins, W., Saha, S., White, G., Woollen, J., Chelliah, M., Ebisuzaki, W., Kanamitsu, M., Kousky, V., van den Dool, H., Jenne, R.** and **Fiorino, M.** 2001: The NCEP-NCAR 50-year reanalysis: monthly means CD-ROM and documentation. *Bulletin of the American Meteorological Society* 82, 247–67.
- Koerner, R.M.** 1977: Ice thickness measurements and their implications with respect to past and present ice volumes in the Canadian High Arctic ice caps. *Canadian Journal of Earth Sciences* 14, 2697–705.
- Koerner, R.M.** and **Fisher, D.A.** 1990: A record of Holocene summer climate from a Canadian high-Arctic ice core. *Nature* 343, 630–31.
- Krabill, W., Frederick, E., Manizade, S., Martin, C., Sonntag, J., Swift, R., Thomas, R., Wright, W.** and **Yungel, J.** 1999: Rapid thinning of parts of the southern Greenland ice sheet. *Science* 283, 1522–24.
- Lamoureux, S.** 2000: Five centuries of interannual sediment yield and rainfall-induced erosion in the Canadian High Arctic recorded in lacustrine varves. *Water Resources Research* 36, 309–18.
- Lamoureux, S.F.** and **Bradley, R.S.** 1996: A late Holocene varved sediment record of environmental change from northern Ellesmere Island, Canada. *Journal of Paleolimnology* 16, 239–55.
- Lamoureux, S.F.** and **Gilbert, R.** 2004: A 750-yr record of autumn snowfall and temperature variability and winter storminess recorded in the varved sediments of Bear Lake, Devon Island, Arctic Canada. *Quaternary Research* 61, 134–47.
- Lamoureux, S.F., England, J.H., Sharp, M.J.** and **Bush, A.B.G.** 2001: A varve record of increased ‘Little Ice Age’ rainfall associated with volcanic activity, Arctic Archipelago, Canada. *The Holocene* 11, 243–49.
- Mann, M.E., Bradley, R.S.** and **Hughes, M.K.** 1998: Global-scale temperature patterns and climate forcing over the past six centuries. *Nature* 392, 779–87.
- Marshall, S.J., Sharp, M.J., Burgess, D.O.** and **Anslow, F.S.** 2007: Near-surface temperature lapse rates on the Prince of Wales Icefield, Ellesmere Island, Canada: implications for regional downscaling of temperature. *International Journal of Climatology* 27, 385–98.
- Maxwell, J.B.** 1981: Climatic regions of the Canadian Arctic islands. *Arctic* 34, 225–40.
- Mysak, L.A., Ingram, R.G., Wang, J.** and **van der Baaren, A.** 1996: The anomalous sea-ice extent in Hudson Bay, Baffin Bay and the Labrador Sea during three simultaneous NAO and ENSO episodes. *Atmosphere-Ocean* 34, 313–43.
- Overpeck, J.K., Hughen, K., Hardy, D., Bradley, R., Case, R., Douglas, M., Finney, B., Gajewski, K., Jacoby, G., Jennings, A., Lamoureux, S., Lasca, A., MacDonald, G., Moore, J., Retelle, M., Smith, S., Wolfe, A.** and **Zielinski, G.** 1997: Arctic environmental change of the last four centuries. *Science* 278, 1251–56.
- Parkinson, C.L., Cavalieri, D.J., Gloersen, P., Zwally, H.J.** and **Comiso, J.C.** 1999: Arctic sea ice extents, areas, and trends, 1978–1996. *Journal of Geophysical Research-Oceans* 104, 20837–56.
- Perren, B.B., Bradley, R.S.** and **Francus, P.** 2003: Rapid lacustrine response to recent High Arctic warming: a diatom record from Sawtooth Lake, Ellesmere Island, Nunavut. *Arctic Antarctic and Alpine Research* 35, 271–78.
- Rogers, J.C., Wang, C.C.** and **McHugh, M.J.** 1998: Persistent cold climatic episodes around Greenland and Baffin Island: links to decadal-scale sea surface temperature anomalies. *Geophysical Research Letters* 25, 3971–74.
- Serreze, M.C.** and **Barry, R.G.** 2005: *The Arctic climate system*. Cambridge University Press, 402 pp.
- Serreze, M.C.** and **Hurst, C.M.** 2000: Representation of mean Arctic precipitation from NCEP-NCAR and ERA reanalyses. *Journal of Climate* 13, 182–201.
- Serreze, M.C.** and **Maslanik, J.A.** 1997: Arctic precipitation as represented in the NCEP/NCAR reanalysis. *Annals of Glaciology* 25, 429–33.
- Serreze, M.C., Clark, M.P.** and **Bromwich, D.H.** 2003: Monitoring precipitation over the Arctic terrestrial drainage system: data requirements, shortcomings, and applications of atmospheric reanalysis. *Journal of Hydrometeorology* 4, 387–407.
- Smith, S.V., Bradley, R.S.** and **Abbott, M.B.** 2004: A 300 year record of environmental change from Lake Tuborg, Ellesmere Island, Nunavut, Canada. *Journal of Paleolimnology* 32, 137–48.
- Smith, T.M.** and **Reynolds, R.W.** 2004: Improved extended reconstruction of SST (1854–1997). *Journal of Climate* 17, 2466–77.
- Thompson, D.W.J.** and **Wallace, J.M.** 1998: The Arctic Oscillation signature in the wintertime geopotential height and temperature fields. *Geophysical Research Letters* 25, 1297–300.
- Vinnikov, K.Y., Robock, A., Stouffer, R.J., Walsh, J.E., Parkinson, C.L., Cavalieri, D.J., Mitchell, J.F.B., Garrett, D.** and **Zakharov, V.F.** 1999: Global warming and northern Hemisphere sea ice extent. *Science* 286, 1934–37.
- Wolken, G.J., England, J.H.** and **Dyke, A.S.** 2008: Changes in late-Neoglacial perennial snow/ice extent and equilibrium-line altitudes in the Queen Elizabeth Islands, Arctic Canada. *The Holocene* 18, 000–000, this issue.
- Zakharov, V.F.** 1997: *Sea ice in the climate system*. WMO Technical Document 782. World Climate Research Programme, Arctic Climate System Study, 80.

Recent Changes in Areal Extent of the Devon Ice Cap, Nunavut, Canada

David O. Burgess and

Martin J. Sharp

Department of Earth and Atmospheric
Sciences, University of Alberta, Edmonton,
Alberta, T6G 2E3, Canada.
dob@ualberta.ca

Abstract

Image data from the years 1959/1960 and 1999/2000 reveal a 2.4% decrease in the surface area of the Devon Ice Cap, Nunavut, over the last 40 yr. This has resulted primarily from extensive retreat of tidewater glacier margins on the eastern side of the ice cap, and shrinkage of its near-stagnant southwestern arm. Thinning of the ice cap has also increased bedrock exposure in the ice cap interior. However, since 1960 the northwestern margin of the ice cap has advanced slightly. Volume loss associated with these changes was estimated at $-67 \pm 12 \text{ km}^3$ as calculated from two independent techniques. A digital elevation model (DEM) of the ice cap surface was used to delineate interior ice divides allowing patterns of change to be investigated at the drainage basin scale. Strong correlation between the hypsometric characteristics of drainage basins and the observed changes in ice-cap geometry suggests that these changes reflect interbasin differences in the inherent sensitivity of glacier mass balance to recent climate forcing. Response time calculations indicate that most of the ice cap is responding to recent climate warming, whereas the northwestern region is likely still responding to cooler conditions that prevailed during the Little Ice Age (LIA).

Introduction

Global climate models consistently predict that anthropogenic climate warming will be manifested most strongly in northern high latitudes (Mitchell, 1995; Johns et al., 1997; IPCC, 2001). There is already considerable evidence that predicted changes are occurring (Overpeck et al., 1997; Serreze et al., 2000). The predicted temperature changes would impact strongly on the mass balance and extent of the glaciers, ice caps, and ice sheets in the region, and the resulting shrinkage of these ice masses could contribute significantly to global sea-level change over the next century (Meier, 1984; Van de Wal and Wild, 2001; Meier and Dyurgerov, 2002).

Outside Greenland, the largest amounts of land ice ($\sim 150,000 \text{ km}^2$) in the Northern Hemisphere are found in the Canadian Arctic islands (Koerner, 1966). However, little is known about recent changes in the extent of these ice masses. Areal change measurements have been made for a section of the Barnes Ice Cap on Baffin Island (Jacobs et al., 1996) and for the small, stagnant Murray Ice Cap on northern Ellesmere Island (Braun et al., 2001). Over the period 1961 to 1993, the area of the measured sector of the Barnes Ice Cap decreased by $\sim 1\%$, while that of the Murray Ice Cap decreased by $\sim 28\%$ between 1959 and 2000. Here we report results of an investigation into recent changes in the extent of the Devon Ice Cap, Nunavut. Investigation of glacier change at the scale of the whole ice cap is of particular interest because there are strong spatial gradients in climate, mass balance characteristics, glacier geometry, and terminus conditions across the ice cap. Thus, different sectors of the ice cap may be subjected to different climate forcings, they may have different inherent mass-balance sensitivity to specific forcings, and they may respond to these forcings at different rates.

Glacier response times are influenced by a combination of ice-mass geometry, mass-balance gradient, and terminus ablation rates (Johannesson, 1989; Bahr et al., 1998). All of these factors vary significantly across the Devon Ice Cap. Differences in mass-balance gradient between the east and west sides of the ice cap have been attributed to the effect of the Baffin Bay moisture source on regional accumulation patterns. These patterns are believed to have influenced

the long-term evolution of the ice-cap geometry such that glaciers draining to its eastern margin occupy larger basins and descend to lower elevations than glaciers draining to the west (Koerner, 1977a). Asymmetry of mass-balance gradient and ice-cap geometry resulting in large differences in terminus ablation rates between the east and west margins may have a significant effect on response times characteristic of these regions.

This study quantifies recent changes in the areal extent of the Devon Ice Cap by comparing the position of ice margins extracted from 1959/1960 aerial photographs and 1999/2000 satellite imagery. Information on the topography of the ice-cap surface, obtained from the Canadian Digital Elevation Dataset (CDED), was used to delineate drainage basins within the ice cap, and changes were analyzed at the scale of individual drainage basins. Relationships among the magnitudes of observed changes, the characteristic response times, and the hypsometry of drainage basins were investigated to provide insight into the mechanisms controlling ice margin variations. Also, two independent methods were used to estimate volume change for selected basins and for the ice cap as a whole.

Study Area

The Devon Ice Cap occupies approximately $14,400 \text{ km}^2$ (between $74^\circ 30' \text{N}$ and $75^\circ 50' \text{N}$ and $80^\circ 00' \text{W}$ and $86^\circ 00' \text{W}$) on Devon Island, which is located in the southeast of the Queen Elizabeth Islands, Nunavut, Canada (Fig. 1). Recent radio echo sounding data indicate that the current ice-cap volume is $4110 \pm 140 \text{ km}^3$ with a maximum ice thickness of approximately 880 m at the head of the eastward flowing basins (Dowdeswell et al., submitted). The highest elevation is 1921 m at the ice-cap summit. The eastern margin of the ice cap faces the North Open Water (NOW) polynya at the head of Baffin Bay. Large outlet glaciers that descend to sea level in this region experience high rates of accumulation (up to $500 \text{ kg m}^{-2} \text{ a}^{-1}$) and surface ablation (up to $2000 \text{ kg m}^{-2} \text{ a}^{-1}$) as well as mass loss by iceberg calving, resulting in relatively steep mass-balance–elevation gradients ($2.7 \text{ kg m}^{-2} \text{ a}^{-1} \text{ m}^{-1}$; Koerner, 1970). Smaller tidewater glaciers reach the

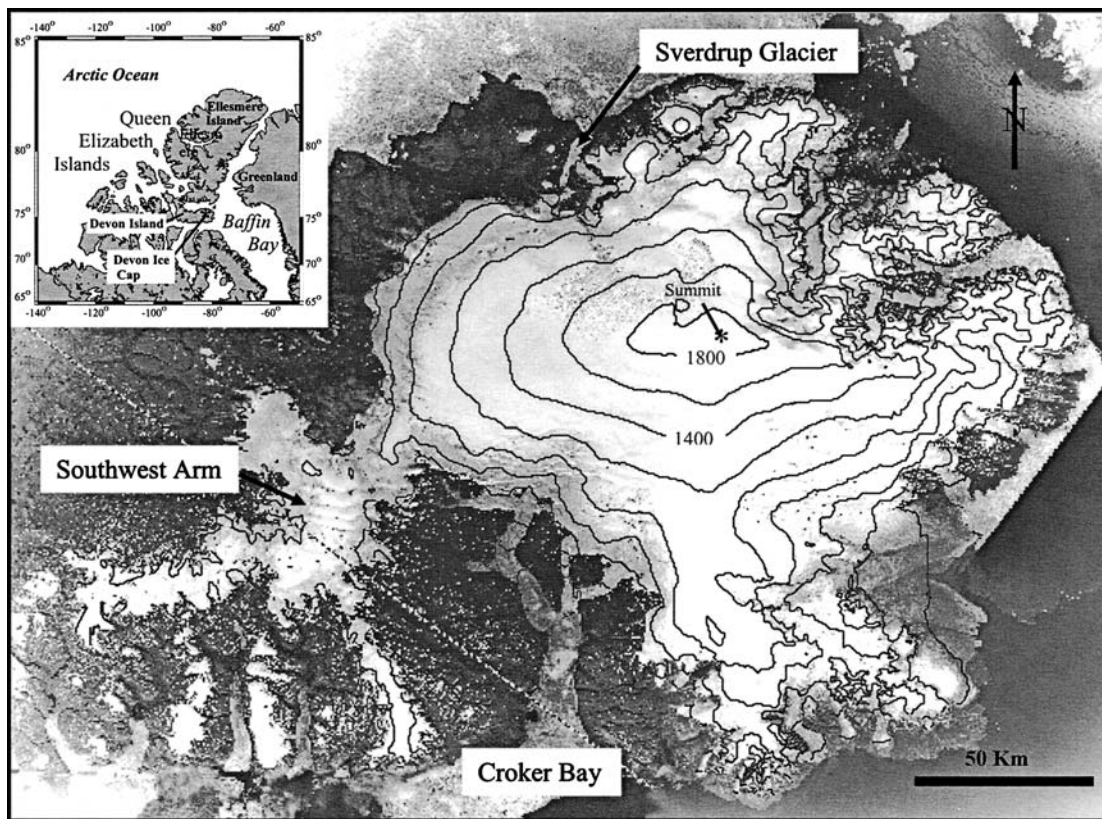


FIGURE 1. Location of the Devon Ice Cap in the Canadian Arctic Archipelago. Image of the ice cap is an orthorectified mosaic of Landsat 7 satellite panchromatic data acquired on 13 July 1999 and 2 August 2000. Contour interval is 200 m.

ocean along the northern and southern margins of the ice cap. By contrast, the western margin of the ice cap terminates entirely on land at elevations of 300 to 500 m. This part of the ice cap is located in a precipitation shadow, where rates of accumulation and ablation (up to $200 \text{ kg m}^{-2} \text{ a}^{-1}$ and $\sim -1000 \text{ kg m}^{-2} \text{ a}^{-1}$, respectively), along with mass-balance gradients ($1.5 \text{ kg m}^{-2} \text{ a}^{-1} \text{ m}^{-1}$) are much reduced. An arm extending approximately 80 km to the southwest of the main ice cap consists largely of near-stagnant, ablating ice. Nearly this entire sector of the ice cap lies below the equilibrium-line altitude (ELA) as defined by mass-balance data compiled by Koerner (1970).

Proxy data and field measurements provide insight into the climate history of the ice cap since the end of the Little Ice Age (LIA). Records of summer melt layers from ice cores in the Canadian Arctic indicate an abrupt warming trend beginning ca. AD 1850, with a second significant temperature increase after ca. 1925 (Koerner, 1977b). Stake measurements made across the northwest part of the ice cap (Sverdrup Glacier) since 1960 indicate a negative mass balance since observations began, with a trend towards increasingly negative balances since the late 1980s (Koerner and Lundgaard, 1995).

Methods

Changes in the surface area of the Devon Ice Cap were determined from remotely sensed imagery acquired in 1959/1960 and 1999/2000. Ice margins were digitized for each data set and drainage basin boundaries common to both data sets were delineated. Overlay analysis and raster cartographic techniques were then employed to detect and quantify areal differences between the extracted data sets.

DATA SOURCES

The satellite image data used in this study were obtained from 3 Landsat 7 ETM+ panchromatic (15-m resolution) scenes acquired on

13 July 1999 (path 38 rows 6 and 7) and 2 August 2000 (path 36 row 7). All satellite imagery was purchased as L1G (radiometrically and geometrically corrected) processed data. The aerial photography consisted of 250 1:60,000 photographs acquired in late July and early August of 1959/1960 by the Government of Canada. The digital elevation model (DEM) used in this study was a subset of the Canadian Digital Elevation Dataset (CDED) produced from the National Topographic System (NTS) 1:250,000 map sheets which, in turn, were derived from the 1959/1960 aerial photography mentioned above. The DEMs were re-projected from the WGS-84 geographic coordinate system (3×6 arcsec) to a 100 m resolution NAD83 UTM grid. Vertical accuracy of the DEM is ± 20 m over bedrock and ice margins decreasing to ± 50 m throughout the interior regions of the ice cap (Gagne, pers. comm., 2002).

IMAGE PREPARATION

All image data were referenced to the UTM projection on the NAD83 datum. Satellite images were georeferenced to the 1:250,000 NTS map sheets using at least 40 ground control points (GCPs) that were clearly identified in both images (RMS error < 60 m). The satellite imagery was orthorectified in PCI Orthoengine™ V8.0 using the CDED DEM to correct for terrain distortions. The orthorectified images were manually mosaiced to produce a 15-m resolution ortho-image of the entire Devon Ice Cap. The aerial photographs were obtained as contact prints and digitized at 300 dpi (5 m ground resolution) using a Vidar 36" upright scanner. Each digital photograph was georeferenced to the Landsat 7 orthomosaic by selecting between 7 and 12 GCPs (depending on the amount of exposed bedrock) over bedrock features clearly identifiable in both images (RMS error < 15 m). The digital photos were then orthorectified in the PCI Orthoengine™ V8.0 using the CDED DEM to correct for terrain distortions. Four mosaics of the aerial photography were generated in

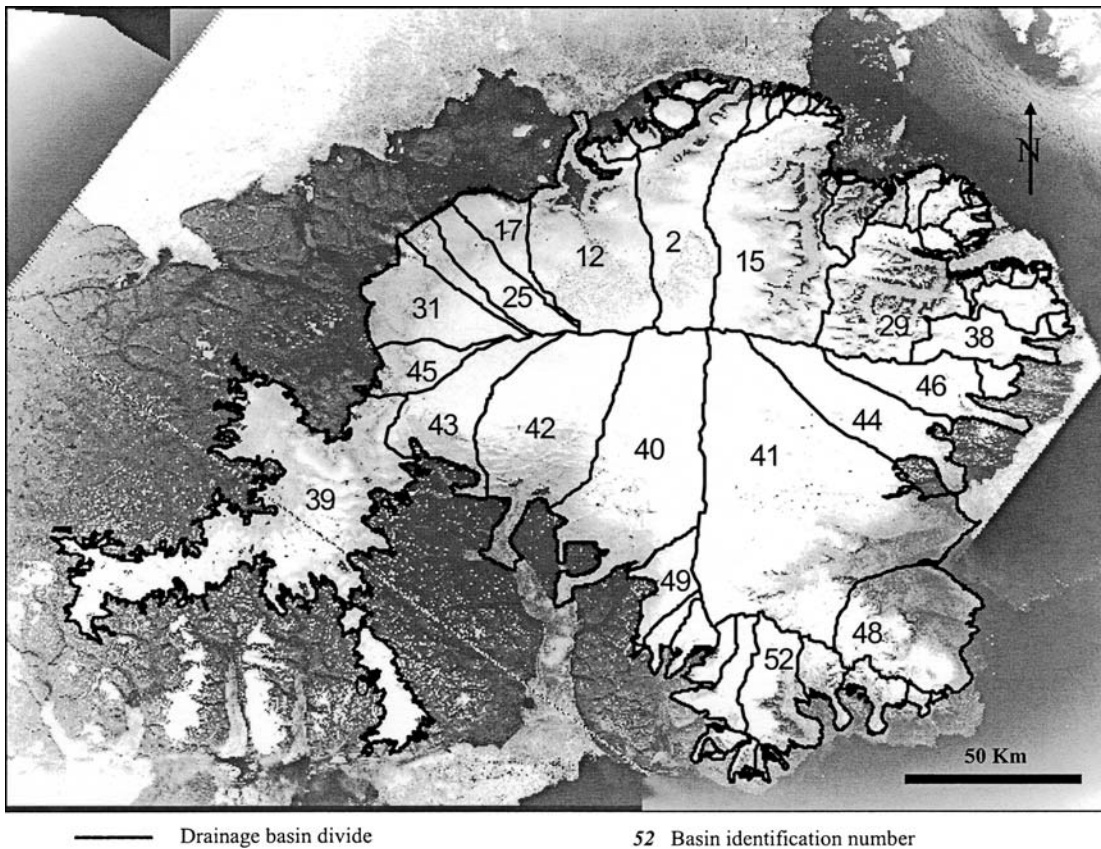


FIGURE 2. Drainage basins of the Devon Ice Cap. Only the basins labeled with unique identification numbers were used for analysis in this study.

Orthovista™ (image mosaicing software) and clipped to the geographic extents of the corresponding 1:250,000 map sheets.

LINWORK CAPTURE

Ice margins and boundaries of interior bedrock regions were captured through on-screen digitizing techniques in ArcView 3.2™ geographic information system from both orthorectified digital data sets. Linework representing ice margins was digitized in “point mode” as a series of line segments and later converted to single polygon coverage in ArcInfo 8.0™. Interior bedrock regions were digitized directly as polygons in ArcView 3.2™. The 1960 ice margin was digitized from the contiguous ice mass. Any parts of the ice cap that were separated from the main ice cap by melting between 1960 and 1999 were included in the 1999 surface area calculations.

DRAINAGE BASIN DELINEATION

Drainage basins were delineated to allow areal changes to be associated with distinct catchment regions (Fig. 2). A river drainage network for the ice-cap surface was initially simulated from the DEM and overlaid on the satellite image mosaic.

Using the “Basin” utility in ArcView 3.2™, outlet locations (points where the simulated drainage paths flow off the ice-cap edge) were identified interactively and the associated catchment areas were delineated based on flow accumulation and direction grids. Due to inaccurate representation of the ice surface by the DEM in some areas, particularly towards the margins, ice flow (as observed from the Landsat image) is not always consistent with the downslope direction derived from the DEM. In these cases, manual editing of the boundaries was necessary to prevent drainage basin boundaries from cross-cutting ice-flow lines. This was done through visual

interpretation of the Landsat orthomosaic. Drainage basin boundaries were then clipped by both the 1960 and 1999 ice-margin polygons.

AREA CALCULATIONS

Calculation of area change in each drainage basin was performed using raster overlay techniques in ArcView GIS. The drainage basin boundary layer was clipped by the 1960 and 1999 ice-margin polygons to produce the same internal drainage divide structure for both years. The polygon coverages and interior bedrock regions were then converted to a 15-m resolution raster grid. Cells were coded with unique arbitrary values assigned to each polygon with the same polygons having the same coded value for both years. For each data set (1959/1960 and 1999/2000) the interior bedrock regions were subtracted from the ice surface polygon coverage, resulting in “ice surface only” coverages. Areal changes were then calculated by comparing tabulated pixel counts for each gridded ice-surface coverage on a per polygon basis.

ERROR ANALYSIS

Errors associated with the ice-cap area measured from the air photos were a function of both the accuracy of the coregistration between the air photos and the Landsat 7 ETM+ orthomosaic and the accuracy with which the ice-cap margin was identified and digitized. Errors of the Landsat 7 ETM+ derived areas were a function of the accuracy with which the ice-cap margin was identified and digitized only. Ice-cap margins were digitized using on-screen digitizing in ArcView GIS that allowed the operator to zoom in to the pixel level for point data collection. Digitizing inaccuracies over unobscured sections of the ice-cap margin were therefore based on (a) image resolution and (b) contrast between the ice-cap surface and the adjacent terrain.

TABLE 1

Summary of error associated with extracting linework from the satellite and aerial photography image data

	Error Source	Line Segment Length (km)	Line Placement Error (m)	Area Estimate Error (\pm km ²)
Landsat 7	Digitizing	2678	15	40
Landsat 7	Cloud	19	90	2
Landsat 7	Shadow	14	90	1
Landsat 7	Snow	50	120	6
Landsat 7 Total				40
Aerial Photography	Digitizing	2546	5	13
Aerial Photography	Coregistration	2567	11	28
Aerial Photography	Obscured and missing imagery	21	75	2
Aerial Photography Total				31

Coregistration errors between the air photo orthomosaics and the Landsat 7 ETM+ orthomosaic were estimated to be ± 22 m based on residual values between 40 (10 points from each air photo mosaic) independent checkpoints identified in each data set. However, for the area measurement to be affected by the maximum residual distance, the coregistration error would have to displace each mosaic in equal and opposite directions from the other mosaics. Since it is more likely that these errors are random, a value of ± 11 m (50% of the coregistration error) was chosen as a more realistic estimate of the error attributed to coregistration (see Table 1).

Measurement uncertainty of the unobscured sections of the ice margin was judged to be no greater than the pixel size of the image being digitized (± 15 m for the satellite mosaic and ± 5 m for the aerial photography mosaic). This error was calculated as the product of the total ice-cap boundary length minus the length obscured, and the pixel width. For obscured sections of the ice-cap perimeter, error was estimated as the product of the obscured segment length and a maximum estimated line offset value applied to each type of obscurity (Table 1). Because all missing or obscured sections of the aerial photography orthomosaic were digitized from the 1:250,000 NTS map sheets, estimated offset distances were based on the coregistration accuracy between the aerial photography orthomosaic and the 1:250,000 NTS map sheets (± 75 m).

Offset distances were estimated for the satellite orthoimage based on the confidence with which the ice margin could be identified within each type of obscurity. Because the margin was generally not completely obscured by cloud and shadow, error along these sections was estimated at ± 90 m. Sections of the ice margin under cloud were faintly (intermittently) identified through semitransparent (broken) cloud cover. Similarly, sections of the ice-cap margin obscured by shadow were enhanced by applying a contrast stretching function to the imagery that allowed the margin to be identified with some degree of confidence in these areas. Ice margins obscured by late-lying snow-pack, however, were less distinct and identification accuracy was estimated at ± 120 m. Along these sections, the margin was digitized at the angle of inflection between the ice-cap boundary and the snow-covered ground that was highlighted by differential illumination as a result of the local incidence angle of the sun. In total, the ice-cap margin was obscured (either partially or fully) by 3% and 0.8% in the satellite imagery and the aerial photography, respectively.

Additional error could potentially have been generated in the orthorectification process due to registration errors between the imagery and the DEM. The DEM used in this study is essentially

a digital version of the NTS topographic map sheets to which the Landsat 7 imagery was georeferenced with an RMS error of ± 75 m. The aerial photography was subsequently georeferenced to the Landsat 7 imagery (RMS error of ± 15 m) increasing the registration error between the aerial photography and the DEM to ± 90 m. Therefore, the uncorrected aerial photography and Landsat 7 imagery may have been orthorectified based on topographic information offset by up to 90 m from the associated features on the imagery. Orthorectification errors resulting from inaccurate coregistration between the DEM and imagery however were not considered in this study because both data sets would be affected equally by this problem therefore the relative difference in area measurements would be minimal.

AREA ESTIMATES AND TOTAL ERROR

The total error (TE) of the area measured from each data source was computed from the formula;

$$TE = \sqrt{g1^2 + g2^2 + \dots + gn^2}$$

where $g1 \dots gn$ represent the individual sources of error as specified in Table 1. The total area (TA) and the associated error as measured from the 1999 Landsat imagery therefore is;

$$TA_{Landsat} = 14,010 \pm 40 \text{ km}^2$$

and for the 1960 aerial photography is;

$$TA_{aerial \text{ photography}} = 14,342 \pm 31 \text{ km}^2$$

The error associated with the change of areal extent (difference between the 1999 area and the 1960 area measurement) was taken as the greater of the two error estimates.

Therefore,

$$\text{Total area change} = 332 \pm 40 \text{ km}^2$$

The minimum error of the area change measurements derived for an individual drainage basin was estimated to be accurate to within $\pm 11\%$ for basins with unobscured margins. For all other drainage basins, error was estimated as a function of the length (and type) of the obscured margin within the basin.

The error analysis presented in this study likely overestimates the actual error because it assumes a maximum digitizing offset along the entire perimeter of the ice-cap boundary. Previous work based on repeat digitizing experiments has demonstrated that errors associated with digitizing points along the perimeter of a polygon are limited to a statistically derived epsilon band which is significantly smaller than the maximum offset width (Dunn et al., 1990). It is beyond the scope of this study however, to minimize the stated error by deriving a statistical distribution of digitized points about the ice-cap margin.

Results

The Devon Ice Cap has experienced a net decrease in area of $338 \pm 40 \text{ km}^2$ over the past 40 yr. Surface area changes were most significant in four distinct regions of the ice cap.

1. Retreat of the four major tidewater glaciers on the east coast (Fig. 3) accounted for $38 \pm 4 \text{ km}^2$ of the decrease in area of the ice cap. The most northerly glaciers (i) and (ii) experienced retreat of up to 1300 m from the 1960 terminus location and the central glacier (iii) retreated approximately 750 m. The most southerly glacier (iv) experienced maximum retreat of up to 3000 m.
2. Increase in the area of exposed bedrock in the interior regions of the ice cap accounted for $45 \pm 5 \text{ km}^2$ of the decrease in ice

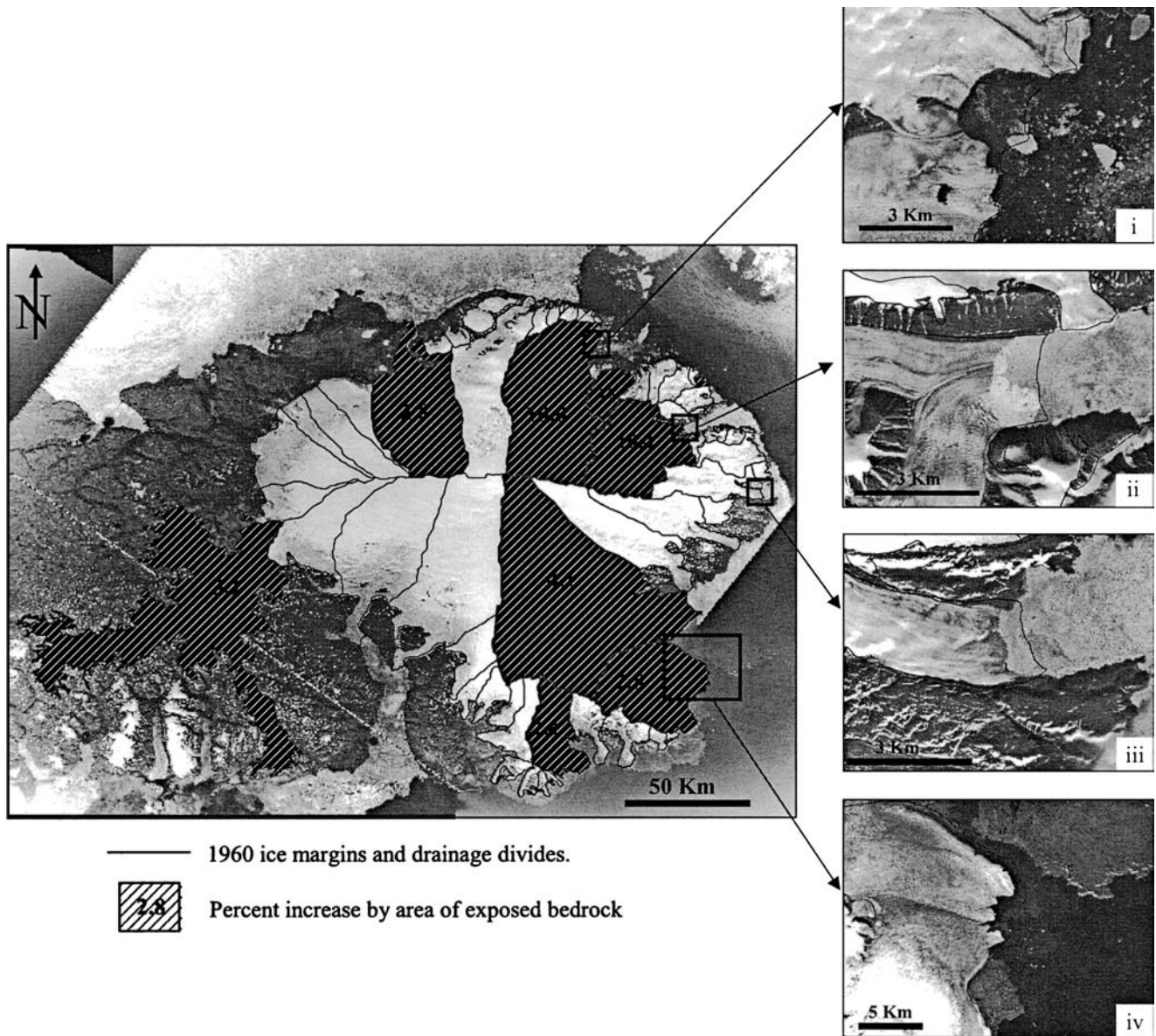


FIGURE 3. 1960 ice margins superimposed on 1999/2000 Landsat image mosaics highlight retreat of the major tidewater glaciers over the past 40 yr. Shaded basins have experienced a minimum increase of 2 km² of exposed bedrock area between 1960 and 1999 within the ice cap interior.

surface area (Fig. 3). The basins affected the greatest are located in the mountainous northeast and southeast regions of the ice cap. The increase in exposed bedrock area in these regions indicates a lowering of the ice-cap surface.

3. Marginal retreat of the southwest arm (Fig. 4) accounted for a 200 ± 17 km² decrease in surface area of the ice cap.
4. Ice margin advance by an average of 130 m along a 80 km section of the northwest margin (Fig. 5) accounted for a 10.5 ± 2 km² increase in surface area of the ice cap.

The changes described above account for approximately 76% of the total change experienced by the Devon Ice Cap. The remaining changes in terms of area decrease have occurred primarily as a result of glacier retreat within small basins located throughout the south and northeast sectors of the ice cap. The remaining increases in area have resulted from advance of the Sverdrup Glacier (basin 12) by up to 250 m and the two major outlet glaciers that drain south into Croker Bay (basins 42 and 40) which have experienced advance of between 100 and 400 m along their termini.

Analysis

Variability in the areal changes observed could be due to regional differences in climate forcing, to variations in the sensitivity of glacier mass balance to given changes in climate, or to differences in the response time of different sectors of the ice cap to mass-balance changes. It is also probable, however, that the variations in ice-margin fluctuations have resulted from a complex interaction of these factors.

PREVAILING CLIMATE PATTERN

Differential changes at the ice margin may reflect growth related to the influence of a prevailing climate pattern on the ice-cap geometry. The predominant moisture supply for the ice cap is derived from the North Open Water (NOW) polynya that is located at the north end of Baffin Bay. Cyclonic weather systems that develop over this region deposit over two times the amount of precipitation over the east sector of the ice cap than the west (Koerner, 1977a). Ice-cap growth in the extreme southeast is also encouraged by the maritime effect associated

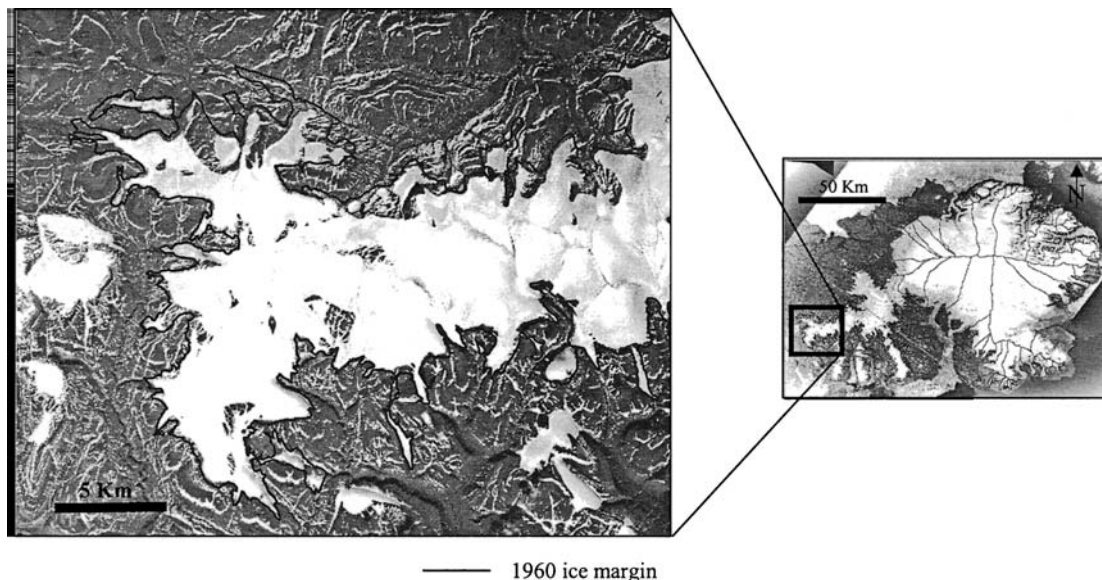


FIGURE 4. Ice margin retreat and apparent thinning of the southwest arm.

with the NOW, which suppresses summer melt in this region (Koerner, pers. comm., 2002). Koerner (1977a) has suggested that this pattern has likely persisted since at least the Climatic Optimum period (6000–5000 yr BP) to produce the asymmetric geometry of the ice cap that exists today. The eastern basins are typically larger and descend to lower elevations than basins in the west. This results in the east side of the ice cap being subjected to greater amounts of surface ablation and mass loss due to iceberg calving than basins on the west side. Significant mass losses that have occurred along the east side of the ice cap (in contrast to growth along the west) therefore suggest that regions of the ice cap that have experienced preferential growth in the past as a result of this prevailing climate pattern appear to be the most susceptible to increases in average temperature.

BASIN HYSOMETRY

Analysis of the hypsometry of the major basins was performed to investigate the influence of basin topography on ice-cap response to recent climate changes. Two parameters were used to characterize the basin topography: a Balance Ratio (BR; Furbish and Andrews, 1984)

and a sensitivity index derived in this study which provides a measure of the relative change in glacier mass balance resulting from a prescribed change in ELA.

The balance ratio (BR) was calculated from the equation;

$$BR = (Z_m - ELA) / (ELA - Z_t) \quad (1)$$

where Z_m = maximum elevation of the glacier, Z_t = terminus elevation of the glacier, and ELA = equilibrium-line altitude. For a rectangular glacier, the change in the altitude of the glacier terminus that results from a prescribed change in the ELA is an inverse linear function of the BR. For glaciers with other shapes, the relationship is still inverse, but nonlinear (Furbish and Andrews, 1984: 202–203). Thus if the ice cap as a whole were subjected to a spatially uniform change in ELA, the change in terminus position resulting from that ELA change would primarily be a function of the BR and planimetric shape of the basin.

BRs were calculated for the major drainage basins of the Devon Ice Cap using ELA estimates derived from the 1960–1966 mass-balance observations by Koerner (1970). The ice cap was divided into quadrants, with boundaries following the watershed divides and

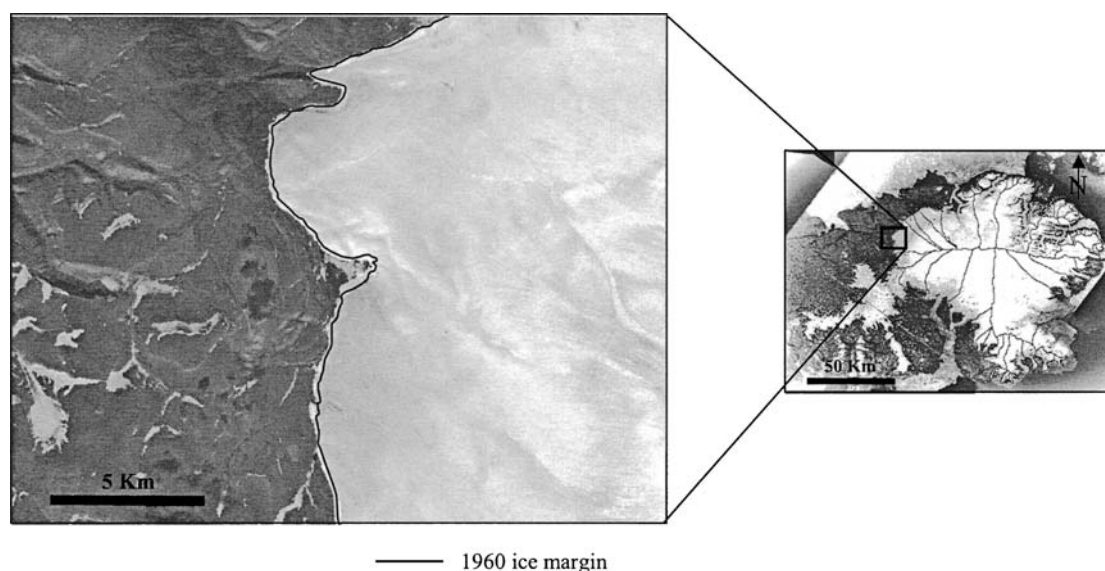


FIGURE 5. Section of the advancing northwest margin.

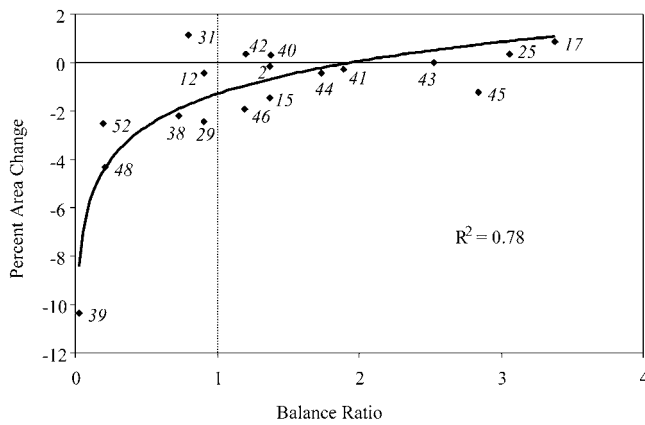


FIGURE 6. Plot of the logarithmic relationship between calculated balance ratios and percent area change of glaciers in the major drainage basins between 1959/1960 and 1999/2000.

appropriate ELA values were applied to each region. ELAs for the northwest and southeast zones were identified directly from Koerner's measurements (950 m a.s.l. and 800 m a.s.l., respectively) and ELAs within the northeast and southwest zones were taken as the average of the two adjacent zones (875 m a.s.l.). Basin hypsometry was derived from the CDED data and analysis was limited to basins larger than 170 km², which comprise more than 85% of the total ice-cap area.

Although the ELA used to calculate the balance ratio index should be that for an ice cap in steady state, the mass balance associated with the ELAs chosen above is slightly negative. On the basis of analysis of the mass balance/ELA relationship, Koerner (1970), however, suggests that a steady state ELA for the northwest sector of the ice cap is 920 ± 80 m. As the ELA assumed for the northwest region of 950 m falls in this range, we are therefore confident that our method of estimating the ELA for the rest of the ice cap is adequate for proper balance ratio calculations.

The calculated BRs display a strong logarithmic relationship ($R^2 = 0.78$) with percent area change of the major drainage basins (Fig. 6). Most basins with BR values below 1.0 have experienced a significant reduction in surface area. Maximum elevations of these basins are

collectively among the lowest on the ice cap (Table 2) resulting in a relatively small altitudinal range above the ELA. In particular, basins 39 and 48 reach maximum elevations of only 998 and 1169 m a.s.l., respectively, resulting in extremely low BR values for these basins. Basins with BRs greater than 1.0 have experienced much less of an area decrease, and in some cases, these basins have increased in size. Those that have experienced growth (42, 40, 25, and 17) are concentrated mainly along the western margin. Although these basins only reach 1500–1600 m a.s.l., their average terminus elevation is 400 m a.s.l., which results in a small elevational range below the ELA. Also, because the termini of these basins are relatively high, they experience cooler temperatures that inhibit glacier retreat. Basins that have experienced limited shrinkage (< -1%) and have BRs greater than 1.0 (2, 44, 41, 43 and 45) extend up to elevations equal to or close to those of the ice-cap summit. These basins generally have larger accumulation area ratios (AARs) than glaciers that have shrunk significantly, and their mass balance was presumably less strongly affected by the post-LIA rise in ELA.

Excluding the southwest arm, basin shape appears to have had some influence on the amount of area loss at the ice-cap margin. Basin shapes were grouped into three main categories according to the Furbish and Andrews (1984) classification scheme: Type "A"—rectangular shaped basins, type "C"—basins that taper up-glacier, and type "D"—basins with wide mid sections that narrow in both up and down glacier directions. For glaciers with BRs less than 1.0, type "D" shaped basins have decreased in size by an average of 3.4% whereas those in type "A" basins have only shrunk by an average of 1.7%. Areal change of glaciers in basins with balance ratios greater than 1.0, show no correlation with shape, however.

Basin hypsometry was analyzed further to determine the sensitivity of major drainage basins to climate warming. Basin sensitivity (BS) values were estimated as the fractional change in AAR resulting from a 100-m rise in the ELA:

$$BS = \Delta AAR_{+100m} / AAR \quad (2)$$

where

$$AAR = \text{Accumulation area} / \text{Total basin area} \quad (3)$$

AAR (accumulation area ratio) represents the proportion of the basin area within the accumulation zone and ΔAAR_{+100m} is the change

TABLE 2

Hypsometrically derived index values and associated glacier attributes for all major drainage basins. Shaded rows indicate basins with balance ratios below 1.0

Basin ID	ELA Zone	Balance Ratio	Basin Sensitivity	% Area Change	Basin Shape	Accumulation Area Ratio	Minimum Elevation (m)	Max. Elevation (m a.s.l.)
12	NW	0.91	L(0.09)	-0.4	A	0.83	0	1854
42	SW	1.2	L(0.09)	0.3	D	0.77	0	1835
2	NE	1.37	L(0.07)	-0.2	A	0.82	0	1901
40	SW	1.38	L(0.09)	0.3	A	0.81	5	1897
46	SE	1.2	M(0.14)	-1.9	C	0.65	0	1674
15	NE	1.37	M(0.13)	-1.4	A	0.69	0	1901
44	SE	1.74	M(0.10)	-0.4	A	0.77	0	1853
41	SE	1.89	M(0.14)	-0.3	D	0.57	0	1901
25	NW	3.06	M(0.14)	0.3	A	0.87	540	1667
31	NW	0.8	H(0.23)	1.1	C	0.59	312	1521
29	NE	0.91	H(0.18)	-2.4	D	0.61	0	1708
43	SW	2.53	H(0.16)	0	C	0.73	398	1633
45	SW	2.84	H(0.20)	-1.2	C	0.77	538	1443
17	NW	3.38	H(0.22)	0.8	C	0.73	561	1666
39	SW	0.03	VH(0.90)	-10.3	N/A	0	119	998
52	SE	0.2	VH(0.46)	-2.5	A	0.45	34	1141
48	SE	0.21	VH(0.59)	-4.3	D	0.01	0	1169
38	SE	0.73	VH(0.31)	-2.2	A	0.43	0	1484

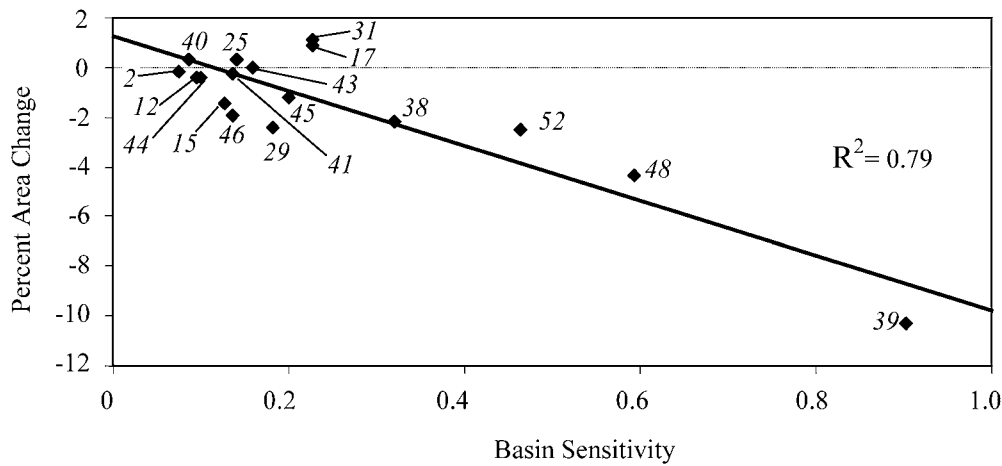


FIGURE 7. Plot of the linear relationship between basin sensitivity and percent area change of glaciers in the major drainage basins measured between 1959/1960 and 1999/2000.

in accumulation area ratio resulting from a 100-m rise in ELA as documented in the CDED DEM for 1959/1960 (year of the aerial photography used to derive the CDED DEM).

Overall, the calculated BS values display a strong linear relationship ($R^2 = 0.79$) with percent area change of the major drainage basins (Fig. 7). This relationship is controlled mainly by BS values of the basins situated at lower elevations (i.e. basins 38, 52, 48, and 39). These basins have relatively high BS values (>0.2) and have experienced significant areal change over the past 40 yr. The trend is less obvious for basins with BS values <0.2 .

The spatial distribution of BS values highlights the relative susceptibility of various regions of the ice cap to climate warming (Fig. 8; Table 2). Basins with BS values greater than 0.23 (“VH”; basins 38, 39, 48, 52) have small AARs and have experienced the greatest average retreat of all major basins since 1960. These basins are restricted to lower elevations (i.e. have low maximum and terminus elevations; see Table 2) where shrinkage appears to be a direct function of the relative loss of accumulation area due to raising the ELA. Drainage basins classified as “highly sensitive” (“H”; 31, 29, 43, 45, 17, and 25) include those that occupy the western margin and have experienced recent advance. These basins are predominantly type “C” in shape implying that the accumulation area ratio increases rapidly as

the ELA is lowered. Recent advance throughout this region indicates that these basins may not yet have reacted fully to recent climate warming. Medium sensitivity basins (“M”; 46, 15, 44, and 41) are concentrated on the eastern side of the ice cap. They are predominantly type “A” in planimetric shape (accumulation area ratio decrease is directly proportional to a rise in ELA) and reach near-summit elevations with AARs averaging 0.71. Finally, low sensitivity drainage basins (“L”; 12, 42, 2, and 40) have properties very similar to the “M” basins except that they drain towards the north and south coasts and have an average AAR of 0.81.

The hypsometric curves plotted in Figure 9 indicate the distribution of surface area within a basin in relation to elevation above or below the ELA. Basins in which the ELA intersects the steepest section of the curve (basins 38 and 52) are most sensitive to climate change because moving the ELA from the current location results in changes in accumulation area that are large relative to the total basin area. In some cases however, the ELA intersects the hypsometric curve close to the upper limit of the cumulative basin area (basins 39 and 48). The accumulation areas within these basins have almost entirely disappeared resulting in consistently high ELAs regardless of fluctuations of the ELA. The ELAs of highly sensitive basins (“H”) intersect steep sections of the hypsometric curves. The sensitivity of these basins is

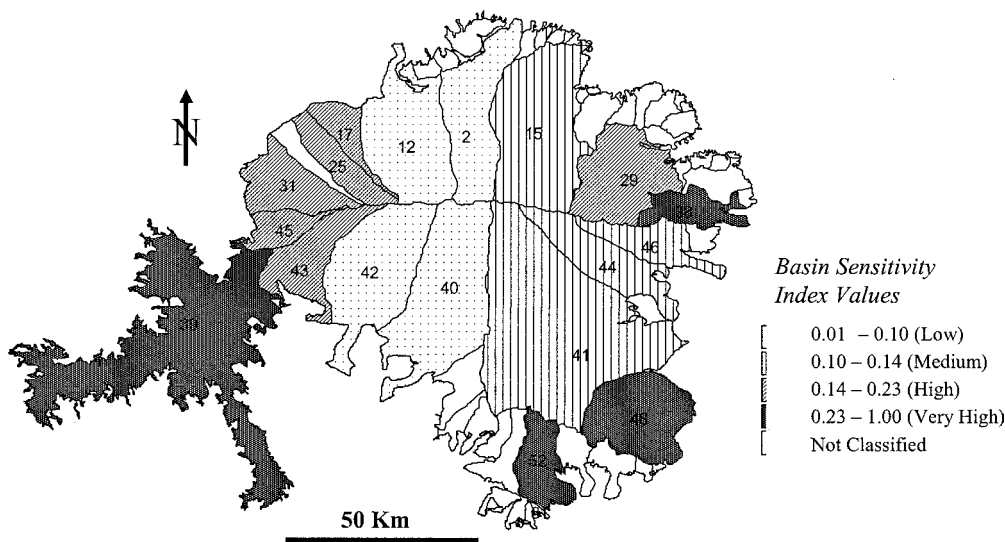


FIGURE 8. Relative sensitivity of glaciers in the major drainage basins to increasing the ELA by 100 m.

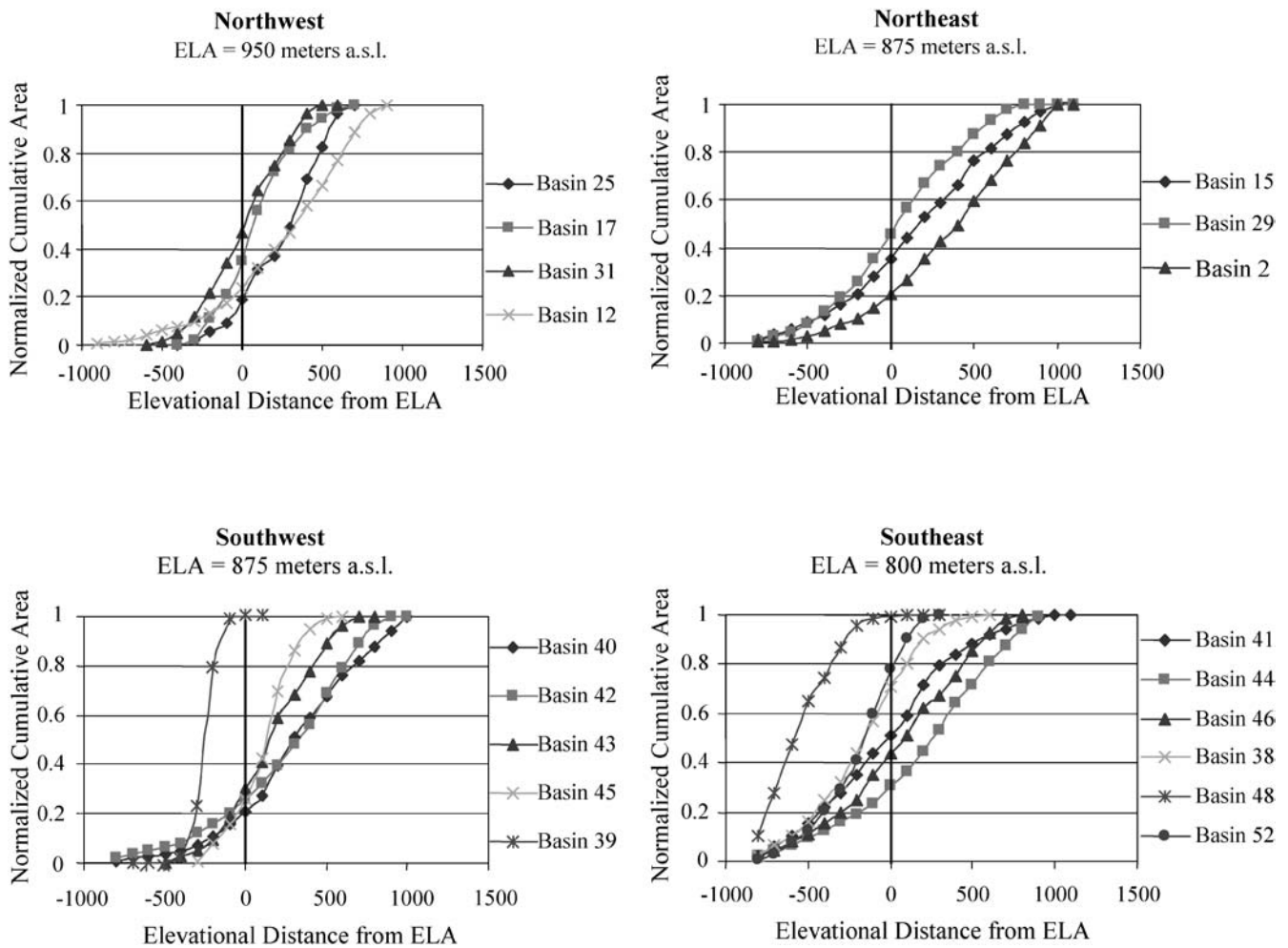


FIGURE 9. Hypsometric curves of the normalized cumulative area for each major drainage basin plotted in relation to the ELA (vertical line at 0) for each quadrant of the ice cap.

reduced however by the fact that the cumulative area below the ELA of these basins is generally less than 0.4. Medium-sensitivity basins (“M”) have between 0.2 and 0.3 of their cumulative area below the ELA whereas low-sensitivity basins consistently have less than 0.2 of their area below the ELA. Both of these basin types intersect relatively low sloping sections near the inflection point along the hypsometric curves indicating that the accumulation area of these basins will decrease at a much faster rate as the ELA is raised than it will increase as the ELA is lowered.

RESPONSE TIME

Approximate response times (RT) were calculated for each of the major drainage basins using the volume time scale formula in Johannesson et al. (1989):

$$RT = H/b_i \tag{4}$$

where H is the maximum thickness of ice within the basin and b_i is the mass balance at the glacier terminus. Ice thickness data were obtained from Dowdeswell’s 2000 RES data set (Dowdeswell et al., in press) and terminus ablation rates were interpolated from Koerner’s, 1961–1998 mass-balance observations as compiled by Dyurgerov (2002).

A moderate inverse relationship ($R^2 = 0.65$) exists between RT and percent area change of the major basins across the ice cap (Fig. 10). This relationship indicates that maximum areal changes have occurred for basins with the shortest calculated response times, and that

the magnitude of change decreases logarithmically (and in some cases the basins grow rather than shrink) as the calculated response times increase.

Three distinct groupings emerged from these RT calculations (Table 3). RTs in the first group of basins range from ca. 125 yr to ca. 380 yr. This group includes ~70% of all major basins. Although all basins in this group terminate at or near sea level where ablation rates are highest, basins with the shortest RTs in this group (29, 38, 39, 46, 48, and 52) are restricted to the peripheral regions (i.e., their source regions do not extend to the ice-cap summit region) where the ice is thinnest. Except for basin 39 (southwest arm), all basins in this category

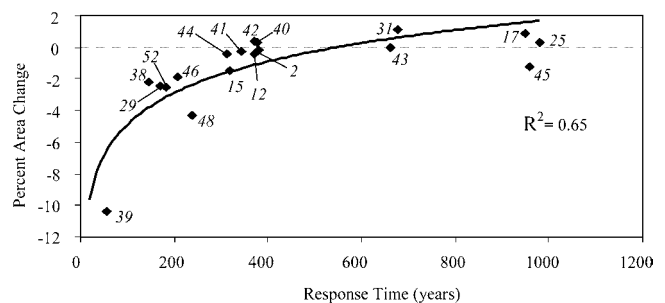


FIGURE 10. Plot of the logarithmic relationship between response time and percent area change of glaciers in the major drainage basins measured between 1959/1960 and 1999/2000.

TABLE 3

Response time estimates and associated glacier attributes for each major drainage basin across the ice cap. Shaded rows highlight the intermediate class of response time estimates

Basin ID	Quadrant	% Area Change	Terminus Mass Balance (kg m ⁻² a ⁻¹)	Maximum Thickness (m)	Response Time (yr)
25	Nw	0.3	-680	666	979
45	Sw	-1.2	-595	571	959
17	Nw	0.8	-620	589	950
31	Nw	1.1	-850	576	677
43	Sw	0	-940	621	660
2	Ne	-0.2	-1875	712	379
40	Sw	0.3	-1875	705	376
42	Sw	0.3	-1875	695	370
12	Nw	-0.4	-1500	555	370
41	Se	-0.3	-2250	775	344
15	Ne	-1.4	-1875	597	318
44	Se	-0.4	-2250	706	313
48	Se	-4.3	-2250	539	239
46	Se	-1.9	-2250	463	205
52	Se	-2.5	-2200	403	183
29	Ne	-2.4	-1875	318	169
38	Se	-2.2	-2250	330	146
39	Sw	-10.3	-1600	200	125

are located along the east or south margins of the ice cap. Other basins within this group (2, 40, 42, 12, 41, 15, and 44) extend farther inland towards the ice-cap summit, lengthening the RT due to increased ice thickness. Basins exhibiting intermediate (ca. 700 yr) and long (ca. 950 yr) RTs terminate at higher elevations (500–600 m a.s.l.) where terminus ablation rates are relatively small. These basins are concentrated along the western margin and they also extend inland towards the interior summit region where ice thickness is greatest.

The RTs calculated here are consistent with characteristic RTs suggested by Bahr et al. (1998). Glaciers in larger basins with steeper mass-balance gradients (east side) have significantly shorter RTs than glaciers in smaller basins with shallower mass-balance gradients (west margin). This difference suggests that the east and west sectors of the ice cap may be responding to distinctly separate periods of climate forcing.

MULTIPLE REGRESSION ANALYSIS OF AREAL CHANGE

To determine the influence of BS, BR, and RT on the areal changes (AC) measured, multiple regression analysis was next performed resulting in the equation:

$$AC = (-9.87(\pm 0.86)BS) + (0.002(\pm 0.0005)RT) \quad (5)$$

BR was highly correlated with RT ($r^2 = 0.86$) and was therefore excluded from this analysis. *P*-values of 0.00001, and 0.002, were obtained for the coefficients of BS and RT, respectively. The coefficient of multiple determination ($R^2 = 0.854$) indicated that 85.4% of the total variance of AC is explained by BS and RT.

VOLUME CHANGE ESTIMATES

Volume change was calculated for the ice cap using two independent methods. The first method was based on calculating the difference between the 1960 ice-cap volume, derived from the volume-area scaling (VA) technique (Bahr et al., 1997), and the 2000 ice-cap volume derived from Dowdeswell et al.'s (in press) RES data. Using this method, the 1960s volume was calculated for the southwest arm and the main ice cap separately, and summed for a total ice-cap volume

estimate. The second technique was the method presented by Hooke (1998: 219), which calculates the change in volume of a glacier as the product of the maximum thickness and the length change at the terminus (MT). In order to account for the influence of glacier width, however, the total area of change measured in each basin was multiplied by the maximum thickness to estimate the resulting change in volume. Using this method, volume change was calculated for each major drainage basin separately and summed to estimate the total ice-cap volume change.

The 1960 ice-cap volume (VOL_{1960}) was calculated from the VA method using the formula:

$$VOL_{1960} = SC(A_{1960}^{1.25}) \quad (6)$$

where, A_{1960} is the area of the ice cap in 1960 and 1.25 is the appropriate exponent for small ice caps (Bahr et al., 1997). The scaling constant (SC) is derived from the formula:

$$SC = VOL_{2000}/(A_{1999}^{1.25}) \quad (7)$$

where A_{1999} is the area in 1999 and VOL_{2000} is the volume in 2000 taken from Dowdeswell et al.'s (in press) 2000 RES data. VOL_{2000} measurements of 3854 km³ and 130 km³ produced scaling constants of 0.031525 and 0.009968 for the main ice cap and the southwest arm, respectively. Applying the scaling constants to the 1960 measurements resulted in a total volume estimate of 4181 km³ (146 and 4034 km³ for the southwest arm and main ice cap respectively). Error was estimated for the VA method at ± 12 km³ based on the 1960s area measurement error of ± 30 km². Error for the MT method of ± 9 km³ was calculated as a product of the average area measurement error between 1960 and 1999 (± 35 km²) and the average ice-cap thickness (284 m).

Differences between the 1960 and 2000 volume estimates derived from the VA method and from Dowdeswell et al.'s (in press) RES measurements respectively indicate a loss of 71 km³ for the entire ice cap and 16 km³ for the southwest arm over the past 40 yr. Volume changes derived from the MT method were similarly estimated as a loss of 62 km³ for the ice cap in total and 18 km³ over the southwest arm. Total volume loss of the Devon Ice Cap between 1960 and 1999 was therefore estimated as 67 ± 12 km³. These estimates of volume loss imply a thinning of ~ 3 m averaged over the main part of the ice cap and ~ 8 m over the southwest arm.

Our computed volume loss of 67 km³ equates to a 0.17 mm contribution to global sea level between 1960 and 1999. When extrapolated to all ice cover in the Canadian Arctic, this would represent a total contribution of ~ 1.7 mm. This is approximately one-sixth the current estimated contribution from all Alaskan glaciers (Arendt, et al., 2002) which cover $\sim 40\%$ less surface area than ice in the Canadian Arctic.

Conclusions

Remotely sensed imagery acquired in 1959/1960 and 1999/2000 reveals a net decrease in surface area of the Devon Ice Cap of 332 ± 40 km² with an associated volume loss of 67 ± 12 km³. The dominant trends in geometric change currently being experienced by the Devon Ice Cap are retreat (thinning) of the eastern margin, growth of the western basins, and rapid shrinkage of the southwest arm. Major tidewater glaciers along the east coast have retreated up to 1.3 km over the past 40 yr. These glaciers drain from basins that have experienced increased bedrock exposure indicating that the ice surface within these basins has lowered. Advance of the northwest margin suggests either that conditions favourable to ice sheet growth are prevalent in this region, or that this sector of the ice cap is still responding to the cooler conditions of the Little Ice Age. The southwest arm of the Devon Ice Cap lies almost entirely below the regional ELA (Koerner, 1970).

Thus, rapid retreat of the ice margin in this region reflects the loss of the accumulation area for this sector as a result of ELA rise driven by post-LIA warming.

Statistical analysis has shown that 85.4% of the variance in basin area change is explained by variations in the balance ratio, basin sensitivity, and response times of different drainage basins. The logarithmic relationship between BR and AC suggests that the ice cap will shrink at a much faster rate in response to a given rise in the ELA than it will grow in response to an equivalent lowering of the ELA. Similarly, cumulative area curves for most basins indicate that the rate of accumulation area loss as the ELA is raised is greater than the rate of accumulation area gain when the ELA is lowered. Finally, response times of 700 to 1000 yr throughout the western region indicate that the advance of these basins is likely a delayed response to cooler LIA climatic conditions. In contrast, shorter response times (100–400 yr) for the remaining basins suggest that the observed retreat over these regions is likely a response to post-LIA warming.

Acknowledgments

Financial support for this research was provided by an NSERC Discovery grant to Dr. Martin Sharp. Funding for David Burgess was provided through an NSERC IPS-2 scholarship sponsored by Land Data Technologies Inc. of Edmonton, Canada. Landsat 7 ETM+ imagery and Canadian Digital Elevation Data (CDED) were purchased through support from CRYSYS (Cryospheric System to Monitor Global Change in Canada), the Meteorological Services of Canada (MSC) and the Canadian Space Agency (CSA—Climate and Cryosphere Initiative). Aerial photography was provided by the National Hydrology Institute and Art Dyke of the Geological Survey of Canada. We thank Prof. J. Dowdeswell for making available radio echo sounding data for the Devon Ice Cap, Dr. John Andrews and an anonymous reviewer for their comments to the manuscript, and Dr. R. M. Koerner for his comments on an earlier draft.

References Cited

Arendt, A., Eckelmeyer, K., Harrison, W. D., Lingle, C. S., and Valentine, V. B., 2002: Rapid wastage of Alaska glaciers and their contribution to rising sea level. *Science*, 297(5580): 382–386.

Bahr, D. B., Meier, M. F., and Peckham, S. D., 1997: The physical basis of glacier volume-area scaling. *Journal of Geophysical Research*, 102(20): 355–362.

Bahr, D. B., Pfeffer, W. T., Sassolas, C., and Meier, M. F., 1998: Response time of glaciers as a function of size and mass balance: 1. Theory. *Journal of Geophysical Research*, 103(B5): 9777–9782.

Braun, C., Hardy, D., and Bradley, R., 2001: Recent recession of a small plateau ice cap, Ellesmere Island, Canada. *Journal of Glaciology*, 47(156): 154.

Dowdeswell, J. A., Benham, T. J., Gorman, M. R., Burgess, D., and Sharp, M., in press: Form and flow of the Devon Island Ice Cap, Canadian Arctic. *Journal of Geophysical Research*.

Dunn, R., Harrison, A. R., and White, J. C., 1990: Positional accuracy and measurement error in digital databases of land use: an empirical study. *International Journal of Geographical Information Systems*, 4(4): 385–398.

Dyurgerov M., 2002: Glacier mass balance and regime: Data of measurements and analysis. Meier, M. and Armstrong, R. (eds.) University of Colorado, Institute of Arctic and Alpine Research, Occasional Paper, 55. various paging, CD-ROM.

Furbish, D. J. and Andrews, J. T., 1984: The use of hypsometry to

indicate long-term stability and response of valley glaciers to changes in mass transfer. *Journal of Glaciology*, 30(105): 199–210.

Gagne, A., 2002: Personal communication. Geomatics Canada, 615 Booth St., Ottawa, Canada.

Hooke, R. LeB., 1998: *Principles of Glacier Mechanics*. Upper Saddle River, NJ: Prentice Hall. 248 pp.

IPCC, 2001: *Climate Change 2001: Impacts, Adaptation, and Vulnerability*. McCarthy, J. J., Canziani, O. F., Leary, N. A., Dokken, D. J., White, K. S. (eds.). Cambridge: Cambridge University Press for Intergovernmental Panel on Climate Change. 1032 pp.

Jacobs, J. D., Simms, E. L., and Simms, A., 1996: Recession of the southern part of Barnes Ice Cap, Baffin Island, Canada, between 1961 and 1993, determined from digital mapping of Landsat TM. *Journal of Glaciology*, 3(143): 98–102.

Johannesson, T., Raymond, C. F., and Waddington, E. D., 1989: A simple method for determining the response time of glaciers. In Oerlemans, J. (ed.), *Glacier Fluctuations and Climate Change*. Dordrecht: Kluwer, 343–352.

Johns, T. C., Carnell, R. E., Crossley, J. F., Gregory, J. M., Mitchell, J. F. B., Senior, C. A., Tett, S. F. B., and Wood, R. A., 1977: The second Hadley Centre coupled ocean–atmosphere GCM: Model description, spinup and validation. *Climate Dynamics*, 13. 103–134.

Koerner, R. M., 1966: Accumulation on the Devon Island ice cap, Northwest Territories, Canada. *Journal of Glaciology*, 6(45): 383–392.

Koerner, R. M., 1970: The mass balance of Devon Island ice cap Northwest Territories, Canada, 1961–1966. *Journal of Glaciology*, 9(57): 325–336.

Koerner, R. M., 1977a: Ice thickness measurements and their implications with respect to past and present ice volumes in the Canadian High Arctic ice caps. *Canadian Journal of Earth Sciences*, 14: 2697–2705.

Koerner, R. M., 1977b: Devon Island ice cap: core stratigraphy and paleoclimate. *Science*, 196: 15–18.

Koerner, R. M., 2002: Personal communication. Geological Survey of Canada, Terrain Sciences Division, 601 Booth St., Ottawa, Canada.

Koerner, R. M. and Lundgaard, L., 1995: Glaciers and global warming. *Géographie physique et Quaternaire*, 49(3): 429–434.

Meier, M. F., 1984: Contribution of small glaciers to global sea level. *Science*, 226(4681): 1418–1420.

Meier, M. F. and Dyurgerov, M. B., 2002: How Alaska affects the world. *Science*, 297(5580): 350–351.

Mitchell, J. F. B., Johns, T. C., Gregory, J. M., and Tett, S. F. B., 1995: Climate response to increasing levels of greenhouse gases and sulphate aerosols. *Nature*, 376: 501–504.

Overpeck, J., Hughen, K., Hardy, D., Bradley, R., Case, R., Douglas, M., Finney, B., Gajewski, K., Jacoby, G., Jennings, A., Lamoureux, S., Lasca, A., MacDonald, G., Moore, J., Retelle, M., Smith, S., Wolfe, A., and Zielinski, G., 1997: Arctic environmental change of the last four centuries. *Science*, 278: 1251–1256.

Serreze, M. C., Walsh, J. E., Chapin, III, F. E., Osterkamp, T., Dyurgerov, M., Romanovsky, V., Oechel, W. C., Morison, J., Zhang, T., and Barry, R. G., 2000: Observational evidence of recent change in the northern high latitude environment. *Climatic Change*, 46: 159–207.

Van de Wal, R. S. W. and Wild, M., 2001: Modelling the response of glaciers to climate change by applying volume-area scaling in combination with a high resolution GCM. *Climate Dynamics*, 18: 359–366.

Ms submitted December 2003

Influence of the Arctic Circumpolar Vortex on the Mass Balance of Canadian High Arctic Glaciers

ALEX S. GARDNER AND MARTIN SHARP

Department of Earth and Atmospheric Sciences, University of Alberta, Edmonton, Alberta, Canada

(Manuscript received 25 July 2006, in final form 15 November 2006)

ABSTRACT

Variability in July mean surface air temperatures from 1963 to 2003 accounted for 62% of the variance in the regional annual glacier mass balance signal for the Canadian High Arctic. A regime shift to more negative regional glacier mass balance occurred between 1986 and 1987, and is linked to a coincident shift from lower to higher mean July air temperatures. Both the interannual changes and the regime shifts in regional glacier mass balance and July air temperatures are related to variations in the position and strength of the July circumpolar vortex. In years when the July vortex is “strong” and its center is located in the Western Hemisphere, positive mass balance anomalies prevail. In contrast, highly negative mass balance anomalies occur when the July circumpolar vortex is either weak or strong without elongation over the Canadian High Arctic, and its center is located in the Eastern Hemisphere. The occurrence of westerly positioned July vortices has decreased by 40% since 1987. The associated shift to a dominantly easterly positioned July vortex was associated with an increased frequency of tropospheric ridging over the Canadian High Arctic, higher surface air temperatures, and more negative regional glacier mass balance.

1. Introduction

Global climate models consistently predict that climate warming associated with increasing atmospheric concentrations of greenhouse gases will be largest in northern high latitudes (Houghton et al. 2001; Johannessen et al. 2004). The response of Arctic glaciers, ice caps, and ice sheets to this warming may therefore be a significant influence on the eustatic component of global sea level rise. In the long term, changes in the volume of the Greenland Ice Sheet are likely to have the greatest impact on sea level, but in the short term (the next century or so) contributions from ice caps and glaciers may be more significant (Meier 1984; Houghton et al. 2001; Raper and Braithwaite 2006). There is therefore considerable interest in characterizing the mass balance of these smaller ice masses and their relationship to climate trends and variability (Cogley et al. 1996; Dowdeswell et al. 1997; Dyurgerov and Meier 1997, 2000; McCabe et al. 2000; Braithwaite and Raper

2002; Hagen et al. 2003; Dyurgerov and Meier 2005; Dyurgerov and McCabe 2006).

In this paper, ~40-yr records of the surface mass balance of four ice masses in the Canadian High Arctic (>75°N) and their relationship to regional temperature trends and Arctic atmospheric circulation changes are analyzed. The Canadian High Arctic is a region of particular importance for this type of study because it contains the largest area of land ice in the world outside Greenland and Antarctica, and has the highest density of long-term glacier mass balance records in the Arctic.

The records used come from four ice masses in the Queen Elizabeth Islands (QEI), Nunavut, Canada: Devon Island Ice Cap, Meighen Ice Cap, Melville Island South Ice Cap (Koerner 2002; Dyurgerov and Meier 2005), and White Glacier, on Axel Heiberg Island (Cogley et al. 1996; Dyurgerov and Meier 2005) (Fig. 1). All four glaciers are located in the “polar desert” climatic region, where annual precipitation is often <200 mm, with minimal interannual variability. Surface air temperatures (SATs) over glaciers in this region only exceed the freezing temperature during two–three months of the year. For the four glaciers examined, variability in summer (June–August) mass balance accounts for 93%–98% of the variation in annual mass balance. This indicates that summer melt has

Corresponding author address: Alex Gardner, Department of Earth and Atmospheric Sciences, University of Alberta, 1-16B Earth Sciences Building, Edmonton, AB T6G 2E3, Canada.
E-mail: alexg@ualberta.ca

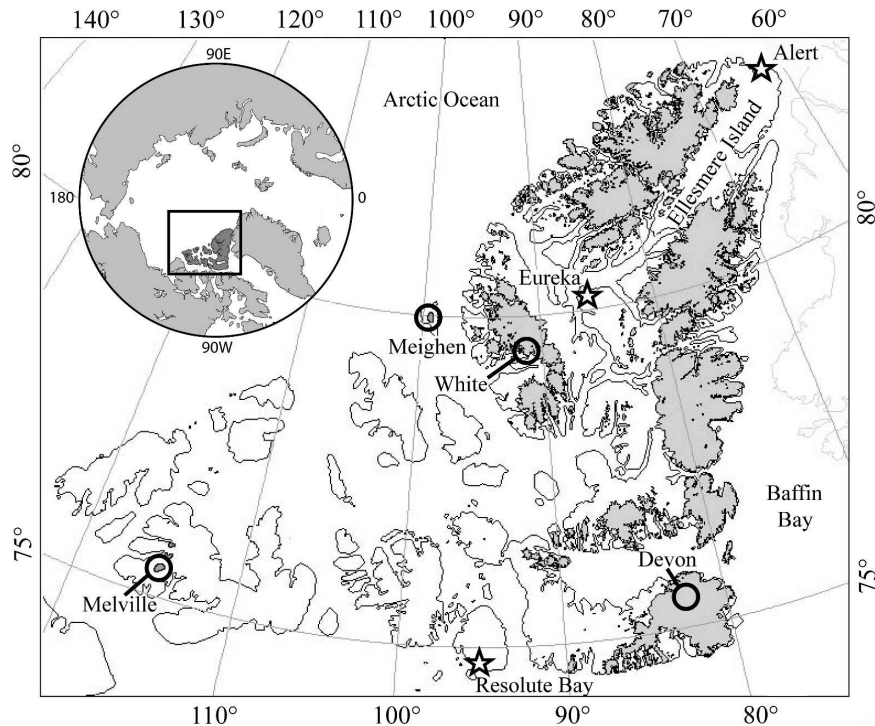


FIG. 1. Canadian High Arctic: Locations at which long term glacier mass balance records have been collected (circles) and locations of long term Environment Canada meteorological stations (stars).

a dominant influence on variability in both the summer and annual mass balances. This allows variability in annual mass balance to be used as a measure of summer climate influences on glaciers and ice caps in the Canadian High Arctic.

Previous studies of glacier mass balance in the Canadian High Arctic (Meier 1984; Alt 1987; Dowdeswell et al. 1997; Dyurgerov and Meier 1999; Braun et al. 2004; Dyurgerov and McCabe 2006) have documented trends in mass balance, but only Alt (1987) has attempted to explain the variability in annual mass balance in terms of synoptic-scale climatic forcing. Building on previous studies of synoptic climate controls on the mass balance of the Devon Island (Alt 1978) and Meighen Ice Caps (Alt 1979), Alt (1987) identified the synoptic conditions associated with extreme mass balance years on three ice masses in the QEI: the Meighen Ice Cap, Devon Island Ice Cap, and White Glacier. By examining surface and upper-air synoptic charts and climatic parameters over a 16-yr period (1960–76), Alt identified the following three sets of synoptic conditions associated with extreme mass balance years:

(i) high melt conditions, associated with the intrusion of a ridge from the south into the QEI at all levels in the troposphere;

(ii) melt suppression conditions, associated with the maintenance of a deep, cold trough across Ellesmere Island; and

(iii) summer snow accumulation conditions, which occur when cold polar lows track south and southeast across the QEI from the Arctic Ocean.

These three situations were related to differences in the position and shape of the July 500-mbar circumpolar vortex (Alt 1987). This midtropospheric feature consists of a cyclonic system with strong winds rotating counterclockwise about the cold polar air mass in its center, and is widely recognized as being the dominant factor in Arctic summer atmospheric circulation (Maxwell 1980). Unlike the stratospheric circumpolar vortex, which breaks down in summer, the tropospheric vortex, although weaker in summer, is present year-round (Serreze and Barry 2005). On a daily time scale, the July 500-mbar circumpolar vortex can split into several centers, spawning smaller cyclones that often move in a westerly direction around the pole. On a monthly time scale, the July mean polar vortex is most often characterized by a single, well-defined annular geopotential low with its center located between 80° and 90°N or by two weaker cyclonic systems with one system located near the pole and the other located over Baffin Bay.

Glaciers in the Canadian High Arctic have experienced a sharp reduction in mass balance since the late 1980s (Dyurgerov and McCabe 2006). In the work presented here, we investigate whether the relationships recognized by Alt (1987) can be used to explain this marked change in regional glacier surface mass balance. In particular, this research aims to characterize the interannual variability in the July 500-mbar circum-polar vortex and to define its relationship to both interannual and longer-term changes in the mass balance of glaciers in the Canadian High Arctic.

2. Methods

Long-term (1963–2003) mass balance records for the four target ice masses in the Canadian High Arctic were obtained from syntheses of global glacier mass balance (Dyurgerov 2002; Dyurgerov and Meier 2005). Missing mass balance records for White Glacier and the Devon Island Ice Cap from 2002 and 2003 were obtained from the World Glacier Monitoring Service (IAHS/UNESCO 2005) and R. M. Koerner (2006, personal communication), respectively. Glacier mass balance measurements are made by monitoring a network of stakes drilled into the glacier ice and firn in both the accumulation and ablation areas. Measurements are made in spring, before the onset of summer melt. In the ablation area, the required measurements include the change in stake height, and the depth and density of the snowpack overlying glacier ice. In the accumulation area, snow depth is measured to the dense melt surface formed at the end of the previous summer and, in addition to measurements of stake height and snow density, it is necessary to estimate the fraction of summer melt retained by refreezing within the snowpack and underlying firn. This is accomplished by measuring ice accumulation in buried collection trays, and average snow densities. Cogley et al. (1996) estimated the error in annual glacier mass balance measured at each stake on White Glacier to be ± 200 -mm water equivalent. This single stake error can be used as a conservative estimate of the error in whole glacier mass balance estimates for all monitored glaciers in the Canadian High Arctic (Cogley and Adams 1998). These measurements document the surface mass balance and do not account for mass loss resulting from glacier calving or basal melt, which may be significant in some cases (Burgess et al. 2005). For a more detailed description of the physical characteristics and methods used to determine the surface mass balance of each of the four glaciers, see Koerner (1996, 2002) and Cogley et al. (1996).

Nonrotated principal component analysis (PCA) was used to extract the primary modes of variance from

standardized time series of the four mass balance records. Time series were standardized by subtracting the mean of the series from each value and dividing the resulting values by the standard deviation of the series. Because this study is concerned with long-term changes in mass balance, the individual mass balance records were not detrended prior to PCA (Venegas 2001). To select modes for further analysis, the Kaiser criterion (Kaiser 1960) was used, which excludes any factors with an eigenvalue of less than one, thereby excluding any factors that explain less variance than a single original variable. Because the first principal component (PC1) explains 53% of the variance in the original four mass balance time series and is the only component with an eigenvalue greater than one, all other principal components were excluded.

A sequential algorithm developed for the detection of climate regime shifts from empirical data (Rodionov 2004) was used to determine whether and when any significant shifts in the mean of the PC1 anomalies occurred. Unlike commonly used confirmatory statistical methods for identifying climate regime shifts, such as those employed by Mantua et al. (1997), which require an a priori hypothesis about the timing of the shift, this method allows for the automatic detection of discontinuities in the time series. Another advantage of this method is that it can detect regime shifts toward the end of a time series, which is not the case for other automatic detection methods. Only regime shifts detected using a cutoff length of 20 years and having a probability level $p \leq 0.05$ were considered. A Huber parameter (Huber 1964) of two was used to reduce the weighting of outliers that deviate by more than two standard deviations from the expected mean value of a new regime when calculating the regime shift. The red noise component of the time series to which this technique was applied was removed prior to applying the regime shift detection algorithm by “prewhitening” the time series (Rodionov 2006). The autoregressive parameter used in the prewhitening procedure was calculated using the method of inverse proportionality with four corrections (IPN4), with a subsample size of 10 (Rodionov 2006). Using these criteria, only one regime shift was detected.

The magnitude of glacier ablation, and thus the annual surface mass balance of glaciers in the Canadian High Arctic, depends on the energy balance at the glacier surface. Quantifying the historical net surface energy balance for this data-sparse region is extremely difficult. For this reason, the relationship between glacier mass balance and near-surface air temperatures (a commonly used proxy for the surface energy balance) was examined to investigate surface climate–glacier in-

TABLE 1. Principal component analysis of four Canadian High Arctic glacier mass balance records (1963–2003).

Component	Eigenvalue	% of variance	Component loading			
			White Glacier	Devon Ice Cap	Melville Island Ice Cap	Meighen Ice Cap
1	2.13	53.30	0.71	0.75	0.81	0.64
2	0.85	21.22	−0.53	0.30	−0.30	0.62
3	0.58	14.53	0.29	−0.12	−0.12	0.45

teractions. SAT records were obtained for local Environment Canada meteorological stations (available at <http://www.climate.weatheroffice.ec.gc.ca>). Because only three meteorological stations in the Canadian High Arctic (Alert, Eureka, and Resolute Bay; Fig. 1) have continuous SAT records over the period of study (1963–2003), gridded 850-mbar air temperatures from the National Centers for Environmental Prediction–National Center for Atmospheric Research (NCEP–NCAR) climate reanalysis (Kalnay et al. 1996; Kistler et al. 2001; available at <http://www.cdc.noaa.gov>) were also utilized. These were used to provide a more location-independent measure of regional-scale temperature and to investigate the spatial pattern of temperature changes. The 850-mbar pressure level (≈ 2 km above sea level) NCEP–NCAR-reanalyzed atmospheric temperatures were used in place of reanalyzed SATs because they are less affected by the spectrally defined topography used in the NCEP–NCAR climate reanalysis (Kalnay et al. 1996). This topography is too coarsely resolved to capture the complex orography of the Canadian High Arctic. An additional reason for selecting the 850-mbar pressure level was to reduce possible SAT biases resulting from erroneously defined snow cover within the NCEP–NCAR reanalysis model (Kanamitsu et al. 2002). SAT measurements from the three meteorological stations located in the region of interest were compared with mean monthly 850-mbar NCEP–NCAR air temperatures from the respective overlying grid cells to determine the degree of agreement between the records.

Both regional glacier mass balance and air temperatures were examined in relation to interannual variations in the position and strength of the circumpolar vortex. The location and standardized magnitude of the absolute minimum July NCEP–NCAR 500-mbar geopotential height north of the equator were used to characterize the center location and strength of the circumpolar vortex. The time series of minimum July 500-mbar geopotential height was standardized and inverted to provide a relative index of vortex strength. Years with positive strength indices have relatively low absolute minimum July 500-mbar geopotential heights

with strong cyclonic circulation and were classified as years with a strong July vortex. In contrast, years with negative strength indices have relatively high absolute minimum July 500-mbar geopotential heights with weak cyclonic circulation and were referred to as years with a weak July vortex. Locations of July 500-mbar vortices were divided into three regional groups. We then investigated the relationships between the strength and position of the circumpolar vortex and the regional glacier mass balance.

To study the causes of the reduction in regional glacier mass balance in the late 1980s, differences between the NCEP–NCAR reanalysis fields for 850-mbar temperature and 500-mbar geopotential height for the years prior to and after 1987 were examined.

All correlation values presented in this paper are expressed in terms of r , Pearson's product-moment coefficient of correlation. The significance of the correlations was determined using a two-tailed Student's t test with the null hypothesis that the time series are uncorrelated ($r = 0$). All r values quoted are significant at the 0.05 level.

3. Results

a. Glacier mass balance

The four annual surface mass balance records, spanning the 41 yr from 1963 to 2003, are not well correlated with each other ($r = 0.23$ – 0.52), but they nevertheless display strong underlying similarities. PC1 of these records has an eigenvalue of 2.13 and accounts for 53% of the variance across the four time series (Table 1). The loadings of the four mass balance time series on PC1 are similar in magnitude and sign, ranging between 0.64 and 0.81, suggesting that PC1 identifies a regional climatic influence on glacier mass balance. The standardized PC1 was therefore taken as a measure of the regional mass balance history of Canadian High Arctic glaciers for the period of 1963–2003, and is hereafter referred to as the *regional glacier mass balance*. Individual standardized glacier mass balance records are compared with PC1 in Fig. 2. Over the period of 1961–2003, PC1 has a weak but significant linear trend to

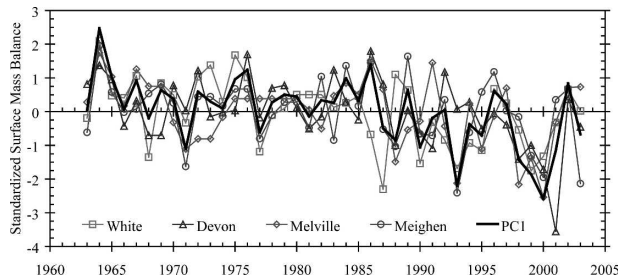


FIG. 2. Annual mass balance records from individual glaciers expressed as standardized anomalies with the first principal component (PC1) plotted in bold.

ward more negative regional glacier mass balance anomalies ($r^2 = 0.27$).

Applying the regime shifts detection algorithm outlined in section 2, only one regime shift was detected in the regional glacier mass balance signal. This occurred between 1986 and 1987 (Fig. 3), in agreement with the findings of Dyrgerov and McCabe (2006). This method of regime shift detection is most sensitive to the user-defined variables of cutoff length and probability level. To determine the robustness of the identified regime shift, similar analyses were conducted using other cutoff lengths. For all cutoff lengths between 12 and 30 years, a 1986–87 regime shift in the mean of the regional glacier mass balance signal was detected. A significant difference in mean between the periods of 1963–86 and 1987–2003 is also found when using the traditional two-tailed Student's *t*-test method, assuming unequal variance. The 24-yr period prior to 1987 contains only 4 years with negative mass balance anomalies and has a mean standardized regional glacier mass balance anomaly of 0.46 with no linear trend. In contrast, the 17-yr period after 1987 includes 12 years with negative mass balance anomalies, and has a mean standardized anomaly of -0.66 . While there are too few points to identify a significant trend in the later 17-yr period, there is a tendency toward increasingly negative anomalies toward the end of the series, with 4 of the 5 most negative mass balance anomaly years in the entire 41-yr period occurring during the last 6 years of record (Fig. 3).

b. Air temperature

Interannual variability in Canadian High Arctic annual glacier mass balance is governed almost entirely by variation in summer glacier surface melt, which occurs mainly in the month of July (Wang et al. 2005). For this reason, only the relationships between regional annual mass balance and summer air temperatures were investigated. Average June, July, August, and summer (June–August) SATs for Alert, Eureka, and Resolute Bay

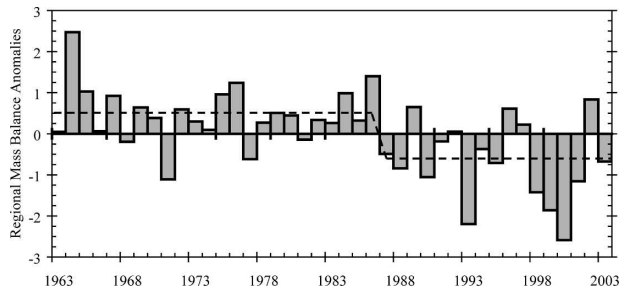


FIG. 3. Standardized anomalies of the first principal component (PC1) of the four glacier mass balance records. Inferred mass balance regimes are represented by a dashed line.

were correlated with the regional glacier mass balance signal. Of the 12 SAT series, only June, July, and summer SATs from Eureka and Resolute Bay are significantly correlated with the regional glacier mass balance. On average, July SATs from Eureka and Resolute Bay account for 56%, 44%, and 26% more variance in the regional glacier mass balance than mean August, June, and summer SATs, respectively. In addition, when average July SATs from Eureka or Resolute Bay were used to model regional glacier mass balance, there were no significant correlations between the linear regression residuals and any June, August, or summer SAT series. This strong relationship between Canadian High Arctic glacier mass balance and mean July temperature has long been recognized (Bradley and England 1978; Dowdeswell 1995). Because the majority of the variance in the Canadian High Arctic regional glacier mass balance signal is captured in the July SATs from Eureka and Resolute Bay, and there is minimal correlation with the SATs from the neighboring months, we focus solely on July atmospheric variables in the remainder of this analysis.

The average July SATs from Eureka and Resolute Bay are highly correlated ($r = 0.85$), however, no significant correlation exist between these two records and July SATs from Alert. This suggests that northern Ellesmere Island SATs may be influenced by different synoptic conditions than those that affect the more southern parts of the Canadian Arctic Archipelago. The implications of this for the glacier mass balance of the region will be discussed in section 5.

The average July SATs from both Eureka and Resolute Bay were correlated with the 850-mbar temperatures in the $2.5^\circ \times 2.5^\circ$ reanalysis grid cell located directly over each station. Reanalysis 850-mbar air temperatures and station SATs are reasonably well correlated ($r = 0.65$ – 0.87). To estimate how well regional variability in station-derived SATs is captured by the NCEP–NCAR 850-mbar air temperatures, these

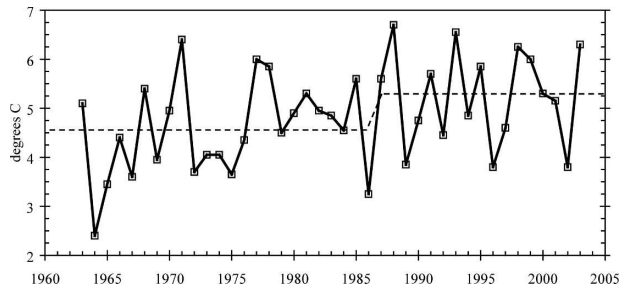


FIG. 4. Regional mean July station derived surface air temperature (SAT), taken as the average temperature observed at the Environment Canada meteorological stations of Eureka and Resolute Bay. The dashed line displays the two significant temperature regimes.

temperatures (averaged over the region of interest: 75° – 80° N, 75° – 115° W) were correlated with the average Eureka and Resolute Bay July temperature ($r = 0.82$).

The average Eureka/Resolute Bay SATs are highly correlated with the regional glacier mass balance (PC1) ($r = 0.79$). July SATs also show a significant regime shift from cooler to warmer temperatures between 1986 and 1987, with a 1° C increase in mean July SAT between earlier and later time periods (Fig. 4). The SAT series also contains a weakly significant linear trend toward warmer temperatures ($r^2 = 0.13$). This shift in regional temperature corresponds with the 1987 acceleration in the rate of annual glacier mass loss identified in section 3a. A similar shift is found in the regionally averaged NCEP–NCAR 850-mbar air temperatures.

It should be noted that in the 15 yr prior to 1963 (the first year of record used in this study) mean July SATs taken from the Environment Canada meteorological stations of Resolute Bay and Eureka were 1° C warmer than those in the period of 1963–86. The difference between the two is statistically significant and has previously been documented by Bradley and England (1978).

c. 500-mbar Arctic circumpolar vortex

For all years examined, the center locations of the July circumpolar vortices were grouped into the following three sectors (Fig. 5a): sector I: 75° – 90° N, 0° – 180° E; sector II: 75° – 90° N, 0° – 180° W, and sector III: 60° – 75° N, 90° – 60° W. To show the relationship between the position and strength of the circumpolar vortex and the mass balance of Canadian High Arctic glaciers, the relative vortex strength (standardized and inverted minimum Northern Hemisphere July 500-mbar geopo-

tential height) and the Canadian High Arctic regional glacier mass balance signal (PC1) have been grouped by the sector in which the vortex center is located and sorted from the strongest to the weakest strength vortex within that group (Fig. 5b).

For sector I vortices there is a well-defined linear relationship between vortex strength and regional glacier mass balance, wherein strong vortices result in moderately positive mass balance anomalies and weak vortices result in extremely negative mass balance anomalies. A similar relationship exists for sector II vortices, except that strong vortices produce extremely positive mass balance anomalies and weak vortices produce neutral to moderately negative mass balance anomalies. As for sector III vortices, there is little variation in vortex strength or regional glacier mass balance, with both indices close to neutral. If the extreme year of 1993 (discussed further in section 4) is excluded from the analysis, there are statistically significant relationships between vortex strength and regional glacier mass balance for both Eastern (sector I) and Western (sectors II and III) Hemisphere-centered vortices.

Looking solely at the relationship between vortex location and regional glacier mass balance, 67% of all negative mass balance anomalies exceeding one standard deviation from the mean occurred during years when the vortex was located in the Eastern Hemisphere. Of all positive mass balance anomalies exceeding one standard deviation from the mean, 67% occurred during years when the vortex was located in the Western Hemisphere. In 18 of the 24 yr prior to the 1987 decrease in regional glacier mass balance, the July vortex center was located in the Western Hemisphere. In contrast, the July vortex was centered in the Western Hemisphere in only 6 of the 17 yr between 1987 and 2003. Analysis of the NCEP–NCAR climate reanalysis data available for the 15 yr prior to 1963 shows an equal distribution of Eastern and Western Hemisphere-centered vortices.

d. 1987–2003 atmospheric anomalies

To examine atmospheric differences between the time periods before and after the 1987 shift in regional glacier mass balance, the differences between the 1963–86 and 1987–2003 mean July NCEP–NCAR 850-mbar atmospheric temperature and 500-mbar geopotential height anomalies were determined. Relative to 1963–86, the mean 1987–2003 July 850-mbar temperature increased by 1° – 2° C over the Canadian High Arctic, Siberia, and the Barents Sea and decreased by 1° – 2° C over the Kara and Labrador Seas (Fig. 6a). The mean July 500-mbar geopotential height shows a similar pat-

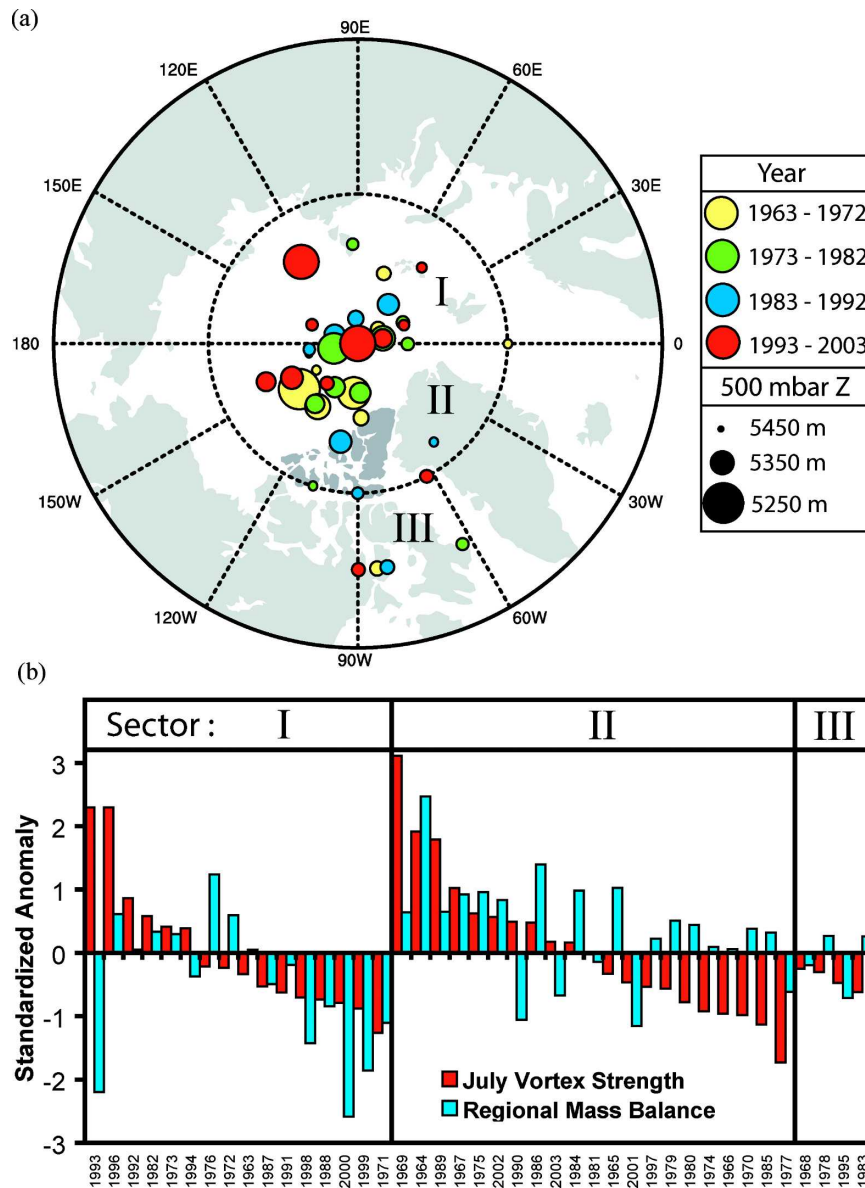


FIG. 5. (a) Sector boundaries and July 500-mbar Arctic circumpolar vortex center location and strength, defined as the location and magnitude of the minimum Northern Hemisphere 500-mbar geopotential height. Years of anomalously low (high) minimum geopotential heights are classified as years with a “strong” (“weak”) circumpolar vortex. (b) Inverse of the standardized minimum Northern Hemisphere 500-mbar geopotential height (vortex strength) and Canadian high Arctic regional glacier mass balance (PC1) grouped by year into the sectors in which the vortex center is located and sorted by vortex strength.

tern, with increases in geopotential height over regions where there was atmospheric warming and decreases in geopotential height over regions with atmospheric cooling (Fig. 6b). The 1987–2003 decrease in mean July 500-mbar geopotential height in the region bounded by 75°–90°N, 0°–180°E and the increase in 500-mbar geopotential height in the region bounded by 75°–90°N, 0°–180°W reflects the increasing tendency for the July

circumpolar vortex to be centered in the Eastern Hemisphere during the period of 1987–2003.

A time series (1963–2003) of mean area-weighted July 500-mbar geopotential height over the region 70°–85°N, 75°–115°W was created to determine whether there were any significant regime shifts in mean 500-mbar geopotential height over the Canadian Arctic and whether they corresponded with the abrupt change in

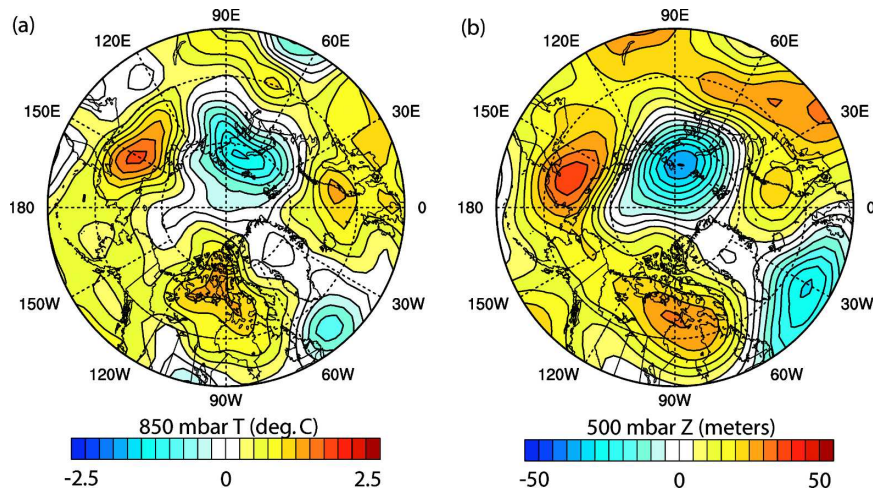


FIG. 6. Mean July 1987–2003 (a) 850-mbar air temperature (T) and (b) NCEP/NCAR 500-mbar geopotential height anomalies based on a 1963–86 base period.

regional glacier mass balance. No significant shift or trend was identified. Regional 500-mbar geopotential heights are however highly correlated with the time series of regional glacier mass balance ($r = 0.66$).

4. Discussion

On a hemispheric scale, both Angell (1998, 2006) and Frauenfeld and Davis (2003) have shown that variability in the extent of the summer midtropospheric Arctic circumpolar vortex, as defined by the 700–300-mbar geopotential height contour that consistently falls within the primary baroclinic zone, is significantly correlated with variability in Northern Hemisphere mid- to lower-tropospheric temperatures. Alt (1987) showed that interannual changes in the shape, strength, and position of the July 500-mbar Arctic circumpolar vortex have a strong influence on Canadian High Arctic regional glacier surface mass balance.

To illustrate the influence of both vortex strength and position on the regional glacier mass balance, July vortices were categorized into four types: I-A, I-B, II-A, II-B, and III. The first, type I-A, includes years when the July 500-mbar circumpolar vortex was strong and its center was located in the Eastern Hemisphere. This type included all years with July vortices that had centers located in sector I with positive strength anomalies. For type-I-A years it was most common for the area of low geopotential height surrounding the vortex center to extend into Baffin Bay (1973, 1982, 1992, 1994, 1996, and 2003). July 1992 exemplifies the regional influence of vortices with these characteristics (Fig. 7a). Under these conditions, the regional influence of

continental high pressure systems over the Canadian High Arctic during July is greater than in years when a strong July vortex is located in the Western Hemisphere (type II-A). In type-I-A years, average July temperatures result in neutral regional glacier mass balance anomalies.

In years when the July vortex is either weak (negative strength anomaly) and centered in the Eastern Hemisphere (type-I-B conditions: 1963, 1971, 1972, 1976, 1987, 1988, 1991, 1998, 1999, and 2000) or is strong but the region of lowest geopotential height is not elongated over the Canadian High Arctic (1993) (Fig. 7b), the Canadian High Arctic becomes almost thermally homogeneous with continental North America. This results in anomalously warm July SATs and extremely negative regional glacier mass balance. The 11 yr with these characteristics contain 4 of the 5 warmest years in the 41-yr record and 6 of the 8 most negative regional glacier mass balance years. Type-I-B conditions compare well with Alt's (1987) synoptic analog for an extreme melt year (1962), when there was an anomalously high percentage of open water in the Queen Elizabeth Islands channels and a cloud cover minimum. Type-I-B vortices were identified either as having centers located in sector I with negative strength anomalies or as having centers located in sector I with the area of low geopotential heights constrained strictly to the Eastern Hemisphere with positive strength anomalies.

For years when the July 500-mbar vortex is strong and centered in the Western Hemisphere (type-II-A conditions) cyclonic conditions prevail over the Canadian High Arctic. July 1964 (Fig. 7c) was selected as a

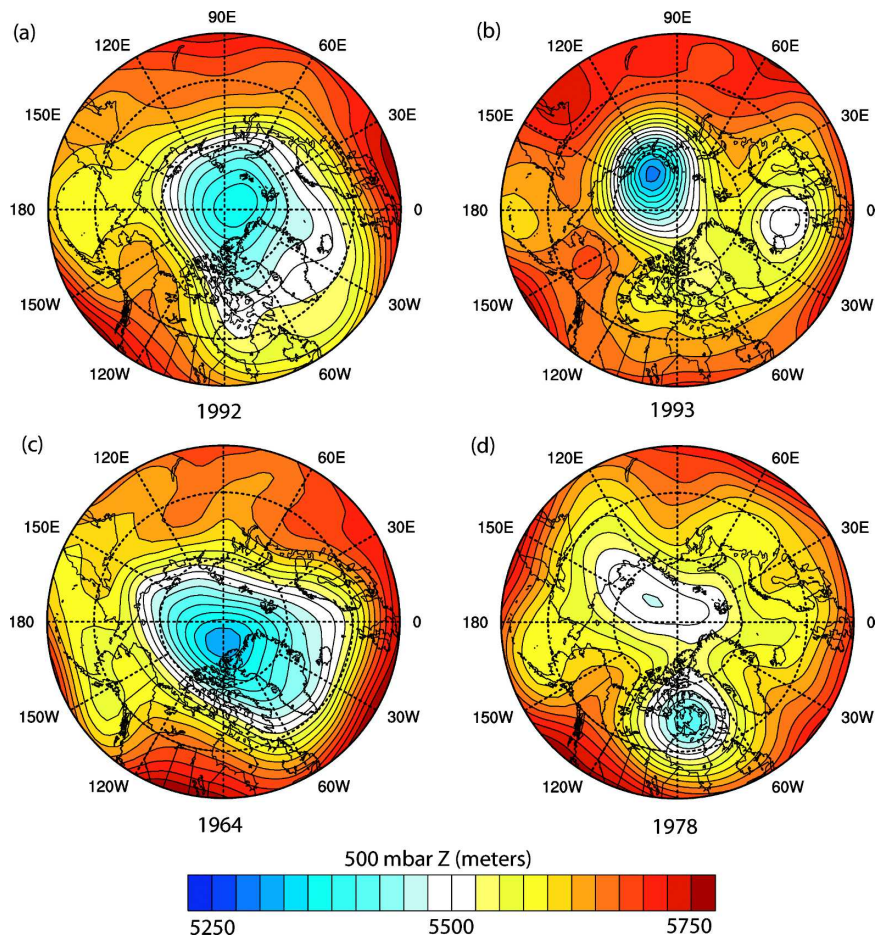


FIG. 7. Mean July NCEP/NCAR 500-mbar geopotential height for 1992, 1993, 1964, and 1976 (a)–(d), representative examples of type-I-A, -I-B, -II-A, and -III July vortex types.

representative year with these vortex characteristics. During this year, strong cyclonic conditions prevented North American high pressure ridges from extending northward over the Canadian High Arctic, keeping July SATs exceptionally low. Cold SATs, in turn, resulted in below-average glacier ablation rates and highly positive annual glacier mass balance anomalies. Also, 1964 was a year of above-average summer precipitation, which resulted from a succession of barotropic cyclones that transported Arctic Ocean moisture southward and deposited snow over the Canadian high Arctic (Alt 1987). Of the 41 yr investigated, 1964 had the coldest mean July SAT, and the most positive annual regional glacier mass balance. Similar July vortex characteristics prevailed during 9 out of the 41 yr investigated (1964, 1967, 1969, 1975, 1984, 1986, 1989, 1990, and 2002). Out of these 9 yr, 8 were among the 10 most positive mass balance years on record. All years with vortex centers located in sector II with positive strength anomalies were grouped in this category.

In years when the July circumpolar vortex is located in the Western Hemisphere but the vortex strength is decreased (higher minimum geopotential height) (type-II-B conditions: 1965, 1966, 1970, 1974, 1977, 1979, 1980, 1981, 1985, 1997, and 2001), the circumpolar vortex does not so effectively block warm North American continental air from moving into the Canadian High Arctic. These conditions result in average regional SATs and neutral regional glacier mass balance anomalies. All vortices with centers located in sector II and having negative strength anomalies where placed in this category.

The last grouping of July vortices consists of years when there are two 500-mbar geopotential minima, the strongest of which (lowest geopotential height) is located in sector III. The two minima are located to the south of, and to the north of, the Canadian High Arctic (type III: 1968, 1978, 1983, and 1995). The 500-mbar geopotential height contours for 1978, a representative year, are shown in Fig. 7d. These vortex characteristics

are associated with above-average July SATs and below-average Canadian High Arctic regional glacier mass balance.

Analysis of the NCEP–NCAR climate reanalysis data for the 15-yr period prior to 1963 shows a much higher occurrence (40%) of type-I-B vortices, which are associated with extreme melt conditions, and a reduced occurrence (20%) of type-II-B vortices, which are associated with average glacier mass balance conditions, relative to the period of 1963–86. This suggests that the period of 1948–62 closely resembles the 1987–2003 period, when there was a more negative glacier mass balance regime. This is also consistent with the above-average July SATs observed during this period.

Analysis of July mean precipitation records from the Environment Canada meteorological stations at Eureka and Resolute Bay shows that in years when the vortex is strong and located in the Western Hemisphere (type II-A) there is a nearly threefold increase (~20 mm) in total July precipitation compared to years when the vortex is either weak and located in the Eastern Hemisphere (type I-B), or located to the south of the Canadian High Arctic (type III). During type-I-B and -III years average regional July SATs measured at Eureka and Resolute Bay, both of which are located at elevations near sea level, are 5.6°C, compared to 3.8°C for type-II-A years. Assuming a cooling factor of 3°C for SATs over glaciers, as was done by Atkinson and Gajewski (2002) when estimating high-resolution summer SATs for the Canadian Arctic Archipelago, this lowers the mean July sea level SATs over glaciers to 2.6° and 0.8°C for type-I-B-III and -I-A years, respectively. Because type-II-A years have mean July temperatures near 0°C, it is likely that more of the precipitation will fall as snow during type-II-A years than in type-II-B and -III years. Thus, the influence of vortex characteristics on summer precipitation in the Canadian High Arctic likely amplifies the thermally driven response of regional glacier mass balance to changes in the strength and location of the July 500-mbar circumpolar vortex.

Comparing the mean July 500-mbar geopotential heights in the 24-yr period prior to the 1987 shift in regional glacier mass balance with those in the following 17 yr (Fig. 6b), there is a large decrease (40 m) in mean geopotential height on the eastern side of the Arctic Ocean and a large increase (30 m) on the western side. This is consistent with Angell's (1998, 2006) conclusion that the summer circumpolar vortex adopted a more easterly position in the latter part of the period of 1963–2001.

In more general terms, when the mean July 500-mbar vortex is located in the Western Hemisphere the mass

of cold polar air is more frequently situated over the Canadian High Arctic and warm high pressure ridges that build over continental Canada are more effectively blocked from moving northward over this region. When the mean July vortex is centered in the Eastern Hemisphere, warm continental high pressure ridges are not so effectively blocked from pushing northward and the Canadian High Arctic becomes more thermally homogeneous with continental North America. In terms of the influence of vortex characteristics on the Canadian High Arctic glacier mass balance, only 17% of years between 1963 and 1986 had easterly positioned type-I-B July vortices, which result in extreme glacier melt conditions. In the 17 yr that followed, 41% of the years had type-I-B July vortices and the overall occurrence of westerly positioned July vortices (types II-A, II-B, III) decreased by 40%.

In section 3d it was shown that regional July 500-mbar geopotential heights are significantly correlated with the regional glacier mass balance, but the regional 500-mbar geopotential height time series does not show the 1986–87 regime shift identified in both the air temperature and regional glacier mass balance time series. This suggests that it is not solely the absolute change in July 500-mbar height over the region that resulted in the inferred 1986–87 shift in regional glacier mass balance, but rather the combination of changes in the strength and position of the July circumpolar vortex. This can be illustrated by comparing regional July 500-mbar geopotential heights during type-I-A and -II-B vortex years. During type-I-A vortex years (strong vortex centered in the Eastern Hemisphere), regional July 500-mbar geopotential heights over the Canadian High Arctic are on average 0.32 standard deviations below the 41-yr mean. During type-II-B vortex years (weak vortex centered in the Western Hemisphere) regional 500-mbar geopotential heights over the Canadian High Arctic are on average 0.40 standard deviations greater than for type-I-A vortex years. Despite the higher regional 500-mbar geopotential heights for years with type-II-B vortices, there is little difference in the regional glacier balance or station-derived July SATs between years with type-II-B vortices and years with type-I-A vortices. This suggests that the combination of vortex position and strength must be accounted for when describing the relationship between the circumpolar vortex and the regional glacier mass balance.

The absence of significant correlations between the regional glacier mass balance record and the July temperature record from Alert (Fig. 1), and between the Alert and Resolute Bay/Eureka July temperature records suggests that mass balance variations of glaciers located in northern Ellesmere Island might differ from

the pattern depicted by the regional glacier mass balance signal (PC1) of the four existing mass balance records for the Canadian High Arctic, and therefore their relationships with the July 500-mbar vortex may differ from those presented here.

Other climate regime shifts that have previously been identified and shown to influence climate in Arctic regions are briefly examined. One of the most well known climate regime shifts is the 1976 shift in North Pacific sea surface temperatures, which is commonly referred to as the 1976 shift in the Pacific decadal oscillation (PDO; Mantua et al. 1997). By inspection of Fig. 3, it can clearly be seen that the shift in PDO had little if any impact on the regional glacier mass balance of the Canadian High Arctic. Additional statistical analysis of the relationship between monthly and annual PDO indices [taken as the first empirical orthogonal function (EOF) of Pacific sea surface temperatures poleward of 20°N; information available at <http://jisao.washington.edu/pdo/>] shows no significant correlation between the PDO and the regional glacier mass balance. Another well-studied climate regime shift is the 1989 upward shift in the wintertime North Atlantic Oscillation (NAO; Hurrell 1995)/Arctic Oscillation (AO; Thompson and Wallace 1998) index, taken here as the first EOF of sea level pressure poleward of 20°N. The majority of the variability in the Canadian High Arctic regional glacier mass balance is governed by melt processes that occur during summer months, so it is not surprising that no significant correlation exists between the National Weather Service Climate Prediction Center's winter AO index (available at <http://www.cpc.noaa.gov>) and the regional glacier mass balance. The only significant correlation that exists between monthly AO indices and the regional glacier mass balance signal is for the month of July ($r = 0.42$). The July AO is also significantly correlated ($r = 0.50$) with the average area-weighted regional 500-mbar geopotential height and, like the regional 500-mbar geopotential height, the July AO does not contain a 1986–87 regime shift. Less well known regime shifts that did occur in 1987 affected central Arctic annual sea level pressures (Walsh et al. 1996) and Northern Hemisphere snow extent (Robinson and Frei 2000), suggesting that the inferred 1987 climate regime shift may have affected areas beyond the Canadian High Arctic.

5. Conclusions

A significant decrease in the Canadian High Arctic mean regional glacier mass balance anomaly, as represented by our 41-yr time series of the first principal component of four glacier mass balance records, was detected between 1986 and 1987. For the four glaciers

examined, variability in summer mass balance determines variability in the annual glacier mass balance. Regional glacier mass balance is strongly correlated with July mean air temperature at Eureka and Resolute Bay and with the regionally averaged 850-mbar July temperature from the NCEP–NCAR climate reanalysis. Significant shifts to higher July mean temperatures after 1987 were found in both station-derived SATs and NCEP–NCAR 850-mbar temperatures.

Consistent with the findings of Alt (1987), interannual changes in the strength and position of the July 500-mbar circumpolar vortex exert a strong influence on Canadian High Arctic regional SATs and glacier mass balance. In general, when the July circumpolar vortex is strong and its center is located in the Western Hemisphere, positive mass balance anomalies prevail. In contrast, when the July circumpolar vortex is either weak or strong without elongation over the Canadian High Arctic, and the vortex center is located in the Eastern Hemisphere, highly negative mass balance anomalies prevail. Since the late 1980s there has been a significantly higher occurrence of July vortex types that produce anomalously high SATs over the Canadian High Arctic. This, in turn, has resulted in a sharp decrease in the regional glacier mass balance. The tendency for more easterly centered July circumpolar vortices is reflected in 1987–2003 anomalies in NCEP–NCAR 500-mbar geopotential heights (Fig. 6), which show a decrease of up to 40 m in mean geopotential height over the eastern side of the Arctic Ocean and an increase of up to 30 m in geopotential height over the Canadian Arctic relative to the 1963–87 period.

These findings highlight the importance of understanding the dynamics behind the climatic forcings that have resulted in accelerated glacier melt in the Canadian High Arctic and show that the observed changes in July mean SATs and glacier mass balance in the region are not appropriately characterized by simple linear trends. To identify the mechanisms behind the regional patterns of warming and mass balance change in the Canadian High Arctic, it is necessary to analyze the dominant synoptic-scale pressure systems and regional circulation patterns over the Arctic. The results presented here clearly show that changes in the strength and center position of the July 500-mbar circumpolar vortex have resulted in the acceleration of glacier ablation in the Canadian high Arctic since 1986–87. Further research is needed to determine what has caused these changes in the July 500-mbar circumpolar vortex.

Acknowledgments. This work was supported by NSERC (through a discovery grant to M. Sharp, and an undergraduate summer research award and Canada

graduate scholarship to A. S. Gardner), the Alberta Ingenuity Fund (through a scholarship to A. S. Gardner), the Meteorological Service of Canada (through a scholarship supplement to A. S. Gardner), and by the Canadian Foundation for Climate and Atmospheric Sciences through the Polar Climate Stability Network. We gratefully acknowledge the sustained efforts of Roy Koerner, Peter Adams, Graham Cogley, Miles Ecclestone, and coworkers to produce long time series of surface mass balance measurements for glaciers and ice caps in the Queen Elizabeth Islands. We also thank Lindsey Nicholson and two anonymous reviewers for their comments and insights.

REFERENCES

- Alt, B. T., 1978: Synoptic climate controls of mass balance variations on Devon Island Ice Cap. *Arct. Alp. Res.*, **10**, 61–80.
- , 1979: Investigation of summer synoptic climate controls on the mass balance of Meighen Ice Cap. *Atmos.–Ocean*, **17**, 181–199.
- , 1987: Developing synoptic analogs for extreme mass balance conditions on Queen Elizabeth Island ice caps. *J. Climate Appl. Meteor.*, **26**, 1605–1623.
- Angell, J. K., 1998: Contraction of the 300 mbar north circumpolar vortex during 1963–1997 and its movement into the Eastern Hemisphere. *J. Geophys. Res.*, **103**, 25 887–25 893.
- , 2006: Changes in the 300-mb north circumpolar vortex, 1963–2001. *J. Climate*, **19**, 2984–2994.
- Atkinson, D. E., and K. Gajewski, 2002: High-resolution estimation of summer surface air temperature in the Canadian Arctic Archipelago. *J. Climate*, **15**, 3601–3614.
- Bradley, R. S., and J. England, 1978: Recent climatic fluctuations of the Canadian high Arctic and their significance for glaciology. *Arct. Alp. Res.*, **10**, 715–731.
- Braithwaite, R. J., and S. C. B. Raper, 2002: Glaciers and their contribution to sea level change. *Phys. Chem. Earth*, **27**, 1445–1454.
- Braun, C., D. R. Hardy, and R. S. Bradley, 2004: Mass balance and area changes of four High Arctic plateau ice caps, 1959–2002. *Geogr. Ann.*, **86A**, 43–52.
- Burgess, D. O., M. J. Sharp, D. W. F. Mair, J. A. Dowdeswell, and T. J. Benham, 2005: Flow dynamics and iceberg calving rates of Devon Ice Cap, Nunavut, Canada. *J. Glaciol.*, **51**, 219–230.
- Cogley, J. G., and W. P. Adams, 1998: Mass balance of glaciers other than the ice sheets. *J. Glaciol.*, **44**, 315–325.
- , —, M. A. Ecclestone, F. Jung-Rothenhäusler, and C. S. L. Ommanney, 1996: Mass balance of White Glacier, Axel Heiberg Island, NWT, Canada, 1960–91. *J. Glaciol.*, **42**, 548–563.
- Dowdeswell, J. A., 1995: Glaciers in the high Arctic and recent environmental change. *Philos. Trans. Roy. Soc. London*, **352A**, 321–334.
- , and Coauthors, 1997: The mass balance of circum-Arctic glaciers and recent climate change. *Quat. Res.*, **48**, 1–14.
- Dyurgerov, M. B., 2002: Glacier mass balance and regime: Data of measurements and analysis. INSTAAR, University of Colorado Occasional Paper 55, 268 pp.
- , and M. F. Meier, 1997: Year-to-year fluctuations of global mass balance of small glaciers and their contribution to sea-level changes. *Arct. Alp. Res.*, **29**, 392–402.
- , and —, 1999: Analysis of winter and summer glacier mass balances. *Geogr. Ann.*, **81A**, 541–554.
- , and —, 2000: Twentieth century climate change: Evidence from small glaciers. *Proc. Natl. Acad. Sci. USA*, **97**, 1406–1411.
- , and —, 2005: Glaciers and the changing earth system: A 2004 snapshot. INSTAAR, University of Colorado Occasional Paper 58, 117 pp.
- , and G. J. McCabe, 2006: Associations between accelerated glacier mass wastage and increased summer temperature in coastal regions. *Arct. Antarct. Alp. Res.*, **38**, 190–197.
- Frauenfeld, O. W., and R. E. Davis, 2003: Northern Hemisphere circumpolar vortex trends and climate change implications. *J. Geophys. Res.*, **108**, 4423, doi:10.1029/2002JD002958.
- Hagen, J. O., K. Melvold, F. Pinglot, and J. A. Dowdeswell, 2003: On the net mass balance of the glaciers and ice caps in Svalbard, Norwegian Arctic. *Arct. Antarct. Alp. Res.*, **35**, 264–270.
- Houghton, J. T., Y. Ding, D. J. Griggs, M. Noguer, P. J. Van Der Linden, D. Xiaosu, K. Maskell, and C. A. Johnson, Eds., 2001: *Climate Change 2001: The Scientific Basis*. Cambridge University Press, 881 pp.
- Huber, P. J., 1964: Robust estimation of location parameter. *Ann. Math. Stat.*, **35**, 73–101.
- Hurrell, J. W., 1995: Decadal trends in the North Atlantic Oscillation: Regional temperatures and precipitation. *Science*, **269**, 676–679.
- IAHS/UNESCO, 2005: *Glacier Mass Balance Bulletin*. No. 8, 108 pp.
- Johannessen, O. M., and Coauthors, 2004: Arctic climate change: Observed and modeled temperature and sea-ice variability. *Tellus*, **56A**, 559–560.
- Kaiser, H. F., 1960: The application of electronic-computers to Factor-Analysis. *Educ. Psychol. Meas.*, **20**, 141–151.
- Kalnay, E., and Coauthors, 1996: The NCEP/NCAR 40-Year Reanalysis Project. *Bull. Amer. Meteor. Soc.*, **77**, 437–471.
- Kanamitsu, M., W. Ebisuzaki, J. Woollen, S. K. Yang, J. J. Hnilo, M. Fiorino, and G. L. Potter, 2002: NCEP–DOE AMIP-II Reanalysis (R-2). *Bull. Amer. Meteor. Soc.*, **83**, 1631–1643.
- Kistler, R., and Coauthors, 2001: The NCEP–NCAR 50-Year Reanalysis: Monthly means CD-ROM and documentation. *Bull. Amer. Meteor. Soc.*, **82**, 247–267.
- Koerner, R. M., 1996: Canadian Arctic. Report on Mass Balance of Arctic Glaciers, Working Group on Arctic Glaciology, International Arctic Science Committee Rep. 5, 5–8.
- , 2002: Glaciers of the Arctic Islands. Glaciers of the High Arctic Islands, USGS Professional Paper 1386-J-1, J111–J146.
- Mantua, N. J., S. R. Hare, Y. Zhang, J. M. Wallace, and R. C. Francis, 1997: A Pacific interdecadal climate oscillation with impacts on salmon production. *Bull. Amer. Meteor. Soc.*, **78**, 1069–1079.
- Maxwell, J. B., 1980: *The Climate of the Canadian Arctic Islands and Adjacent Waters: Climatological Studies No. 30*. Vol. 1, Atmospheric Environmental Services, Environment Canada, 532 pp.
- McCabe, G. J., A. G. Fountain, and M. Dyurgerov, 2000: Variability in winter mass balance of Northern Hemisphere glaciers and relations with atmospheric circulation. *Arct. Antarct. Alp. Res.*, **32**, 64–72.
- Meier, M. F., 1984: Contribution of small glaciers to global sea-level. *Science*, **226**, 1418–1421.
- Raper, S. C. B., and R. J. Braithwaite, 2006: Low sea level rise

- projections from mountain glaciers and icecaps under global warming. *Nature*, **439**, 311–313.
- Robinson, D. A., and A. Frei, 2000: Seasonal variability of Northern Hemisphere snow extent using visible satellite data. *Prof. Geogr.*, **52**, 307–315.
- Rodionov, S. N., 2004: A sequential algorithm for testing climate regime shifts. *Geophys. Res. Lett.*, **31**, L09204, doi:10.1029/2004GL019448.
- , 2006: Use of prewhitening in climate regime shift detection. *Geophys. Res. Lett.*, **33**, L12707, doi:10.1029/2006GL025904.
- Serreze, M. C., and R. G. Barry, 2005: *The Arctic Climate System*. 1st ed. Cambridge University Press, 385 pp.
- Thompson, D. W. J., and J. M. Wallace, 1998: The Arctic Oscillation signature in the wintertime geopotential height and temperature fields. *Geophys. Res. Lett.*, **25**, 1297–1300.
- Venegas, S. A., 2001: Statistical methods for signal detection in climate. Danish Center for Earth System Science Rep. 2, 96 pp.
- Walsh, J. E., W. L. Chapman, and T. L. Shy, 1996: Recent decrease of sea level pressure in the central Arctic. *J. Climate*, **9**, 480–486.
- Wang, L., M. J. Sharp, B. Rivard, S. Marshall, and D. Burgess, 2005: Melt season duration on Canadian Arctic ice caps, 2000–2004. *Geophys. Res. Lett.*, **32**, L19502, doi:10.1029/2005GL023962.

Thirty-seven year mass balance of Devon Ice Cap, Nunavut, Canada, determined by shallow ice coring and melt modeling

Douglas Mair

Department of Geography and Environment, University of Aberdeen, Aberdeen, UK

David Burgess and Martin Sharp

Department of Earth and Atmospheric Sciences, University of Alberta, Edmonton, Alberta, Canada

Received 8 October 2003; revised 18 November 2004; accepted 30 November 2004; published 22 February 2005.

[1] In April–May 2000, eight boreholes were drilled to ~15–20 m depth on the Devon Ice Cap. ^{137}Cs γ activity profiles of each borehole showed a peak count rate at depth that is associated with fallout from atmospheric thermonuclear weapons testing in 1963. Snow, firn, and ice densities were measured at each core site and were used to estimate the average pattern of mass balance across the accumulation zone of the ice cap over the period 1963–2000. The average mass balance across the entire ice cap for the period 1960–2000 was also estimated using a degree-day model driven by data derived from on-ice temperature sensors and long-term measurements at Resolute Bay. Best fitting degree-day factors were determined for different sectors of the ice cap by comparing model output with repeated annual mass balance measurements made along two transects (Koerner, 1970). The results suggest that the ice cap has lost ~1.6 km³ water per year, equivalent to a mean net mass balance of approximately $-0.13 \text{ m We a}^{-1}$. Estimates of the mean mass balance for individual drainage basins reveal regions of positive and negative mass balance that are consistent with remotely sensed observations of advancing and retreating ice cap margins, respectively.

Citation: Mair, D., D. Burgess, and M. Sharp (2005), Thirty-seven year mass balance of Devon Ice Cap, Nunavut, Canada, determined by shallow ice coring and melt modeling, *J. Geophys. Res.*, 110, F01011, doi:10.1029/2003JF000099.

1. Introduction

[2] Global climate models consistently predict that anthropogenic climate warming will be strongest at high northern latitudes [*Intergovernmental Panel on Climate Change*, 2001; *Mitchell et al.*, 1995]. Such a change in climate may cause significant changes in the mass and geometry of high Arctic ice masses, and there is evidence that such changes may be underway [e.g., *Dowdeswell et al.*, 1997; *Paterson and Reeh*, 2001; *Burgess and Sharp*, 2004]. To help elucidate the causes of these changes, it is necessary to gather baseline information on the mass balance of whole ice caps. The ice caps of the Canadian high Arctic are ideally suited to this challenge. They occupy an area in which there are strong spatial gradients in both mass balance and the magnitude and seasonality of predicted climate changes [*Maxwell*, 1997], and they will have shorter response times to climate change than the larger Greenland ice sheet. In addition, there is substantial variability in ice dynamics between different basins within the same ice cap. Typically, these ice caps have both terrestrial and tidewater margins, and they may contain fast flowing outlet glaciers, surge-type glaciers and more slowly moving lobate sectors. They can thus be expected to display a

diversity of responses to climate change. The main aim of this paper is to determine the contribution of surface mass balance to observed changes in the geometry of a high Arctic ice cap over the last 4 decades.

[3] We use a combination of long-term mass balance field measurements from the accumulation area and degree-day melt model output to present a spatially resolved reconstruction of 37 year average accumulation and ablation rates across the Devon Ice Cap (Figure 1) in the Canadian high Arctic. The contribution of surface mass balance to observed changes in the geometry and volume of the ice cap over the last 4 decades [*Burgess and Sharp*, 2004] is then determined for the ice cap as a whole and for each of the major drainage basins. This research is part of an integrated study of the area/volume change and dynamics of the Canadian Arctic ice caps and will provide the necessary baseline data required to estimate balance fluxes for the ice cap (following *Budd and Warner* [1996]).

2. Field Site

[4] Devon Ice Cap covers ~14,000 km² on eastern Devon Island, Nunavut, Canada (Figure 1). It has a maximum elevation of 1930 m above sea level (asl). It is slightly asymmetrical, with an east-west summit ridge, which is more pronounced in the east, and a southern ridge that begins ~20 km south of the summit and extends south to

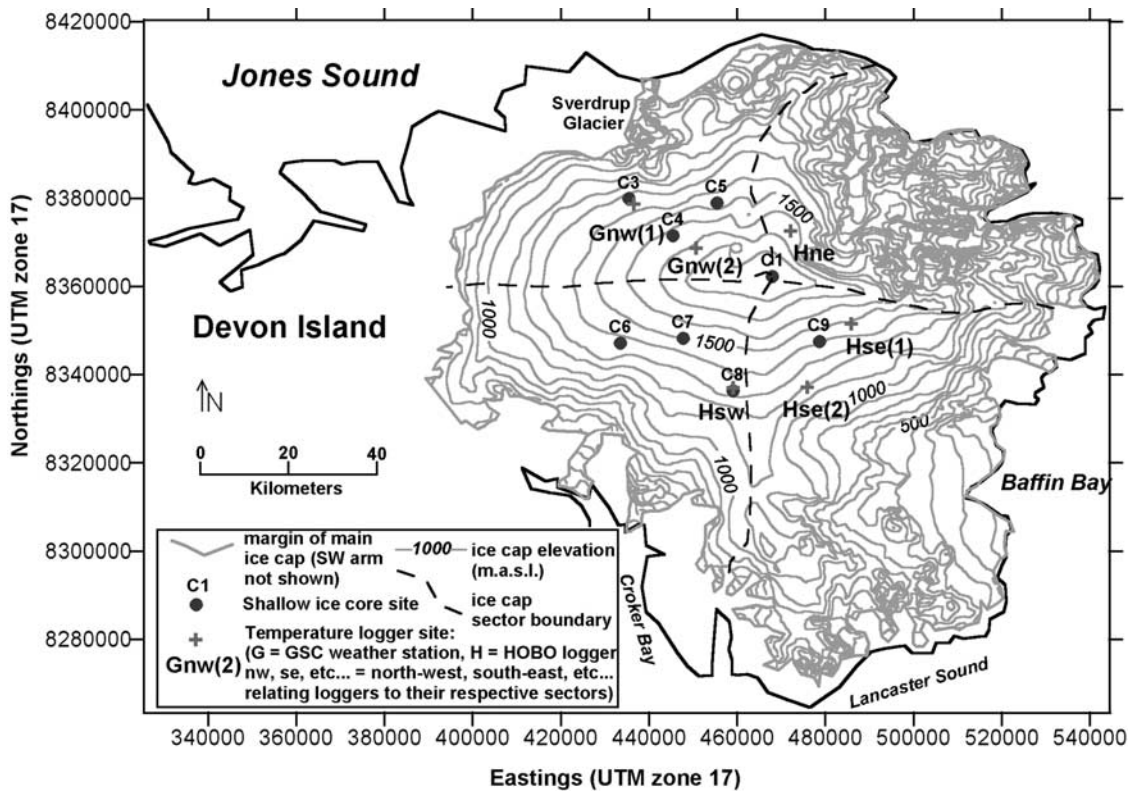


Figure 1. Devon Ice Cap fieldwork locations.

within a few kilometers of Lancaster Sound. The ice cap has been the focus of mass balance measurements since the early 1960s [Koerner, 1966, 1970; Koerner and Taniguchi, 1976]. Maps of mass accumulation were produced from snow depth measurements along several profiles across the ice cap [Koerner, 1966]. An annual mass balance measurement program was conducted along profiles that ran from the summit of the ice cap, northwest along the Sverdrup glacier basin to the coast, and southeast toward Lancaster Sound [Koerner, 1970]. In the mid-1970s, longer-term average accumulation rates were estimated from laboratory analyses of two shallow ice cores retrieved from the northwest transect [Koerner and Taniguchi, 1976]. The cores were analyzed to detect the radioactive layer deposited in 1963 as a result of H-bomb tests in 1962. Measurements of ice density above this layer allowed estimation of average accumulation between 1963 and 1974. Mass balance monitoring has continued and is ongoing along the northwest transect across Devon Ice Cap [Dyurgerov, 2002]. However, repeat measurements of stake arrays on remote ice masses are very time consuming and expensive [Fountain et al., 1999], so no continuous measurements of mass balance have been made across the rest of the ice cap.

3. Methods and Data Acquisition

[5] In this study, a combination of shallow ice core measurements and degree-day modeling is used to map the spatial distribution of average mass balance across the Devon Ice Cap. A combination of methodologies is used because (1) long-term field measurements can effectively constrain the spatial pattern of mass balance across much of the accumulation area, but are not of sufficiently good

spatial and temporal coverage to simply carry out a statistical extrapolation of measurements across large ablation areas of the ice cap at lower elevations and (2) simple degree-day melt modeling works fairly well for lower elevations across the ablation area, but struggles with the highly nonlinear snow accumulation/elevation relationship which exists at Devon Ice Cap, particularly within the accumulation area.

3.1. Shallow Ice Coring

[6] During April–May 2000, eight shallow (<20 m) ice cores were drilled across the accumulation area of Devon Ice Cap (Figure 1, C1–C9) using a Kovacs Mark II ice corer. The corer produces cores with diameters of 9 cm and average lengths of ~40 cm. Snow and firn densities were determined immediately after retrieval of cores by measuring the diameter, length and weight of each core section.

[7] Using a down-borehole gamma spectrometer (NaI(Tl) detector with photomultiplier tube and MicroMCB multi-channel analyzer software), gamma activity profiles of each borehole were measured using a method similar to that described by Dunphy and Dibb [1994]. Measurements of gamma ray counts accumulated over 1200 s were made for the energy bands of a ^{109}Cd reference source, ^{137}Cs and 2 other spectral intervals. Counts were conducted at 40 cm intervals, working upward from the bottom of each borehole. Profiles for all spectral intervals except ^{109}Cd show an exponential increase toward the surface that is most likely due to cosmic ray–produced gamma rays [Dunphy and Dibb, 1994]. The count profiles for ^{137}Cs showed a secondary peak at depth (e.g., Figure 2) that is associated with peak fallout from atmospheric testing of thermonuclear weapons in 1962–1963. Profiling resolution was increased

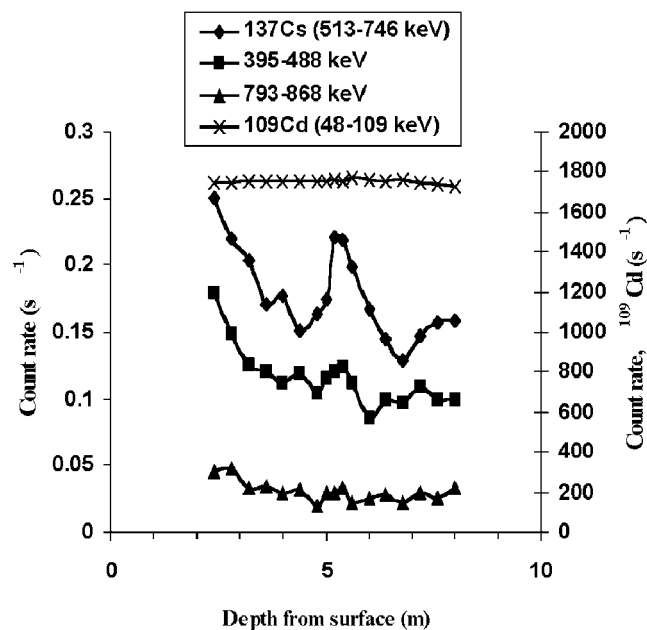


Figure 2. Gamma ray count-depth profiles for four energy ranges at core C3.

to 20 cm intervals around the peak to determine its location more accurately.

[8] Using the depth of the 1963 radioactive fallout layer and measurements of the densities of firn and snow above this layer, the average mass balance over the period 1963–2000 was estimated at each core site in the field. There are errors associated with in situ density profiling. Determining the average density of the core is relatively straightforward at higher elevations (e.g., core 1 at the summit), where coherent sections of relatively low-density firn were retrieved. Closer to the equilibrium line (e.g., core 3), within the “saturation zone,” core sections were composed of refrozen slush which frequently broke into more irregularly shaped sections that were more difficult to measure. The error in determining the average density of the entire core was, however, likely reduced by the relatively uniform density and character (e.g., bubble content) of firn from these regions. We estimate that (1) the error in total volume of the core above the bomb layer is $\sim 10\%$, (2) the error in the weight of the core is $\sim 1\%$, and (3) the error in the depth of the bomb layer is $\sim 0.5\text{--}2\%$. We therefore estimate that the long-term mass balance at a point can be determined with an accuracy of $\sim 12\%$.

[9] A more fundamental uncertainty concerns the ability of a measurement based on a single core to represent the average accumulation rate across a larger area. Variations in annual accumulation can occur, for instance due to the formation of sastrugi, over spatial scales of $10^{-2}\text{--}10^2$ m. Since we do not know spatial covariance functions for the mean accumulation rates across the ice cap this uncertainty cannot be resolved, although it is likely to be diminished over a period of 37 years.

3.2. Air Temperature Loggers

[10] In May 2000, four 8K HOBO™ temperature loggers were deployed to measure average daily surface air temperature within the northeastern, southeastern and southwestern

sectors of the ice cap at elevations of ~ 1640 m, 1530 m, 1190 m and 1320 m respectively (Figure 1, Hne, Hse(1), etc.). The Geological Survey of Canada (GSC) has deployed automatic weather stations (AWS) and recorded air temperatures at sites within the northwestern sector of the ice cap (two of these are located in Figure 1: Gnw(1) and Gnw(2)) almost continuously during the 1990s and periodically before this, but has no record of air temperatures elsewhere on the ice cap. Data from HOBO loggers and AWSs were downloaded in April 2001 and used to generate input for degree-day melt modeling (see Appendix A).

3.3. Degree-Day Melt Modeling

[11] The daily snow or ice melt at any point is often assumed to be proportional to the daily mean air temperature at that location so long as the mean air temperature is positive. The constant of proportionality between the melt rate and the air temperature is termed the “degree-day factor,” and is generally lower for snow (DDF_s) than for ice (DDF_i) [Braithwaite, 1995]. This method of estimating ablation has been applied effectively in Greenland [Braithwaite and Olesen, 1989; Huybrechts et al., 1991], and to John Evans Glacier, Ellesmere Island [Arendt and Sharp, 1999] and several glaciers in the Swiss Alps [Braithwaite and Zhang, 2000]. DDF_s and DDF_i are not universal across all ice masses [Braithwaite and Zhang, 2000], however, since they depend on the energy balance at each location. Although the method is a crude simplification of the complex processes involved in the surface energy balance, it is very useful for application to areas for which input data are sparse. Using this approach, temporal patterns of melt at a specific glacier can be estimated from measurements at remote stations so long as (1) some measurements of mass balance are available to constrain the degree-day factors for the glacier and (2) there are sufficient temperature data from the glacier to determine a relationship with measurements at the remote station.

4. Results

4.1. Shallow Ice Coring

[12] Depth profiles of density and ^{137}Cs gamma count rates for four sites within the northwest sector of the ice cap are shown in Figure 3. At higher altitudes, firn densities are low at the surface and increase gradually with depth. At lower altitudes the annual accumulation consists of refrozen saturated snow, and firn densities are closer to that of pure ice. The ^{137}Cs profiles each show a distinct peak at depth (peak ~ 0.25 ^{137}Cs counts s^{-1} compared with a background count rate at depth of ~ 0.15 ^{137}Cs counts s^{-1}). In the northwest sector of the ice cap the peaks are generally closer to the surface at lower elevations.

[13] At the summit, two gamma profiles were measured; one in a shallow borehole (C1, Figure 3a), and one in a slightly narrower borehole drilled to ~ 60 m depth by the GSC (C2, Figure 3a). The ^{137}Cs peak appears on both profiles ~ 18 m from the surface. Assuming that this peak represents the 1963 fallout layer, the average mass balance at the summit for the period 1963–2000 was calculated as 0.241 ± 0.03 meters water equivalent per year (mWe a^{-1}). This compares with values in the range $0.216\text{--}0.234$ mWe a^{-1} calculated by the GSC based on identification of annual layers

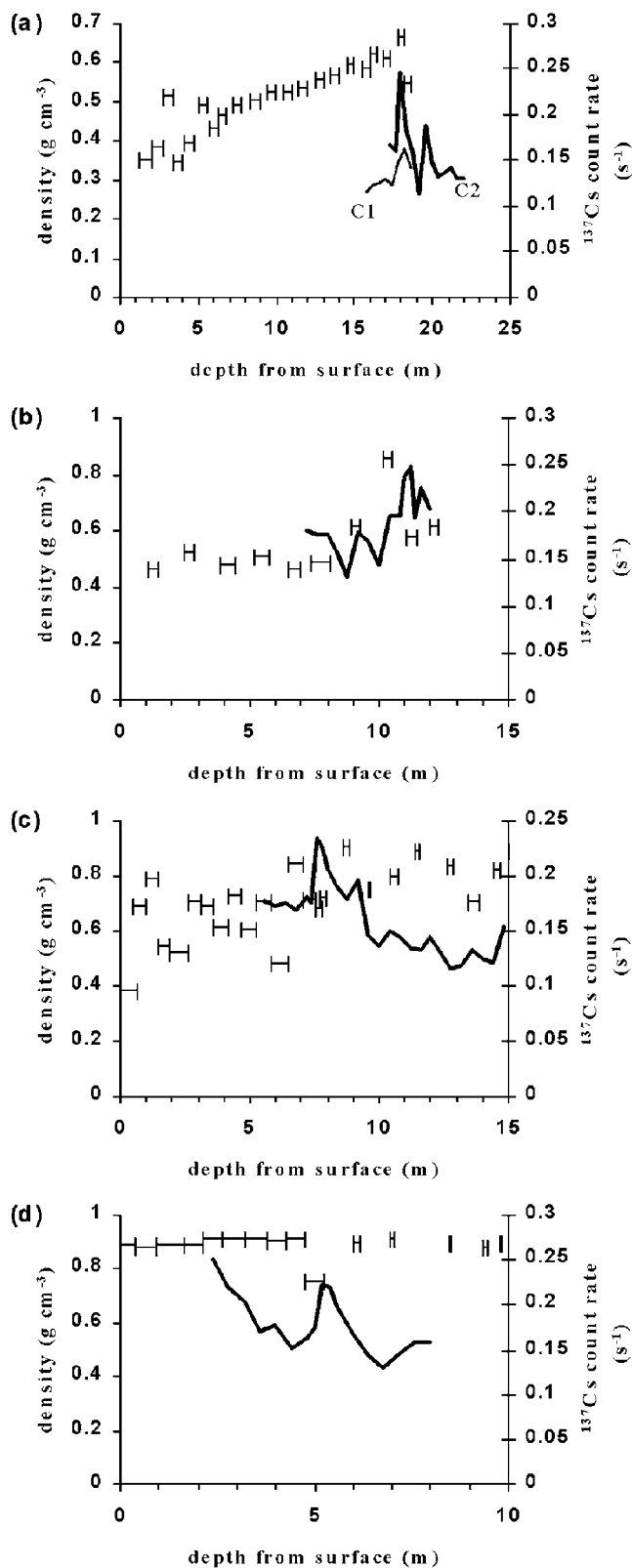


Figure 3. Density and ^{137}Cs count rates: (a) summit cores, C1 and C2 (GSC core), 1930 m asl; (b) C4, 1640 m asl; (c) C5, 1508 m asl; and (d) C3, 1340 m asl.

Table 1. Mass Balance Calculated From Shallow Ice Core Measurements on Devon Ice Cap, April–May 2000^a

Core Site	Elevation, m asl	Depth of 1963 Layer in 2000, m	Mass Balance 1963–2000, mWe
C1	1930	18.0	0.241
C4	1640	11.2	0.159
C5	1508	7.6	0.138
C3	1340	5.2	0.127
C7	1504	10.2	0.159
C9	1470	10.6	0.218
C6	1367	10.4	0.201
C8	1325	15.2	0.267

^aC1–C5 are in northern half of ice cap; C6–C9 are in southern half of ice cap.

using major ion concentrations and laboratory density measurements over a range of timescales dating back to the Laki eruption of 1783 [Pinglot *et al.*, 2003]. The consistency between GSC measurements and shallow ice core results gives us confidence that the ^{137}Cs peak at depth clearly represents the 1963 radioactive fallout layer and that the method is successful in determining the long-term, average mass balance.

[14] The 1963 fallout layer was also located at four sites across the southern half of the ice cap (C6–C9, Figure 1; Table 1). Estimates of the long-term average mass balance for all 8 sites, distributed across the accumulation area of the ice cap, are presented in Table 1. Long-term mass balance, estimated from shallow ice cores in the northwest sector of the ice cap, is generally consistent with a range of previous stake measurements from the 1960s and core measurements from 1963–1974 (Figure 4a). Note that there was an exceptionally high level of melt across the ice cap in 1962 [Koerner, 1970]. In contrast to the northwest sector of the ice cap, both shallow ice cores and annual mass balance measurements show that there is no clear relationship between mass balance and elevation to the south and east (Figure 4b).

[15] A comparison of the 1963–1974 and 1963–2000 ice core measurements reveals two patterns (Figure 4a). Firstly the better spatial resolution of the 1963–2000 core measurements identifies a slightly nonlinear mass balance–elevation relationship. Mass balance falls rapidly from the summit (1930 m) to ~ 1600 m and decreases more gradually from there toward ~ 1300 m. This pattern is likely to reflect the erosive action of katabatic winds, which are most persistent from ~ 1600 to 1800 m. These winds remove winter snowfall from these altitudes and deposit it at lower elevations [Koerner, 1966]. Secondly, there may have been a reduction in the net mass balance since 1974 at lower elevations in the accumulation area (~ 1300 m), though some of this may be accounted for by errors.

[16] The lack of a clear relationship between mass balance and elevation in the south and southeast sectors of the ice cap probably reflects the strong influence of Baffin Bay on patterns of accumulation in these areas. Northern Baffin Bay remains ice-free for most of the year and cyclones bring moist air across the southern and eastern regions of the ice cap. Most of the moisture is deposited as snow as it reaches the eastern slopes of the cold ice cap [Koerner, 1966]. Higher melt at lower altitudes will be balanced by higher accumulation rates nearer Baffin Bay. Net mass balance can

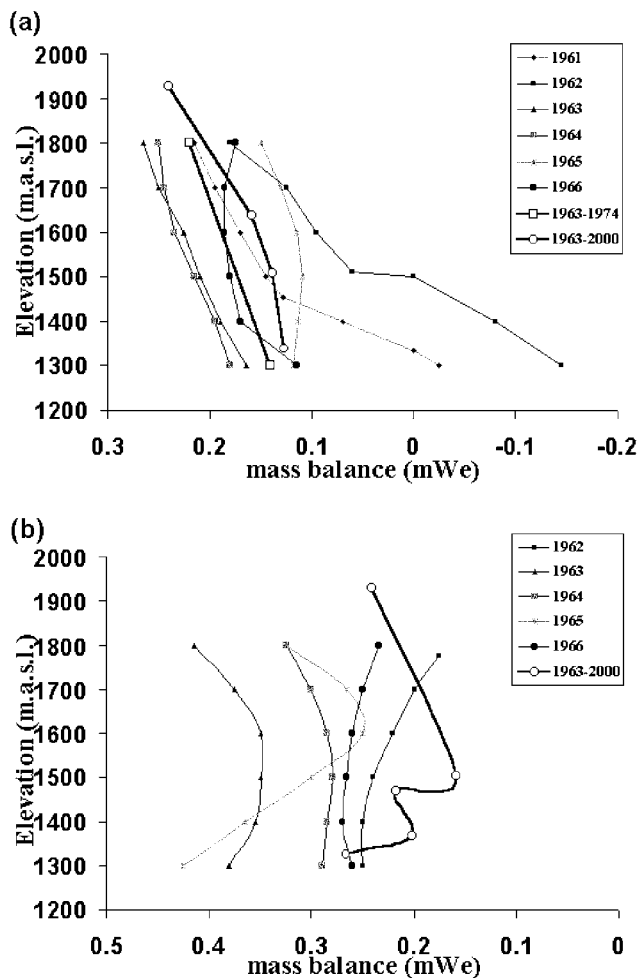


Figure 4. Mass balance from cores over period 1963–2000 compared with annual mass balance measurements from the 1960s [Koerner, 1970] and (in Figure 4a) with shallow ice core experiments in 1974 [Koerner and Taniguchi, 1976]. (a) Northwest sector accumulation area. (b) South and southeast sectors accumulation areas.

therefore even out at values similar to those measured at higher elevations.

4.2. Degree-Day Modeling: Simulation of Long-Term Temperature Data for Different Sectors of the Ice Cap

[17] Summer melt over the ice cap was simulated using the degree-day model of *Arendt and Sharp* [1999]. For the purposes of degree-day modeling, the ice cap was subdivided into four sectors (Figure 1). Temperature data from different loggers were used to generate input data for modeling melt in each sector. On-ice temperature data for all sectors were gathered for the period May 2000–April 2001 only. Thus to model the mass balance of the ablation zone over a period of ~ 40 years, it was necessary to determine the relationship between air temperatures on the ice cap and those at the nearest location for which records extend back to the early 1960s (Resolute Bay). For the purposes of degree-day modeling, it is important that the simulated long-term temperature records predict accurately the number of positive degree-days at each temperature logger site.

[18] Linear regression equations were derived to express the relationship between daily average temperatures at Resolute Bay and in each sector of the ice cap for the period day of year 150 (D150) to D250 (May 30 to September 7), 2000 (e.g., Figures 5a and 5b). Surface melt is not expected outside this period. These equations were used to predict temperatures on the ice cap from the Resolute Bay time series. The predicted temperatures (e.g., “predGnw(1),” Figure 5c) seriously underestimate the number of positive degree-days recorded on the ice cap. It is assumed that the difference between predicted and recorded temperature series was due to two factors: (1) different synoptic weather conditions over Resolute Bay and Devon Ice Cap and (2) error induced by the simple linear regression. Synoptic differences are expected to average out over seasonal and multiyear periods. Error in the regression was corrected for as follows. It was assumed that half the difference between each predicted and recorded temperature was due to error in the regression and the rest due to synoptic effects. The time series of half the difference between the predicted and recorded ice cap temperatures for the period D150–250, 2000, was therefore used to create a distribution of error terms. These errors were randomly redistributed and then added to the predicted temperature series for the potential melt period (i.e., D150–250). This process was repeated 37 times for each year from 1963–2000. The resulting time series for the potential melt period of the year 2000 (“corrpredGnw(1),” Figure 5d) has a similar number of positive degree-days to the original temperature time series recorded on the ice cap. The process was repeated for all four sectors of the ice cap, and the resulting simulated 1963–2000 temperature records were used as input to the degree-day model. This method assumes that the error distribution is stationary throughout the study period, an assumption that has not been tested.

4.3. Running the Degree-Day Model

[19] Other input data required to run the model were as follows: (1) altitude of temperature record, derived from differential GPS measurements; (2) surface air temperature lapse rate (the average summer lapse rate $(-0.0048^{\circ}\text{C m}^{-1})$ was calculated using data from GSC AWSs located at 1930 m, 1730 m, 1340 m and 330m elevations within the northwest sector); (3) accumulation, specified as a multiple, k , of the sum of daily accumulation measured at Resolute, where k is the average winter snow fall at each ice cap sector temperature logger elevation (recorded in May 2000 and 2001) divided by total winter snowfall at Resolute up to the same date; (4) accumulation lapse rate, derived from measurements of snow depth at ice cap temperature loggers and at the ice cap summit ($0.00002 \text{ mWe m}^{-1}$ for the southwest sector, $0.00005 \text{ mWe m}^{-1}$ for the other 3 sectors); (5) maximum amount of superimposed ice formed during the melt season, calculated using the temperature method [Woodward *et al.*, 1997], which requires the mean annual sea level temperature for Devon Island (-13.6°C). This was extrapolated from the linear relationship between annual average air temperatures and elevation determined using data from GSC AWS.

[20] A potentially significant limitation of the melt model is that temperature and accumulation lapse rates are taken as constants when there is field evidence which suggests they

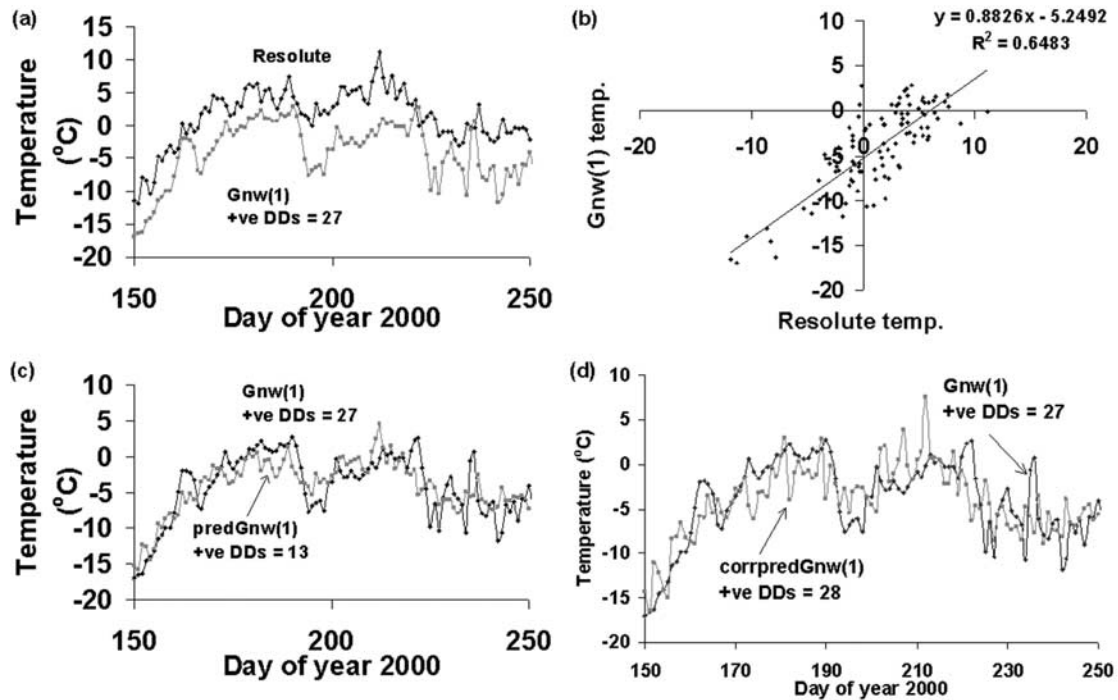


Figure 5. Stages in the simulation of daily average temperatures for the northwest sector of the ice cap from Resolute Bay temperature data. (a) Daily average temperatures at Resolute Bay and at AWS Gnw(1) over period D150–250, 2000. (b) Linear regression relationship between Resolute Bay and Gnw(1) temperature data over same period. (c) Gnw(1) data compared with predicted temperature data (predGnw(1)) from linear regression with Resolute Bay data. (d) Gnw(1) data compared with corrected, predicted temperature data (corrpredGnw(1)) after random redistribution of error terms.

are not. The average temperature lapse rate calculated from AWS measurements along the northwest transect, masks frequent temperature inversions and is likely to be very dependent on variations in katabatic winds [Denby and Greuell, 2000]. The effect of inversions and katabatic winds will be particularly significant when they occur during the summer when temperatures approach 0°C. Winter accumulation patterns across Devon Ice Cap do not show a linear decrease with altitude. According to Koerner [1966], accumulation actually reaches a maximum around the equilibrium line in the southeast sector. Although the melt model is primarily used to estimate mass balance in the ablation areas of the ice cap, accumulation lapse rates were calculated from measurements made in the accumulation area only. A more general limitation of the melt model is that a considerable amount of empirical data is needed to calibrate and/or constrain model output. Devon Ice Cap is a good place to apply such a model because of the existence of field measurements of mass balance across different sectors of the accumulation and ablation areas. Where fewer empirical data are available to constrain model output, the selection of degree-day factors will be even more subjective.

4.4. Model Tuning

[21] Since previous research (summarized by Braithwaite and Zhang [2000, Table 4]) has shown that no unique set of DDFs can be applied to all ice masses, DDF_s and DDF_i must be assumed to be unknown. The following steps were followed to determine the most appropriate DDFs for each sector of the ice cap.

[22] 1. The melt model was run for the periods for which stake measurements of annual mass balance exist at 100 m altitude intervals: 1961–1966 in the northwest sector; 1962–1966 in the southeast sector.

[23] 2. For each of these sectors the model was run forty times with different sets of DDFs for snow and ice: DDF_s was varied between 2.5 and 4 mm d⁻¹ °C⁻¹ with an interval of 0.5; DDF_i was varied between 5 and 14 mm d⁻¹ °C⁻¹ with an interval of 1. These values cover the typical range of DDFs for Arctic and Alpine glaciers (summarized by Braithwaite and Zhang [2000, Table 4]).

[24] 3. The accuracy of each model run was expressed by the error, e , between the mean values of modeled and measured mass balance at the j th altitude, b_j^* and b_j respectively, such that

$$e = \sqrt{\left(1/J \sum_{j=1}^{j=J} ((b_j^* - b_j)/2)^2\right)}, \quad (1)$$

where J is the number of elevation intervals. Thus e is the square root of the mean of the squares (rms) of half of the differences between measured and modeled values.

[25] 4. The DDFs from the best fit model runs were used with the simulated 1963–2000 temperature data to calculate long-term mass balance for the northwest and southeast sectors.

[26] 5. In the absence of stake or core measurements for the northeast sector, best fit DDFs from the northwest sector were applied to simulated temperature data for the adjacent

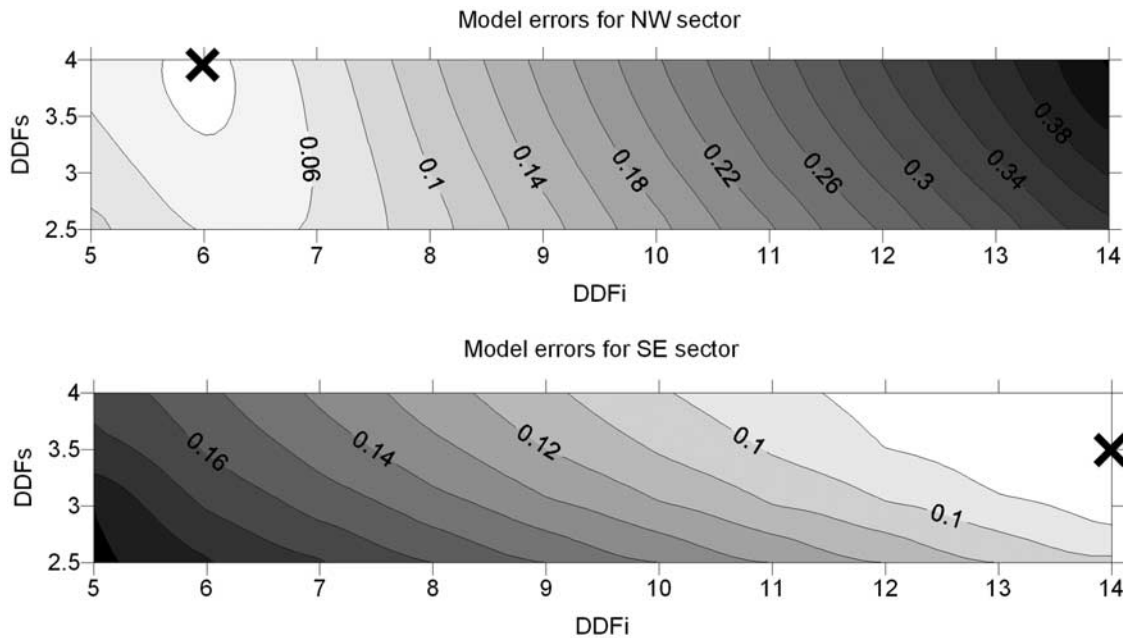


Figure 6. Model errors for northwest and southeast sectors. Lowest errors are run 32 for the northwest sector and run 30 for the southeast sector.

northeast sector. Since core measurements from the southwest sector and stake measurements from the southeast sector both display a nonlinear relationship between mass balance and elevation (Figure 4b), it was assumed that best fit DDFs from the southeast sector could be applied to simulated temperature data for the southwest sector.

[27] The areas of each elevation interval were not factored into equation (1) since, unlike well-defined valley glacier catchments, these are highly dependent upon the fairly arbitrary nature of the sector boundaries. This could lead to the undesirable situation where the most appropriate DDFs for each sector may become as dependent on the exact locations of the sector boundaries as on the comparison with measured data. The model errors and DDF ranges for each model run are shown for the northwest and southeast sectors in Figure 6. A number of model runs give low errors. The best fit values for the northwest sector are $DDF_s = 4 \text{ mm d}^{-1} \text{ } ^\circ\text{C}^{-1}$ and $DDF_i = 6 \text{ mm d}^{-1} \text{ } ^\circ\text{C}^{-1}$ (model run 32); and for the southeast sector, $DDF_s = 3.5 \text{ mm d}^{-1} \text{ } ^\circ\text{C}^{-1}$ and $DDF_i = 14 \text{ mm d}^{-1} \text{ } ^\circ\text{C}^{-1}$ (model run 30). These DDFs lie within the range of values used previously [Braithwaite and Zhang, 2000, Table 4]. The differences in these DDFs for different sectors should not be physically interpreted since these are sensitive to varying winter accumulation which, as mentioned above, is not well constrained by linear lapse rates. Despite this, modeled mass balance compares favorably with the limited number of shallow ice core measurements averaged over the period 1963–2000 in the northwest, southeast and southwest sectors and with 1960s stake measurements (Figure 7). No long-term data exist for the northeast sector.

4.5. Combining Modeled and Measured Mass Balance

[28] For each sector of the ice cap, high-order polynomial regression trend lines were fitted to plots of modeled mass balance against elevation. The regression equations were

used to predict the mass balance distribution across the ice cap with 1 km spatial resolution using 1 km digital elevation models (DEMs) of each sector.

[29] Shallow ice coring experiments provide long-term measurements of mass balance, and are assumed to be more accurate and reliable than modeled mass balance. Therefore across most of the accumulation area, mass balance was interpolated from the distribution of core measurements (using a 1 km grid block kriging routine) and then combined with modeled mass balance associated with the remainder of the ice cap. This was carried out as follows.

[30] Net accumulation in the west of the ice cap is well constrained by core measurements from an ice cap summit value of 0.241 mWe a^{-1} to 0.127 mWe a^{-1} at C3 (Figure 1). Melt model output for the western half of the ice cap was therefore only used to predict mass balance across those areas where modeled values were less than 0.1 mWe a^{-1} . Accumulation in the east is less well constrained by measurements (0.241 mWe a^{-1} at summit to 0.217 mWe a^{-1} at C9), so modeled mass balance values less than 0.15 mWe a^{-1} were retained. By choosing this higher value, model output is used to predict mass balance across inaccessible mountainous areas in the northeast and southeast that show evidence of accumulation (e.g., extensive areas of ice-covered summits). A 1 km grid of surface mass balance across the entire ice cap was therefore created from merging five grids; the shallow ice core-constrained grid, covering most of the accumulation area, and melt model grids from each of the four sectors covering the remainder of the accumulation area and ablation area. A contour map of mass balance was created from these merged grids using the Golden Software, Inc. “Surfer” program (Figure 8). The error distribution across the ice cap was calculated by assuming an error of 12% in the core measurements, and using equation (1) to estimate errors averaged across different sectors of the rest of the ice cap (inset of Figure 8).

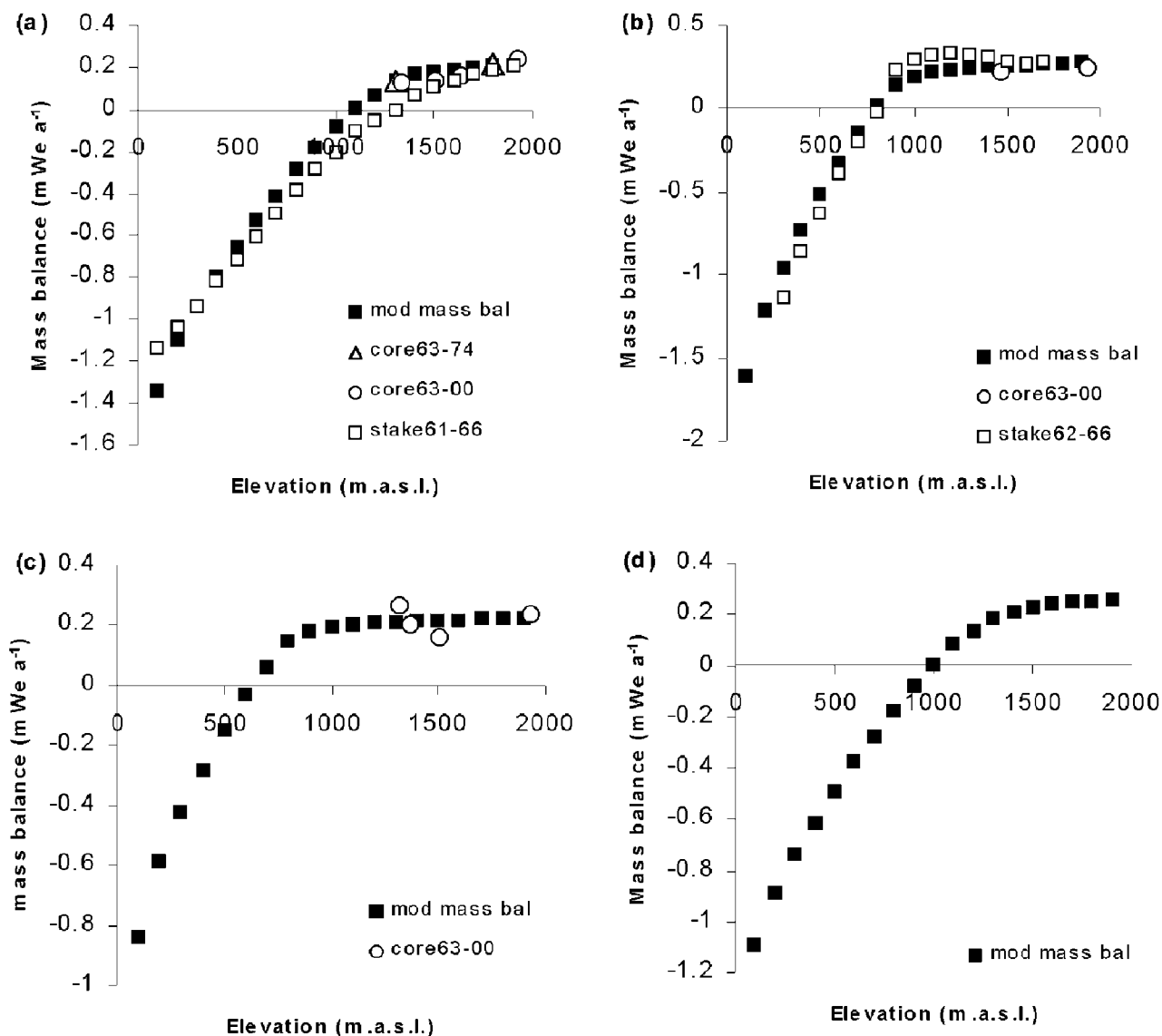


Figure 7. Modeled mass balance, shallow ice core and stake measurements of mass balance for different sectors of Devon Ice Cap. (a) Northwest sector. (b) Southeast sector. (c) Southwest sector. (d) Northeast sector.

4.6. Contribution of Surface Mass Balance to Volume Change of Devon Ice Cap

[31] The contribution of surface mass balance to observed changes in volume of the ice cap can now be estimated by calculating the net “volume” of the mass balance grid upon which Figure 8 is based. This was done using the “Surfer” Grid/Volume function that calculates the net volume between a grid surface and a horizontal plane, which, in this case, is where mass balance equals zero. Three methods were used to determine volumes: Extended Trapezoidal Rule, Extended Simpson’s Rule, and Extended Simpson’s 3/8 Rule [Press *et al.*, 1988, section 4.1]. The difference in the volume calculations by the three different methods measures the accuracy of the volume calculations. In all cases the volume calculations were very close (within $0.005 \text{ km}^3 \text{ We a}^{-1}$), so an average of the three values was taken.

[32] The northwest sector of the ice cap (Figure 1) has lost $6.4 \pm 3 \text{ km}^3$ water over the period 1963–2000. This equates to an average surface mass balance of $-0.067 \pm 0.03 \text{ mWe a}^{-1}$ which compares with the value of $-0.049 \text{ mWe a}^{-1}$ calculated based on repeat annual mass balance stake measurements over the period 1963–1998 in this region (measured by Koerner, quoted by *Dyurgerov* [2002]). The main part of Devon Ice Cap (i.e., excluding the southwest arm) has lost $59.2 \pm 26.6 \text{ km}^3$ (or $1.6 \pm 0.7 \text{ km}^3 \text{ a}^{-1}$) over the period 1963–2000. This equates to an average surface mass balance (SMB) of $-0.13 \pm 0.056 \text{ mWe a}^{-1}$. This result can be compared with completely independent volume change estimates for a similar time period, which we now summarize.

[33] *Burgess and Sharp* [2004] calculated volume change of the Devon Ice Cap over a 40 year period using two independent methods based on areal changes measured from 1959/1960 aerial photography and 1999/2000 Landsat 7 ETM+ satellite imagery. The first method estimates the

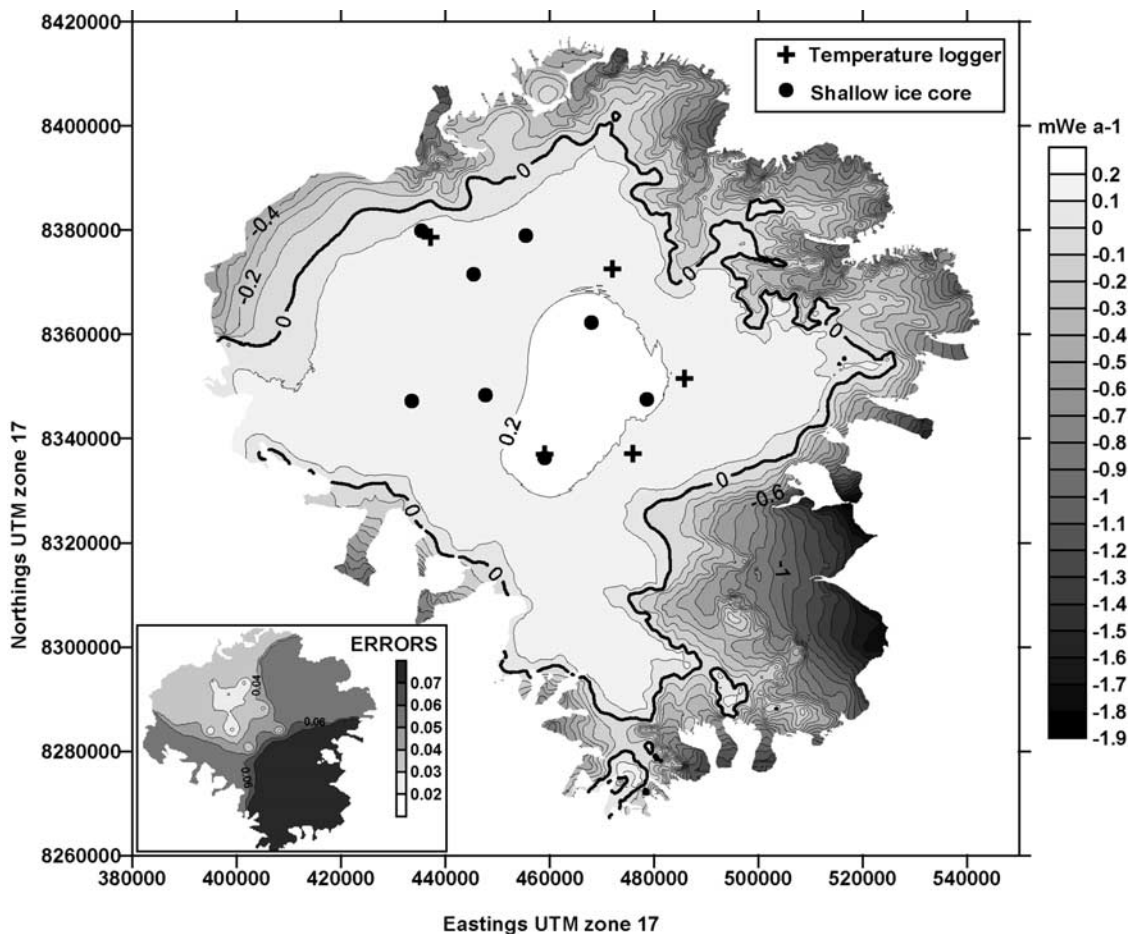


Figure 8. Spatial pattern of mass balance determined from combination of shallow ice core measurements and degree-day melt model output (units of mass balance in mWe a^{-1}). Equilibrium line highlighted.

change in cross sectional area of a longitudinal profile of a glacier as the product of the maximum glacier thickness (MT) and the length change at the terminus [Hooke, 1998, p. 219]. However, to account for glacier width, the total area change (instead of the length change alone) calculated for each individual drainage basin (Figure 9), was multiplied by the maximum ice thickness within the associated catchment area (obtained from recent radio echo sounding (RES) data collected by J. Dowdeswell, Cambridge University, UK, 2000). Volume change measurements were calculated over 86% of the ice cap area and extrapolated over the remaining 14% indicating a total volume change of $44 \pm 9 \text{ km}^3$ (excluding the southwest arm), or 1.1 km^3 per year over the period 1960–1999. The second method used volume-area (VA) scaling techniques [Bahr et al., 1997], and estimated volume change for the main portion of the ice cap as $52 \pm 5 \text{ km}^3$. Given the large scope for measurement and methodological errors, the three different methods (SMB, MT and VA) give comparable total volume loss estimates for Devon Ice Cap over approximately the last 4 decades.

5. Analysis and Discussion of Spatial Variations in Mass Balance and Volume Change

[34] Burgess and Sharp [2004] identified significant spatial changes in the geometry of Devon Ice Cap since

1960. These included (1) the retreat of major tidewater glaciers along the east coast, (2) an increase in exposed bedrock area in mountainous northeast and southeast regions, indicating lowering of the ice cap surface, (3) an ice margin advance of $\sim 130 \text{ m}$ along an 80 km section of the northwest margin, and (4) minor marginal advance of smaller glaciers in the northwest (Sverdrup Glacier) and south of the ice cap (Croker Bay glacier catchments). In order to determine the contribution of SMB to these changes, we compared SMB estimates of volume change with estimates using the MT method described above for each of the largest major drainage basins (17 basins, excluding the southwest arm (Figure 9)). Volume change estimates derived from the MT method were used for the comparison because this method allowed volume changes to be calculated for individual drainage basins whereas volume change estimates derived from the volume-area scaling technique were calculated for the ice cap as a whole only. SMB estimates are extrapolated over a 39 year period in order to facilitate comparison with volume change estimates derived from the MT method.

[35] The relationship between the MT and SMB estimates of volume change (over the 17 basins for which the MT method was used) is quite strong (Figure 10a, $r^2 = 0.68$). There is no significant relationship between the area of each

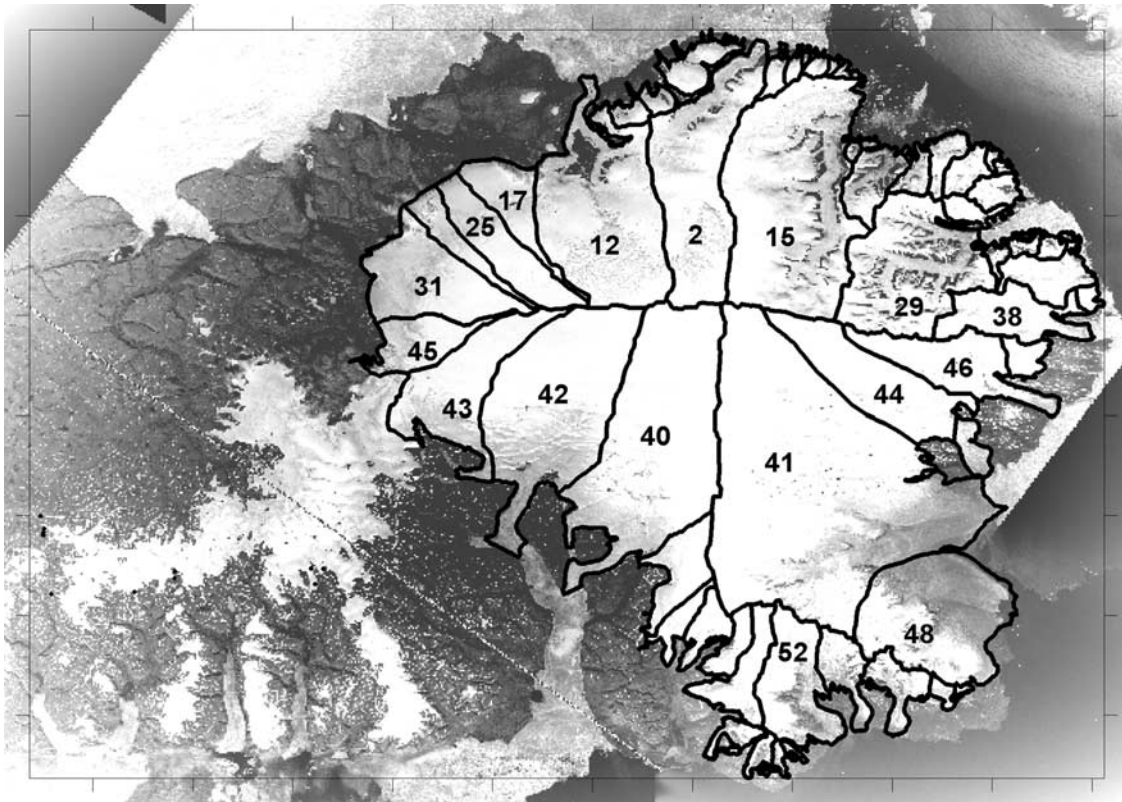


Figure 9. Drainage basins of the Devon Ice Cap. The southwest arm was not included in this analysis.

drainage basin and the difference between these two estimates of volume change. The largest 17 basins account for 86% of the area of the ice cap (excluding the southwest arm) but only ~68% of the total volume loss estimated from SMB measurements. The remaining 14% of the ice cap accounts for ~32% of mass loss due to SMB. Thus the

small basins may make a disproportionately high contribution to the overall mass loss. This makes physical sense. These basins are found near the ice cap margins, particularly in the southern and eastern sectors, and do not extend to the high interior elevations that the larger basins reach. They have much larger ablation areas in proportion to the total

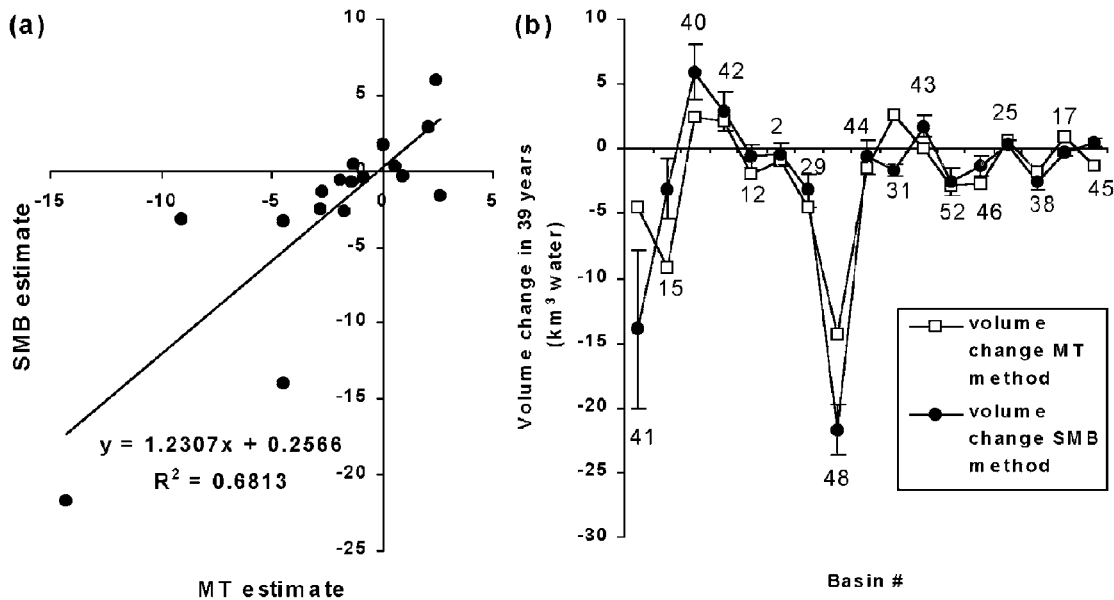


Figure 10. Surface mass balance (SMB) estimate of volume change extrapolated over 39 years and compared with maximum thickness (MT) estimate. (a) Linear regression relationship between SMB and MT volume change estimates. (b) Individual basin comparison (with error bars on SMB estimate).

basin area (lower accumulation area ratios). Preferential thinning of up to 10 cm a^{-1} was detected from repeat airborne laser altimetry profiles flown by NASA in 1995 and 2000 [Abdalati *et al.*, 2005] at two locations along the northwest and southwest margins. This also indicates relatively high rates of ablation at lower elevations of the ice cap. The linear extrapolation of the MT volume change estimates from the largest basins (86% ice cap area) across the rest of the ice cap (i.e., across the smaller basins) will therefore be likely to underestimate the total ice cap mass loss.

[36] A basin by basin comparison of SMB and MT estimates of total mass change over a 39 year period (Figure 10b) identifies very similar patterns of spatial variation in volume change across the largest drainage basins of the ice cap. These are (1) volume loss across many easterly basins (e.g., basins 15, 29, 38, 46, 41, 48, and 52); (2) very little change across much of the western half of the ice cap (e.g., basins 2, 12, 17, 25, 43, and 45); and (3) significant volume increase in southern glacier basins flowing into Croker Bay (i.e., basins 40 and 42).

[37] There are, however, differences between the two sets of estimates that are now discussed further. For eight basins, differences between SMB and MT volume change estimates can be accounted for by errors in the SMB estimate (basins 42, 12, 2, 29, 44, 52, 25, and 38). Other differences could be due to the possibility that the true volume change differs from that determined from the area change, calculated as part of the MT method. If there has been a significant change in the maximum thickness of a basin this will affect the accuracy of the MT estimate of volume change. Figure 10b suggests that highly negative SMB across basins 41 and 48 in the southeast sector should have led to much greater values of volume loss than estimated by the MT method. The discrepancy could be due to thinning of the ice in these basins which has not been accounted for in the MT method. Burgess and Sharp [2004] identified an increase in the area of exposed bedrock in interior regions of the southeast sector of the ice cap, indicating surface lowering of the ice cap over the period 1960–2000. Thus given the error in the SMB estimates and the unknown error in ice thickness used in the MT method, it is likely that SMB can account for mass loss across 10 (65%) of the 17 largest drainage basins.

[38] SMB across basin 31 in the northwest sector suggests this basin has experienced an overall negative balance in recent decades despite the fact that its margin has advanced 130 m between 1960 and 2000. It may be that the maximum ice thickness of this basin has decreased and that marginal advance is a delayed response to a period of positive mass balance at some time in the past. Burgess and Sharp [2004] calculated response times of each drainage basin following the method of Johannesson *et al.* [1989] and found that basin 31 has a response time of 677 years. Burgess and Sharp [2004, p. 270] came to the conclusion that the advance of the northwest margin “suggests either that conditions favorable to ice sheet growth are prevalent in this region, or that this sector of the ice cap is still responding to the cooler conditions of the Little Ice Age.” From the SMB evidence presented here, it would appear that the latter explanation is more likely.

[39] The MT and SMB volume change estimates for the remaining six basins (15, 40, 43, 46, 17, and 45) are -4.6 km^3 and $+3.5 \text{ km}^3$ respectively. Most of this difference of 8.1 km^3 can be attributed to basin 15. It is likely that iceberg calving accounts for the difference in volume change estimate for this basin where tidewater glaciers have retreated up to 1300 m from 1960 to 2000 [Burgess and Sharp, 2004] and where imagery shows the highest concentrations of icebergs in coastal waters.

6. Summary and Conclusions

[40] The spatial pattern of mass balance across Devon Island Ice Cap was reconstructed from two data sources. These were (1) shallow ice core measurements of net mass balance in the accumulation area since the deposition of the 1963 radioactive H-bomb test layer and (2) output (predicted net mass balance) from degree-day melt modeling driven by simulated long-term daily average air temperatures and snow accumulation. Despite potentially significant sources of error, results compared well with previous mass balance measurements from stakes and ice cores. We estimate that Devon Ice Cap (excluding the southwest arm) has lost an average of $1.6 \pm 0.7 \text{ km}^3$ water per year over the period 1963–2000. Although the estimated margin of error is large, this estimate compares favorably with completely independent volume change estimates over a similar time period based on measured area changes [Burgess and Sharp, 2004]. The contribution of mass balance to recent changes in ice cap geometry was investigated across the largest individual ice drainage basins by comparing mass balance estimates of volume change with estimates based upon measurements of maximum ice thickness and area change. The spatial patterns of mass change across these basins were similar for both sets of estimates. The comparison suggests that surface mass balance is the main cause of volume change. Where differences between the estimates were more significant, these could largely be explained by recognizing that (1) the relationship between volume and area of drainage basins may change through time, so the MT estimates of volume change are incorrect for such cases, that (2) the response times of some drainage basins may be such that recently observed changes in basin area are not a consequence of the recent mass balance regime, and (3) the exclusion of the component of mass loss due to iceberg calving.

[41] This research will provide important input data for balance flux and coupled mass balance dynamics modeling of high Arctic ice caps, and a baseline data set against which to compare future measurements of mass balance to detect evidence for spatial and temporal change.

Appendix A

[42] HOBOs were not placed within mini-radiation covers. This did lead to days of inflated air temperatures due to insulation. The nonshielded HOBO data was compared with a properly shielded AWS data set, where these were at the most similar elevation and location, i.e., Gnw(2) and Hne, located at 1731 m asl and 1637 m asl, respectively (Figure 1). It was realized that HOBO data could be used to derive a good estimate of the temperature over the ice

cap. The best relationship between AWS and HOBO data was obtained if HOBO daily minima were used on days when HOBO daily maxima exceeded 0°C ($r^2 = 0.76$ for the potential melt period JD150–250, $r^2 = 0.967$ for the entire year) instead of always using the HOBO daily average ($r^2 = 0.67$ for JD150–250). Average summer (i.e., D150–250) temperatures of this HOBO derived data were 0.9°C higher than AWS data. About half of this difference could be accounted for by the average lapse rate over the same period (calculated from four GSC AWSs from 1930 m to 330 m as $0.0048^{\circ}\text{C m}^{-1}$). The same daily minimum criterion was applied to each HOBO logger data set and the derived data were used to form regression relationships with the Resolute Bay temperature time series. It was decided that this routine was preferable to rejecting all the HOBO data on the basis that they were not properly shielded. This method is likely to overestimate the average temperatures across the ice cap, however this will be a systematic error that subsequent tuning of the model will account for by producing DDFs with lower values.

[43] HOBO loggers were deployed ~ 1.0 m above snow surface. Difference in height between deployment and downloading varied between 20 cm and 40 cm. All HOBO loggers were closer to the surface when retrieved. Monitoring height above snow surface is usually done using ultrasonic depth gauges (UDGs). UDG data from GSC AWSs have often proved unreliable due to problems with excessive rime ice buildup around sensors (R. M. Koerner, personal communication, 2000). However, summit (1930 m) records show a maximum variation in height of ~ 50 cm and annual difference (D114 2000 to D113 2001) of ~ 40 cm. The variation in height of the logger above the snow surface during the potential melt period (D150–250) was just 20 cm. At 1340 m maximum change in height is ~ 40 cm, annual difference is just 10 cm and from D150–250 the height change was 25 cm. Our measurements of HOBO annual height changes are consistent with changes in height of this magnitude. The literature on vertical gradients in air temperature over melting glaciers usually concentrates on larger-scale variations using vertical profile data from high AWS masts and/or balloons. The literature is dominated by work from Alpine glaciers or Iceland [e.g., Oerlemans *et al.*, 1999; Denby and Greuell, 2000; Greuell and Smeets, 2001]. At Pasterze, Austria, Denby and Greuell [2000] recorded temperatures at a range of heights including 1.0 m and 0.7 m, comparable to the heights of our HOBO loggers. A graph of average temperature over a 2 day fair weather period shows a difference of about 0.5°C between 1.0 m and 0.7 m [Denby and Greuell, 2000, Figure 1b]. Vertical temperature gradients are likely to be smaller over a high Arctic polar ice cap than over this warm temperate glacier, but we are unaware of any empirical study of high-resolution, near-surface temperature variations over melting surfaces of much higher latitude ice masses. However, if we take this (probably high) value from the literature we can estimate by how much this error would cause us to underestimate the total PDDs. In the northwest sector of the ice cap (where we use AWS data rather than HOBO data) the PDD total for 2000–2001 was 27.13. If we assume that the height varied linearly during the melt season (D150–250) from 0 to 30 cm, and equate this to a temperature error

from 0° – 0.5°C , then the PDD total would rise to 32.48, i.e., about a 20% increase. This systematic error will be accounted for by subsequent tuning of the model by producing DDFs with higher values (for the HOBO temp records it will to some extent cancel out the logger shielding error discussed above).

[44] **Acknowledgments.** We thank Roy Koerner, Mike Demuth, and Chris Zdanowicz, National Glaciology Program-Environment Canada/Natural Resources Canada for their logistical support and AWS data, the Leverhulme Trust for a Research Fellowship to D.M., NSERC for an Industrial Postgraduate Scholarship (IPS) to D.B. and for Discovery and equipment grants to M.S., Land Data Technologies (Edmonton), sponsor of an IPS Scholarship to D.B., Canadian Space Agency, Meteorological Service of Canada-CRYSYS, Canadian Circumpolar Institute, and Polar Continental Shelf Project for funding and logistical support, and the Meteorological Service of Canada for providing Resolute meteorological data through the CRYSYS program. We thank the Nunavut Research Institute and the communities of Grise Fjord and Resolute Bay for permission to work on Devon Island. This paper is PCSP contribution number 01603.

References

- Abdalati, W., W. Krabill, E. Frederick, S. Manizade, C. Martin, J. Sonntag, R. Swift, R. Thomas, J. Yungel, and R. Koerner (2005), Elevation changes of ice caps in the Canadian Arctic Archipelago, *J. Geophys. Res.*, *110*, F04007, doi:10.1029/2003JF000045.
- Arendt, A., and M. Sharp (1999), Energy balance measurements on a high Arctic glacier and their implications for mass balance modelling, *IAHS Publ.*, *256*, 165–172.
- Bahr, D. B., M. F. Meier, and S. D. Peckham (1997), The physical basis of glacier volume-area scaling, *J. Geophys. Res.*, *102*, 355–362.
- Braithwaite, R. J. (1995), Positive degree-day factors for ablation on the Greenland ice sheet studied by energy-balance modelling, *J. Glaciol.*, *41*, 153–160.
- Braithwaite, R. J., and O. B. Olesen (1989), Calculation of glacier ablation from air temperature, West Greenland, in *Glacier Fluctuations and Climate Change*, edited by J. Oerlemans, pp. 219–233, Springer, New York.
- Braithwaite, R. J., and Y. Zhang (2000), Sensitivity of mass balance of five Swiss glaciers to temperature changes assessed by tuning a degree-day model, *J. Glaciol.*, *46*, 7–14.
- Budd, W. F., and R. C. Warner (1996), A computer scheme for rapid calculations of balance-flux distributions, *Ann. Glaciol.*, *23*, 21–27.
- Burgess, D. O., and M. J. Sharp (2004), Recent changes in areal extent of the Devon Ice Cap, Nunavut, Canada, *AAAR*, *36*, 261–271.
- Denby, B., and W. Greuell (2000), The use of bulk and profile methods for determining surface heat fluxes in the presence of glacier winds, *J. Glaciol.*, *46*, 445–452.
- Dowdeswell, J. A., et al. (1997), The mass balance of circum-Arctic glaciers and recent climate change, *Quat. Res.*, *48*, 1–14.
- Dunphy, P. P., and J. E. Dibb (1994), ^{137}Cs gamma-ray detection at Summit, Greenland, *J. Glaciol.*, *40*, 87–92.
- Dyrugerov, M. (2002), Glacier mass balance and regime: Data of measurements and analysis, *Occas. Pap.* 55, Inst. of Arct. and Appl. Res. Univ. of Colo., Boulder.
- Fountain, A. G., P. Jansson, G. Kaser, and M. Dyrugerov (1999), Summary of the workshop on methods of mass balance measurements and modelling, Tarfala, Sweden, August 10–12, 1998, *Geogr. Ann.*, *81A*, 461–465.
- Greuell, W., and P. Smeets (2001), Variations with elevation in the surface energy balance on the Pasterze (Austria), *J. Geophys. Res.*, *106*, 31,717–31,727.
- Hooke, L. R. (1998), *Principles of Glacier Mechanics*, 248 pp., Prentice Hall, Upper Saddle River, N. J.
- Huybrechts, P., A. Letreguilly, and N. Reeh (1991), The Greenland ice sheet and greenhouse warming, *Palaeoogeogr. Palaoclimatol. Palaeoecol.*, *89*, 399–412.
- Intergovernmental Panel on Climate Change (2001), *Climate Change 2001: Impacts, Adaptation, and Vulnerability*, edited by J. J. McCarthy et al., Cambridge Univ. Press, New York.
- Johannesson, T., C. F. Raymond, and E. D. Waddington (1989), A simple method for determining the response time of glaciers, in *Glacier Fluctuations and Climate Change*, edited by J. Oerlemans, pp. 343–352, Springer, New York.
- Koerner, R. M. (1966), Accumulation on the Devon Island Ice Cap, Northwest Territories, Canada, *J. Glaciol.*, *6*, 383–392.

- Koerner, R. M. (1970), The mass balance of Devon Island Ice Cap Northwest Territories, Canada, 1961–1966, *J. Glaciol.*, *9*, 325–336.
- Koerner, R. M., and H. Taniguchi (1976), Artificial radioactivity layers in the Devon Island Ice Cap, Northwest Territories, *Can. J. Earth Sci.*, *13*, 1251–1255.
- Maxwell, B. (1997), *Responding to Global Climate Change in Canada's Arctic*, vol. 2, *The Canada Country Study: Climate Impacts and Adaptation*, 82 pp., Environ. Can., Downsview, Ont., Canada.
- Mitchell, J. F. B., T. C. Johns, J. M. Gregory, and S. F. B. Tett (1995), Climate response to increasing levels of greenhouse gases and sulphate aerosols, *Nature*, *376*, 501–504.
- Oerlemans, J., H. Bjornsson, M. Kuhn, F. Obleiter, F. Obleiter, F. Palsson, C. J. J. P. Smeets, H. F. Vugts, and J. De Wolde (1999), Glacio-meteorological investigations on Vatnajökull, Iceland, summer 1996, *Boundary Layer Meteorol.*, *92*, 3–26.
- Paterson, W. S. B., and N. Reeh (2001), Thinning of the ice sheet in north-west Greenland over the past forty years, *Nature*, *414*, 60–62.
- Pinglot, J. F., et al. (2003), Ice cores from Arctic sub-polar glaciers: Chronology and post-depositional process deduced from radioactivity measurements, *J. Glaciol.*, *49*, 149–158.
- Press, W. H., B. P. Flannery, S. A. Teukolsky, and W. T. Vetterling (1988), *Numerical Recipes in C*, Cambridge Univ. Press, New York.
- Woodward, J., M. Sharp, and A. Arendt (1997), The effect of superimposed ice formation on the sensitivity of glacier mass balance to climate change, *Ann. Glaciol.*, *24*, 186–190.

D. Burgess and M. Sharp, Department of Earth and Atmospheric Sciences, University of Alberta, Edmonton, Alberta, Canada T6G 2E3. (dob@ualberta.ca; martin.sharp@ualberta.ca)

D. Mair, Department of Geography and Environment, University of Aberdeen, Elphinstone Road, Aberdeen, AB24 3UF, UK. (d.mair@abdn.ac.uk)

Mass balance of Devon Ice Cap, Canadian Arctic

Andrew SHEPHERD,^{1*} Zhijun DU,¹ Toby J. BENHAM,¹ Julian A. DOWDESWELL,¹
Elizabeth M. MORRIS²

¹Scott Polar Research Institute, University of Cambridge, Lensfield Road, Cambridge CB2 1ER, UK
E-mail: andrew.shepherd@ed.ac.uk

²British Antarctic Survey, Natural Environment Research Council, Madingley Road, Cambridge CB3 0ET, UK

ABSTRACT. Interferometric synthetic aperture radar data show that Devon Ice Cap (DIC), northern Canada, is drained through a network of 11 glacier systems. More than half of all ice discharge is through broad flows that converge to the southeast of the ice cap, and these are grounded well below sea level at their termini. A calculation of the ice-cap mass budget reveals that the northwestern sector of DIC is gaining mass and that all other sectors are losing mass. We estimate that a 12 489 km² section of the main ice cap receives 3.46 ± 0.65 Gt of snowfall each year, and loses 3.11 ± 0.21 Gt of water through runoff, and 1.43 ± 0.03 Gt of ice through glacier discharge. Altogether, the net mass balance of DIC is -1.08 ± 0.67 Gt a⁻¹. This loss corresponds to a 0.003 mm a⁻¹ contribution to global sea levels, and is about half the magnitude of earlier estimates.

1. INTRODUCTION

The 3980 km³ Devon Ice Cap (DIC) in the Canadian Arctic is among the largest of Earth's ice caps, and forms a significant fraction of all land ice volume that lies beyond the Antarctic and Greenland ice sheets. While DIC's geographical location has exposed it to a range of climatic conditions (Paterson and others, 1977; Dowdeswell and others, 1997), general circulation models (Church and Gregory, 2001) consistently predict continued warming throughout the coming century. Moreover, recent studies (Braun and others, 2004) have shown that fluctuations in the mass of the world's smaller ice bodies will constitute the greatest cryospheric component of future sea-level rise, so a knowledge of the present state of balance of DIC is a subject of considerable interest (Burgess and Sharp, 2004).

Persistent monitoring of the DIC surface mass balance began in the early 1960s with sparse ($\sim 10^{-2}$ sites km⁻²) field surveys of accumulation and other parameters (Koerner, 1966). More recently, a change in the ice-cap volume has been reported (Abdalati and others, 2004) based on repeat sorties of an airborne laser altimeter, and an estimate of the DIC surface mass balance has been produced (Mair and others, 2005) using accumulation data from eight boreholes and a model of ablation. From these surveys, it was concluded that the ice cap lost 0.8 km³ of ice each year between 1995 and 2000, and 1.6 ± 0.7 km³ a⁻¹ over the longer period 1963–2000. Another study (Burgess and others, 2005) used satellite interferometric synthetic aperture radar (InSAR) and other data to estimate the rate of mass loss due to iceberg calving between 1960 and 1999, and concluded the ice cap was losing 0.57 ± 0.12 km³ of ice each year through glacier outflow. Although separate studies, these works put the long-term (30 year) mass balance of DIC at about -2.2 ± 0.7 Gt a⁻¹, a loss sufficient to raise global sea levels by 0.006 mm a⁻¹. Here, we use InSAR measurements of ice discharge, in situ records of snow accumulation, and a positive degree-day model of summer ablation, to reach a new, absolute estimate of the DIC mass balance.

2. DATA

We use European Remote-sensing Satellite (ERS) synthetic aperture radar (SAR) data recorded during the tandem-repeat phase to produce repeat-pass interferograms from two separate satellite ground tracks. No ERS data were recorded during descending orbits at DIC, so we used data from ascending orbits only (their trajectory is shown in Fig. 1a). The distribution of our SAR dataset allowed us to form interferograms with temporal baselines of 1 or 35 days in spring 1996 (Table 1); data were not available for other time periods. The width of the SAR images was ~ 100 km, so it was necessary to mosaic data from two adjacent ERS tracks in order to survey the entire DIC.

2.1. InSAR DEM

Although a recent airborne survey has provided models of the DIC surface and bedrock elevations (Dowdeswell and others, 2004), their ~ 1 km horizontal resolution is lower than that required for InSAR processing. Instead, we derived a new, fine spatial resolution digital elevation model (DEM) to facilitate our InSAR estimates of the ice-cap surface deformation, ice-flow direction and mass flux. We formed the DEM using differential interferograms from the two ERS tandem (1 day) pairs (Table 1). Their baselines were constrained (Zebker and others, 1994) with ground-control points (GCPs) of known elevation. The spatial resolution of the new InSAR DEM is 40 m, ~ 250 times finer than that of the airborne survey. To assess its accuracy, we re-sampled the InSAR DEM to the same ground resolution as the airborne DEM, and the root-mean-square (rms) deviation between the two models was 18 m. This was comparable to the precision of the airborne dataset, so we conclude that the two elevation models were indistinguishable.

2.2. Ice surface velocity

We used InSAR to measure the DIC surface displacement in the look direction of the SAR sensor (e.g. Joughin and others, 1996; Shepherd and others, 2001) from data recorded during ascending orbits only (Table 1). In the absence of data from alternate viewing geometries, it was necessary to make assumptions as to the ice-flow direction in order to derive

*Present address: School of GeoSciences, University of Edinburgh, Drummond Street, Edinburgh EH8 9XP, UK.

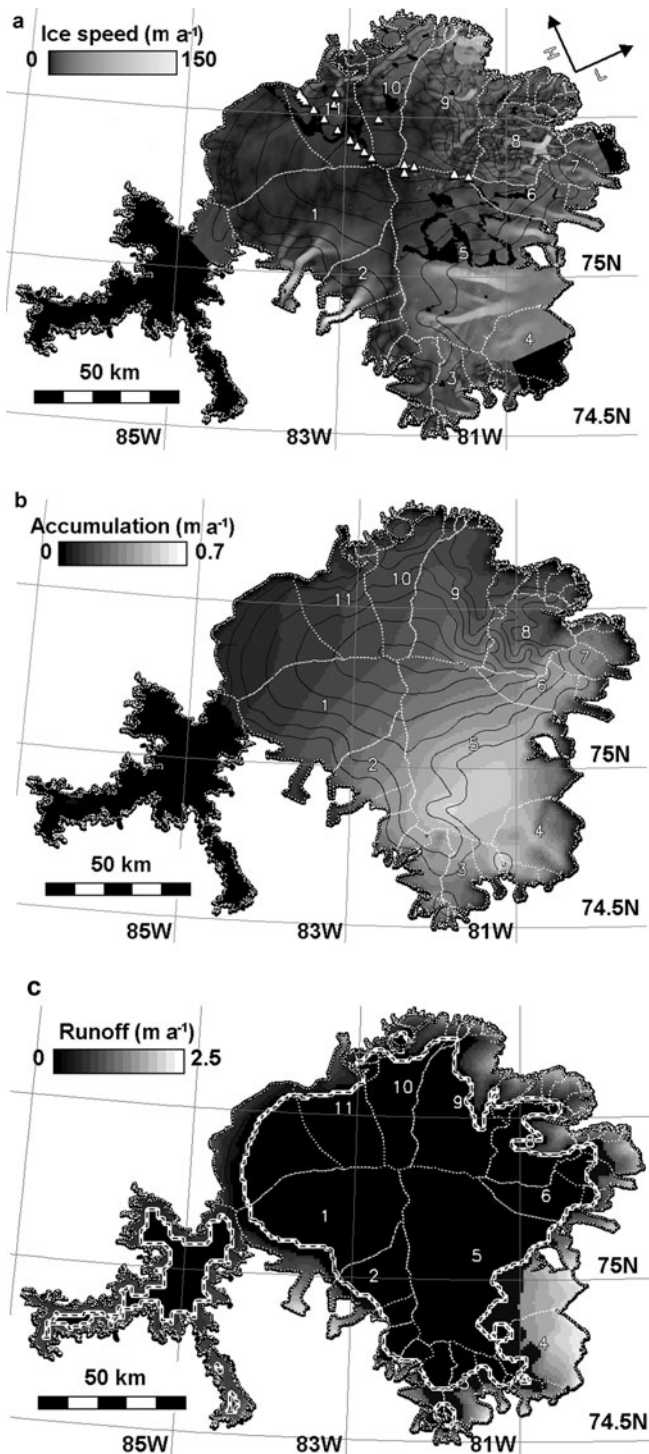


Fig. 1. (a) Ice speed (greyscale in m a^{-1}) of DIC measured in spring 1996 from 1 day repeat-pass InSAR. Dotted white lines mark the boundaries of the major drainage basins (numbered as in Table 2), where mass flux was determined through gates bisecting glacier flows near to their termini. Ice surface elevation contours are shown in black. White triangles mark a northwestern traverse along which field measurements of ice motion were recorded. Also shown are the trajectories of the satellite heading (H) and the satellite look direction (L). (b) Snow accumulation (greyscale in m a^{-1}) derived (see text) from a collection of in situ measurements distributed across the ice-cap centre, and meteorological records at sea level. (c) Runoff (greyscale in m a^{-1}) derived (see text) from a PDD model of ablation and estimated accumulation (b). The modelled equilibrium line is also shown (bold, dotted line). Areas of no data are shown in black.

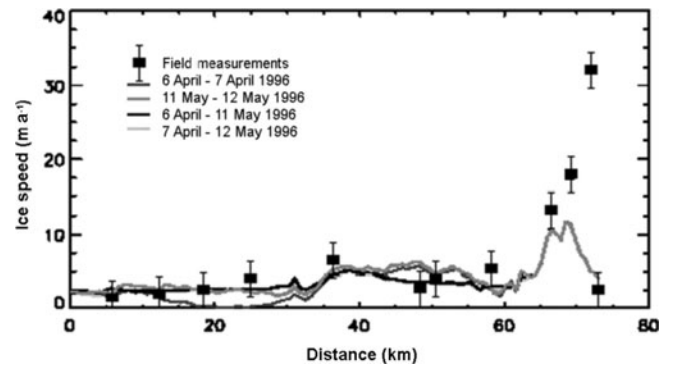


Fig. 2. Ice velocity determined along a profile of DIC extending from the summit to the ice-cap margin. The profile bisects the field measurement locations shown in Figure 1a. Filled squares are annual velocity measurements recorded as the motion of stakes on the ice-cap surface between 1999 and 2001. Grey lines are velocity measurements determined from four separate satellite radar interferograms of data recorded in spring 1996. Coherence is lost in radar interferograms formed over 35 day periods at speeds greater than $\sim 5 \text{ m a}^{-1}$. There is no significant variation in ice-flow rates during the ~ 1 month period of the satellite measurements.

estimates of the ice velocity. As a common practice, we adopted the assumption of surface-parallel ice flow (Kwok and Fahnestock, 1996). By subtracting a model of the interferometer phase due to topography, we obtained the signal due to surface displacement (Goldstein and others, 1993). To minimize the error due to non-parallel flow, we calculated the direction of maximum slope from a smoothed version of the InSAR DEM, averaged horizontally over a distance equal to ten times the ice thickness. In this way, the effects of short-scale variations in surface topography were eliminated. We determined the DIC ice-flow velocity in April and May 1996 (Table 1; Figs 1a and 2).

Errors in estimating the interferometer baseline, and our potentially inaccurate prescription of the ice-flow direction, will affect the accuracy of ice velocity data. After applying the GCPs, we estimated the error due to baseline uncertainties by considering the interferometer phase in areas of exposed bedrock. The standard deviation of the interferometer phase was 2.7 rad, corresponding to a velocity uncertainty of 3.8 m a^{-1} . The residual signal due to uncompensated vertical motion (after applying a slope correction (Joughin and others, 1996)) is difficult to estimate. Comparison of velocity results with and without corrections for vertical velocity led to erroneous short-scale variability, and the mean deviation was 4.7 m a^{-1} . Assuming half of this variability remains after applying the correction, the combined estimate of velocity errors was 4.5 m a^{-1} . Finally, because the InSAR observations are sensitive to the SAR look direction, estimates of ice velocity in areas where the flow direction was within 5° of the SAR ground track direction were discarded (about 5% of all data).

The InSAR data record springtime velocity at DIC, and the maximum rate of flow measured was 175 m a^{-1} at the terminus of a glacier flowing into Croker Bay (73.57° N , 82.92° W). We compared the satellite observations to a set of field measurements recorded between 1999 and 2001 at 23 stakes located along a northwestern traverse of DIC (see Fig. 1a). Stakes were positioned in April 1999, and re-surveyed in April 2000 and April 2001. Their locations were recorded using standard differential global positioning

Table 1. ERS-1/-2 data used in this study. SD: single difference; DD: double difference

Data	Orbits	Track	Dates (in 1996)	Perpendicular baseline m
ERS-1/-2 SD	e1 24712/e2 05039	175	6 Apr./7 Apr.	60
ERS-1/-2 SD	e1 25213/e2 05540	175	11 May/12 May	-3
ERS-1/-2 SD	e1 24898/e2 05225	361	19 Apr./20 Apr.	62
ERS-1/-2 SD	e1 25399/e2 05726	361	24 May/25 May	12
ERS-1/-2 DD	e1 24712/e2 05039e1 25213/e2 05540	175	6 Apr./7 Apr., 11 May/12 May	63
ERS-1/-2 DD	e1 24898/e2 05225e1 25399/e2 05726	361	19 Apr./20 Apr., 24 May/25 May	50
ERS-1 SD	e1 24712/e1 25213	175	6 Apr./11 May	175
ERS-2 SD	e2 05039/e2 05540	175	7 Apr./12 May	117

system (GPS) surveying techniques. On average, the difference between the 1999–2001 annual velocity measurements and those derived from InSAR in spring 1996 was only 5%, within the relative precision of the two datasets. However, there were five stakes located in the ablation zone near to Sverdrup Glacier (75.67° N, 83.25° W) where flow speeds exceed 50 m a⁻¹. At these locations, the average difference between annual and springtime velocities was 16%, exceeding the measurement error at all fast-flowing locations (Fig. 2).

3. MASS BALANCE

Several approaches have been used to determine ice mass balance in glaciology. The approach we consider here is commonly referred to as the mass-budget method (e.g. Rignot and others, 1997). It compares mass accumulation in the interior with runoff and ice discharge across its boundary. The difference between these typically large values determines whether the ice body is losing or gaining mass.

3.1. Ice discharge

We calculated the ice discharge of DIC through flux gates close to the termini of all outlet glaciers (e.g. Rott and others, 1998) from the InSAR ice velocity mosaic and a model of the ice-cap thickness. Errors in this estimation were introduced

by uncertainties in ice thickness, estimated to be accurate to within 10 m, and, to a lesser degree, by uncertainties in ice velocity, estimated to be 4.5 m a⁻¹. The majority of ice discharge from DIC was through 11 fast-flowing glacier systems, and we determined the mass flux across gates near to the termini of each of these outlets (Table 2). The greatest outflows were at two unnamed glaciers (basin 5) to the southeast of DIC, and their total mass transport was 0.32 ± 0.02 Gt a⁻¹, 73% of the glacier flux from basin 5. In spring 1996, the total rate of ice discharge from DIC glaciers was 0.80 ± 0.02 Gt a⁻¹ (Table 2).

Phase noise and incoherence in the InSAR dataset prevented us from marking the absolute terminus of each outlet glacier, and because of this there was a measure of ice mass transport in slow-moving sectors of the ice sheet proximal to each gate. We marked a boundary just inland (a few km) of the ice-cap margin and adjacent to glacier flux gates to compute the ice export from adjacent, slow-moving sectors. Together, this boundary and the glacier flux gates (hereafter the DIC boundary) enclose 12 489 km² of the main DIC, and form the limit of our mass-balance calculations. The mechanism of mass loss beyond the DIC boundary does not affect our calculation; we simply omit those regions and present the mass balance of the main ice cap. Our velocity data also exclude the 1980 km² western arm, east of 84° W and south of 75° N, so our survey omits ~15% of the ice covered area.

Table 2. Drainage basins, boundary flow, accumulation, runoff and ice mass balance of DIC. Drainage basins 1–11, as defined in Figure 1, comprise 77% of the ice-cap area. Mass balance is calculated as the summation of accumulation (+), annual boundary flow (–) and runoff (–)

Basin	Area km ²	Winter glacier flux Gt a ⁻¹	Winter boundary flux Gt a ⁻¹	Annual flux Gt a ⁻¹	Accumulation Gt a ⁻¹	Runoff Gt a ⁻¹	Mass balance Gt a ⁻¹
1	1667	0.07 ± 0.01	0.03 ± 0.00	0.10 ± 0.01	0.31 ± 0.06	0.27 ± 0.01	-0.05 ± 0.06
2	516	0.08 ± 0.01	0.02 ± 0.00	0.11 ± 0.01	0.16 ± 0.03	0.14 ± 0.02	-0.09 ± 0.04
3	286	0.01 ± 0.00	0.00 ± 0.00	0.02 ± 0.00	0.10 ± 0.02	0.12 ± 0.03	-0.03 ± 0.04
4	581	0.05 ± 0.01	0.08 ± 0.01	0.14 ± 0.01	0.23 ± 0.04	0.66 ± 0.06	-0.57 ± 0.07
5	2631	0.32 ± 0.02	0.10 ± 0.01	0.44 ± 0.02	1.12 ± 0.21	0.57 ± 0.02	0.11 ± 0.21
6	404	0.02 ± 0.00	0.03 ± 0.00	0.05 ± 0.00	0.15 ± 0.03	0.07 ± 0.01	0.03 ± 0.03
7	191	0.03 ± 0.00	0.02 ± 0.00	0.05 ± 0.00	0.07 ± 0.01	0.05 ± 0.02	-0.03 ± 0.03
8	628	0.03 ± 0.00	0.01 ± 0.00	0.05 ± 0.00	0.16 ± 0.03	0.08 ± 0.01	0.04 ± 0.03
9	1182	0.14 ± 0.01	0.01 ± 0.00	0.16 ± 0.01	0.25 ± 0.05	0.16 ± 0.01	-0.07 ± 0.05
10	669	0.04 ± 0.00	0.00 ± 0.00	0.05 ± 0.00	0.12 ± 0.02	0.04 ± 0.01	0.04 ± 0.02
11	808	0.02 ± 0.00	0.01 ± 0.00	0.03 ± 0.00	0.12 ± 0.02	0.06 ± 0.01	0.03 ± 0.02
1 to 11	9563	0.80 ± 0.02	0.31 ± 0.01	1.16 ± 0.03	2.80 ± 0.53	2.20 ± 0.15	-0.56 ± 0.55
DIC total	12489	0.80 ± 0.02	0.58 ± 0.02	1.43 ± 0.03	3.46 ± 0.65	3.11 ± 0.21	-1.08 ± 0.68

Old ground-based measurements of glacier velocity at DIC (Cress and Wyness, 1961) show strong seasonal variations, and we observe a similar difference between the InSAR and field measurements in this study, which survey different time periods. Our estimates (see section 3.3) of summer melting at DIC show that surface waters, which are often presumed to affect glacier speed (e.g. Zwally and others, 2002), are present between June and August. In 1996, melting was first detected on 9 June at sea level, so we conclude that our InSAR estimates of ice motion (recorded before 25 May) are representative of the winter velocity minima. To estimate the rate of annual ice discharge, we determined an empirical relationship between the InSAR spring velocities and the mean annual rate of ice flow, based on in situ observations of annual speeds and a hypothesis of summertime acceleration. This adjustment is applied to the fast-flowing outlets only. We suppose that the annual velocity distribution is bimodal, with enhanced flow for the duration of each summer at a rate that equals a constant multiple of the winter value. In this simple model (Equation (1)), the mean annual ice velocity (\bar{v}) varies according to the winter velocity (v_w) and the melt season duration (d) via the summertime enhancement factor (f) which we determined empirically to be 1.6 ± 0.4 . This value is comparable to the ratio of summertime and springtime velocities (1.8) recorded at Sverdrup Glacier in 1961 (Cress and Wyness, 1961). Using Special Sensor Microwave/Imager data (unpublished), we estimate that between 1998 and 2002 the summer melting season on DIC was, on average, 40 ± 16 days long. With these parameters, our model predicts that mean annual glacier velocities at DIC are, on average, $6.5 \pm 3.1\%$ greater than winter values.

$$\bar{v} = v_w \left(1 + \frac{d(f-1)}{365} \right) \quad (1)$$

Using the wintertime ice outflow across the slow-moving sectors of the DIC boundary (Table 1) and our model of the seasonal velocity variations (Equation (1)) to predict the annual fast-flowing glacier outflow, we estimate the average annual DIC outflow is $1.43 \pm 0.03 \text{ Gt a}^{-1}$. This value is $\sim 4\%$ larger than the combined winter outflow. More detailed summertime velocity data are required to clarify the exact nature of the seasonal fluctuation we have recorded here.

3.2. Snow accumulation

Field measurements (Koerner, 1966) recorded during the 1960s show that the average winter snow depth across a 5127 km^2 sector of DIC was equivalent to 23 cm of water (cm w.e.), and that summer accumulation added a further $\sim 10\%$ to this value (Koerner, 1970). Since then, winter snow depth at an annually sampled northwestern traverse has barely fluctuated, with a 40 year mean value of $11 \pm 2 \text{ cm w.e.}$ (Haeberli and others, 1998) and similar rates ($11 \pm 3 \text{ cm w.e.}$) for the periods 1962, 1963, 1965 and 1988–2002, during which spatially extensive measurements exist. We adopt the spatially extensive accumulation data (Koerner, 1966) and characterize their temporal variability from that of the 40 year dataset (Haeberli and others, 1998). These data, however, span only the central region (about 50%) of DIC, and provide no coverage of the ice-cap perimeter. To augment these data, we derived estimates of spring snow depth from the ten meteorological stations surrounding DIC that meet World Meteorological Organization (WMO) standards for climatology (Environment

Canada, http://www.climate.weatheroffice.ec.gc.ca/climateData/canada_e.html), and interpolated the combined dataset onto a regular grid (Fig. 1b). The resulting accumulation model agrees well with estimates derived from eight ice cores drilled on the central ice cap (Mair and others, 2005), and the rms difference in the annual accumulation rate determined from the independent datasets was $52 \text{ mm w.e. a}^{-1}$. From our combined dataset, we estimate that the average annual accumulation rate within the DIC boundary was $3.46 \pm 0.65 \text{ Gt a}^{-1}$ (Table 2).

3.3. Water runoff

We simulated runoff in 1996 (the year of our velocity data) from DIC using a positive degree-day (PDD) model (Reeh, 1991). To drive this model, we used sea-level temperature data from the International Arctic Buoy Program (IABP) database (Rigor and others, 2000) at nine locations surrounding DIC, and in situ temperatures recorded at an automatic weather station (AWS) sited near to the ice-cap summit (1900 m elevation) (Koerner, 2005). We determined an atmospheric lapse rate of $-4.575^\circ\text{C km}^{-1}$ from these records, and modelled the number of PDDs across the ice cap from the IABP dataset and our DEM of the surface elevation. For the Greenland ice sheet, melting factors are generally assumed to be $3 \text{ mm w.e. PDD}^{-1}$ for snow and $8 \text{ mm w.e. PDD}^{-1}$ for ice (Braithwaite, 1995). Although higher PDD factors (up to $14 \text{ mm w.e. PDD}^{-1}$) have been estimated (Mair and others, 2005) for individual sectors of DIC, when compared to other empirically derived estimates, these appear excessive, and our analysis of the IABP database suggests that they may be affected by an underestimate of the degree of melting in this region. For instance, sea-level temperatures to the southeast of DIC are consistently 2°C warmer than those to the northwest, leading to summer melting seasons that are, on average, 32 days longer in Baffin Bay (109 ± 8 days) than those north of Sverdrup Glacier (77 ± 7 days). In the absence of more detailed in situ measurements, we make no attempt to derive empirical degree-day factors here, and we adopt standard values of Braithwaite (1995) for ice- and snowmelting. However, while the melting factors of Mair and others (2005) are 25–40% higher than those we adopt here, the annual degree-day total at Sverdrup is 30% lower than that at Baffin Bay, so it seems likely that the two models will concur within the bounds of experimental error. Using the PDD values of Braithwaite (1995), we estimate (see Fig. 1c) that runoff from the DIC surface in 1996 was $3.11 \pm 0.21 \text{ Gt a}^{-1}$.

3.4. Net mass balance

The net mass balance of the main DIC is the difference between the accumulation and the sum of annual boundary flow and the total runoff from the ice-cap surface. Based on our estimates of these quantities, we are able to conclude that at present DIC is losing mass at a rate of $1.08 \pm 0.66 \text{ Gt a}^{-1}$ (Table 2). A more detailed inspection, however, reveals a marked geographical trend. Many basins (e.g. basins 2–7) in the southeastern sector of DIC are losing mass, whereas those to the northwest (basins 10–11) are gaining mass. This result is in qualitative agreement with the conclusions of a recent study of the surface mass balance (Mair and others, 2005), since both reveal mass gains in the northwest, although there is a substantial difference in the overall mass trend. A direct comparison can only be made between the sum of surface mass balance and glacier

discharge, that is a combination of the Burgess and others (2005) and Mair and others (2005) trends. Together, those studies suggest DIC has lost $2.17 \pm 0.71 \text{ Gt a}^{-1}$. While this value agrees with our estimate within error bounds, the central values are a factor of two apart.

4. DISCUSSIONS AND CONCLUSIONS

A new velocity map derived from InSAR data shows that DIC is drained through a network of 11 major glacier systems. Whilst the fastest rate of flow is along a narrow outlet at the southwest of the ice cap, the greatest mass transport drains through three broad southeastern glaciers that converge near Philpots Island (74.9° N , 80.0° W). These glaciers, and others of DIC, flow at rates greatly exceeding those due to gravitational creep deformation – typically $< 2 \text{ m a}^{-1}$ – and are presumably enhanced by some other mechanism that provides spatial variations in glacier traction. Field measurements suggest that there is a near-twofold increase in ice-flow speeds during summer months, a change that we hypothesize is related to seasonal variations in glacier lubrication. Accounting for this increase, the annual ice discharge is, on average, 7% greater than during the winter quiescent period.

We find that the main DIC is presently losing mass at a rate of $1.08 \pm 0.66 \text{ Gt a}^{-1}$, equivalent to a global sea-level contribution of $+0.003 \text{ mm a}^{-1}$ or 31% of the mean annual accumulation rate. This value is half that of an estimate based on the results of two past studies (Burgess and others, 2005; Mair and others, 2005) which considered partial components of the mass budget, albeit within allowed error bounds. Since the study areas considered were not dissimilar, it appears that the departure is related to experimental methods. We suggest that the most likely source of difference lies in the assessment of surface mass balance. Although our estimates of snow accumulation and water runoff consider both altitudinal and geographical trends associated with climatic gradients, the results of earlier studies (Mair and others, 2005) are of insufficient detail to make a useful or meaningful comparison. Nonetheless, there is good evidence (Koerner, 1966) to suggest that katabatic winds redistribute snowfall in an asymmetric manner, and that rates of melting in the southeastern sector are governed by temperature gradients (Rigor and others, 2000) and not locally high ablation factors. Of course, in the absence of more detailed in situ measurements, it is equally possible that this and earlier estimates of the DIC mass balance concur.

Because the field data (Koerner, 1966; Haeberli and others, 1998) show that there has been no significant variation in snow accumulation over the past 40 years, and because the velocity data (Cress and Wyness, 1961) show a seasonal variation, it seems reasonable to suppose that any future increase in the DIC temperature will exacerbate today's rate of attrition. It would not only lead to increased rates of ablation, but it may also accelerate glacier ice discharge (e.g. Zwally and others, 2002). While it is possible that the growth of the northwestern DIC reflects a delayed ice-dynamic response to the cooler conditions (Fisher and others, 1998) that prevailed during the Little Ice Age, it seems certain that the remainder of the ice cap is already out of balance with contemporary accumulation rates. The data do, therefore, support the notion that projected trends in climate warming during the 21st century provide clear mechanisms for rapid fluctuations in the grounded ice mass of the Arctic region.

ACKNOWLEDGEMENTS

This research was supported by the UK Natural Environment Research Council Centre for Polar Observation and Modelling. We thank the European Space Agency Vectra consortium for provision of ERS data, and I. Joughin for helpful comments on the manuscript.

REFERENCES

- Abdalati, W. and 9 others. 2004. Elevation changes of ice caps in the Canadian Arctic Archipelago. *J. Geophys. Res.*, **109**(F4), F04007. (10.1029/2003JF000045.)
- Braithwaite, R.J. 1995. Positive degree-day factors for ablation on the Greenland ice sheet studied by energy-balance modelling. *J. Glaciol.*, **41**(137), 153–160.
- Braun, C., D.R. Hardy and R.S. Bradley. 2004. Mass balance and area changes of four High Arctic plateau ice caps, 1959–2002. *Geogr. Ann.*, **86A**(1), 43–52.
- Burgess, D.O. and M.J. Sharp. 2004. Recent changes in areal extent of the Devon Ice Cap, Nunavut, Canada. *Arct. Antarct. Alp. Res.*, **36**(2), 261–271.
- Burgess, D.O., M.J. Sharp, D.W.F. Mair, J.A. Dowdeswell and T.J. Benham. 2005. Flow dynamics and iceberg calving rates of Devon Ice Cap, Nunavut, Canada. *J. Glaciol.*, **51**(173), 219–230.
- Church, J.A. and J.M. Gregory. 2001. Changes in sea level. In Houghton, J.T. and 7 others, eds. *Climate change 2001: the scientific basis. Contribution of Working Group I to the Third Assessment Report of the Intergovernmental Panel on Climate Change*. Cambridge, etc., Cambridge University Press, 639–693.
- Cress, P. and R. Wyness. 1961. The Devon Island expedition, observations of glacial movements. *Arctic*, **14**(4), 257–259.
- Dowdeswell, J.A. and 10 others. 1997. The mass balance of circum-Arctic glaciers and recent climate change. *Quat. Res.*, **48**(1), 1–14.
- Dowdeswell, J.A., T.J. Benham, M.R. Gorman, D. Burgess and M. Sharp. 2004. Form and flow of the Devon Island ice cap, Canadian Arctic. *J. Geophys. Res.*, **109**(F2), F02002. (10.1029/2003JF000095.)
- Fisher, D.A. and 12 others. 1998. Penny Ice Cap cores, Baffin Island, Canada, and the Wisconsinan Foxe Dome connection: two states of Hudson Bay ice cover. *Science*, **279**(5351), 692–695.
- Goldstein, R.M., H. Engelhardt, B. Kamb and R.M. Frolich. 1993. Satellite radar interferometry for monitoring ice sheet motion: application to an Antarctic ice stream. *Science*, **262**(5139), 1525–1530.
- Haeberli, W., M. Hoelzle, S. Suter and R. Frauenfelder, comps. 1998. *Fluctuations of glaciers 1990–1995 (Vol. VII)*. Wallingford, Oxon., IAHS Press; Nairobi, UNEP; Paris, UNESCO.
- Joughin, I., R. Kwok and M. Fahnestock. 1996. Estimation of ice-sheet motion using satellite radar interferometry: method and error analysis with application to Humboldt Glacier, Greenland. *J. Glaciol.*, **42**(142), 564–575.
- Koerner, R.M. 1966. Accumulation on the Devon Island ice cap, Northwest Territories, Canada. *J. Glaciol.*, **6**(45), 383–392.
- Koerner, R.M. 1970. The mass balance of the Devon Island ice cap, Northwest Territories, Canada, 1961–66. *J. Glaciol.*, **9**(57), 325–336.
- Koerner, R.M. 2005. Mass balance of glaciers in the Queen Elizabeth Islands, Nunavut, Canada. *Ann. Glaciol.*, **42**, 417–423.
- Kwok, R. and M.A. Fahnestock. 1996. Ice sheet motion and topography from radar interferometry. *IEEE Trans. Geosci. Remote Sens.*, **34**(1), 189–200.
- Mair, D., D. Burgess and M. Sharp. 2005. Thirty-seven year mass balance of Devon Ice Cap, Nunavut, Canada, determined by shallow ice coring and melt modelling. *J. Geophys. Res.*, **110**(F1), F01011. (10.1029/2003JF000099.)

- Paterson, W.S.B. and 7 others. 1977. An oxygen-isotope climatic record from the Devon Island ice cap, Arctic Canada. *Nature*, **266**(5602), 508–511.
- Reeh, N. 1991. Parameterization of melt rate and surface temperature on the Greenland ice sheet. *Polarforschung*, **59**(3), 113–128.
- Rignot, E.J., S.P. Gogineni, W.B. Krabill and S. Ekholm. 1997. North and north-east Greenland ice discharge from satellite radar interferometry. *Science*, **276**(5314), 934–937.
- Rigor, I.G., R.L. Colony and S. Martin. 2000. Variations in surface air temperature observations in the Arctic, 1979–97. *J. Climate*, **13**(5), 896–914.
- Rott, H., M. Stuefer, A. Siegel, P. Skvarca and A. Eckstaller. 1998. Mass fluxes and dynamics of Moreno Glacier, Southern Patagonia Icefield. *Geophys. Res. Lett.*, **25**(9), 1407–1410.
- Shepherd, A., D.J. Wingham, J.A.D. Mansley and H.F.J. Corr. 2001. Inland thinning of Pine Island Glacier, West Antarctica. *Science*, **291**(5505), 862–864.
- Zebker, H.A., C.L. Werner, P.A. Rosen and S. Hensley. 1994. Accuracy of topographic maps derived from ERS-1 interferometric radar. *IEEE Trans. Geosci. Remote Sens.*, **32**(4), 823–836.
- Zwally, H.J., W. Abdalati, T. Herring, K. Larson, J. Saba and K. Steffen. 2002. Surface melt-induced acceleration of Greenland ice-sheet flow. *Science*, **297**(5579), 218–222.

Sensitivity of net mass balance estimates to near-surface temperature lapse rates when employing the degree day method to estimate glacier melt

Alex S. GARDNER, Martin SHARP

*Department of Earth and Atmospheric Sciences, University of Alberta, Edmonton, Alberta, Canada, T6G 2E3
E-mail: alexg@ualberta.ca*

ABSTRACT. Glacier mass balance models that employ the degree day method of melt modeling are most commonly driven by surface air temperatures that have been downscaled over the area of interest, using digital elevation models and assuming a constant free air lapse rate that is often taken to be the moist adiabatic lapse rate (MALR: $-6.5^{\circ}\text{C km}^{-1}$). Air temperature lapse rates measured over melting glacier surface are, however, consistently less steep than free air values and have been shown to vary systematically with lower tropospheric temperatures. In this study the implications of including a variable near-surface lapse rate in a 26 year (1980–2006) degree day model simulation of the surface mass balance of the Devon Ice Cap, Nunavut, Canada are examined and compared with estimates derived from surface air temperatures downscaled using a constant near-surface lapse rate equal to the measured summer mean ($-4.9^{\circ}\text{C km}^{-1}$) and the MALR. Our results show that degree day models are highly sensitive to the choice of lapse rate. When compared with 23 years of surface mass balance measurements from the northwest sector of the ice cap, model estimates are significantly better when surface air temperatures are downscaled using a modeled daily lapse rate rather than a constant lapse equal to either the summer mean or the MALR.

INTRODUCTION

The magnitude of glacier ablation depends on the energy balance at the glacier surface. For remote glacier locations, the large amounts of data required to determine this balance are often unavailable. For this reason, degree day models (DDMs) based on the strong observed relationship between glacier melt and near-surface air temperatures are often used to estimate surface melt. Most studies that employ DDMs must downscale or interpolate climate model output and/or station observations to the area of interest. For spatially distributed models, temperature fields must be generated to reflect local conditions, which often include complex topography. This is most commonly done through the use of digital elevation models and a constant free air lapse rate that is often assumed to be the moist adiabatic lapse rate ($6\text{--}7^{\circ}\text{C km}^{-1}$). The problem with this approach is that temperature lapse rates measured over melting glacier surfaces have been found to be systematically less steep than the free air values (Greuell and Böhm, 1998; Braun and Hock, 2004; Hanna and others, 2005; Marshall and others, 2007). These deviations are mainly the result of temperatures over melting surfaces being fixed at 0°C , while free atmospheric temperatures generally increase with decreasing elevation. This can generate strong temperature gradients between the surface and overlying atmosphere that increase with decreasing elevation when air temperature is above 0°C . The strong temperature gradients drive a sensible heat flux that cools the near-surface atmosphere at lower elevations and effectively reduces the magnitude of the near-surface temperature lapse rates (Greuell and Böhm, 1998).

Recent investigations into near-surface temperature lapse rates in the Canadian High Arctic show that lapse rates vary on both seasonal and daily timescales (Marshall and others, 2007). Gardner and others (in press) found that during the

summer months (JJA) lapse rates vary systematically with daily mean air temperatures in the lower (i.e. 750 mbar) troposphere. They concluded that much of the observed covariability was due to an increase in the climate sensitivity of screen-level temperatures with increasing elevation (c.f. Denby and others, 2002), where ‘climate sensitivity’ is defined as the change in near-surface temperature relative to a change in the free atmospheric temperature.

In this study we examine the implications of including variable near-surface lapse rates (VLR) in DDM simulations of the surface mass balance of the Devon Ice Cap, Nunavut, Canada. Surface mass balance estimates are determined for the years 1980–2006 and are evaluated against 23 years (1980–2003) of surface mass balance measurements from the northwest sector of the ice cap (Koerner, 1970). These results are also compared with estimates derived using the assumption that model temperatures can be downscaled using a constant near-surface lapse rate equal to either the measured summer (JJA) mean lapse rate (GLR) or the moist adiabatic lapse rate (MALR).

SITE AND DATA DESCRIPTION

The Devon Ice Cap is a large ($14\,000\text{ km}^2$; Dowdeswell and others, 2004) dome-shaped ice mass covering much of the eastern part of Devon Island, Nunavut, Canada (Fig. 1). From 1961 to present, the Geological Survey of Canada (GSC) has made physical measurements of the net surface mass balance b_n along a 40 km-long stake network following a path from the glacier summit (1880 m a.s.l.) to the terminus of the Sverdrup outlet glacier in the northwest sector of the ice cap (Fig 1; Koerner, 2005). Previous estimates of surface mass balance (mm w.e. a^{-1}) for the main ice cap (excluding the southwest arm) vary greatly between study periods: -76 ± 50 (1961–66; Koerner, 1970), -30 ± 60 (1963–2000:

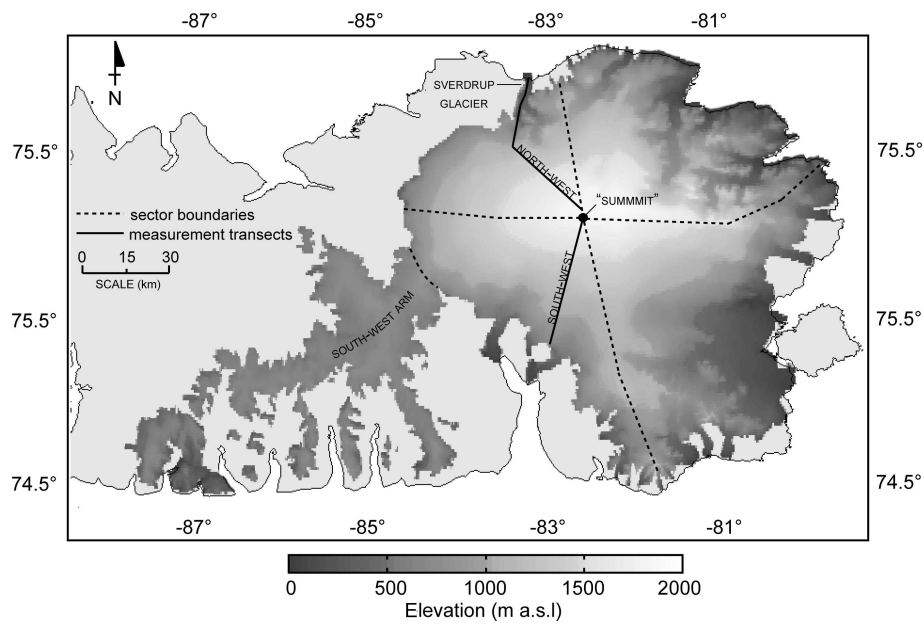


Fig. 1. The Devon Ice Cap shown with region boundaries and transects along which field measurements have been taken.

Mair and others, 2005) and $+28 \pm 70$ (1996: Shepherd and others, 2007).

Continuous meteorological measurements have been made on the ice cap since 1997, with as many as 7 automatic weather stations and 13 temperature sensors operating along 2 transects in 2004 (Fig. 1). Near-surface temperature lapse rates derived from these transects show strong linear relationships ($r = 0.72$) with summit elevation temperatures (Fig. 2).

MASS BALANCE MODEL

Glacier melt

The Degree Day glacier Mass Balance model (DDM) determines the daily quantity of melt m_t (mm w.e.) as a function of the mean daily air temperature T_t ($^{\circ}\text{C}$) using a factor of proportionality referred to as the degree day factor DDF (units: $\text{mm d}^{-1} \text{ } ^{\circ}\text{C}$):

$$m_t = DDF \cdot T_t \quad T_t \geq 0 \text{ deg C}$$

$$m_t = 0 \quad T_t < 0 \text{ deg C}$$

Owing to differences in the surface energy balance characteristics of snow and ice (including albedo, shortwave penetration, thermal conductivity and surface roughness),

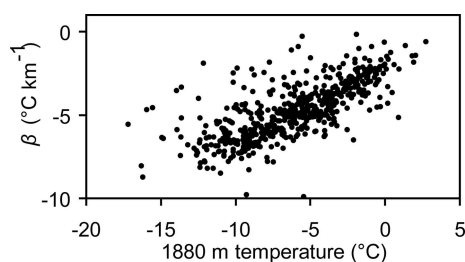


Fig. 2. Average daily lapse rates (β) for the northwest transects plotted against respective mean daily summit air temperatures.

separate values are used for snow (DDF_s) and ice (DDF_i). Reported factors vary greatly from study to study, depending on local variations in the surface energy balance (albedo, incoming solar radiation, surface roughness, wind speed and air temperature), how melt was determined (measured or modeled), the time period over which the study was conducted, and how air temperatures were determined (daily or hourly mean). Hock (2003) provides a comprehensive review of the temperature-index melt modeling method. For this study we adopt the values $DDF_s = 3.3 \text{ mm d}^{-1} \text{ } ^{\circ}\text{C}$ and $DDF_i = 8.2 \text{ mm d}^{-1} \text{ } ^{\circ}\text{C}$, which are the mean values determined by Braithwaite (1995) at two locations (880 and 790 m a.s.l.) on the Greenland ice sheet. Braithwaite (1995) obtained these values through the use of an energy balance model over a 6 year period and they agree well with factors determined from stake measurements made at the same locations. These are the same factors used by Shepherd and others (2007) to model melt over the Devon Ice Cap for 1996 and compared with $DDF_s = 4$ and $DDF_i = 6\text{--}14 \text{ mm d}^{-1} \text{ } ^{\circ}\text{C}$ used by Mair and others (2005) to model melt over the ice cap for the years 1963–2000.

Surface air temperature and downscaling

Daily mean surface air temperatures were downscaled to the entire ice cap from summit elevation temperatures using both modeled mean daily and assumed constant lapse rates and a 30×30 sec digital elevation model (DEM, Canada3D: available from Natural Resources Canada). Daily mean 2 m air temperatures from the North American Regional Reanalysis (NARR: Mesinger and others, 2006) were extracted for the model grid cell centered on the summit of the ice cap and were corrected for a mean summer (JJA) temperature offset of $+4^{\circ}\text{C}$ relative to 8 years (1997–2004) of air temperature measurements from an on-glacier weather station located near the summit of the ice cap. The 4°C offset in the NARR air temperature is partly due to the coarse resolution of the NARR model topography, which models the maximum elevation of the Devon Ice Cap at an elevation 400 m lower than the true summit elevation. After adjusting

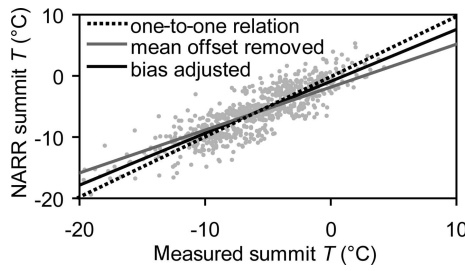


Fig. 3. NARR bias adjusted summer (JJA) daily summit air temperatures (T) plotted against measured summit temperatures (1880 m). The two solid lines show the linear regression relationship between NARR and measured summit temperatures before (grey: $r = 0.86$) and after (black: $r = 0.85$) the temperatures have been adjusted for overly warm temperatures on relatively cool days and overly cool temperatures on relatively warm days.

for the mean difference, measured and modeled summer daily mean summit air temperatures show good agreement ($r = 0.86$) except for systematic underestimations of maximum and overestimation of minimum summer summit temperatures. To correct for this bias, we add or subtract corrections drawn randomly from a normal distribution with a range of 0 to 2°C to all NARR summer temperatures above -4.5°C and below -7.5°C , respectively (Fig. 3). Surface air temperatures were generated for both ablation season days and non-ablation season days in order to determine mean annual and winter temperatures needed for the calculation of maximum meltwater refreeze amounts, which are discussed below.

To investigate the impact on mass balance of using different near-surface temperature lapse rates β to down-scale air temperatures, three separate surface air temperature fields were generated. The first was generated using a near-surface lapse rate equal to the moist adiabatic lapse rate ($\bar{\beta}_{MML} = -6.5^{\circ}\text{C km}^{-1}$), the second using mean measured lapse rates ($\bar{\beta}_{MMLR} = -4.9^{\circ}\text{C km}^{-1}$) for all days during the ablation season (15 May–15 September) and all winter days (16 September–14 May: $\bar{\beta}_{MMLR_w} = -3.3^{\circ}\text{C km}^{-1}$), and the third using a modeled variable daily lapse rate (β_{VLR} in $^{\circ}\text{C km}^{-1}$) during the ablation season and $\bar{\beta}_{MMLR_w}$ in winter. β_{VLR} was estimated using the lapse rate equation developed from over 10 years of screen-level air temperature measurements made over the Devon Ice Cap (Gardner and others, 2007):

$$\beta_{VLR} = 0.2T_{750} - 4.9$$

where T_{750} is the 3 day running mean of the daily anomaly (summer mean removed) in NARR 750 mbar temperature. T_{750} was derived from a 6 grid cell domain (64×86 km) centered over the ice cap. To illustrate the range in variability of β_{VLR} , mean daily summit temperatures are plotted with β_{VLR} for the highest (1986: Fig. 4a) and lowest (2001: Fig. 4b) measured mass balance years in the study period. On 26 July 2001, when temperatures peaked at 5°C , $\beta_{VLR} = -3^{\circ}\text{C km}^{-1}$. On this day, downscaling summit temperatures with β_{VLR} results in sea level temperatures that are 4°C and 7°C cooler than temperatures downscaled using $\bar{\beta}_{MMLR_w}$ and $\bar{\beta}_{MALR_w}$, respectively. This represents ~ 30 – 55 mm w.e. less ice melt for this day.

The three model runs forced with mean daily air temperature fields downscaled using β_{VLR} , $\bar{\beta}_{MMLR_w}$ and

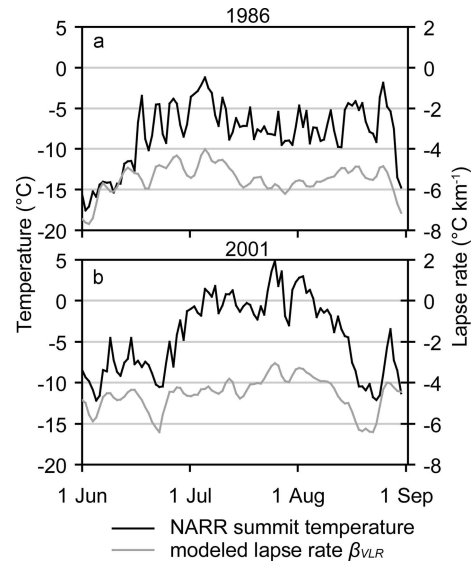


Fig. 4. NARR summit elevation temperatures plotted with variable modeled daily lapse rates β_{VLR} for representatively (a) cold and (b) warm years. Modeled lapse rates are less steep when temperatures are anomalously warm and steeper when temperatures are anomalously cold.

$\bar{\beta}_{MALR_w}$ are referred to throughout this paper as the VLR, MMLR and MALR runs, respectively.

Precipitation

Daily precipitation was derived from the NARR and corrected for a mean over-precipitation bias of 100 mm w.e. a^{-1} , which was determined from the comparison of NARR mean annual precipitation at the summit with the net mass balance measured at the same location for the years 1979–2003 (Koerner, personal communication). Taking point values at the center of the NARR grid cells, the bias adjusted coarse resolution (3×32 km), NARR daily precipitation fields were linearly interpolated based on horizontal distance to match the resolution of the DEM ($\sim 200 \times 1000$ m). The phase of the daily precipitation P_t (mm w.e.) was determined at each grid cell based on the estimated mean daily grid cell air temperature T_t :

$$P_t = \text{snow} \quad T_t \leq 0^{\circ}\text{C}$$

$$P_t = \text{rain} \quad T_t > 0^{\circ}\text{C}$$

Here we have chosen the critical surface temperature for phase change as 0°C (Bassford and others, 2006). Other studies use values as high as 2°C (Oerlemans, 1993). Using a critical value of 2°C would increase net mass balance estimates of the Devon Ice Cap on average by 40 ± 14 mm w.e. relative to the value used here. At the summit of the ice cap, the standard error of the interpolated precipitation was determined as 40 mm w.e. a^{-1} .

Refreezing of meltwater

All liquid water (melt or rain) generated within any grid cell in a given year is assumed to refreeze in that grid cell until the volume of refrozen water $F = F_{max}$, where F_{max} is the maximum amount of refreeze that can occur in that grid cell. Once the liquid water exceeds F_{max} , all additional rain or melt generated in that year is assumed to leave the glacier as runoff. We use the term ‘refreeze’ to refer to the total amount

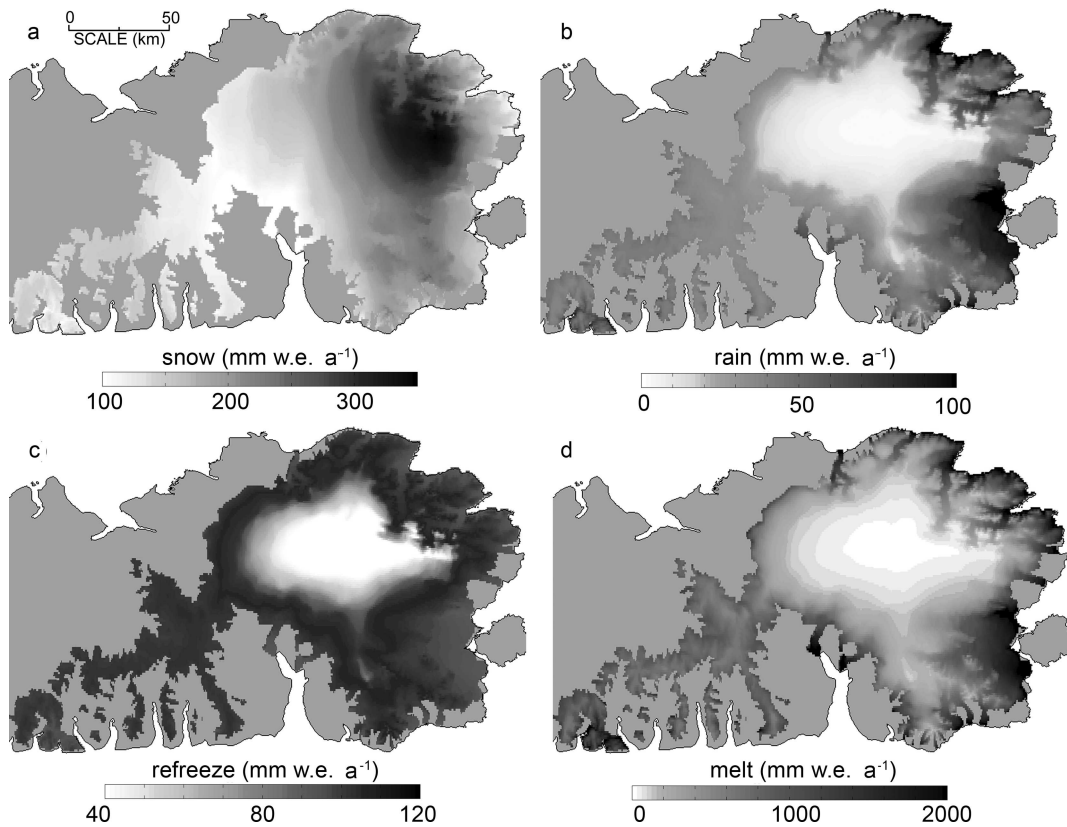


Fig. 5. (a) Mean annual snow, (b) rain, (c), melt water refreeze and (d) melt, for the Devon Ice Cap averaged over the years 1980–2006. Values determined from the VLR model run (see text for details).

of meltwater and rain that refreezes on the glacier during a given mass balance year and can re-melt later in that year and run off; the term ‘internal accumulation’ refers to the amount of water that refreezes, does not run off, and remains on the glacier into the following mass balance year. There is no communication between grid cells, so meltwater only affects refreeze and internal accumulation quantities of the cell in which that meltwater is generated.

F_{max} was determined at each grid cell using the method proposed by Wright (2007). This method determines F_{max} based on a simplified estimate of the total amount of energy required to change the temperature profile of the upper 10–15 m of the glacier from an end of winter temperature profile to a post-refreezing profile:

$$F_{max} = \frac{c_i d_i}{2L_f} \left(\left(1 - \frac{\pi}{2}\right) \bar{T}_a - \bar{T}_w \right),$$

where c_i is the specific heat capacity of ice at 0°C (2097 J kg⁻¹ °C⁻¹), d_i is the maximum depth to which the annual temperature cycle penetrates, L_f is the latent heat of fusion for water (333.5 kJ kg⁻¹), \bar{T}_a is the mean annual air temperature and \bar{T}_w is the mean winter temperature (here taken as the mean temperature outside of the ablation season). On the Devon Ice Cap the annual temperature cycle penetrates to a depth of ~10–15 m. Using this value for d_i results in F_{max} values which are much too large (>1000 mm w.e.). We instead set $d_i = 1$ m, which gives mean F_{max} values at the summit of the ice cap that are ~60% (130 mm) of the annual snowfall, the value often used for the upper threshold for meltwater refreezing on the Greenland ice sheet (Reeh, 1991) and is supported by field measure-

ments made near the equilibrium line altitude of the Greenland ice sheet (Braithwaite and others, 1994).

RESULTS

Mass balance components

Average (1980–2006) annual snowfall, rainfall, refreeze and melt generated from the VLR model run are shown in Figure 5. Similar spatial patterns in the four mass balance components are seen in all three model runs, but magnitudes vary as all components are dependent on the surface air temperature. Averaged over the entire ice cap (including the southwest arm) for the period of study, mean annual snowfall (156 ± 11 mm w.e. a⁻¹), rainfall (43 ± 10 mm w.e. a⁻¹) and meltwater refreeze (90 ± 7 mm w.e. a⁻¹) vary little between model runs with slightly lower (20 mm w.e. a⁻¹) snowfall and slightly higher (20 mm w.e. a⁻¹) rainfall amounts for the MALR run due to a higher frequency of above zero temperatures in that run. There are, however, large differences in melt quantities, with mean annual estimates of 730 ± 250 , 960 ± 350 and 1840 ± 440 mm w.e. a⁻¹ for the VLR, MMLR and MALR model runs, respectively. Because the model runs differ greatly in both the melt amounts and the altitudes at which melt occurs, the three model runs produce very different internal accumulation distributions (Fig. 6) and thicknesses (8, 12 and 3 mm w.e. a⁻¹ for the VLR, MMLR and MALR model runs, respectively).

Comparison with measurements (northwest sector)

Modeled point-location net mass balance (b_n) estimates were extracted from the model output along the GSC’s northwest

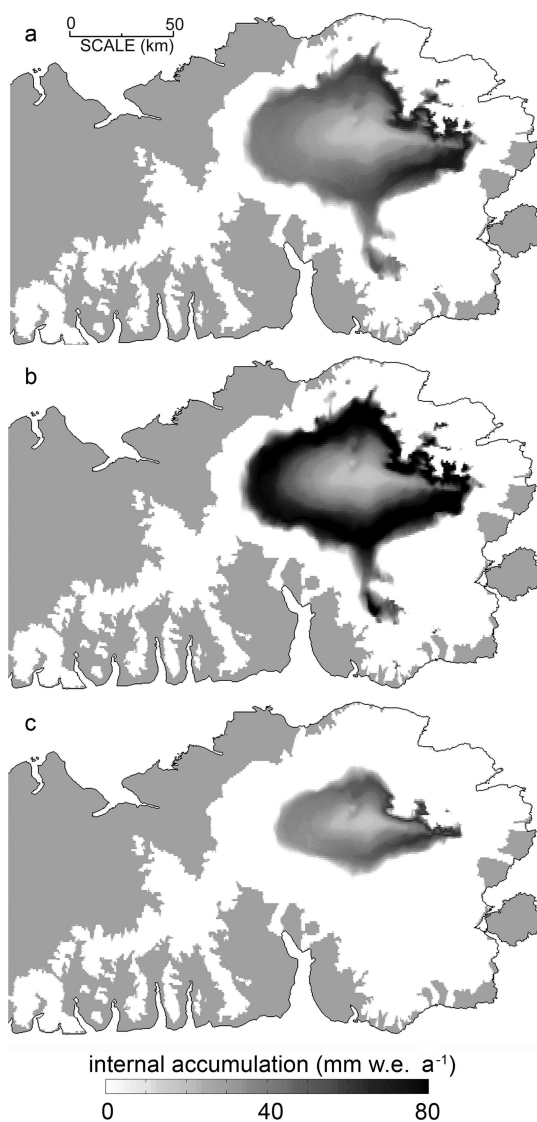


Fig. 6. Annual mean internal accumulation formation estimated from the (a) VLR, (b) MMLR (c) MALR model runs.

transect and compared with their respective stake measurements at 100 m elevation intervals from 150–1750 m a.s.l. for the period of available data (1980–2003: Koerner, personal communication) (Fig. 7). All model estimates are similar and agree well with the stake measurements at elevations above 1450 m, but they diverge with decreasing elevation as estimated melt quantities increase. At 150 m, all model runs significantly overestimate melt quantities relative to measurements by as much as 2800 mm for the MALR run. Overall, the VLR and MMLR model runs significantly outperform the MALR model run, with 23 year mean \pm standard errors averaged across all elevations of $+25 \pm 260$ and -140 ± 340 mm w.e. a⁻¹, respectively compared with -880 ± 920 mm w.e. a⁻¹ for the MALR. Using the sector boundaries outlined by Koerner (1970), cumulative annual net mass balances B_n for the three model runs were estimated for the northwest sector of the ice cap and are shown together with an estimate derived from stake measurements in Figure 8. B_n estimates vary greatly between model runs with mean \pm standard errors of 9 ± 120 , -113 ± 150 , -577 ± 223 mm w.e. a⁻¹ for the VLR, MMLR and MALR runs relative to measured values. The VLR model run produces B_n

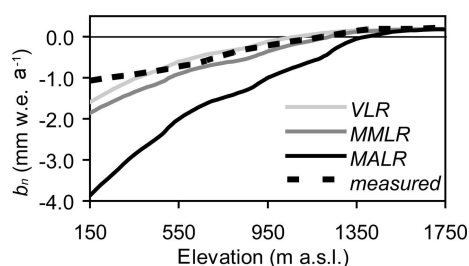


Fig. 7. Average (1980–2001) annual point-location net mass balance (b_n) model estimates extracted at 100 m intervals along the northwest transect shown with respective mass balance stake network measurements.

that are close to measured values with a 1980–2003 cumulative difference of only 0.2 m w.e.

Net mass balance of the Devon Ice Cap

Annual B_n values were calculated for the main portion of the ice cap (southwest arm excluded: 12 100 km²: Dowdeswell and others, 2004) and are shown in Figure 9. The MALR model run produces mass balance values that are, on average, 4 times more negative than values determined from the VLR model run and ~ 2.5 times more negative than values determined from the MMLR run. During more positive mass balance years (e.g. 1986 and 2004) there is good agreement between the VLR and MMLR model runs, but the differences are larger during more negative years (e.g. 2001 and 2006). This is because the total annual Positive Degree Days (PDDs) for the two runs are most similar when lower tropospheric temperatures are seasonally low and most different when temperatures are seasonally warm (i.e. during high melt years). For the whole ice cap (southwest arm included), B_n values are 24–41% more negative than for the main ice cap because the entire southwest arm lies below 900 m and often lies completely within the ablation zone (Fig. 10).

Using perturbed historical accumulation measurements and a constant lapse rate of $-4.6^\circ\text{C km}^{-1}$ (mean 2001 lapse rate measure over the Devon Ice Cap) to extrapolate sea level temperature data from the International Arctic Buoy Program over different sectors of the ice cap, Shepherd and others (2007) estimated the 1996 net mass balance for the main ice cap to be 28 mm w.e. This value is 42, 140 and 730 mm w.e. larger than 1996 estimates computed using the VLR, MMLR and MALR, respectively. We attribute most of the difference between the VLR model run and this estimate to the slightly higher (12 mm w.e.) snowfall estimate used by

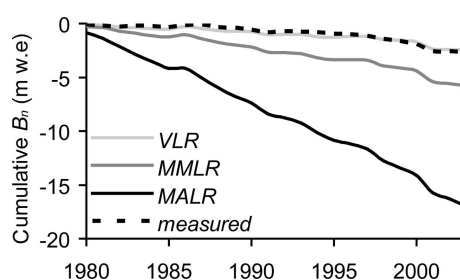


Fig. 8. Modeled cumulative surface mass balance B_n for the northwest sector of the Devon Ice Cap plotted with estimates derived from measurements.

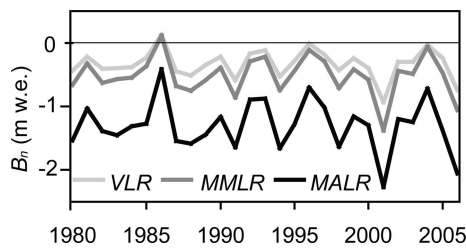


Fig. 9. Net mass balance B_n for the main Devon Ice Cap (southwest arm excluded) for all three model runs.

Shepherd and others (2007), which results in both greater net accumulation at higher elevations and less melt at lower elevations, since snow has a lower DD in ice. The differences between the estimate of Shepherd and others (2007) and the estimates generated using MMLR and MALR are attributed to an overestimation of surface air temperatures in the MMLR and MALR simulations (much higher melt and slightly lower snowfall) due to the use of overly steep lapse rates.

Based on our comparisons with independent model estimates of the 1996 net glacier mass balance for the main ice cap and 24 years of measurements made along the northwest stake transect, we take the VLR model results as the best estimate of surface mass balance. We estimate that the main ice cap lost an average of 333 ± 120 mm w.e. a^{-1} over the period 1980–2006, where the error associated with this estimate is taken to be the standard error of the modeled, relative to measured, net mass balance for the northwest sector.

DISCUSSION AND CONCLUSION

The use of different air temperature lapse rates in the downscaling of surface air temperatures over the Devon Ice Cap has a large impact on estimates of glacier mass balance produced with the Degree Day method. Using the moist adiabatic lapse rate ($-6.5^\circ\text{C km}^{-1}$) to downscale summit elevation temperatures over the ice cap generates net mass balance estimates that are 4 times more negative than estimates made using a modeled variable lapse rate and ~ 2.5 times more negative than estimates made using a mean measured summer lapse rate. Over the main ice cap, mass balance estimates made from temperature fields downscaled with the mean measured summer lapse rate overestimate melt by $\sim 180 \pm 100$ mm w.e. a^{-1} on average relative to estimates made from temperature fields downscaled using a modeled variable lapse rate. During more positive mass balance years, model results generated using the two methods agree closely, but they diverge by as much as 550 mm w.e. a^{-1} during the most negative mass balance years.

When the DDM is forced with surface air temperature fields downscaled using modeled variable daily lapse, it produces estimates of net surface mass balance that agree well (9 ± 120 mm) with the 23 years of measurements made along the northwest transect. This same method produces a 1996 estimate of net mass balance for the main ice cap that agrees closely (42 mm w.e. higher) with the previous 1996 estimate made by Shepherd and others (2007). However, forcing the model with these surface air temperatures only results in a 25% (80 mm w.e. a^{-1}) improvement in the

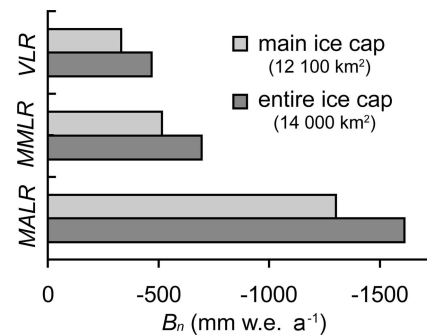


Fig. 10. Model run estimates of mean annual net mass balance B_n for the main (excluding southwest arm) and whole Devon Ice Cap.

standard error of point location net mass balance estimates relative to estimates made from temperature fields downscaled using a mean summer lapse rate. Like all DDMs, model results are highly sensitive to the choice of degree day factors. While we have chosen not to tune the model using the degree day factors, similar model root-mean-square errors, as those achieved when the DDM is forced with a variable lapse rate, could be achieved by adjusting the degree day factor for ice to ~ 4.5 – 6.5 and ~ 2 – 3.5 mm w.e. d^{-1} when employing the mean measured summer lapse rate and the moist adiabatic lapse rate, respectively. When comparing against previously published values (Hock, 2003), a degree day factor < 5.0 mm w.e. d^{-1} for ice is unrealistic. Therefore, the model can only be tuned with a realistic degree day factor for ice to produce comparable results to those achieved using the untuned variable lapse rate when the mean measured summer lapse rate is employed. The root-mean-square error across all three models is relatively insensitive to degree day factor for snow between 2 – 6 mm w.e. d^{-1} .

Our best estimate of the net surface mass balance of the main ice cap over the years 1980–2006 is -330 ± 120 mm w.e. a^{-1} , which is much lower than previous estimates of -76 ± 50 (1961–66: Koerner 1970), -130 ± 60 (1963–2000: Mair and others, 2005) and 28 ± 70 mm w.e. a^{-1} (1996: Shepherd and others, 2007). The more negative model estimate can be attributed to differences in mean summer conditions between the different time periods for which estimates have been derived and to large uncertainties in estimated accumulation rates due to large spatial variations in snowfall (Koerner, 1966), which are poorly reproduced by the 32×32 km resolution NARR output. In particular, total accumulation amounts measured by Koerner (1966) were found to be 2–6 times larger for the southeast (largest sector) than for the northwest sector of the ice cap and are nearly equivalent to the regridded NARR model output.

In conclusion, DDMs are highly sensitive to the choice of lapse rate when models are forced with downscaled temperature fields. For the DDM used in this study, use of a variable daily lapse rate estimated from lower tropospheric (750 mbar) temperatures to downscale surface air temperatures gives significantly better mass balance estimates than a constant lapse equal to either the summer mean or the moist adiabatic lapse rate.

ACKNOWLEDGMENTS

This work was supported by NSERC Canada (through Discovery, Northern Supplement and Equipment Grants to

M. Sharp, and an Alexander Graham Bell Canada Graduate Scholarship to A.S. Gardner), the Canadian Foundation for Climate and Atmospheric Sciences through the Polar Climate Stability Network, Environment Canada through the CRYSYS program, the Northern Scientific Training Program (Indian and Northern Affairs Canada), the Institute for Geophysical Research and Circumpolar Boreal Alberta Research Grant fund (University of Alberta), and by the Alberta Ingenuity Fund (through scholarships to A. S. Gardner). We thank the late R.M Koerner for making available surface mass balance and temperature datasets.

REFERENCES

- Bassford, R.P., M.J. Siegert and J.A. Dowdeswell. 2006. Quantifying the mass balance of ice caps on Severnaya Zemlya, Russian High Arctic. III: Sensitivity of ice caps in Severnaya Zemlya to future climate change. *Arct. Antarct. Alp. Res.*, **38**(1), 21–33.
- Braithwaite, R.J., M. Laternser and W.T. Pfeffer. 1994. Variations of near-surface firn density in the lower accumulation area of the Greenland ice sheet, Pâkitsoq, West Greenland. *J. Glaciol.*, **40**(136), 477–485.
- Braithwaite, R.J. 1995. Positive degree day factors for ablation on the Greenland ice sheet studied by energy-balance modelling. *J. Glaciol.*, **41**(137), 153–160.
- Braun, M. and R. Hock. 2004. Spatially distributed surface energy balance and ablation modelling on the ice cap of King George Island (Antarctica). *Global Planet. Change*, **42**, 45–58.
- Denby, B., W. Greuell and J. Oerlemans. 2002. Simulating the Greenland atmospheric boundary layer. Part II: Energy balance and climate sensitivity. *Tellus A*, **54**(5), 529–541. [AUTHOR: Not cited in text]
- Dowdeswell, J.A., T.J. Benham, M.R. Gorman, D. Burgess and M. Sharp. 2004. Form and flow of the Devon Island ice cap, Canadian Arctic. *J. Geophys. Res.*, **109**(F2), F02002. (10.1029/2003JF000095.)
- Gardner and others. Near-surface temperature lapse rates... [AUTHOR: only accepted papers can be cited – please provide publication details]
- Greuell, W. and R. Böhm. 1998. 2 m temperatures along melting mid-latitude glaciers, and implications for the sensitivity of the mass balance to variations in temperature. *J. Glaciol.*, **44**(146), 9–20.
- Hanna, E., P. Huybrechts, I. Janssens, J. Cappelen, K. Steffen and A. Stephens. 2005. Runoff and mass balance of the Greenland ice sheet: 1958–2003. *J. Geophys. Res.*, **110**(D13), D13108. (10.1029/2004JD005641.)
- Hock, R. 2003. Temperature index melt modelling in mountain areas. *J. Hydrol.*, **282**(1–4), 104–115.
- Koerner, R.M. 1966. Accumulation on the Devon Island ice cap, Northwest Territories, Canada. *J. Glaciol.*, **6**(45), 383–392.
- Koerner, R.M. 1970. The mass balance of the Devon Island ice cap, Northwest Territories, Canada, 1961–66. *J. Glaciol.*, **9**(57), 325–336.
- Koerner, R.M. 2005. Mass balance of glaciers in the Queen Elizabeth Islands, Nunavut, Canada. *Ann. Glaciol.*, **42**, 417–423.
- Mair, D., D. Burgess and M. Sharp. 2005. Thirty-seven year mass balance of Devon Ice Cap, Nunavut, Canada, determined by shallow ice coring and melt modelling. *J. Geophys. Res.*, **110**(F1), F01011. (10.1029/2003JF000099.)
- Marshall, S.J., M.J. Sharp, D.O. Burgess and F.S. Anslow. 2007. Near-surface-temperature lapse rates on the Prince of Wales Icefield, Ellesmere Island, Canada: implications for regional downscaling of temperature. *Int. J. Climatol.*, **27**(3), 385–398.
- Mesinger, F. and 18 others. 2006. North American regional reanalysis. *Bull. Am. Meteorol. Soc.*, **87**(3), 343–360.
- Oerlemans, J. 1993. A model for the surface balance of ice masses: Part 1. Alpine glaciers. *Z. Gletscherkd. Glazialgeol.*, **27**, 63–83.
- Reeh, N. 1991. Parameterization of melt rate and surface temperature on the Greenland ice sheet. *Polarforschung*, **59**(3), 113–128.
- Shepherd, A., Du Z., T.J. Benham, J.A. Dowdeswell and E.M. Morris. 2007. Mass balance of Devon Ice Cap, Canadian Arctic. *Ann. Glaciol.*, **46**, 249–254.
- Wright, A.P., J.L. Wadham, M.J. Siegert, A. Luckman, J. Kohler and A.M. Nuttall. 2007. Modeling the refreezing of meltwater as superimposed ice on a high Arctic glacier: a comparison of approaches. *J. Geophys. Res.*, **112**(F4), F04016. (10.1029/2007JF000818.) [AUTHOR: Not cited in text]

Melt season duration on Canadian Arctic ice caps, 2000–2004

L. Wang,¹ M. J. Sharp,¹ B. Rivard,¹ S. Marshall,² and D. Burgess¹

Received 1 July 2005; revised 30 August 2005; accepted 2 September 2005; published 7 October 2005.

[1] The extent and duration of summer melt on ice caps in the Queen Elizabeth Islands (QEI), Nunavut, Canada, in 2000–2004 were mapped using enhanced resolution QuikSCAT (QSCAT) scatterometer images. The mean melt duration depends mainly on surface elevation and distance from Baffin Bay. Over most ice caps, inter-annual variations in melt duration and the variation in melt duration with elevation are closely related to variations in the July 500 hPa height over the QEI. Pressure-related variability in the vertical gradient of near-surface air temperature appears to be a major control on the inter-annual variations in average melt duration. **Citation:** Wang, L., M. J. Sharp, B. Rivard, S. Marshall, and D. Burgess (2005), Melt season duration on Canadian Arctic ice caps, 2000–2004, *Geophys. Res. Lett.*, 32, L19502, doi:10.1029/2005GL023962.

1. Introduction

[2] Melting of all glaciers and ice caps (excluding the Antarctic and Greenland ice sheets) would raise sea level by ~0.5 m [Church *et al.*, 2001]. 46% of the area of these glaciers and ice caps is in the Arctic [Dyurgerov, 2002], where there was strong warming in the 20th century [Johannessen *et al.*, 2004]. General Circulation Model simulations predict that this trend will continue and likely increase in the 21st century due to anthropogenic forcing [Houghton *et al.*, 2001]. It is therefore important to understand how and why the extent and volume of glacier ice in the Arctic have changed in the recent past.

[3] There is over 110,000 km² of glacier ice in Canada's Queen Elizabeth Islands (QEI) [Koerner, 2002]. Variations in summer melt drive the inter-annual variability in glacier mass balance in the QEI [Koerner, 2002], so there is a strong interest in monitoring summer melt across the region. Satellite-borne Ku- and C-band radar scatterometers have been used to detect melt on the Greenland Ice Sheet [Wismann, 2000; Nghiem *et al.*, 2001; Steffen *et al.*, 2004]. Smith *et al.* [2003] used this method to detect melt within single pixels on several small Arctic ice caps, but could not undertake synoptic melt mapping because of the coarse resolution of the sensors (~25 km). In this study, enhanced resolution data from QSCAT [Long and Hicks, 2005] were used to detect the dates of melt onset and freeze-up, and determine annual melt extent and duration across all major ice caps in the QEI for the period 2000–2004. The results provide a measure of variability in summer climate over ice-covered areas remote from long-term weather

stations and may prove useful in the development of methodologies for up-scaling site-specific measurements of glacier mass balance [Koerner, 2002] to the regional ice cover.

2. Methods

2.1. Data

[4] The SeaWinds scatterometer on QSCAT makes measurements at Ku-band frequency with two constant incidence angles: 46° at H-pol over a 1400 km swath, and 54° at V-pol over an 1800 km swath. The resolution of the original data is low. Due to its wide swath and orbit geometry, however, QSCAT observes the Polar Regions multiple times each day, allowing reconstruction of surface backscatter at finer spatial resolution using the Scatterometer Image Reconstruction (SIR) algorithm [Long and Hicks, 2005]. Ascending and descending pass images produced with this algorithm are available daily for the Arctic since July 1999. These images have a nominal pixel spacing of 2.225 km and an estimated effective resolution of 5 km [Long and Hicks, 2005]. Due to ascending-to-descending swath overlap and day boundary effects in the Polar Regions, there is large temporal variability in the measurements used to construct each (ascending/descending) image [Hicks and Long, 2005]. The majority of effective measurement times (local) over the QEI are 10 pm for descending pass images, and 2 am for ascending pass images. Since ice caps are more likely to be melting at 10 pm, descending pass images (H-pol) were used to detect melt in this study.

[5] 1:250,000 NTDB (National Topographic Data Base) shapefiles of permanent ice were used to extract ice pixels from the QSCAT data. These shapefiles are based on aerial photographs taken in 1959/1960, and many glaciers and ice caps have changed significantly since then. The ice mask thus includes many mixed pixels along the ice margins and in areas surrounding nunataks. Landsat7 ETM+ (30 m) or MODIS (250 m) images from 1999 to 2002 were used to identify these mixed pixels and remove them from the ice mask.

[6] To validate the use of QSCAT images for detecting surface melt, 25 air temperature loggers (either Onset HOBO H8-PRO loggers or Veriteq SP2000 temperature-relative humidity loggers with an accuracy of ±0.25°C) were deployed at elevations from 130–2010 m on the Prince of Wales (POW) Icefield, Ellesmere Island, from 2001–2003. Sensors were installed in Onset radiation shields (without ventilation) and recorded near-surface (1–1.5 m) air temperatures at 30-minute intervals (S. J. Marshall *et al.*, Surface temperature lapse rate variability on the Prince of Wales Icefield, Ellesmere Island, Canada: Implications for regional-scale downscaling of temperature, submitted to *International Journal of Climatology*, 2005, hereinafter referred to as Marshall *et al.*, submitted manuscript, 2005).

¹Earth and Atmospheric Sciences, University of Alberta, Edmonton, Alberta, Canada.

²Department of Geography, University of Calgary, Calgary, Alberta, Canada.

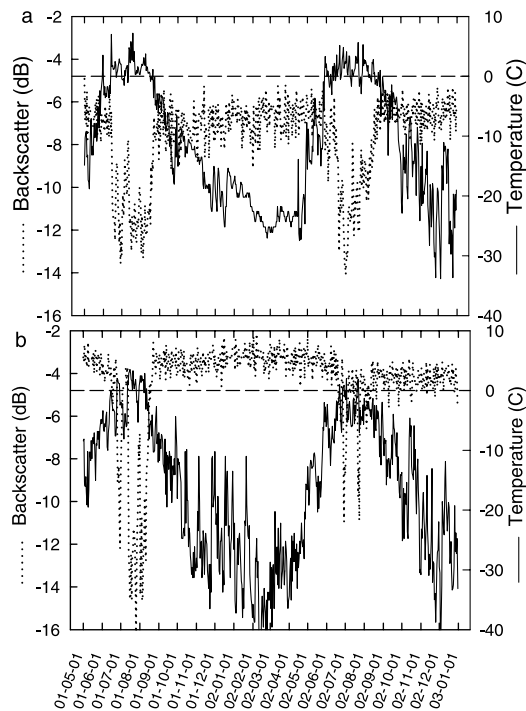


Figure 1. Time series of QSCAT σ^0 and surface air temperature during 2001–2002 for 2 locations on POW Icefield, (a) 78.68°N, 74.96°W, 400 m a.s.l., (b) 78.61°N, 78.63°W, 1300 m a.s.l.

2.2. Melt Threshold and Melt Detection

[7] The basis for melt mapping is the reduction in Ku-band radar backscatter (σ^0) that occurs during the melt season. Liquid water in snow dramatically increases microwave absorption and masks out subsurface scattering, resulting in decreased σ^0 at the onset of snowmelt [Ulaby *et al.*, 1981]. Transient increases in σ^0 occur during subsequent periods of refreezing, but σ^0 falls again if snowmelt resumes. At low elevations, the snow pack may be removed completely in summer, exposing glacier ice. Backscatter may then increase over time due to the relative roughness of the ice surface, but detailed comparisons of σ^0 and air temperature records from POW indicate that these increases are significantly less than those associated with refreezing.

[8] During winter (December to February), mean σ^0 values (W_{mn}) increase with elevation, while the standard deviations (W_{sd}) decrease (auxiliary Figure A1¹). Since dry snow is almost transparent at Ku-band frequency [Ulaby *et al.*, 1981], this is mainly due to elevation dependent differences in the physical properties (grain size, surface roughness, density, ice layers) of near surface snow and firn at the end of the previous summer. Nevertheless, this result implies that the magnitude of σ^0 that indicates melting during the following summer will vary with W_{mn} and W_{sd} . Two dynamic thresholds were therefore used to detect melt in each pixel:

$$M_1 = W_{mn} - a(W_{sd})^{-b} \quad (1)$$

$$M_2 = cM_1 \quad (2)$$

Here a , b , and c are user defined constants. Using trial and error and the air temperature records, optimal values for a , b , and c were identified as: $a = c = 1.3$, $b = -1.1$. For each pixel, all periods when either (A) σ^0 remained below M_1 for 3 or more consecutive days, or (B) σ^0 dropped below M_2 for 1 day, were categorized as melt days. Step (A) eliminates possible “false starts” in melt onset; and step (B) makes it possible to capture short periods of melt at high elevations on the ice caps. The first melt day and last melt day plus one were used as melt onset and freeze-up dates respectively. The number of melt days in each pixel was determined as the time period between melt onset and freeze-up minus the duration of any periods without melt within the melt season.

[9] At all elevations on POW, there is a close correspondence between the periods of decreased σ^0 (MD_{QS}) and positive air temperatures (MD_T) in the 20:00–23:00 time window (Figure 1). Linear regression gives $MD_{QS} = 0.9 MD_T + 9$ days ($r^2 = 0.78$, $P < 0.001$, standard error of the estimate = 10.1 days). There is also a good relationship between MD_{QS} and the annual positive degree-day total ($\Sigma PDD = 0.11 + 0.6036 MD_{QS} + 0.01430 MD_{QS}^2$, $r^2 = 0.74$, $p < 0.001$, standard error of the estimate = 20 PDD).

3. Results and Discussion

3.1. Melt Climatology

[10] Average melt onset dates range from late May to mid-July (Figure 2a), and freeze-up dates range from mid-July to early September (Figure 2b). Melt duration ranges from 1 day or less at high elevations to 100 days at low elevations in areas facing Baffin Bay in the southeast QEI (Figure 2c). For the whole QEI, the average is 37.7 days (standard deviation (s.d.) = 4.9 days, Table 1). Ice cap margins facing either Baffin Bay to the southeast or the Arctic Ocean to the northwest have significantly longer melt seasons than margins facing the interior of the QEI. Areas with longer melt seasons tend to have both earlier melt onset and later freeze-up dates.

[11] The spatial pattern of melt duration can be well explained in terms of surface elevation and distance from Baffin Bay (measured relative to 74.010°N, 75.042°W) – a

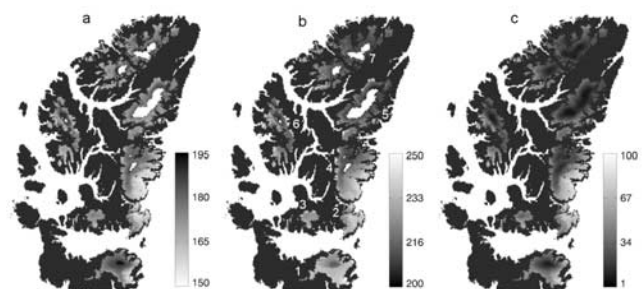


Figure 2. Melt climatology for the QEI for the period 2000–2004, (a) melt onset dates; (b) freeze-up dates; (c) the number of melt days. Anomalies in onset and freeze-up dates cannot be calculated for areas shown in white, as melt was not detected in these areas in all years. Numbers in (b) indicate major ice caps: 1~Devon; 2~Manson; 3~Sydkap; 4~POW; 5~Agassiz; 6~Axel Heiberg Island; 7~Northern Ellesmere Island. See color version of this figure in the HTML.

¹Auxiliary material is available at <ftp://ftp.agu.org/apend/gl/2005GL023962>.

Table 1. Average Melt Duration Over the Whole QEI and Each Major Ice Cap, for the Summers of 2000–2004^a

Ice Cap	Melt Duration, days							Mean Elevation, m	Area Above 1000 m, %	Correlation With 500 hPa
	2000	2001	2002	2003	2004	Mean	S.D.			
QEI	39.1	42.6	30.9	41.4	34.7	37.7	4.9	998	58	0.96
Devon	40.8	50.9	37.5	45.7	35.4	42.1	6.3	1080	56	0.93
Manson	61.6	63.4	62.4	57.6	63.4	61.7	2.4	585	4	-0.2
Sydkap	49.0	49.2	32.7	44.1	45.1	44.0	6.7	827	23	0.77
POW	47.6	53.9	40.1	51.0	44.7	47.4	5.4	967	49	0.95
Agassiz	29.8	32.6	16.2	29.8	22.9	26.3	6.7	1286	77	0.92
Axel Heiberg	40.4	39.0	31.8	40.4	36.0	37.5	3.7	1073	57	0.93
N. Ellesmere	31.4	32.7	23.9	37.1	26.6	30.3	5.2	1171	68	0.97

^aThe mean elevation and the percentage of area above 1000 m for each ice cap, and the correlation between melt duration and July 500 hPa height are also shown.

source of warm maritime air masses. Multiple regression gives: $MD_{QS} = 87.98 - 0.0346h - 0.0461x$ ($r^2 = 0.69$, $p < 0.001$), where h is surface elevation (m) and x is distance from Baffin Bay (m). The correlation with distance from Baffin Bay alone is -0.44 , while that with elevation is -0.80 , so surface elevation is the main influence on melt duration in the QEI. MD_{QS} ranges from 26.3 days (s.d. = 6.7 days) on the Agassiz Ice Cap to 61.7 days (s.d. = 2.4) on the Manson Icefield (Table 1). This is consistent with the mean elevations of the ice caps: 1286 m for Agassiz and 585 m for Manson.

3.2. Melt Anomalies

[12] For the whole QEI, the longest melt season was 2001 (42.6 days) and the shortest 2002 (30.9 days) (Table 1). The pattern for individual ice caps was similar (Table 1), although 2003 was the longest melt season on the Northern Ellesmere and Axel Heiberg Island ice caps, and the shortest season on the Manson Icefield. 2004 was the shortest melt season on the Devon Ice Cap. In relatively cool years, like 2002 and 2004, no melt was detected in some high elevation areas of Ellesmere Island and Axel Heiberg Island (Figure 2).

[13] In the southeast QEI, the melt duration anomalies in 2001 and 2002 were of opposite sign at high and low elevations (Figure 3, auxiliary Figure A2). At low elevations, the anomalies were extremely negative in 2001 and extremely positive in 2002 (i.e. the low elevation anomalies were of opposite sign to the anomalies for the ice caps as a whole). On POW, the decrease in melt duration with increasing elevation was almost linear in 2001 (Figure 4). In 2002 the melt duration decreased abruptly between 700 m

(68 days) and 1100 m (29 days), resulting in a much steeper average rate of decrease of melt duration with increasing elevation. Consistent with this, lapse rates in daily mean surface air temperature in June–August were $-3.7^\circ\text{C km}^{-1}$ in 2001 and $-5.1^\circ\text{C km}^{-1}$ in 2002 (Marshall et al., submitted manuscript, 2005). In 2001, the melt duration at elevations below 700 m was less than in the generally shorter melt season of 2002. This suggests that in some years, like 2002, the temperature regimes of the high and low elevation regions of the Icefield are partially decoupled, while in other years, like 2001, they are more closely related. The correlation coefficient between the June–August daily mean air temperatures at stations at 130 m and 1300 m was 0.74 in 2001, but only 0.56 in 2002.

[14] Alt [1987] found that high melt years on QEI ice caps were associated with the intrusion of a ridge into the QEI at all levels in the troposphere, while low melt years were associated with the maintenance of a deep cold trough across Ellesmere Island and down Baffin Bay, which resulted in northwest flow off the Polar Ocean. In addition, on POW, less negative vertical gradients in daily mean surface air temperature (2001) are associated with high pressure and anticyclonic flow, while more negative gradients (2002) are associated with low pressure and generally cyclonic flow (Marshall et al., submitted manuscript, 2005). It was thus hypothesized that melt season duration would vary systematically with geopotential height over the QEI. Indeed, the correlation between the mean melt season duration over the QEI and the mean July 500 hPa height over the region $74\text{--}83^\circ\text{N}$, $70\text{--}92^\circ\text{W}$ (as derived from the NCEP-CDAS Reanalysis [Kalnay et al., 1996]) was $+0.96$ (Table 1). Similar relationships were found for all the

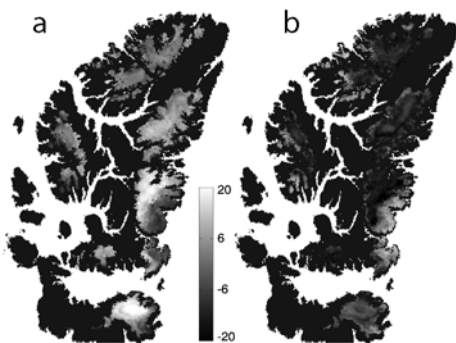


Figure 3. Anomalies in melt duration over QEI relative to the 2000–2004 climatology for the summers of (a) 2001 and (b) 2002. See color version of this figure in the HTML.

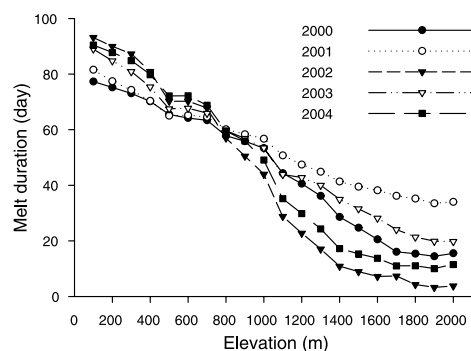


Figure 4. Average melt duration in each 100 m elevation band on POW Icefield in the summers of 2000–2004.

individual ice caps except the Manson Icefield and, possibly, Sydkap, which have low mean surface elevations and relatively small areas above 1000 m (Table 1). Although these results are based on only 5 years of data, they suggest that the less negative surface air temperature gradients associated with high mean geopotential heights result in longer than average melt seasons at higher elevations on the QEI ice caps, and in longer melt seasons overall. In contrast, lower mean geopotential heights are associated with more negative surface air temperature gradients, shorter melt seasons at high elevations, and shorter melt seasons overall.

[15] In the QEI, 2002 was the shortest melt season in the period 2000–2004. On the Greenland Ice Sheet, however, unusually extensive melt in northeast Greenland made 2002 the year with the most extensive melt in the period 1979–2003 [Steffen *et al.*, 2004]. NCEP-CDAS Reanalysis data reveal a positive 500 hPa geopotential height anomaly over northeast Greenland in June and July 2002, while the anomaly was negative over the QEI. This suggests that changes in melt extent and duration in the QEI and northern Greenland may have a common relationship to changes in the distribution of atmospheric mass.

4. Summary and Conclusions

[16] The extent and duration of summer melt on the QEI ice caps from 2000–2004 were mapped using enhanced resolution QSCAT backscatter time-series. The 5-year mean melt duration pattern was largely a function of surface elevation, with shorter melt seasons at higher elevations. No melt was detected over some high-elevation regions in 2002 and 2004. For monitoring sites on the POW Icefield, QSCAT derived melt durations correspond well with those derived from air temperature measurements, and are well correlated with the annual positive degree-day total. This suggests that it may be possible to use maps of melt duration to derive positive degree-day fields that could be used to compute summer melt volume using temperature index melt models.

[17] The annual mean melt duration over the larger ice caps is positively correlated with the local 500 hPa height. In a given year, however, the sign of melt duration anomalies may be opposite at high and low elevations on an ice cap. This phenomenon appears to be linked to pressure-related variations in the vertical gradient of surface air temperature over the ice caps, which is more negative in years with relatively low pressure. Thus, in high-pressure years, ice caps with relatively large areas at high elevations experience

longer than average melt seasons, which increases the mean melt duration over the whole ice cap. The mean melt duration over these ice caps can therefore be inversely correlated to the duration at elevations near sea level.

[18] **Acknowledgments.** This research was supported financially by the Meteorological Service of Canada's CRYSYS program, and logistically by the Polar Continental Shelf Project, Natural Resources Canada. The Microwave Earth Remote Sensing Laboratory, Brigham Young University provided the QSCAT data. We thank D.G. Long for his help with reading the QSCAT data and for discussions. The Nunavut Research Institute and the peoples of Grise Fjord and Resolute Bay gave permission to conduct the field component of this research.

References

- Alt, B. T. (1987), Developing synoptic analogues for extreme mass balance conditions on Queen Elizabeth Island ice caps, *J. Clim. Appl. Meteorol.*, *26*, 1605–1623.
- Church, J., et al. (2001), Changes in sea level, in *Climate Change 2001: The Scientific Basis*, edited by J. T. Houghton et al., pp. 639–693, Cambridge Univ. Press, New York.
- Dyrugerov, M. (2002), Glacier mass balance and regime: Data of measurements and analysis, *Occas. Pap. 55*, Univ. of Colo., Boulder.
- Hicks, B. R., and D. G. Long (2005), Improving temporal resolution of SIR images for QuikSCAT in the polar regions, report, Brigham Young Univ., Provo, Utah.
- Houghton, J. T., et al. (Eds.) (2001), *Climate Change 2001: The Scientific Basis*, Cambridge Univ. Press, New York.
- Johannessen, O. M., et al. (2004), Arctic climate change: Observed and modelled temperature and sea-ice variability, *Tellus, Ser. A*, *56*, 328–341.
- Kalnay, E., et al. (1996), The NCEP/NCAR 40-year reanalysis project, *Bull. Am. Meteorol. Soc.*, *77*, 437–471.
- Koerner, R. M. (2002), Glaciers of the High Arctic Islands, in *Satellite Image Atlas of Glaciers of the World: Glaciers of North America—Glaciers of Canada*, edited by R. S. Williams Jr. and J. G. Ferrigno, *U.S. Geol. Surv. Prof. Pap. 1386-J*, j111–j146.
- Long, D. G., and B. R. Hicks (2005), Standard BYU QuikSCAT/SeaWinds land/ice image products, report, Brigham Young Univ., Provo, Utah.
- Nghiem, S. V., K. Steffen, R. Kwok, and W. Y. Tsai (2001), Detection of snowmelt regions on the Greenland ice sheet using diurnal backscatter change, *J. Glaciol.*, *47*, 539–547.
- Smith, L. C., Y. Sheng, R. R. Forster, K. Steffen, K. E. Frey, and D. E. Alsdorf (2003), Melting of small Arctic ice caps observed from ERS scatterometer time series, *Geophys. Res. Lett.*, *30*(20), 2034, doi:10.1029/2003GL017641.
- Steffen, K., S. V. Nghiem, R. Huff, and G. Neumann (2004), The melt anomaly of 2002 on the Greenland Ice Sheet from active and passive microwave satellite observations, *Geophys. Res. Lett.*, *31*, L20402, doi:10.1029/2004GL020444.
- Ulaby, F. T., R. K. Moore, and A. K. Fung (1981), *Microwave Remote Sensing: Fundamentals and Radiometry*, Addison-Wesley, Boston, Mass.
- Wismann, V. (2000), Monitoring of seasonal snowmelt in Greenland with ERS scatterometer data, *IEEE Trans. Geosci. Remote Sens.*, *38*, 1821–1826.

D. Burgess, B. Rivard, M. J. Sharp, and L. Wang, Earth and Atmospheric Sciences, University of Alberta, Edmonton, AB, Canada T6G 2E3. (libo@ualberta.ca)

S. Marshall, Department of Geography, University of Calgary, Calgary, AB, Canada T2N 1N4.

Flow dynamics and iceberg calving rates of Devon Ice Cap, Nunavut, Canada

David O. BURGESS,¹ Martin J. SHARP,¹ Douglas W.F. MAIR,²
Julian A. DOWDESWELL,³ Toby J. BENHAM³

¹Department of Earth and Atmospheric Sciences, University of Alberta, Edmonton, Alberta T6G 2E3, Canada,
E-mail: dob@ualberta.ca

²Department of Geography, University of Aberdeen, Elphinstone Road, Aberdeen AB24 3UF, UK

³Scott Polar Research Institute, University of Cambridge, Lensfield Road, Cambridge CB2 1ER, UK

ABSTRACT. The surface velocity field of Devon Ice Cap, Nunavut, Canada, was mapped using interferometric synthetic aperture radar (InSAR). Ascending European Remote-sensing Satellite 1 and 2 (ERS-1/-2) tandem mode data were used for the western and southeast sectors, and 3 day repeat pass ERS-1 imagery for the northeast sector. Speckle-tracking procedures were used with RADARSAT 1 imagery to obtain surface velocities over the terminus of Belcher Glacier (a major calving front) where decorrelation between ERS data occurred. The InSAR data highlight a significant contrast in ice-flow dynamics between the east and west sides of the ice cap. Ice movement west of the main north–south divide is dominated by relatively uniform ‘sheet’ flow, but three fast-flowing outlet glaciers that extend 14–23 km beyond the ice-cap margin also drain this region. Several outlet glaciers that extend up to 60 km inland from the eastern margin drain the eastern side of the ice cap. The dominant ice-flow regimes were classified based on the relationship between the driving stress (averaged over a length scale of ten ice thicknesses) and the ratio of surface velocity to ice thickness. The mapped distribution of flow regimes appears to depict the spatial extent of basal sliding across the ice cap. This is supported by a close relationship between the occurrence of flow stripes on the ice surface and flow regimes where basal sliding was found to be an important component of the glacier motion. Iceberg calving rates were computed using measured surface velocities and ice thicknesses derived from airborne radio-echo sounding. The volume of ice calved between 1960 and 1999 was estimated to be $20.5 \pm 4.7 \text{ km}^3$ (or $0.57 \text{ km}^3 \text{ a}^{-1}$). Approximately 89% of this loss occurred along the eastern margin. The largest single source is Belcher Glacier, which accounts for ~50% of the total amount of ice calved.

INTRODUCTION

Most of the outlet glaciers that drain the interior regions of Devon Ice Cap, Nunavut, Canada, terminate in tidewater, making them potentially sensitive to changes in both climate and sea level. Iceberg calving from the termini of these glaciers has not previously been quantified, but may constitute a significant mode of mass loss from the ice cap. The rate of calving may be sensitive to changes in the flow dynamics of the glaciers and to changes in terminus position related to instabilities of the grounding line. Knowledge of the velocity structure of the ice cap is essential for identifying the major pathways by which ice is removed from the ice cap, and for estimating the rate of mass loss by iceberg calving and its relative contribution to overall changes in the mass of the ice cap. A recent study by Burgess and Sharp (2004) estimated that Devon Ice Cap has decreased in volume by $\sim 67 \text{ km}^3$ between 1960 and 1999. Mair and others (2004) suggest that surface melting may account for 60–90% of this loss, indicating that iceberg calving may account for up to 40% (27 km^3) of the total mass loss over this time interval.

In this study, surface velocities were derived for almost the entire Devon Ice Cap using interferometric synthetic aperture radar (InSAR). The pattern of surface velocities in the look direction of the satellite was analyzed to identify the dominant ice-flow regimes and the spatial relationships between slow- and fast-flowing sectors of the ice cap. Downslope surface velocities were projected from look

direction velocities in order to quantify the flow rates of all major glaciers on the ice cap. Ice-thickness data acquired using airborne radio-echo sounding (Dowdeswell and others, 2004) were used in conjunction with surface velocity values to calculate calving fluxes at the terminus of 94% of all tidewater glaciers draining the ice cap. The velocity and ice-thickness data were also used to investigate the nature of the transition zones between slow and fast ice flow, and the mechanisms of ice flow along the major glaciers that drain the interior regions of the ice cap.

STUDY AREA

Devon Ice Cap occupies approximately $14\,000 \text{ km}^2$ of the eastern part of Devon Island, Nunavut, in the Canadian High Arctic (Fig. 1). Landsat 7 Enhanced Thematic Mapper Plus (ETM+) imagery acquired in 1999 suggests that ice-flow patterns are strongly influenced by the form of the underlying bedrock surface, and that they differ significantly between the east and west sides of the ice cap. West of the central north–south divide, the ice cap rests on a relatively flat plateau, and flows westwards as a single broad lobe ($\sim 82 \text{ km}$ long) that terminates on land between 400 and 600 m a.s.l. This region is also drained by two outlet glaciers that flow south into Croker Bay and by Sverdrup Glacier which flows north into Jones Sound (Fig. 2). These glaciers all extend $>14 \text{ km}$ beyond the main ice-cap margin. East of the central divide, the topography

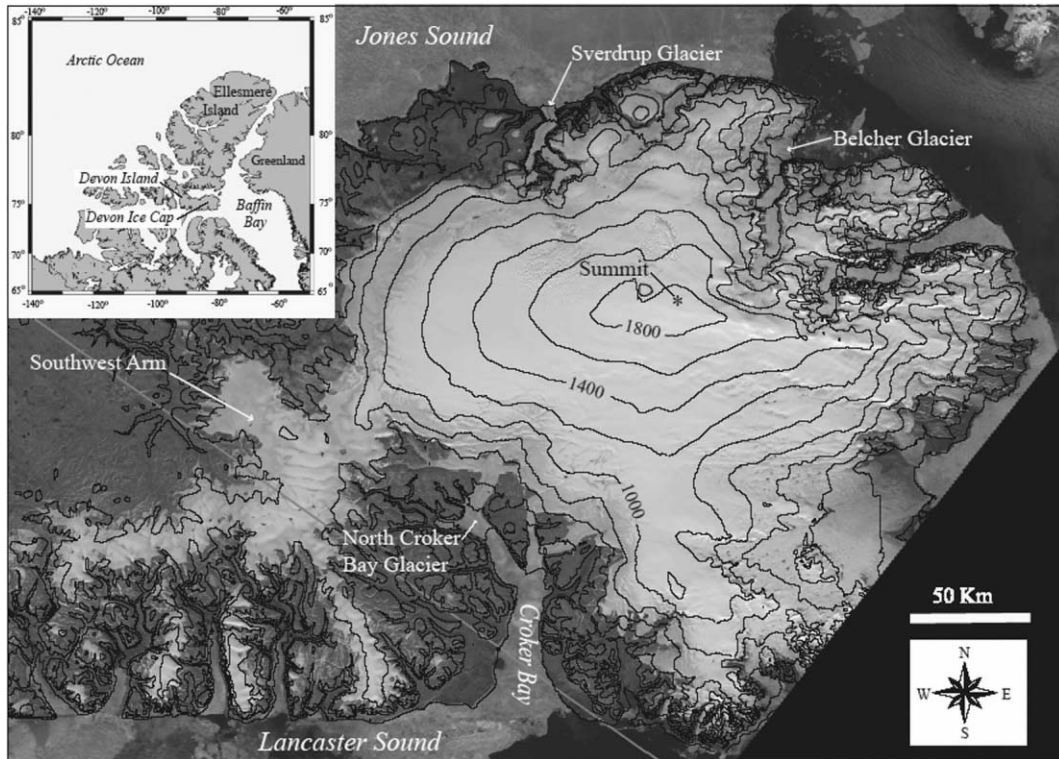


Fig. 1. 1999 Landsat 7 ETM+ ortho-mosaic of Devon Ice Cap. Inset shows the location of Devon Ice Cap in the Canadian Arctic Archipelago.

is primarily mountainous. Large outlet glaciers that extend up to 41 km inland from the coast drain the northeast sector. The east-central region is dissected by a series of outlet glaciers that extend up to 60 km inland from the ice-cap margin. Most of these outlet glaciers terminate in tidewater, and they comprise 89% of the 73 km of the ice-cap margin that reaches the sea (Dowdeswell and others, 2004). Flow stripes are characteristic surface features along these glaciers (see Fig. 3), indicating that ice motion is likely due to sliding at the glacier bed (Gudmundsson and others, 1998, 2003). Margin-parallel layering and surface-parallel meltstreams are surface features common to the remaining areas of the ice cap below ~ 1000 m a.s.l.

INTERFEROMETRIC MEASUREMENTS

Surface velocity fields across Devon Ice Cap were derived from InSAR which measures topography and displacement of the Earth's surface as a result of the interference pattern created between a coherent pair of radar images acquired from successive satellite passes along the same orbital path

(Massonnet and Feigl, 1998). In order to isolate the component of surface motion in the interferogram, the effects of topography must be removed either by subtracting an independent digital elevation model (DEM) from the InSAR pair (Joughin and others, 1996) or through double-differencing with a second coherent InSAR pair (Gabriel and others, 1989). In this study, double-differencing was performed with two radar pairs acquired over the southeast region of the ice cap during the European Remote-sensing Satellite 1 and 2 (ERS-1/-2) tandem mode mission in 1996 (see Table 1 for orbital pairs and Fig. 2 for the footprint of the radar images). Topography was removed from the interferograms over the western half and the northeast region (where only single radar pairs were available) using the Canadian digital elevation dataset (CDED) as the external DEM. The 'motion-only' interferograms were unwrapped and converted to absolute values by referencing bedrock features identifiable in the radar imagery to zero velocity (Zebker and others, 1994). The three 'motion-only' interferograms were then manually mosaicked to produce line-of-sight velocity fields (V_{LOS}) over 98% of the ice-cap surface (Fig. 2). Line-of-sight

Table 1. Orbit numbers and dates of radar imagery used for mapping surface velocities of the Devon Ice Cap

Ice-cap region	RADARSAT orbit	ERS orbit	ERS image dates	Perpendicular baseline m
Southeast	–	24397/4724, 24898/5225	15–16 Mar., 19–20 Apr. 1996	187, 64
West	–	24894/5311	25–26 Apr. 1996	–1
Northeast	–	2924/2967	6/9 Feb. 1992	60
Belcher terminus	25810/26153	–	14 Oct–7 Nov. 2000	–
Belcher terminus	26345/26688	–	20 Nov.–14 Dec. 2000	–

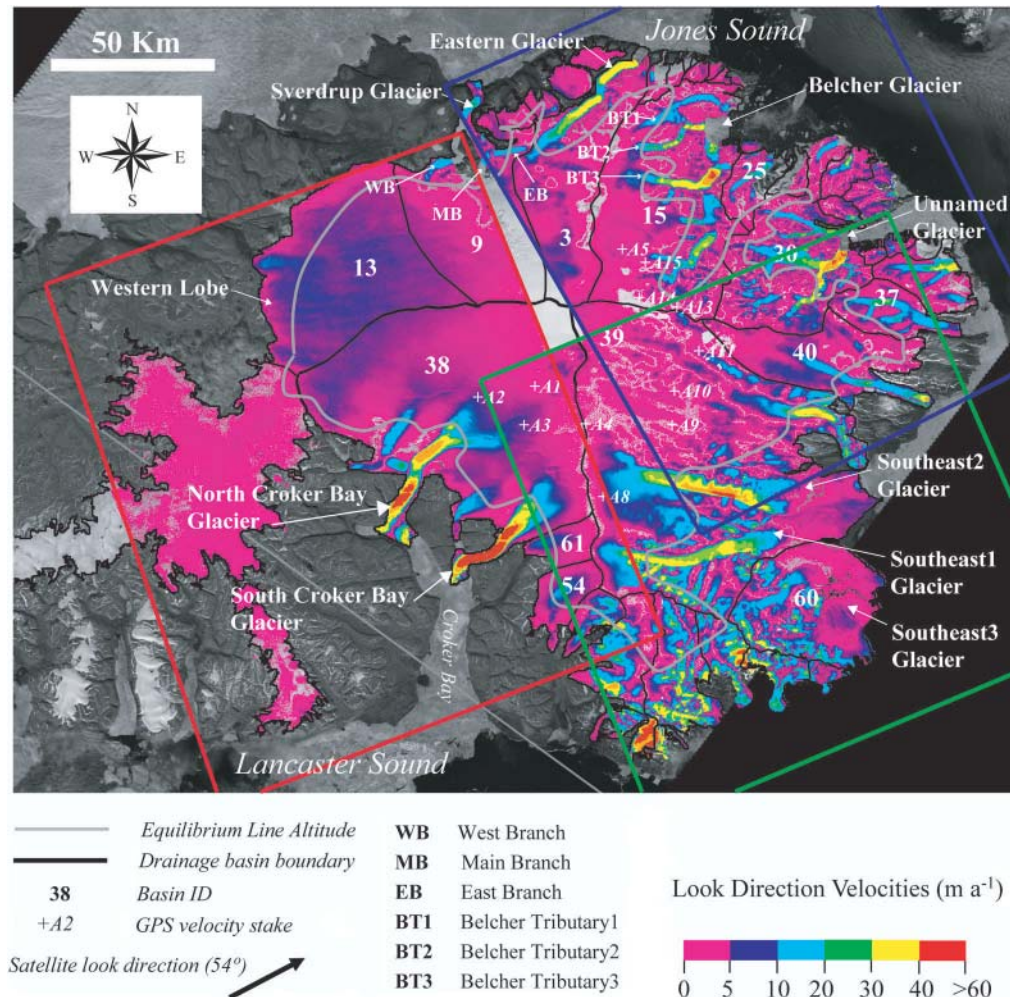


Fig. 2. Look direction surface velocities overlaid onto a 1999 Landsat 7 ETM+ satellite ortho-mosaic of Devon Ice Cap. Accelerated glacier flow is identified by the closely spaced coloured fringes which are evident along the entire length of most of the major outlet glaciers. Red, green and blue boxes outline the footprints for the west, southeast and northeast ERS radar image pairs respectively. Orbital numbers are listed in Table 1. The ELA used here is situated at ~ 800 m a.s.l. throughout the southeast, ~ 950 m a.s.l. throughout the northwest and 875 m a.s.l. throughout the southwest and northeast regions of the ice cap (Koerner, 1970).

velocities were projected to true downslope velocities (V_{DS}) based on the satellite ice surface geometry (Vachon and others, 1996; Cumming and Zhang, 2000) according to the formula:

$$V_{DS} = \frac{V_{LOS}}{(\cos \alpha \sin \nu \sin \theta) + (\sin \alpha \cos \theta)}, \quad (1)$$

where α is the slope of the ice-cap surface, ν is the angle between the look direction of the satellite and the direction of ice flow, and θ is the incidence angle of the radar beam (33 for the ERS satellites). Throughout the interior regions of the ice cap, ice was assumed to flow in the direction of maximum slope of ice-cap surface. Surface slopes were computed from the CDED that was smoothed at a horizontal scale equivalent to ~ 6 times the local ice thickness. The direction of ice flow over outlet glaciers was mapped from the orientation of flow stripes visible in the Landsat 7 ETM+ imagery. Projecting line-of-sight velocities to downslope velocities produces unreliable results over regions where ice flow is nearly perpendicular to the look direction of the satellite (Unwin, 1998). Therefore, since InSAR from only a single look direction was available, true surface velocities could be computed for only $\sim 75\%$ of the ice-cap surface.

Error estimates for InSAR measurements

The main source of velocity error (V_{error}) associated with the measurements of downslope surface displacement derives from projecting the line-of-sight velocities from a single look angle. Throughout the interior regions where ice velocity is generally < 20 m a⁻¹, V_{error} was quantified by comparing the projected InSAR data with point velocity values from repeat differential global positioning system (DGPS) measured in the field. The positions of 13 velocity stakes deployed above the equilibrium-line altitude (ELA; Fig. 2) were measured during May 2000 using Leica Geosystems Series 500 GPS dual frequency antennae. GPS tracking data were collected for 3–4 hours at each site. The data were post-processed using the GIPSY-OASIS II software package (Webb and Zumbege, 1995), which includes models and estimation algorithms, developed by NASA's Jet Propulsion Laboratory (JPL), that account for orbit, Earth orientation, clock biases and a range of other geodetic and astronomical parameters. The 1σ uncertainty in horizontal positioning was < 0.02 m (personal communication from J.F. Zumbege, 2004). Repeat measurements were made at each stake in April 2001. Slight measurement errors may have been incurred in the repositioning of antennae on the stakes and from

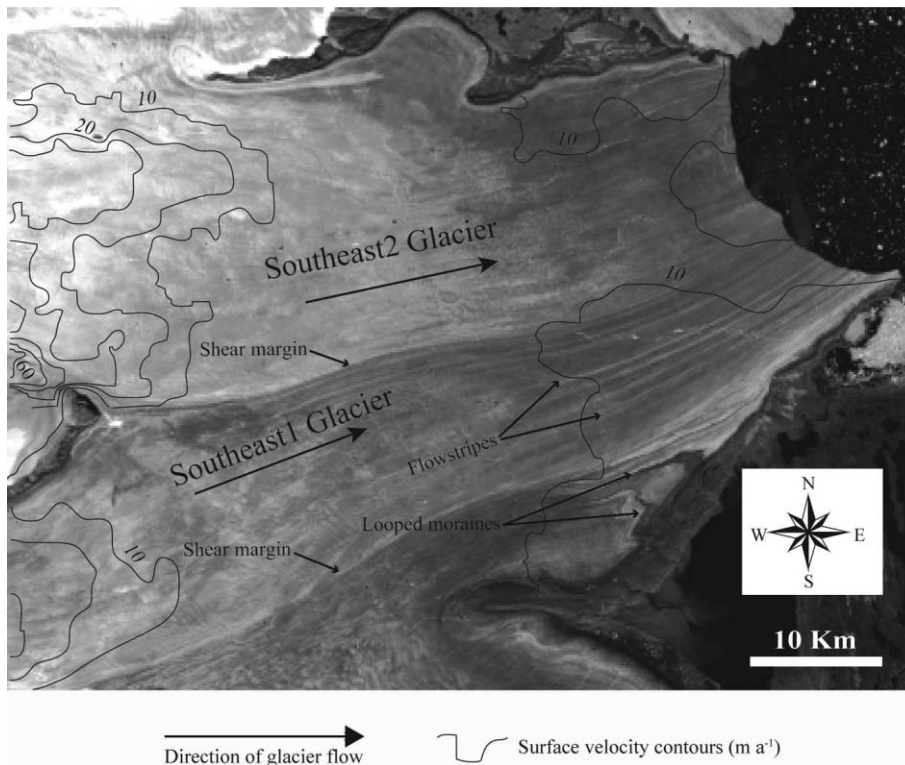


Fig. 3. A subset of a 2000 Landsat 7 ETM+ image mosaic highlighting surface features indicative of fast glacier flow throughout the terminus region of the Southeast 1 and Southeast 2 glaciers.

wind-induced movement during measurement periods. We estimate the error in the annual surface displacement measurements to be <0.05 m. Measured annual surface displacements ranged from 2.33 m, near the saddle of the southern half of the north–south ice divide, to 12.24 m just above the equilibrium line in the southeastern sector (A8 and A9 respectively in Fig. 2). The average discrepancy between the velocity stake data and the associated InSAR pixel data agreed to within an average of $\pm 2.54 \text{ m a}^{-1}$, indicating a conservative V_{error} of $\pm 3 \text{ m a}^{-1}$ throughout the interior regions of the ice cap. V_{error} over ice moving $>20 \text{ m a}^{-1}$ (where DGPS velocity measurements were not performed) was found to be a function of the accuracy with which the direction of ice flow was measured. The direction of ice flow over these regions was determined from the visual inspection of flow stripes in the Landsat 7 imagery and was estimated to be accurate to within $\pm 2^\circ$ in azimuth. This error translated into an accuracy of 2–10% of the projected surface velocity values, depending on the angle between the direction of ice flow and the look angle of the satellite. Significant variability in seasonal velocity measured over several High Arctic glaciers (Cress and Wyness, 1961; Iken, 1972; Bingham and others, 2003; Copland and others, 2003a) suggests that additional error may be introduced when extrapolating InSAR-derived velocity measurements to annual values. Summer velocities up to 100% higher than winter velocities were recorded at certain low-elevation velocity stakes by Copland and Sharp (2001) on John Evans Glacier, Nunavut. Such variability would not be detected in the short-term (1–3 day) InSAR velocity measurements. Although the effects of seasonal variability cannot be quantified due to a lack of summer velocity measurements over the ice cap, it is likely that the areas affected are restricted to the main outlet glaciers. Since the radar imagery

used in this study was acquired in the winter and spring months (before the onset of melt), velocities derived from these data likely represent minimum annual values.

SPECKLE-TRACKING MEASUREMENTS

Intense crevassing and relatively high velocities at the termini of Eastern, Belcher and Unnamed Glaciers caused decorrelation between the ERS 3 day repeat pass image pairs over these regions. The technique of speckle tracking (Gray and others, 2001; Joughin, 2002) was therefore used to measure surface velocities over the terminus of Belcher Glacier. Speckle tracking measures movement of the surface of the Earth between two coherent radar images acquired from successive orbital cycles (Gray and others, 2001). Coherence is based on the backscatter properties of each image, which allow the pairs to be co-registered to within a fraction of a pixel. In this study, pixels were resampled to 250 m resolution. Displacement rates and directions are measured by matching the speckle pattern of a roving chip (several pixels in size) to a reference image. Unfortunately, poor coherence between the RADARSAT 1 pairs precluded the application of this technique to other areas of the ice cap. Ice velocities of $180\text{--}300 \text{ m a}^{-1}$ were measured throughout the terminal reaches of Belcher Glacier. Velocities of up to 21 m a^{-1} were, however, measured over adjacent bedrock outcrops (where velocity should be 0 m a^{-1}), indicating that the error of the velocity estimates is up to 10% of the measured value.

ICEBERG CALVING RATE

The volume of ice calved was quantified for 94% of that part of the perimeter of the ice cap that terminates at sea level.

Total discharge was calculated as:

$$Q_{\text{Total}} = Q_{\text{flux}} + Q_{v_loss}, \quad (2)$$

where Q_{flux} is the volume of ice flux discharged at the tidewater termini between 1960 and 1999, and Q_{v_loss} is the volume loss due to the observed change of terminus position over that interval (Burgess and Sharp, 2004).

Although the predominant ice-flow regimes at the location of the flux gates for which Q_{flux} was determined are known (derived in a later section), the exact ratio of sliding to ice deformation at each gate is not known. A range of estimates of Q_{flux} was therefore made, based on different assumptions regarding the contribution of internal deformation to overall glacier motion. The maximum estimate was based on the assumption that glacier flow was entirely by basal sliding or bed deformation ($V_{\text{sliding}} = V_{\text{DS}}$). The minimum estimate assumed that internal deformation also contributed to glacier flow, and that the depth-averaged velocity was equal to 80% of the measured downslope surface velocity ($V_{\text{depth_avg}} = V_{\text{DS}} \times 0.8$; Paterson, 1994). The occurrence of flow stripes on all major glaciers, however, suggests that basal motion is likely more important to glacier flow than internal deformation, indicating that the upper velocity estimate is probably closer to the actual value.

Flux gates were located as close as possible to the termini of all tidewater glaciers. However, flux gates of Eastern and Unnamed Glaciers had to be positioned 3 km up-glacier from their termini due to a lack of surface velocity data for regions further downstream. Also, ice flux from 6% of that part of the ice-cap perimeter that terminates at sea level could not be derived due to an absence of surface velocity data. The glaciers concerned originate from relatively small basins isolated from the main ice cap, however, and probably do not contribute significantly to the volume of ice discharged from the ice cap.

Another important source of error associated with the iceberg calving flux measurements (besides V_{error}) is inaccuracies in the ice-thickness data (h_{error}). Point measurements of ice thickness were obtained in 2000 (Dowdeswell and others, 2004) along transects flown 5–10 km apart in north–south and east–west directions across the main part of the ice cap, and up the centre lines of most of the main outlet glaciers. The data were then interpolated across the entire ice cap using an inverse distance-weighted surfacing algorithm constrained by exposed bedrock visible in the 1999 Landsat ETM+ imagery in order to properly constrain channelized flow (Dowdeswell and others, 2004). The spatial resolution of the resultant gridcells was 1 km, with an estimated error in ice thickness of ± 10 m. Errors associated with glacier width (W) at the location of the flux gate were considered insignificant.

Other sources of error associated with extrapolating calving flux estimates over the period 1960–99 are introduced by the variability in velocity of these glaciers on seasonal and/or long-term time-scales. As mentioned above, velocities near the glacier termini may fluctuate on a seasonal time-scale, indicating that the spring InSAR data used to derive velocity estimates in this study likely underestimate the actual annual velocities, and hence rates of calving flux. Since significant summer melting generally only extends from early July to early August (Alt, 1978), the resulting fluctuations in flow rate should not affect the annual velocity measurements by more than $\sim 10\%$. It is difficult to estimate the long-term variability in glacier flow,

due to the lack of velocity data across most of the ice cap over the past 40 years. However, a point velocity of 36 m a^{-1} measured on Sverdrup Glacier by Cress and Wyness (1961) agrees to within 5 m a^{-1} with the 1996 InSAR measured velocity, suggesting a reasonably consistent rate of flow at this location since 1960. On the other hand, evidence of fast glacier flow (see Fig. 3) near the termini of the Southeast 1 and Southeast 2 glaciers indicates that the velocity throughout this region (which is currently $< 15 \text{ m a}^{-1}$) has decreased significantly since the formation of these surface features. If this apparent reduction in velocity has occurred since 1960, the extrapolated calving flux derived from the InSAR data would be an underestimate of the 40 year average across this calving front.

Upper and lower estimates of flux (Q_{max} and Q_{min} respectively) at each gate were calculated from the formulae:

$$Q_{\text{max}} = VT_{\text{max}}W \quad (3)$$

$$Q_{\text{min}} = VT_{\text{min}}W, \quad (4)$$

where

$$VT_{\text{max}} = (V_{\text{sliding}} + V_{\text{error}})(h + h_{\text{error}}) \quad (5)$$

and

$$VT_{\text{min}} = (V_{\text{depth_avg}} - V_{\text{error}})(h - h_{\text{error}}). \quad (6)$$

VT_{max} and VT_{min} represent average values across the flux gates which were then multiplied by the flux gate width. This technique of averaging pixel values along the flux gate, as opposed to a summation of the pixel values, was chosen to avoid including extra pixels in the calculation which can occur when representing irregular or diagonal lines in a gridded format.

The value of Q_{v_loss} was calculated as the product of the 1960–99 area change and the average of all gridded ice-thickness values across the tidewater terminus of each outlet glacier. Area changes were determined as the difference between the 1960 and 1999 outlines of the ice-cap margin (Burgess and Sharp, 2004). The estimated accuracy of volume-change measurements at the glacier termini was derived by assuming a ± 15 m digitizing error around the perimeter of the area of change and a ± 10 m error in the measured ice thickness. Due to the absence of bathymetry data beyond the tidewater termini, volume changes were derived assuming that the thickness of ice throughout the area of change is consistent with ice thickness along the current ice margin.

RESULTS

Flow pattern of Devon Ice Cap

The line-of-sight velocity map reveals a significant difference in the pattern of ice flow between the eastern and western sectors of Devon Ice Cap (Fig. 2). In the western half of the ice cap, ice movement occurs predominantly by slow ‘sheet’ flow ($< \sim 15 \text{ m a}^{-1}$), although several areas of more rapid flow occur along the southwest margin. The largest of these areas occurs up-glacier of North Croker Bay Glacier, where more rapid flow penetrates up to 30 km inland from the ice-cap margin. Flow associated with South Croker Bay Glacier penetrates up to 20 km inland of the ice-cap margin. The Croker Bay glaciers terminate in Lancaster Sound, and their velocities reach maxima of ~ 210 and $\sim 240 \text{ m a}^{-1}$ for the

north and south glaciers respectively. A third region of more rapid flow is associated with Sverdrup Glacier which flows north into Jones Sound. Unfortunately, a lack of velocity data precludes analysis of the inland extent of enhanced glacier flow in this region. However, R.M. Koerner (personal communication, 2004) indicated that the inland extent of fast glacier flow associated with Sverdrup Glacier is defined by the concave-up form of the ice-cap surface which extends ~ 5 km inland of where the glacier enters the main valley. Sverdrup Glacier draws ice from both its main tributary (main branch; Fig. 2), and an eastern arm (east branch; Fig. 2), the up-glacier extension of which is restricted by the head of Eastern Glacier. Enhanced ice flow at the head of a third flow feature to the west of the main tributary (west branch; Fig. 2) is limited as it terminates approximately 14 km down-glacier of its head and does not contribute to the flow of Sverdrup Glacier.

Ice drainage from the northeast sector of the ice cap occurs primarily via large outlet glaciers that flow through mountain valleys to reach sea level. Most of the glaciers in this region originate at valley heads that restrict the inland extension of fast ice flow. Exceptions to this are Eastern Glacier (basin 3) and three tributary glaciers to the Belcher (Belcher tributaries 1–3; Fig. 2), all of which draw from the slower-flowing ice of the interior region. Belcher Glacier itself originates along the north slope of the main east–west ice divide. In the upper reaches of this glacier, velocity increases to $\sim 75 \text{ m a}^{-1}$ upstream of the confluence with Belcher tributary 1 ~ 15 km up-glacier from the terminus. Velocities increase to $\sim 120 \text{ m a}^{-1}$ at this confluence, reaching maximum values of $\sim 290 \text{ m a}^{-1}$ at the glacier terminus. Belcher tributaries 2 and 3 merge with the main glacier at the terminus, forming the widest ‘fast-flowing’ calving front on the ice cap.

Velocities of Eastern Glacier increase over approximately 30 km from the slow-moving interior regions to reach a maximum of $\sim 120 \text{ m a}^{-1}$, 10 km up-glacier from the terminus. Although velocities at the terminus of Eastern Glacier could not be measured, intense crevassing suggests that the speed of this glacier increases as it approaches marine waters. The remaining ice in the northeast sector is drained through a series of tidewater glaciers that range in maximum speed from 30 to 100 m a^{-1} . These glaciers drain relatively small basins ($< \sim 15 \text{ km}^2$) that are separate from the main ice-cap accumulation area.

‘Fast’ flow along Southeast 1 and Southeast 2 glaciers extends farther into the accumulation zone than any other flow feature across the ice cap (Fig. 2). The ice divide at the head of Southeast 1 has a convex up-glacier form, suggesting that this outlet glacier may be extending headwards into the less active basin to the west (basin 54). Both glaciers converge 40 km down-glacier from the head, resulting in a near-stagnant region ($< 10 \text{ m a}^{-1}$) approximately 250 km^2 in area that terminates along an 8 km ice front in Hyde Inlet (Fig. 2). Despite low velocities throughout this region, flow stripes visible on the surface of Southeast 1 Glacier suggest that this feature was once flowing faster than at present (Fig. 3). Sharp shear zones along both margins and folded moraines near the terminus are indicators that this glacier may indeed have surged in the past (Dowdeswell and Williams, 1997; Copland and others, 2003b).

Ice from the southern slopes of the Cunningham Mountains drains through a series of steep valley glaciers towards Lancaster Sound, most of which terminate on land.

Included in this group is a possible surge-type glacier identified by Copland and others (2003b). Measured velocities on this glacier reach a maximum of $\sim 150 \text{ m a}^{-1}$, but the surface morphology of the glacier suggests that, if it is indeed a surge-type glacier, it is currently in the quiescent phase of a surge cycle.

Glacier flow regimes

Four major flow regimes were identified based on the relationship between the ratio of surface velocity to ice thickness (v/h) and the driving stress (τ_d) along four flowlines across the ice cap (Fig. 6 below). When the ice flow is solely due to ice deformation, the parameter (v/h) represents the mean shear strain rate in a vertical profile through the ice. When basal motion is important, this parameter no longer represents the shear strain rate in the ice, but the inverse of the ratio of v/h to τ_d has units of Pa s and is therefore a measure of the ‘effective viscosity’ of the glacier system.

τ_d was derived from:

$$\tau_d = \rho_i g h \sin \alpha, \quad (7)$$

where ρ_i is the density of ice (910 kg m^{-3}) and g is the acceleration due to gravity (9.81 m s^{-2}). The effects of local variations in surface slope due to longitudinal stress gradients in the ice were removed by averaging surface slope values over distances equivalent to ~ 10 times the ice thickness.

Flow regime 1 is distinguished by values of $v/h < 0.075 \text{ a}^{-1}$ and a high positive correlation with τ_d ($r^2 > 0.85$), though the sensitivity of v/h to changes in τ_d is low (Fig. 4a–d). This behaviour suggests that the ice is frozen to the bed, and glacier movement is by internal deformation alone (Budd and Smith, 1981; Cooper and others, 1982). Within this flow regime, however, the ratio of v/h to τ_d may increase downstream (Fig. 4a–c). This is probably a reflection of softening of the ice as it warms up with increasing distance of transport.

Flow regime 1 is characteristic of the upper reaches leading into major outlet glaciers (Fig. 5a–c) and of the whole western lobe (Fig. 5d). In these regions, glaciers have convex upward surface profiles (Fig. 6a–d), and flow is not constrained laterally by bedrock topography. Flow regime 1 is also observed in the terminal reaches of the Southeast 1 Glacier flowline where the velocity, and hence v/h , is low (Figs 3 and 6c). In this region, v/h decreases as τ_d rises, suggesting increased flow resistance and ‘effective viscosity’ towards the glacier terminus. This may be indicative of a frozen bed at the glacier margin.

The relationship between v/h and τ_d changes significantly at $v/h \sim 0.075 \text{ a}^{-1}$ (flow regime 2; Fig. 4a–c). In this flow regime, the ratio of v/h to τ_d is generally higher, the relationship between the two variables is more sensitive, and the sign of the relationship may be opposite to that observed in flow regime 1 (Fig. 4b and c). This is not, however, always the case (Fig. 4a). The ensemble of changes observed suggests a down-flow reduction in ‘effective viscosity’ and flow resistance, and a contribution of basal motion to the surface velocity. The beginning of flow regime 2 coincides with convergent flow at the head of the major outlet glaciers (Fig. 5a and c) and the appearance of flow stripes on the ice surface (Fig. 5a–c). Gudmundsson and others (1998) argued that flow stripes form only where the velocity at the bed is large relative to shearing through the ice thickness, supporting the argument that basal motion must be

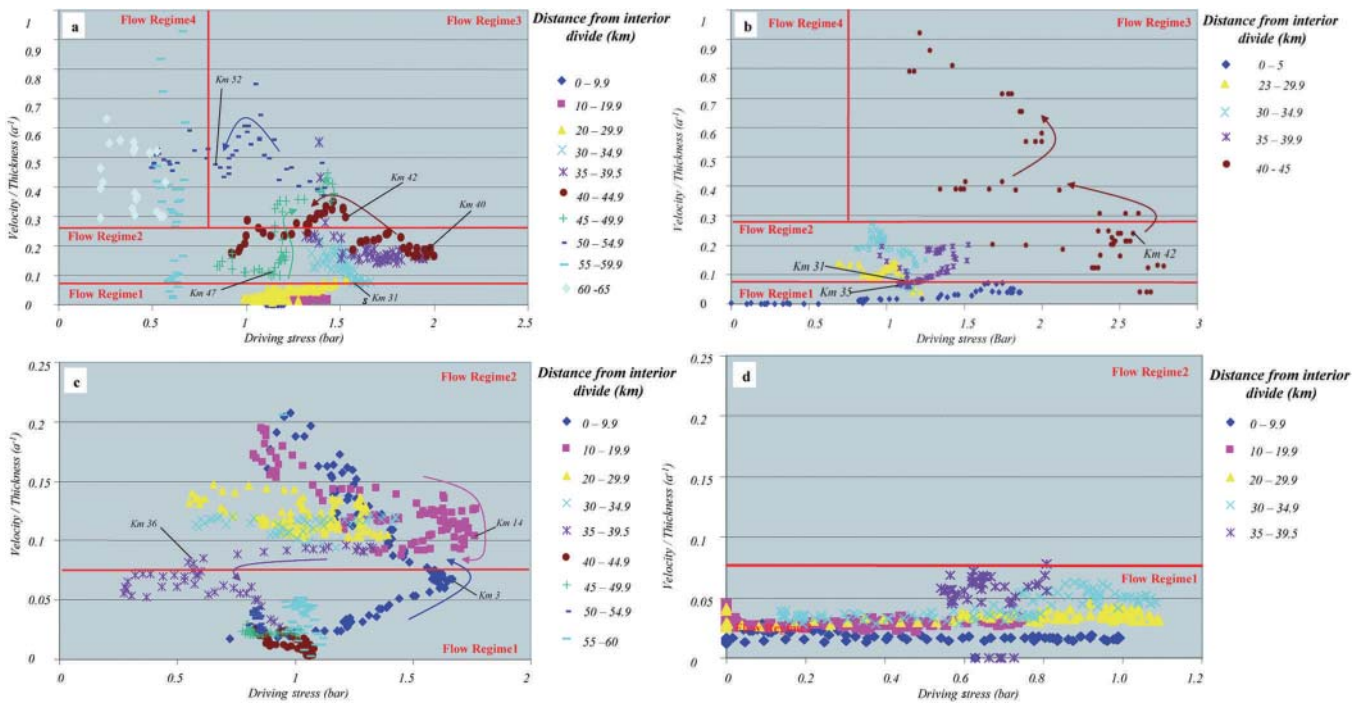


Fig. 4. The predominant modes of glacier flow across Devon Ice Cap are identified based on the relationship between mean shear strain rate (v/h) and driving stress (τ_d) along profiles of (a) North Croker Bay Glacier, (b) Belcher Glacier, (c) Southeast 1 Glacier and (d) the western lobe. Threshold values (red lines) separate each distinct ice-flow regime based on changes in the relative slope of the clusters in each feature space. Coloured arrows in (a–c) indicate the down-glacier direction of ice flow.

significant in regions with this flow regime. Flow regime 2 commences ~ 5 km up-glacier from steps in the bedrock topography along North Croker Bay and Southeast 1 Glaciers (Fig. 6a and c). These locations also coincide with the transformation to a concave-up surface profile (Fig. 6a–c) from the convex-up profile which is characteristic of flow regime 1. Rapid acceleration of V_{DS} and ice thinning at the cusp of the bedrock steps (Fig. 6a and c) indicate that the onset of basal sliding is controlled primarily by the subglacial topography at these locations (McIntyre, 1985).

Ice-flow regime 3 appears to be defined by threshold values of $v/h > \sim 0.28 a^{-1}$ and $\tau_d > \sim 0.075$ MPa (Fig. 4a and b). In this region, v/h is inversely related to τ_d , and the slope of the relationship between the two variables is steeper than in flow regime 2. The ratio of v/h to τ_d is higher again than in flow regime 2, implying a further reduction in viscosity and probably an increase in the relative contribution of basal motion to the surface velocity. Regions of flow regime 3 occur throughout the mid- to lower reaches of the major glaciers where flow stripes are well developed on the ice surface. Along the North Croker Bay Glacier flowline, flow regime 3 begins where the glacier enters the bedrock valley at km 48 (Fig. 5a) and V_{DS} increases rapidly (60 – 170 $m a^{-1}$ over a 1 km distance). A rapid increase of V_{DS} (and hence v/h) marks the beginning of flow regime 3 at km 42 along the Belcher Glacier flowline (Fig. 5b). In contrast to North Croker Bay Glacier, however, the flow of ice within this region is driven mainly by large values of τ_d that occur over steeply sloping (and rough) bed topography that descends to ~ 300 m below sea level within 2 km of the glacier terminus. In both situations, intense crevassing at the onset of flow regime 3 suggests that an increase in the rate of ice deformation occurs at the transition from flow regime 2 to flow regime 3. In addition, meltwater channels terminating

at these crevasse fields (visible in the 1960s aerial photography) indicate that surface run-off may penetrate to the glacier bed via the crevasses and potentially enhance flow rates throughout this zone during the summer months. A fourth regime, flow regime 4, is defined by threshold values of $v/h > 0.28 a^{-1}$ and $\tau_d < 0.075$ MPa (Fig. 4a). In this region, the wide range of values of v/h for consistently low values of τ_d is indicative of low friction at the glacier bed. This may suggest that deformation of subglacial sediments contributes to basal motion, which remains a major component of the surface velocity of the glacier. Flow regime 4 is characteristic of the terminal reaches of North Croker Bay Glacier, where the glacier is grounded below sea level (Fig. 6a). It is not, however, found along Belcher and Southeast 1 Glaciers which are also grounded below sea level.

Identification of distinct flow regimes across the ice cap indicates that the mode of ice movement evolves as one of a few possible sequences along a flowline between the interior region and the ice-cap margin. The initial transition occurs at the head of the outlet glaciers where cold-based ice moving by internal deformation only (Bentley, 1987) transforms to warm-based flow, and basal sliding commences. This mode of flow continues until the glacier either (a) reverts back to cold-based where flow is by internal deformation only, or (b) is enhanced by high driving stresses or narrowing bedrock valleys. Glaciers that transform into (b) likely experience high rates of internal deformation (Truffer and Echelmeyer, 2003) and enhanced basal sliding as a result of the penetration of surface meltwater through crevasses during the summer melt season (Zwally and others, 2002; Boon and Sharp, 2003; Copland and Sharp, 2003a). A third transition occurs near the termini of a few glaciers where τ_d is greatly reduced but high velocities are maintained. The mechanics of this mode of glacier flow are

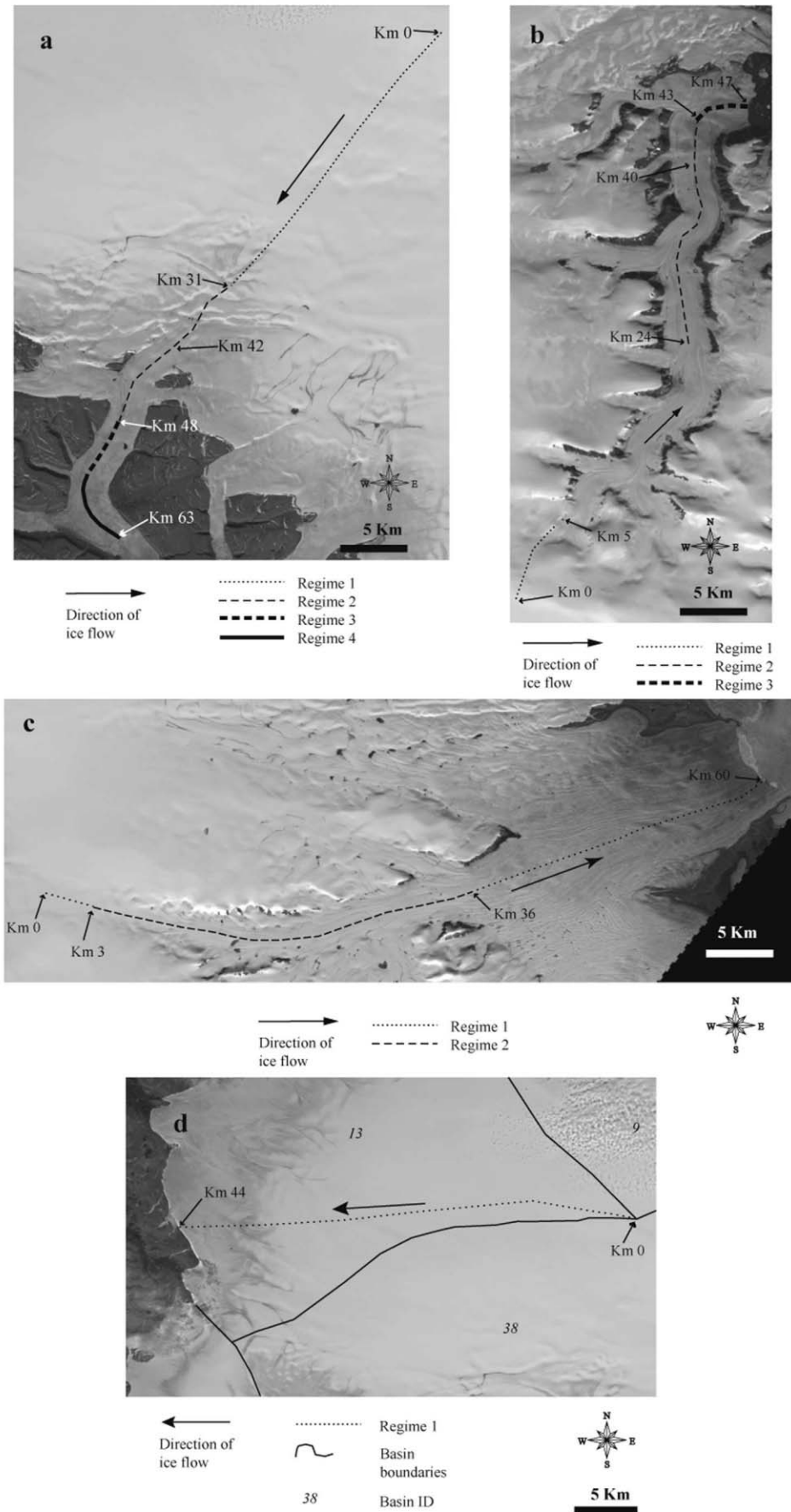


Fig. 5. Planimetric view of the dominant flow regimes along (a) North Croker Bay Glacier, (b) Belcher Glacier, (c) Southeast 1 Glacier and (d) the western lobe. Centre-line profiles are superimposed on a subset of the 1999 Landsat ETM+ satellite imagery. Locations of image subsets and profiles are identified in Figure 7.

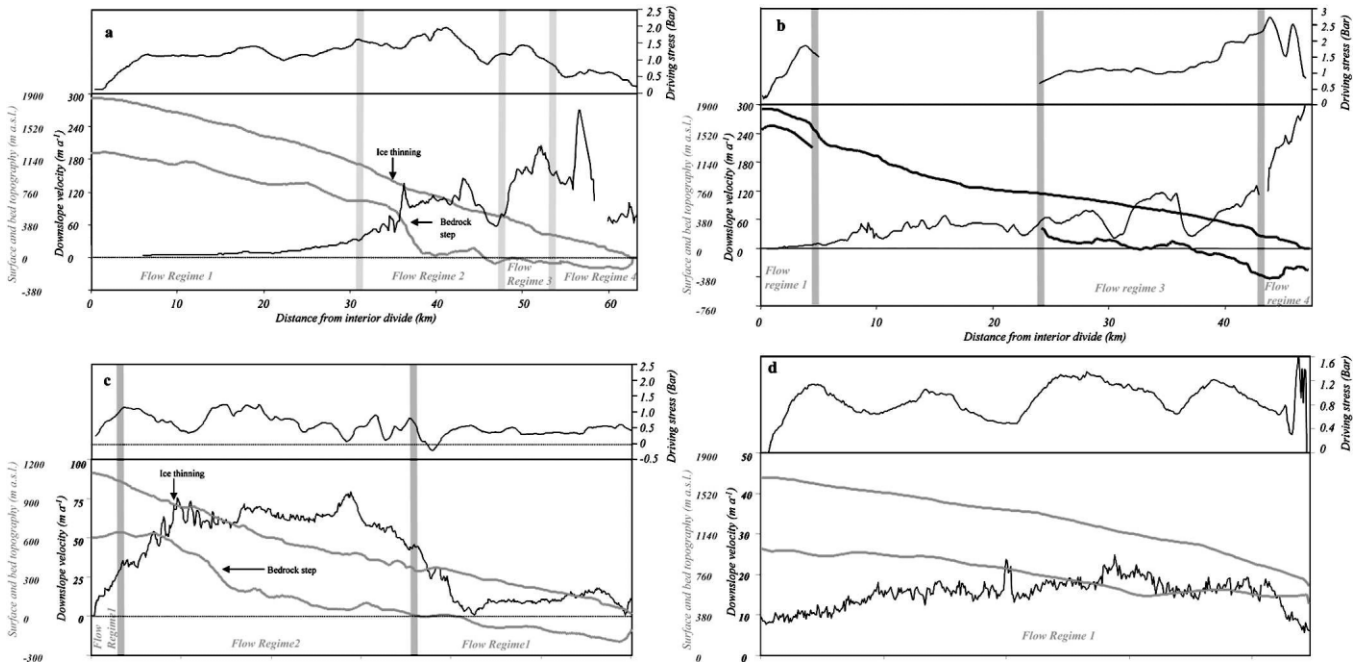


Fig. 6. Profiles of driving stress, surface and bed topography, and downslope velocity along (a) North Croker Bay Glacier, (b) Belcher Glacier, (c) Southeast 1 Glacier and (d) the western lobe. Gaps in the downslope velocity profile of (a) between km 0–5 and km 58–59 represent sections where InSAR data could not be derived. The absence of bed topography data in (b) between km 4 and 24 precluded calculation of τ_d throughout this zone.

likely similar to ice-stream flow where glacier movement occurs over a highly deformable and/or lubricated bed and the main resistive forces to flow occur at the glacier margins (Bentley, 1987; Truffer and Echelmeyer, 2003).

Threshold values of v/h and τ_d separating the four distinct flow regimes in the scatter plots were applied to raster datasets of these parameters in order to map the distribution of ice-flow regimes across the entire ice cap. For the raster grids, surface slope was averaged as a function of area rather than in an along-profile direction. This spatial averaging has the effect of slightly over- (under-) estimating the slope relative to the profile analyses over high (low) slope areas. These variations, however, had no effect on the flow regime classification.

Further uncertainties in τ_d may derive from the fact that the glacier shape factors were not included in the computed values of τ_d . A few representative shape factor values were computed along the major outlet glaciers (assuming a parabolic glacier cross-section; Paterson, 1984) and indicated that applying this correction could reduce the computed values of τ_d by up to $\sim 25\%$. It is also possible that the longitudinal averaging used in this study ($10h$) was inadequate to fully remove the effects of longitudinal stress gradients from τ_d . In particular, near the glacier termini where averaging was $<10h$, computed values of τ_d may be slightly higher than the true values. In any case, slight discrepancies between the actual and computed values of τ_d would have only minor implications for flow-regime classification relating exclusively to the separation of flow regime 3 from flow regime 4.

Approximately 50% of the mapped area of the ice cap was classified as flow regime 1 which includes the interior region above 1000 m a.s.l. as well as $\sim 600 \text{ km}^2$ of the southeast sector which lies below 300 m a.s.l. (Fig. 7). Flow regime 2 is confined mainly to the outlet glaciers, but it also

occurs in some small areas along the western margin. Excluding the areas that were not mapped, this regime comprises approximately 22% of the total area east of the central divide (basins 3, 10, 11, 15, 20, 24, 25, 29, 30, 33, 35, 36, 37, 40, 39, 60, 66, 70 and 73) but only 8% of the area west of the central divide (basins 9, 13, 38, 43, 54, 61, 65 and 67), indicating that basal motion is much more prevalent in the east. Flow regime 3 occurs up to 22 km up-glacier from the termini of North and South Croker Bay Glaciers and up to 25 km up-glacier from the terminus of Belcher Glacier (along Belcher tributary 2), reflecting the combination of relatively high driving stresses and high velocities in these regions. Flow regime 4 is confined to the termini of North Croker Bay, East 3, East Central 1 and South Cunningham Glaciers as well as a small section along Southeast 2 Glacier. The glaciers classified as flow regime 4 are all grounded above sea level except for the terminus region of North Croker Bay Glacier, suggesting that reduced basal friction of these glaciers may be attributed to the presence of deformable sediments at the bed rather than to buoyancy effects at tidewater margins.

Rates of iceberg calving

The rate of ice calved directly into the ocean due to flux at the tidewater margins was estimated to be $0.42 \pm 0.14 \text{ km}^3 \text{ a}^{-1}$. This equates to a calving flux rate of $16.8 \pm 5.7 \text{ km}^3$ between 1960 and 1999, assuming invariant glacier flow velocities over this time interval. Volume loss due to retreat of the tidewater termini increases the total mass loss by $3.6 \pm 0.026 \text{ km}^3$, resulting in a total volume loss due to iceberg calving of $20.5 \pm 4.7 \text{ km}^3$ over the past 40 years. The northeast sector (basins 10, 11, 15, 20, 24, 25, 29, 30, 31, 33 and 36) produced 67% of the total volume of ice calved. Belcher Glacier alone was responsible for 70% of this amount, which equates to almost half (47%) of the ice-cap

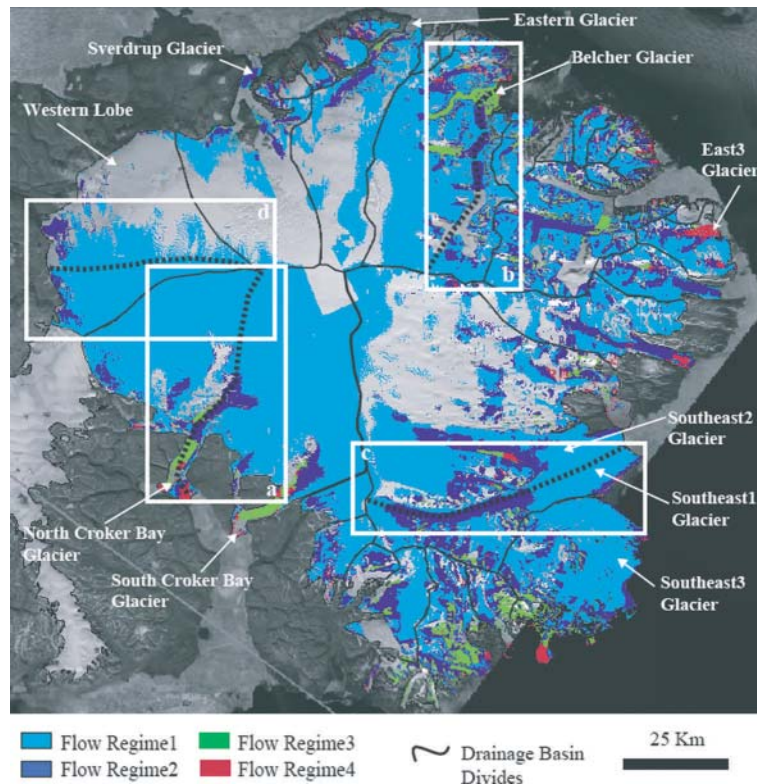


Fig. 7. Mapped distribution of classified flow regimes across Devon Ice Cap. White boxes indicate the location of image subsets and centre-line profiles in Figure 5.

total (Fig. 8). Most of the mass lost from Belcher Glacier ($\sim 93\%$) is accounted for by ice flux as opposed to terminus change. This reflects the relatively thick ice ($\sim 250\text{ m}$) and high velocity (up to 290 m a^{-1}) at this ice front. Although two major glaciers terminating at the southeast margin of the ice cap (basins 39 and 60) have extensive calving fronts ($\sim 18\text{ km}$ long), this region accounts for only 16% of the total calving flux. This is due mainly to the low surface velocities of these glaciers. The southernmost calving front (basin 60) is unique in that the majority of mass calved from this terminus is due to retreat of the ice front ($\sim 60\%$) rather than ice flux. North and South Croker Bay Glaciers have advanced since 1960. This reduces the calculated volume loss due to flux by 12%. Similarly, glacier advance reduced the calculated calving flux of Sverdrup Glacier by 13%. Mass loss due to calving from the western glaciers accounts for $\sim 10\%$ of the total volume of ice calved from Devon Ice Cap. In total, the eight major tidewater glaciers draining the ice cap (indicated in Fig. 8) are responsible for $\sim 90\%$ of the total discharge of ice calved. The rest is derived from small alpine glaciers (generally $<1\text{ km}$ wide) that flow from basins in the northeast and eastern sectors.

CONCLUSIONS

The continuous surface velocity field of Devon Ice Cap mapped using InSAR techniques reveals a significant contrast in ice-flow dynamics between the east and west sides of the ice cap. The eastern half of the ice cap is drained by several fast-flowing outlet glaciers that extend up to 60 km inland from the ice-cap margin, and in some cases reach within a few kilometres of the central ice divides. The western half of the ice cap is drained primarily by sheet flow,

but also by a few outlet glaciers that are restricted to within $<30\text{ km}$ of the ice-cap margins.

The predominant ice-flow regimes were classified based on the relationship between the ratio of surface velocity to ice thickness and the driving stress derived along four flowlines from distinctly different regions across the ice cap. The classified regimes were mapped across $\sim 75\%$ of the ice-cap surface for which both surface velocity and ice-thickness data are available. The interior and southeast ice regions were classified as flow regime 1 type flow and are characterized by frozen bed conditions where ice movement is by internal deformation alone. The main sections of most outlet glaciers were classified as flow regime 2, in which basal motion occurs. The transition to flow regime 2 along a flowline marks the onset of basal sliding and is usually associated with ice flow over a step in the bedrock topography. The appearance of flow stripes on the ice surface in regions of flow regime 2 supports the argument that basal motion makes a major contribution to the surface velocity in these regions. Flow regime 3 is characterized by enhanced basal motion and internal deformation due to a significant increase in driving stress. Flow regime 4 is characterized by a wide range in values of v/h (including maximum values) within sections of the glacier with consistently low values of driving stress. This flow regime occurs within a few kilometres of the termini and is indicative of minimal basal friction that may result from the presence of deformable sediments at the glacier bed.

Approximately 20.5 km^3 of ice was calved from Devon Ice Cap between 1960 and 1999. Approximately 89% of the total volume of ice calved was discharged from the eastern margin, with the largest single source being Belcher Glacier which was responsible for $\sim 50\%$ of the total amount.

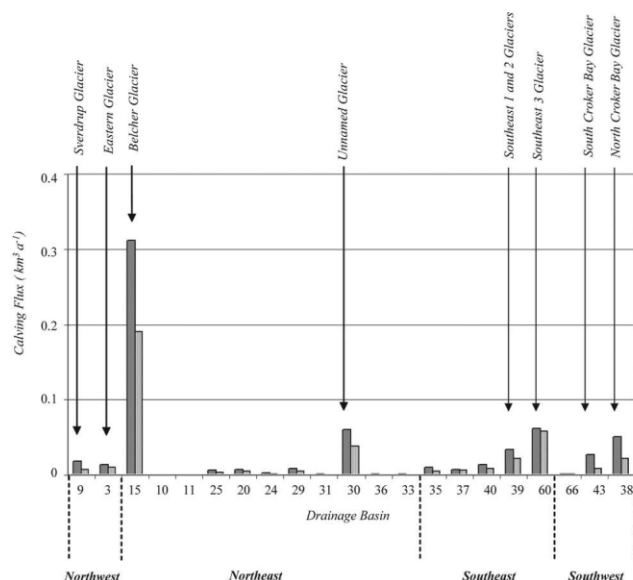


Fig. 8. Distribution of iceberg calving rates on Devon Ice Cap. Solid bars represent the upper calving flux estimate, and the shaded bars represent the lower calving flux estimate.

Comparing the total volume of ice lost due to calving and total mass loss of $\sim 67 \text{ km}^3$ from Devon Ice Cap between 1960 and 1999 (Burgess and Sharp, 2004) indicates that iceberg calving may account for up to 30% of the total volume loss over the past 40 years. Iceberg calving therefore represents a significant form of ablation from Devon Ice Cap and should be accounted for when determining the state of health of this ice mass as a whole. Dowdeswell and others (2002) also found that about 40% of mass loss from the 5575 km^2 Akademii Nauk ice cap, Severnaya Zemlya, Russia, was lost by iceberg calving. Together with the evidence from Devon Ice Cap, this suggests that iceberg production is an important component of the total mass loss from large Arctic ice caps.

ACKNOWLEDGEMENTS

This work was supported by grants from the Natural Sciences and Engineering Research Council (NSERC), Canada, and the Meteorological Service of Canada (CRYSYS program) to M. Sharp. D. Burgess received an IPS-2 scholarship from NSERC and Land Data Technologies Inc., and grants from the Canadian Circumpolar Institute and Northern Scientific Training Program (Department of Indian and Northern Affairs Canada), and D. Mair was supported by a Research Fellowship from the Leverhulme Trust. We also acknowledge Innovation and Science Research Investments Program (ISRIP) for a grant to purchase a DGPS, and NASA/Alaska Satellite Facility (ASF) for providing the ERS-1/-2 radar imagery. Logistical support in the field was provided by the Polar Continental Shelf Project, Natural Resources Canada (contribution No. 628-00). UK funding for the acquisition, analysis and interpretation of airborne radio-echo sounding data was provided by Natural Environment Research Council grant GR3/12469 and the European Union SPICE (Software Process Improvement and Capability determination) project. Finally, we thank L. Gray and N. Short (Canada Centre for Remote Sensing) for software training and access to the speckle-tracking programs.

REFERENCES

- Alt, B.T. 1978. Synoptic climate controls of mass-balance variations on Devon Island Ice Cap. *Arct. Alp. Res.*, **10**(1), 61–80.
- Bentley, C.R. 1987. Antarctic ice streams: a review. *J. Geophys. Res.*, **92**(B9), 8843–8858.
- Bingham, R.G., P.W. Nienow and M.J. Sharp. 2003. Intra-annual and intra-seasonal flow dynamics of a High Arctic polythermal valley glacier. *Ann. Glaciol.*, **37**, 181–188.
- Boon, S. and M. Sharp. 2003. The role of hydrologically-driven ice fracture in drainage system evolution on an Arctic glacier. *Geophys. Res. Lett.*, **30**(18). (10.1029/2003GL018034.)
- Budd, W.F. and I.N. Smith. 1981. The growth and retreat of ice sheets in response to orbital radiation changes. *International Association of Hydrological Sciences Publication 131* (Symposium at Canberra 1979 – *Sea Level, Ice and Climatic Change*), 369–409.
- Burgess, D.O. and M.J. Sharp. 2004. Recent changes in areal extent of the Devon ice cap, Nunavut, Canada. *Arct. Antarct. Alp. Res.*, **36**(2), 261–271.
- Cooper, A.P.R., N.F. McIntyre and G. de Q. Robin. 1982. Driving stresses in the Antarctic ice sheet. *Ann. Glaciol.*, **3**, 59–64.
- Copland, L. and M. Sharp. 2001. Mapping thermal and hydrological conditions beneath a polythermal glacier with radio-echo sounding. *J. Glaciol.*, **47**(157), 232–242.
- Copland, L., M.J. Sharp and J.A. Dowdeswell. 2003a. The distribution and flow characteristics of surge-type glaciers in the Canadian High Arctic. *Ann. Glaciol.*, **36**, 73–81.
- Copland, L., M.J. Sharp, P.W. Nienow and R.G. Bingham. 2003b. The distribution of basal motion beneath a High Arctic polythermal glacier. *J. Glaciol.*, **49**(166), 407–414.
- Cress, P. and R. Wyness. 1961. Observations of glacial movements. *Arctic*, **14**(4), 257–259.
- Cumming, I. and J. Zhang. 2000. Measuring the 3-D flow of the Lowell Glacier with InSAR. In *Fringe '99: Second ESA International Workshop on ERS SAR Interferometry, Liège, Belgium, 10–12 November 1999*. European Space Agency, 1–9.
- Dowdeswell, J.A. and M. Williams. 1997. Surge-type glaciers in the Russian High Arctic identified from digital satellite imagery. *J. Glaciol.*, **43**(145), 489–494.
- Dowdeswell, J.A. and 10 others. 2002. Form and flow of the Academy of Sciences ice cap, Severnaya Zemlya, Russian High Arctic. *J. Geophys. Res.*, **107**(B4). (10.1029/2000JB000129.)
- Dowdeswell, J.A., T.J. Benham, M.R. Gorman, D. Burgess and M. Sharp. 2004. Form and flow of the Devon Island ice cap, Canadian Arctic. *J. Geophys. Res.*, **109**(F02002). (10.1029/2003JF000095.)
- Gabriel, A.K., R.M. Goldstein and H.A. Zebker. 1989. Mapping small elevation changes over large areas: differential radar interferometry. *J. Geophys. Res.*, **94**(B7), 9183–9191.
- Gray, L., N. Short, K.E. Mattar and K.C. Jezek. 2001. Velocities and flux of the Filchner Ice Shelf and its tributaries determined from speckle tracking interferometry. *Can. J. Remote Sensing*, **27**(3), 193–206.
- Gudmundsson, G.H., C.F. Raymond and R. Bindschadler. 1998. The origin and longevity of flow stripes on Antarctic ice streams. *Ann. Glaciol.*, **27**, 145–152.
- Gudmundsson, G.H., G. Adalgeirsdóttir and H. Björnsson. 2003. Observational verification of predicted increase in bedrock-to-surface amplitude transfer during a glacier surge. *Ann. Glaciol.*, **36**, 91–96.
- Iken, A. 1972. Measurements of water pressure in moulins as part of a movement study of the White Glacier, Axel Heiberg Island, Northwest Territories, Canada. *J. Glaciol.*, **11**(61), 53–58.
- Joughin, I. 2002. Ice-sheet velocity mapping: a combined interferometric and speckle-tracking approach. *Ann. Glaciol.*, **34**, 195–201.
- Joughin, I., R. Kwok and M. Fahnestock. 1996. Estimation of ice-sheet motion using satellite radar interferometry: method and error analysis with application to Humboldt Glacier, Greenland. *J. Glaciol.*, **42**(142), 564–575.

- Koerner, R.M. 1970. The mass balance of the Devon Island ice cap, Northwest Territories, Canada, 1961–66. *J. Glaciol.*, **9**(57), 325–336.
- Mair, D.W.F., D.O. Burgess and M.J. Sharp. 2004. Thirty-seven year mass balance of the Devon Ice Cap, Nunavut, Canada determined by shallow ice coring and melt modelling. *J. Geophys. Res.* **110**(F01011). (doi: [10.1029/2003JF000099](https://doi.org/10.1029/2003JF000099).)
- Massonnet, D. and K.L. Feigl. 1998. Radar interferometry and its application to changes in the Earth's surface. *Rev. Geophys.*, **36**(4), 441–500.
- McIntyre, N.F. 1985. The dynamics of ice-sheet outlets. *J. Glaciol.*, **31**(108), 99–107.
- Paterson, W.S.B. 1994. *The physics of glaciers. Third edition.* Oxford, etc., Elsevier.
- Truffer, M. and K.A. Echelmeyer. 2003. Of isbræ and ice streams. *Ann. Glaciol.*, **36**, 66–72.
- Unwin, B.V. 1998. Arctic ice cap velocity variations revealed using ERS SAR interferometry. (PhD thesis, University College London.)
- Vachon, P.W., D. Geudtner, K. Mattar, A.L. Gray, M. Brugman and I. Cumming. 1996. Differential SAR interferometry measurements of Athabasca and Saskatchewan glacier flow rate. *Can. J. Remote Sensing*, **22**(3), 287–296.
- Webb, F.H. and J.F. Zumberge. 1995. *An introduction to GIPSY/OASIS-II.* Pasadena, CA, California Institute of Technology. US National Aeronautics and Space Administration. Jet Propulsion Laboratory.
- Zebker, H.A., P.A. Rosen, R.M. Goldstein, A. Gabriel and C.L. Werner. 1994. On the derivation of coseismic displacement fields using differential radar interferometry: the Landers earthquake. *J. Geophys. Res.*, **99**(B10), 19,617–19,634.
- Zwally, H.J., W. Abdalati, T. Herring, K. Larson, J. Saba and K. Steffen. 2002. Surface melt-induced acceleration of Greenland ice-sheet flow. *Science*, **297**(5579), 218–222.

MS received 21 July 2004 and accepted in revised form 30 January 2005



Recent changes in thickness of the Devon Island ice cap, Canada

David Burgess^{1,2} and Martin J. Sharp¹

Received 19 June 2007; revised 28 March 2008; accepted 8 April 2008; published 19 July 2008.

[1] Long-term rates of thickness change were derived at several spatial scales using a variety of methods for most of the Devon Island ice cap, Nunavut, Canada. Basin-wide thickness change calculations were derived for the accumulation zones of all major drainage basins as the area-averaged volume difference between balance and InSar fluxes at the altitude of the long-term equilibrium line (ELA). Thickness changes for ablation zones were derived as a function of the surface mass balance, flux across the EL and calving flux, averaged across the ablation areas. Average rates of thickness change are near zero in the accumulation zones of the northern and southwestern basins but reach $-0.23 \pm 0.11 \text{ m a}^{-1}$ w.e. in the southeast basin due to dynamic thinning. Thickness changes were also estimated along five major outlet glaciers as a function of flux divergence and net surface mass balance and along the Belcher Glacier by comparing elevation values derived from 1960s aerial photography with those derived from 2005 NASA Airborne Topographic Mapper (ATM) surveys. Ice dynamics have had a significant influence on the pattern of thickness change of all outlet glaciers examined in this study. Volume changes derived from the basin-wide values indicate a net loss of $-76.8 \pm 7 \text{ km}^3$ water equivalent from the main portion of the ice cap from 1960 to 1999, contributing $0.21 \pm 0.02 \text{ mm}$ to global sea level over this time. This value is $\sim 44\%$ greater than previous estimates of volume change based on volume-area scaling methods and surface mass balance alone.

Citation: Burgess, D., and M. J. Sharp (2008), Recent changes in thickness of the Devon Island ice cap, Canada, *J. Geophys. Res.*, 113, B07204, doi:10.1029/2007JB005238.

1. Introduction

[2] Knowledge of the rates of thickness change of the Earth's large ice masses is crucial to understanding their state of balance and contribution to global sea level change. Combined, the Greenland and Antarctic ice sheets would raise sea level by $>80 \text{ m}$ if they were to disintegrate completely. Smaller ice caps and glaciers pose a more immediate concern, however, and may have accounted for a significant fraction ($>50\%$) of total sea level rise over the last century [Dyurgerov and Meier, 2005]. Currently, model predictions of volume loss from these ice masses are based on changes in surface mass balance alone [Intergovernmental Panel on Climate Change (IPCC), 2007]. Recent studies have, however, demonstrated that climate induced changes in ice dynamics can significantly influence the net mass balance of high-latitude ice masses [Rignot and Kanagaratnam, 2006]. It is therefore essential to determine the relative impact of changes in ice dynamics, iceberg calving, and surface mass balance in order to properly assess how large ice masses in the polar regions may respond to future climate warming.

[3] The Devon Island ice cap occupies approximately $14,000 \text{ km}^2$ of the eastern half of Devon Island, Nunavut (Figure 1), which makes it one of the largest ice masses in

the Canadian high Arctic. This ice cap derives a significant proportion of its accumulation from the North Open Water Polynya in Baffin Bay [Koerner, 1977]. According to field measurements collected by R. Koerner, the net mass balance of the northwest sector of the Devon Island ice cap (Figure 2) over the period 1961–2001 was -0.086 m a^{-1} water equivalent (w.e.). Interannual variations in net mass balance on the ice cap arise mainly from variations in the summer balance [Koerner, 2002].

[4] One estimate of volume change of the Devon Island ice cap, which is based on in situ mass balance data collected in the northwest sector of the ice cap by R. Koerner between 1961 and 2003, indicates that the main part of the ice cap has decreased in volume by $\sim 42 \text{ km}^3$ w.e. This value is a minimum estimate however, as it does not account for losses due to iceberg calving. An independent volume loss estimate of $-0.81 \text{ km}^3 \text{ a}^{-1}$ (of ice) was derived from surface elevation changes measured from repeat laser altimetry performed by NASA in 1995 and 2000 (lines NASA_EW1, NASA_EW2, and NASA_NS1; Figure 2) [Abdalati et al., 2004]. This yields a total loss of -31 km^3 w.e. when extrapolated over the 42 year period. Both sets of observations are of limited value in terms of estimating volume change for the Devon Island ice cap as a whole due to the large extrapolations involved.

[5] Comparison of the ice margins identified on 1960 aerial photography and on 1999 Landsat7 ETM+ imagery reveals significant spatial variability in the rate and sign of fluctuations of the margins of the Devon Island ice cap

¹Department of Earth and Atmospheric Sciences, University of Alberta, Edmonton, Alberta, Canada.

²Now at Canada Centre for Remote Sensing, Ottawa, Ontario, Canada.

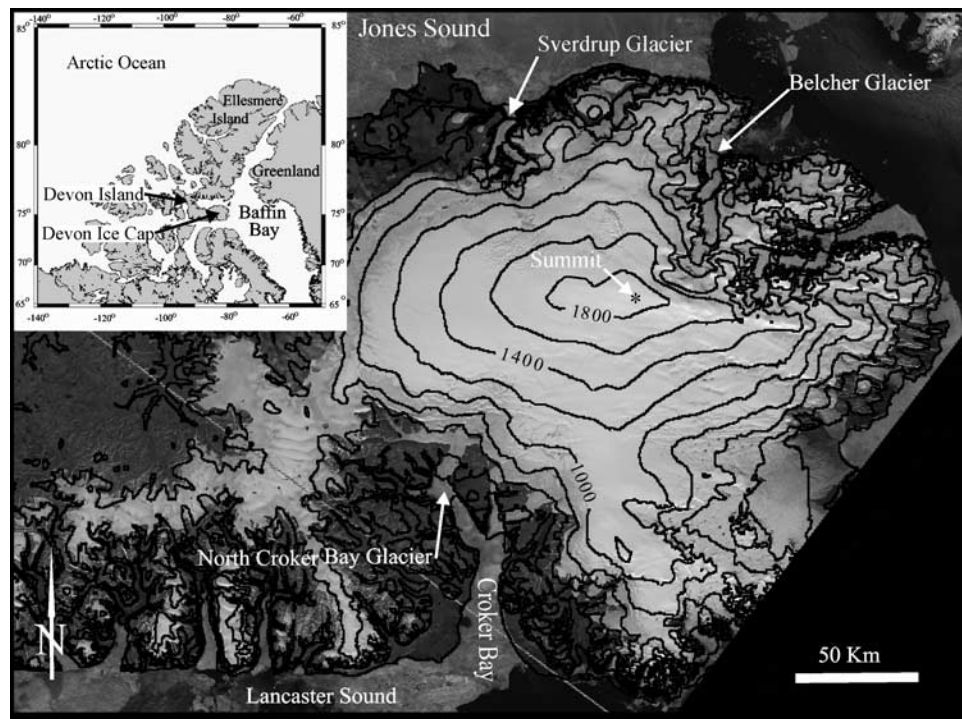


Figure 1. 1999 Landsat 7 ETM+ orthomosaic of the Devon ice cap, Nunavut, Canada. Inset shows the location of the Devon ice cap in the Canadian Arctic Archipelago.

[Burgess and Sharp, 2004]. The dominant changes identified include retreat of most of the larger tidewater glaciers (by as much as 3 km in the southeast region) and advance of the western margin by up to 120 m. The net volume decrease of the main ice cap (excluding the stagnant southwest arm) was estimated to be $-44 \pm 5 \text{ km}^3$ w.e. using volume-area scaling techniques [Burgess and Sharp, 2004]. Using a combination of ice core derived estimates of net accumulation and melt modeling, Mair *et al.* [2005] estimated the net volume reduction of the ice cap to be $-59 \pm 26 \text{ km}^3$ w.e. between 1963 and 2000 due to net surface mass balance alone. They identified the southeast region as the area where the greatest volume changes are occurring. Combined with mass loss due to iceberg calving ($-19 \pm 5 \text{ km}^3$ water equivalent between 1960 and 1999) [Burgess *et al.*, 2005], it is estimated that total loss from the Devon Island ice cap over the past 40 years may be as great as -78 km^3 water equivalent. It seems likely that there is significant variability in the magnitude and sign of volume change across the Devon Island ice cap, and accounting for this variability results in estimates of volume change that are consistently larger than those derived from “localized” mass balance observations and altimetry.

[6] In this study, estimates of the long-term (40 years) rates of thickness change of the Devon Island ice cap, Nunavut, Canada, are derived using several approaches. First, average rates of thickness change were calculated for the accumulation zones of individual drainage basins as the area weighted difference between the measured ice flux and balance flux at the altitude of the equilibrium line (ELA). For the ablation zones of these basins, average rates of thickness change were calculated from the difference between the mass flux at the ELA and the sum of the volume

losses from the ablation area by surface mass balance and iceberg calving. Second, in situ measurements of rates of thickness change were obtained for three sites in the southwest region of the ice cap using (1) the “coffee can” technique developed by Hamilton and Whillans [2000] and (2) measurements of the 40 year surface mass balance and vertical strain across a $1 \text{ km} \times 1 \text{ km}$ grid. Third, rates of thickness change along five major outlet glaciers (the Fitzroy, North and South Croker Bay, and the Southeast 1 and 2 Glaciers) were derived as a function of the difference in ice flux between successive gates spaced 5–8 km apart, and the average net surface mass balance between the fluxgates. For the Belcher Glacier only, direct measurements of surface lowering were obtained by comparing surface elevations obtained from analytical stereo photogrammetry from 1960s aerial photography with values obtained from an airborne laser altimetry survey conducted by NASA in the spring of 2005.

[7] These measurements should allow us to answer important questions concerning the state of balance of the Devon Island ice cap. These include: (1) What is the magnitude of volume loss from the ice cap since 1960 and how much does this contribute to global sea level change? (2) How is volume change distributed between drainage basins? (3) Is area change at the scale of individual drainage basins a good guide to volume change? (4) How is volume change distributed between the accumulation and ablation zones? (5) Are there distinctive longitudinal patterns of elevation change along outlet glaciers, and how do these patterns compare with those at the basin-wide scale? (6) Is there evidence from the patterns of thickness change, either within whole basins or along outlet glaciers, for recent changes in flow dynamics that have resulted in rates

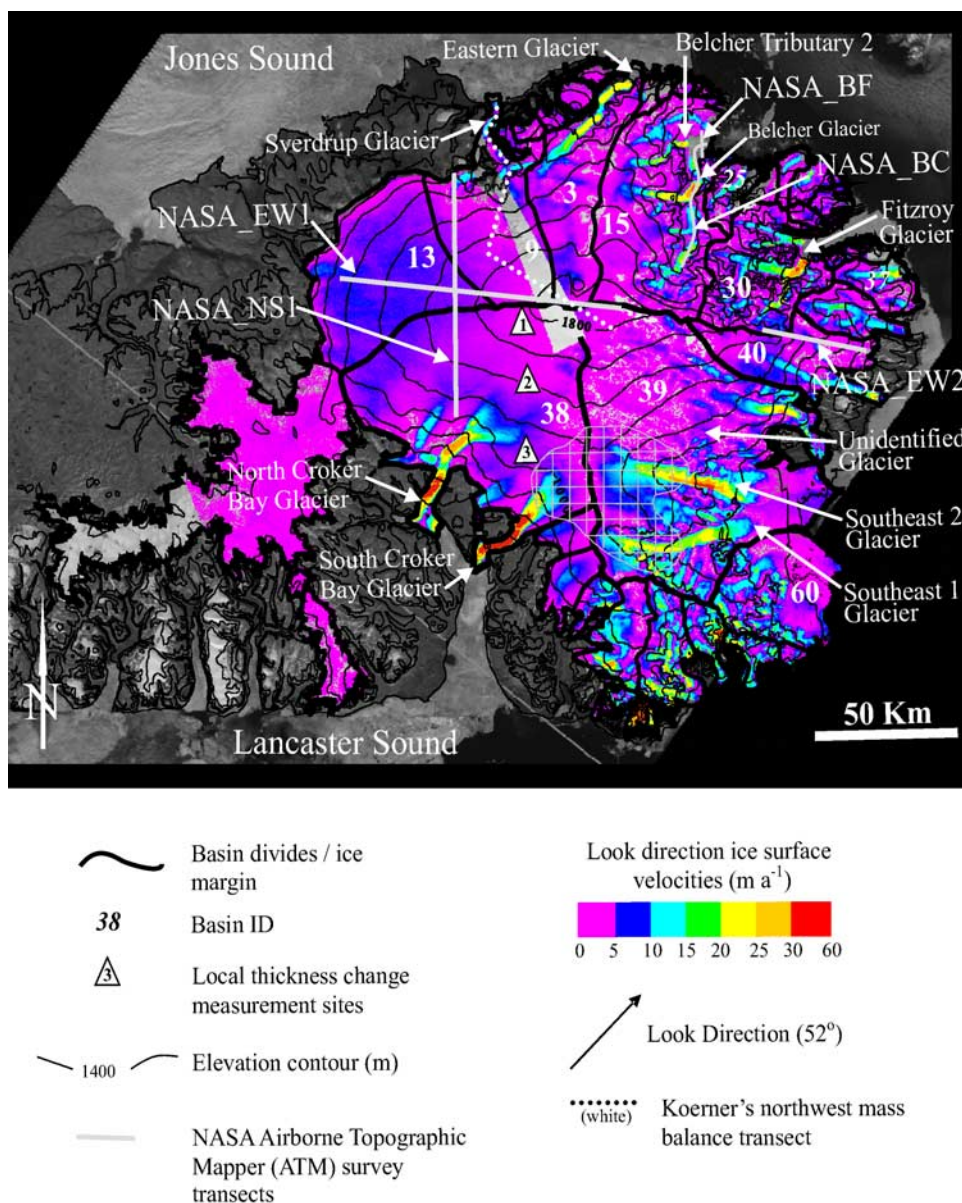


Figure 2. InSAR look direction surface velocities across the Devon Ice Cap derived from the ERS 1/2 satellite data. The gray gridded area in the southern region of the ice cap indicates the location where surface accumulation rates were increased by 1.5 times the amount derived by *Mair et al.* [2005].

of thinning/thickening that are not easily accounted for by changes in surface mass balance alone?

2. Data Sets

[8] Calculations of rates of thickness change were made possible by the recent development of ice thickness, topography, surface mass balance, and ice surface velocity data sets for the Devon Island ice cap. Ice thickness data across most of the ice cap were derived from airborne radio echo sounding measurements obtained during the spring of 2000 [Dowdeswell et al., 2004]. These data are accurate to ± 10 m, whereas the ice surface elevation values are accurate to ± 7 m. Surface mass balance data for the accumulation zone were derived from interpolation of long-term net accumulation rates measured at eight sites in the accumulation area

of the ice cap. Net accumulation at each site was determined using down-borehole ^{137}Cs gamma ray spectrometry to detect the depth to the 1963 “bomb” layer that was deposited as fallout from atmospheric thermonuclear weapons testing in the Russian high Arctic in 1962 [Mair et al., 2005]. Mean net accumulation rates over the 37-year period (1963–2000) were calculated as a function of depth to the reference layer and the density of the overlying firn. On the basis of field measurements of net accumulation performed at three sites in the southern region of the ice cap in Spring 2005, the accumulation grid developed by *Mair et al.* [2005] was modified to take into account accumulation rates that locally exceeded those shown by *Mair et al.* [2005] by a factor of 1.5. The area affected encompassed the source regions of the South Croker Bay, Southeast 1, and Southeast 2 Glaciers (see Figure 2). This modifica-

tion had the effect of raising the mass balance of basin 38 by 2.5% and basin 39 by 6%, resulting in a net increase of $0.017 \text{ km}^3 \text{ a}^{-1}$ in the mass balance of the whole ice cap. For the ablation zone, the net balance was calculated using a positive degree-day model driven by air temperature data from Resolute Bay, Nunavut, corrected for conditions specific to the ice cap [Mair *et al.*, 2005]. Surface velocity fields for the ice cap were derived by satellite radar interferometry (InSAR) using ascending pass ERS 1 and 2 data obtained during the tandem mode mission in the spring of 1996 and the 3-day repeat pass mission in February 1992 [Burgess *et al.*, 2005]. Errors associated with these data are $\pm 3 \text{ m a}^{-1}$ throughout the interior regions of the ice cap, and from 10% to 30% of the measured velocity along the fast flowing outlet glaciers, depending on the angle between the satellite look direction and the direction of ice flow. Since these data represent ice velocities over a 1–3 day time interval, uncertainties related to possible temporal variations in flow rates also exist when comparing InSAR derived ice fluxes with balance flux values derived from the 37 year accumulation values as described above. The lack of data on seasonal variability in rates of flow of the Devon Island ice cap precludes us from quantifying this uncertainty. Finally, the surface topography of the ice cap was obtained from the Canadian Digital Elevation Data set (CDED) with a horizontal resolution of 100 m. It was produced from 1:60,000 aerial photography acquired in 1959–1960 by the Government of Canada. Errors associated with limited bedrock control, problems with photogrammetric data capture over low contrast regions, and conversion of data from analog to digital format result in surface elevation errors of $\pm 50 \text{ m}$ along the main outlet glaciers and up to $\pm 100 \text{ m}$ throughout the ice cap interior. These errors are considered random at the ice cap-wide scale. A second DEM of the Belcher Glacier, with a grid cell resolution of 20 m, was recently produced from this photography. Ground control points obtained from differential GPS (DGPS) measurements in the spring of 2005 indicate that these raw data are accurate to $\pm 2 \text{ m}$ in the vertical and $\pm 1 \text{ m}$ in the horizontal dimensions. Along- and cross-profiles of surface and bed elevation of the Belcher Glacier were also obtained in 2005 from NASA's Airborne Topographic Mapper (ATM) and the University of Kansas Coherent Radar Depth Sounder (CoRDS), respectively (lines NASA_BC and NASA_BF; Figure 2) [Krabill *et al.*, 2006]. Vertical resolutions of the ATM and CoRDS data are $\pm 10 \text{ cm}$ and $\pm 10 \text{ m}$, respectively.

3. Methods

3.1. Basin-Wide Thickness Changes

[9] Average rates of thickness change were calculated for the accumulation and ablation zones of 10 major ($>100 \text{ km}^2$) drainage basins, excluding the western lobe of the ice cap, for which InSAR derived surface velocities are sparse. Basins for which the accumulation area comprises $<5\%$ of the total basin area (basins 60, 37, and 25) were considered to consist of ablation zones only.

[10] For the accumulation zone, the mean rate of thickness change was calculated from the difference between the

balance and observed water equivalent flux values (Q_{Balance} and Q_{InSAR} , respectively) across the ELA:

$$\partial H / \partial t_{\text{acc}} = ((Q_{\text{Balance}} - Q_{\text{InSAR}}) / A_{\text{acc}}) \quad (1)$$

where

$$Q_{\text{balance}} = HV_{\text{Balance}} \text{ ELA}_{\text{length}} \quad (2)$$

and

$$Q_{\text{InSAR}} = HV_{\text{InSAR}} \text{ ELA}_{\text{length}} \quad (3)$$

V_{balance} is the balance velocity (the depth averaged flow rate required to maintain profile equilibrium in an ice mass; km a^{-1}) [Paterson, 1994] and A_{acc} is the area of the accumulation zone within a particular basin (km^2). V_{InSAR} is the depth averaged velocity derived by applying a correction value (explained below) to the surface velocity measured from satellite radar interferometry (km a^{-1}) [Burgess *et al.*, 2005]. HV_{InSAR} (HV_{balance}) ($\text{km}^2 \text{ a}^{-1}$) is the average for all grid cells along the ELA within a particular basin, where the value for each grid cell is the product of V_{InSAR} (V_{Balance}) and ice thickness (H) (km) in that grid cell. The long-term ELA was estimated as 950 m a.s.l. for the northwest, 800 m a.s.l. for the southeast, and 875 m a.s.l. for both the northeast and southwest regions [after Koerner, 1970]. The boundaries of these regions are indicated in Figure 3.

[11] V_{balance} was derived from the model of Budd and Warner [1996] using surface mass balance [Mair *et al.*, 2005] modified as described above, ice thickness [Dowdeswell *et al.*, 2004], and surface topography (CDED), as input data. The pattern of glacier flow produced by the balance velocity model (Figure 4) closely reflects the InSAR-derived flow pattern (Figure 2), with the exception of four flow features that are not observed in the InSAR data (identified as A, B, C, and D in Figure 4). Since these features are embedded within much larger drainage basins, the misrouting of flow along them would not affect balance flux calculations at the basin scale. Flow unit A, however, appears to divert modeled flux from the South Croker Bay Glacier. Flow unit D is located in the southeast region and drains directly south from the summit region to join up with the Southeast 2 Glacier approximately 30 km up glacier from its terminus. Discontinuous patches of enhanced velocity in the InSAR data along the path of this feature support the existence of a major flow unit in this area (unidentified glacier; Figure 2). It is likely that this feature was not fully resolved by the InSAR data because ice flow in this region is nearly perpendicular to the look angle of the satellite (52°). Despite these differences, the overall similarity between the flow structures produced by the balance velocity model and the InSAR measurements provides confidence in the comparability of these data.

[12] In order to make V_{InSAR} , which is a surface quantity, compatible with V_{balance} , which is a depth-averaged quantity, V_{InSAR} was multiplied by 0.8 over regions where the predominant mode of ice flow is inferred to be by internal

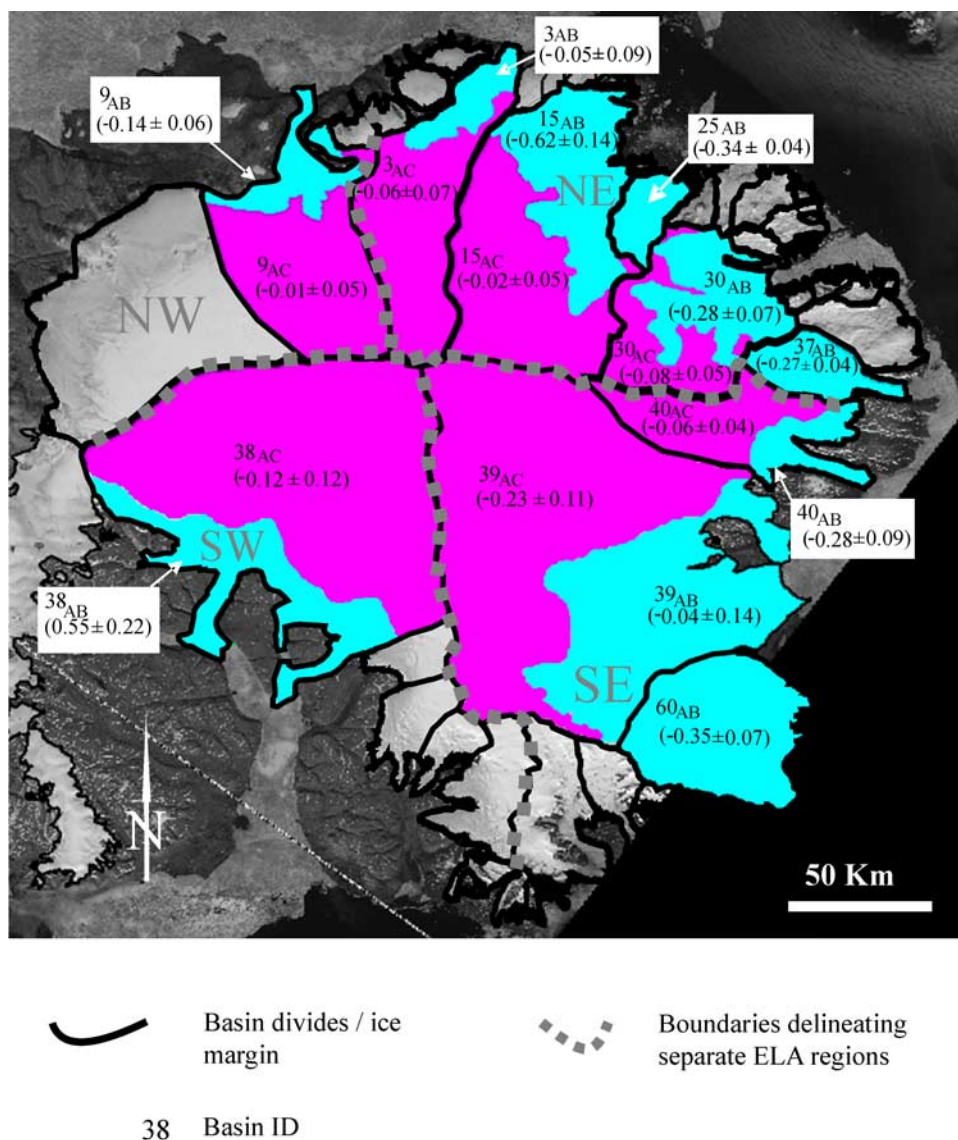


Figure 3. Basin-wide thickness changes of the accumulation (AC) and ablation (AB) zones of the Devon Island ice cap (m a^{-1} w.e.). The ELA is specified to be 950 m in northwest (NW), 800 m in the southeast (SE), and 875 m in the southwest (SW) and northeast (NE) quadrants [Koerner, 1970]. Light blue represents the ablation zone and purple the accumulation zone.

deformation. This value is a conservative approximation based on the ratio of surface velocity to velocity measurements at depth measured near the summit of the Devon Island ice cap by Reeh and Paterson [1988]. V_{InSAR} was assumed to be equal to the depth-averaged velocity in areas where sliding is inferred to be the predominant mode of ice flow [Burgess et al., 2005]. Although internal deformation may still occur where basal sliding dominates, this contribution is expected to be small (<5%) relative to the uncertainties in the InSAR-derived surface velocities (15–20%), which are accounted for in the calculations of ice flux. Inferences of whether ice movement is predominantly by internal deformation or sliding are based on an analysis of the relationship between the ratio of velocity to ice thickness (V/H) and the driving stress [Burgess et al., 2005].

[13] The uncertainty (σ) associated with the application of equation (1) to each basin was estimated as:

$$\sigma(\partial H / \partial t_{\text{acc}}) = \left(\sqrt{(\sigma(Q_{\text{balance}}))^2 + (\sigma(Q_{\text{InSAR}}))^2} \right) / A_{\text{acc}} \quad (4)$$

where $\sigma Q_{\text{balance}}$ (and σQ_{InSAR}) was calculated as the difference between an upper estimate of flux ($Q_{\text{balance_upper}}$ (and $Q_{\text{InSAR_upper}}$)), and the best estimate of flux (Q_{balance} (and Q_{InSAR})) (see Table 1). $Q_{\text{balance_upper}}$ was derived as the product of the upper estimate of ice thickness ($H_{+10\text{m}}$) and $V_{\text{balance_upper}}$, where $V_{\text{balance_upper}}$ was produced from the balance flux model using upper estimates of net surface mass balance ($b + \sigma b$) [Mair et al., 2005]. $Q_{\text{InSAR_upper}}$ was derived as the product of $H_{+10\text{m}}$ and $V_{\text{InSAR_upper}}$, where $V_{\text{InSAR_upper}}$ was derived by adding the estimated ice

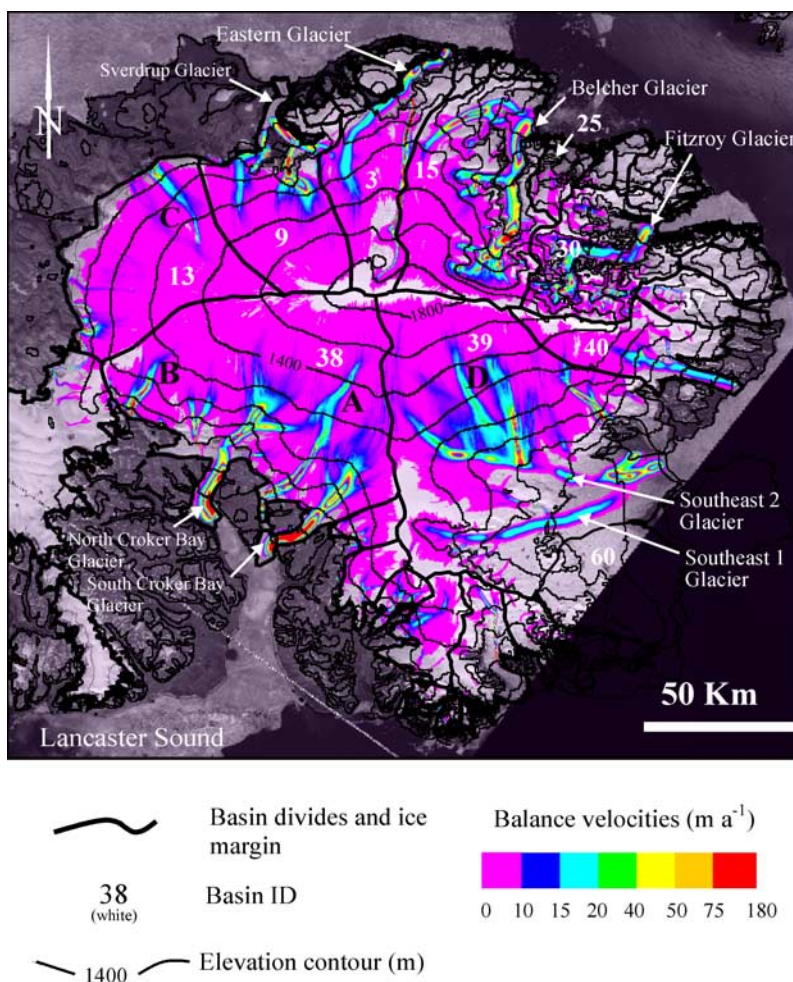


Figure 4. Modeled balance velocities across the Devon Island ice cap. Areas of missing data represent sections of the ice cap where the modeled balance velocity is less than 1 m a^{-1} . Flow units not evident in the InSAR derived velocity fields are indicated as A, B, C, and D.

velocity error (specified in the work of Burgess *et al.* [2005]), to V_{InSAR} . Error associated with A_{acc} had a negligible effect on the final value of $\partial H/\partial t_{\text{acc}}$.

[14] For the ablation zones, the average rate of thickness change in water equivalent was calculated from the differ-

ence between the measured flux across the ELA and the sum of the mass loss rates by surface ablation and calving:

$$\partial H/\partial t_{\text{abl}} = (Q_{\text{InSAR}} + Q_{\text{abl}} + Q_{\text{calving}})/\text{Area}_{\text{abl}} \quad (5)$$

Table 1. Rates of Water Equivalent Volume Change Throughout the Accumulation and Ablation Zones of the Major Tidewater Terminating Basins Across the Devon Island Ice Cap^a

Basin ID	Accumulation Zone		Ablation Zone		
	Net Volume Change ($\text{km}^3 \text{ a}^{-1} \text{ w.e.}$)	Net Volume Change ($\text{km}^3 \text{ a}^{-1} \text{ w.e.}$)	Measured Flux at the ELA ($\text{km}^3 \text{ a}^{-1} \text{ w.e.}$)	Surface Mass Balance ($\text{km}^3 \text{ a}^{-1} \text{ w.e.}$)	Calving Flux ($\text{km}^3 \text{ a}^{-1} \text{ w.e.}$)
3	-0.036 ± 0.020	-0.017 ± 0.024	0.089	-0.075	-0.028
9	-0.003 ± 0.025	-0.046 ± 0.016	0.058	-0.092	-0.011
15	-0.013 ± 0.031	-0.274 ± 0.070	0.074	-0.162	-0.21
25	n/a	-0.045 ± 0.006	n/a	-0.041	-0.003
30	-0.029 ± 0.013	-0.08 ± 0.026	0.059	-0.104	-0.032
37	n/a	-0.053 ± 0.008	n/a	-0.051	-0.002
38	-0.213 ± 0.180	0.357 ± 0.111	0.479	-0.072	-0.046
39	-0.385 ± 0.137	-0.114 ± 0.142	0.512	-0.606	-0.018
40	-0.018 ± 0.010	-0.046 ± 0.141	0.027	-0.066	-0.006
60	n/a	-0.532 ± 0.042	n/a	-0.528	-0.003

^aNet volume change of the accumulation zone represents the difference between balance and observed flux at the ELA. Individual components contributing to net volume change of the ablation zone are shown separately.

where Q_{abl} (see Table 1) is the volumetric net surface balance of the ablation zone as obtained from *Mair et al.* [2005], $Q_{calving}$ (see Table 1) is the water equivalent mass lost by iceberg calving as computed by *Burgess et al.* [2005], and $Area_{abl}$ is the total area of the ablation zone in 1999. As indicated in Table 1, mass loss rates due to net surface ablation and iceberg calving are negative values.

[15] Since a positive net balance could have the effect of glacier advance as well as thickening, the apparent thickness change estimate for a basin in which the ice cap was growing was adjusted by the formula:

$$\partial H / \partial t_{ablLadvance} = \partial H / \partial t_{abl} - (Q_{adv} / Area_{abl}) \quad (6)$$

where Q_{adv} is the average annual rate of volume increase due to glacier advance in the basin since 1960 [*Burgess and Sharp, 2004*]. This correction factor was applied to basin 38, which is the only sector of the ablation zone that has experienced net growth over the past 40 years.

[16] The total error associated with equation (5) was calculated as:

$$\sigma(\partial H / \partial t_{abl}) = \left(\frac{\sqrt{(\sigma(Q_{InSAR}))^2 + (\sigma(Q_{abl}))^2 + (\sigma(Q_{calving}))^2)}}{Area_{abl}} \right) \quad (7)$$

where σQ_{abl} was obtained from *Mair et al.* [2005] and $\sigma Q_{calving}$ was obtained from *Burgess et al.* [2005]. Errors in $Area_{abl}$ had an insignificant effect on the estimate of $\sigma(\partial H / \partial t_{abl})$.

3.2. In Situ Measurements of Rates of Ice Thickness Change

[17] In situ measurements of rates of ice thickness change were made at three locations in the southwest region of the ice cap in 2004 and 2005 (site 1, 1800 m; site 2, 1400 m; and site 3, 1000 m a.s.l.; see Figure 2 for locations). These measurements, which were derived using two separate methods, provide independent checks on estimates produced using remote sensing techniques.

[18] The first estimate was made using:

$$\partial H / \partial t_{strain} = b_{40} - F(H(\varepsilon_x + \varepsilon_y) + u(\partial H / \partial x)) \quad (8)$$

[*Paterson, 1994; p. 257*] where b_{40} is the accumulation rate averaged over the 40 year time period (1963–2003) measured using down borehole ^{137}Cs gamma spectrometry and firn core density profiling as described above. The majority of ice core segments extracted from all three sites were intact and ranged from 30 to 50 cm in length, with a diameter assumed to be 2 mm smaller than the inside diameter of the ice core barrel. Density measurements from all sites were estimated to be accurate to $\pm 5\%$ based on measured core lengths and weights. Here ε_x and ε_y are surface strain rates in the directions along flow and transverse to flow, respectively. Strain rates were calculated from repeat differential global positioning system (DGPS) measurements of the magnitude and direction of displacement of four stakes arranged in a 1 km \times 1 km grid determined between spring 2004 and 2005. F was assigned a value of 0.8 (based on *Reeh and Paterson [1988]*) in order

to relate strain rates measured at the ice cap surface to depth-averaged values. Here, u is the downslope velocity derived from repeat DGPS stake measurements and ∂H was calculated over a 1 km distance (∂x) from the ice thickness grid produced by *Dowdeswell et al.* [2004].

[19] The second method used was the “coffee can” technique [*Hamilton and Whillans, 2000*] which derives the long-term rate of thickness change at a single point from the equation:

$$\partial H / \partial t_{cc} = (b_{40} / \rho) + z + u v \quad (9)$$

where b_{40} (positive for accumulation) is the net mass balance averaged over the period from 1963 to 2003, z is the ice submergence velocity derived from precise GPS measurements of a marker anchored 20 m below the ice surface (negative downward), ρ is the firn density at the marker depth, and v is the surface slope measured across one ice thickness in the direction of flow (positive downward). The value of z was calculated as the average of three measurements performed each spring from 2004 to 2007.

[20] The validity of this method relies on the assumption that ρ increases consistently with depth implying that b and z have been relatively constant over the last 40 years or more. To test this, a suite of “coffee cans” were installed at each site in order to determine whether or not a linear relationship between z and $1/\rho$ exists at depths of 20, 16, 12, 8, and 4 m, as would be expected from *Sorge’s Law* [*Hamilton and Whillans, 2000*]. The data from sites 1 and 2 do show such a linear relationship, indicating that compaction rates have not been significantly influenced by recent changes in temperature or precipitation. The “coffee can” method should therefore result in valid calculations of the rate of thickness change at these locations [*Hamilton and Whillans, 2000*]. The upper 20 m of the ice cap at site 3 was composed entirely of ice with a density of 917 kg m^{-3} ; therefore submergence velocity measured at the ice surface was assumed equal to submergence velocity at marker depth. Uncertainties of the “coffee can” measurements are largely a function of the accuracy of the GPS measurements of vertical position, which were $\pm 3, 5, \text{ and } 6 \text{ cm a}^{-1}$ for sites 1, 2, and 3, respectively.

3.3. Rates of Thickness Changes Along Major Outlet Glaciers

[21] Rates of thickness change along five major outlet glaciers (North and South Croker Bay, Southeast 1 and 2, and Fitzroy Glaciers) were computed from the divergence of ice flux between successive gates along the glaciers and the average surface mass balance between these gates:

$$\partial H / \partial t_{Glacier} = [(Q_{InSARg1} - Q_{InSARg2}) / Area_{gLg2}] + SMB_{gLg2} \quad (10)$$

where $g1$ and $g2$ are fluxgates positioned at the up- and down-glacier ends of 5–8 km long glacier segments. Fluxgates were chosen to enclose sections of the glacier that were relatively homogeneous in terms of lateral constraints along the margins. As for (3), Q_{InSAR} ($\text{m}^3 \text{ a}^{-1}$ w.e.) was derived as the product of HV_{InSAR} ($\text{m}^2 \text{ a}^{-1}$) and

Table 2. Volume Change Estimates of All Major Drainage Basins According to Flux Imbalance as Derived in This Study and the Maximum Thickness Area Change Technique as Derived by *Burgess and Sharp* [2004]^a

Basin ID	Volume Change Derived From Flux Imbalance × 39 Years (km ³ w.e.)	Volume Change Derived From Areal Changes 1960–1999 (km ³ w.e.)
9	−1.91 ± 0.19	−1.76 ± 0.21
25	−1.76 ± 0.04	−1.62 ± 0.19
40	−2.46 ± 0.88	−2.56 ± 0.31
37	−2.07 ± 0.05	−1.46 ± 0.18
30	−4.25 ± 0.18	−4.66 ± 0.40
3	−2.07 ± 0.20	−0.66 ± 0.08
15	−11.19 ± 1.44	−8.11 ± 0.62
38	5.62 ± 1.32	2.66 ± 0.33
39	−19.46 ± 1.23	−5.15 ± 0.62
60	−20.75 ± 0.26	−12.19 ± 1.48
Total	−60.33 ± 5.8	−35.47 ± 4.6

^aCells in boldface represent volume changes that agree to within the specified margin of error.

the glacier width ($Width_{Glacier}$) (m), where HV_{InSAR} was obtained as an average value across the width of the glacier at each fluxgate. $Area_{g1-g2}$ (m²) is the area between $g1$ and $g2$ and SMB_{g1-g2} (m³ a^{−1} w.e.) is the average net surface mass balance between fluxgates obtained from *Mair et al.* [2005].

[22] In addition to quantifying the rate of thickness change between fluxgates, equation (10) provides the basis for identifying the main driver behind the measured changes. The relative magnitudes of Term1 and Term2 (as shown in Figures 6b–10b) indicate whether the resultant changes are caused primarily by the prevailing surface mass balance in the region, ice dynamics, or both.

[23] The error associated with equation (10) was estimated as:

$$\sigma(\partial H/\partial t_{Glacier}) = \sqrt{(\sigma(Term1))^2 + (\sigma(SMB))^2} \quad (11)$$

where

$$\sigma Term1 = \left(\sqrt{\sigma Q_{g1}^2 + \sigma Q_{g2}^2} \right) / Area_{g1-g2} \quad (12)$$

and

$$\sigma(Q) = Q \left(\sqrt{\left(\frac{\sigma(Width)}{Width} \right)^2 + \left(\frac{\sigma(H)}{H} \right)^2 + \left(\frac{\sigma(V_{InSAR})}{V_{InSAR}} \right)^2} \right) \quad (13)$$

Direct measures of surface elevation change along the entire length of the Belcher Glacier, and along a 5 km transect parallel to its terminus (lines NASA_BC and NASA_BF; Figure 2), were computed as the difference between elevations derived from analytical stereo photogrammetry from 1960 aerial photography ($ELEV_{1960}$; ±2 m) and the 2005 ATM data. Individual NASA ATM laser shots (horizontal spacing of ~2 m) were interpolated to 20 × 20 m grid cells (using an inverse distance weighted function) in order to match the resolution of the 1960 DEM. Total error associated with these elevation change

measurements, calculated as the square root of the sum of the squared errors divided by the 45-year time interval between data set acquisitions, was estimated to be ±0.04 m a^{−1}.

4. Results

4.1. Post-1960 Volume Change of the Ice Cap and Its Contribution to Global Sea Level

[24] The average volume loss from the main part of the Devon Island ice cap between 1960 and 1999 derived from the basin-wide calculations was -60.3 ± 6 km³ w.e. (-5.0 ± 0.5 m w.e.). This estimate is derived for basins that constitute 78% of the main part of the ice cap. Volume loss from the remaining 22% of the ice cap was estimated as the sum of the volume change attributed to net surface mass balance (-16.5 ± 2 km³ water equivalent) [*Mair et al.*, 2005] and iceberg calving (-0.014 ± 0.007 km³ w.e.) [*Burgess et al.*, 2005]. This equates to a total loss of -76.8 ± 7 km³ w.e. (or -6.3 ± 0.6 m w.e. thinning) between 1960 and 1999, or an average annual loss rate of -1.9 km³ a^{−1} w.e. (or -0.16 m a^{−1} w.e. thinning) over this period of time. Assuming that the total area of the Earth's oceans is 360×10^6 km², this implies that the Devon Island ice cap contributed $+0.21 \pm 0.02$ mm to global sea level between 1960 and 1999. This amounts to approximately 2% of the worldwide input from small ice caps and glaciers based on the current contribution from these sources, estimated to be $+0.59$ mm a^{−1} between 1960 and 2003 [*Dyrgerov and Meier*, 2005].

4.2. Distribution of Volume Change Between Basins

[25] All basins examined in this study lost net volume between 1960 and 1999, except for basin 38 where volume increased by 5.62 ± 1.32 km³ w.e. (see Table 2). The greatest losses were from basins 39 and 60 in the southeast region, where volume decreased by -19.46 ± 1.23 km³ and -20.75 ± 0.26 km³ w.e., respectively. Volume also decreased significantly in basin 15 in the northeast region by -11.19 ± 1.44 km³ w.e. Basins 9, 25, 30, 37, 40, and 3 experienced an average net loss of -2.4 ± 0.25 km³ w.e. Among these basins, the greatest ice volume loss occurred from basin 30 (-4.25 ± 0.18 km³ w.e.).

4.3. Distribution of Ice Thickness and Volume Changes Between Accumulation and Ablation Areas and Factors Controlling the Changes Observed

[26] Basin-wide estimates indicate that thickness changes across the accumulation zones of the northern basins (9, 3, and 15) are indistinguishable from zero, while the accumulation zones of basins 30 and 40 along the eastern margin are thinning slightly (Figure 3). Basins 38 and 39 in the southern region are thinning throughout their accumulation zones at rates of -0.12 ± 0.12 m a^{−1} w.e. and -0.23 ± 0.11 m a^{−1} w.e., respectively (Figure 3). In situ measurements indicating near-zero thickness change conditions at site 1 and slight thinning at site 2 in the southwest accumulation zone (Table 3) agree closely with the basin-wide values for this region. The significant thinning estimated for the 1 × 1 km grid at site 3 (-0.23 ± 0.07 m a^{−1} w.e.) is likely due to the fact that the easternmost pole in this grid is located in ice that is accelerating eastward toward the

Table 3. Rates of Thickness Change Derived From in Situ Four GPS Measurements Obtained Annually Each Spring Between April 2004 and May 2007 at Three Study Sites in the Southwest Region of the Devon Island Ice Cap

Site	Coffee Can Method (m a^{-1} w.e.)	Thickness Change Across 1 \times 1 km Strain Grid (m a^{-1} w.e.)
1	-0.02 ± 0.03	$+0.03 \pm 0.04$
2	-0.11 ± 0.05	-0.05 ± 0.05
3	$+0.04 \pm 0.06$	-0.23 ± 0.07

South Croker Bay Glacier whereas the remaining poles in the grid are moving southward. Divergent ice motion across the 1×1 km grid thus results in a higher rate of thinning than was estimated from the “coffee can” method at a single point. With the exception of this value, the in situ measurements are likely representative of thickness changes over a broader area because they are located in regions of

low flow rates ($<15 \text{ m a}^{-1}$) where seasonal velocity fluctuations are minimal ($<1 \text{ m a}^{-1}$).

[27] The average rates of thickness change for the ablation zones of basin 39 in the southeast region and basin 3 along the north coast are near zero (Figure 3). In these basins, mass loss due to surface melt is replaced almost entirely by influx across the ELA (see Table 1). In basin 38, flux across the ELA exceeds mass loss due to surface melt resulting in net thickening of the southwest ablation zone by $0.55 \pm 0.22 \text{ m a}^{-1}$ w.e. The ablation zones of the remaining basins in the north and northeast regions (9, 15, and 30) are thinning by -0.14 ± 0.06 , -0.62 ± 0.14 , and $-0.28 \pm 0.07 \text{ m a}^{-1}$ w.e., respectively (Figure 3). Surface lowering by $-0.30 \pm 0.1 \text{ m a}^{-1}$ w.e. as detected along the NASA_EW2 transect (see Figure 2) in basin 40 [Abdalati *et al.*, 2004], agrees with the basin-wide thinning rate of $-0.28 \pm 0.09 \text{ m a}^{-1}$ w.e. in this area. Basins 9, 30, and 40 are losing mass primarily by surface melt (Table 1) whereas more than half of the annual mass loss from basin 15 is by

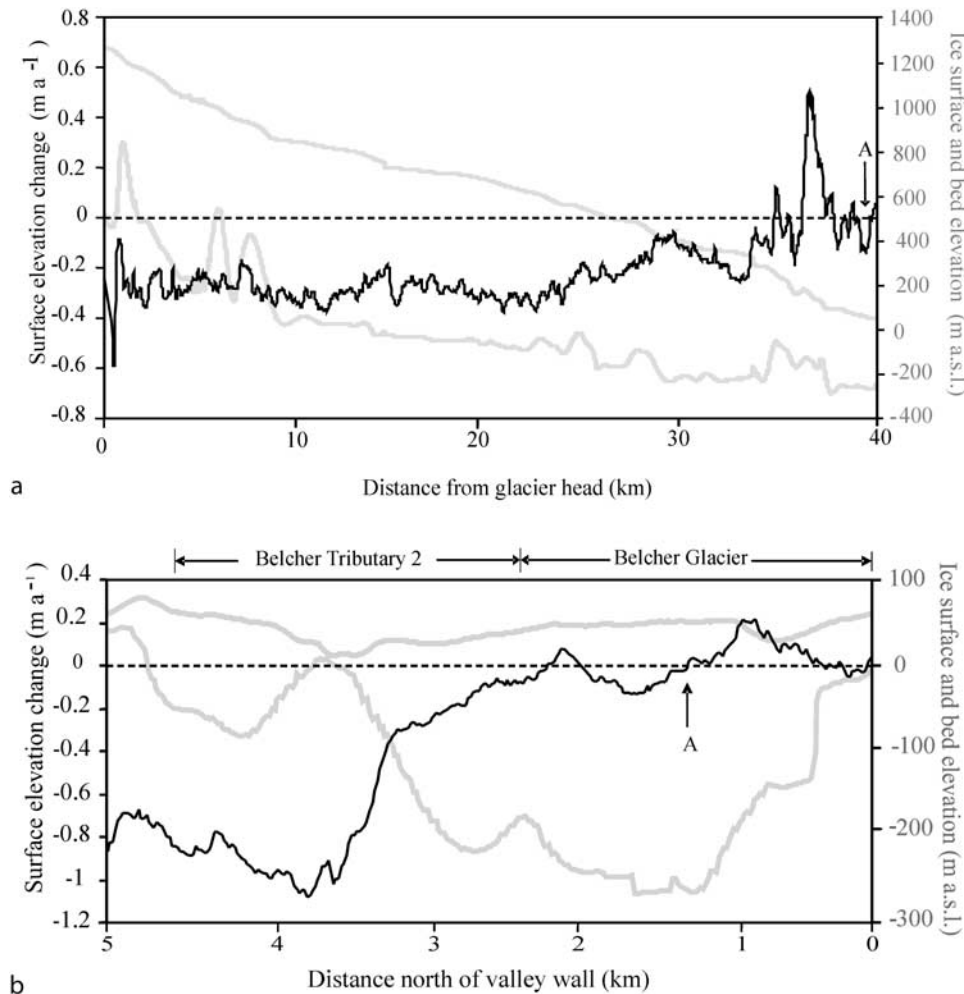


Figure 5. (a) Average annual rate of surface elevation change (black line) along the Belcher Glacier between 1960 and 2005. (b) Average annual rate of surface elevation change (black line) along a 5 km transect running parallel to the terminus of the Belcher Glacier. Ice surface and bed elevations (gray lines) in Figures 5a and 5b were obtained in 2005 from NASA’s Airborne Topographic Mapper and the University of Kansas Coherent Radar Depth Sounder instruments, respectively. “A” indicates the point of intersection between the two transects.

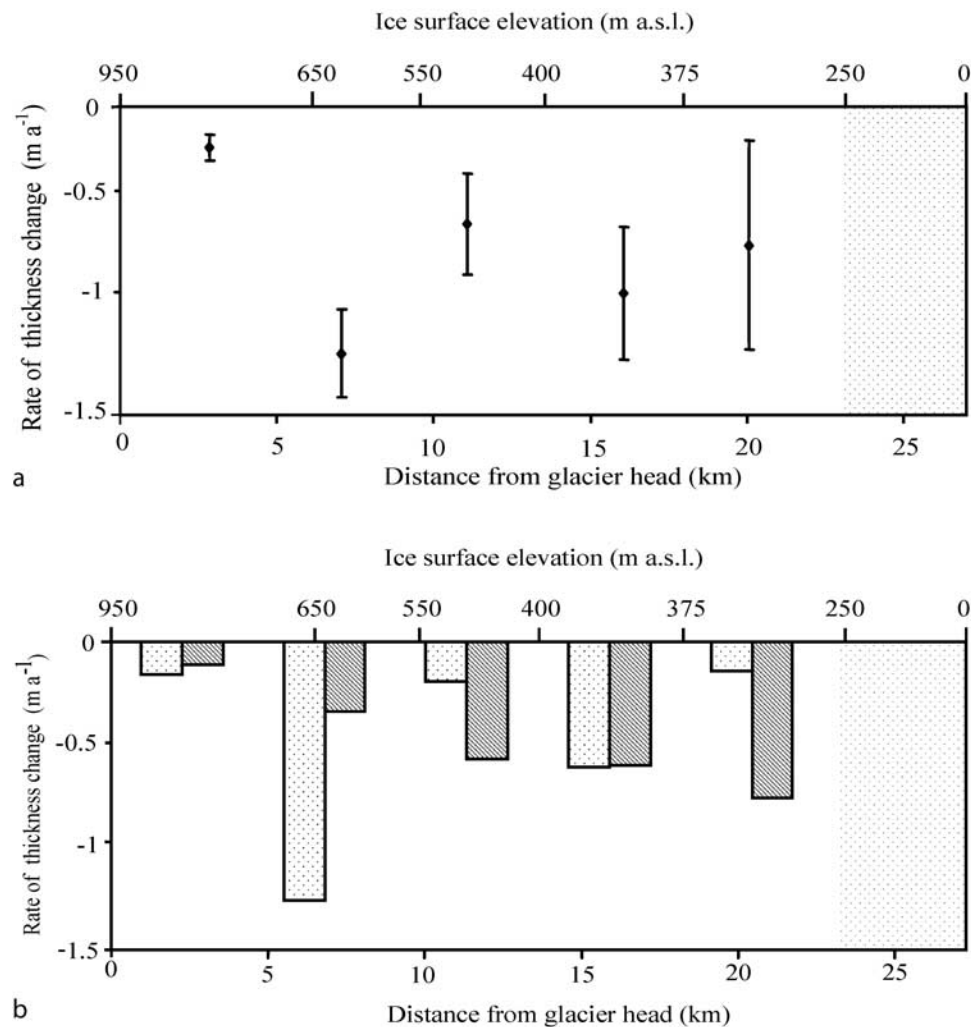


Figure 6. (a) Net thickness change averaged between fluxgates along the Fitzroy Glacier. Values along the top axis indicate the elevation of each fluxgate location. (b) Contributions of surface mass balance (dark shade) and flux divergence (light shade) to net thickness change. The gray stippled area between km 23 and the terminus indicates the region of the glacier where InSar velocity data are not available.

iceberg calving ($-0.21 \text{ km}^3 \text{ a}^{-1}$ w.e.) [Burgess *et al.*, 2005]. Basins 25, 37, and 60 are situated almost entirely below the ELA and experience net losses of -0.045 ± 0.006 , -0.053 ± 0.008 , and $-0.53 \pm 0.042 \text{ km}^3 \text{ a}^{-1}$ w.e., respectively, due primarily to surface melt (see Table 1).

4.4. Relationship Between Basin-Wide Area Changes and Volume Changes Derived From Mass Flux Imbalance

[28] The estimate of volume change for the main portion of the Devon Island ice cap derived from area change measurements [Burgess and Sharp, 2004] is -43 km^3 w.e. compared with $-76.8 \pm 7 \text{ km}^3$ w.e. as derived in this study. There is however a relatively strong relationship ($r^2 = 0.8$) between the two estimates of volume loss for individual basins. Volume changes estimated using the two methods agree to within 1.41, 0.4, and 0.6 km^3 w.e. for basins 3, 30, and 37, and to within measurement uncertainty for basins 9, 25, and 40. The volume-area scaling technique therefore provides a reasonable estimate of volume change for these basins. This is not, however, the case for basins 39, 60, 38,

and 15 where estimates of volume change based on changes in area are lower than the values calculated in this study by 14.31, 8.56, 2.96, and 3.08 km^3 w.e., respectively (see Table 2). Three of these basins are experiencing significant thickness changes due to changes in ice dynamics within either their accumulation (basin 39) or ablation zones (basins 15 and 38) (see below), while basin 60 is thinning throughout due primarily to surface melt. In all of these cases, volume loss is not proportionally reflected in changes at the ice cap margin.

4.5. Longitudinal Patterns of Thickness Change on Outlet Glaciers and Comparison With Thickness Changes at the Basin-Wide Scale

[29] Direct observations of surface elevation change on the Belcher Glacier indicate lowering of the ice surface by $-0.4 \pm 0.04 \text{ m a}^{-1}$ (of ice) along most of its length, with localized thickening near the terminus (Figure 5a). Similarly, elevation change measurements along an across-glacier profile near the glacier terminus indicate slight thickening or near-zero change across the main Belcher

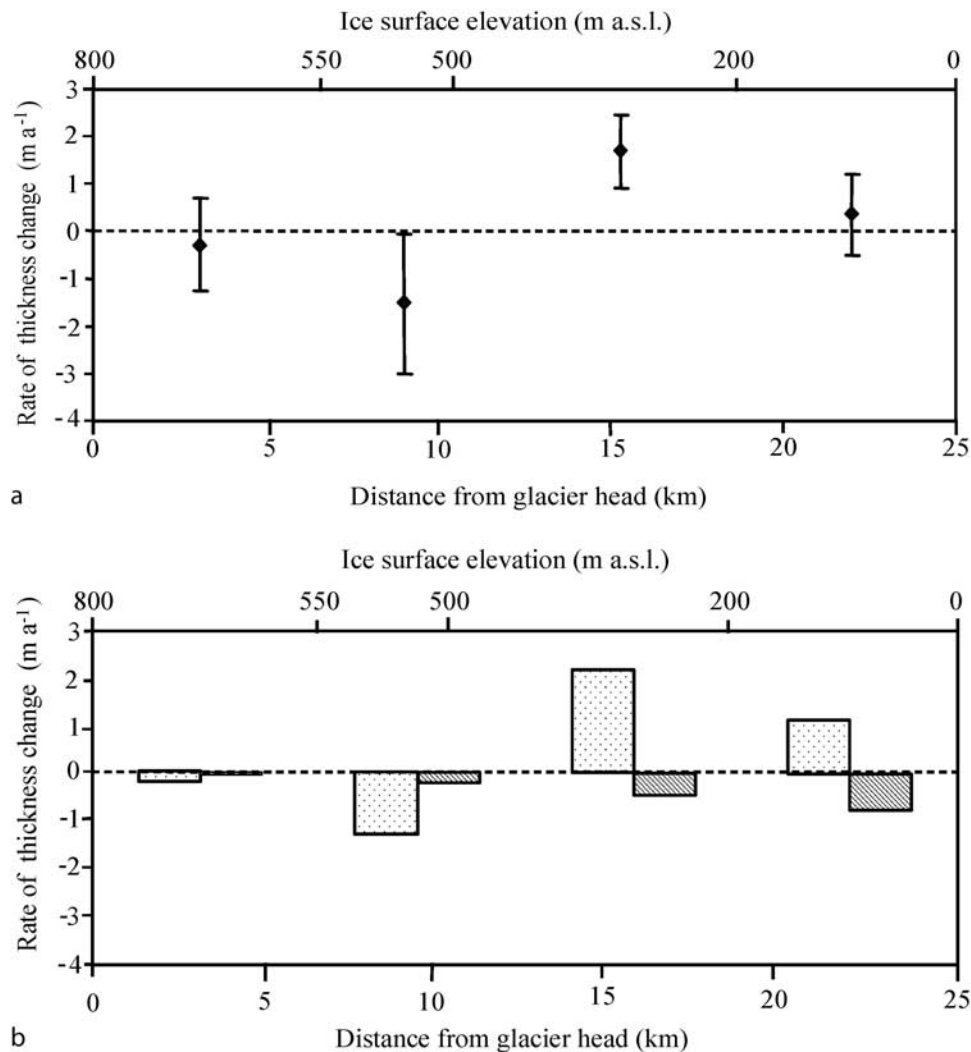


Figure 7. (a) Net thickness change averaged between fluxgates along the North Croker Bay Glacier. Values along the top axis indicate the elevation of each fluxgate location. (b) Contributions of surface mass balance (dark shade) and flux divergence (light shade) to net thickness change.

Glacier channel (Figure 5b). Overall thinning of the ablation zone in basin 15 by $-0.62 \pm 0.14 \text{ m a}^{-1} \text{ w.e.}$ is significantly greater than the average rate of surface lowering along the Belcher Glacier below the ELA ($-0.3 \pm 0.04 \text{ m a}^{-1} \text{ w.e.}$). Since the Belcher Glacier occupies approximately 37% of the ablation zone of basin 15, it is likely that thinning throughout the less dynamic portions of this ablation zone is greater than it is along the main flow unit. This is supported by the higher rate of surface lowering ($-0.8 \pm 0.1 \text{ m a}^{-1}$ of ice) near the terminus in the region of the less active Belcher Tributary 2 Glacier (Figure 5b).

[30] The Fitzroy Glacier is thinning along most of its length, with maximum rates of $-1.2 \text{ m a}^{-1} \text{ w.e.}$ occurring 20 km from the ice front (Figure 6a). The section of this glacier along which thickness changes were computed represents approximately 30% of total area of the ablation zone, which is thinning by $-0.28 \pm 0.07 \text{ m a}^{-1} \text{ w.e.}$ (Figure 3).

[31] In the southwest region, the North and South Croker Bay Glaciers occupy only 18% of the ablation zone of basin 38. Both of these glaciers exhibit near-zero thickness change conditions close to their heads and thinning between 7 and 12 km along these flow units. Thickening by $1.7 \pm 0.7 \text{ m a}^{-1} \text{ w.e.}$ along the lower reaches of the North Croker Bay glacier (Figure 7a) is consistent with, but greater than, the pattern of thickening that prevails throughout the ablation zone of this basin ($0.55 \pm 0.22 \text{ m a}^{-1} \text{ w.e.}$). By contrast, thinning of up to $-2.4 \pm 0.75 \text{ m a}^{-1} \text{ w.e.}$ prevails throughout the lower reaches (<400 m a.s.l.) of the South Croker Bay Glacier (Figure 8a).

[32] In the southeast region (basin 39), thinning by up to $-1 \text{ m a}^{-1} \text{ w.e.}$ along the upper 15 km of the Southeast 1 outlet glacier (Figure 9a) is consistent with, but greater than, basin-wide thinning of this accumulation zone by $-0.23 \pm 0.12 \text{ m a}^{-1} \text{ w.e.}$ (Figure 3). The Southeast 1 and 2 glaciers however are thickening by up to $1 \text{ m a}^{-1} \text{ w.e.}$, approximately 20 km inland from their termini, while their lower-

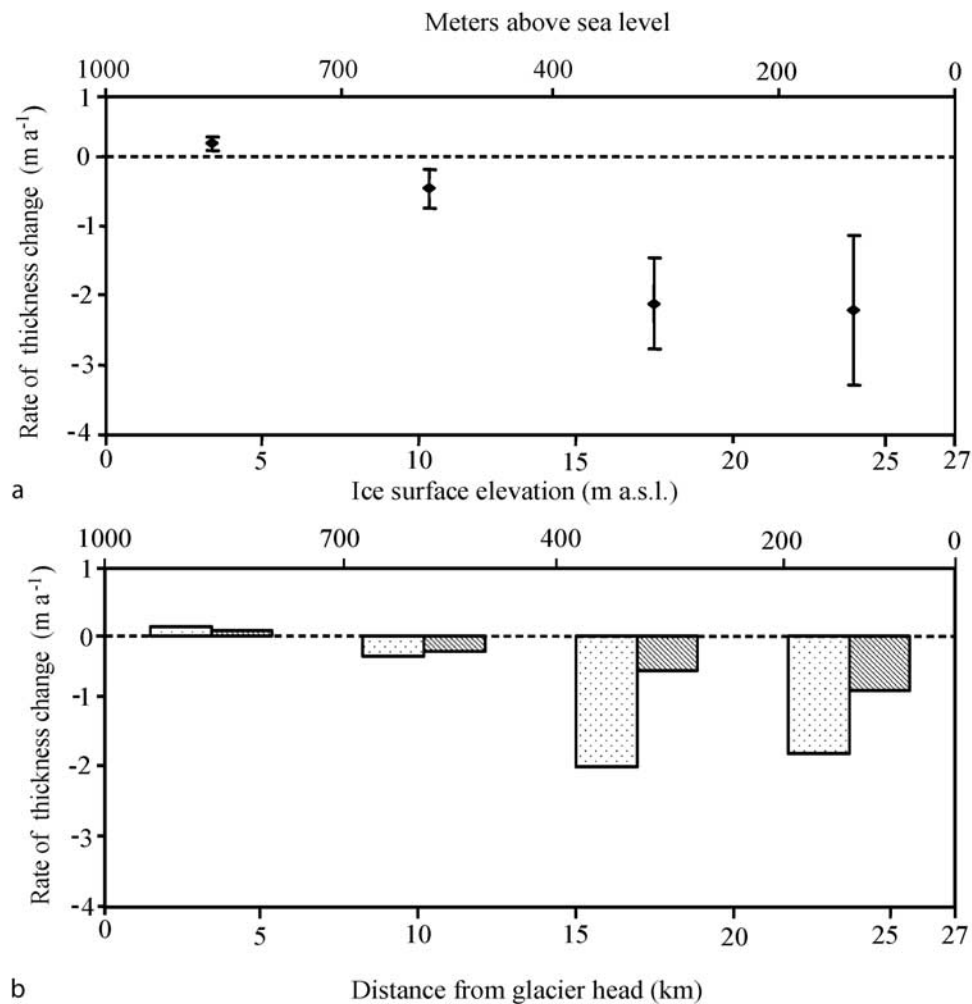


Figure 8. (a) Net thickness change averaged between fluxgates along the South Croker Bay Glacier. Values along the top axis indicate the elevation of each fluxgate location. (b) Contributions of surface mass balance (dark shade) and flux divergence (light shade) to net thickness change.

most reaches are thinning by -1 m a^{-1} w.e. (Figures 9a and 10a). These glaciers occupy approximately 50% of the ablation zone of this basin and draw sufficient mass from higher elevations to offset mass loss due to surface melt below the ELA.

4.6. Evidence for Recent Changes in Flow Dynamics That Have Resulted in Rates of Thinning/Thickening That Are Not Easily Accounted for by Surface Mass Balance

[33] Direct observations of surface elevation change along the Belcher Glacier indicate that the surface of this glacier has been lowering by $-0.35 \pm 0.04 \text{ m a}^{-1}$ of ice, up to and beyond 1400 m a.s.l. (Figure 5a), or approximately 400 m above the long-term ELA. Mass balance data obtained over the past 4 decades from the summit region reveal a near-zero trend in surface mass balance across the Devon Island ice cap above the ELA (1000 m a.s.l.) (R. Koerner, personal communication, 2007). *Colgan and Sharp* [2008], however, do report a negative trend (-0.06 m a^{-1} w.e.) in surface mass balance in this region since the late 1980s. Although this trend may have contributed slightly to

net lowering of the Belcher Glacier, it would not be sufficient to account for the total amount of thinning observed in this study. Most of the surface lowering has therefore likely been dynamically driven and possibly linked to an increased rate of ice flux at lower elevations. In situ measurements of surface mass balance obtained from the northwestern sector of the ice cap (60 km due west of the Belcher Glacier terminus) show a trend toward slightly greater rates of surface ablation below 700 m a.s.l. since 1960. Summer melt below 500 m a.s.l. in this region has increased significantly since the late 1980s (R. Koerner, personal communication, 2007). Thickening of the near-terminus section of the glacier (<300 m a.s.l.) is therefore also likely to be dynamically driven and may be influenced by the recent increase in ice flux from the upper reaches of this glacier.

[34] For the remaining glaciers, dynamically induced thickness changes were identified by comparing the relative contributions of flux divergence and surface mass balance, with the net thickness change between fluxgates. Briefly, a positive (or negative) flux imbalance occurs where flux at the lower gate is greater (or less) than flux at the upper gate

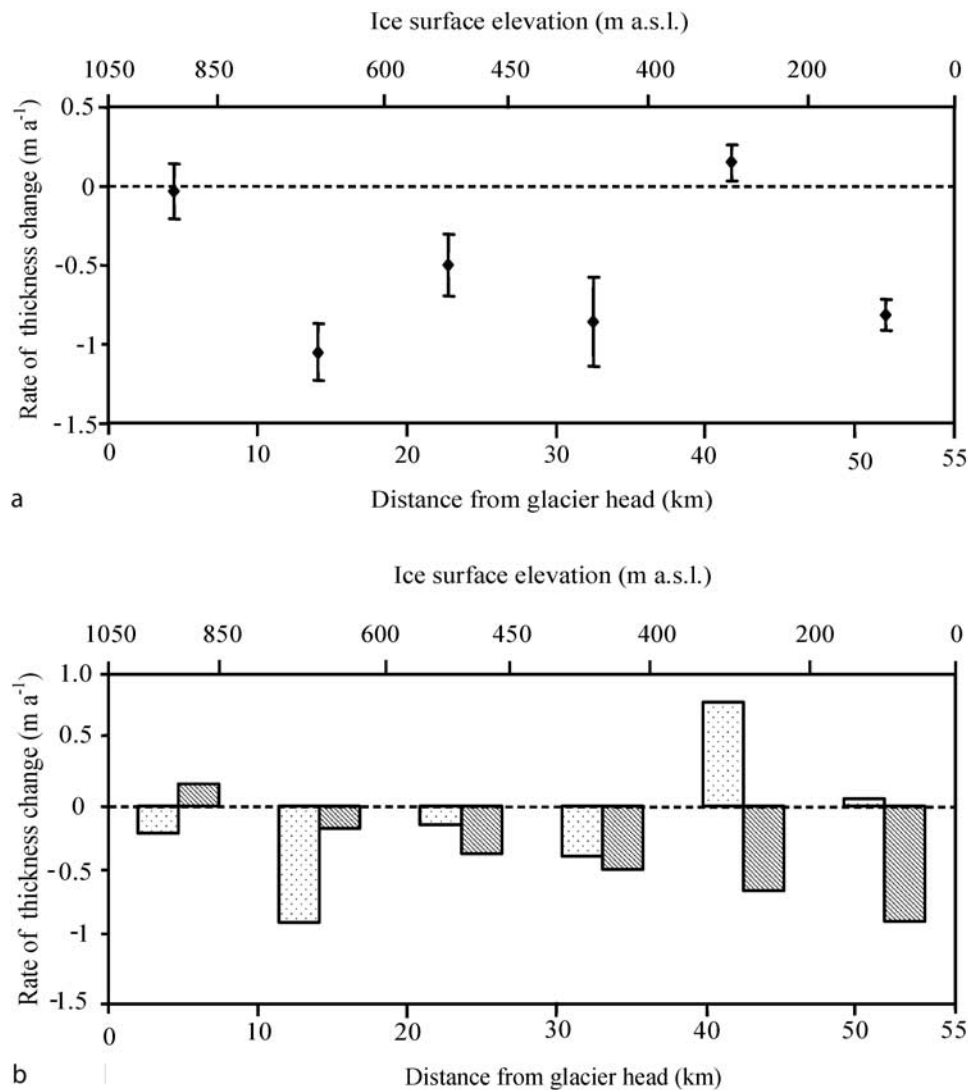


Figure 9. (a) Net thickness change averaged between fluxgates along the Southeast 1 Glacier. Values along the top axis indicate the elevation of each fluxgate location. (b) Contributions of surface mass balance (dark shade) and flux divergence (light shade) to net thickness change.

plus the net surface mass balance between gates. In these situations, flux at the lower gate is enhanced (or inhibited) relative to the net balance integrated over the area between fluxgate locations, leading to dynamically driven thinning (or thickening). Mechanisms influencing variability in the rate of flow along the glaciers examined in this study are discussed in the next section.

[35] Thinning of up to $-1.3 \pm 0.3 \text{ m a}^{-1}$ w.e. within 7 km of the head of the Fitzroy Glacier (Figure 6a) coincides with a positive flux gradient that exceeds local surface ablation rates by a factor of almost three (Figure 6b) suggesting that change within this area is dynamically driven. The limited spatial extent over which the thinning occurs is more suggestive of a local change in ice dynamics than of variability in surface mass balance, which would likely affect a greater spatial region. In the southwest region of the ice cap, thinning near the head of the North Croker Bay Glacier (Figure 7a) appears to be largely attributable to a

positive flux gradient (Figure 7b) that is associated with the acceleration of flow into a bedrock valley. The net surface mass balance at this location is only slightly negative (-0.15 m a^{-1} w.e.) suggesting that thinning is driven primarily by recent increases in the rate of ice flow. Reduced rates of ice flux toward the terminus however are, however, causing dynamic thickening by $1.7 \pm 0.8 \text{ m a}^{-1}$ w.e. and near-zero thickness change where surface mass balance is -0.55 and -0.95 m a^{-1} w.e., respectively (Figure 7b). Along the lower 10 km of the South Croker Bay Glacier (Figure 8a), thinning is probably driven by recent changes in ice dynamics as a positive flux gradient in this segment of the glacier accounts for more than twice the rate of thinning that is attributable to surface mass balance alone (Figure 8b). Increased rates of iceberg calving and terminus advance of this glacier by up to 600 m since 1960 [Burgess and Sharp, 2004] likely represent the main sinks for increased flux from this glacier.

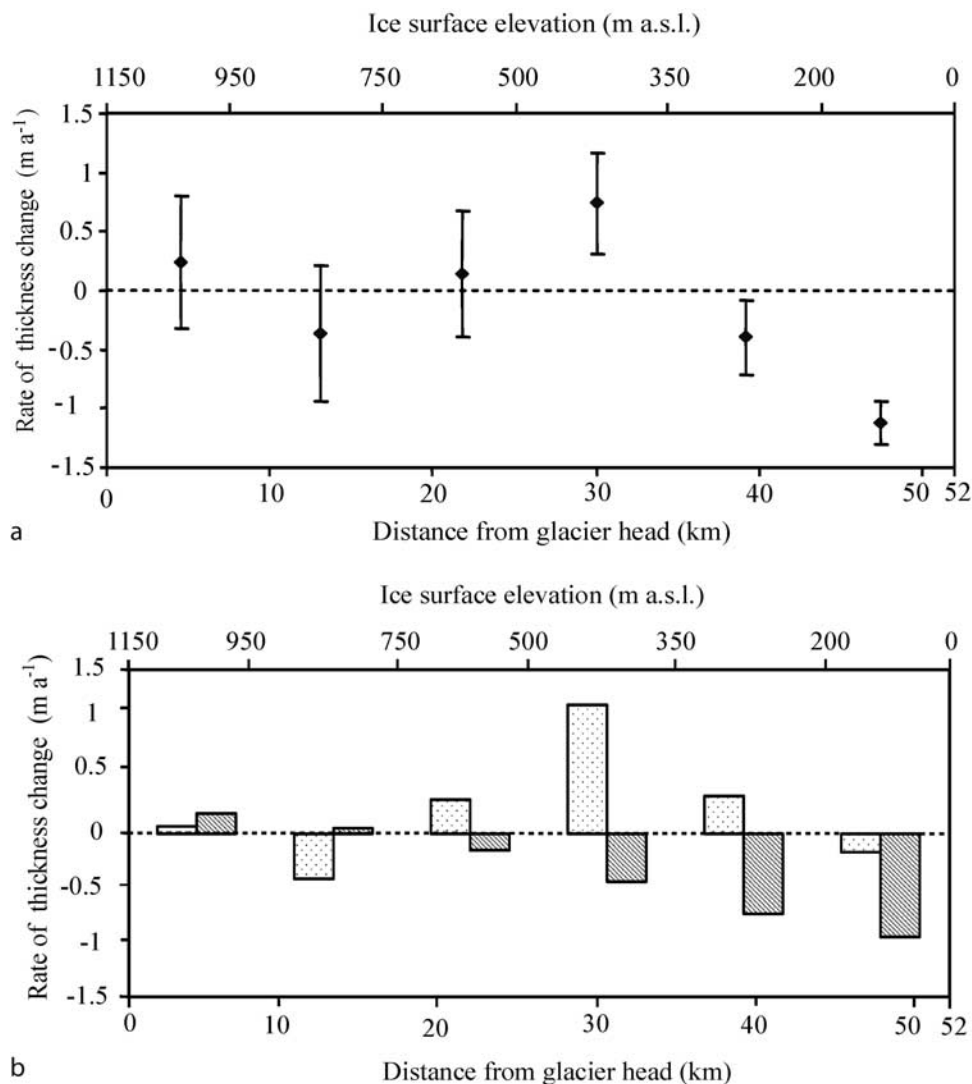


Figure 10. (a) Net thickness change averaged between fluxgates along the Southeast 2 Glacier. Values along the top axis indicate the elevation of each fluxgate location. (b) Contributions of surface mass balance (dark shade) and flux divergence (light shade) to net thickness change.

[36] The general patterns of thickness change along those sections of the Southeast 1 and 2 Glaciers above 350 m a.s.l. are indicative of dynamically induced changes in ice thickness, whereas thinning near the glacier termini is due almost entirely to surface melt. Net thinning by $-1.1 \pm 0.2 \text{ m a}^{-1}$ w.e. between 10 and 20 km down-glacier from the head of the Southeast 1 Glacier is associated with a positive flux gradient (Figure 9a) that causes thinning at a rate that is roughly 5 times greater than that due to the local surface mass balance (Figure 9b). A positive flux gradient also occurs near the head of the Southeast 2 Glacier (Figure 10b), but uncertainties in this estimate, combined with slightly positive surface mass balance make net thickness change in this area indistinguishable from zero (Figure 10a). The lower reaches of the Southeast 1 and 2 Glaciers both experience net thickening in the region 20 km up-glacier of their termini (Figures 9a and 10a) where faster flowing ice from higher elevations runs into slower flowing ice at lower elevations (Figure 11). Decelerating ice flow along

these glaciers results in dynamic thickening that more than compensates for mass loss due to local net surface ablation.

5. Discussion

[37] The patterns of dynamic thickness change identified in this study provide some important clues concerning the mechanisms responsible for nonsteady flow along many of the outlet glaciers that drain the Devon Island ice cap. As mentioned above, net surface lowering along the Belcher Glacier between 300 and 1400 m a.s.l. most likely reflects an excess of outflow over net accumulation from this glacier system due to recent increases in the rate of ice flow. Analysis of aerial photographs and field observations reveal a system of meltwater channels that begin at 1500 m a.s.l. and terminate in crevasse fields or moulins at lower elevations. These features may provide surface water with access to the glacier bed, thus enhancing flow through basal lubrication or by reducing the effective ice overburden

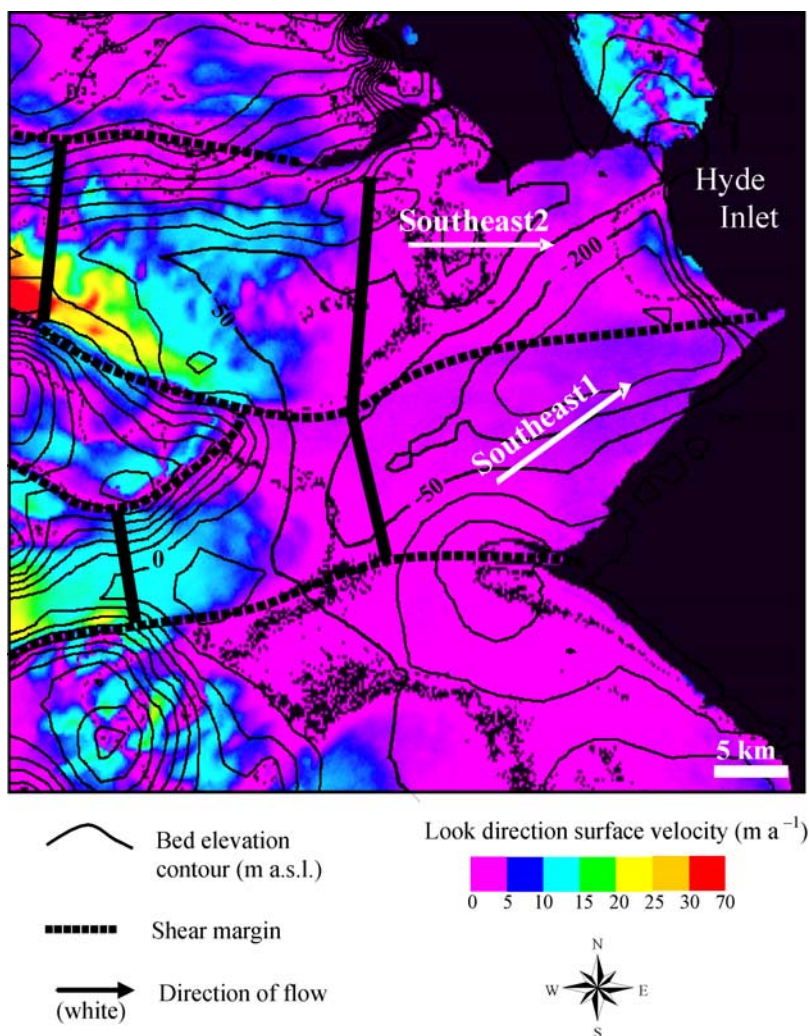


Figure 11. Bedrock topography and InSAR derived surface velocities in the look direction of the satellite across the terminus region of the Southeast 1 and 2 outlet glaciers. The heavy lines perpendicular to flow demarcate the zones of dynamic thickening along the Southeast 1 and 2 Glaciers, respectively. The transition from warm- to cold-based ice as inferred by *Burgess et al.* [2005] corresponds roughly to the color transition from dark blue to purple in the direction of glacier flow.

pressure. Predominant thickening near the terminus of the Belcher Glacier is likely driven by compressive forces as it experiences a sharp reorientation of flow and converges with the slower moving Belcher Tributary 2 glacier flowing in from the west (Figure 12). Lateral compression is inferred from a reduction in the width of the channel along the eastward flowing segment by ~ 500 m relative to the channel up-glacier from the curve. Narrowing of the glacier channel may induce higher ice velocities, which reach $\sim 300 \text{ m a}^{-1}$ along this eastward flowing segment of the glacier [*Burgess et al.*, 2005]. Enhanced flow within this segment occurs over topographic ridges at the glacier bed (Figure 5a) which would result in longitudinal compression and likely contribute to the thickening that is observed at these locations. Predominant thickening of the near-terminus region of the Belcher Glacier, combined with the fact that there has been minimal net change in position of this margin since 1960 (Figure 12), suggests that the stability of this ice front has not been significantly affected by recent

climate warming. By contrast, significant thinning across the less dynamic (and thinner; see Figure 5b) portions of the Belcher Tributary 2 glacier reflects the vulnerability of this margin to the effects of floatation and retreat due to calving. Thinning across this northern segment of the cross-flow profile is likely due to the fact that ice flux to this part of the terminus is insufficient to replace mass loss due to surface melt. Factors similar to these may be responsible for the $\sim 3 \text{ km}^2$ portion of ice lost sometime between 1984 and 1999 from the northern part of this margin (Figure 12). The timing of this event was determined from analysis of video from an aerial survey conducted in 1983 [*Taylor and Frobel*, 1984] and the 1999 Landsat ETM+ image used in this study.

[38] The patterns of ice dynamics and thickness change along the Southeast 1 and 2 Glaciers suggest that nonsteady flow in this region may be controlled by a surge-type mechanism. Thinning along the upper reaches of the Southeast 1 (and possibly Southeast 2) Glacier(s) coincides with

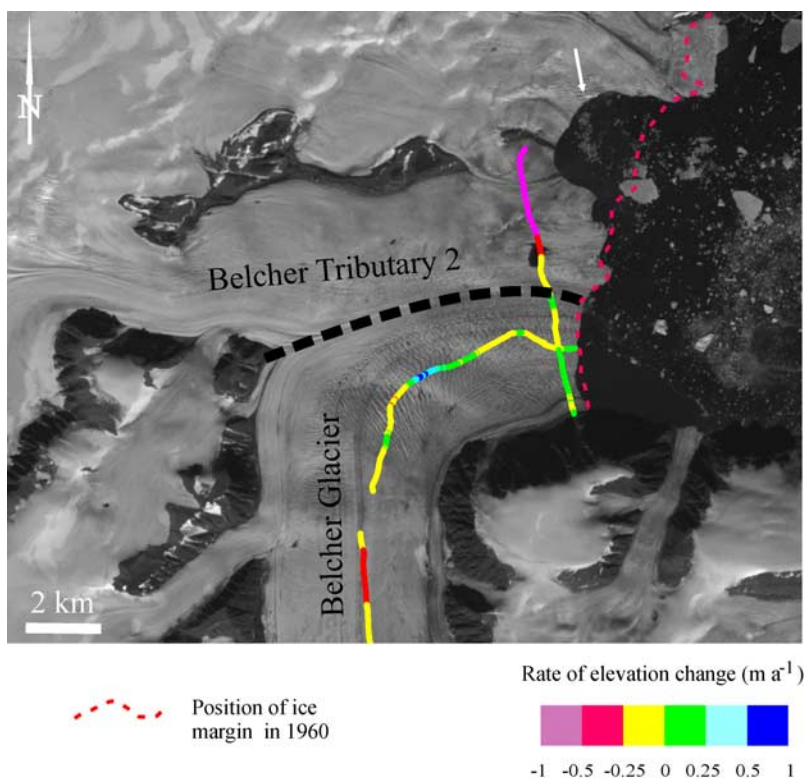


Figure 12. Rates of surface elevation change (m a^{-1}) in the Belcher Glacier terminus region (1960–2005) overlaid on a July 1999 Landsat ETM+ panchromatic orthoimage. Arrow points to a $\sim 3 \text{ km}^2$ portion of ice that calved sometime between 1983 and 1999.

maximum flow rates along these glaciers. These sectors may represent the actively surging portions of the glaciers where dynamic lowering of the ice surface is occurring. Maximum thickening on the other hand occurs where “fast” flowing ice from the upper reaches of these glaciers runs into near-stagnant ice at lower elevations (Figure 11). These zones of thickening coincide with strong longitudinal velocity gradients that likely represent surge fronts propagating into the slower moving ice at lower elevations [Sharp *et al.*, 1988; Murray *et al.*, 1998]. The presence of looped moraines and degraded flow stripes near the stagnant margin of these glaciers provides evidence that fast flow did extend into this region in the past. This near-stagnant terminus region, which is currently thinning, presumably has yet to be reactivated by the surge.

[39] The estimate of total volume change of the main part of the Devon Island ice cap of -32 km^3 water equivalent over the past 40 years derived from extrapolation of airborne laser altimetry measurements [Abdalati *et al.*, 2004], is significantly lower than our estimate of $-76 \pm 7 \text{ km}^3$ water equivalent. This may reflect a difference in thinning rates between the period covered by our assessment and that covered by the NASA measurements, but it may also derive from the fact that the NASA transects did not sample the regions where the most significant changes are occurring. The NASA transects from which these changes were derived (NASA_EW1, NASA_EW2, and NASA_NS1; Figure 2) are confined primarily to the main east-west divide and the western lobe, which are relatively inactive regions. The most significant changes however are occurring within the accumulation zone of the southeast region, the lower reaches of the

South Croker Bay Glacier, the ablation zone of basin 15 and in the low-lying basins that are almost entirely below the current ELA such as basin 60 (see Table 2). Since these areas are not sampled by the airborne laser altimetry surveys, estimates of volume change based on the results of those surveys may be too low.

[40] In many ways, the pattern of thickness changes observed over the Devon Island ice cap is similar to that measured over the Greenland ice sheet [Thomas *et al.*, 2001; Thomas *et al.*, 2005; Luthcke *et al.*, 2006; Stearns and Hamilton, 2007; Joughin *et al.*, 2008]. The broad scale pattern of thickness change over both Greenland and the Devon Island ice cap is one of near balance at high elevations and thinning near the ice cap margins [Krabill *et al.*, 2000]. Accumulation zone thinning rates of -29 cm a^{-1} and -23 cm a^{-1} do, however, occur in the southeast regions of Greenland [Thomas *et al.*, 2000] and Devon respectively. In both cases, these basins are likely influenced significantly by the behavior of the major outlet glaciers that drain them (King Christian IV, Pikiutdleg, and Helheim for Greenland [Abdalati *et al.*, 2001] and Southeast 1 and 2 for Devon). Dynamic thinning occurs well into the accumulation zones along these glaciers. Finally, several major tidewater glaciers that drain the Greenland Ice Sheet (Rink Isbrae, Kangerdlugsuup, Kjer, King Oscar, Humboldt North, Eqalorutsit East, Eqalorutsit West, Storsstrommen North) have zones of dynamic thinning similar to those along sections of the Belcher and South Croker Bay Glaciers on Devon. As on Greenland, some regions of surface lowering within the Devon Island ice cap appear to be attributable to recent changes in ice dynamics. Mass

loss due to these changes must therefore be accounted for to provide a reliable basis for assessing volume change of the ice mass as a whole [Abdalati *et al.*, 2001].

6. Conclusions

[41] Indirect measurements of rates of thickness change performed across the Devon Island ice cap, Nunavut, Canada reveal significant variability in the sign and magnitude of thickness changes between basins over the period from 1960 to 2003. The accumulation zones of the south and east regions of the ice cap are thinning slightly while rates of thickness change across the accumulation zones of the northern basins are indistinguishable from zero. Maximum thinning by $-0.23 \pm 0.11 \text{ m a}^{-1}$ w.e. occurs in the accumulation zone of the southeast basin. Thickness changes indistinguishable from zero prevail in the ablation zone of the southeast region while the southwest ablation zone is thickening by $0.55 \pm 0.22 \text{ m a}^{-1}$ w.e. The ablation zones of most basins in the northern region are thinning slightly with maximum rates of -0.62 m a^{-1} w.e. in the northeast sector. Overall, the main part of the Devon Island ice cap has decreased in volume by $-76.8 \pm 7 \text{ km}^3$ w.e. between 1963 and 2000, resulting in a net contribution of $+0.21 \pm 0.02 \text{ mm}$ to global sea level rise over this period of time. This estimate is up to $\sim 44\%$ greater than independent estimates based on volume-area scaling methods and surface mass balance alone, suggesting that ice dynamics must be included in models aimed at assessing the net mass balance of a large ice cap as a whole.

[42] Along glacier thickness change measurements suggest that all of the outlet glaciers examined in this study exhibit nonsteady, transient flow controlled by mechanisms operating either internally or externally to these systems. Thinning by $-0.35 \pm 0.04 \text{ m a}^{-1}$ of ice along almost the entire length of the Belcher Glacier may be an indirect result of recent warming trends that have occurred over the past 25 years. Dynamic thickening of the Belcher Glacier terminus has probably stabilized this tidewater margin, making it relatively insensitive to recent climate warming. The pattern of thickness change along the Southeast 1 and 2 outlet glaciers, combined with the presence of looped moraines and flow stripes on the surfaces of their near-stagnant termini suggest that these glaciers are characterized by surge-type flow, thus they are likely controlled by mechanisms internal to these systems. The diversity of patterns and rates of thickness change across the Devon Island ice cap suggests a complex interplay exists between changes in ice flow behavior and mass balance.

[43] This study provides insight into the impact of ice dynamics on changes in geometry and net mass balance of a high Arctic ice cap. A major drawback of recent efforts to predict the response of ice caps and glaciers to climate warming is that only changes in volume due to changes in surface mass balance are taken into account [e.g., IPCC, 2007]. Although the rates of volume change associated with changes in the flow of these glaciers are much less than those observed recently over Greenland, they are nonetheless significant for the overall balance of these ice masses.

[44] **Acknowledgments.** This work was supported by grants from NSERC (Canada) and the Meteorological Service of Canada (CRYSYS

program) to M. Sharp. D. Burgess received an IPS-2 scholarship from NSERC and Land Data Technologies Inc. and grants from the Canadian Circumpolar Institute and Northern Scientific Training Program (Department of Indian and Northern Affairs Canada). Gridded ice thickness data set provided by J. Dowdeswell were collected under NERC grant GR3/12469 and the EU SPICE project. Ice thickness profile data were obtained from S.P. Gogenini at the Center for Remote Sensing of Ice Sheets (CReSIS), University of Kansas. Airborne Laser Altimetry data were obtained from Bill Krabill of NASA Wallops Flight Facility, Virginia, U.S.A. Logistical support in the field was provided by the Polar Continental Shelf Project, Natural Resources Canada. We thank the Nunavut Research Institute and the hamlets of Grise Fiord and Resolute Bay for their permission to conduct this research on the Devon Island ice cap. Finally, we thank A. Arendt for many insightful comments on this paper.

References

- Abdalati, W., W. Krabill, E. Frederick, S. Manizade, C. Martin, J. Sonntag, R. Swift, R. Thomas, W. Wright, and J. Yungel (2001), Outlet glacier and margin elevation changes: Near-coastal thinning of the Greenland Ice Sheet, *J. Geophys. Res.*, *106*(D24), 33,729–33,741, doi:10.1029/2001JD900192.
- Abdalati, W., W. Krabill, E. Frederick, S. Manizade, C. Martin, J. Sonntag, R. Swift, R. Thomas, J. Yungel, and R. Koerner (2004), Elevation changes of ice caps in the Canadian Arctic Archipelago, *J. Geophys. Res.*, *109*, F04007, doi:10.1029/2003JF000045.
- Budd, W. F., and R. C. Warner (1996), A computer scheme for rapid calculations of balance-flux distributions, *Ann. Glaciol.*, *23*, 21–27.
- Burgess, D. O., and M. J. Sharp (2004), Recent changes in areal extent of the Devon Island ice cap, Nunavut, Canada, *Arct. Antarct. Alp. Res.*, *36*(2), 261–271, doi:10.1657/1523-0430(2004)036[0261:RCIAEO]2.0.CO;2.
- Burgess, D. O., M. J. Sharp, D. W. F. Mair, J. A. Dowdeswell, and T. J. Benham (2005), Flow dynamics and iceberg calving rates of the Devon Island ice cap, Nunavut, Canada, *J. Glaciol.*, *51*(173), 219–238, doi:10.3189/172756505781829430.
- Colgan, L., and M. Sharp (2008), Combined oceanic and atmospheric influences on net accumulation on Devon Ice Cap, Nunavut, Canada, *J. Glaciol.*, *54*(184), 28–40, doi:10.3189/002214308784409044.
- Dowdeswell, J. A., T. J. Benham, M. R. Gorman, D. Burgess, and M. Sharp (2004), Form and flow of the Devon Island ice cap, Canadian Arctic, *J. Geophys. Res.*, *109*, F02002, doi:10.1029/2003JF000095.
- Dyrugerov, M. B., and M. F. Meier (2005), *Glaciers and the Changing Earth System: A 2004 Snapshot*, 117 pp., Univ. of Colo. Inst. of Arctic and Alpine Res., Boulder, Colo.
- Hamilton, G. S., and I. M. Whillans (2000), Point measurements of mass balance of the Greenland Ice Sheet using precision vertical Global Positioning System (GPS) surveys, *J. Geophys. Res.*, *105*(B7), 16,295–16,301, doi:10.1029/2000JB900102.
- Intergovernmental Panel on Climate Change (2007), *Climate Change 2007: The Physical Science Basis: Contribution of Working Group I to the Fourth Assessment Report of the Intergovernmental Panel on Climate Change*, edited by S. Solomon *et al.*, Cambridge Univ. Press, New York.
- Joughin, I. J., I. Howat, R. B. Alley, G. Ekstrom, M. Fahnestock, T. Moon, M. Nettles, M. Truffer, and V. C. Tsai (2008), Ice-front variation and tide-water behaviour on Helheim and Kangerdlugssuaq Glaciers, Greenland, *J. Geophys. Res.*, *113*, F01004, doi:10.1029/2007JF000837.
- Koerner, R. (1970), Mass balance of the Devon Island ice cap, Northwest Territories, Canada, 1961–66, *J. Glaciol.*, *6*(45), 383–392.
- Koerner, R. (1977), Ice thickness measurements and their implications with respect to past and present ice volumes in the Canadian High Arctic ice caps, *Can. J. Earth Sci.*, *14*, 2697–2705.
- Koerner, R. (2002), Glaciers of the High Arctic Islands, in *Satellite Image Atlas of Glaciers of the World. Glaciers of North America—Glaciers of Canada*, edited by R. S. Williams Jr. and J. G. Ferrigno, *U.S. Geol. Surv. Prof. Pap.*, *1386-J-1*, 111–146.
- Krabill, W., W. Abdalati, E. Frederick, S. Manizade, C. Martin, J. Sonntag, R. Swift, R. Thomas, W. Wright, and J. Yungel (2000), Greenland Ice Sheet: High-elevation balance and peripheral thinning, *Science*, *289*, 428–429, doi:10.1126/science.289.5478.428.
- Krabill, W., P. Gogenini, and M. N. Demuth (2006), Glacier elevation and ice thickness data derived from Airborne LiDAR and Ice Penetrating RaDAR surveys over the reference monitoring glaciers and ice caps of the Canadian Arctic Islands, 2005, 2006, Geol. Surv. of Canada, Ottawa, Ontario, Canada.
- Luthcke, S. B., H. J. Zwally, W. Abdalati, D. D. Rowlands, R. D. Ray, R. S. Nerem, F. G. Lemoine, J. J. McCarthy, and D. S. Chinn (2006), Recent Greenland ice mass loss by drainage system from satellite gravity observations, *Science*, *314*, 1286–1289, doi:10.1126/science.1130776.

- Mair, D. W. F., D. O. Burgess, and M. J. Sharp (2005), Thirty-seven year mass balance of the Devon Island ice cap, Nunavut, Canada determined by shallow ice coring and melt modeling, *J. Geophys. Res.*, *110*, F01011, doi:10.1029/2003JF000099.
- Murray, T., J. A. Dowdeswell, D. J. Drewry, and I. Frearson (1998), Geometric evolution and ice dynamics during a surge of Bakaninbreen, Svalbard, *J. Glaciol.*, *44*(147), 263–272.
- Paterson, W. S. B. (1994), *The Physics of Glaciers*, 3rd ed., Elsevier, Oxford, U. K.
- Reeh, N., and W. S. B. Paterson (1988), Application of a flow model to the ice-divide region of Devon Island Ice Cap, Canada, *J. Glaciol.*, *34*(116), 55–63.
- Rignot, E., and X. Kanagaratnam (2006), Changes in the velocity structure of the Greenland Ice Sheet, *Science*, *311*, 986–987, doi:10.1126/science.1121381.
- Sharp, M., W. Lawson, and R. S. Anderson (1988), Tectonic processes in a surge-type glacier, *J. Struct. Geol.*, *10*, 499–515, doi:10.1016/0191-8141(88)90037-5.
- Stearns, L. A., and G. S. Hamilton (2007), Rapid volume loss from two East Greenland outlet glaciers quantified using repeat stereo satellite imagery, *Geophys. Res. Lett.*, *34*, L05503, doi:10.1029/2006GL028982.
- Taylor, R. B., and D. Frobel (1984), Coastal surveys, Jones Sound, District of Franklin, in *Current Research, Part B, Geol. Surv. Can. Pap.*, *84-1B*, 25–32.
- Thomas, R. H., T. Akins, B. Csatho, M. Fahnestock, P. Gogineni, C. Kim, and J. Sonntag (2000), Mass balance of the Greenland Ice Sheet at high elevations, *Science*, *289*, 426–429, doi:10.1126/science.289.5478.426.
- Thomas, R. H., et al. (2001), Program for Arctic regional climate assessment (PARCA): Goals, key findings, and future directions, *J. Geophys. Res.*, *106*(D24), 33,691–33,705, doi:10.1029/2001JD900042.
- Thomas, R., E. Frederick, W. Krabill, S. Manizade, C. Martin, and A. Mason (2005), Elevation changes on the Greenland ice sheet from comparison of aircraft and ICESat laser-altimeter data, *Ann. Glaciol.*, *42*, 77–82, doi:10.3189/172756405781813050.

D. Burgess, Canada Centre for Remote Sensing, 588 Booth Street, Ottawa, ON K1A 0Y7, Canada. (david.burgess@nrcan.gc.ca)

M. J. Sharp, Department of Earth and Atmospheric Sciences, University of Alberta, Edmonton, AB T6G 2E3, Canada.

Combined oceanic and atmospheric influences on net accumulation on Devon Ice Cap, Nunavut, Canada

William COLGAN,^{1,2} Martin SHARP¹

¹Arctic and Alpine Research Group, Department of Earth and Atmospheric Sciences, University of Alberta, Edmonton, Alberta T6G 2E3, Canada

²Cooperative Institute for Research in Environmental Sciences, University of Colorado, Boulder, Colorado 80309-0216, USA
E-mail: liam.colgan@colorado.edu

ABSTRACT. An annual net accumulation history of the high-elevation region of Devon Ice Cap, Nunavut, Canada, was reconstructed for the period 1963–2003 using five shallow firn cores. Annual net accumulation decreased significantly after 1989. To explain variability in the reconstructed annual net accumulation record, monthly and seasonal moisture-source probabilities were calculated for gridcells throughout the Arctic during 1979–2003. Seasonally, moisture-source probabilities reach a maximum in northern Baffin Bay in late summer/early fall and approach zero throughout the Arctic in winter. Late-summer/early-fall moisture-source probabilities were significantly higher around the North Open Water (NOW) Polynya during the 4 year period of highest annual net accumulation during the 1979–2003 period (1984–87), than during the 4 year period with the lowest annual net accumulation (1994–97). This is due to both a significant decrease in the sea-ice fraction and a significant increase in low-elevation atmospheric transport over the NOW area during the high net accumulation period. Anomalously low net accumulation and anomalously high firnification rates during the 1989–2003 period suggest that a change in ice dynamics, rather than a change in surface mass balance, may explain recent ice-cap thickening observed by laser altimetry.

NOTATION

$\sigma[c]$	Total uncertainty in annual net accumulation (m w.e. a ⁻¹)
$\sigma[c_c]$	Uncertainty in annual net accumulation due to m to m w.e. conversion (%)
$\sigma[c_l]$	Uncertainty in annual net accumulation due to peak location (%)
$\sigma[c_p]$	Uncertainty in net accumulation due to meltwater percolation between layers (%)
A	Area (km ²)
b	Back-trajectory points below 500 m elevation (hours)
c	Mean annual net accumulation rate (m w.e. a ⁻¹)
d	Number of days
D	Site-specific low-elevation atmospheric transport density (km ⁻²)
D'	Theoretical maximum site-specific low-elevation atmospheric transport density (km ⁻²)
m	Given month
M	Moisture-source index value (km ⁻²)
M'	Theoretical maximum moisture-source index value (km ⁻²)
O	Open-water fraction (dimensionless)
O'	Theoretical maximum open-water fraction (dimensionless)
P	Relative moisture-source probability (dimensionless)
s	Given season
S	Sea-ice fraction (dimensionless)
w	Number of points in a running mean
x	Given G814 cell
y	Given G4640 cell

1. INTRODUCTION

There is a significant discrepancy between the observed rate of sea-level rise ($1.5 \pm 0.5 \text{ mm a}^{-1}$) and the rate calculated from the sum of the best estimates of freshwater inputs to the ocean and thermal expansion of sea water ($0.7 \pm 1.5 \text{ mm a}^{-1}$; Cazenave and Nerem, 2004). This discrepancy indicates that inaccuracies are likely to exist in sea-level observations or calculations of the major contributions to sea-level rise, or both. This provides a motivation to improve the quantification of glacier and ice-cap contributions to sea-level change (Cazenave and Nerem, 2004). Outside of Greenland and Antarctica, the Canadian Arctic Archipelago contains the largest area of glaciated terrain in the world (Dyrgerov and Meier, 2005). Although the potential contribution of the Canadian Arctic ice caps to sea-level rise is far less than that of the ice sheets in Greenland and Antarctica, their smaller size and more temperate environs make them potentially significant short-term contributors to eustatic sea-level rise (Dowdeswell, 1995; Abdalati and others, 2004). The 14 010 km² Devon Ice Cap (75° N, 82° W; Fig. 1) is 880 m thick at its deepest point, and has an estimated volume of 3980 km³, equivalent to $\sim 10 \text{ mm}$ sea-level rise if melted completely (Dowdeswell and others, 2004). It is believed to be in long-term negative mass balance (Koerner, 2005), losing an estimated $1.6 \pm 0.7 \text{ km}^3$ of water equivalent (w.e.) per year since 1960 (Burgess and Sharp, 2004).

Although only 19% of the area of Devon Ice Cap lies above 1200 m (Dowdeswell and others, 2004), the high-elevation region is of interest because its mass-balance variations are poorly correlated with the overall net balance of the northwest sector of the ice cap, which has been measured annually since 1961 (personal communication from R. Koerner, 2005; Fig. 2). In the northwest sector as a whole, the annual and summer net balances are well

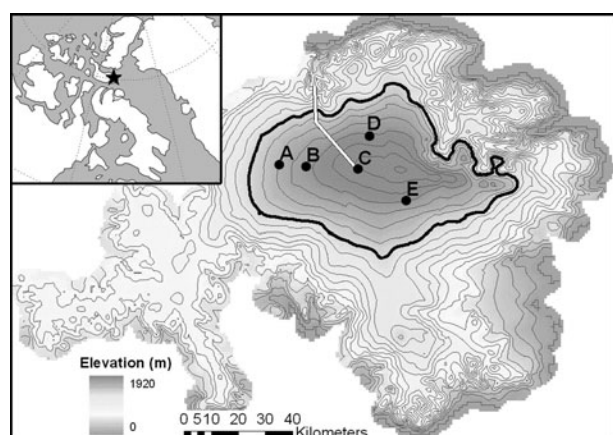


Fig. 1. Shaded contour map of Devon Ice Cap (100 m interval), with the high-elevation region enclosed by the 1200 m contour (black). The locations of the five shallow firn-core sites (A–E) and the northwest sector mass-balance transect (white; Koerner, 1970) are shown. Inset: Devon Ice Cap in the Canadian Arctic Archipelago.

correlated, which suggests that interannual net mass-balance variability is controlled largely by summer melt processes at lower elevations (<1200 m; Koerner, 2002; Abdalati and others, 2004). At higher elevations, even the summer balance may be positive, and variability in snow accumulation may account for much of the variability in annual net balance. Airborne laser altimetry surveys in 1995 and 2000 suggested that the high-elevation region (>1200 m) of the ice cap was thickening at a rate of up to 20 cm a^{-1} , and the low-elevation region (<1200 m) was thinning at a rate of up to 40 cm a^{-1} (Abdalati and others, 2004). Although it has been suggested that the recent high-elevation thickening may be due to anomalous accumulation during the 1995–2000 period (Abdalati and others, 2004), a decrease in the rate of firn densification or a long-term reduction in ice outflow from the accumulation zone could also explain the laser altimetry observations.

In order to best predict how the mass balance of Devon Ice Cap will respond to future climatic conditions, present-day climatic controls on mass balance must be well understood. This study aims to create an annually resolved record of the recent (1963–2003) net accumulation history of the high-elevation region of the ice cap from measurements on shallow firn cores. This record is used to (i) investigate the

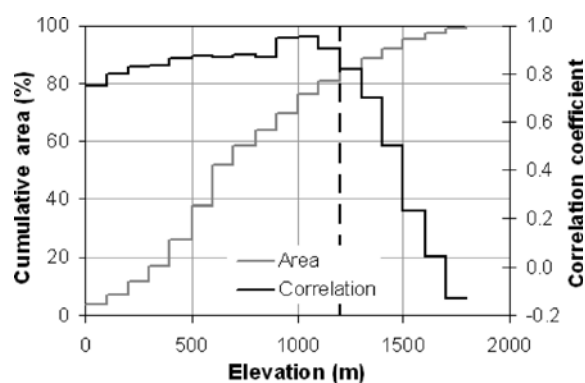


Fig. 2. Correlation between the overall northwest transect annual mass balance and the net balance of individual elevation bands over the period 1961–98 (personal communication from R. Koerner, 2005). The cumulative area of the ice cap with elevation is also shown (Dowdeswell and others, 2004). The dashed curve denotes 1200 m elevation.

influences of changing atmospheric transport and regional sea-ice cover variability on the annual net accumulation at high elevations and (ii) assess whether the thickening observed by laser altimetry can be explained by anomalous net accumulation or firnification rates.

2. METHODS

2.1. Shallow firn-core recovery

To reconstruct a net accumulation record for the high-elevation region of Devon Ice Cap, five shallow ($\sim 20 \text{ m}$) firn cores (cores A–E) were recovered in April 2004 and April 2005 (Fig. 1; Table 1). The cores were recovered using a Kovacs Mk II corer with a 90 mm internal barrel diameter. The average measured core diameter was 88 mm. The length and mass of each $\sim 30 \text{ cm}$ firn core section were recorded in the field in order to construct a density profile for each core. The core sections were then wrapped in polyethylene and shipped frozen to the University of Alberta for further analysis.

To constrain the dating of the cores, in situ ^{137}Cs gamma spectrometry was performed in each borehole using an NaI(Tl) detector connected to a multi-channel analyzer (Dunphy and Dibb, 1994) to identify the depth of the 1963

Table 1. Characteristics of the five shallow firn cores recovered from Devon Ice Cap: recovery year, location and elevation, drill depth, mean number of glaciochemical samples per year, mean net accumulation (c ; \pm standard deviation), uncertainty in annual net accumulation ($\sigma[c]$), mean annual ice fraction (\pm standard deviation) and the mean number of melt days for the 2000–04 period (Wang and others, 2005)

	Core A	Core B	Core C	Core D	Core E
Recovery year	2005	2005	2004	2005	2005
Latitude ($^{\circ}$ N)	75.3448	75.3427	75.3399	75.2390	75.4494
Longitude ($^{\circ}$ W)	83.7015	83.3525	82.6763	82.0310	82.5305
Elevation (m)	1415	1630	1825	1525	1525
Drill depth (m)	20.5	18.5	21.0	20.6	20.7
Samples (a^{-1})	10.8	13.4	9.6	7.3	13.1
c (m w.e. a^{-1})	0.22 ± 0.09	0.22 ± 0.07	0.25 ± 0.06	0.17 ± 0.06	0.23 ± 0.07
$\sigma[c]$ (m w.e. a^{-1})	± 0.08	± 0.06	± 0.07	± 0.06	± 0.07
Ice fraction	0.62 ± 0.34	0.26 ± 0.24	0.16 ± 0.17	0.49 ± 0.36	0.46 ± 0.28
Melt days	31	24	18	27	29

'bomb' layer resulting from fallout from atmospheric thermonuclear weapons testing. Gamma emissions were counted for 20 min periods at 20 cm intervals in three discrete energy windows: a background window (885–1001 keV), the ^{137}Cs window (626–749 keV) and a ^{109}Cd control window (49–117 keV). The background band registers gamma emissions over a randomly selected energy band. These background emissions are expected to remain constant at depths below the level to which cosmic radiation penetrates. In addition to showing the near-surface increase due to cosmic radiation, the ^{137}Cs band also demonstrates a clear secondary peak at depth that is taken to be the 1963 ^{137}Cs peak (Dunphy and Dibb, 1994). The observed ^{109}Cd activity originated from a ^{109}Cd source fixed to the detector and was monitored to ensure the absence of drift in peak locations. As counts were performed in each of the three bands at 20 cm intervals from the bottom of the borehole upwards, the 1963 ^{137}Cs peak is resolved to within ± 10 cm.

2.2. Reconstructing annual net accumulation

The five firn cores were dated by counting annual layers defined by high-resolution physical and chemical stratigraphy. A detailed description of the physical stratigraphy of each core was made before the cores were sectioned with a bandsaw into slices of 3.1 ± 0.8 cm for anion and $\delta^{18}\text{O}$ analyses (Table 1). Individual slices were melted at room temperature in Whirlpak bags and decanted and stored in 20 mL vials prior to analysis. A Dionex ICS-2500 ion chromatograph was used to measure the concentrations of methanesulphonic acid (MSA: $\text{CH}_3\text{SO}_3\text{H}$), sulphate (SO_4^{2-}), nitrate (NO_3^-) and chloride (Cl^-) in each sample. The limits of detection (LOD), defined here as three times the standard deviation of the lowest concentration standard in a randomly selected sequence of eight consecutive runs, were $0.086 \mu\text{Eq L}^{-1}$ for SO_4^{2-} , $0.109 \mu\text{Eq L}^{-1}$ for NO_3^- , $0.079 \mu\text{Eq L}^{-1}$ for MSA and $0.097 \mu\text{Eq L}^{-1}$ for Cl^- . The $\delta^{18}\text{O}$ ratios in samples from the highest-elevation core (core C) were measured with a GV Isoprime continuous-flow mass spectrometer with EuroEA combustion chamber using an injection volume of 0.1 μL . The instrument was calibrated with SMOW1675, GISP1381 and SLAP1499, with CO_2 as a reference gas.

Annual layers in each core were identified by counting annual SO_4^{2-} , Cl^- , MSA and $\delta^{18}\text{O}$ (when available) peaks. The net accumulation of a given year is defined as the accumulation between a given pair of SO_4^{2-} peaks. Snowfall SO_4^{2-} concentrations in the Canadian High Arctic peak in February/March (Toom-Saunty and Barrie, 2002), so the net accumulation in a given year represents the net accumulation from February/March of that year to February/March of the following year. The July/August MSA and $\delta^{18}\text{O}$ (when available) maxima and the January/February $\delta^{18}\text{O}$ (when available) minimum and Cl^- maximum (Toom-Saunty and Barrie, 2002) are identifiable in most annual layers (Fig. 3). In addition, common horizons defined by, for example, unusually high Cl^- concentrations were used for core correlation when present in all five records (Fig. 3). The net accumulation (in m.w.e.) was derived for the annual layers in each core using the density profiles measured in the field. This created a record of annual net accumulation between 1963 and 2003 for each core site. As the ice content of the core was assessed during logging of the physical stratigraphy (Fig. 3), the ice fraction of each annual layer could be calculated. The annual ice fraction is defined

as the fraction of the w.e. net accumulation present as ice, rather than firn, in each annual layer (Table 1). The thinning of annual layers with depth, due to ice deformation, is often a concern when using ice cores to reconstruct annual net accumulation records. In a previous study, however, Pohjola and others (2002) considered the top 18.5 m of an ice core to be minimally influenced by deformation. We likewise assume negligible flow-induced layer thinning in our annual net accumulation record.

2.3. Uncertainty in reconstructed net accumulation

There are three main sources of uncertainty in the reconstructed net accumulation in a given annual layer. Firstly, there is uncertainty in the precise location of seasonal anion concentration peaks. This is the result of uncertainties in (i) the use of discrete samples to define the chemical stratigraphy of the core, (ii) the timing of the deposition of the annual SO_4^{2-} concentration peak used to define annual layers and (iii) the displacement of the anion peak by melt (Gjessing and others, 1993; Moore and others, 2005). We estimate the uncertainty due to discrete sampling as the fraction of the annual layer represented by a single sample. For example, in core A there are 10.8 samples per year, which means that one sample represents $\sim 9\%$ of a given annual layer (Table 1). As the seasonal peak in snowfall SO_4^{2-} concentration spans a 3 month period (Toom-Saunty and Barrie, 2002), we estimate the uncertainty in the deposition timing of the annual SO_4^{2-} concentration peak as $\pm 25\%$. We have no way of estimating the displacement of this peak by melt. These uncertainties were combined to give a root-mean-square (rms) uncertainty due to peak location ($\sigma[c_l]$) of between ± 26 and $\pm 29\%$ depending on core (core A: 27%, B: 26%, C: 27%, D: 29% and E: 26%). The second main source of uncertainty in net accumulation is due to the transfer of mass between annual layers by meltwater percolation ($\sigma[c_p]$). We estimate this uncertainty as the mean decrease in net accumulation variability in each core record between periods of lower (1963–88) and higher (post-1989) meltwater percolation. (The calculation of $\sigma[c_p]$ (core A: 23%, B: 9%, C: 0%, D: 18% and E: 4%) is described in section 3.2 below.) Thirdly, there is uncertainty in annual net accumulation due to the conversion of annual layer thicknesses from m to m.w.e. ($\sigma[c_d]$) using the density profiles and core geometries measured in the field. The core sections recovered have a mean length of 29.8 ± 2 cm and a mean mass of 1187 ± 50 g. The uncertainties in these measurements were taken as a percentage of the mean length and mass of the ice-core sections ($\pm 5\%$ and $\pm 4\%$, respectively), giving a combined rms error $\sigma[c_c]$ of $\pm 6\%$. The total uncertainty in the mean annual net accumulation at a core site ($\sigma[c]$) was calculated as:

$$\sigma[c] = c \sqrt{(\sigma[c_l])^2 + (\sigma[c_p])^2 + (\sigma[c_c])^2}. \quad (1)$$

The resulting uncertainty varied between ± 0.06 and ± 0.08 m.w.e. a^{-1} (± 28 to $\pm 36\%$ of the mean annual net accumulation) depending on the core site (Table 1).

This analysis of uncertainty excludes the uncertainty associated with the dating of the core. Dating errors can result in true annual layers being split or combined, which has consequences for the assessment of the accumulation they contain. This source of uncertainty is presumably lowest near those horizons that can be dated independently (the surface and the 1963 ^{137}Cs bomb layer) and potentially

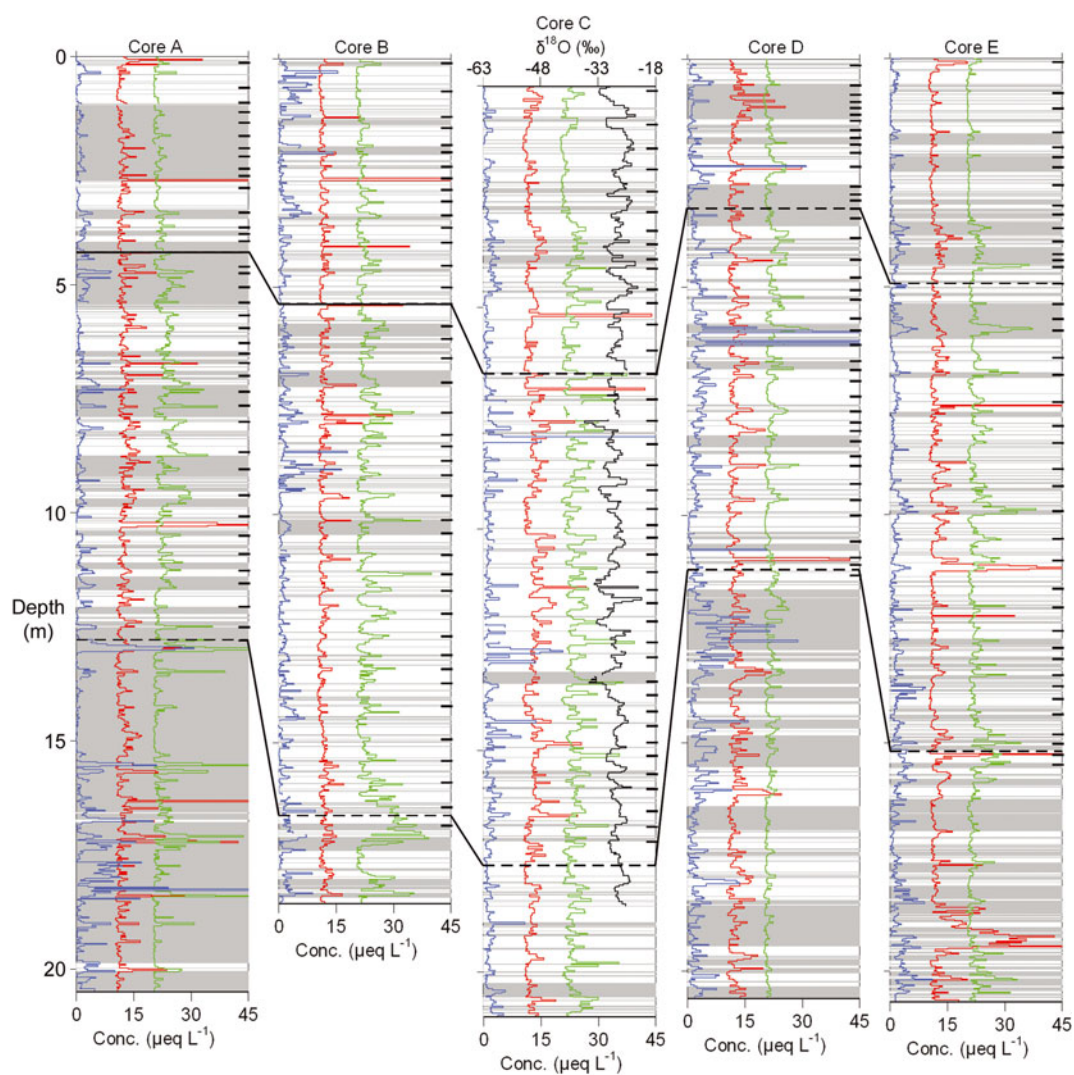


Fig. 3. MSA (blue), Cl^- (red), SO_4^{2-} (green) and $\delta^{18}\text{O}$ (black) records with depth in the five shallow firn cores. To facilitate interpretation, MSA concentrations have been multiplied by 100, and Cl^- and SO_4^{2-} concentrations have been translated from zero by 10 and $20 \mu\text{Eq L}^{-1}$, respectively. Grey shading indicates the portions of the cores composed of ice, both clear and bubbly, as opposed to firn (white shading). The 1963 ^{137}Cs 'bomb' horizon and the 1989 annual layer are connected between cores (dashed lines). The annual layers are identified in each core (dashes).

greatest near the middle of the reconstructed record. Because of this variability, we chose not to combine this dating-related uncertainty with the uncertainties included in Equation (1), and evaluated it separately. For all the cores, we estimated a dating uncertainty of ± 1 year during the 1963–73 and 1993–2003 periods, and a dating uncertainty of ± 2 years during the 1973–93 period. The associated maximum uncertainty in the accumulation associated with a single annual layer can thus be assumed to be one or two times the mean annual net accumulation rate for each core, but the actual error will be much less than this for most layers because the number of annual layers counted in each core is constrained to match the time interval between 1963 and the year of core recovery. To minimize the impact of this uncertainty on the analyses reported here, all time-series analyses were performed on 3 year running means of the reconstructed annual net accumulation records.

2.4. Potential moisture-source areas

To investigate the causes of variability in annual net accumulation on the ice cap, we attempted to evaluate

temporal changes in the potential supply of moisture to the ice cap that resulted from variations in the pattern of atmospheric transport to the ice cap and the extent and distribution of areas of open water along the transport pathways. Potential moisture-source areas, defined as regions with open water that have a relatively high probability of being traversed by low-elevation (< 500 m) air masses en route to Devon Ice Cap, were reconstructed for the 1979–2003 period. We focused on low-elevation air masses because previous work indicates that air masses travelling close to open-water surfaces are more likely to acquire moisture by evaporation than higher-elevation air masses (Reijmer and others, 2002).

Daily 120 hour kinematic back-trajectories for the period 1979–2003 were calculated for the summit of Devon Ice Cap (75°N , 82°W) using the METEX model (Zeng and others, 2003) and US National Centers for Environmental Prediction/US National Center for Atmospheric Research (NCEP/NCAR) re-analysis data (Kalnay and others, 1996). Each trajectory describes the most probable upwind path taken by a parcel of air arriving 500 m above ground level at

the summit of Devon Ice Cap at 0000 h local time each day. Similarly, Kahl and others (1997) compiled a 44 year daily back-trajectory record for the summit of the Greenland ice sheet using the once-daily (0000 h) 400 m arrival. The choice of a once-daily sampling interval is justified on the grounds that we are interested in reconstructing synoptic-scale (day to week) and seasonal variations in regional air-mass transport pathways (Kahl and others, 1997; Reijmer and others, 2002).

To identify those regions of the Arctic crossed by low-elevation air masses en route to Devon Ice Cap, all hourly back-trajectory points below 500 m in a given month were gridded on an 814-cell conic grid centred on the North Pole (hereafter G814). For a given G814 cell (indicated by subscript x), the monthly site-specific low-elevation atmospheric transport density (D_{mx}) was computed according to:

$$D_{mx} = \frac{b_{mx}}{A_x \times d_m \times 24 \text{ hours d}^{-1}}, \quad (2)$$

where b_{mx} is the number of hourly back-trajectory points below 500 m elevation counted in a given G814 cell (hours), A_x is the area of the given G814 cell and d_m is the number of days in the given month.

Although site-specific low-elevation atmospheric transport provides a physical mechanism to link the ice cap with potential moisture-source regions, sea-ice cover is also an important control on the distribution of moisture sources (open water) in the polar regions. To improve the identification of potential moisture-source regions for Devon Ice Cap, we combined the monthly site-specific low-elevation atmospheric transport density history with a monthly open-water fraction (O_{my}) history. Monthly open-water fraction values were obtained from the US National Snow and Ice Data Center (NSIDC) Northern Hemisphere monthly sea-ice fraction dataset, gridded in a 4640-cell standard 1° latitude cylindrical projection grid (hereafter G4640), and derived from passive microwave remote sensing using the NASA Team algorithm (Walsh, 1978; <http://arctic.atmos.uiuc.edu/SEACE>). Monthly open-water fraction is given by:

$$O_{my} = 1 - S_{my}, \quad (3)$$

where S_{my} is the monthly sea-ice fraction in a given G4640 cell (indicated by subscript y) in a given month (indicated by subscript m).

Each G814 gridcell in the monthly site-specific low-elevation atmospheric transport dataset encompasses multiple G4640 cells in the monthly open-water fraction dataset. Each G4640 cell was therefore assigned the monthly low-elevation atmospheric transport history of the G814 cell within which its centre coordinates reside. Monthly moisture-source index values (M_{my}) were generated for each G4640 cell in a given month by combining monthly low-elevation atmospheric transport and open-water fraction histories according to:

$$M_{my} = D_{mx} \times O_{my}. \quad (4)$$

To express the monthly moisture-source index value of each G4640 cell as a dimensionless relative probability, monthly moisture-source index values were divided by a theoretical monthly maximum moisture-source index value (M'_m), which is the theoretical limit that would be reached if both monthly low-elevation atmospheric transport density and monthly open-water fraction reached maxima (D'_m and O'_m) within a single cell which served as the sole moisture source

for Devon Ice Cap in a given month:

$$M'_m = D'_m \times O'_m. \quad (5)$$

To achieve this theoretical maximum moisture-source index value, all daily back-trajectory points in a given month would have to lie below 500 m elevation and have access to perpetually open water within the single G814 cell at the summit of Devon Ice Cap in which all trajectories terminate. Equation (2) is used to find D'_m , with b_{mx} taken as the theoretical maximum number of daily low-elevation back-trajectory points that could occur in a given gridcell in a given month ($120 \text{ hours d}^{-1} \times d_m$) and A_x as the area of the terminal gridcell ($77\,788 \text{ km}^2$). Equation (5) gives M'_m ; assuming an open-water fraction of 1 it has a value of $6.42 \times 10^{-4} \text{ km}^{-2}$.

The relative probability that a given G4640 cell acts a moisture source in a given month (P_{my}) is then:

$$P_{my} = \frac{M_{my}}{M'_m}. \quad (6)$$

If $P_{my} = 0.01$, then an air mass transits within 500 m of open water in G4640 cell y and goes on to travel to the summit of Devon Ice Cap approximately once every 100 hours in month m . Although calculated P_{my} values ranged between zero and 0.1, only G4640 cells where the P_{my} value surpassed 0.001 for at least one month a year were chosen for further study. Cells where P_{my} values are perpetually below 0.001 are unlikely to be important moisture-source areas. Monthly values of site-specific low-elevation atmospheric transport density (D_{mx}), sea-ice fraction (S_{my}) and relative moisture-source probability (P_{my}) were averaged for three seasons: late summer/early fall (July, August, September, October (JASO)); late spring/early summer (March, April, May, June (MAMJ)) and winter (November, December, January, February (NDJF)) (see Figs 4–6). Seasonal values were weighted according to the differing number of days in each month, and denoted as D_{sx} , S_{sy} and P_{sy} . These seasonal divisions were chosen because approximately twice as much accumulation occurs on Devon Ice Cap in JASO as in MAMJ, and little accumulation occurs during NDJF (Koerner, 2002). The NDJF season comprises January and February of a given year, and November and December of the previous year.

This simple calculation of P_{my} values provides only a first approximation of the likely location of moisture sources, since important parameters that influence evaporative moisture uptake, such as air-mass temperature, relative humidity and wind speed, are ignored. Warmer air masses can hold more moisture than colder air masses (Serreze and Barry, 1999). Moisture-source probabilities may therefore be underestimated (overestimated) during the JASO (NDJF) season, as the air masses in all seasons are treated as equal when, in reality, a given JASO air mass probably takes up and transports more moisture than a given NDJF air mass. Similarly, the amount of moisture an air mass can take up decreases as the relative humidity of an air mass increases (Serreze and Barry, 2005). Therefore, relative moisture-source probabilities may be slightly enhanced (depressed) in the more continental (maritime) regions of the Arctic, such as the Queen Elizabeth Islands, Baffin Bay, where relative humidity is probably low (high). Finally, evaporation is also enhanced by higher wind speeds. Although moisture is transferred from open water to the shallow surface boundary layer primarily through diffusion, turbulent eddies are the

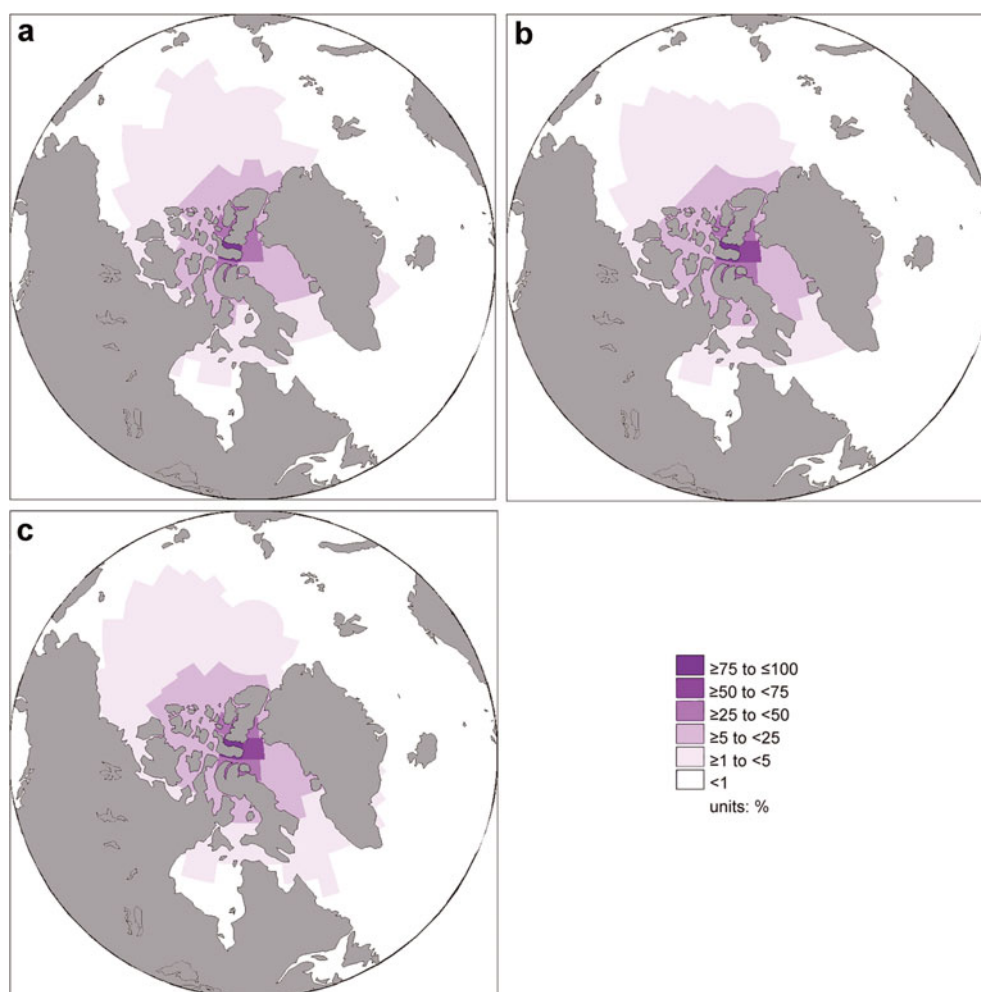


Fig. 4. The seasonal site-specific low-elevation atmospheric transport density (D_{sx}), during the period 1979–2003, in (a) the winter (NDJF), (b) late-spring/early-summer (MAMJ) and (c) late-summer/early-fall (JASO) seasons. D_{sx} values for each G814 cell are expressed as a percentage of the maximum D_{sx} value achieved in each season.

main method by which moisture is transferred to the rest of the troposphere (Serreze and Barry, 2005). Therefore, regions with relatively high mean wind speeds may have higher moisture-source probabilities than reported here, due to the effective transfer of moisture from the boundary layer to the rest of the troposphere.

2.5. Annual net accumulation variability

The influence of seasonal moisture-source probability variability on net accumulation was examined for the moisture-source region of interest (defined by $P_{my} > 0.001$) during the 1979–2003 period. Within this region, the mean relative moisture-source probabilities of the 4 year periods of highest (1984–87) and lowest (1994–97) annual net accumulation during the 1979–2003 period were compared. One-tailed t tests, assuming equal variance, were performed for each gridcell to ensure that only cells exhibiting significant differences in JASO moisture-source probabilities between the high and low net accumulation 4 year periods were mapped. To examine the relative role of atmospheric and oceanic influences on relative moisture-source probability differences, significant differences in the sea-ice fraction and site-specific low-elevation air-mass transport density between the high and low net accumulation periods were also mapped.

3. RESULTS

3.1. Reconstructed annual net accumulation

Similar standard deviations of the annual net accumulation records indicate that the five cores exhibit similar amounts of interannual variability (Table 1). The stacked mean of the five reconstructed annual net accumulation records shows distinct periods of above (1964–67, 1971–79 and 1984–88) and below (1968–70, 1981–83 and 1989–2003) average annual net accumulation (Fig. 7). A two-tailed t test, assuming equal variance, reveals that the mean annual net accumulation during the 1989–2003 period (0.18 ± 0.05 m w.e.) was significantly lower ($p < 0.05$) than in the 1963–88 period (0.24 ± 0.07 m w.e.).

As the reconstructed annual net accumulation records exhibit clear periods with above and below average annual net accumulation, they can be characterized as datasets dominated by red-noise processes as opposed to white-noise processes. This distinction is important when examining the significance of relationships between these core records. As the autocorrelation within these records is most likely to be physically based (i.e. meteorological explanations for the autocorrelation probably exist), white-noise statistics, which assume no autocorrelation, are not suitable for analyzing these relationships. Fleming and Clarke (2002) argued that

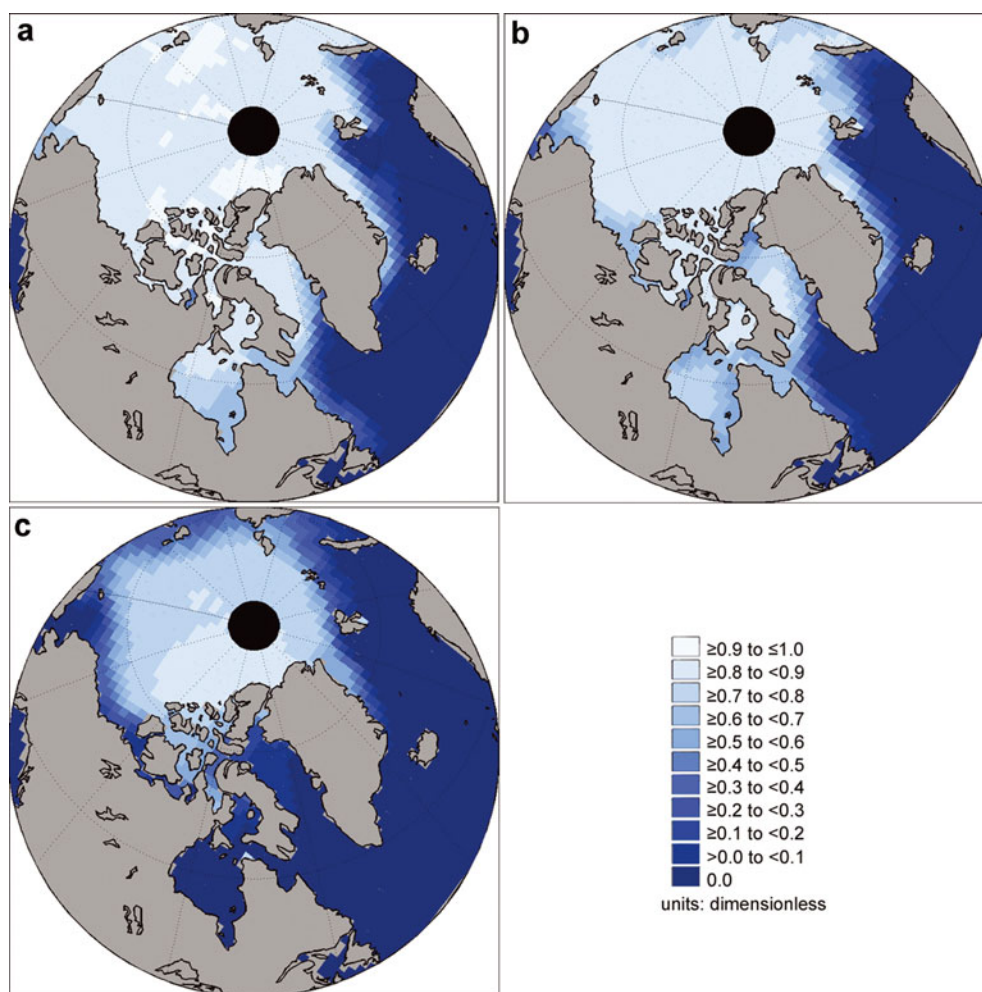


Fig. 5. The sea-ice fraction (S_{sy}), during the period 1979–2003, in (a) the winter (NDJF), (b) late-spring/early-summer (MAMJ) and (c) late-summer/early-fall (JASO) seasons (<http://arctic.atmos.uiuc.edu/SEAICE>). S_{sy} values for each G4640 cell are expressed as a fraction between 0 and 1.

the use of white-noise approaches to examine relationships between datasets with physically based autocorrelation ‘can substantially and inappropriately reduce the power of trend significance tests’. To address this problem, they argued that non-parametric statistical approaches, such as Spearman’s rank correlation, should be used to overcome the difficulties of autocorrelation in red-noise datasets, and evaluate the significance of relationships between time series (Fleming and Clarke, 2002).

The coherence of the net accumulation signal contained within the five ice cores was assessed through the cross-correlation of the five individual reconstructed 3 year running mean net accumulation records and the 3 year running mean stacked net accumulation record, using Spearman’s rank correlation. Although the use of a 3 year running mean compensates for dating uncertainty, it introduces non-physically based autocorrelation into the datasets. A running mean reduces the effective sample size of a dataset by $1.5/w$, where w is the number of points used in the running mean (Moore and others, 2006). Therefore, a 3 year running mean results in an effective sample size of half the original sample size, which means correlations between 40 year datasets, for example, should be assessed using 19 degrees of freedom (Moore and others, 2006).

All five individual core records were found to be positively correlated ($p < 0.01$, $r > 0.52$ for $df = 19$) to the

3 year stacked mean net accumulation record (Table 2). Therefore, we find the 3 year stacked mean net accumulation record to be representative of the individual core records which comprise it. The Spearman’s rank correlation coefficient between individual core records is negatively correlated with the distance between core sites ($p < 0.05$, $r = 0.60$ for $df = 9$), which suggests that some spatial variability exists in the history of net accumulation on Devon Ice Cap and supports the stacking of the shallow firn-core records to produce a composite history (Table 2; Fig. 1).

Good correlation between the annually measured mass-balance record and the reconstructed net accumulation record is of paramount importance to instil faith in the use of shallow firn cores to reconstruct the net accumulation history. The measured mass-balance record used here is the mean of the annual mass-balance measurements at 1250, 1350, 1450, 1550, 1650 and 1750 m elevations (the range covered by the firn cores) in the northwest sector of Devon Ice Cap (personal communication from R. Koerner, 2005; Fig. 7). Previous work has found that the mass balance of the northwest sector is a good proxy for the mass balance of the entire ice cap (Koerner, 1970). The significance of the relationship between 3 year running means of the reconstructed net accumulation record and the measured mass-balance record was also examined using Spearman’s rank correlation. Although there was a positive correlation

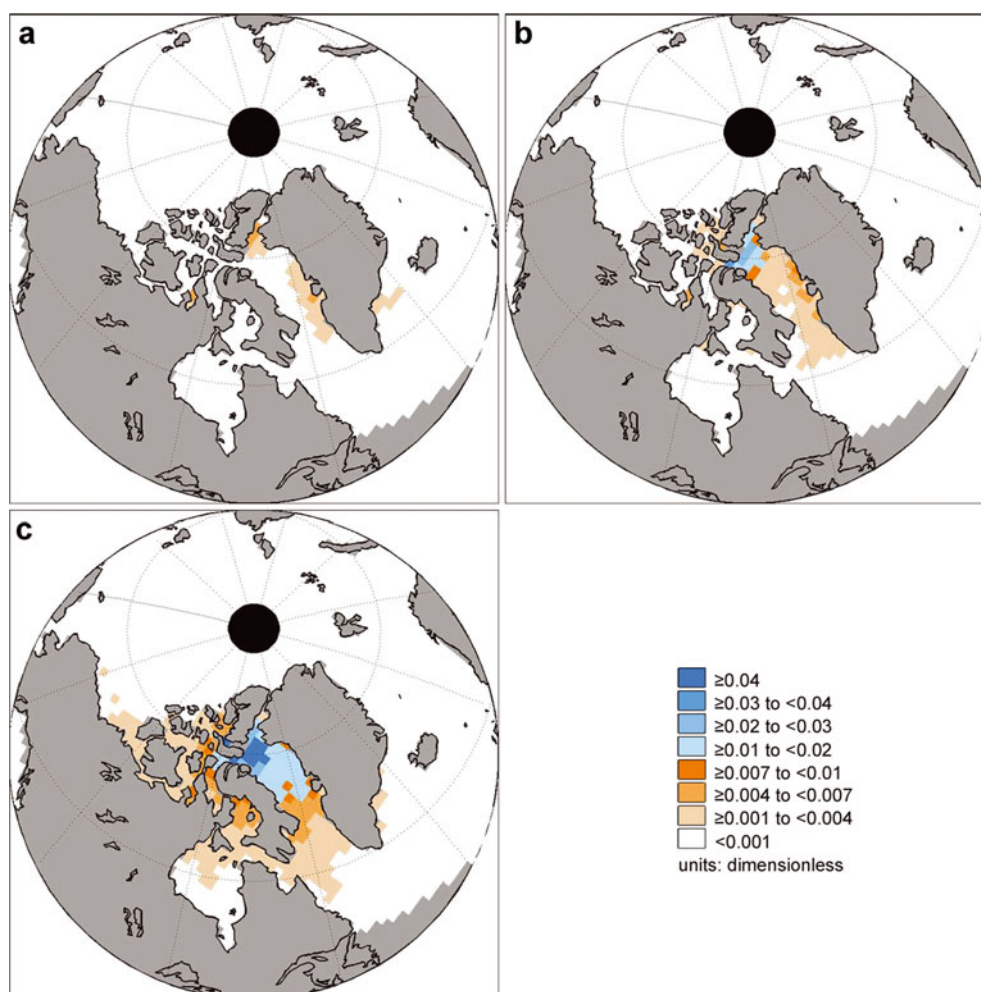


Fig. 6. Relative moisture-source probabilities (P_{sy}) in (a) the winter (NDJF), (b) late-spring/early-summer (MAMJ) and (c) late-summer/early-fall (JASO) seasons, during the 1979–2003 period. P_{sy} values for each G4640 cell are expressed as a dimensionless probability.

($p < 0.05$, $r = 0.39$ for $df = 19$) between the records during the whole 1963–2003 period, it was stronger ($p < 0.05$, $r = 0.62$ for $df = 12$) during the period of higher net accumulation (1963–88). There is no correlation ($p > 0.05$, $r = -0.24$ for $df = 6$) during the post-1989 period of significantly lower net accumulation (Fig. 7), when the stacked mean net accumulation record consistently underestimates the measured mass balance (Fig. 7). As these two records pertain to different portions of the high-elevation region of Devon Ice Cap, the differences between them are likely to be real and indicative of spatial differences in net accumulation rates (Fig. 1).

3.2. High-elevation melt

The unfortunate result of meltwater percolation is that ‘any one annual layer contains accumulation from more than one year, and yet does not contain all the accumulation from the year when the layer was deposited’ (Koerner, 1970). This problem is probably most severe for those cores which experience the most melt and, within a single core, for periods of more intense melt. It is likely to influence both the reliability of the reconstructed net accumulation records and the comparison between the ice-core records and the measured mass balance of the ice cap. To characterize the spatial variation in the melt regime of the region of the ice cap from which the cores were collected, the mean number

of melt days experienced at each core site between 2000 and 2004 was estimated using the regression model developed from QuikSCAT scatterometer data by Wang and others (2005). This model, which incorporates the influences of both site elevation and the distance of each core site from a fixed point in Baffin Bay, predicts annual melt durations of 18–31 days depending on core site (Table 1). The mean annual ice fraction in each ice core provides an independent measure of the melt intensity at each core site. During the 1963–2003 period, this fraction

Table 2. Spearman’s rank correlation coefficients between the five individual 3 year mean net accumulation records and their stacked 3 year mean over the 1963–2003 period. The distances between core sites (in km) are shown in parentheses

	Core A	Core B	Core C	Core D	Core E
Core B	0.45* (10)	–	–	–	–
Core C	0.47* (29)	0.68† (19)	–	–	–
Core D	–0.11 (48)	0.42* (39)	0.33 (21)	–	–
Core E	0.25 (35)	0.33 (26)	0.28 (14)	0.27 (27)	–
Mean	0.66†	0.82†	0.78†	0.49†	0.62†

Note: * indicates $p < 0.05$ and † indicates $p < 0.01$ for $df = 19$.

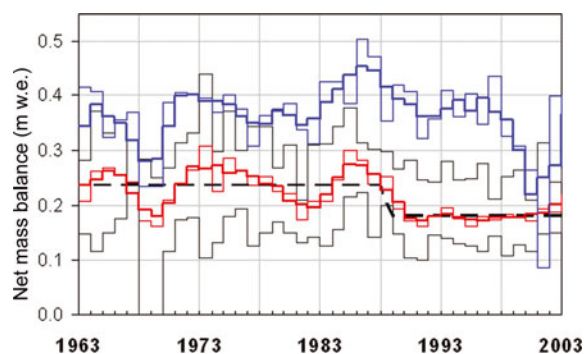


Fig. 7. The 3 year mean measured surface mass balance (blue) and 3 year stacked mean reconstructed net accumulation (red) are shown during the 1963–2003 period, as well as their respective annual records (thin black). The annual maximum and minimum reconstructed net accumulation values are indicated with thin grey lines. A significant decrease ($p < 0.05$; t test) in the mean annual net accumulation after 1988 is shown (dashed line).

varied between 0.16 and 0.62, depending on the core site (Table 1) and was well correlated to the calculated number of melt days at each core site ($p < 0.01$, $r = 0.95$ for $df = 4$).

Reliable ice-core chemistry records have been recovered from ice cores with annual ice fractions of close to 0.8 (Moore and others, 2005). The mean annual ice fraction in the five cores increased between the 1963–88 period (0.33 ± 0.24) and the post-1989 (0.51 ± 0.30) period (Table 3; Fig. 8). Significantly greater ($p < 0.05$; two-tailed t test assuming equal variance) $\delta^{18}\text{O}$ values in core C during the 1989–2003 period ($-27.5 \pm 2.2\text{‰}$), in comparison to the 1963–88 period ($-28.8 \pm 2.1\text{‰}$), indicate warmer atmospheric temperatures in the later period that could account for the increase in annual ice fraction. However, the mean annual net accumulation rate also decreased between the 1963–88 period ($0.24 \pm 0.07 \text{ m w.e. a}^{-1}$) and the post-1989 ($0.18 \pm 0.05 \text{ m w.e. a}^{-1}$) period, and this would also affect the annual ice fraction. The mean annual ice fraction of the earlier period corresponds to a mean annual ice thickness of $\sim 0.08 \text{ m w.e.}$ ($0.33 \times 0.24 \text{ m w.e.}$), while the mean annual ice thickness during the more recent period was $\sim 0.09 \text{ m w.e.}$ ($0.51 \times 0.18 \text{ m w.e.}$). Therefore, the amount of ice contained within the annual layers did increase (by $\sim 11\%$) between the two periods, confirming that melt was probably more intense during the post-1989 period.

A homogenization of the anion chemistry, as evidenced by a decrease in the variability (standard deviation) of anion concentration measurements between the 1963–88 period and the 1989–2003 period, also suggests increased meltwater percolation during the recent period (Fig. 3; Moore and others, 2005). The mean variability in the five records decreased by 18% for MSA (from ± 0.020 to $\pm 0.016 \mu\text{Eq L}^{-1}$), 6% for Cl^- (from ± 1.89 to $\pm 1.78 \mu\text{Eq L}^{-1}$) and 38% for SO_4^{2-} (from ± 2.45 to $\pm 1.54 \mu\text{Eq L}^{-1}$) between these two periods (Table 3). Although meltwater percolation has apparently increased over time, with annual percolation probably reaching greater depths in the recent period, it has failed to fully homogenize the annual layers (Fig. 3).

Although all five cores demonstrated an increase in annual ice fraction between the 1963–88 and 1989–2003 periods, the increase was only significant ($p < 0.05$) in cores C, D and E, according to two-tailed t tests assuming

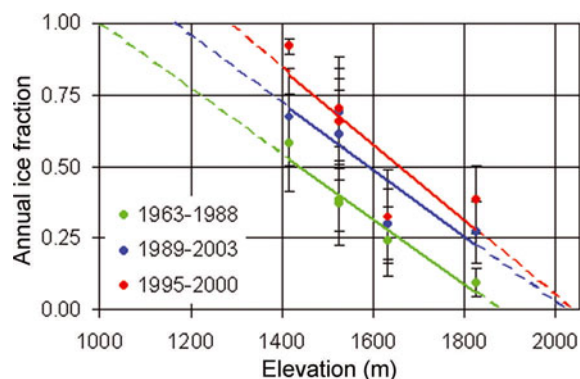


Fig. 8. The annual ice fraction–elevation relationships for the five shallow firn cores during the 1963–88, 1989–2003 and 1995–2000 periods. Vertical bars represent a half standard deviation in the annual ice fraction. The lower elevation limit of the dry snow zone (ice fraction = 0) and upper elevation limit of the superimposed ice zone (ice fraction = 1) can be approximated through extrapolation of regressions.

two samples with equal variance. Extrapolation of annual ice fraction–elevation relationships for the five core sites suggests that the upper limit of the superimposed ice zone (the lower limit of the wet snow zone), defined by a mean annual ice fraction of 1, was found at $\sim 1000 \text{ m}$ elevation during the 1963–88 period and 1160 m during the 1989–2003 period (Fig. 8). Likewise, the upper limit of the percolation zone (the lower limit of the dry snow zone), defined by a mean annual ice fraction of 0, was found at $\sim 1880 \text{ m}$ elevation during the 1963–88 period and 2025 m during the 1989–2003 period, well above the 1930 m summit of Devon Ice Cap (Fig. 8).

The reconstructed net accumulation record exhibits decreased variability during the post-1989 period of poorer correlation with the measured record, in comparison to the 1963–88 period of better correlation (Fig. 7). This decrease in variability can be quantified by examining the change in the standard deviation of the net accumulation record of each core. The change ranged from 0 m w.e. in core C (the highest-elevation core) to -0.05 m w.e. (23% of the mean annual net accumulation) in core A (the lowest-elevation core; Table 3). If we assume no change in the interannual variability of snowfall between the two periods, this change in standard deviation provides a measure of the change in the redistribution of mass between annual layers by percolating meltwater between the two periods. The change in the standard deviation of net accumulation was calculated as a percentage of the 1963–2003 mean net accumulation rate for each core, and used as an estimate of the uncertainty in net accumulation due to mass transfer between annual layers by meltwater percolation ($\sigma[\text{c}_p]$) in section 2.3 above (A: $\pm 0.05 \text{ m w.e.}$ (23%); B: $\pm 0.02 \text{ m w.e.}$ (9%); C: $\pm 0.00 \text{ m w.e.}$ (0%); D: $\pm 0.03 \text{ m w.e.}$ (18%); and E: $\pm 0.01 \text{ m w.e.}$ (4%) (Table 3)).

3.3. Site-specific low-elevation atmospheric transport density

Variations in atmospheric transport pathways to the ice cap can result in variations in both firn chemistry and accumulation. Maps of seasonal (JASO, MAMJ and NDJF) site-specific low-elevation atmospheric transport densities provide a clear picture of the relative frequency with which

Table 3. Comparisons between 1963–88 (in parentheses) and 1989–2003: mean annual net accumulation (c ; \pm std dev.), mean annual ice fraction (\pm std dev.) and the mean MSA, Cl^- and SO_4^{2-} concentrations of all samples (\pm std dev.) during both periods

	Core A	Core B	Core C	Core D	Core E	Mean
c (m.w.e. a^{-1})	0.19 ± 0.05 (0.24 ± 0.10)	0.17 ± 0.04 (0.25 ± 0.06)	0.21 ± 0.05 (0.26 ± 0.05)	0.14 ± 0.03 (0.19 ± 0.06)	0.20 ± 0.06 (0.25 ± 0.07)	0.18 ± 0.05 (0.24 ± 0.07)
Ice fraction	0.67 ± 0.34 (0.58 ± 0.34)	0.30 ± 0.25 (0.24 ± 0.24)	0.27 ± 0.21 (0.09 ± 0.10)	0.69 ± 0.39 (0.37 ± 0.29)	0.61 ± 0.31 (0.38 ± 0.22)	0.51 ± 0.30 (0.33 ± 0.24)
[MSA] ($\mu\text{Eq L}^{-1}$)	0.005 ± 0.011 (0.009 ± 0.019)	0.014 ± 0.025 (0.011 ± 0.019)	0.009 ± 0.015 (0.013 ± 0.022)	0.011 ± 0.019 (0.022 ± 0.021)	0.005 ± 0.011 (0.010 ± 0.018)	0.009 ± 0.016 (0.013 ± 0.020)
$[\text{Cl}^-]$ ($\mu\text{Eq L}^{-1}$)	2.26 ± 1.59 (3.01 ± 1.73)	1.81 ± 1.40 (1.79 ± 1.42)	2.47 ± 1.38 (3.65 ± 2.30)	3.25 ± 2.96 (2.58 ± 1.94)	1.81 ± 1.59 (2.23 ± 2.07)	2.32 ± 1.78 (2.65 ± 1.89)
$[\text{SO}_4^{2-}]$ ($\mu\text{Eq L}^{-1}$)	1.51 ± 1.15 (3.61 ± 2.44)	2.03 ± 1.60 (3.78 ± 3.02)	2.32 ± 1.75 (3.38 ± 2.31)	1.50 ± 1.39 (2.41 ± 2.01)	1.48 ± 1.82 (2.88 ± 2.45)	1.77 ± 1.54 (3.21 ± 2.45)

air masses arriving at the summit of Devon Ice Cap cross different regions of the Arctic at elevations below 500 m (Fig. 4). Site-specific low-elevation atmospheric transport density patterns are similar for all three seasons. Transport density is an inverse function of distance from the back-trajectory termination point, and values reach a maximum in all seasons where back-trajectories converge on the common G814 termination cell of Devon Ice Cap. Values of seasonal site-specific low-elevation atmospheric transport density range over three orders of magnitude across the Arctic. In all seasons, northern Baffin Bay and the Queen Elizabeth Islands (QEI) appear to be the primary regions crossed by low-elevation air masses en route to Devon Ice Cap, while southern Baffin Bay, the western Arctic Ocean and Foxe Basin/northern Hudson Bay are crossed less often. The Atlantic Ocean east of Greenland and the Eurasian portion of the Arctic Ocean are not traversed frequently in any season (Fig. 4). Either Greenland acts as an effective block to low-elevation air-mass transport from Europe and the east (Kahl and others, 1997), or the 120 hour back-trajectories are too short to capture transport paths from Eurasia.

3.4. Regional sea-ice fraction

During the NDJF season, high sea-ice fractions (low open-water fractions) occur throughout the Canadian Arctic Archipelago and Baffin Bay (Fig. 5). During the MAMJ season, as the polar pack margin migrates northward, the sea-ice fraction begins to decrease in both Hudson and Baffin Bays, along the Eurasian shelves and in the North Open Water (NOW) Polynya (Fig. 5). During the JASO season, Baffin Bay has a low sea-ice (high open-water) fraction, and sea-ice fractions also reach a minimum along the Eurasian shelves, in the coastal zone of the Beaufort Sea, throughout the QEI and in Hudson Bay (Fig. 5).

3.5. Moisture-source probabilities

The coupling of site-specific low-elevation atmospheric transport densities with the observed regional open-water fraction record allows investigation of temporal and spatial variations in the relative probability that a given G4640 cell acts as a moisture source for Devon Ice Cap in a given season. Primary moisture-source areas were defined as regions where $P_{\text{sy}} \geq 0.01$ (blue in Fig. 6), while secondary moisture-source areas were defined as regions where $0.001 < P_{\text{sy}} \leq 0.01$ (orange in Fig. 6). During the NDJF season, no primary moisture-source areas are found within

5 days transit time of Devon Ice Cap, as relative moisture-source probabilities drop to near zero in most G4640 cells. Only localized bands of secondary moisture-source areas are inferred along the Greenland coast and in the NOW region (Fig. 6). During the MAMJ season, a primary moisture-source area is inferred in the NOW region, and the remainder of Baffin Bay is inferred to be a secondary moisture source (Fig. 6). During the JASO season, the main accumulation season on Devon Ice Cap (Koerner, 2002), the northern half of Baffin Bay is inferred to be a primary moisture-source area, while the southern half of Baffin Bay, the Labrador Sea, the QEI, the southeast Beaufort Sea and Foxe Basin/northern Hudson Bay are inferred to be secondary moisture-source regions (Fig. 6). Relative moisture-source probabilities surpass 0.04 in northern Baffin Bay in JASO, which represents one air mass passing within 500 m of open water en route to the summit of Devon Ice Cap every 25 hours, or almost daily, for the entire season in this region. These findings are consistent with the observation that most accumulation on Devon Ice Cap occurs during the JASO season, with the least accumulation during the NDJF season, and intermediate accumulation during the MAMJ season (Koerner, 2002).

A comparison of the JASO relative moisture-source probabilities during the 4 year periods of highest (1984–87) and lowest (1994–97) net accumulation shows significantly higher ($p < 0.05$; t test) relative moisture-source probabilities during the high net accumulation period in the region of the NOW Polynya (Fig. 9). The magnitude of this increase ($\Delta P_{\text{sy}} > 0.01$) is $\sim 25\%$ of the mean 1979–2003 JASO season P_{sy} value in the NOW region ($P_{\text{sy}} \approx 0.04$; Fig. 6). There is also a significant decrease ($p < 0.05$; t test) in relative moisture-source probabilities in the Beaufort Sea and the QEI, and a significant increase ($p < 0.05$; t test) in Ungava Bay during the high net accumulation period (Fig. 9).

The significant increase in relative moisture-source probabilities in the NOW region appears to be caused by both a significant decrease ($p < 0.05$; t test) in sea-ice fraction and a significant increase ($p < 0.05$; t test) in site-specific low-elevation atmospheric transport density (Fig. 9). Barber and others (2001) found that the deepening of a Greenland low-pressure trough, due to an east–west temperature gradient across the NOW region and Baffin Bay, enhances northerly winds across the NOW region, which results in a cyclonic gyre in northern Baffin Bay and the formation of an ice bridge across Nares Strait that leads to the opening of the NOW Polynya. This link between

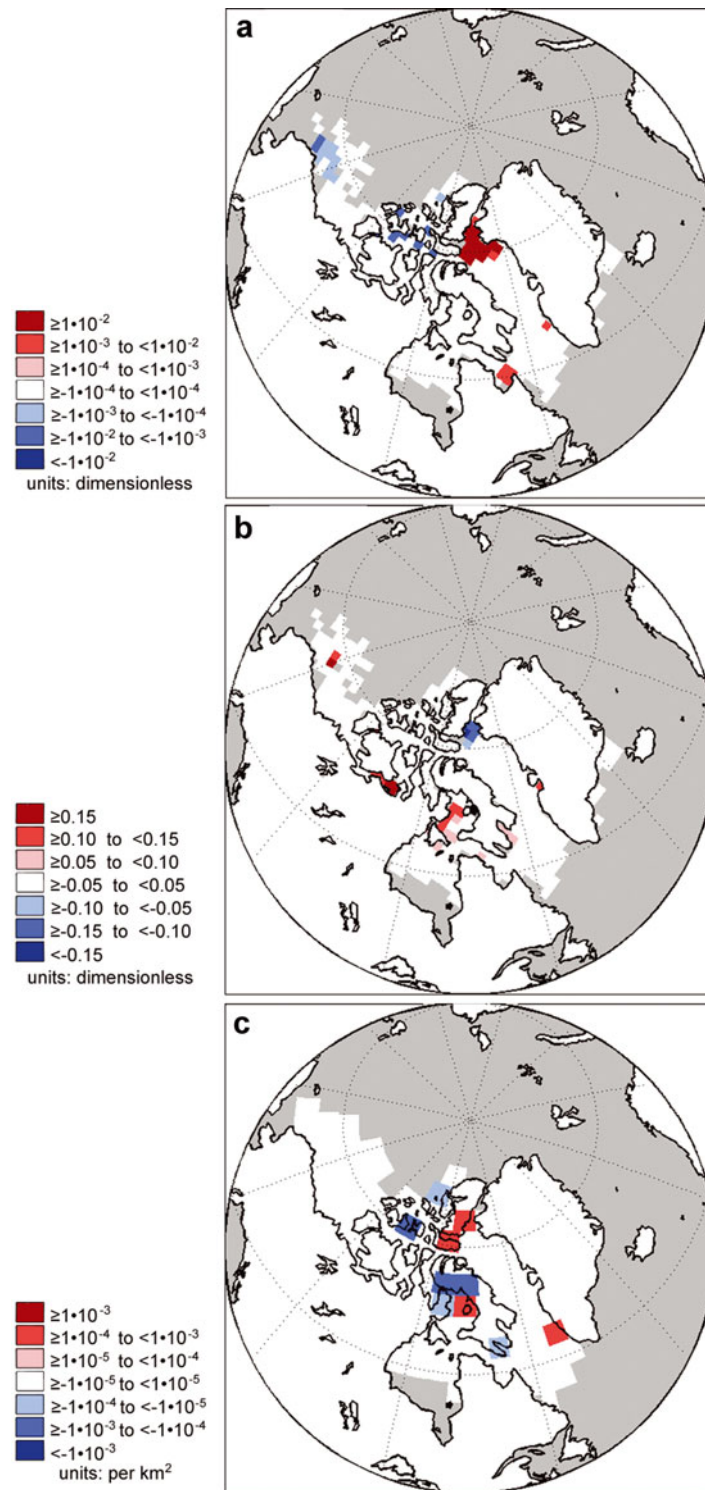


Fig. 9. Significant differences ($p < 0.05$; t test) in JASO relative moisture-source probabilities (P_{sy}) (a), sea-ice fraction (S_{sy}) (b) and site-specific low-elevation atmospheric transport density (D_{sxi} ; km^{-2}) (c) between high (1984–87) and low net accumulation (1994–97) periods. Red indicates significantly higher values during the high net accumulation period. Grey areas indicate regions with $P_{my} < 0.001$ throughout the year.

atmospheric circulation and sea-ice motion, extent and concentration could therefore account for the history of moisture-source probabilities in the NOW region.

The significant decrease in relative moisture-source probabilities in the Beaufort Sea during the high net accumulation period may be due to a small area of significantly increased ($p < 0.05$; t test) sea-ice fraction, as there is no significant change ($p > 0.05$; t test) in site-specific

low-elevation atmospheric transport density in this region (Fig. 9). The significant decrease in relative moisture-source probabilities in the QEI during the high net accumulation period is probably due to a significant decrease ($p < 0.05$; t test) in site-specific low-elevation atmospheric transport density from this region, as there is no significant change ($p > 0.05$; t test) in the sea-ice fraction within the QEI between the high and low net accumulation periods.

4. DISCUSSION: HIGH-ELEVATION THICKENING

Airborne laser altimetry measurements, conducted in 1995 and 2000, suggested that the high-elevation region of Devon Ice Cap thickened at a rate of up to 20 cm a^{-1} , while the low-elevation region thinned at a rate of up to 40 cm a^{-1} (Abdalati and others, 2004). Although Abdalati and others (2004) suggested that these observations can be explained by anomalously high accumulation throughout the Arctic during the observation period (1995–2000), compared to the 52 year mean from three weather stations in the Canadian Arctic (Iqaluit, Clyde River and Eureka), our reconstructed record clearly demonstrates anomalously low mean annual net accumulation during this period ($0.18 \pm 0.01 \text{ m.w.e. a}^{-1}$) in comparison to the mean annual net accumulation for the entire 1963–2003 period ($0.22 \pm 0.04 \text{ m.w.e. a}^{-1}$). This finding is supported by the measured mass-balance record from the high-elevation region (1250–1750 m) of the northwest sector of the ice cap (Fig. 7), as well as by the measured mean mass balance at all elevations (0–1750 m), which was anomalously low during the 1995–2000 period ($-0.43 \pm 0.17 \text{ m.w.e.}$) in comparison to the 1961–2003 mean ($-0.31 \pm 0.17 \text{ m.w.e.}$; cf. fig. 2 in Koerner, 2005). This decrease in annual net accumulation during the 1995–2000 period, relative to the ~ 40 year mean, would be expected to result in surface lowering or ice-cap thinning, rather than the thickening observed by altimetry.

Changes in the rate of firnification, which may be indicated by changes in the annual ice fraction, also influence the relative elevation of an ice-cap surface. The reconstructed annual ice fraction record of Devon Ice Cap suggests that the mean annual ice fraction of the five cores was higher during the post-1989 period (0.51 ± 0.30) than during 1963–88 period (0.33 ± 0.24). The mean annual ice fraction during the 1995–2000 laser altimetry survey period was even higher (0.60 ± 0.24 ; Fig. 8). Trends of increasing annual ice fraction, over the last 70–130 years, have been recognized on ice caps throughout the Arctic, and are interpreted as evidence of climate change (Dowdeswell, 1995). Given the firn-core evidence presented above for increased air temperatures, meltwater percolation and annual ice fractions after 1989, it seems certain that the rate of firnification was higher during the 1989–2003 period than during the 1963–1988 period. An increase in the rate of firnification would be expected to result in overall surface lowering, especially when accompanied by a decrease in net accumulation. Given this conclusion, a reduction in ice outflow from the high-elevation region of the ice cap may be a more plausible explanation of the thickening of the high-elevation parts of the ice cap between 1995 and 2000 than a change in surface mass balance.

A fuller discussion of the apparent inconsistency between the laser altimetry observations and current surface mass-balance trends will be presented elsewhere. One possible explanation of a reduction in outflow from the high-elevation regions of the ice cap is that neoglaciation cooling has only recently reached the bed of Devon Ice Cap and begun to stiffen the basal ice, resulting in reduced internal deformation and outflow velocities.

5. CONCLUSIONS

A reconstructed annual net accumulation record for the period 1963–2003 was derived from five shallow firn cores

recovered from the high-elevation region of Devon Ice Cap. The stacked mean annual net accumulation was significantly lower during the 1989–2003 period than in the 1963–88 period. Conversely, the mean annual ice fraction in the five cores was higher (significantly higher in three cores) during the post-1989 period than in the 1963–88 period. There appears to be a good correlation between the reconstructed mean net accumulation record and the observed northwest sector high-elevation surface mass-balance record.

Relative moisture-source probabilities reach a maximum in northern Baffin Bay in JASO, and a minimum throughout the Arctic in NDJF. A comparison of the JASO relative moisture-source probabilities during the 4 year periods of highest (1984–87) and lowest (1994–97) annual net accumulation shows significantly higher relative moisture-source probabilities during the high annual net accumulation period in the NOW Polynya region. These elevated moisture-source probabilities appear to be the result of both a significant increase in low-elevation atmospheric transport density and a significant decrease in sea-ice fraction.

The firn-core records indicate that the rate of annual net accumulation was lower, and the rate of firnification (indicated by the water equivalent ice thickness within annual layers) was higher than the 1963–2003 mean during the laser altimetry survey period (1995–2000). We therefore suggest that a change in ice dynamics, such as a decrease in ice outflow from the accumulation zone of the ice cap (possibly related to the penetration of the neoglaciation cold wave to the bed of the ice cap), may be responsible for the observed high-elevation thickening of Devon Ice Cap during this period, rather than a change in surface mass balance.

ACKNOWLEDGEMENTS

We thank the Polar Continental Shelf Project (PCSP contribution No. 029-07), the Natural Sciences and Engineering Research Council of Canada, the ArcticNet Network of Centres of Excellence, the Canadian Foundation for Innovation, the Canadian Circumpolar Institute, the Northern Scientific Training Program, the Alberta Science and Research Investment Program and the Alberta Ingenuity Fund for financial and logistical support. We also thank the Nunavut Research Institute and the communities of Resolute Bay and Grise Fjord for permission to conduct fieldwork. H. Bigelow, L. Hyrciw, L. Nicholson, J. Barker and N. Atkinson provided assistance in the laboratory, and J. Davis, D. Burgess, F. Cawkwell, C. Bell and S. Williamson assisted with the fieldwork.

REFERENCES

- Abdalati, W. and 9 others. 2004. Elevation changes of ice caps in the Canadian Arctic Archipelago. *J. Geophys. Res.*, **109**(F4), F04007. (10.1029/2003JF000045.)
- Barber, D.G., J.M. Hanesiak, W. Chan and J. Piwowar. 2001. Sea-ice and meteorological conditions in northern Baffin Bay and the North Water polynya between 1979 and 1996. *Atmos.–Ocean*, **39**(3), 343–359.
- Burgess, D.O. and M.J. Sharp. 2004. Recent changes in areal extent of Devon ice cap, Nunavut, Canada. *Arct. Antarct. Alp. Res.*, **36**(2), 261–271.
- Cazenave, A. and R.S. Nerem. 2004. Present-day sea level change: observations and causes. *Rev. Geophys.*, **42**(3), RG3001. (10.1029/2003RG000139.)

- Dowdeswell, J.A. 1995. Glaciers in the High Arctic and recent environmental change. *Philos. Trans. R. Soc. London, Ser. A*, **352**(1699), 321–334.
- Dowdeswell, J.A., T.J. Benham, M.R. Gorman, D. Burgess and M. Sharp. 2004. Form and flow of Devon Island ice cap, Canadian Arctic. *J. Geophys. Res.*, **109**(F2), F02002. (10.1029/2003JF000095.)
- Dunphy, P.P. and J.E. Dibb. 1994. ^{137}Cs gamma-ray detection at Summit, Greenland. *J. Glaciol.*, **40**(134), 87–92.
- Dyrugerov, M.B. and Meier, M.F. 2005. *Glaciers and the changing Earth system: a 2004 snapshot*. Boulder, CO, University of Colorado. Institute of Arctic and Alpine Research. (INSTAAR Occasional Paper 58).
- Fleming, S.W. and G.K.C. Clarke. 2002. Autoregressive noise, deserialization, and trend detection and quantification in annual river discharge time series. *Can. Water Res. J.*, **27**(3), 335–354.
- Gjessing, Y., I. Hanssen-Bauer, Y. Fujii, T. Kameda, K. Kamiyama and T. Kawamura. 1993. Chemical fractionation in sea ice and glacier ice. *Bull. Glacier Res.*, **11**, 1–8.
- Kahl, J.D.W., D.A. Martinez, H. Kuhns, C.I. Davidson, J.L. Jaffrezo and J.M. Harris. 1997. Air mass trajectories to Summit, Greenland: a 44-year climatology and some episodic events. *J. Geophys. Res.*, **102**(C12), 26,861–26,875.
- Kalnay, E. and 21 others. 1996. The NCEP/NCAR 40-year reanalysis project. *Bull. Am. Meteorol. Soc.*, **77**(3), 437–471.
- Koerner, R.M. 1970. The mass balance of the Devon Island ice cap, Northwest Territories, Canada, 1961–66. *J. Glaciol.*, **9**(57), 325–336.
- Koerner, R.M. 2002. Glaciers of the High Arctic islands. In Williams, R.S. and J.G. Ferrigno, eds. *Satellite image atlas of glaciers of the world*. *US Geol. Surv. Prof. Pap.* 1386-J, J111–J146.
- Koerner, R.M. 2005. Mass balance of glaciers in the Queen Elizabeth Islands, Nunavut, Canada. *Ann. Glaciol.*, **42**, 417–423.
- Moore, J.C., A. Grinsted, T. Kekonen and V. Pohjola. 2005. Separation of melting and environmental signals in an ice core with seasonal melt. *Geophys. Res. Lett.*, **32**(10), L10501. (10.1029/2005GL023039.)
- Moore, J.C., T. Kekonen, A. Grinsted and E. Isaksson. 2006. Sulfate source inventories from a Svalbard ice-core record spanning the Industrial Revolution. *J. Geophys. Res.*, **111**(D15), D15307. (10.1029/2005JD006453.)
- Pohjola, V.A. and 6 others. 2002. Reconstruction of three centuries of annual accumulation rates based on the record of stable isotopes of water from Lomonosovfonna, Svalbard. *Ann. Glaciol.*, **35**, 57–62.
- Reijmer, C.H., M.R. van den Broeke and M.P. Scheele. 2002. Air parcel trajectories and snowfall related to five deep drilling locations on Antarctica based on the ERA-15 dataset. *J. Climate*, **15**(14), 1957–1968.
- Serreze, M. and R.G. Barry. 2005. *The Arctic climate system*. Cambridge, etc., Cambridge University Press. (Cambridge Atmospheric and Space Science Series.)
- Toom-Sauntry, D. and L.A. Barrie. 2002. Chemical composition of snowfall in the high Arctic: 1990–1994. *Atmos. Environ.*, **36**(15–16), 2683–2693.
- Walsh, J. E. 1978. A data set on Northern Hemisphere sea ice extent, 1953–76. *Glaciol. Data, World Data Center A for Glaciol. <Snow and Ice>*, Boulder, **GD-2**, part 2, 49–51.
- Wang, L., M.J. Sharp, B. Rivard, S. Marshall and D. Burgess. 2005. Melt season duration on Canadian Arctic ice caps, 2000–2004. *Geophys. Res. Lett.*, **32**(19), L19502. (10.1029/2005GL023962.)
- Zeng, J., M. Katsumoto, R. Ide, M. Inagaki, H. Mukai and Y. Fujinuma. 2003. Development of meteorological data explorer for Windows. In Fujinuma, Y., ed. *Data analysis and graphic display system for atmospheric research using PC*. Tsukuba, Ibaraki, National Institute for Environmental Studies. Center for Global Environmental Research, 19–73. (CGER-M012–2003.)

MS received 7 May 2007 and accepted in revised form 2 September 2007

Is the high-elevation region of Devon Ice Cap thickening?

William COLGAN,^{1,2} James DAVIS,¹ Martin SHARP¹

¹Arctic and Alpine Research Group, Department of Earth and Atmospheric Sciences, University of Alberta, Edmonton, Alberta T6G 2E3, Canada

E-mail: william.colgan@colorado.edu

²Cooperative Institute for Research in Environmental Sciences, UCB 216, University of Colorado, Boulder, Colorado, 80309-0216, USA

ABSTRACT. Devon Ice Cap, Nunavut, Canada, has been losing mass since at least 1960. Laser-altimetry surveys, however, suggest that the high-elevation region (>1200 m) of the ice cap thickened between 1995 and 2000, perhaps because of anomalously high accumulation rates during this period. We derive an independent estimate of thickness change in this region by comparing ~40 year mean annual net accumulation rates to mean specific outflow rates for 11 drainage basins. The area-averaged rate of thickness change across the whole region is within error of zero ($0.01 \pm 0.12 \text{ m.w.e. a}^{-1}$), but two drainage basins in the northwest are thickening significantly, and two basins in the south are thinning significantly. The laser-altimetry observations are biased towards the drainage basins where we find thickening. Recent changes in the rate of accumulation or the rate of firnification cannot explain the observed thickening, but decreased ice outflow, due to the penetration of Neoglacial cooling to, and subsequent stiffening of, the basal ice, may provide an explanation. Thinning in the south may result from increased ice outflow from basins in which fast flow and basal sliding extend above 1200 m.

NOTATION

A_B	Area of a given drainage basin (m^2)
a_c	Measured annual net accumulation (m.w.e. a^{-1})
A_G	Cross-sectional area of a given flux gate (m^2)
a_m	MLR (multiple linear regression) interpolated annual net accumulation (m.w.e. a^{-1})
d_G	Width across a given flux gate (m)
dh/dt	Change in surface elevation (m.w.e. a^{-1})
dh_A/dt	Change in surface elevation due to net accumulation (m.w.e. a^{-1})
dh_O/dt	Change in surface elevation due to specific outflow (m.w.e. a^{-1})
\bar{h}_G	Mean ice thickness across a given flux gate (m)
n	Glen's flow-law parameter
u_G	Horizontally averaged surface velocity perpendicular through a given gate (m a^{-1})
\bar{u}_G	Width- and depth-averaged velocity profile through a given flux gate (m a^{-1})
V_B	Volumetric outflow of ice from a given basin ($\text{m}^3 \text{ a}^{-1}$)
Y	UTM northing (m)
Z	Elevation (m)
β	Angle between the ice flow and satellite-look directions ($^\circ$)
ρ_i	Density of ice (kg m^{-3})
ρ_w	Density of water (kg m^{-3})
$\sigma[x]$	Uncertainty in parameter x (units of x)

INTRODUCTION

The net transfer of land-based ice into the oceans is the second greatest contributor to contemporary sea-level rise after the thermal expansion of ocean water (Braithwaite and Raper, 2002; Raper and Braithwaite, 2006). Between 2001 and 2004, ice caps and alpine glaciers outside Greenland and Antarctica contributed $\sim 0.77 \pm 0.15 \text{ mm a}^{-1}$ to sea-level rise, although the contribution of calving glaciers to this estimate may well be underestimated (Kaser and others, 2006; Meier and others, 2007). The Canadian Arctic Archipelago contains the largest glaciated area in the world outside Greenland and Antarctica (Dyurgerov and Meier, 2005). Although the potential sea-level rise contribution from these ice caps is far less than that from Greenland or Antarctica, their more temperate environs and shorter response times make them potentially more reactive to changes in climate (Raper and Braithwaite, 2006).

Although recent estimates of the current sea-level rise contribution of Devon Ice Cap, Nunavut, Canada (75°N , 82°W ; Fig. 1) range over an order of magnitude, from 0.003 mm a^{-1} (Shepherd and others, 2007) to 0.036 or 0.046 mm a^{-1} (Abdalati and others, 2004; Burgess and Sharp, 2004), they agree that Devon Ice Cap is a net contributor to sea-level rise. Laser-altimetry surveys in 1995 and 2000 suggested that the high-elevation region (>1200 m) of the ice cap was thickening by up to 0.20 m a^{-1} , while the low-elevation region (<1200 m) was thinning by up to 0.40 m a^{-1} (Abdalati and others, 2004). These trends were, however, derived from relatively limited altimetry measurements along two flight-lines that intersect in the western part of the ice cap (Fig. 1; Abdalati and others, 2004). There is therefore a question whether the changes detected by altimetry are representative of the entire ice cap.

On the basis of meteorological records from weather stations at Iqaluit, Clyde River and Eureka, thickening of the high-elevation region was originally attributed to anomalously high snowfall during the 1995–2000 period (Abdalati

and others, 2004). However, both in situ measurements of surface mass balance (Koerner, 2005) and reconstructions of net annual snow accumulation on the ice cap derived from shallow firn cores (Colgan and Sharp, 2008) show that the annual net accumulation rate at high elevations on the ice cap, during the 1995–2000 period, was anomalously low in comparison to the 1963–2003 mean. A number of factors may explain this apparent discrepancy. First, net accumulation, which is measured by mass-balance programs and deduced from ice-core measurements, is different from snowfall, in that melt-induced runoff can potentially remove a fraction of the annual accumulation from any site on the ice cap. Therefore, these two types of records are not strictly comparable. Second, problems with measuring snowfall in polar regions, where precipitation totals are low, trace falls are common and wind redistribution of snow is frequent, are well known (Woo and others, 1983). Finally, station records of snowfall are typically derived from coastal sites that are often remote from the ice-cap locations in which we are interested.

An alternative explanation of the thickening would be that the rate of firnification on the ice cap was unusually low during the 1995–2000 period, resulting in a reduction in the density of the near-surface snow and firn. However, the ice content of firn deposited in 1995–2000 is anomalously high relative to the 1963–2003 mean, which suggests that the observed thickening is unlikely to reflect anomalously low rates of firn compaction during that period (Colgan and Sharp, 2008). Thus, if the observed thickening is real, its cause may lie in a recent change in the dynamics of the ice cap.

Mean annual rates of ice-thickness change can be estimated by comparing mean annual net accumulation rates to mean specific outflow rates for individual drainage basins (cf. Thomas and others, 1998, 2000). Comparison of these measurements (which have units $\text{kg m}^{-2} \text{a}^{-1}$) with laser-altimetry measurements (m a^{-1}) requires conversion of accumulation rates to thickness changes using an assumed density for the material added to or removed from the ice column. In this study, estimates of rates of thickness change in the high-elevation region of Devon Ice Cap were derived using in situ measurements of annual surface velocity for 11 flux gates aligned along the 1200 m contour. For four of these basins, we compared these estimates with estimates derived using shorter-term, but spatially denser, measurements of surface velocity derived using interferometric synthetic aperture radar (InSAR).

METHODS

Surface velocities

The specific ice outflow through each flux gate was calculated using measurements of ice thickness (Dowdeswell and others, 2004) and ice surface velocities. Seventeen 4 m wooden stakes were installed along the 1200 m contour of the ice cap in April 2005 and re-surveyed in April 2006. Stake locations were determined with Leica Geosystems series 500 dual-frequency global positioning system (GPS) instruments using static differential methods. Multiple base station locations were used to ensure a maximum distance of 25 km between the base station and stake positions during each survey. Data were processed in Leica Geo Office (version 1.0) and achieved phase position solutions accurate

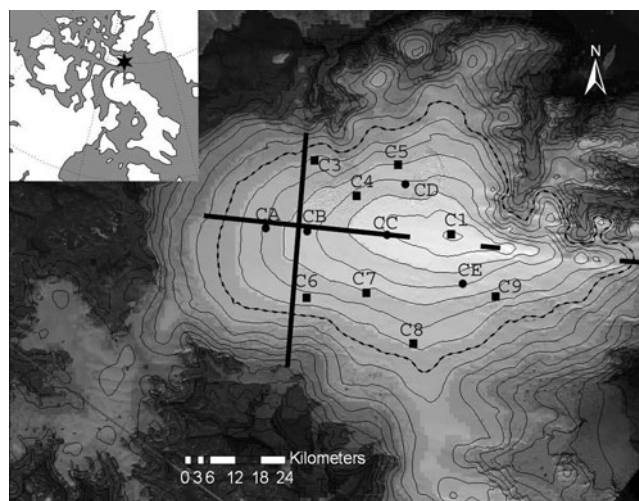


Fig. 1. Devon Ice Cap, in the Canadian High Arctic (inset), shown in an orthorectified mosaic of Landsat 7 images acquired in July and August 1999, overlaid with a 1 km digital elevation model (DEM) based on the measurements of Dowdeswell and others (2004). Contour spacing is 100 m, with the 1200 m contour highlighted. The locations of the shallow firn cores (Mair and others, 2005: squares; Colgan and Sharp, 2008: circles) and the approximate NASA altimetry flight-lines are shown (Abdalati and others, 2004).

to better than ± 0.5 cm in the horizontal (x, y) and ± 2.0 cm in the vertical (z). At each survey point, the GPS antenna was mounted on top of the stake, and the vertical dimension of the GPS position was corrected to a base-of-stake position to within ± 2 cm. For stakes that did not tilt between surveys, the total positional error (the combination of position and manual measurement errors over the two seasons) was estimated to be ± 2.5 cm in the x , y and z directions. For stakes 6 and 17, which became tilted between surveys (10° and 20° , respectively), the GPS antenna was mounted on a survey tripod centred over the point where the stake protruded from the snow surface, and trigonometry was used to estimate the base-of-stake position. For these two stakes, the total positional error was estimated as 25% of the trigonometrically corrected horizontal distance in the x and y directions (± 8.8 and 2.8 cm, respectively) and 10% of the trigonometrically corrected vertical distance in the z direction (± 6.2 and 9.6 cm, respectively). The azimuth and magnitude of annual horizontal stake velocities were computed from the difference in stake positions and the time elapsed between surveys.

Six stakes were lost between 2005 and 2006, which forced a redefinition of the flux gates and resulted in flux gates of unequal width. To compensate for the paucity of repeat GPS measurements in the east of the study region, one 'dummy' velocity (derived by InSAR using winter–spring 1996 European Remote-sensing Satellite (ERS-1/2) imagery; Burgess and others, 2005) was included with the ten measured stake velocities (Fig. 2).

Shepherd and others (2007) calculated the specific mass balance of Devon Ice Cap using an approach similar to that adopted here, but they used velocity measurements derived by InSAR rather than stake-derived velocities to compute ice fluxes. Although these InSAR measurements have high spatial resolution, and can identify narrow bands of faster flow within flux gates, they relate to relatively short periods of time (~ 30 days) and may not provide reliable estimates of

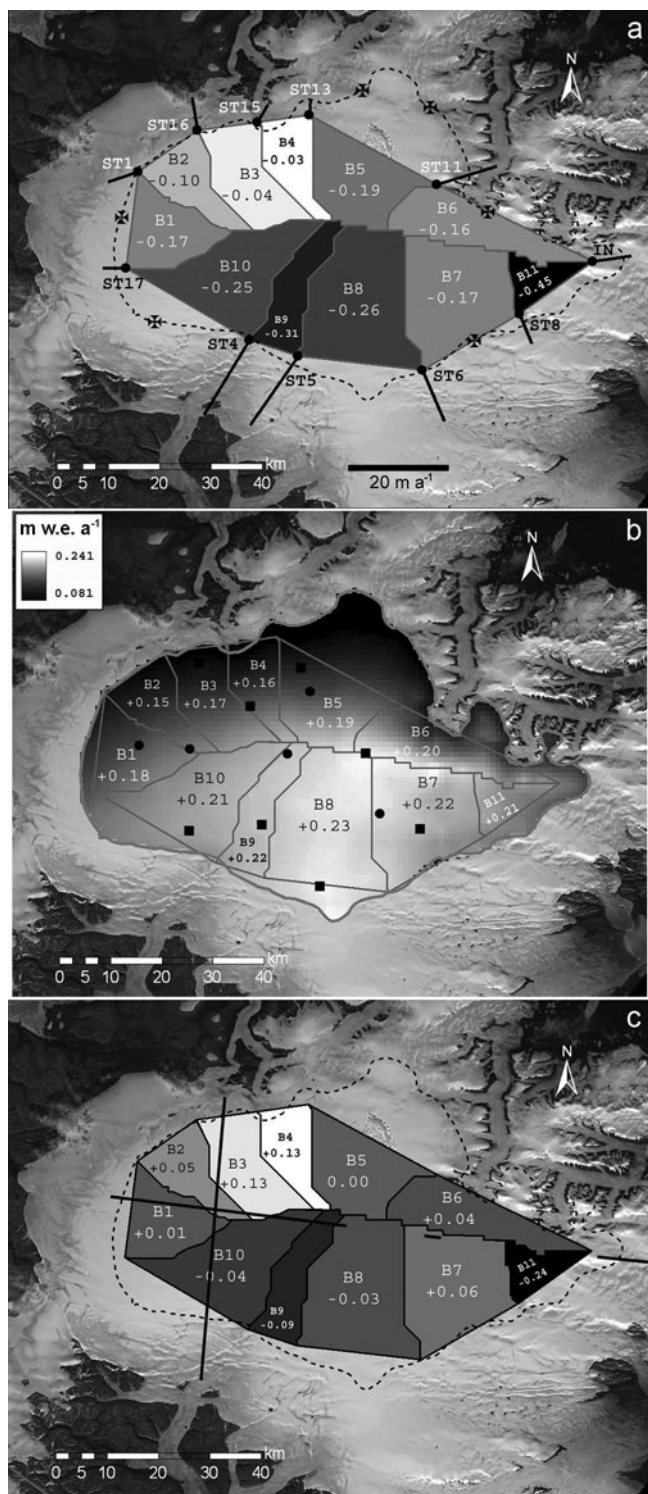


Fig. 2. (a) The mean annual rate of specific outflow (dh_O/dt ($m.w.e.a^{-1}$)). The ten stakes (ST) and one InSAR-derived velocity point (IN) are shown with velocity vectors. Stakes lost between surveys are shown with crosses. (b) The mean annual net accumulation rate (dh_A/dt ($m.w.e.a^{-1}$)), based on net accumulation rates at 13 core sites (Mair and others, 2005: squares; Colgan and Sharp, 2008: circles). (c) The mean annual rate of thickness change (dh/dt ($m.w.e.a^{-1}$)). The approximate locations of the NASA laser-altimetry flight-lines are also shown (Abdalati and others, 2004).

annual average velocities. They also lack true three-dimensional resolution, as only ascending orbit data are available, and they were produced by resolving the satellite-look direction velocities onto the calculated direction of

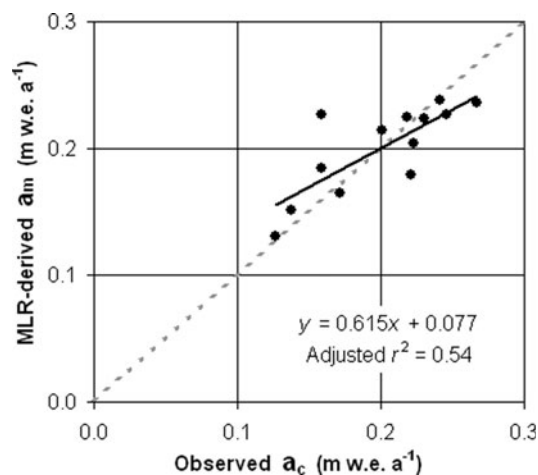


Fig. 3. MLR-derived annual net accumulation rate (a_m) versus observed mean annual net accumulation rate (a_c) at the 13 core sites (residuals: Table 2). Line $y = x$ is shown for reference (dashed).

steepest down-glacier slope. The uncertainty in these velocities increases with (1) increasing angle between the ice flow and satellite-look directions (β ($^\circ$)) and (2) decreasing surface slope. The limitations of these measurements therefore justify the use of stake-based measurements of true annual mean velocities as an alternative means of estimating rates of thickness change.

Drainage basin delineation

The ten velocity stakes and one dummy point were used to define 11 flux gates and the drainage basins that feed them. Stake 12 was not used for this purpose because of its proximity to stake 11. Drainage basins were delineated using a 1 km resolution digital elevation model (DEM) of the ice cap (Dowdeswell and others, 2004). The flow direction tool in ArcGIS 9.0 was used to compute the flow direction in each DEM cell, based on the DEM slope direction field. Once the flow direction in each DEM cell was known, the upslope source cell of each DEM cell could be identified. Flowlines leading to each stake were then extracted manually from the flow direction field (Le Brocq and others, 2006) by connecting successive upslope source cells from the stake back to the main drainage divide of the ice cap (Fig. 2). Flowlines leading from the stakes to the main drainage divide were used to define the drainage basin boundaries for each flux gate (Thomas and others, 1998).

Annual specific outflow

To calculate the mean annual specific outflow through a given flux gate, the horizontally averaged surface ice velocity perpendicular to the flux gate (u_G ($m.a^{-1}$)) was calculated as the mean of the perpendicular velocities at either end of the flux gate. The vertically averaged ice velocity through the flux gate (\bar{u}_G ($m.a^{-1}$)) was taken as 0.8 times the horizontally averaged surface velocity on the assumption that flow through each flux gate occurred primarily by ice deformation and that the value of the exponent, n , in Glen's flow law for ice = 3 (Reeh and Paterson, 1988; Paterson, 1994). Our error analysis uses a ± 0.5 range in n values to accommodate threads of fast flow, which influence small portions of some gates (cf. fig. 7 in Burgess and others, 2005), causing the n value across a given gate to vary from 3 (see Appendix). The annual

Table 1. The drainage basin area ($A_B \pm \sigma[A_B]$), flux gate width (d_G), flux gate mean ice thickness ($\bar{h}_G \pm \sigma[\bar{h}_G]$) and across-gate InSAR coverage for the 11 drainage basins

Drainage basin	$A_B \pm \sigma[A_B]$ 10^8 m^2	d_G m	$\bar{h}_G \pm \sigma[\bar{h}_G]$ m	InSAR %
1	2.1 ± 0.11	18 865	505 ± 10	82
2	1.7 ± 0.08	14 112	430 ± 10	7
3	2.4 ± 0.12	11 734	251 ± 10	35
4	1.5 ± 0.08	10 290	220 ± 10	12
5	2.8 ± 0.14	28 350	423 ± 10	40
6	2.6 ± 0.13	33 838	123 ± 10	93
7	4.1 ± 0.20	21 839	476 ± 10	5
8	4.8 ± 0.24	24 389	547 ± 10	60
9	1.8 ± 0.09	10 008	494 ± 10	100
10	3.7 ± 0.18	27 884	468 ± 10	85
11	0.9 ± 0.05	17 608	341 ± 10	37

volumetric outflow through each gate (V_B ($\text{m}^3 \text{a}^{-1}$)) was calculated by multiplying the vertically averaged ice velocity by the cross-sectional area of the gate (A_G (m^2)), which was determined from ice-thickness values interpolated at 1 km intervals across a given gate (Dowdeswell and others, 2004). To allow comparison with measurements of net accumulation rate in the basin draining through the flux gate, the volumetric outflow was converted into a rate of specific outflow, equivalent to a surface-elevation change in each basin (dh_O/dt (m w.e. a^{-1})) according to:

$$\frac{dh_O}{dt} = \left(\frac{V_B}{A_B} \right) \left(\frac{\rho_i}{\rho_w} \right), \quad (1)$$

where ρ_i is the density of ice, ρ_w is the density of water and A_B is the area of the drainage basin (m^2 ; Table 1). To allow for the presence of firn in each ice column, we assume an ice density (900 kg m^{-3}) less than that of pure ice (917 kg m^{-3}). By comparing the calculated annual specific outflow with measurements of mean annual net accumulation for 1963–2003 we implicitly assume no change in specific ice outflow over that period. We have no way of assessing the validity of this assumption.

Annual specific net accumulation

The mean annual change in surface elevation due to net accumulation over the 1963–2003 period (dh_A/dt (m w.e. a^{-1})) was determined for each drainage basin using mean annual net accumulation rates determined from 13 shallow firn cores (Mair and others, 2005; Colgan and Sharp, 2008; Table 2). The mean annual net accumulation rate at each core site was calculated by dividing the water equivalent depth of the 1963 ‘bomb’ layer by the number of years between 1963 and the year the core was recovered. The bomb layer is the result of fallout from atmospheric thermonuclear weapons testing and is easily identified as a layer of high ^{137}Cs activity by down-borehole gamma spectrometry (Dunphy and Dibb, 1994). The relationship between mean annual net accumulation and elevation and latitude at each core site was derived using multiple linear regression (MLR; cf. Van der Veen and others, 2001):

$$\frac{dh_A}{dt} = (1.09 \times 10^{-4})Z - (2.46 \times 10^{-6})Y + 20.6, \quad (2)$$

Table 2. The observed net accumulation rate (Mair and others, 2005; Colgan and Sharp, 2008), multiple linear regression (MLR) residuals and latitude and longitude of each shallow core site (Fig. 1)

Core site	Net accumulation rate m w.e. a^{-1}	MLR residual m w.e. a^{-1}	Latitude $^{\circ}\text{N}$	Longitude $^{\circ}\text{W}$
C1	0.24	0.00	75.34	82.14
C3	0.13	0.00	75.49	83.31
C4	0.16	0.03	75.42	82.95
C5	0.14	0.01	75.49	82.60
C6	0.20	0.01	75.20	83.33
C7	0.16	0.07	75.21	82.84
C8	0.27	−0.03	75.11	82.43
C9	0.22	0.01	75.21	81.75
CA	0.22	−0.04	75.34	83.70
CB	0.22	−0.02	75.34	83.35
CC	0.25	−0.02	75.34	82.68
CD	0.17	−0.01	75.24	82.53
CE	0.23	−0.01	75.02	82.13

where Z is the elevation (m) and Y is the Universal Transverse Mercator (UTM) northing (m) ($p < 0.01$; adjusted $r = 0.73$ for $df = 12$; Fig. 3). The standard error of the multiple linear regression (MLR) estimate is $0.02 \text{ m w.e. a}^{-1}$, with residuals of up to $|0.07| \text{ m w.e. a}^{-1}$, distributed randomly across the high-elevation region (Table 2). The inclusion of longitude as an explanatory variable did not improve the performance of the regression. Equation (2) was used to estimate the mean annual net accumulation rate in each 1 km DEM cell. An area-weighted mean of the estimated net accumulation rates in all gridcells was computed for each basin (Fig. 2).

Annual specific rate of thickness change

Several studies have used the mass imbalance approach, in which specific net accumulation and outflow rates are compared, to infer basin-scale rates of thickness change (Thomas and others, 1998, 2000, 2001). This method assumes that any surplus (deficit) of mass in a given basin will result in an increase (decrease) in the snow surface elevation or ice-cap thickness, rather than an increase (decrease) in the firnification rate. Hence:

$$\frac{dh}{dt} = \left(\frac{dh_A}{dt} \right) + \left(\frac{dh_O}{dt} \right). \quad (3)$$

Results of this calculation for the 11 drainage basins are presented in Table 3. For the four gates for which InSAR-derived across-gate velocity profiles were available (1, 6, 9 and 10), InSAR-derived specific outflows were also compared with calculated specific net accumulation rates to obtain independent estimates of rates of thickness change (Table 4).

RESULTS

Basin-scale thickness changes

There is a clear contrast between the in situ derived rates of specific outflow, net accumulation and thickness change in drainage basins south of the main east–west drainage divide (basins 7–11; hereafter southern basins) and the basins north

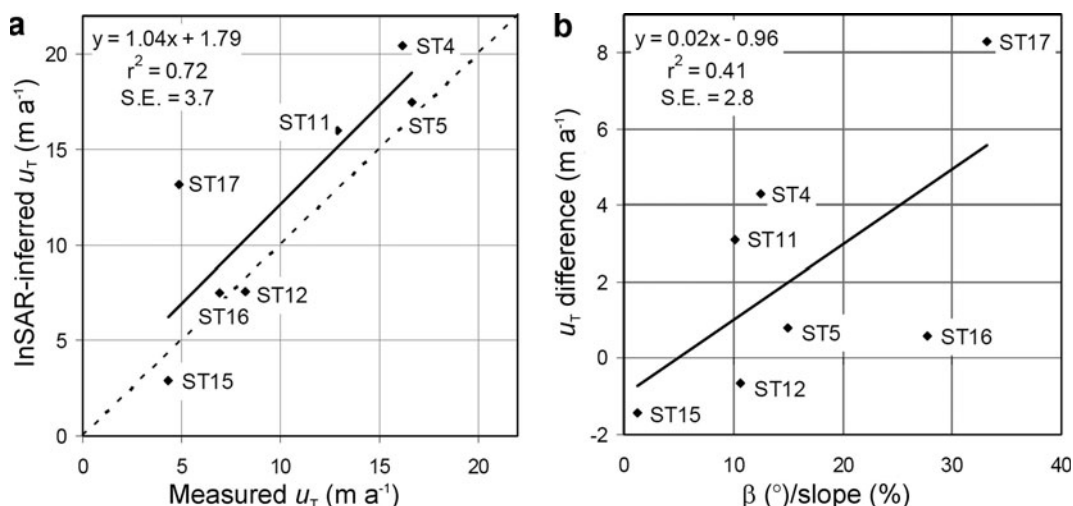


Fig. 4. (a) InSAR-derived downslope surface velocities (Burgess and others, 2005) regressed against measured stake velocities for the seven stakes for which data are available. Line $y = x$ is shown for reference (dashed). (b) The difference between InSAR-derived and measured stake velocities regressed against the ratio of the angle between the satellite-look and ice-flow directions (β) to surface slope.

of that divide (basins 1–6; hereafter northern basins). The annual specific outflow from the southern basins (area average: -0.25 ± 0.16 m w.e. a⁻¹) is significantly greater (two-tailed t test assuming equal variance, $p < 0.01$) than that from the northern basins (area average: -0.12 ± 0.13 m w.e. a⁻¹; Fig. 2). Similarly, the annual specific net accumulation rate in the southern basins (area average: 0.22 ± 0.02 m w.e. a⁻¹) is significantly ($p < 0.01$) greater than that in the northern basins (area average: 0.18 ± 0.02 m w.e. a⁻¹; Fig. 2). The variation in net accumulation rate is explained primarily by latitude rather than by elevation, leading to a strong north–south net accumulation gradient across the study region (Fig. 2). The rate of thickness change in the northern basins (area average: 0.05 ± 0.14 m w.e. a⁻¹) is significantly ($p < 0.05$) greater than that in the southern basins (area average: -0.03 ± 0.16 m w.e. a⁻¹;

Fig. 2). The area-averaged mean annual rate of thickness change for all 11 basins (0.01 m w.e. a⁻¹) differs from zero by much less than the estimated margin of uncertainty (± 0.12 m w.e. a⁻¹; Table 3).

Regression of InSAR-derived velocities against in situ stake velocities yields a slope of 1.04 ($r^2 = 0.72$, standard error of the estimate = 3.7 m a⁻¹; Fig. 4). The difference between InSAR-derived and measured-stake velocities is, however, variable. The combined effects of β and slope (taken as the quotient of β over slope) account for 41% of the variability in the differences between the measured and InSAR-derived velocities (Fig. 4). The residual variability may result from either differences in the length of the measurement periods or from true changes in surface velocity between the 1996 InSAR observations and the 2005–06 in situ velocity measurements.

There is significant variability within the across-gate InSAR-derived horizontal velocity profiles that cannot be captured by linear interpolation between the stake measurements (Fig. 5). The InSAR-derived specific outflow estimates are always of the same sign as the stake-derived estimates, but they are greater than the stake-derived estimates in basins 1 (-0.59 versus -0.17 m w.e. a⁻¹) and 10 (-0.33 versus -0.25 m w.e. a⁻¹), and less than the stake-derived estimates in basin 6 (-0.08 versus -0.16 m w.e. a⁻¹). The InSAR- and in situ-derived specific outflow estimates are not independent in basin 9, as the single InSAR dummy point used to supplement the stake data was located in this basin (Table 4).

Table 3. The in situ-derived mean annual rate of specific outflow ($dh_O/dt \pm \sigma[dh_O/dt]$), mean annual net accumulation rate ($dh_A/dt \pm \sigma[dh_A/dt]$) and mean annual rate of thickness change ($dh/dt \pm \sigma[dh/dt]$) for the 11 drainage basins, as well as the area-averaged mean for the entire high-elevation region (Fig. 2)

Drainage basin	$dh_O/dt \pm \sigma[dh_O/dt]$	$dh_A/dt \pm \sigma[dh_A/dt]$	$dh/dt \pm \sigma[dh/dt]$
	m w.e. a ⁻¹	m w.e. a ⁻¹	m w.e. a ⁻¹
1	-0.17 ± 0.07	0.18 ± 0.02	0.01 ± 0.07
2	-0.10 ± 0.08	0.15 ± 0.02	0.05 ± 0.08
3	-0.04 ± 0.02	0.17 ± 0.02	$0.13 \pm 0.03^*$
4	-0.03 ± 0.02	0.16 ± 0.02	$0.13 \pm 0.03^*$
5	-0.19 ± 0.22	0.19 ± 0.02	0.00 ± 0.22
6	-0.16 ± 0.10	0.20 ± 0.02	0.04 ± 0.11
7	-0.17 ± 0.10	0.22 ± 0.02	0.05 ± 0.10
8	-0.26 ± 0.12	0.23 ± 0.02	-0.03 ± 0.13
9	-0.31 ± 0.07	0.22 ± 0.02	$-0.09 \pm 0.07^*$
10	-0.25 ± 0.21	0.21 ± 0.02	-0.04 ± 0.21
11	-0.45 ± 0.20	0.21 ± 0.02	$-0.24 \pm 0.20^*$
Mean	-0.19 ± 0.12	0.20 ± 0.02	0.01 ± 0.12

* $|dh/dt| > \sigma[dh/dt]$.

DISCUSSION

Level of uncertainty

The calculation of uncertainty estimates for the results presented here is explained in the Appendix. Uncertainties in the horizontally and vertically averaged velocities are the main sources of uncertainty in the calculated rates of thickness change. The area-averaged rate of thickness change across all drainage basins (0.01 m w.e. a⁻¹) is much smaller than the associated uncertainty (± 0.12 m w.e. a⁻¹), so we find no significant thickness change for the high-elevation region as a whole. However, the calculated rates of thickness

Table 4. The InSAR-derived mean annual rate of specific outflow ($dh_O/dt \pm \sigma[dh_O/dt]$), and its resulting mean annual rate of thickness change ($dh/dt \pm \sigma[dh/dt]$) for the four drainage basins with good (>80%) InSAR coverage. Differences between InSAR thickness change estimates and in situ estimates are also shown

Drainage basin	$dh_O/dt \pm \sigma[dh_O/dt]$	$dh/dt \pm \sigma[dh/dt]$	InSAR vs in situ dh/dt
	m w.e. a ⁻¹	m w.e. a ⁻¹	m w.e. a ⁻¹
1	-0.59 ± 0.08	-0.41 ± 0.08	-0.42
6	-0.08 ± 0.01	0.12 ± 0.03	+0.08
9	-0.30 ± 0.04	-0.08 ± 0.04	+0.01
10	-0.33 ± 0.04	-0.12 ± 0.05	-0.08

change do exceed the associated uncertainty in four drainage basins. Two drainage basins in the northwest (3 and 4) show significant thickening, and two (9 and 11) in the south and east show significant thinning. Shepherd and others (2007) also report positive mass balance in the northwest sector of the ice cap and negative mass balance in the southeast, though their calculations relate to entire drainage basins while ours only relate to regions above 1200 m.

Comparison with laser altimetry

NASA laser-altimetry observations over the high-elevation region suggest a maximum rate of thickening between 1995 and 2000 of 0.20 m a^{-1} , while figure 3 in Abdalati and others (2004) suggests a mean thickening rate of $\sim 0.05 \text{ m a}^{-1}$. To facilitate a direct comparison between the observed and calculated rates of thickness change, the measurements derived from laser altimetry were converted from an absolute rate of thickness change (m a^{-1}) to an estimated water-equivalent thickening rate (m w.e. a^{-1}). These conversions were performed using two distinct density scenarios: (1) density close to ice (900 kg m^{-3}), which assumes that the observed thickening is the result of decreased ice outflow from the high-elevation region, as suggested by the recent decrease in the annual net accumulation rate and increase in the rate of firnification in the high-elevation regions of the ice cap (Colgan and Sharp, 2008); and (2) density of fresh snow (300 kg m^{-3}), which assumes that the observed changes are the result of a short-term increase in the accumulation rate during the measurement period (Abdalati and others, 2004). These two scenarios correspond to mean rates of thickness change within the high-elevation region of between ~ 0.015 and $\sim 0.045 \text{ m w.e. a}^{-1}$. Although these values are substantially greater than the area-averaged rate of thickness change reported in this study ($0.01 \text{ m w.e. a}^{-1}$), they do lie within our estimated range of uncertainty ($\pm 0.12 \text{ m w.e. a}^{-1}$). When making this comparison however, we recognize that it is difficult to estimate the area-averaged rate of thickness change and its associated uncertainty using data from the two laser-altimetry flight-lines.

Our results do not indicate a widespread thickening trend across the high-elevation region of the ice cap, such as was inferred from the altimetric measurements. Our best estimate of the overall area-averaged thickening rate is within error of zero, and significant thickening is found only in basins 3 and 4. The two laser-altimetry flight-lines provide only partial coverage of the ice cap (Fig. 2) and are biased towards the western portion of the high-elevation region,

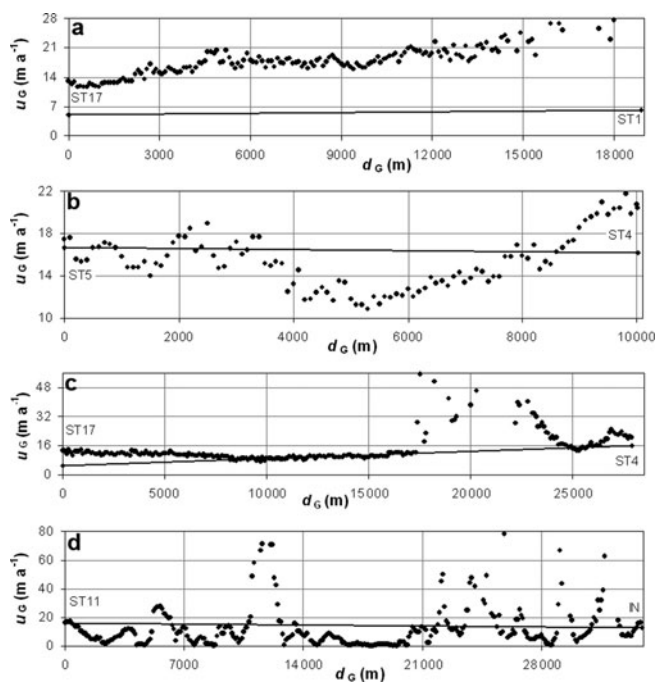


Fig. 5. InSAR-derived across-gate (d_G) surface velocity (u_G) profiles (points) are compared to the two-point stake velocity profiles (lines) across flux gates 1 (a), 9 (b), 10 (c) and 6 (d).

where we find thickening at a rate much higher than the average for the high-elevation region (0.13 ± 0.03 and $0.01 \pm 0.12 \text{ m w.e. a}^{-1}$, respectively; Table 3). The rates of thickness change observed by laser altimetry over the high-elevation parts of the ice cap range between approximately -0.15 and $+0.20 \text{ m a}^{-1}$, but the majority of observations lie between zero and 0.10 m a^{-1} . Only $\sim 10\%$ of the laser-altimetry observations from the high-elevation region suggest thinning (Abdalati and others, 2004). The altimetry coverage, however, is poor or non-existent in basins 9 and 11, where we find significant thinning. Thus, the differences between our estimated rates of thickness change and those of Abdalati and others (2004) might be due to the difference in the areas sampled in the two sets of measurements.

Ice dynamics

Over short measurement periods, laser-altimeter measurements of ice-thickness change can be strongly influenced by interannual variability in the height of the snow surface (Thomas and others, 2001). However, the laser-altimetry observations of high-elevation thickening of the northwest region of Devon Ice Cap are unlikely to reflect anomalously high net accumulation between 1995 and 2000, because both in situ surface mass-balance measurements (Koerner, 2005) and ice-core measurements suggest anomalously low net accumulation at high elevations on the ice cap during this period (Colgan and Sharp, 2008). It is also unlikely that a decrease in the rate of firnification can explain the laser-altimetry observations (Thomas and others, 2001), as the ice content of shallow firn cores recovered from the high-elevation region of Devon Ice Cap increased between 1995 and 2000, relative to the 1963–2003 mean (Colgan and Sharp, 2008). Increased ice content is more likely to be indicative of more rapid firnification.

We therefore suggest that longer-term trends in ice outflow provide the most likely explanation for the thickening

in the northwest region of the ice cap. Decreased ice outflow over time might result from the downwards diffusion of a cold wave associated with Neoglacial cooling in the Canadian High Arctic. As ice deformation is concentrated near the glacier bed, the cooling and stiffening of basal ice reduces the outflow from a basin (Reeh and Gundestrup, 1985). If the Neoglacial cooling of Devon Island began approximately 1050 years BP and peaked approximately 150 years BP (Blake, 1981), this temperature cycle would have a period of ~1800 years. The amplitude of such a cycle would reach 5% of its surface value at ~430 m depth (Paterson, 1994, p. 204–211). Peak cooling at this depth will lag peak cooling at the surface by ~860 years. The ice depth in basins 3 and 4 ranges from ~650 m near the ice divide to ~250 m at the flux gates (Dowdeswell and others, 2004). Thus, Neoglacial cooling of basal ice in these basins may have begun only in the last few centuries, and it could account for reduced outflow from these basins.

The calculated thinning in the southern drainage basins (9 and 11) has not been independently validated by laser-altimetry observations. The observed decrease in the net accumulation rate (~25% after 1989; Colgan and Sharp, 2008) and inferred increase in the firnification rate may be sufficient to explain the thinning in basin 9, but are probably not sufficient to account for the thinning in basin 11 (-0.24 ± 0.20 m w.e. a⁻¹). Increased ice outflow may therefore be a factor in the thinning of this basin, which is one of three drainage basins in the eastern region of the ice cap where threads of fast flow (and probably basal sliding) extend above the 1200 m contour (fig. 7 in Burgess and others, 2005). A possible cause of increased ice outflow is increased meltwater penetration to the glacier bed as a result of recent climate warming (e.g. Zwally and others, 2002).

Another factor that must be borne in mind when comparing the two estimates of rates of thickness change is that the estimates pertain to different time periods. We differenced a 40 year mean specific net accumulation rate with a 1 year specific outflow rate to obtain our estimate, while the laser-altimetry observations describe a 5 year mean rate of thickness change. If the specific outflow rate from any sector of the ice cap has changed systematically over the past 40 years, this has implications for the comparison. If the specific outflow has been decreasing relative to specific net accumulation rate (as postulated for northwest basins 3 and 4), then our estimate of the specific outflow will be below the 40 year average and we will have overestimated the 40 year mean rate of thickening. Equally, if specific outflow from basin 11 has been increasing over time, we will have overestimated the rate of outflow and the long-term thinning rate may be less than we have suggested.

CONCLUSIONS

The rate of thickness change of the entire high-elevation region of Devon Ice Cap appears to be within error of zero (0.01 ± 0.12 m w.e. a⁻¹). A non-uniform pattern of thickness change across the ice cap is, however, suggested by our observations. We find significant thickening in two drainage basins (basins 3 and 4), and significant thinning in another two (basins 9 and 11). Estimates of the rate of high-elevation thickening derived from laser altimetry are likely to be affected by a spatial bias towards the northwestern region of the ice cap where we find significant thickening. A possible ice-dynamic mechanism to explain the thickening in the

northwest high-elevation region of Devon Ice Cap is the downward diffusion of the Neoglacial cooling wave. This may be responsible for a recent stiffening of the basal ice in these basins, and a decrease in outflow. In contrast, meltwater-induced enhancement of already fast ice flow may account for the thinning observed in basins 9 and 11.

ACKNOWLEDGEMENTS

This work was supported by the Polar Continental Shelf Project (PCSP contribution No. 030-07), the Natural Sciences and Engineering Research Council of Canada (NSERC), the ArcticNet Network of Centres of Excellence, the Canadian Circumpolar Institute (CCI), the Northern Scientific Training Program (NSTP) and the Alberta Ingenuity Fund. We thank the Nunavut Research Institute and the communities of Resolute Bay and Grise Fjord for permission to conduct fieldwork. D. Burgess, F. Cawkwell and S. Williamson assisted with the fieldwork. J. Dowdeswell and T. Benham kindly provided ice-thickness measurements. We also thank W. Abdalati for his thorough review of the manuscript.

REFERENCES

- Abdalati, W. and 9 others. 2004. Elevation changes of ice caps in the Canadian Arctic Archipelago. *J. Geophys. Res.*, **109**(4), F04007. (10.1029/2003JF000045.)
- Blake, W., Jr. 1981. Neoglacial fluctuations of glaciers, southeastern Ellesmere Island, Canadian Arctic Archipelago. *Geogr. Ann.*, **63A**(3–4), 201–218.
- Braithwaite, R.J. and S.C.B. Raper. 2002. Glaciers and their contribution to sea level change. *Phys. Chem. Earth*, **27**(32–34), 1445–1454.
- Burgess, D.O. and M.J. Sharp. 2004. Recent changes in areal extent of the Devon Ice Cap, Nunavut, Canada. *Arct. Antarct. Alp. Res.*, **36**(2), 261–271.
- Burgess, D.O., M.J. Sharp, D.W.F. Mair, J.A. Dowdeswell and T.J. Benham. 2005. Flow dynamics and iceberg calving rates of Devon Ice Cap, Nunavut, Canada. *J. Glaciol.*, **51**(173), 219–230.
- Colgan, W. and M. Sharp. 2008. Combined oceanic and atmospheric influences on net accumulation on Devon Ice Cap, Nunavut, Canada. *J. Glaciol.*, **54**(184), 28–40.
- Dowdeswell, J.A., T.J. Benham, M.R. Gorman, D. Burgess and M. Sharp. 2004. Form and flow of the Devon Island ice cap, Canadian Arctic. *J. Geophys. Res.*, **109**(F2), F02002. (10.1029/2003JF000095.)
- Dunphy, P.P. and J.E. Dibb. 1994. ¹³⁷Cs gamma-ray detection at Summit, Greenland. *J. Glaciol.*, **40**(134), 87–92.
- Dyurgerov, M.B. and M.F. Meier. 2005. Glaciers and the changing Earth system: a 2004 snapshot. Boulder, CO, University of Colorado. Institute of Arctic and Alpine Research. (INSTAAR Occasional Paper 58.)
- Kaser, G., J.G. Cogley, M.B. Dyurgerov, M.F. Meier and A. Ohmura. 2006. Mass balance of glaciers and ice caps: consensus estimates for 1961–2004. *Geophys. Res. Lett.*, **33**(19), L19501. (10.1029/2006GL027511.)
- Koerner, R.M. 2005. Mass balance of glaciers in the Queen Elizabeth Islands, Nunavut, Canada. *Ann. Glaciol.*, **42**, 417–423.
- Le Brocq, A.M., A.J. Payne and M.J. Siegert. 2006. West Antarctic balance calculations: impact of flux-routing algorithm, smoothing algorithm and topography. *Comput. Geosci.*, **32**(10), 1780–1795.
- Mair, D., D. Burgess and M. Sharp. 2005. Thirty-seven year mass balance of Devon Ice Cap, Nunavut, Canada, determined by shallow ice coring and melt modelling. *J. Geophys. Res.*, **110**(F1), F01011. (10.1029/2003JF000099.)

- Meier, M.F. and 7 others. 2007. Glaciers dominate eustatic sea-level rise in the 21st century. *Science*, **317**(5841), 1064–1067.
- Paterson, W.S.B. 1994. *The physics of glaciers. Third edition.* Oxford, etc., Elsevier.
- Raper, S.C.B. and R.J. Braithwaite. 2006. Low sea level rise projections from mountain glaciers and icecaps under global warming. *Nature*, **439**(7074), 311–313.
- Reeh, N. and N.S. Gundestrup. 1985. Mass balance of the Greenland ice sheet at Dye 3. *J. Glaciol.*, **31**(108), 198–200.
- Reeh, N. and W.S.B. Paterson. 1988. Application of a flow model to the ice-divide region of Devon Island Ice Cap, Canada. *J. Glaciol.*, **34**(116), 55–63.
- Shepherd, A., Z. Du, T.J. Benham, J.A. Dowdeswell and E.M. Morris. 2007. Mass balance of Devon Ice Cap, Canadian Arctic. *Ann. Glaciol.*, **46**, 249–254.
- Thomas, R.H., B.M. Csathó, S. Gogineni, K.C. Jezek and K. Kuivinen. 1998. Thickening of the western part of the Greenland ice sheet. *J. Glaciol.*, **44**(148), 653–658.
- Thomas, R. and 6 others. 2000. Mass balance of the Greenland ice sheet at high elevations. *Science*, **289**(5478), 426–428.
- Thomas, R. and 7 others. 2001. Mass balance of higher-elevation parts of the Greenland ice sheet. *J. Geophys. Res.*, **106**(D24), 33,707–33,716.
- Van der Veen, C.J., D.H. Bromwich, B.M. Csatho and C. Kim. 2001. Trend surface analysis of Greenland accumulation. *J. Geophys. Res.*, **106**(D24), 33,909–33,918.
- Woo, M.K., R. Heron, P. Marsh and P. Steer. 1983. Comparison of weather station snowfall with winter snow accumulation in High Arctic basins. *Atmos–Ocean*, **21**(3), 312–325.
- Zwally, H.J., W. Abdalati, T. Herring, K. Larson, J. Saba and K. Steffen. 2002. Surface melt-induced acceleration of Greenland ice-sheet flow. *Science*, **297**(5579), 218–222.

APPENDIX ERROR ANALYSIS

Traditional error analysis was used to quantify the uncertainty associated with estimates of specific outflow, net accumulation and thickness change. The largest sources of uncertainty in computing the rate of specific outflow for a given drainage basin lie in the calculation of the horizontally and vertically averaged ice velocities. Uncertainty in the vertically averaged velocity ($\sigma_V[\bar{u}_G]$ (m a^{-1})) due to the choice of n was taken as the difference between estimates derived assuming $n = 2.5$ and 3.5 for a given flux gate. Uncertainty in the horizontally averaged velocity ($\sigma_H[u_G]$ (m a^{-1})) is a function of how well two stakes in a flux gate represent the ‘true’ horizontal surface velocity profile perpendicular to the gate. To quantify this uncertainty, across-gate InSAR velocity profiles (Burgess and others, 2005; Fig. 5) were linearly detrended and compared with the two-point velocity profiles derived from stakes. The standard error of the differences between the detrended InSAR profile and the two-point profile was taken to represent the uncertainty in the horizontally averaged velocity across each flux gate ($\sigma_H[u_G]$; Table 5). The standard errors are relatively low for gates that do not contain threads of fast-flowing ice (e.g. 1.6 m a^{-1} for gate 1), but much higher for those flux gates within which fast flow does occur (e.g. 6.6 and 13.3 m a^{-1} for flux gates 10 and 6, respectively). As variability in the surface velocity profile is likely to increase with flux gate width, uncertainties in the horizontally averaged velocities through the remaining seven flux gates were estimated using a regression ($r^2 = 0.76$) of the uncertainty in the horizontally averaged velocity against flux gate width for the four flux gates for which data were available (Table 5).

Table 5. The in situ-derived uncertainty in the horizontally averaged velocity ($\sigma_H[u_G]$), uncertainty in the vertically averaged velocity ($\sigma_V[\bar{u}_G]$) and total uncertainty in the width- and depth-averaged velocity ($\sigma[\bar{u}_G]$) for the 11 drainage basins

Drainage basin	$\sigma_H[u_G]$ m a^{-1}	$\sigma_V[\bar{u}_G]$ m a^{-1}	$\sigma[\bar{u}_G]$ m a^{-1}
1	1.6	0.21	1.6
2	2.1	0.16	2.2
3	1.1	0.18	1.1
4	0.5	0.10	0.5
5	8.4	0.25	8.4
6	13.3	0.55	13.3
7	5.5	0.37	5.6
8	6.7	0.53	6.7
9	2.5	0.64	2.6
10	6.6	0.39	6.6
11	3.7	0.39	3.7

Assuming that the errors in both the horizontally and vertically averaged velocities are independent and random, the total error in the width- and depth-averaged velocity through a given flux gate ($\sigma[\bar{u}_G]$ (m a^{-1})) can be estimated as the quadratic sum of the fractional uncertainties in the two terms (Thomas and others, 1998):

$$\sigma[\bar{u}_G] = \sqrt{(\sigma_H[u_G])^2 + (\sigma_V[\bar{u}_G])^2}. \quad (\text{A1})$$

Likewise, assuming that the errors in each term used to compute the specific outflow are independent and random, the error in the mean annual change in surface elevation due to specific outflow from a given drainage basin ($\sigma[dh_O/dt]$ (m w.e. a^{-1}); Table 3) can be estimated as (Thomas and others, 1998):

$$\sigma\left[\frac{dh_O}{dt}\right] = \left[\left(\frac{\sigma[A_B]}{A_B}\right)^2 + \left(\frac{\sigma[d_G]}{d_G}\right)^2 + \left(\frac{\sigma[\bar{u}_G]}{\bar{u}_G}\right)^2 + \left(\frac{\sigma[\bar{h}_G]}{\bar{h}_G}\right)^2 + \left(\frac{\sigma[\rho_i]}{\rho_i}\right)^2 \right]^{\frac{1}{2}} \left(\frac{dh_O}{dt}\right), \quad (\text{A2})$$

where $\sigma[A_B]$ is the uncertainty in drainage basin area, assessed as 5% of A_B through repeat flowline traces, $\sigma[d_G]$ is the GPS position measurement error at each stake, $\sigma[\bar{u}_G]$ is calculated according to Equation (A1) for a given flux gate, $\sigma[\bar{h}_G]$ is an assumed ice-thickness error of $\pm 10 \text{ m}$ (Dowdeswell and others, 2004) and $\sigma[\rho_i]$ is an assumed ice-density uncertainty of $\pm 50 \text{ kg m}^{-3}$.

Two sources of uncertainty affect the computation of the rate of surface-elevation change due to net accumulation in a given basin: (1) the uncertainty associated with the calculation of the mean annual net accumulation rate at each ice-core site, and (2) the uncertainty introduced by the use of MLR to predict the variation in net annual accumulation rates across the high-elevation region. The uncertainty in the mean annual net accumulation rate ($\sigma[a_c]$ (m w.e. a^{-1})) is assumed to be the quotient of the uncertainty in the water equivalent depth of the 1963 ^{137}Cs horizon ($\pm 0.1 \text{ m w.e.}$) over 40 years ($\pm 0.0025 \text{ m w.e. a}^{-1}$). As the differences between observed and predicted net accumulation rates at the 13 core sites appear to be randomly distributed across

the high-elevation region (Table 2), the uncertainty in the use of MLR to interpolate net accumulation rates ($\sigma[a_m]$ (m w.e. a⁻¹)) was taken as the standard error of the MLR regression estimate (0.023 m w.e. a⁻¹). The uncertainty in the mean annual change in surface elevation due to net accumulation ($\sigma[dh_A/dt]$ (m w.e. a⁻¹); Table 3) was estimated as 0.023 m w.e. a⁻¹ for all basins, according to (Thomas and others, 1998):

$$\sigma\left[\frac{dh_A}{dt}\right] = \sqrt{(\sigma[a_c])^2 + (\sigma[a_m])^2}. \quad (\text{A3})$$

Assuming that the errors in both of the terms used to arrive at the calculated rate of thickness change are independent and random, the error in the mean annual change in surface elevation in a given drainage basin ($\sigma[dh/dt]$ (m w.e. a⁻¹); Table 3) can therefore be estimated as the quadratic sum of the fractional uncertainties in the mean annual changes in surface elevation due to both specific outflow and net accumulation (Thomas and others, 1998):

$$\sigma\left[\frac{dh}{dt}\right] = \sqrt{\left(\sigma\left[\frac{dh_O}{dt}\right]\right)^2 + \left(\sigma\left[\frac{dh_A}{dt}\right]\right)^2}. \quad (\text{A4})$$

MS received 27 April 2007 and accepted in revised form 4 March 2008

Spatial and temporal variability in the snowpack of a High Arctic ice cap: implications for mass-change measurements

Christina BELL,¹ Douglas MAIR,¹ David BURGESS,² Martin SHARP,³
Michael DEMUTH,⁴ Fiona CAWKWELL,⁵ Robert BINGHAM,⁶ Jemma WADHAM⁷

¹Department of Geography and Environment, University of Aberdeen, Elphinstone Road, Aberdeen AB31 3UF, UK
E-mail: christina.bell@abdn.ac.uk

²Natural Resources Canada, Canada Centre for Remote Sensing, 588 Booth Street, Ottawa, Ontario K1A 0Y7, Canada

³Department of Earth and Atmospheric Sciences, University of Alberta, Edmonton, Alberta T6G 2E3, Canada

⁴Natural Resources Canada, National Glaciology Group, 562 Booth Street, Ottawa, Ontario K1A 0E4, Canada

⁵Department of Geography, University College Cork, Cork, Ireland

⁶British Antarctic Survey, Natural Environment Research Council, Madingley Road, Cambridge CB3 0ET, UK

⁷Bristol Glaciology Centre, School of Geographical Sciences, University Road, Bristol BS1 8SS, UK

ABSTRACT. Interpretation of ice mass elevation changes observed by satellite altimetry demands quantification of the proportion of elevation change which is attributable to variations in firn densification. Detailed stratigraphic logging of snowpack structure and density was carried out at ~1 km intervals along a 47 km transect on Devon Ice Cap, Canada, in spring (pre-melt) and autumn (during/after melt) 2004 and 2006 to characterize seasonal snowpack variability across the full range of snow facies. Simultaneous meteorological measurements were gathered. Spring (pre-melt) snowpacks show low variability over large spatial scales, with low-magnitude changes in density. The end-of-summer/autumn density profiles show high variability in both 2004 and 2006, with vastly different melt regimes generating dissimilar patterns of ice-layer formation over the two melt seasons. Dye-tracing experiments from spring to autumn 2006 reveal that vertical and horizontal distribution of meltwater flow within and below the annual snowpack is strongly affected by the pre-existing, often subtle stratigraphic interfaces in the snowpack, rather than its bulk properties. Strong interannual variability suggests that using a simple relationship between air temperature, elevation and snowpack densification to derive mass change from measurements of elevation change across High Arctic ice caps may be misguided. Melt timing and duration are important extrinsic factors governing snowpack densification and ice-layer formation in summer, rather than averaged air temperatures.

INTRODUCTION

Changes in ice-sheet thickness with time have been inferred from aircraft (Thomas and others 2003; Abdalati and others, 2004) and from satellite data (e.g. Davis and others 1998; Zwally and others, 1998, 2005). Two key issues arise when attempting to determine mass-balance change from remote-sensing platforms. Firstly, satellite radar altimeter (SRA) measurements of ice-cap elevation change are dependent on correct identification of snow surfaces, which may be ambiguous owing to strong internal reflections in the near-surface snow and firn, known as 'volume backscatter' (Ridley and Partington, 1988; Davis and Moore, 1993). Secondly, remote-sensing techniques which measure *elevation* change over large ice masses need to account for temporal and spatial changes in near-surface *density* if they are to be successfully used to estimate ice volume change (e.g. Braithwaite and others, 1994).

Changes in the shape of radar power returns from ice sheets are strongly linked to structural and/or density changes in the near-surface snowpack associated with melting (Jezek and others, 1994). If predictions of high-latitude warming (e.g. Houghton and others, 2001) are correct, it is likely that dry snow zones will shrink due to the gradually increasing elevations of the upper boundaries of all the zones between the rising equilibrium line and the dry snow zone. Quantification of spatial and temporal variability

in the near-surface stratigraphy of ice sheets is thus of interest from a mass-balance perspective, but in addition is vital to assist in identification of where and when volume backscatter may adversely affect SRA measurements of elevation change across an ice mass. Volume backscatter is a particular concern in the percolation facies, which covers in excess of one-third of the Greenland ice sheet (Nghiem and others 2005), owing to extensive melt-derived ice layers and lenses in the near-surface stratigraphy (e.g. Thomas and others, 2001; Scott and others, 2006).

Interpretation of ice mass volume change from SRA measurements requires accurate estimation of the proportion of elevation change attributable to firn densification. Near-surface firn densification has been shown to be largely controlled by the formation of ice layers and denser firn from refreezing of meltwater (Braithwaite and others, 1994; Reeh and others, 2005). It has been documented that a slight change in annual melt can have a significant impact on ice density profiles and therefore surface elevation change, even if accumulation remains constant (Braithwaite and others, 1994). Existing firn densification models adopt a simple temperature-driven positive-degree-day approach (e.g. Reeh and others, 2005; Li and others, 2007). It is therefore vital that the relationship between air temperature and firn densification (particularly near-surface ice-layer formation) is fully explored if such models are to be applied in varying spatial and temporal contexts.

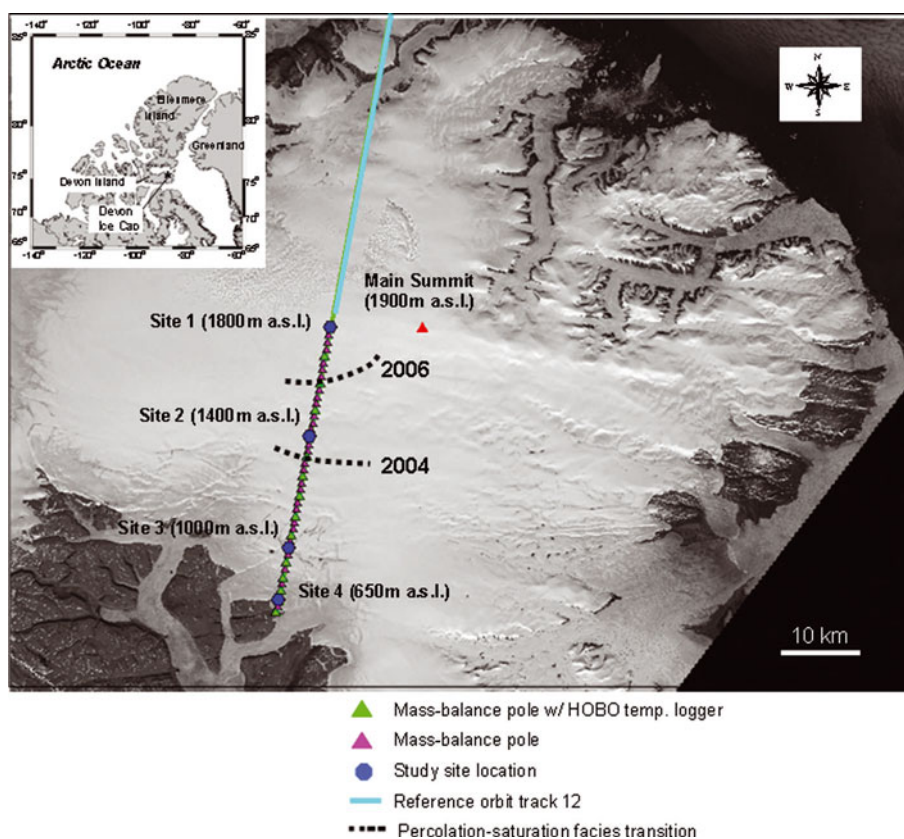


Fig. 1. Devon Ice Cap and CryoSat reference orbit track 12 transect showing nested grid sites 1–4.

Recent studies of snowpack variability tend to focus on small spatial areas (e.g. Harper and Bradford, 2003; Parry and others, 2007). There is a need to extend studies of spatial variability in snowpack density over a range of snow facies, and during more than one melt season, since annual melt timing, duration and intensity across High Arctic ice caps can vary substantially (e.g. Wang and others, 2005).

In this paper, we present data from a transect across a High Arctic ice cap which spans several snow facies, in order to:

1. Quantify seasonal densification across a range of snow facies on a High Arctic ice cap, to highlight levels of spatial variability and assess the role of air temperature as a first-order control.
2. Determine the structure and stratigraphic distribution of densification in the snowpack, which will highlight areas of the ice cap where intense volume scatter from near-surface ice layers, lenses and pipes may result in ambiguous surface returns.

FIELD SITE AND METHODS

Field site

Devon Ice Cap is situated on the eastern end of Devon Island, in the southeastern Queen Elizabeth Islands, Nunavut, Canada, where it covers an area of some 14 400 km² (Fig. 1). Previous studies on this ice cap have highlighted the importance and complexity of refreezing processes on surface mass balance (e.g. Koerner, 1970a, b, 1977, 1997) and an overall mass budget controlled mainly by changes in surface mass balance (Koerner, 2002; Mair

and others, 2005). Repeat airborne laser surveys conducted in 1995 and 2000 across the ice caps of the Canadian Arctic Archipelago (including Devon Ice Cap) revealed a common pattern of thinning in marginal areas, accompanied by little change or slight thickening of the ice masses in high-elevation areas (Abdalati and others 2004). Regional relationships between elevation and elevation change, and comparison with in situ data dating back to the 1960s from across many of the ice caps of the Queen Elizabeth Islands indicate that the mass balance between 1995 and 2000 was more negative than observed over the last two or three decades. The changes in elevation are thought to be strongly melt-driven (Abdalati and others, 2004).

The present study focuses on a ~47 km long transect (CryoSat reference orbit track 12) which spans several snow facies from near the summit at 1800 m a.s.l. to a south-southwest land-terminating margin at ~400 m a.s.l. (Fig. 1). This drainage basin is dynamically stable, with a slightly positive mass balance (Burgess and Sharp, 2004; Mair and others, 2005).

Field methods

Detailed stratigraphic logging of the physical properties of the snowpack was undertaken in spring and autumn 2004 and repeated in spring and summer/autumn 2006, in order to record snowpack variability prior to and after summer melting. An earlier second field season in 2006 coincided with a period of strong surface melting, giving an insight into summer snowpack evolution and its controlling processes.

Meteorological data

Three automatic weather stations (AWS) were set up in spring 2004 at nested grid sites 1–3 along the transect (Fig. 1).

Combined with 15 HOBOTM temperature data loggers, spaced approximately every 3 km, these measured temporal and spatial variation in air temperatures along the transect.

Snow pits

Snow pits were dug to the previous end-of-summer layer. This was identifiable in spring by a ~10 cm depth hoar immediately overlying a distinctive hard crust of coarse-grained freeze-thaw ice or firn. Late summer and autumn is when most depth hoar forms, making it a useful end-of-summer marker horizon (e.g. Steffen and others, 1999). In autumn, care was taken to ensure that these layers were relocated by careful re-examination of the snowpack. Snow-pit stratigraphy, density, grain size, grain type, hardness and temperature were logged on north-facing pit walls. Density measurements involved weighing a sample of known volume (100 cm³) from each stratigraphic layer. Harper and Bradford (2003) found that measurement errors associated with this type of density sampling were ~10%. In spring seasons, pits were dug at 1 km intervals along the full length of the transect. In autumn seasons, pits were dug as far along the length of the transect as was possible owing to snowpack removal, saturation, or time constraints of digging pits dominated by thick (>~10 cm) ice layers at lower elevations. The August 2006 field data are referred to as 'late-summer' rather than 'autumn'; a reminder that the snowpack was still wet for much of the field season. Refreezing began towards the end of the field season (31 August 2006). A few snow pits were backlit in both spring and autumn seasons, following the method of Koerner (1971), to reveal fine-resolution horizontal and vertical features in the snowpack at the 10⁻²–10⁻³ m scale, which are otherwise not obvious.

Dye-tracing experiments

Dye tracing was carried out to identify controls on meltwater routing, ice-layer formation and changes in the physical properties of the snowpack as a result of melting. A concentrated solution of Rhodamine WT liquid dye was sprayed as a thin mist onto 1 m² patches on the snowpack surface in spring 2006 at sites 1–3. Dye patches were

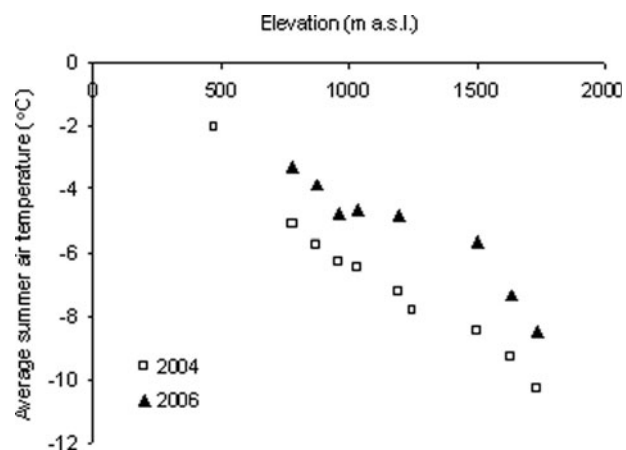


Fig. 2. Average summer air temperatures plotted against elevation, from HOBO loggers along the length of the CryoSat line in 2004 (squares) and 2006 (black triangles).

excavated in late summer 2006. The stained snow pits were photographed and logged.

RESULTS

Meteorological conditions in the measured periods of 2004 and 2006

The summer months of 2004 and 2006 exhibited very different melt conditions. Average summer temperatures were 2–3°C higher in 2006 than in 2004 (Fig. 2). Wang and others (2005) documented that Devon Ice Cap experienced low melt in summer 2004. In contrast, US National Centers for Environmental Prediction (NCEP) re-analysis data indicate that August 2006 was the warmest August in 33 years. Temperature data from the upper accumulation area of the CryoSat transect (HOBO logger at 1636 m a.s.l.) show that during 2004 there were no positive degree days at this elevation, and periods of cold summer temperatures (e.g. –12°C on Julian day (JD) 196), whilst in 2006 there were sustained periods where temperatures exceeded 0°C at the same high-elevation site (Fig. 3).

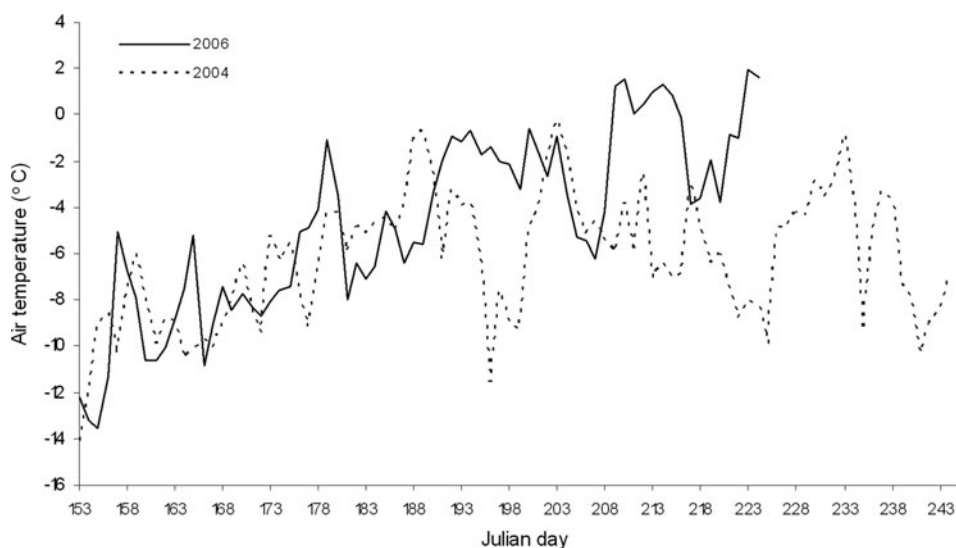


Fig. 3. Daily average air temperatures from a HOBO logger in the upper reaches of the CryoSat transect (1636 m a.s.l.) between 1 June (JD 153) and mid- to late August in 2004 and 2006. The record is truncated at 11 August (JD 224) in 2006 and 31 August in 2004.

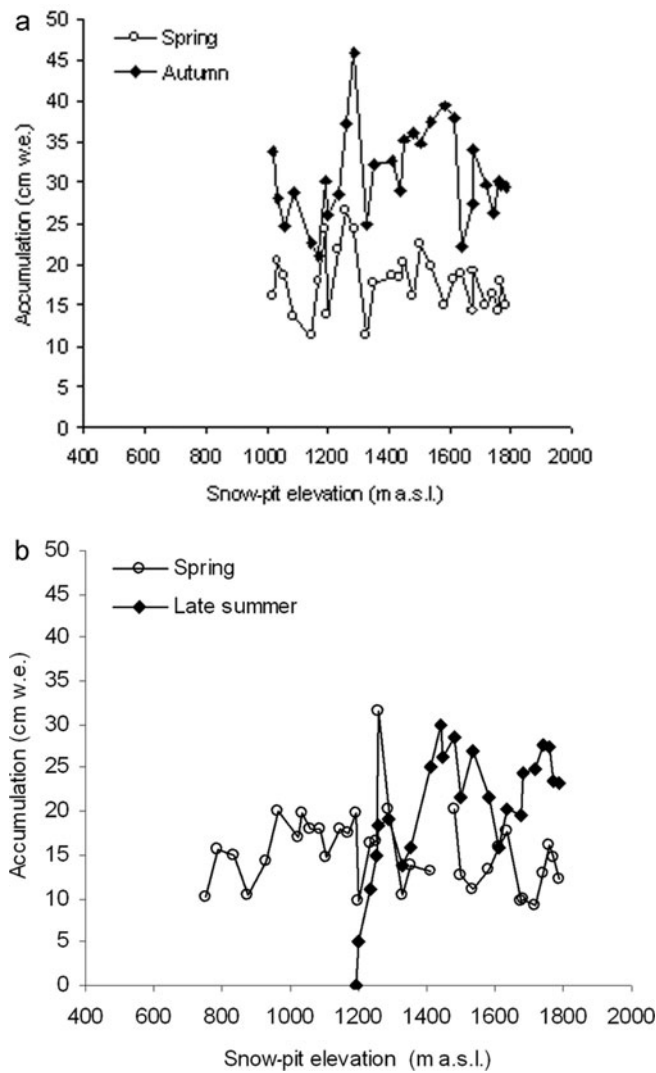


Fig. 4. Spring and autumn accumulation plotted against elevation, from snow-pit measurements along the length of the CryoSat line for (a) 2004 and (b) 2006.

Examination of Envisat advanced synthetic aperture radar (ASAR) Global Monitoring Mode (GMM) imagery for summer 2004 and 2006 shows a progression of melt across Devon Ice Cap, indicating profound differences in melt timing and geographical extent between and within these two summer seasons. Dark surface returns (indicative of surface moisture) show that in 2004 the first melt event which affected much of the ice cap, including the CryoSat transect region, occurred on 6–9 July (JD 188–191). Another widespread melt event was evident on 21 July, lasting a few days. A melt event around 20 August 2004 affected the lower CryoSat line area, but was predominantly confined to the southeast corner of the ice cap. In contrast, dark surface returns from the Envisat imagery indicate that widespread summer melt in 2006 commenced on 29 June (JD 179), over a week earlier than in 2004. This was followed by other melt events in early to mid-July. Beyond 22 July (JD 203), very dark surface returns indicate heavy and sustained melting across almost the entire ice cap until 25 August (JD 237), when melt became confined to the southeast corner of Devon Ice Cap once again.

In summary, summer 2004 was cool, characterized by short, intermittent melt events with cold periods in between.

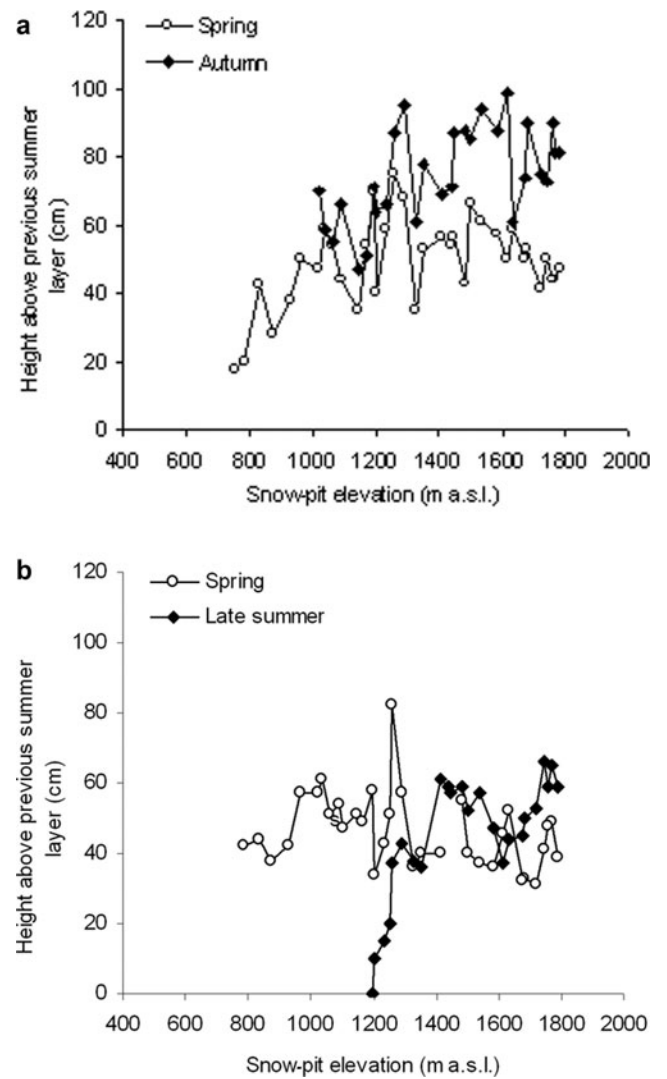


Fig. 5. Spring and autumn snowpack height above previous summer layer, plotted against surface elevation for (a) 2004 and (b) 2006, along the CryoSat transect.

Summer 2006 melting began earlier and finished later, with the most notable difference being the sustained late-summer warmth throughout late July and August.

Seasonal variability in annual snowpack depth, accumulation and bulk density

Measured *spring* snowpack accumulation (Fig. 4a and b), depth (Fig. 5a and b) and average density (Fig. 6a and b) were similar in 2004 and 2006. In both 2004 and 2006, spring snow-pit depth was variable along the length of the transect. This variability was not related to elevation. Mid-transect snow pits (km 12–34) had the highest variability in winter accumulation (Fig. 4a and b), in 2004 ranging from 26.4 cm w.e. at 1259 m a.s.l. to 11.2 cm w.e. at 1328 m a.s.l., and in 2006 ranging from 31.6 cm w.e. at 1290 m a.s.l. to 9.57 cm w.e. at 1236 m a.s.l. The average bulk density of the annual snowpack along the transect in spring 2004 and 2006 was $\sim 300\text{--}350\text{ kg m}^{-3}$ (Fig. 6a and b).

By *autumn* 2004, snow depth and accumulation had increased at all sites. The summer increase in accumulation was lower at lower elevations. The *late-summer* accumulation pattern in 2006 (Fig. 4b) was very different to that in 2004 (Fig. 4a). Above 1290 m a.s.l. (km 22.6) the snowpack

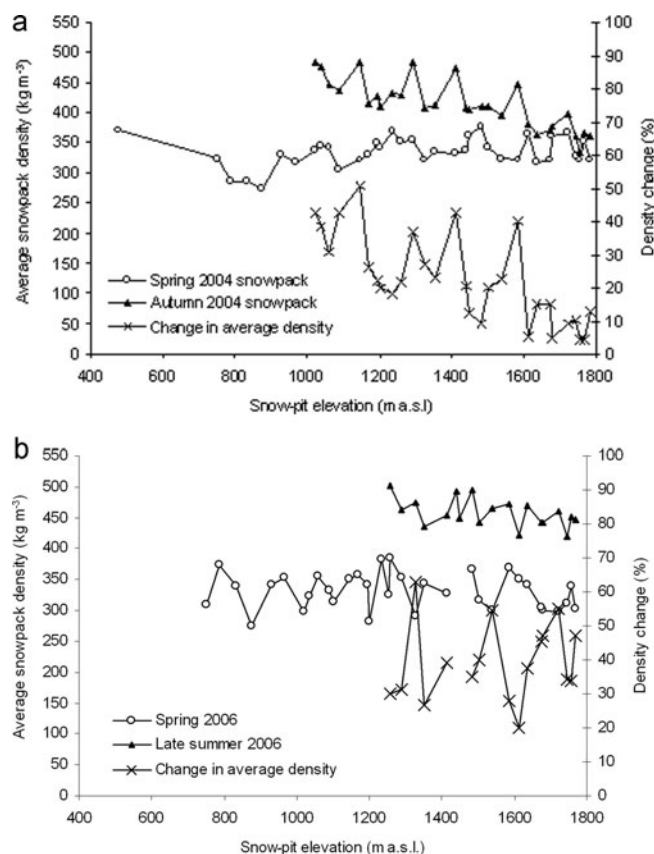


Fig. 6. Average bulk density of snowpack in (a) spring and autumn 2004 and (b) spring and late summer 2006, and associated percentage density change over summer along the length of the CryoSat line.

gained mass during the summer. Below this, there was a rapid drop in accumulation. Between 1259 and 1201 m a.s.l. (km 23.6 and km 26.8), the snowpack was saturated from the bottom up, with water observed to gradually seep upwards at the bottom of the snow pit, indicating that the subsurface water table lay below the 2006 annual snowpack. Where a topographic gradient allowed, this zone of saturation reached the surface as either a supraglacial stream or lake (Fig. 7). At 1194 m a.s.l. (km 27.9) the snowpack was completely removed and replaced by a supraglacial lake.

In 2004, average bulk densities of the annual snowpack generally increased as elevation decreased (Fig. 6a) and temperature increased (Fig. 8). In 2006 the pattern was different, with average densities generally decreasing as elevation decreased (Fig. 6b) and temperature increased (Fig. 8).

Seasonal variations in stratigraphic depth–density structure of the snowpack

The *spring* snowpack density profiles show little variability across upper and mid- to lower elevations (Figs 9 and 10). A low-density hoar layer was traced the full length of the transect in both years. In 2004 (Fig. 9), ice layers formed immediately above the hoar, after a short-lived autumn melt event which followed heavy snowfall (29 August 2003) identified from QuikSCAT data (personal communication from L. Wang, 2005). The melt event was detected across the entire ice cap.

Autumn/late-summer snowpack density structures were more variable than in spring in both 2004 and 2006. In

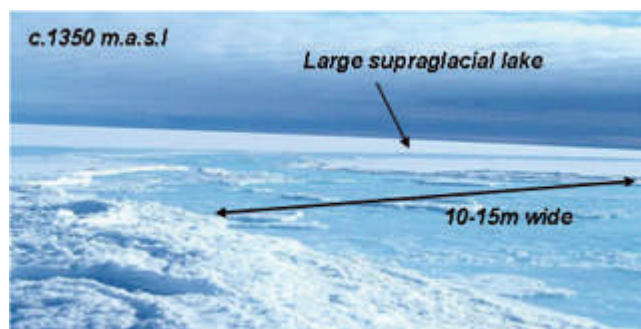


Fig. 7. Surface runoff (fed by a perched runoff horizon) near km 23.6 in mid-August 2006.

2004, ice layers formed at all sites, ranging from three or four fairly thin (0.2–2 cm thick) layers near the snow surface at higher elevations, to thicker (up to 13 cm at 1021 m a.s.l.) and generally more numerous ice layers throughout the snowpack at mid- to lower elevations (maximum of 14 at 1259 m a.s.l. (~km 23.6); Fig. 9). Only at 1259 m a.s.l. and below did ice-layer formation and significant densification occur at the very bottom of the annual snowpack (Fig. 9).

In 2006, late-summer snow pits were logged only as low as 1290 m a.s.l. (km 22.6) owing to saturated conditions in mid-reaches of the transect. Unlike 2004, the most complex snowpack stratigraphies were observed near the summit of the ice cap (1768–1676 m a.s.l.; Fig. 10). At 1502 m a.s.l. (km 13.7) the hoar layer had increased in density (from 230 kg m^{-3} to 380 kg m^{-3}), and at 1290 m a.s.l. (km 22.6) the snowpack had become very uniform in density, with little ice (Fig. 10).

Thus, in 2004, increased snowpack densification with decreasing elevation was dominated by ice-layer formation (Fig. 11), whereas in 2006 ice-layer contribution to annual accumulation decreased with decreasing elevation.

The depth distribution of ice layers in the annual snowpack in both summers showed no clear relationship with

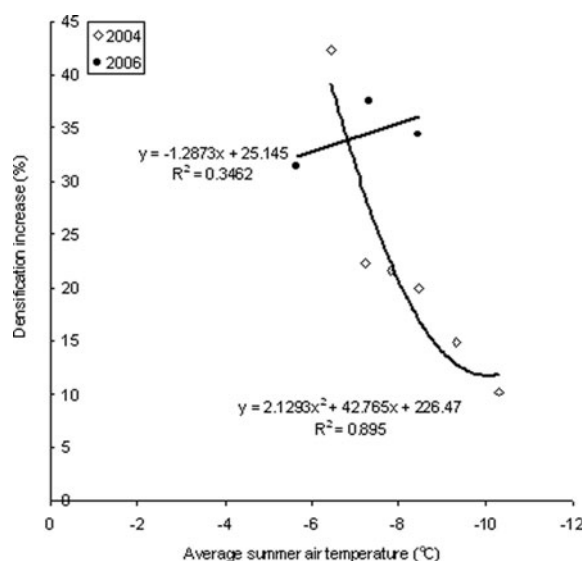


Fig. 8. Relationship between percentage increase in density and average summer air temperature in 2004 and 2006 from snow pits dug within 1 m of a HOBO logger along transect. Snowpack removal and saturation at lower elevations (higher average temperatures) limits the amount of data available in 2006.

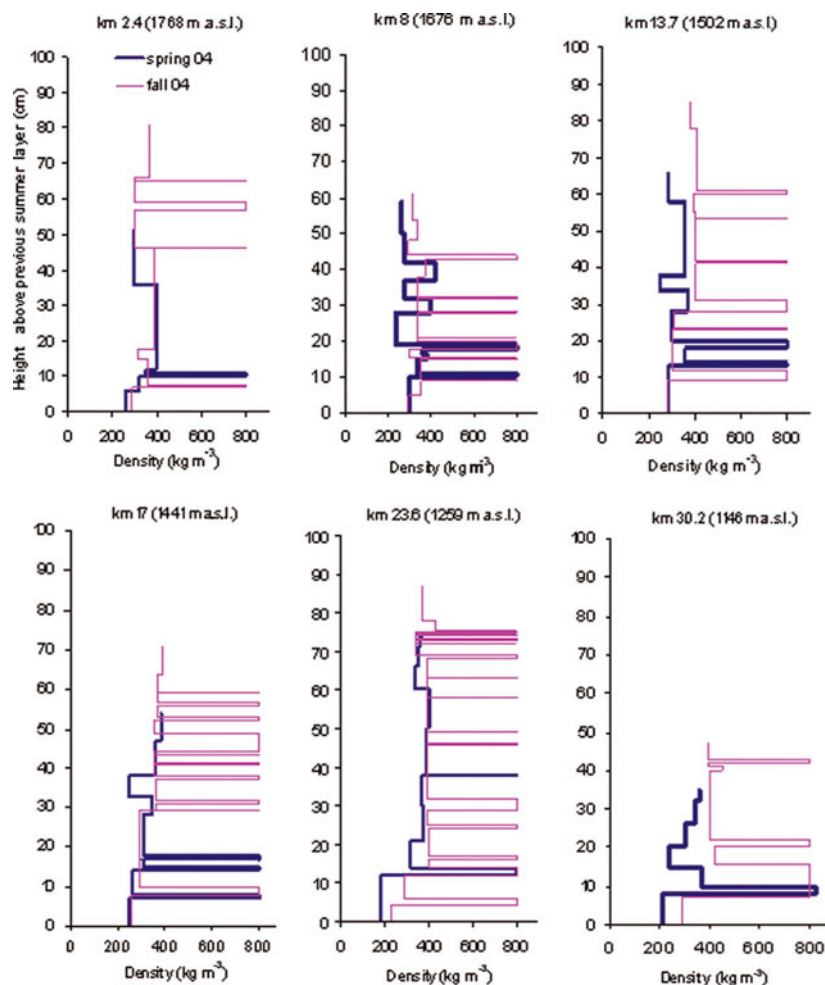


Fig. 9. Kilometre-scale density variability in the annual snowpack from selected snow pits along the CryoSat line in 2004.

elevation. However, in 2004 at the highest elevations, (1768 and 1676 m.a.s.l.) there was little ice in the lower 40% of the snowpack (Fig. 12a). In 2006, ice layers were spread across the full depth of the snowpack in the highest snow pit, but on moving down the transect they became more concentrated in the upper 60% (Fig. 12b).

Dye tracing

The results of the summer 2006 dye-tracing experiments are summarized in Table 1. At site 1, meltwater reached 44 cm depth and revealed structural controls on ice-layer formation (Fig. 13). At site 2, dye penetrated to 150 cm depth, where meltwater refroze as a thick ice accumulation between 150 and 178 cm (Fig. 14). Several ice layers above appeared stratigraphically intact, but stained snow indicates that meltwater passed through/by them.

CONTROLS ON SNOWPACK VARIABILITY

Controls on the observed spatial variability can be subdivided into intrinsic controls (existing features in the snowpack which may affect densification during summer melting) and extrinsic controls (e.g. prevailing meteorological conditions, altitude, surface topography).

Intrinsic controls

The depth–density structure of the spring snowpack plays a role in the subsequent meltwater routing and refreezing

during summer and autumn. Two features of the spring snowpack are discussed in more detail: (1) the depth-hoar layer and (2) crusts.

Depth-hoar control on meltwater penetration and ice-layer formation

The boundary between the depth-hoar layer and the overlying material is characterized by a sharp change in density and grain size (fine-to-coarse transition). Such a transition at the base of the snowpack plays an important role in delaying or preventing meltwater from percolating beyond the depth of the annual snowpack during low melt flux conditions, such as in the short-lived events of 2004. Several previous studies have highlighted the importance of fine-to-coarse transitions in controlling meltwater movement through snowpacks (Wankiewicz, 1979; Marsh and Woo, 1984; Jordan, 1995; Pfeffer and Humphrey, 1996, 1998; Gustafsson and others, 2004; Waldner and others, 2004). Percolating meltwater infiltrates the fine-grained winter snowpack until it reaches the coarse-grained depth-hoar layer, where the contrasting capillary forces between the fine-grained (high-capillarity) snow and the coarse-grained depth hoar (low capillarity) beneath result in downward flow impedance. A zone of saturation then forms, as meltwater is effectively left ‘hanging’ on the bottom of the overlying finer layer where it may refreeze to form an ice layer (evident in Fig. 13). This explains why there is no summer densification at the bottom of the annual snowpack

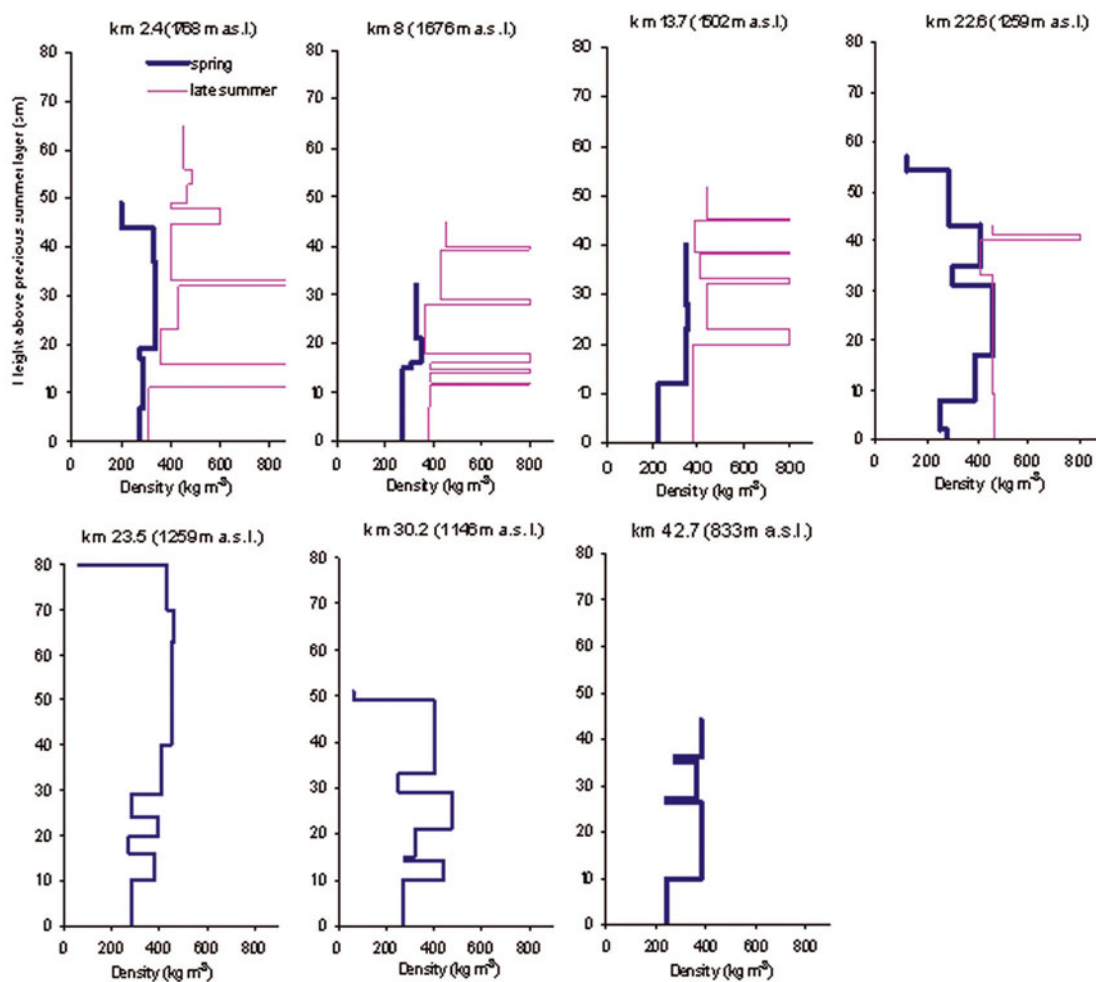


Fig. 10. Kilometre-scale density variability in the annual snowpack from selected snow pits along the CryoSat line in 2006.

in 2004 above ~ 1300 m a.s.l. (Fig. 9). The depth hoar prevents further percolation.

Where the depth-hoar layer is breached by percolating meltwater, flow occurs initially as finger flow, rapidly creating a series of pipes (e.g. Fig. 15). When meltwater is introduced to faceted dry snow, metamorphism occurs rapidly and the depth-hoar grains become rounded (Colbeck, 1989). Where large amounts of meltwater are present, more grains become rounded, growing in size at the expense of smaller grains. A rapid increase in grain size and grain rounding facilitates higher permeabilities (Colbeck, 1983) until the depth-hoar layer no longer prevents meltwater percolating into previous years' firm. Capillary retention may then be replaced by gravity-driven matrix flow. The heavy late-July and August 2006 melt conditions overwhelmed capillary forces associated with the depth hoar, which explains why densification (although not necessarily ice-layer formation) was extensive at the bottom of the snowpack below ~ 1700 m a.s.l. (Fig. 10).

Crust control on meltwater penetration and ice-layer formation

A common feature of spring snowpack stratigraphy along the CryoSat transect was the presence of 1–2 mm thick crust layers, particularly in the upper fine-grained layers of the snowpack. It is unclear whether these crusts are a product of wind, radiation, former rime layers (fog deposits) or some combination. Das and Alley (2005) report similar features

from stratigraphic studies of an Antarctic snowpack. Qualitative observations from our backlit snow pits (in both spring and autumn seasons) and dye-tracing experiments highlight the role of such crusts in forming discontinuous ice lenses in summer and autumn. On inspection with a hand lens, crusts are very fine-grained, frequently sloping and in places are cross-stratified (Fig. 16). Where percolating meltwater encounters a crust in the snowpack, preferential flow occurs laterally along its length; the water is retained within the crust by strong capillary forces (Das and Alley, 2005). It may then refreeze to form an ice layer (evident in Figs 13 and 16). The more crusts there are in the near surface, the more meltwater can be absorbed by them and prevented or delayed from further percolation. The newly formed ice layers may then again form a barrier to percolating meltwater where they are laterally continuous. This is a further example of the importance of capillary forces under conditions of low saturation on ice-layer formation, and in delaying the percolation of meltwater to further depths.

Extrinsic controls

The major extrinsic control on snowpack densification is usually assumed to be surface air temperature (e.g. Reeh and others, 2005). The seasonal increase in snowpack density in 2004 is strongly related to both higher average air temperature (Fig. 8) and lower elevation (Fig. 6a). Furthermore, the high-magnitude density contrasts that characterize the snowpack in autumn 2004 suggest that melt was sporadic,

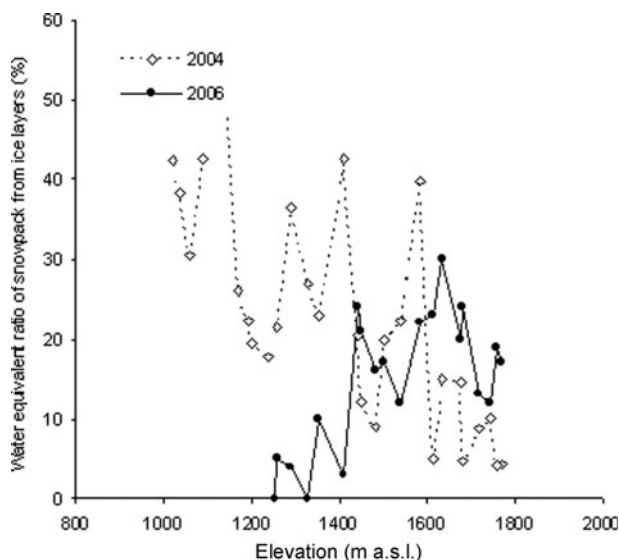


Fig. 11. Percentage of the total water equivalent of the annual snowpack from ice layers in autumn (a) 2004 and (b) 2006.

with preferential flow dominating water routing, under generally non-saturated conditions; a result of the synoptic-scale climatology at our continental site. During the spring and early summer, due to its high altitude, the accumulation area of Devon Ice Cap is rarely exposed to sustained periods of warm conditions resulting in high surface meltwater fluxes over many days (Fig. 3). Instead, frequent cool periods with little or no melt are only briefly interrupted by short-lived warm spells, reducing levels of saturation (and therefore effective permeability) in the snowpack, which favours a preferential flow regime. Thus spatial patterns of ice-layer formation across the ice cap in a *cool* summer with only short bursts of melt activity appear to be predictable.

The late-summer snowpack in 2006 was transformed by relatively high air temperatures, causing sustained melting, with temperatures at high elevations averaging above 0°C for several days at a time in late July and throughout August (Fig. 3). The amount of ice in the annual snowpack *decreases* with lower elevation (Fig. 6b) and warmer temperatures

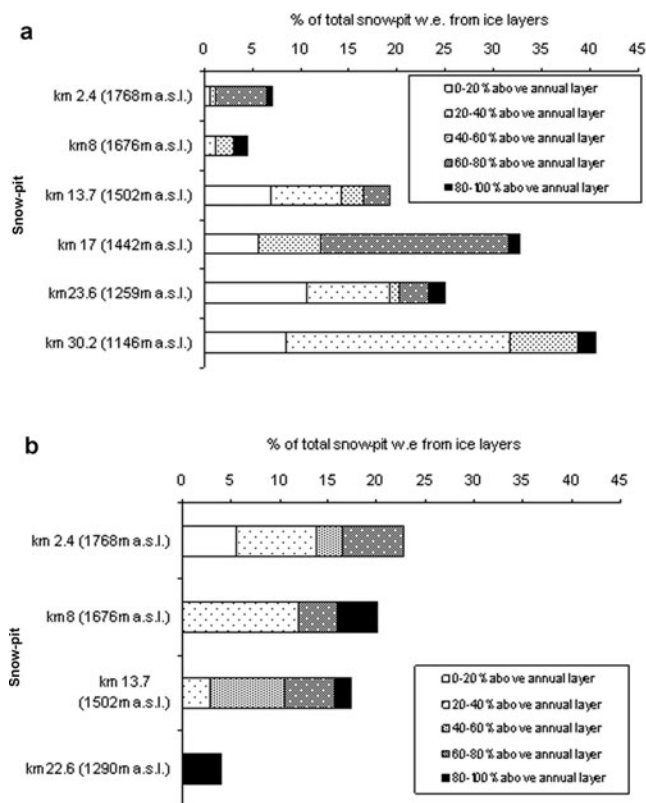


Fig. 12. Depth distribution of ice layers in the annual snowpack at a range of elevations in (a) 2004 and (b) 2006.

(Fig. 8). A similar pattern of ice-layer formation was observed along a 40 km transect in the percolation facies of the Greenland ice sheet, where internal ice layers were found to be ‘a more common element of the higher colder sites, where infiltration of summer melt is more limited than at lower warmer sites’ (Pfeffer and Humphrey, 1998, p. 85). This pattern is a result of the sustained surface melting which occurred in a ripened snowpack in late July and August, instigating a switch from the early-melt-season preferential flow regime to slower, more uniform matrix percolation later

Table 1. Summary of results of dye-tracing experiments

Dye site	Elevation m a.s.l.	Date of application (2006)	Date of retrieval (2006)	Maximum depth penetration of meltwater, from August snow surface cm	Further observations
Site 1	1800	15 May	7 August	44	No meltwater penetration beyond hoar layer. Preferential flow regime evident from piping (Fig. 13)
Site 2	1400	23 April	16 August. No dye visible in snowpack at all	N/A	N/A
Site 2	1400	16 August	26 August	150 (Fig. 14)	Annual snowpack well drained and homogeneous. Dyed meltwater had percolated through several ice lenses
Site 3	1000	19 April	No dye retrieved due to complete snowpack removal	N/A	Bare superimposed ice dissected by meltwater channels

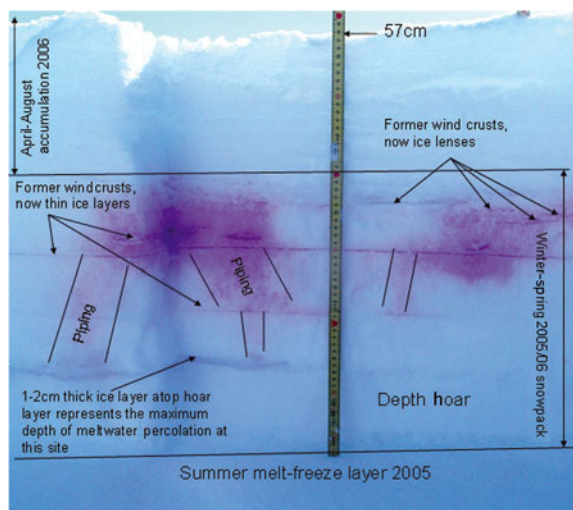


Fig. 13. Annotated stratigraphy from dye-tracing experiments at site 1. Dyed snow shows the pathways of summer 2006 melting through the annual snowpack.

in the melt season. Ice layers which formed early in the 2006 melt season would have initially delayed further percolation, causing saturated conditions immediately above them until broken through. When breakthrough occurred, meltwater would flow rapidly to greater depths in an initially preferential flow regime, where it would refreeze at depth. As this process continued, the snowpack became warmer at depth as the meltwater refroze. Eventually the early-summer formed near-surface ice layers became permeable and matrix flow ensued to depth. The late-summer 2006 melting did not generally therefore create any new ice layers in the near-surface snowpack (except at the highest elevations), instead creating a very homogeneous near-surface snowpack, and a thick ice accumulation at depth (Fig. 14).

There is a common assumption in snow stratigraphy studies that the number of ice layers in any one balance year's accumulation above the firn line is a direct association of the amount of melting during the summer months. Koerner (1970a) addressed this issue, suggesting that in fact the relationship between the two is far from straightforward, mostly owing to the variability in melt timing and the associated thermal properties of the snowpack at melt onset. Koerner (1970a) illustrates this in an example of 1962 summer melting on Devon Ice Cap, when early melting in June of that year produced several pipes and ice layers throughout the depth range of the annual snowpack (0.3–1.2 m), whereas matrix percolation was only observed to reach a few centimetres depth. Further melt in July and August 1962 soaked the annual snowpack but did not lead

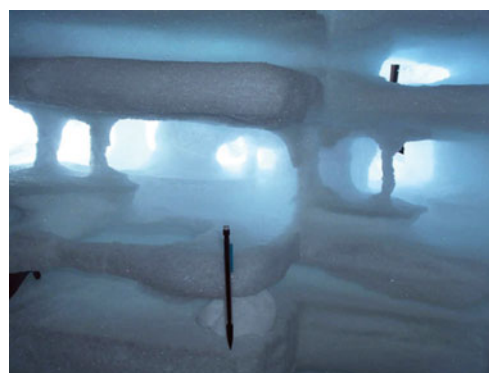


Fig. 15. Backlit snow pit at site 1 in spring 2006. The captured image shows the 2005 firn layer. Excavation of depth-hoar layer revealed extensive piping. This indicates that in 2005 meltwater reached the bottom of the annual snowpack (thus site 1 was verging on saturation in 2005).

to the formation of any further ice layers. It seems that a very similar pattern of melt generation, percolation and ice-layer formation is evident in 2006. Melt timing and duration is therefore a very important extrinsic control on ice-layer formation and furthers the notion that snowpack ice-layer formation cannot be simply related to average air temperature alone.

IMPLICATIONS FOR MASS-BALANCE MONITORING AND MODELLING

Results presented here show that simplistic assumptions relating average air temperature to large-scale patterns of densification and ice-layer formation may represent a significant source of uncertainty when modelling melting and refreezing across Arctic snowpacks. Furthermore, accumulation of mass at depths beyond the annual snowpack due to internal accumulation should be given greater consideration in efforts at modelling High Arctic glacier mass balance. Internal accumulation is widely documented (e.g. Ahlmann, 1948; Benson, 1962; Trabant and Mayo, 1985; Schneider and Jansson, 2004), but it is difficult to quantify its contribution to mass balance since it cannot be measured using traditional techniques (i.e. stake height measurements and snow pits). The consequences of melt percolation and refreezing persist over time since ice layers that develop at depth reduce permeability and therefore affect water movement in future years (e.g. Trabant and Mayo, 1985; Pfeffer and others, 1991).

Where mass was apparently 'lost' from the annual snowpack in several snow pits in 2006 (e.g. at and below 1290 m a.s.l. (~km 22.6), as Fig. 4b shows) or simply where

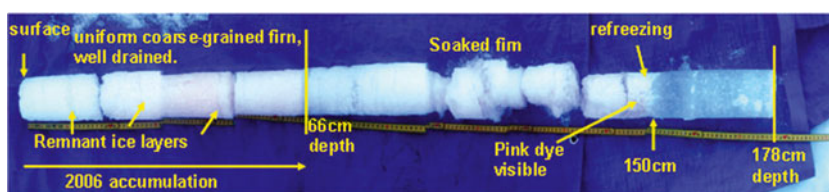


Fig. 14. Ice core extracted from S2 dye-tracer experiment in late August 2006. The annual snowpack (66 cm depth) is fairly homogeneous, with the exception of three relic ice lenses which have allowed meltwater to pass through them into the previous year's firn. A zone of saturation is evident above a large ice accumulation at 150 cm depth. Pink dye is visible up to the depth of this ice layer.

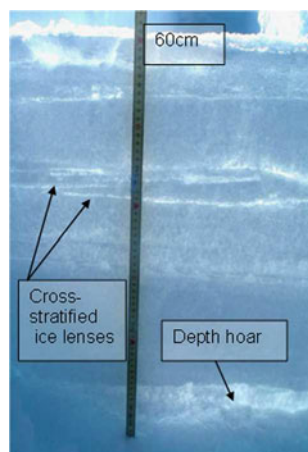


Fig. 16. Backlit snow pit showing cross-stratified ice lenses at site 1 (1800 m a.s.l.) in early August 2006. Cross-stratification of ice lenses makes them highly discontinuous.

very little change in snowpack accumulation was observed between the spring and the end of summer (e.g. 1636, 1613, 1353 and 1328 m a.s.l.), the dye-tracing results from site 2 indicate that melt is unlikely to have left the ice cap, but instead percolated into previous years' firn to refreeze as internal accumulation. The late-summer 2006 snowpack remained relatively intact where this occurred (Fig. 14), but became homogenous and highly permeable owing to grain rounding and isothermal temperatures. The snowpack facilitated rapid meltwater percolation to depth, where, upon reaching a cold, impermeable layer, it refroze. Density was thus more extensive in the layers *beneath* the annual snowpack than within it, which has implications for firn densification models which assume all the percolating meltwater generated at the surface refreezes in the annual snowpack (e.g. Reeh and others, 2005). Such an assumption is likely to underestimate densification and surface lowering in summers where sustained matrix percolation soaks firn beneath the annual layer. Therefore, such models should be limited to areas of very low melt activity, where percolation beyond the annual layer is rare, and where perched runoff does not occur. Under a warming climate, saturated conditions could potentially become more widespread, necessitating use of a model which accounts for densification and ice-layer formation at depths beyond those of an annual snowpack.

Internal accumulation also delays or prevents runoff initiation (Trabant and Mayo, 1985). The key interface for melt retention and meltwater runoff is known as the 'runoff limit' (Kasser, 1959). Pfeffer and others (1991) investigated the potential for a perched runoff surface to shift the runoff limit to a very high elevation and suggested that 'a workable assumption, is to equate the runoff limit with the percolation-wetted zone boundary'. It can be inferred from the results of dye tracing at site 2, and the observed subsurface runoff immediately downslope of this site, that the thick impermeable ice layer which formed at depth is closely related to runoff generation (Fig. 7). The firn immediately above the ice layer was saturated (Fig. 14), and where the capillary forces could no longer retain the liquid water it follows that runoff would occur along the impermeable ice layer. Runoff was not observed to occur until near km 23.7 (1259 m a.s.l.). The boundary between the percolation and saturation facies on

Devon Ice Cap in 2006 (where 'saturation facies' is considered to be where meltwater has wetted the entire depth range of the annual snowpack and densification has occurred at the bottom of the snow pit) was at around km 8 (1676 m a.s.l.). Thus whilst the run-off limit assumption of Pfeffer and others (1991) would result in a considerable overestimation of the runoff limit elevation, stratigraphic observations of the firn core at site 2 (Fig. 14) support the concept of formation of perched runoff horizons. The existence of perched, impermeable flow paths will vary from year to year, requiring a runoff model to consider the past history of melt and accumulation from several years.

Runoff in a saturation zone of a large ice mass where a deep, cold firn pack exists may be entirely dependent on the development of an ice layer formed by refreezing at depth, which is thick enough to remain impermeable, but above which snowpack temperatures are isothermal at 0°C. Ice-layer permeability is therefore an issue which could be more thoroughly addressed in modelling meltwater percolation.

IMPLICATIONS FOR SRA-DERIVED MASS-BALANCE ESTIMATES FROM ELEVATION CHANGE

As previously stated, the interpretation of ice mass change from SRA measurements requires accurate estimation of the proportion of elevation change attributable to firn densification. Our interpretation of results from the Devon Ice Cap clearly demonstrates that a simple derivation of mass change from elevation change based upon a modelled relationship between snowpack densification and air temperature is not applicable. This is because the relationship between mass change and temperature varies depending on accumulation patterns and the intensity of melting (Braithwaite and others, 1994), both of which have been shown to exhibit high inter-annual variability.

A further complication for SRA mass-change interpretation concerns uncertainty about the destination of meltwater contained in supraglacial lakes (Fig. 7). It may appear, from pronounced surface lowering, that mass has been lost (e.g. in 2006 beyond km 22.6), when it may have been redistributed via short-lived perched runoff horizons and refrozen at lower elevations. Thus, again, surface lowering cannot be easily equated to mass loss, since processes of *lateral* redistribution may be significant.

Ice-layer formation in the 2004 snowpack (Fig. 9) produced greater stratigraphic variability in the near surface than in 2006 (Fig. 10). Radar measurements of surface elevation are obfuscated by increased volume backscatter from the near surface where ice layers are abundant (Scott and others, 2006). Ground radar measurements, calibrated by snowpack density sampling from the percolation zone on the Greenland ice sheet, showed that the strongest return from the radar is not necessarily from the surface, but often an ice layer some tens of centimetres below the surface (Scott and others, 2006). In the cooler summer of 2004, ice layers were abundant near the surface of Devon Ice Cap across the entire accumulation zone, potentially increasing volume backscatter and 'dragging down' surface returns (Scott and others, 2006). In 2006, there were generally fewer ice lenses in the annual snowpack from which to generate high levels of volume backscatter, and these were restricted to the highest elevations.

Thus, to summarize, for intermittent melt of a cold snowpack the relationship between average air temperature

and average snowpack densification is stronger, and near-surface ice-layer formation is extensive. Thus, the uncertainty in determining snowpack densification is smaller; however, the uncertainty in identifying the ice cap surface is higher due to potentially high volume backscatter across the accumulation zone. For sustained melting of a warmed snowpack, the relationship between average air temperatures and average snowpack densification is weaker, and ice-layer formation may occur at greater depth, leaving the annual snowpack relatively ice-free. Thus, the uncertainty in determining snowpack densification is greater, but the uncertainty in accurate surface identification may be reduced.

Although our results and interpretation highlight important controls on patterns of near-surface ice-layer formation over large spatial scales and help identify associated potential areas of high volume backscatter, satellite-radar-generated estimates of surface elevation change will remain ambiguous, in the absence of more sophisticated snowpack modelling and further extensive field validation efforts (Parry and others, 2007). Furthermore, following the launch of CryoSat 2, scope for direct intercomparison between in situ and remote observations will provide a means of refining and validating densification modelling.

CONCLUSIONS

Seasonal densification across the varying High Arctic ice-cap snow facies has been quantified over two different years by examining snowpack density properties in spring (pre-melt) and autumn (post-melt). Spring (pre-melt) snowpack profiles in both 2004 and 2006 show low variability over large spatial scales, with low-magnitude changes in density characterizing the stratigraphy. The end-of-summer/autumn density profiles indicate high variability in both 2004 and 2006, although vastly different synoptic conditions generated dissimilar patterns of melting and associated ice-layer formation over the two summers. The relatively cool summer of 2004 generated an annual snowpack characterized by sporadic melt features creating discontinuous ice layers, high-magnitude inter-stratigraphic density contrasts in the near-surface snowpack and very high spatial variability owing to increasing dominance of ice layers towards lower elevations.

In contrast, the sustained warm late-summer meteorological conditions of 2006 produced a very different near-surface snowpack. Strong melting conditions meant a lesser role for intrinsic controls on snowpack variability as saturated conditions ensued. As melting progressed, density structure was lost, creating a more homogeneous annual snowpack, with ice-layer contribution to annual accumulation falling with decreasing elevation and warmer temperatures. Such a reduction in the amount of ice retained in the annual snowpack is shown to be the result of percolation and refreezing at depths below the annual layer. During early-summer melt events and/or short melt events which follow cold periods, the vertical and horizontal routing of meltwater flow within and below the annual snowpack is shown to be strongly affected by the pre-existing, often subtle stratigraphic interfaces in the snowpack, rather than its bulk properties. This is largely a result of capillary action in conditions of low saturation.

In summers where melt occurs early in the summer when the snowpack is cold, or in sporadic bursts with cold periods

dominating in between (2004 on Devon Ice Cap), the high fraction of ice retained in the annual snowpack as multiple ice layers and lenses is likely to create high volume-backscatter returns from satellite radar altimeter measurements, potentially hindering identification of the true surface of the ice mass. This is particularly the case in mid-reaches of the transect where ice-layer formation is shown to be extensive. During summers with spatially extensive and prolonged melting (especially near the end of the melt season when the snowpack is warm, such as in 2006), homogenization of near-surface density could reduce this source of uncertainty in identifying the ice-cap surface. Such interannual variability suggests that using a simple relationship between air temperature, elevation and snowpack densification to derive mass change from measurements of elevation change across High Arctic ice caps may be misguided.

Modelling efforts should take into account the findings in this and other work which identify the importance of densification *below* the annual snowpack, and the complexity of controls on snowpack refreezing, particularly with respect to using temperature simply as a control on the amount of ice formed in the snowpack. The relationship between air temperature and snowpack densification is not straightforward and not transferable from one year to the next.

ACKNOWLEDGEMENTS

This paper is a contribution to the validation of the European Space Agency CryoSat mission. C.B., D.M. and R.B. were funded by the UK Natural Environment Research Council through grant NER/O/S/2003/00620. M.S. was supported by the Natural Sciences and Engineering Research Council, Canada, and the Meteorological Service of Canada (CRYSYS programme), and D.B. was supported by grants from the Canadian Circumpolar Institute and the Northern Scientific Training Program (Department of Indian and Northern Affairs Canada). M.D. was funded by a grant from the Canadian Space Agency GRIP Program. We thank J. Box and R. Koerner for valuable comments which greatly improved the manuscript. In situ data collection was supported by the Polar Continental Shelf Project (an agency of Natural Resources Canada). We also thank the Nunavut Research Institute and the communities of Resolute Bay and Grise Fjord for permission to conduct fieldwork on Devon Ice Cap. We acknowledge field assistance from S. Williamson, A. Gardner, L. Colgan, J. Davis, B. Danielson, J. Sekerka, L. Gray and J. Zheng.

REFERENCES

- Abdalati, W. and 9 others. 2004. Elevation changes of ice caps in the Canadian Arctic Archipelago. *J. Geophys. Res.*, **109**(F4), F04007. (10.1029/2003JF000045.)
- Ahlmann, H.W. 1948. *Glaciological research on the North Atlantic coasts*. London, Royal Geographical Society.
- Benson, C. S. 1962. Stratigraphic studies in the snow and firn of the Greenland ice sheet. *SIPRE Res. Rep.* 70.
- Braithwaite, R.J., M. Latenser and W.T. Pfeffer. 1994. Variations of near-surface firn density in the lower accumulation area of the Greenland ice sheet, Pâkitsoq, West Greenland. *J. Glaciol.*, **40**(136), 477–485.

- Burgess, D.O. and M.J. Sharp. 2004. Recent changes in areal extent of the Devon ice cap, Nunavut, Canada. *Arct. Antarct. Alp. Res.*, **36**(2), 261–271.
- Colbeck, S.C. 1983. Theory of metamorphism of dry snow. *J. Geophys. Res.*, **88**(C9), 5475–5482.
- Colbeck, S.C. 1989. Snow-crystal growth with varying surface temperatures and radiation penetration. *J. Glaciol.*, **35**(119), 23–29.
- Das, S.B. and R.B. Alley. 2005. Characterization and formation of melt layers in polar snow: observations and experiments from West Antarctica. *J. Glaciol.*, **51**(173), 307–313.
- Davis, C.H. and R.K. Moore. 1993. A combined surface- and volume-scattering model for ice-sheet radar altimetry. *J. Glaciol.*, **39**(133), 675–686.
- Davis, C.H., C.A. Kluever and B.J. Haines. 1998. Elevation change of the southern Greenland ice sheet. *Science*, **279**(5359), 2086–2088.
- Gustafsson, D., P.A. Waldner and M. Stähli. 2004. Factors governing the formation and persistence of layers in a subalpine snowpack. *Hydrol. Process.*, **18**(7), 1165–1183.
- Harper, J.T. and J.H. Bradford. 2003. Snow stratigraphy over a uniform depositional surface: spatial variability and measurement tools. *Cold Reg. Sci. Technol.*, **37**(3), 289–298.
- Houghton, J.T. and 7 others, eds. 2001. *Climate change 2001: the scientific basis. Contribution of Working Group I to the Third Assessment Report of the Intergovernmental Panel on Climate Change*. Cambridge, etc., Cambridge University Press.
- Jezek, K.C., P. Gogineni and M. Shanableh. 1994. Radar measurements of melt zones on the Greenland ice sheet. *Geophys. Res. Lett.*, **21**(1), 33–36.
- Jordan, R. 1995. Effects of capillary discontinuities on water flow and water retention in layered snowcovers. In Agrawal, K.C., ed. *International Symposium on Snow and Related Manifestations, 26–28 September 1994, Manali, India. Proceedings*. Manali, Snow and Avalanche Study Establishment, 157–170.
- Kasser, P. 1959. Der Einfluss von Gletscherrückgang und Gletschervorstoß auf den Wasserhaushalt. *Wasser- und Energiewirtschaft.*, **51**(6), 155–168.
- Koerner, R.M. 1970a. The mass balance of the Devon Island ice cap, Northwest Territories, Canada, 1961–66. *J. Glaciol.*, **9**(57), 325–336.
- Koerner, R.M. 1970b. Some observations on superimposition of ice on the Devon Island ice cap, N.W.T. Canada. *Geogr. Ann.*, **52A**(1), 57–67.
- Koerner, R.M. 1971. A stratigraphic method of determining the snow accumulation rate at Plateau Station, Antarctica, and application to South Pole–Queen Maud Land Traverse 2, 1965–1966. In Crary, A.P., ed. *Antarctic snow and ice studies II*. Washington, DC, American Geophysical Union, 225–238. (Antarctic Research Series 16.)
- Koerner, R.M. 1977. Devon Island ice cap: core stratigraphy and paleoclimate. *Science*, **196**(4285), 15–18.
- Koerner, R.M. 1997. Some comments on climatic reconstructions from ice cores drilled in areas of high melt. *J. Glaciol.*, **43**(143), 90–97.
- Koerner, R.M. 2002. Glaciers of the High Arctic islands. In Williams, R.S., Jr and J.G. Ferrigno, eds. *Satellite image atlas of glaciers of the world*. US Geol. Surv. Prof. Pap. 1386-J, J111–J146.
- Li, J., H.J. Zwally and J.C. Comiso. 2007. Ice-sheet elevation changes caused by variations of the firn compaction rate induced by satellite-observed temperature variations (1982–2003). *Ann. Glaciol.*, **46**, 8–13.
- Mair, D., D. Burgess and M. Sharp. 2005. Thirty-seven year mass balance of Devon Ice Cap, Nunavut, Canada, determined by shallow ice coring and melt modelling. *J. Geophys. Res.*, **110**(F1), F01011. (10.1029/2003JF000099.)
- Marsh, P. and M.K. Woo. 1984. Wetting front advance and freezing of meltwater within a snow cover. 1. Observations in the Canadian Arctic. *Water Resour. Res.*, **20**(12), 1853–1864.
- Nghiem, S.V., K. Steffen, G. Neumann and R. Huff. 2005. Mapping of ice layer extent and snow accumulation in the percolation zone of the Greenland ice sheet. *J. Geophys. Res.*, **110**(F2), F02017. (10.1029/2004JF000234.)
- Parry, V. and 6 others. 2007. Investigations of meltwater refreezing and density variations in the snowpack and firn within the percolation zone of the Greenland ice sheet. *Ann. Glaciol.*, **46**, 61–68.
- Pfeffer, W.T. and N.F. Humphrey. 1996. Determination of timing and location of water movement and ice-layer formation by temperature measurements in sub-freezing snow. *J. Glaciol.*, **42**(141), 292–304.
- Pfeffer, W.T. and N.F. Humphrey. 1998. Formation of ice layers by infiltration and refreezing of meltwater. *Ann. Glaciol.*, **26**, 83–91.
- Pfeffer, W.T., M.F. Meier and T.H. Illangasekare. 1991. Retention of Greenland runoff by refreezing: implications for projected future sea level change. *J. Geophys. Res.*, **96**(C12), 22,117–22,124.
- Reeh, N., D.A. Fisher, R.M. Koerner and H.B. Clausen. 2005. An empirical firn-densification model comprising ice lenses. *Ann. Glaciol.*, **42**, 101–106.
- Ridley, J. and K. Partington. 1988. A model of satellite radar altimeter return from ice sheets. *Int. J. Remote Sensing*, **9**(4), 601–624.
- Schneider, T. and P. Jansson. 2004. Internal accumulation in firn and its significance for the mass balance of Storglaciären, Sweden. *J. Glaciol.*, **50**(168), 25–34.
- Scott, J., D. Mair, P. Nienow, V. Parry and E. Morris. 2006. A ground-based radar backscatter investigation in the percolation zone of the Greenland Ice Sheet. *Remote Sens. Environ.*, **104**(4), 361–373.
- Steffen, K., W. Abdalati and I. Sherjal. 1999. Faceted crystal formation in the northeast Greenland low-accumulation region. *J. Glaciol.*, **45**(149), 63–68.
- Thomas, R. and 7 others. 2001. Mass balance of higher-elevation parts of the Greenland ice sheet. *J. Geophys. Res.*, **106**(D24), 33,707–33,716.
- Thomas, R.H., W. Abdalati, E. Frederick, W.B. Krabill, S. Manizade and K. Steffen. 2003. Investigation of surface melting and dynamic thinning on Jakobshavn Isbræ, Greenland. *J. Glaciol.*, **49**(165), 231–239.
- Trabant, D.C. and L.R. Mayo. 1985. Estimation and effects of internal accumulation on five glaciers in Alaska. *Ann. Glaciol.*, **6**, 113–117.
- Waldner, P., M. Schneebeli, U. Schultze-Zimmermann and H. Flühler. 2004. Effect of snow structure on water flow and solute transport. *Hydrol. Process.*, **18**(7), 1271–1290.
- Wang, L., M.J. Sharp, B. Rivard, S. Marshall and D. Burgess. 2005. Melt season duration on Canadian Arctic ice caps, 2000–2004. *Geophys. Res. Lett.*, **32**(19), L19502. (10.1029/2005GL023962.)
- Wankiewicz, A. 1979. A review of water movement in snow. In Colbeck, S.C. and M. Ray, eds. *Modeling of Snow Cover Runoff, 26–28 September 1978, Hanover, New Hampshire. Proceedings*. Hanover, NH, US Army Corps of Engineers. Cold Regions Research and Engineering Laboratory, 222–252.
- Zwally, H.J., A.C. Brenner and J.P. DiMarzio. 1998. Technical comment. Growth of the southern Greenland Ice Sheet. *Science*, **281**(5381), 1251.
- Zwally, H.J. and 7 others. 2005. Mass changes of the Greenland and Antarctic ice sheets and shelves and contributions to sea-level rise: 1992–2002. *J. Glaciol.*, **51**(175), 509–527.